

A framework for the derivation of dynamic process models for sieving

vorgelegt von
M.Sc.
Frederik Elskamp
geb. in Gelsenkirchen

von der Fakultät III - Prozesswissenschaften
der Technischen Universität Berlin
zur Erlangung des akademischen Grades

Doktor der Ingenieurwissenschaften
- Dr.-Ing. -

genehmigte Dissertation

Promotionsausschuss:

Vorsitzender: Prof. Dr.-Ing. Matthias Kraume
Gutachter: Prof. Dr.-Ing. Harald Kruggel-Emden
Gutachter: Prof. Dr. rer. nat. Alfred P. Weber

Tag der wissenschaftlichen Aussprache: 07.12.2018

Berlin 2018

Vorwort

Die vorliegende Arbeit entstand im Rahmen meiner Tätigkeit als wissenschaftlicher Mitarbeiter am Lehrstuhl für Energieanlagen und Energieprozesstechnik (LEAT) der Ruhr-Universität Bochum und dem Fachgebiet für Mechanische Verfahrenstechnik und Aufbereitung (MVTA) der Technischen Universität Berlin. Für die Bereitstellung der finanziellen Mittel im Rahmen des Schwerpunktprogramms SPP 1679 „Dynamische Simulation vernetzter Feststoffprozesse“ unter den Förderzeichen KR3446/7-1, KR3446/7-2 und KR3446/7-3, möchte ich der Deutschen Forschungsgemeinschaft (DFG) danken.

An dieser Stelle möchte ich ebenfalls all denjenigen meinen Dank aussprechen, die mich bei der Ausarbeitung und Fertigstellung dieser Arbeit unterstützt haben. Ein besonderer Dank gilt Herrn Prof. Dr.-Ing. Harald Kruggel-Emden dafür, dass er mich zunächst in seiner Arbeitsgruppe und später an seinem Lehrstuhl aufgenommen und bei der Anfertigung der vorliegenden Dissertation konstruktiv unterstützt hat. Darüber hinaus danke ich ihm für die Übernahme des Hauptreferats.

Ebenso möchte ich Herrn Prof. Dr. rer. nat. Alfred P. Weber für die freundliche Übernahme des Koreferats und das entgegengebrachte Interesse an meiner Arbeit danken.

Ich danke ebenfalls allen Mitarbeitern des LEAT und MVTA für die schöne gemeinsame Zeit. Es war mir eine Freude an diesen Lehrstühlen arbeiten zu dürfen und ich werde diesen Lebensabschnitt immer in guter Erinnerung behalten. Insbesondere danke ich meinen ehemaligen und aktuellen Bürokollegen Peter Fischer, Frederik Bambauer, Bogdan Kravets, Tobias Oschmann und Stephan Gerber. Zudem gilt mein Dank allen technischen und studentischen Mitarbeitern, welche mich in meiner Zeit als wissenschaftlicher Mitarbeiter umfangreich unterstützt haben.

Am meisten möchte ich jedoch meiner Familie und Freunden danken, auf deren Unterstützung ich immer zählen konnte. Ein besonderer Dank an dieser Stelle gilt natürlich meinen Eltern Gisela und Peter, meinem Bruder Björn sowie meiner Freundin Julia.

Kurzfassung

Für ein breites Anwendungsgebiet in der mechanischen Verfahrens- und Aufbereitungstechnik ist das Sieben als technisch einfacher, aber noch nicht ausreichend verstandener Verfahrensschritt gut geeignet, um Schüttgüter nach ihren Korngrößen zu trennen. Häufig liegen Partikel dabei in breiten Größenverteilungen, stark nicht-sphärischer Gestalt und unter feuchten Bedingungen vor, was die Gestaltung und Durchführung von Siebprozessen erschwert. Die Komplexität und Signifikanz dieses Prozesses erhöht sich, wenn das Sieben als Teil vernetzter Feststoffprozesse erfolgt, bei denen definierte, enge Partikelgrößenverteilungen für nachfolgende Prozessschritte benötigt werden. Daher ist es unumgänglich, die Teilprozesse des Siebens (Stratifikation, Partikeldurchtritt und Partikeltransport) und deren Wechselwirkung zu verstehen. Darüber hinaus sind flexible, einfache und prädiktive Werkzeuge für eine quantitative Darstellung des Siebens vor dem Hintergrund einer transienten Beschreibung in industriellen Anwendungen von Bedeutung.

Für die Auslegung und Optimierung von Siebprozessen stehen detaillierte partikelbasierte Simulationsansätze wie die Diskrete-Elemente-Methode (DEM) sowie verschiedene recheneffiziente phänomenologische Prozessmodelle zur Verfügung. Üblicherweise werden die material-, betriebs- und apparatespezifischen Parameter der Prozessmodelle empirisch durch Experimente bestimmt, wohingegen in dieser Arbeit die Parameter für dynamische Siebmodelle direkt aus experimentell validierten DEM-Simulationen gewonnen werden.

Im Rahmen dieser Arbeit werden diskontinuierliche und kontinuierliche Siebungen sowie deren Teilprozesse im Labormaßstab und in wirklichkeitsnahen polydispersen Systemen untersucht. Dabei werden verschiedene Siebgeometrien, -eigenschaften und -anregungen betrachtet, wobei Modellkörper und reale Partikelformen unter dem Einfluss verschiedener Flüssigkeitsmengen herangezogen werden. Neben der instationären Natur der Chargensiebung werden induziert veränderte Betriebsbedingungen von Siebprozessen betrachtet, um deren dynamisches Verhalten zu untersuchen. Für die zuverlässige Durchführung von DEM-Siebsimulationen ist die genaue Bestimmung von Partikeleigenschaften wie Größe, Form, Material- und Kontaktparametern essentiell, was im Vorfeld der Simulationen dieser Dissertation durch einen selbstentwickelten, universell einsetzbaren und unkomplizierten Kalibrierungsansatz erfolgt.

Darüber hinaus werden existierende phänomenologische Prozessmodelle unterschiedlicher Komplexität auf der Grundlage der Durchtrittsrates oder der Rückstandsmasse, die durch DEM-Simulationen stationär betriebener diskontinuierlicher und kontinuierlicher Trockensiebungen erhalten werden, beurteilt. Zusätzlich werden geeignete Prozessmodelle zur Darstellung von Siebprozessen unter veränderten Betriebsbedingungen und unter Feuchteinfluss erweitert. Eine zusätzliche Neuerung besteht in der Vorhersagbarkeit von Siebergebnissen für

verschiedene Betriebsparameter und Flüssigkeitsmengen nach einer material- und apparatespezifischen Parameteranpassung. Die hergeleiteten Prozessmodelle können schlussendlich als Prototypen in dynamischen Prozesssimulationsumgebungen zusammen mit anderen mechanischen Prozessen wie Mahlung, Agglomeration oder Sichtung eingesetzt werden.

Abstract

For a wide field of applications in mechanical process engineering and materials preparation technology, screening as technical simple but still not satisfactorily understood process step is well suited to separate bulk materials according to their particle sizes. Frequently, particles prevail in broad size distributions, highly non-spherical shape and under moist conditions, complicating the handling of screening processes. The complexity and significance of this process even increase when screening is operated within combined solids processes, in which defined narrow particle size distributions are needed for subsequent process steps. Therefore, it is inevitable to understand the subprocesses of screening (stratification, particle passage and particle transport) and their interaction. Furthermore, flexible, simple and predictive tools for a quantitative representation of screening on the background of a transient description are significant in industrial applications.

For the design and improvement of screening processes, detailed particle-based simulation approaches like the discrete element method (DEM) as well as various computational efficient phenomenological process models are available. Usually, the material-, operating-, and apparatus-specific parameters of process models are empirically determined by experiments, whereas, in this work, the parameters for dynamic screening models are directly obtained from DEM simulations, which are validated against experimental investigations.

Within this work, discontinuous and continuous screening as well as its subprocesses in laboratory scale and realistic polydisperse systems are investigated. Therein, different screen geometries and characteristics are considered along with various mechanical excitations applying model and real particle shapes under the influence of various liquid amounts. Besides the inherent transient nature of batch sieving, screening processes under induced altered operational conditions are considered to study their dynamic behavior. In order to perform reliable DEM screening simulations, the exact determination of particle properties like size, shape, material and contact parameters is essential, which is performed in advance of the simulations in this thesis by a self-developed general straightforward calibration procedure.

Furthermore, existing phenomenological process models of differing complexity are benchmarked based on the passage rate or residual mass obtained by DEM simulations of stationary operated discontinuous and continuous dry screening processes. Additionally, suitable process models are extended to represent screening processes under altered operational conditions and under the influence of moisture. A further extension is accomplished in order to predict screening results for different operational parameters and liquid amounts, after a material- and apparatus-specific parameter adjustment. As a result, derived process models can be applied as prototypes in dynamic process simulation frameworks together with other solids processes like grinding, agglomeration or air classifying.

List of publications

Articles in peer reviewed journals and conference contributions that are part of this thesis (articles are all included in “4. Results and publications” as accepted manuscripts)

- [I] Kruggel-Emden H., Elskamp F., 2014, Modeling of Screening Processes with the Discrete Element Method Involving Non-Spherical Particles, *Chemical Engineering & Technology* 37 (5), 847–856, <https://doi.org/10.1002/ceat.201300649>.
- [II] Elskamp F., Kruggel-Emden H., 2015, Review and benchmarking of process models for batch screening based on discrete element simulations, *Advanced Powder Technology* 26 (3), 679-697, <https://doi.org/10.1016/j.appt.2014.11.001>.
- [III] Elskamp F., Kruggel-Emden H., Hennig M., Teipel U., 2015, Benchmarking of process models for continuous screening based on discrete element simulations, *Minerals Engineering* 83, 78-96, <https://doi.org/10.1016/j.mineng.2015.08.011>.
- [IV] Kruggel-Emden H., Elskamp F., 2015, Numerical Investigation of a Continuous Screening Process by the Discrete Element Method, *AIP Conference Proceedings* 1648, 400004, <https://doi.org/10.1063/1.4912624>.
- [V] Elskamp F., Kruggel-Emden H., Hennig M., Teipel U., 2015, Numerical Investigation of Banana Screens Involving Non-Spherical Particles by the Discrete Element Method, *The 8th International Conference for Conveying and Handling of Particulate Solids*, Tel-Aviv, Israel.
- [VI] Elskamp F., Kruggel-Emden H., Hennig M., Teipel U., 2016, Discrete element investigation of process models for batch screening under altered operational conditions, *Powder Technology* 301, 78-95, <https://doi.org/10.1016/j.powtec.2016.05.039>.
- [VII] Elskamp F., Kruggel-Emden H., Hennig M., Teipel U., 2017, A strategy to determine DEM parameters for spherical and non-spherical particles, *Granular Matter* 19:46, <https://doi.org/10.1007/s10035-017-0710-0>.
- [VIII] Spötter C., Elskamp F., Hennig M., Teipel U., Weber A.P., Kruggel-Emden H., 2016, DEM-Simulation der Trennkurven in Siebung und Gegenstromsichtung bei geringen Gutbeladungen, *Chemie Ingenieur Technik* 89 (12), 1726–1738, <https://doi.org/10.1002/cite.201600156>.
- [IX] Elskamp F., Kruggel-Emden H., 2018, DEM simulations of screening processes under the influence of moisture, *Chemical Engineering Research and Design* 136, 593-609, <https://doi.org/10.1016/j.cherd.2018.06.022>.
- [X] Elskamp F., Kruggel-Emden H., 2019, Extension of process models to predict batch screening results under the influence of moisture based on DEM simulations, *Powder Technology* 342, 698-713, <https://doi.org/10.1016/j.powtec.2018.10.039>.

Conference contributions (Article, presentation & poster) that are not part of this thesis

- {1} Kruggel-Emden H., Elskamp F., 2013, Modeling Real Granular Screening Processes of Non-Spherical Particles, Proceedings of the 13th European Symposium on Comminution & Classification ESCC, Brunswick, Germany.
- {2} Hennig M., Elskamp F., Kruggel-Emden H., Teipel U., 2014, Dynamisch-physikalische Modellierung von Siebklassierprozessen, Chemie Ingenieur Technik 86 (9), 1566.
- {3} Elskamp F., Kruggel-Emden H., Komossa H., Scherer V., Hennig M., Teipel U., 2014, A comparative study of phenomenological screening process models based on discrete element simulations, 7th World Congress on Particle Technology, Beijing, China.
- {4} Elskamp F., Kruggel-Emden H., 2015, Entwicklung eines dynamisch-physikalischen Modellrahmens für den Prozessschritt Sieben, Jahrestreffen der Fachgruppe Zerkleinern & Klassieren, Magdeburg, Germany.
- {5} Hennig M., Elskamp F., Spötter C., Kruggel-Emden H., Weber A.P., Teipel U., 2015, Screening Processes at Stationary Conditions, 10th European Congress of Chemical Engineering, Nice, France.
- {6} Elskamp F., Kruggel-Emden H., Hennig M., Teipel U., 2016, Applicability of phenomenological screening models in representing dynamic processes during DEM screening simulations, International Congress on Particle Technology 2016, Nuremberg, Germany.
- {7} Hennig M., Elskamp F., Teipel U., Kruggel-Emden H., 2016, Experimentelle Siebklassierung und deren Abbildung in der DEM, Chemie Ingenieur Technik 88 (9), 1363.
- {8} Markauskas, D., Elskamp F., Kruggel-Emden H., 2017, Investigation of procedures required for modeling of wet sieving using the coupled DEM-SPH method, Particles 2017, Hanover, Germany.
- {9} Elskamp F., Kruggel-Emden H., 2017, DEM simulations of screening processes under the influence of moisture, 10th World Congress of Chemical Engineering, Barcelona, Spain.

Invited Talks (not part of this thesis)

- {1} Elskamp F., Kruggel-Emden H., 2016, Neue numerische Verfahren zur Beschreibung von Siebprozessen, Seminar: Sieben und Siebmaschinen, Haus der Technik, Essen, Germany.
- {2} Elskamp F., Kruggel-Emden H., 2017, Neue numerische Verfahren zur Beschreibung von Siebprozessen, Seminar: Sieben und Siebmaschinen, Haus der Technik, Essen, Germany.

Table of contents

| | |
|---|----|
| Table of contents..... | I |
| 1. Introduction..... | 1 |
| 2. Objectives and document structure | 4 |
| 2.1 Objectives..... | 4 |
| 2.2 Document structure..... | 6 |
| 3. Theoretical foundation and state of research | 7 |
| 3.1 Particle systems and single particles..... | 7 |
| 3.1.1 Disperse systems | 7 |
| 3.1.2 Single particle characterization | 8 |
| 3.1.3 Particle size distribution | 10 |
| 3.2 Separation operations and screening classification..... | 10 |
| 3.2.1 Classification processes | 11 |
| 3.2.2 Basics of sieving and screening..... | 12 |
| 3.2.3 Passage probability and screenability | 14 |
| 3.2.4 Classification machines | 16 |
| 3.3 Discrete element method | 22 |
| 3.3.1 Particle geometries in the DEM | 23 |
| 3.3.2 Equations of motion..... | 24 |
| 3.3.3 Contact detection..... | 25 |
| 3.3.4 Contact forces | 26 |
| 3.3.5 Liquid bridge forces | 29 |
| 3.4 Determination of DEM parameters..... | 31 |
| 3.5 DEM screening validations and investigations | 38 |
| 3.6 Process models | 42 |
| 3.6.1 Flowsheet simulations of solids processes | 42 |
| 3.6.2 Phenomenological process models for screening | 44 |
| 4. Results and publications..... | 47 |

| | |
|---|-----|
| I. Modeling of screening processes with the discrete element method involving non-spherical particles..... | 47 |
| II. Review and benchmarking of process models for batch screening based on discrete element simulations..... | 62 |
| III. Benchmarking of process models for continuous screening based on discrete element simulations..... | 97 |
| IV. Numerical investigation of a continuous screening process by the discrete element method..... | 131 |
| V. Numerical investigation of banana screens involving non-spherical particles by the discrete element method..... | 136 |
| VI. Discrete element investigation of process models for batch screening under altered operational conditions..... | 147 |
| VII. A strategy to determine DEM parameters for spherical and non-spherical particles..... | 184 |
| VIII. Trennkurven in Siebung und Gegenstromsichtung bei geringen Gutbeladungen..... | 202 |
| IX. DEM simulations of screening processes under the influence of moisture..... | 223 |
| X. Extension of process models to predict batch screening results under the influence of moisture based on DEM simulations..... | 257 |
| 5. Conclusions and perspective..... | 289 |
| 5.1 Conclusion..... | 289 |
| 5.2 Perspective..... | 294 |
| References..... | 296 |

1. Introduction

In mechanical process engineering, materials preparation and energy technology, it is often required to classify disperse solid systems according to their particle sizes and shapes or to separate out strongly under- or oversized material from the desired product [1]. In typical processes, particles are often of highly non-spherical shape and of broad size distribution [2,3]. However, in combined solids processes in industrial applications, defined narrow particle size distributions may be necessary for subsequent process steps. In addition, it should be taken into account, that the separation itself often already features dynamic subprocesses or is exposed to dynamic influences (load changes, changes in the feed material, addition and behavior of fluid or mechanical process aids) [4]. A technical simple, but well-suited approach for the separation of solid mixtures is sieving or screening, which can be performed discontinuously and continuously as a stand-alone process or in a process chain with other combined solids processes.

Such an exemplary process chain, including a three-deck vibrating screen, integrated in a comminution classification circuit, is presented in Fig. 1. After the material is supplied and stored in a hopper, the particles are transported over a vibrating conveyor to two different comminution steps (jaw and impact crusher). After the second crusher, the material is screened in four fractions, namely the three products of different size classes and the coarse material, which is returned to the crusher by a recycle stream, mixed with the new material and then crushed and screened again.

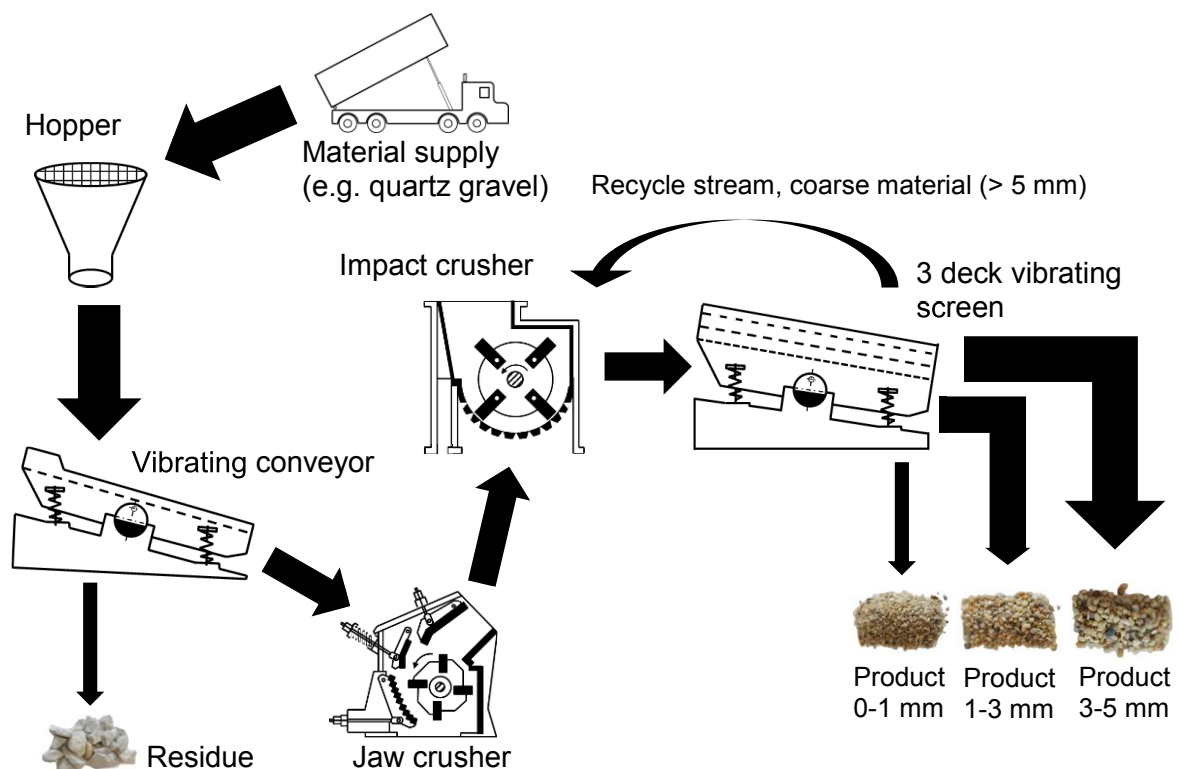


Fig. 1: Exemplary solids production process chain including a comminution classification circuit (comp. [1]).

In order to prevent disturbances in such connected industrial processes, the knowledge of the influence from upstream process steps on the actual process and its impacts on subsequent downstream processes is significant and therefore, the single processes must be at best fully understood. Despite its wide usage in industry and recent promising developments concerning the dynamics of screening and its subprocesses influenced by different mechanical agitations or by a fluid, a satisfactory understanding of screening processes is still not fully given for mixtures of real solids, leaving the design, optimization and scaling of this process operation a challenging task. The underlying different processes (stratification, particle passage and particle transport), their interaction and dynamic behavior still lack detailed understanding [5]. Furthermore, flexible, simple and physically based process models for a quantitative representation of screening on the background of a transient description are not available.

At least the two subprocesses stratification and passage are closely interlinked during screening. Due to the mechanical excitation of the screen, smaller particles move through the interstices of the larger particles in the direction of the screen surface (stratification), whereby particles smaller than the aperture size pass through the screen openings depending on their shapes and the bulk density [6]. In addition, the transport of the bulk material during the continuous screening process and various mechanical excitations also influence the particle passage [7,8]. Furthermore, to counteract material that is difficult to screen, flow processes or mechanical aids can be used during the screening process [9].

For the design and optimization of apparatus-specific and operational parameters of a screening process under stationary conditions, various phenomenological process models are available. Some simple models, which are commonly used in stationary process simulation packages, only consider the integral outcome of the separation operation, while others represent the particle size separation temporally or spatially resolved. In addition, some of the models take the interacting processes of stratification and the actual particle passage through the screen into account. All phenomenological models have in common that they require a set of empirical parameters, which are material, operation and apparatus-specific and are usually determined from experimental investigations. In contrast, particle-based simulation methods such as the discrete element method (DEM), based on the work by Cundall und Strack [10], provide detailed insights into the process of screening and allow, after appropriate validations, the design and optimization of equipment as well as of operating parameters. Up to now, only a few screening investigations addressed systems of realistic particles of complex shape under the influence of liquid due to the high computational demand. Applications of the DEM with the aim to directly derive parameters for dynamic phenomenological models for the process step screening were rarely carried out and are yet not adequately accomplished.

In Fig. 2, an overview of the progression of numerical screening research presented as summed up number of publications per year from 2000 up to the middle of 2018 according to

different criteria from the science database “Web of Science” is presented including the publications in this thesis.

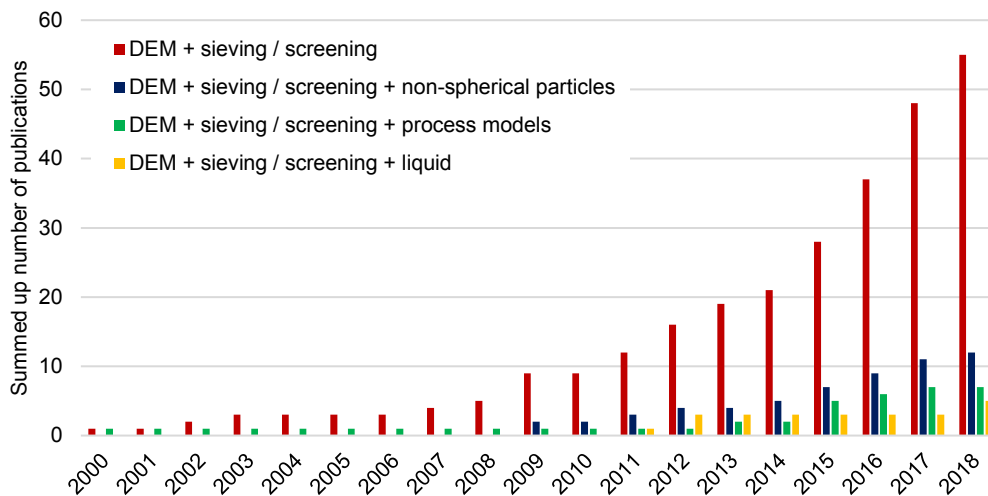


Fig. 2: Overview of numerical screening research presented as summed up number of publications from 2000 up to the middle of 2018 according to different criteria from Web of Science including the publications in this thesis. The search criteria are basically ($TI=$ “sieve” OR “screen” OR “sieving”) AND $TS=$ (“discrete element” OR “distinct element” OR “particle element method”) (red bars) extended by AND $TS=$ (“non-spherical”) (blue bars), AND $TS=$ (“process models” OR “probability” OR “estimate the sieving rate”) (green bars) as well as AND $TS=$ (“moisture” Or “wet” Or “liquid”) (yellow bars). Note that TI and TS are used in this database to search for the title and the topic, respectively.

The first small scale screening simulations were performed in 2000 followed by only a few further investigations in the following eight years. Approximately starting from 2009 until now, many researchers focused on numerical screening simulations due to the increase in available computational power, the unchanged relevance of screening processes and the limitations of experimental investigations. Also in 2009, the first researchers applied non-spherical particles in their DEM screening simulations in order to represent the highly non-spherical shape of the real material more accurately. Despite the importance to model the particle shape adequately, only a few other researchers considered non-spherical particles in screening simulations, which is probably a consequence of the high computational load usually resulting. Even less researchers utilized the detailed and easily accessible information provided by the DEM to derive phenomenological process models for screening. In addition, screening under the influence of various amounts of liquid has rarely been studied with DEM simulations in the past.

2. Objectives and document structure

In this section, the research objectives as well as the structure of this thesis are outlined.

2.1 Objectives

The objectives of this thesis are aligned in accordance to the DFG project “Development of a dynamic-physical process model for sieving” which resembles the framework in which the research outlined throughout this thesis was performed. The DFG project was part of the superordinate DFG priority program SPP 1679 “Dynamic simulation of interconnected solids processes” (DYNSIM-FP). In Fig. 3, the performed investigations within the first two periods of this project (dark blue) as well as current and perspective research (period 3, light blue) are shown. The roman numerals represent the respective publications resulting out of the performed research comprising this thesis.

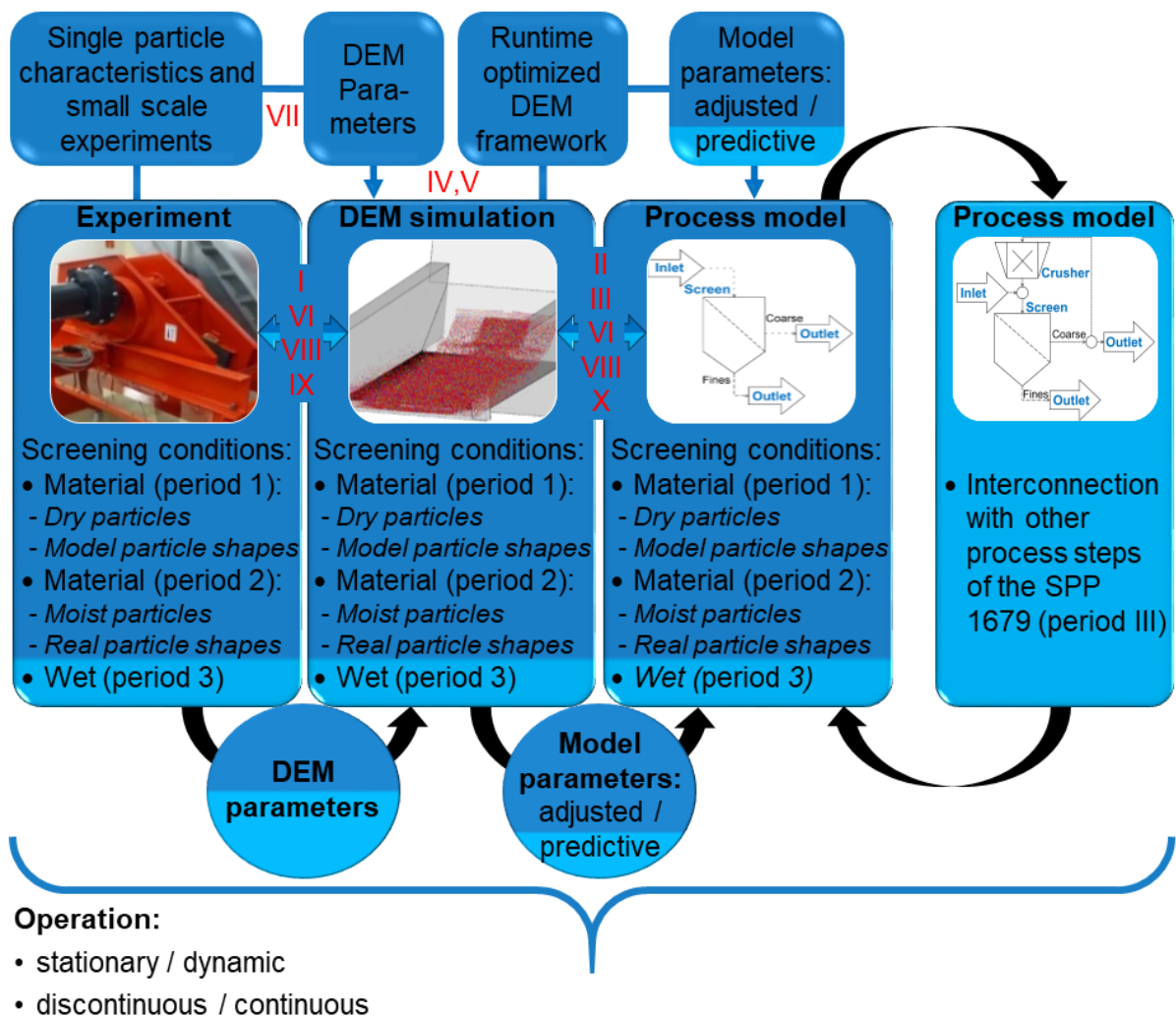


Fig. 3: Performed investigations within the first two periods of the DFG project “Development of a dynamic-physical process model for sieving” as part of SPP 1679 (dark blue) as well as current and perspective research (period 3, light blue). Resulting publications are marked with the respective red roman numerals and associated to the corresponding fields of research.

The objective of the superordinate SPP 1679 is to form a framework to allow the investigation of the dynamics of different representative solids processes and to connect them later as part

of a dynamic flow sheet simulation of bulk solids processes (comp. Fig. 3, period 3). According to this overall aim, the purpose of this thesis is to investigate the dynamics of screening and its subprocesses as well as to provide ways to derive phenomenological process models for the process step screening based on analyzes and benchmarks of existing models.

Therefore, screening processes with model type (period 1) and real shaped (period 2), dry (period 1), moist (period 2) and wet particles (period 3) including particle properties of bulk solids are studied (comp. Fig. 3). In addition, various screen sizes and characteristics, operational parameters and particle compositions as they might be associated with polydisperse particle systems should be addressed.

The necessary model parameters for the process models are not gained from experiments but from DEM simulations and are adjusted to fit respective simulation results of dry screening processes (period 1). Extended process models should be able to represent screening under the influence of moisture (period 2) and wet screening (period 3). However, the benchmarked process models are apparatus and screening material dependent and therefore, they are not predictive and rely on adjustable parameters. An approach, which leads to promising developments, is to improve the predictability of the process models along with a reduction of adjustable parameters by extending them with observed relationships and phenomena (periods 2,3).

The DEM simulations should be performed with a runtime optimized DEM framework and in small dimensions, which are still comparable with realistic screening conditions (comp. Fig. 3). In contrast to experiments, the simulations are more flexibly variable in geometrical dimensions, they need not to be supervised continuously and the respective parameters are easier to obtain due to having the possibility to look into the screening process in more detail leading to a broader range of obtainable parameters. In order to use DEM simulations for this purpose, they must be validated against experiments to prove their reliability (periods 1-3). Additionally, the respective DEM parameters could be gained by these experiments. However, a more effective way is to obtain the DEM parameters by small scale experiments, through single particle characteristics or by a combination of both in a general straightforward calibration procedure (comp. Fig. 3, period 2).

One main intention of the SPP 1679 is to study dynamic processes experimentally and numerically as well as to provide ways to develop dynamic process models. Therefore, the screening processes and the respective extended process models are not limited to stationary conditions but take dynamic changes in operational parameters during the process into account (comp. Fig. 3). In addition, inherent alterations like the decrease of the residues on the screen surface in discontinuous systems are investigated. Furthermore, continuous and discontinuous (batch) screening processes are considered (comp. Fig. 3).

2.2 Document structure

After the introduction, background and objectives, the present thesis is structured as follows. First, a theoretical foundation of screening, DEM simulations, flowsheet simulations and their combination is provided, embedded in the state of research and some extensions of the own performed studies. After this, eight journal publications as well as two conference contributions are part of this thesis (comp. Fig. 3).

In publication I, linear vibrated continuous screening processes are modeled with the discrete element method involving non-spherical particles after a validation against data from literature. Besides the relevant processes for screening, the screen wire geometry and different particle approximations are studied. Batch sieving simulations applying non-spherical particles in the DEM and a sensitivity study including variations in particle and sieve characteristics as well as in operational parameters are carried out in publication II. Based on these simulations and a review of process models for batch sieving, a benchmark of these models is performed. A similar investigation and benchmark for linear vibrated continuously operated screens under different operational parameters as well as particle and screen characteristics is accomplished in publication III. Publications IV and V additionally take a circular vibration as well as the special curved design of banana screens into account. Based on an experimental validation, the investigation in publication VI extends the numerical results and outcomes for batch sieving models by the characteristics and modifications of batch sieving processes, in which the operational conditions are altered during the process. In publication VII, various possibilities to estimate DEM parameters are discussed and a general straightforward procedure for their determination involving spherical and non-spherical particles with a high degree of automation is proposed and later validated against batch sieving experiments. A comparison between continuously operated screening and air classifying experiments of project partners with DEM simulations and process models applying spherical and non-spherical particles is carried out in publication VIII. Batch sieving under the influence of moisture applying spherical particles is performed in publication IX. Therein, DEM simulations considering the forces caused by liquid bridges as well as their formation and rupture are validated against results of an experimental investigation. Following this, the obtained outcome of the DEM simulations is used to benchmark and extend process models to predict batch sieving under the influence of moisture in publication X. After the publications, some concluding remarks and perspectives for future research are provided.

3. Theoretical foundation and state of research

In this section, the basics for the description of particle systems and single particles are introduced. Subsequently, an elementary understanding of screening is provided and common separation processes are presented. Thereafter, the discrete element method is briefly explained including ways of particle approximations, the contact detection as well as contact and liquid bridge forces. In addition, methods for the determination of the relevant particle parameters for DEM simulations are discussed. Based on this knowledge, some simulated screening processes from literature are described and own performed simulations, which are later analyzed in the publications, are illustrated. As a last point, flowsheet simulations of combined solids processes and therein, process models for screening are addressed.

3.1 Particle systems and single particles

In the following, material systems, which are relevant in mechanical process engineering as well as possibilities for the description of single particles will be characterized. In addition, a description of representation variants for particle collectives is provided.

3.1.1 Disperse systems

Material systems treated in mechanical process engineering are usually in the form of granular material or powders. Such particle collectives are generally called disperse material systems. They are subdivided into a disperse phase, which mostly consists of a large number of individual elements and a continuous phase, the surrounding medium [1,11]. Depending on the particle size d of the disperse phase, an additional distinction can be made into coarse ($d > 10^{-6}$ m), colloid (10^{-9} m $< d < 10^{-6}$ m) and molecular disperse systems ($d < 10^{-9}$ m), in which the first size range is of particular importance for mechanical process engineering and in this thesis [1,12].

Dry disperse phases are surrounded by a gas as continuous phase. If a liquid is added, it replaces parts of the continuous phase and can exist in various states depending on the pore saturation in between the particles (comp. Fig. 4).

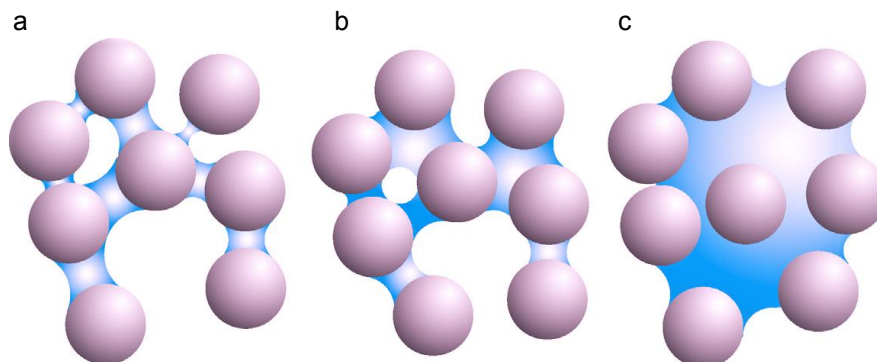


Fig. 4: Different degrees of pore saturation in between particles: (a) pendular state, (b) funicular state, (c) capillary state [13,14].

The pendular state occurs, if individual liquid bridges between pairs of particles form out, due to a small amount of liquid (Fig. 4a). By adding a larger amount of liquid, some pores between the particles are filled, resulting in the connection of more than two particles by one bridge, which is called the funicular state (Fig. 4b). When all pores in between the particles are filled with liquid, the system is in the capillary state (Fig. 4c) [13].

3.1.2 Single particle characterization

The size and shape of particles are the most important distinguishing features in mechanical process engineering. All properties of a particle directly related to its size are called fineness features. Accordingly, properties associated with shape are form factors [15]. The simplest way to characterize the size of a particle is to specify direct geometrical dimensions, such as the diameter d , length l , volume V or surface S of regular shapes like spheres or cylinders. However, the appearance of a particle usually deviates significantly from that of a regularly shaped geometry, resulting in substantial restrictions [1]. Another possibility to characterize the size of a particle is the acquisition of statistical lengths, where a random plane particle projection is generated by an image evaluation method (comp. Fig. 5a). The most important lengths that can be measured by this method are the Feret diameter d_{Fe} (longest distance perpendicular to the measuring direction), the Martin diameter d_{Ma} (chord in measuring direction halving the area) and the longest possible chord in the direction of measurement d_{Cmax} . Additionally, the shortest possible chord of all measured longest chords of a particle projection d_{min} can be obtained, which leads to similar results as a sieve analysis. Note that the values of the measured diameters differ for the same particle due to the random orientation of the projection as well as due to the direction of measurement. Statistical lengths are gained by measuring a sufficient number of particles [1,12,16].

Furthermore, an equivalent diameter of a sphere can be determined, which possesses the same property as the considered irregular shaped particle. Depending on the considered property, a distinction can be made in geometrical and physical equivalent diameters. Thereby, the diameter of a sphere, which is volume equivalent to the particle

$$d_{vol} = \sqrt[3]{6 \cdot V / \pi} \quad (1)$$

is one of the most important geometrical equivalent diameters. The volume V can either be obtained by measuring the displacement of water caused by the respective particles, by the electrical sensing zone method also known as Coulter Counter [17], by 2D image analysis where the projected area diameter is used with various assumptions [18] or by a direct 3D image analysis. In principle, any physical property that is related to the particle size such as the descent rate in liquid during sedimentation can be used to define a physical equivalent

diameter. Depending on the method, after which a particle size distribution is characterized, significant differences can arise for the same particle shape (comp. Fig. 5b) [1,11,12,19].

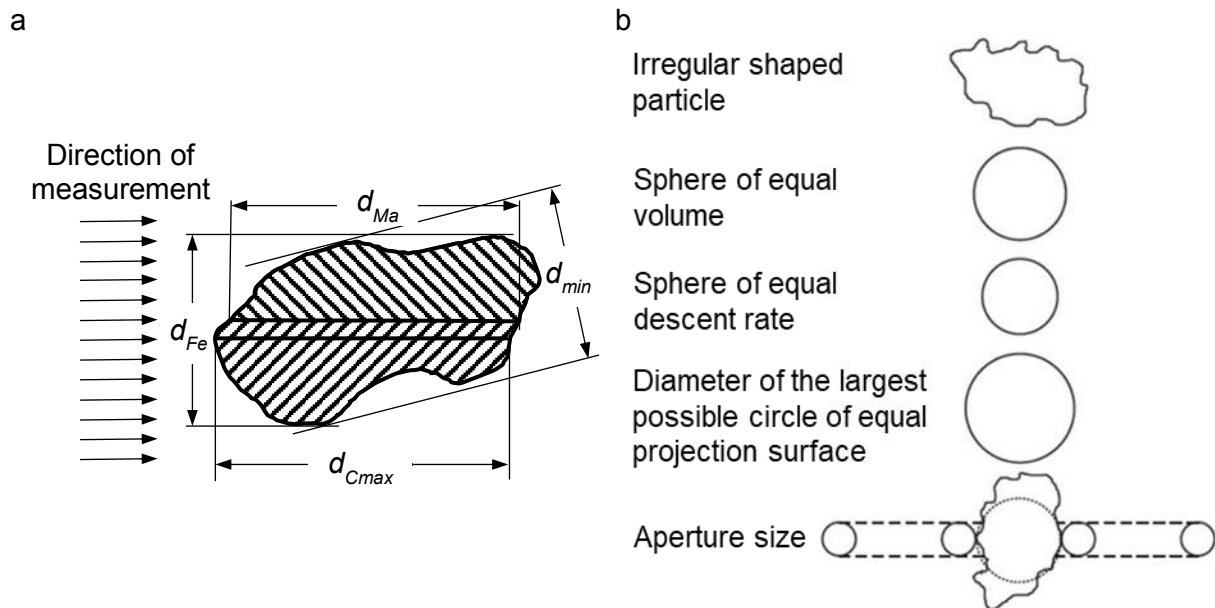


Fig. 5: (a) Statistical lengths of the projection and (b) comparison of various equivalent diameters of an arbitrary shaped particle (comp. [12,15]).

The geometric mean of the diameter of the non-spherical particle most closely corresponds to the diameter of a sphere of equal volume. The diameter of a sphere with the same descent rate in liquid during sedimentation is smaller due to the lower descent rate of an irregularly shaped particle of the same volume. In contrast, when a non-spherical particle is placed on a slide of a microscope, the diameter of the largest possible circle of equal projection surface is always greater than a spherical projection. The characteristic size of a screening process is the nominal aperture size of the screen. A particle, whose average diameter is greater than the nominal aperture size, yet has the ability to pass through the screen bottom if its minor axis (comp. Fig. 5a, d_{min}) is smaller than the aperture size [11,15].

In this thesis, several different materials and shapes, which are adopted from literature or used in experiments, are investigated and some of them are shown in Fig. 6. The first applied material in publication I is a sample of quartz gravel adopted from literature [20], where the size classes were made available through a sieve analysis and the shape was determined by an image analysis of the given sample (comp. Fig. 6a). Various approximations of these particle shapes with given material properties are applied in the investigations of this publication and in the following ones (publications II-VI). In later publications, own experimental validations are performed, in which quartz gravel with different particle size classes (comp. Fig. 6b) obtained by an image analysis of a Camsizer® giving similar results as a sieve analysis ($d = d_{min}$, publication VII, VIII) is applied. In addition, POM spheres with the diameters shown in Fig. 6c are investigated in the publications VII and IX and glass spheres with the same diameters presented in Fig. 6d are applied in the publications IX and X.

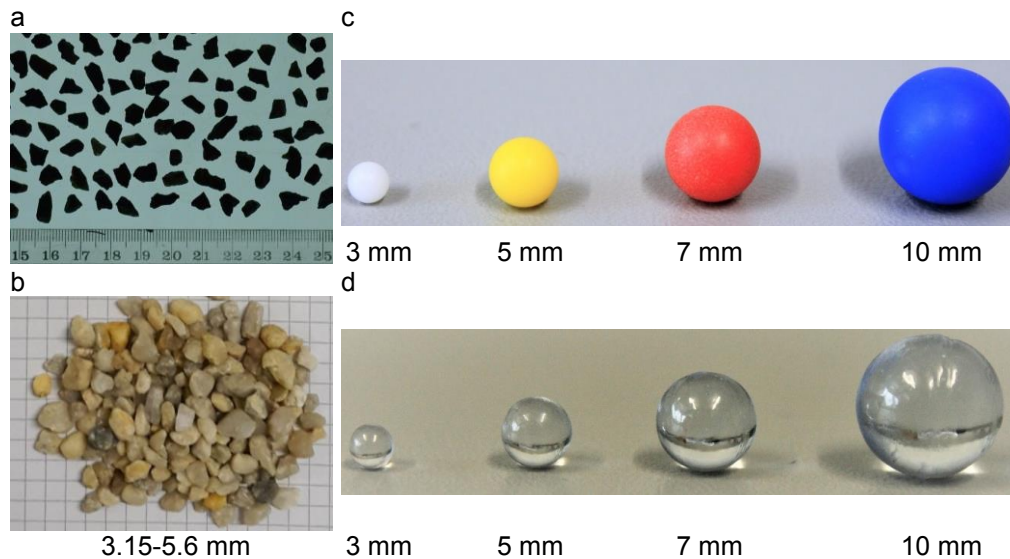


Fig. 6: Applied particle shapes and sizes of the quartz gravel samples (a) adopted from literature [20] and (b) used in own experiments as well as applied particle sizes of (c) POM and (d) glass spheres.

3.1.3 Particle size distribution

Within a particle collective, the individual particles are usually different in size, surface and shape. In order to characterize such a particle collective in more detail, it is mostly presented in the form of a distribution density or cumulative distribution curve. Therein, an arbitrary particle size d (e.g. aperture size or equivalent diameter, comp. section 3.1.2) is assigned on the abscissa. Subsequently, particle classes are formed with a defined interval and frequently with a characteristic average particle size, which is mostly the arithmetic mean in case of small interval widths and less common the geometric mean for large interval widths. When the distribution is represented by a cumulative distribution Q_3 , the proportion of the total amount for each particle size class, which is below a certain particle size d , is calculated and plotted on the ordinate. The resulting curve is monotonically nondecreasing and can be separated in a passing and a residue sum, of which the particle sizes are smaller or larger than a given value, respectively. In case of screening, this value is the aperture size dividing the proportion of passage from the residues. With the distribution density q_3 curve (comp. Fig. 8a), the proportion of the total quantity in a respective size interval relative to the interval width is represented. Referred to screening, this proportion would remain between two screen meshes of different sizes in a sieve analysis. In order to get a usable result, this proportion has to be related to the difference of the aperture sizes, which mainly influences this proportion. Mathematically, the distribution density function is the differential of the sum function, representing its slope at any point d_i [1, 15, 16, 19, 21].

3.2 Separation operations and screening classification

Important terms in the field of separation processes in mechanical process engineering are separation, division, sorting and classification. Separation is the decompositions of an amount

of material into partial quantities, in which the distributions of the considered characteristics are different, while in the division process the distributions of the considered characteristics keep constant. Sorting and classification are separations according to material characteristics like density or according to fineness features like particle size, respectively. Based on this, screening operations are referred to as classification processes [16].

3.2.1 Classification processes

In a classification process, the cut size d_{cut} separates the feed material into the fines and coarse material. Therein, $m_{in} = m_c + m_f$ are the masses and $q_{in}(d)$, $q_c(d)$ and $q_f(d)$ are the particle size distributions of the input feed material, the coarse material and the fines, respectively (comp. Fig. 7). Note that instead of masses, constant mass streams can also be applied in a stationary operated classification process. The share of coarse material of the total feed material is $c = m_c/m_{in}$ and the share of fines is $f = m_f/m_{in}$.

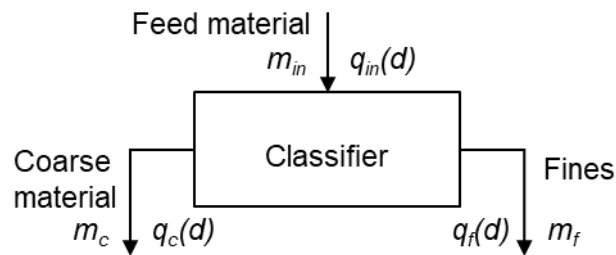


Fig. 7: Terms and principle of classification processes [1].

In an ideal classification, which is not possible in real processes, all particles with a particle size smaller than d_{cut} would be assigned to the fines and vice versa. In practice, a respective amount of particles, which is preferable as low as possible, is classified wrongly and is therefore called outsize. In Fig. 8a, the outsize of the fines and the coarse are the colored areas named (a) and (b), respectively. In addition, it is illustrated in Fig. 8a that $q_{in}(d) = f \cdot q_f(d) + c \cdot q_c(d)$. Another measure for the description of classification processes is the separation efficiency or partition number, which can be determined as

$$T(d) = \frac{c \cdot q_c(d)}{q_{in}(d)}, \quad (2)$$

where it indicates the proportion of the feed material that is contained in the coarse material after the classification process [1, 16, 22, 23]. Note that it is also possible to obtain the separation efficiency with known values of the fines and the input feed particle size distribution or with known values of the fines and the coarse material as

$$T(d) = \frac{q_{in}(d) - f \cdot q_f(d)}{q_{in}(d)}, \quad (3)$$

$$T(d) = \frac{c \cdot q_c(d)}{c \cdot q_c(d) + f \cdot q_f(d)}. \quad (4)$$

Furthermore, it can be calculated when f and c are unknown if all three particle size distributions (input feed, coarse material, fines) are known [1].

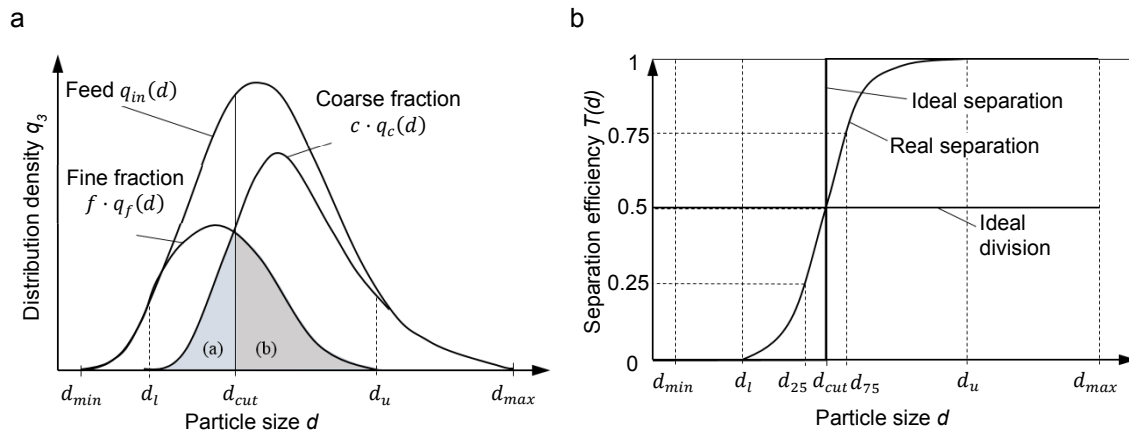


Fig. 8: (a) Density distribution and (b) separation curve [15,16,19].

By calculating the partition number of each particle size, a separation curve, which is also called grade efficiency curve, can be obtained (comp. Fig. 8b). For an ideal division, the value of $T(d)$ constantly equals 0.5. This curve is steeper, if the classification is sharper until an ideal classification is reached, where the curve is a step function. Thereby, the selectivity degree, defined by Eder as $K = d_{25}/d_{75}$, with d_{25} and d_{75} as particle sizes where $T(d_{25}) = 0.25$ and $T(d_{75}) = 0.75$, respectively, is a characteristic value for the quality of the classification [16,21].

3.2.2 Basics of sieving and screening

By definition, classification is the separation of a particle collective according to geometric features. A classic case of classification is the sieving or screening process, which is a relevant topic for experimental research at least since the work by Gaudin from 1939 [24]. Through this process of mechanical process engineering, the material is separated into particle dimensions, whereby ideally, other material properties such as particle density are irrelevant [25]. Characteristic for this process is the comparison of the bulk material with approximately equal sized openings of a solid surface called apertures, which can be meshes, slits or holes. Particles that are smaller than the apertures usually pass in the vertical direction, while larger particles remain as holdup on the screen surface. In accordance to other classification processes, the bulk material supplied on a screen is referred to as feed material. The particles that pass through the apertures are the fines getting in the screen underflow, whereas the particles that remain on the screen are assigned to the coarse material lying in the residue or screen overflow [1,25]. In Fig. 9, the terms in the simple case of a batch sieving process are summarized. Before the beginning of a batch sieving process, a particle collective, which should be separated into size classes, is fed on the classifier in individual charges. The process extends over a predetermined period t_{end} and the feed remains in the sieve box throughout the process.

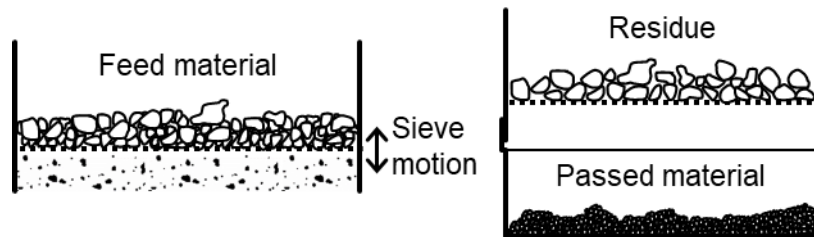


Fig. 9: Terms in the discontinuous sieving process [1].

The amplitude and the frequency of the vibrating sieve surface have a decisive influence on the quality of the batch sieving. The movement of the sieve bottom ensures a vertical loosening of the material layer, so that smaller particles can reach the sieve bottom due to the gaps formed between the larger particles (segregation). In addition, the resulting circulation of the particle layer causes each particle to be compared several times with the aperture size. Since not every small particle passes through the sieve bottom on the first encounter due to local and time-varying forces, it is only possible to separate the sieve material into fines and coarse material over time [1,16]. Note that in the field of sieving or screening, the segregation process followed by the passage of particles through the apertures is called stratification [7].

In industrial processes, predominantly continuous screening machines like the typical one shown in Fig. 10 are used [1].

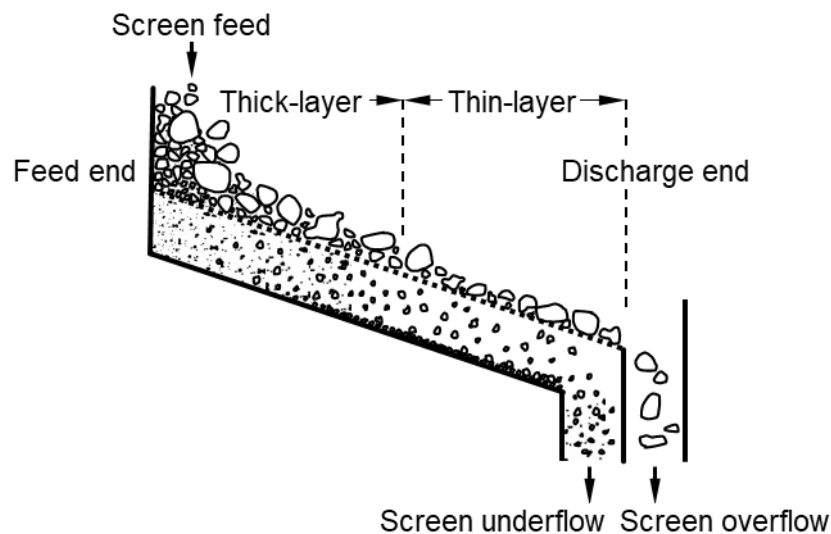


Fig. 10: Continuous production screening (comp. [1]).

In such a continuous screening process, the feed material is fed continuously on a usually slightly inclined screen surface, resulting in several layers of particles at the feed end of the screen apparatus. In addition to the loosening of the feed material, the vibration of the screen also causes the transport of the particle layers along the screen. Thereby, the thickness of the bulk material layers decreases with continuous movement. At the beginning of the screening process, much more particles are near the feed end and only a few are at the discharge end. This state is slightly shifted over time, whereby, it is favorable that the screening process reaches a steady state after a while. This steady state should be maintained but can be interrupted by load changes (mass flow or size distribution) or by a shutdown of the screening

apparatus. In usual operation, a thick layer of particles is at the feed end of the screen and a thin layer at the discharge end. Characteristic of continuous screening operations is a high passage rate in the area of the thick layer, because many particles, which are significantly smaller than the aperture size, pass through the openings here. Accordingly, the passage rate in the area of the thin layer is significantly reduced, where mostly particles with a diameter close to the aperture size are classified to the fines (near mesh sized particles) which have not been able to pass throughout the first period of the screening. Since the passage of these particles is usually more likely over time, the residence time, which is dependent on the length of the screening apparatus and the transport velocity, plays a significant role in terms of separation efficiency. At the end of the screening process, the separated fractions are discharged as overflow and underflow [1,26].

According to the particle size, screening processes can roughly be divided into coarse grain screening ($d > 10^{-2}$ m), normal screening (10^{-3} m $< d < 10^{-2}$ m), which is focused in this thesis, fine screening (10^{-4} m $< d < 10^{-3}$ m) and ultrafine screening ($d < 10^{-5}$ m). Note that for the latter range, cyclones, air or gravitational classifiers are mostly applied in industrial applications instead of screens [25,26].

3.2.3 Passage probability and screenability

Decisive for the passage rate of a particle collective through a screen surface with the aperture size a is the probability of passage p given by

$$p = \frac{(a - d)^2}{(a + w)^2} \quad (5)$$

In addition to the ratio of the particle size d to the aperture size a and the wire thickness w , the orientation of the particle, the impact angle and the forces acting on the particle are of fundamental importance [1,12,16]. The passage probability is described by the simple model of a sphere in relation to a square aperture (comp. Fig. 11a).

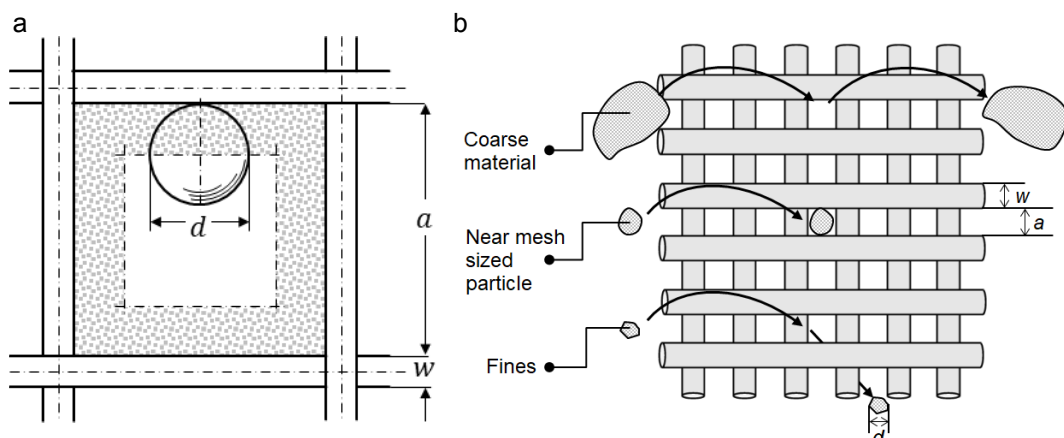


Fig. 11: (a) Model for the passage probability during screening [1] and (b) screening as a comparison of the particle size of the feed material with the mesh size in coarse and fine material [26,27].

In Fig. 11b the screening process as a separation of the feed material depending on the particle and aperture size in coarse $d > a$ and fine material $d < a$ is shown. Therein, particles that are slightly larger than the aperture size ($a < d < 1.2a$) fit into the apertures without passing them and thereby, they peg the apertures and hinder the other particles from passing. Furthermore, near mesh sized particles have diameters slightly smaller than the apertures ($0.8a < d < a$) and reduce the efficiency of the screening process, particularly if the particles are of highly non-spherical shape [26,28]. If the screen is inclined to the horizontal by an angle φ , eq. (5) is extended to

$$p = \frac{((a + w) \cdot \cos \varphi - w - d) \cdot (a - d)}{(a + w)^2 \cdot \cos \varphi} \quad (6)$$

The screenability of particles is not only dependent on the particle and aperture size, but also on the liquid amount in the bulk material (comp. Fig. 12a). It is reduced if the particles contain a low liquid amount or if a small amount of liquid is added to the bulk material until a limiting value is reached. This range is referred to as screening under the influence of moisture in the following.

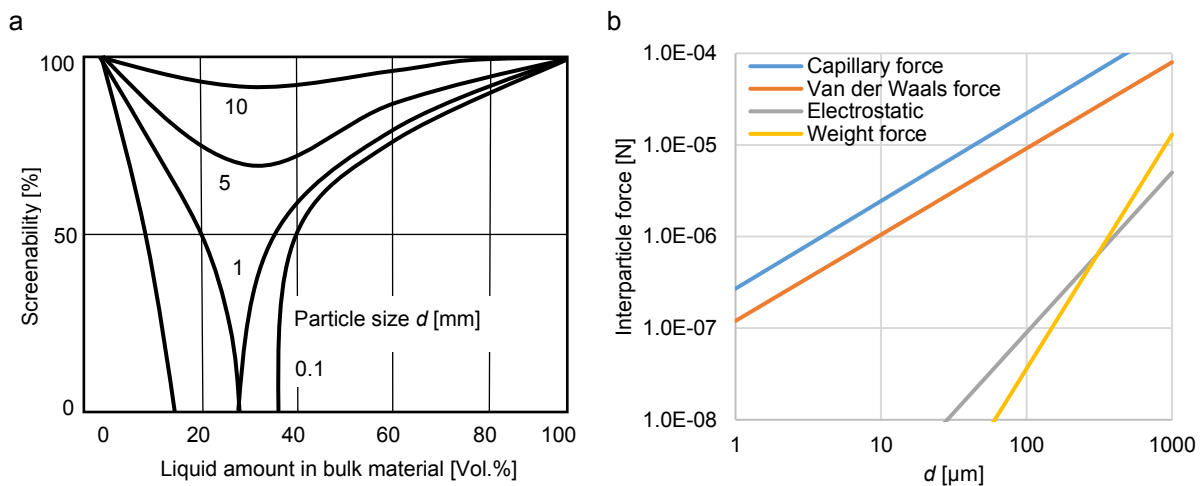


Fig. 12: (a) Screenability depending on the liquid amount in the bulk material and the particle size [26]. (b) Comparison of the magnitude of interparticle forces [29].

The moist particles, particularly the finer ones, stick to each other and accretions can arise. Furthermore, the segregation can be reduced due to adhering fine and coarse particles [9,30]. However, when more liquid is added to the system, the screenability is increased again by supporting the passage of fines and by removing the obstructive influences of moist particles. This solution is referred to as wet screening in the following and is a cheaper alternative to drying for breaking cohesive bonds. In addition, due to the drag force of the liquid, wet screening can lead to better screening results than completely dry screening [9,26].

The influence of the liquid is larger for smaller particles and vice versa. Accordingly, the screenability is only slightly reduced for coarse particles with $d \geq 10$ mm, but can be seriously diminished for small particles with $d \leq 1$ mm. For these small particles, the weight force is low

in comparison to the capillary force (comp. Fig. 12b). With smaller moist particles, the adhesive forces become larger in relation to the mass force, which means that greater accelerations are required for the loosening and hence for the screening of fine products. However, the incline of the weight force is more intensive and even larger than the capillary force for particles with diameters $d > 1$ mm, resulting in a lower liquid influence for larger particles [29].

3.2.4 Classification machines

In the following, several screening machines, their typical fields of application and screen surfaces as well as some flow classifiers are introduced.

Screening machines

In addition to the typical continuously acting screen shown in Fig. 10, a number of other screens exist that are distinguished by their type of movement and their geometry. In addition, air classifiers are mostly categorized according to the direction of the air stream and the movement of relevant components. Fig. 13 provides an overview of some types of classification machines used in practice. Note that machines applied in the publications of this thesis are highlighted in green; whereas devices related to the ongoing and future research in the SPP 1679 are marked light blue.

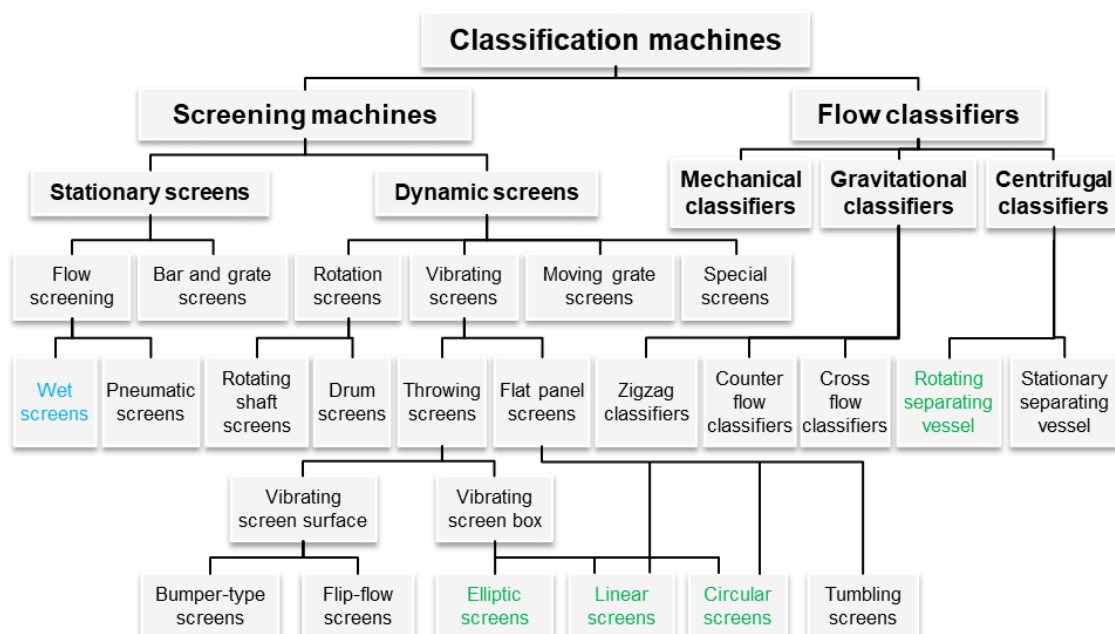


Fig. 13: Overview of classification machines used in industrial applications and researches [12,16,25,26]. Machines applied in the publications of this thesis are marked green, whereas devices related to the ongoing and future research in the SPP 1679 are shown in light blue.

In case of stationary screens, the screen surface remains rigid. Here, the feed material is conveyed over the screen surface either under the influence of gravity (bar and grate screens) or, particularly for finer material, by means of a fluid flow (flow screens) [25]. This fluid can be a liquid (wet screens) or gas (pneumatic screens) and results in a high efficiency of the screening process for various particle and aperture sizes due to the drag force of the fluid. By

means of suitable measures, almost all screening machines can be used for dry and wet screening [26]. Experimental research concerning wet screening applications focused mainly on the observation and optimization of the passage rate [31–33]. Note that studies concerning wet screening are not topic of this thesis, but will be investigated in ongoing/future research related to the SPP 1679.

Suitable coarse screening is achieved by means of inclined and partially vibrated grids or grates. Rotating disc rollers are also a type of grate, which are good in keeping the screen openings free. Furthermore, it is favorable that the vibration induces an oscillating conveying, in particular a throw conveying. Throwing screens are the furthest widespread screening machines (comp. e.g. [34–36] and publications I, III-V, VIII) and operate in industrial applications on the principle of a vibrating conveyor under dry and wet conditions with lowest aperture sizes of a ≈ 6 mm and a ≈ 1 mm, respectively [12,25]. These screening machines are differentiated according to their movement, which can be a linear (publications I, III, V), a circular (comp. Fig. 13a, publication IV) or an elliptical swinging (publication VIII). The movement is described by the parameters amplitude A and frequency f or by the angular velocity ω . The amplitude corresponds to half the double amplitude, the angular velocity is $\omega = 2\pi f$ and a possible inclination of the screen surface to the horizontal is denoted with the angle φ . Additionally, in case of an elliptical and linear vibrating screen, the throwing angle ψ has to be considered. This results in the throwing strength

$$K_v = A\omega^2 \sin(\psi + \varphi) / g \cos \varphi, \quad (7)$$

which is used to define the maximum intensity of the acceleration of a particle related to the gravitational acceleration. In addition, the motion of the screen apparatus is characterized as relation between the acceleration and the gravitation by

$$K = A\omega^2 / g. \quad (8)$$

For $K_v > 1$, the particles lose their contacts to the screen surface and for $K_v = 3.3$, one throw is exactly as long as one oscillation. Typical values are $K_v > 1.5$ for low strains, $3 < K_v < 3.3$ for a sharp screening and $3.3 < K_v < 6.6$ for the screening of material that is difficult to screen [12,26].

Linear vibrating screens operate between $\psi = 30^\circ$ and $\psi = 60^\circ$ and are able to transport the feed material even without an inclination. However, due to accelerating only in one direction, the vertical loosening of the particle layer is low, limiting this design to operate with a thin layer of particles [25,37]. Circular vibrating screens (comp. Fig. 14a) mostly prevent that particles peg the apertures due to transferring the force from the screen surface to the particles from different directions. They normally have a steep discharge angle ψ , resulting in a lower transport speed. Therefore, the screen surface is additionally inclined to achieve a sufficient

transport speed. Ellipse oscillations arise when the circular vibration is damped in one direction or a linear vibration is superimposed. Linear oscillations are technically induced by applying two circular oscillators, which are operated with the same imbalance masses and frequencies in the opposite direction of rotation. In conclusion, the screen inclination angle φ and the discharge angle ψ determine the transport speed over the screen. Thereby, the transport speed is lower for a steeper ψ [25,26].

In order to operate always in the most favorable working range of a thin layer screening, the conveying speed should be faster at the feed end and must decrease along the screen. Accordingly, the possible residence time of the feed material before being assigned to the oversized material, particularly of particles slightly smaller than the aperture size, increases. This is achieved by applying a so-called banana screen, which is still a very current topic in experimental research [38–41]. For a banana screen, several flat screen sections with sometimes decreasing aperture sizes are combined to form a curved screen surface. These screens can be operated in a linear or circular motion [25,26]. Another special screen design is the sizer, whereby the most famous one is the Mogensen Sizer, where several screen surfaces are arranged one above the other with decreasing or constant apertures sizes and increasing inclination angles from the top to the bottom, allowing a large feed rate and several separations simultaneously [12,16,26].

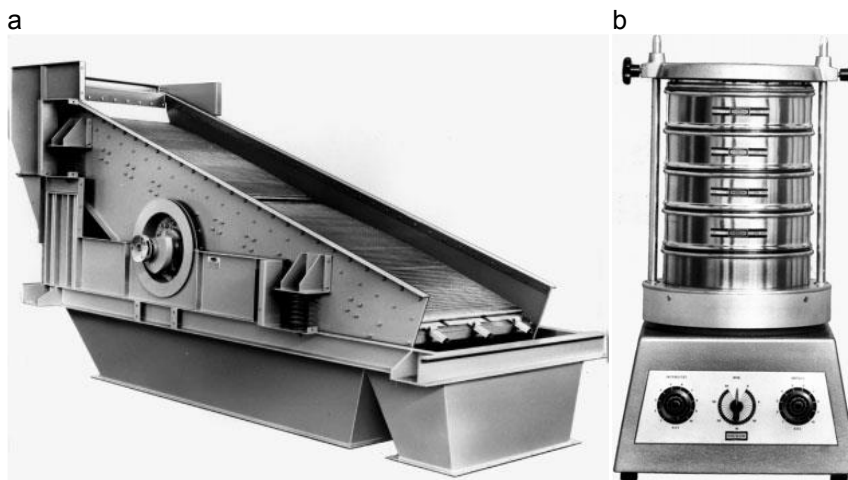


Fig. 14: (a) Circular vibrating throwing screen and (b) batch sieving apparatus [26].

Flat panel screens are horizontal aligned machines whose screen surface vibrates in their screen plane. The swinging motion can be linear or circular and the particles are usually separated with $d_{cut} = 0.25 - 2$ mm (comp. Fig. 15). The grains do not move perpendicular to the screen surface but obliquely to tangentially, sliding and rolling on the screen surface. The result is a significantly smaller cut size than the aperture size, leading to a lower selectivity but nearly to a prevention of pegged apertures. Besides apparatuses with a rectangular floor area and linear or circular motion, a specific type of flat panel screens is the round tumbling screen. Here, the feed material is placed centrally and the overflow is removed at the outer edge. In

addition to a horizontal circular vibration, a tumbling motion is superimposed, leading to a three-dimensional motion [25,26].

Rotation screens convey the feed material in a rolling motion over the screen surface, whereby the entire screen surface is rotated in case of a drum screen which has been studied experimentally among others by Chen et al. [42] for dry material and by Bellocq et al. [43] for wet agglomerates. In contrast, in case of rotating shaft screens, only individual shafts rotate over which the material is transported in the direction of rotation. Therein, a special design of a roller screen ($d_{cut} = 50-150$ mm (comp. Fig. 15)) applied for adhesive particles of $d_{cut} = 10-100$ mm is the self-cleaning star screen (comp. Fig. 15), where star-shaped discs are lined up on shafts [25].

In contrast to vibrating screen boxes, several screening machines with a direct excitation of the screen surface exist. Therein, a differentiation is made between a punctual perpendicular excitation of the screen deck in case of the form-fitting bumper-type screening machine and the newer solution with a force-fitting linear excitation of the mesh by applying vibrating impactor bars under the screen. Moreover, deforming screen surfaces can be applied to avoid pegging particles by self-cleaning of the apertures in a flip-flow screening machine, which operates in the range of $d_{cut} = 3-20$ mm [22,25,26,44] (comp. Fig. 15) and is also studied in current experimental research [40,41].

In Fig. 15 an overview of typical applications of various dry screening machines is given, which operate in a range of $0.0001 \text{ m} < d_{cut} < 1 \text{ m}$.

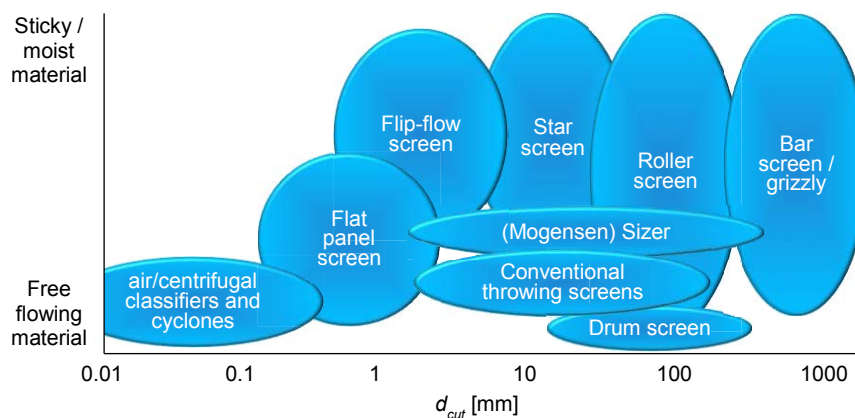


Fig. 15: Typical fields of applications of various dry classification equipment [25].

In addition to the large scale industrial screens, another horizontal aligned apparatus with a round surface is the test sieve shaker, which is applicable for laboratory analysis (comp. Fig. 14b). Such batch sieves have a vertical linear motion like the throwing screens and can comprise of several sieve surfaces to obtain the desired particle size classes [1,12,16]. The advantage of studying sieving processes with this device is the comparatively small amount of particles without an increase by an inflow of feed and the absence of transport processes. Therefore, only particle stratification and passage have to be considered. In addition, batch

sieving processes are transient in nature, providing a good suitability for dynamic process models. Besides several other studies in literature [45–47], batch sieving is investigated in the publications II, VI, VII, IX and X with various intentions.

Screen surfaces

The screen surface as the main element of screening may be formed as a grid, grate, perforated plate or as a harp screen. Today, the screen lining is often made of several rectangular segments of synthetic substances, which are easily exchangeable and good in cleaning the apertures from pegging particles due to their flexibility. In contrast, a wire mesh has the advantage of a larger open area per square meter screen surface $S_f = a^2 / (a + w)^2$ due to the small size of the wires w and low acquisition costs [22,25,26,48]. In Fig. 16, different aperture shapes are presented.

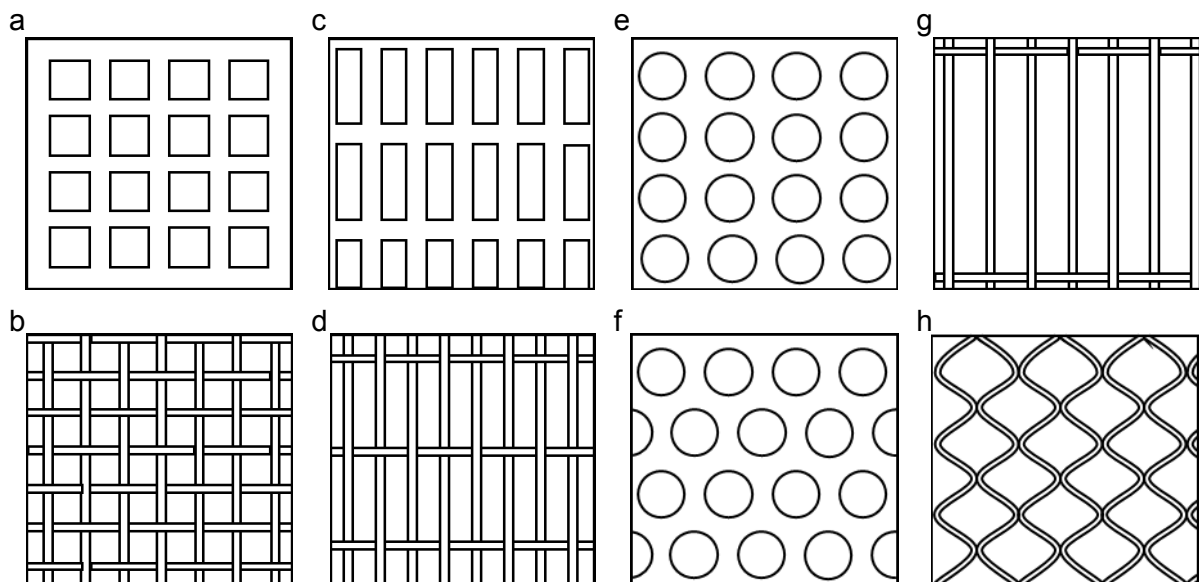


Fig. 16: Overview of different aperture shapes [12,22,25,26].

Usually, square (Figs. 16a,b) (comp. e.g. [49,50]) or rectangular (oblong or broad) apertures (Fig. 16c) (comp. e.g. [51,52]) are applied, whereby in this thesis only perforated square apertures with a rectangular wire profile (comp. publications I-VII) or approximations of woven square apertures with a semicircular wire profile (comp. publications II,III,VIII-X) are considered. However, also slots (Fig. 16d) are not rare in industrial applications and round apertures (Figs. 16e,f) are possible as well. Oblong or broad openings have a length a_l to width a_w ratio of up to 3:1, whereas slots have an even larger ratio. A special design are the so-called harp screens (Fig. 16g), which consist of parallel stretched wires with a ratio of $a_l > 10a_w$. They are effective against pegging particles, but with the drawback, that coarse elongated material is able to pass. A compromise is a corrugated wire with a mainly rectangular mesh cross-section (Fig. 16h) [12,22,25,26].

Flow classifier

For smaller particles, flow classification processes can be applied (comp. Fig. 17). They can be divided into gravity classification processes, mechanical classifiers for medium sized wet particles and centrifugal classifiers which are applied in the case of non-adhesive, free flowing particles (comp. Fig. 13) [25]. Such flow classifiers are devices that separate granular material by means of flow forces of a gas or liquid acting on the particles into precipitating coarse material and fines discharged with the fluid. Thereby, a number of particle size-dependent forces, such as the gravity, the resistance and inertial forces are applied to the solid particles in the separation zone. Similar to screening processes, the behavior of such a classifier is usually described by an experimentally recorded separation curve. In this field, several approaches and improvements for process equations were developed [12,53–57].

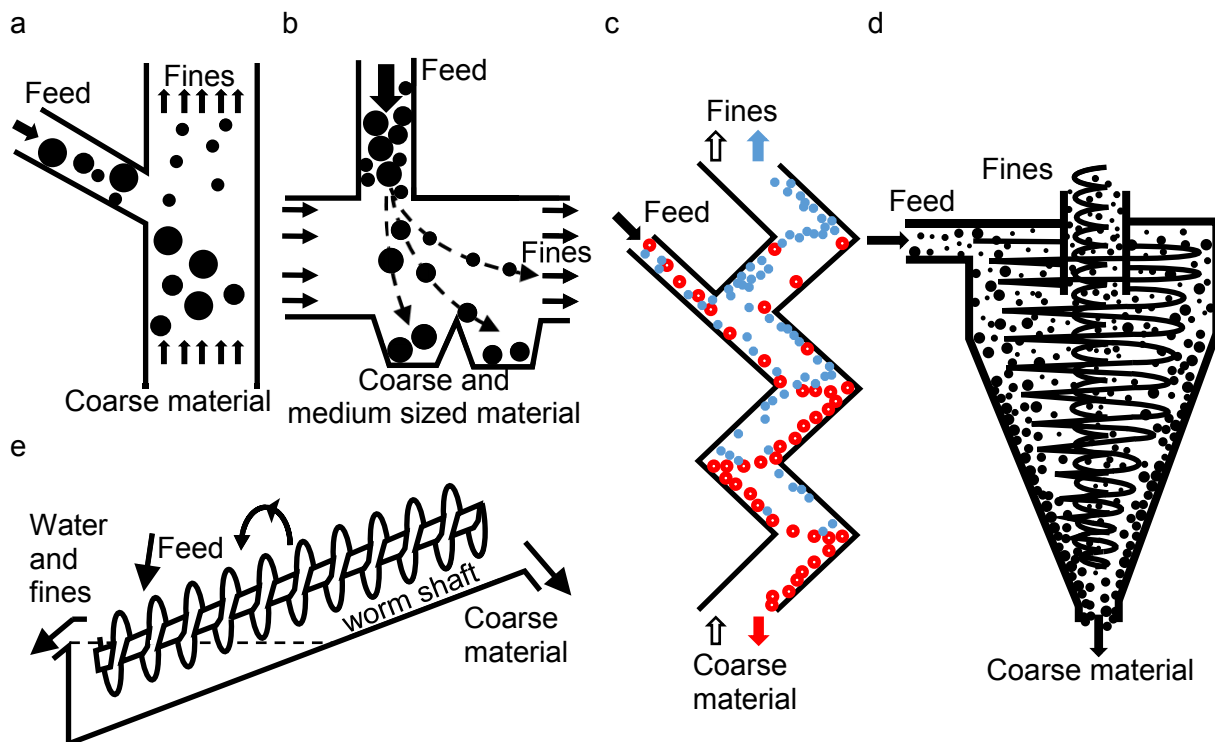


Fig. 17: Examples of flow classifier: (a) counter- and (b) crossflow classifier, (c) zigzag classifier, (d) cyclone and (e) spiral classifier (comp. [25]).

The gravity classification can be further subdivided into the counter- and crossflow classification (Figs. 17a,b). In the first method, the feed material is streamed from below, whereby the fines follow the flow and the coarse material drop down due to its larger descent rate. In the latter variant, the flow direction is horizontal, whereby the feed material is accelerated in this direction. Due to different descent rates, the particles spread out and can be separated into multiple size classes. A combination of both procedures is the zigzag classifier (Fig. 17c), where the particles are separated over several stages with alternating counter- and crossflow sections [12,25].

Mechanical classifiers like the spiral classifier (Fig. 17e) are operated at a higher turbulence than the gravity classifiers. During this wet classification process, fine particles are kept in suspension while coarse particles settle. In case of the spiral classifier, the sedimented coarse material is discharged with a worm shaft over an inclined plane while the water and the fine particles leave the process via an overflow weir.

In order to save required space in industrial applications, compact centrifugal classifiers are applied instead of counter- and crossflow classifiers to perform fine classifications. Therein, a subdivision is made between rotating and stationary separation vessels [11,12,25]. Following the first mentioned principle, a centrifugal field induces a solids vortex like in centrifuges, whereas in the latter, the centrifugal forces result from redirecting the suspension into a potential vortex as in the case of cyclones (Fig. 17d). A special type of centrifugal classifier with a rotating separation vessel is the deflector wheel classifier, in which the feed material is separated through a rotating classifying wheel in fines and coarse material, wherein the particles in the zone between the sight blades undergo inward drag forces and centrifugal forces to the outside [29,58]. This apparatus is studied in detail in publication VIII.

3.3 Discrete element method

The discrete element method (DEM) dating back to Cundall and Strack [10] and Walton and Braun [59] is a particle-based simulation approach that provides detailed insights into various processes and has advanced to a common tool for modeling particulate systems (comp. [60–63] and publications I-X). After an appropriate validation, it provides the possibility to optimize equipment and operating parameters without performing extensive experiments in advance of each study. By applying this method, the motion and interaction of each individual particle within a considered computational domain can be represented and tracked. Contact forces between the particles and the system environment as well as possible additional forces resulting out of the presence of liquid are used to determine velocities, positions and spatial orientations of all particles contained in the system using the Newton's and Euler's equations of motion. Since an exact investigation of the elastic and plastic deformations of the contact partners at the contact points would be too time consuming, various models can be used to approximate the contact forces between the particles. In the soft-sphere approach, which is applied in this thesis, the particles are considered as rigid, elastic bodies, but without allowing deformations. However, the contact forces are determined by virtual overlaps of the discrete elements. The particle collisions are resolved in time, leading to particle contacts lasting over several time steps. In the case of a particulate system under the influence of moisture, the contact between the particles lasts even longer due to the formation of a liquid bridge, which additionally influences the motion of the contact partners after the overlapping phase.

Besides particles, DEM simulations can also contain moving or stationary walls, which are composed of triangular elements in the applied code. In principle, the same force models are used for particle-wall contacts as for particle-particle contacts. Note that the wall positions and wall speeds are unaffected by the resulting contact forces in all simulations performed for the investigations in this thesis (comp. [64]). Various particle shape approximations, the equations of motion, the contact detection and the applied force laws of the DEM are described briefly in the following sub-sections.

3.3.1 Particle geometries in the DEM

Due to its simple geometry, particularly concerning the determination of the contact region, spheres have been used to describe particle geometries in the majority of studies in the field of DEM [65]. If the distance S between the centers of two spheres is lower than the sum of their radii r_{sum} a contact exist and the difference results in the overlap $\delta = r_{sum} - S$. In addition, the determination of the normal vector lying on the connecting line between the two spheres is easy and the tangent vector is given through the relative velocities of the spheres [66]. In contrast, non-spherical particles require in particular a higher complexity of the contact determination [67], which leads to an increased computational effort and to less large scale investigations carried out in the past [68]. However, in most industrial processes where bulk materials are encountered, including screening, real particle geometries deviate significantly from spherical shapes as described in the previous sections. Numerous studies in this context show that spheres behave differently than real, non-spherical particles, so that the findings obtained from such DEM simulations are questionable (comp. publication I and [69]), evoking the need of applying already developed methods to describe complex particle geometries.

For this purpose, a simple approach is to include models for the coefficient of rolling friction (comp. section 3.3.4) in the DEM instead of changing the particle shape to imitate the rolling resistance of non-spherical particles. However, this method is not suitable to represent all phenomena induced by non-spherical particle geometries [70].

A common method for the approximation of non-spherical particles within DEM simulations is to apply superquadrics or -ellipsoids (comp. Fig. 18a). Various studies have shown their ability to represent a greater variety of particle geometries and that they significantly increase the shear strength of loose beds compared to spherical particles [71–73]. However, superellipsoids or -quadrics are limited to mirror-symmetrical body shapes and are not able to image sharp-edged structures.

Another common type for the representation of non-spherical particles within the DEM are polyhedra, which are arbitrary convex bodies defined by surface triangulation (com. Fig. 18b). Since polyhedra can have a variety of structures, the occurring contact geometry can be very

complex. Thereby, several methods for the contact resolution, among others the common plane method [74] and further developments like the fast common plane [75] or the shortest link method [76] as well as a method based on the Gilbert-Johnson-Keerthi algorithm [66], were introduced in the past. Although polyhedra have the advantage of being versatile, the challenging determination of the overlaps and the resulting forces leads to a high computational demand. This limits their applicability for large scale screening simulations, where besides many particle contacts, a large amount of particle-wall contacts is unavoidable.

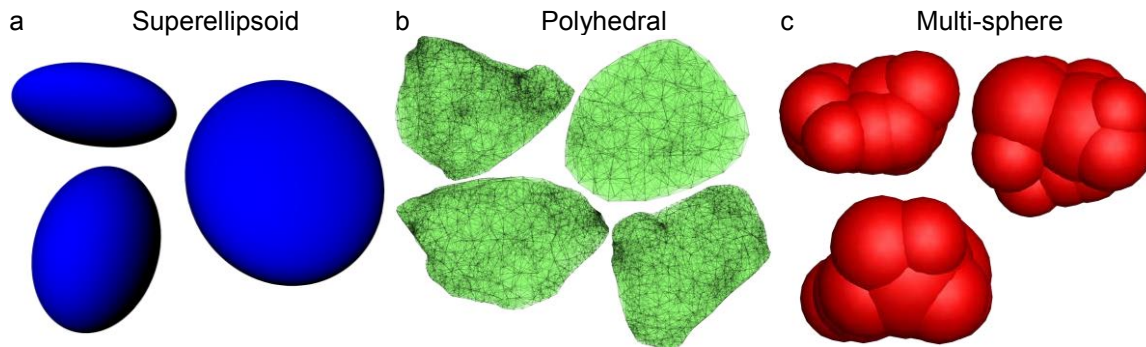


Fig. 18: Comparison of different approximations of non-spherical particles, which are called (a) superellipsoid, (b) polyhedral and (c) multi-sphere method.

In addition, non-spherical particles can be modeled by the multi-sphere method in the DEM (Fig. 18c), which was developed by Jensen et al. [77], Favier et al. [78,79] and Vu-Quoc et al. [80]. Following this flexible approach, a number of arbitrary sized spheres are clustered to adept the desired shape of the non-spherical particle as accurately as possible [69]. Thereby, the spheres are allowed to overlap and the geometry remains unchanged during the simulation. Besides the flexibility to represent a variety of shapes, the advantage of this method is the possibility to apply similar contact force laws as used for spherical particles. In addition, the contact detection is performed analogously to spheres for each single sphere of a multi-sphere particle [65]. Although sharp-edged shapes cannot be represented exactly with the multi-sphere method, it is suitable for screening processes with non-spherical particles (comp. publications I-VIII). It is the most popular method, due to its relatively low computational effort and the flexibility to decrease the particle complexity to a certain extent by reducing the number of single spheres. However, the required number of spheres to properly approximate the real particle is unknown [81]. Note that the multi-sphere approach is not applied for particle systems under the influence of liquid in this thesis (comp. publications IX-X).

3.3.2 Equations of motion

The DEM is routinely utilized for the modeling of systems with spherical particles [60,61]. To obtain the translational and rotational motion of each particle in such a system, the Newton's and Euler's equations are integrated

$$m_i \frac{d^2 \vec{x}_i}{dt^2} = \vec{F}_i^c + m_i \vec{g} + \vec{F}_i^l, \quad (9)$$

$$I_i \frac{d\vec{\omega}_i}{dt} = \vec{M}_i, \quad (10)$$

with particle mass m_i , particle acceleration $d^2 \vec{x}_i / dt^2$, contact force \vec{F}_i^c , forces arising from a possible liquid amount \vec{F}_i^l , gravitational force $m_i \vec{g}$, moment of inertia I_i , angular acceleration $d\vec{\omega}_i / dt$, angular velocity $\vec{\omega}_i$ and external moments resulting out of contact and various additional forces \vec{M}_i .

When the discrete element method is used to represent non-spherical particles, the integration of Euler's equation reads

$$\hat{I}_i \frac{d\vec{W}_i}{dt} + \vec{W}_i \times (\hat{I}_i \vec{W}_i) = \Lambda_i^{-1} \vec{M}_i, \quad (11)$$

with the angular acceleration $d\vec{W}_i / dt$, angular velocity in the body fixed frame \vec{W}_i , external moments resulting out of contact and various additional forces \vec{M}_i , the inertia tensor along the principal axis \hat{I}_i and the rotation matrix converting a vector from the inertial into the body fixed frame Λ_i^{-1} . Therein, explicit integration schemes are used to solve the equations for translational and rotational motion (comp. [82]). In order to apply eqs. (9)-(11), the relevant forces (comp. sections 3.3.4 and 3.3.5), resulting out of respective contacts (comp. section 3.3.3), have to be determined.

3.3.3 Contact detection

As described in the previous section, in addition to the gravitational acceleration, the external forces $\vec{F}_i^c + \vec{F}_i^l$ acting on the particles are responsible for their translational and rotational movements and thus for the mechanical behavior of the particle collective. Within this thesis, these external forces are first (publications I-VIII) limited to the contact forces between particles and those between particles and existing wall elements. Later (publications IX-X), forces arising from the existence of liquid in the bulk material are additionally taken into account. Thus, the contact determination between the individual discrete elements is one of the essential components of DEM simulations in both cases. In principle, the contact determination can be divided into a neighbor search and a subsequent geometric contact resolution. Thereby, in contrast to the neighbor search, the geometric contact resolution depends on the exact geometry of the particles [64]. In the case of a moist particle collective, the contact phase can be further subdivided into the direct contact of the discrete elements without a fluid between them and the contact through a liquid bridge.

In a first step for the purpose of contact detection, each particle is assigned a virtual sphere, whose origin lies in the geometric center of the particle with the perimeter radius of the particle plus a possible liquid film. In a very simple approach for the contact detection in a computational domain, each particle could be tested for contact with any other particle, resulting in a quadratic increase of contact tests for each new particle [83]. In order to reduce the computational effort for systems with large numbers of particles, an effective neighbor search is essential. Therefore, a variety of approaches within the DEM is available, in which a distinction is made between cell-oriented [84–87] and binary-oriented search methods [88,89].

In cell-orientated methods, the computational domain is divided in several cells by a three-dimensional test grid. In a common used method, all particles are smaller than the cells and are assigned to one cell where their center is located. Thereby, the contact determination has to be accomplished for the same and the surrounding cells. In order to save time for calculating polydisperse systems, where many small particles possibly occur in one cell, another cell-oriented search method based on the CGRID algorithm by Williams et al. [85] is applied within the DEM code used in the investigations of this thesis. According to this method, the cubic cells may be smaller than the largest particle in the system and a particle is assigned to each cell that is covered by a part of the virtual sphere around the particle. Thereby, a contact check is only performed between particles that have been assigned to the same grid cell. Since particles can lay in multiple cells, the same contact could be calculated several times. To prevent multiple contact pair calculations, a contact point is determined and uniquely assigned to one grid cell. Details on extensions in the case of spherical particles under the influence of moisture are presented in publication IX. Further information on contacts involving clustered spheres can be found in literature (e.g. [90,91]).

3.3.4 Contact forces

After determining a pair of colliding particles or a contact between a particle and a boundary object, the resulting forces are evaluated by applying a suitable contact force model.

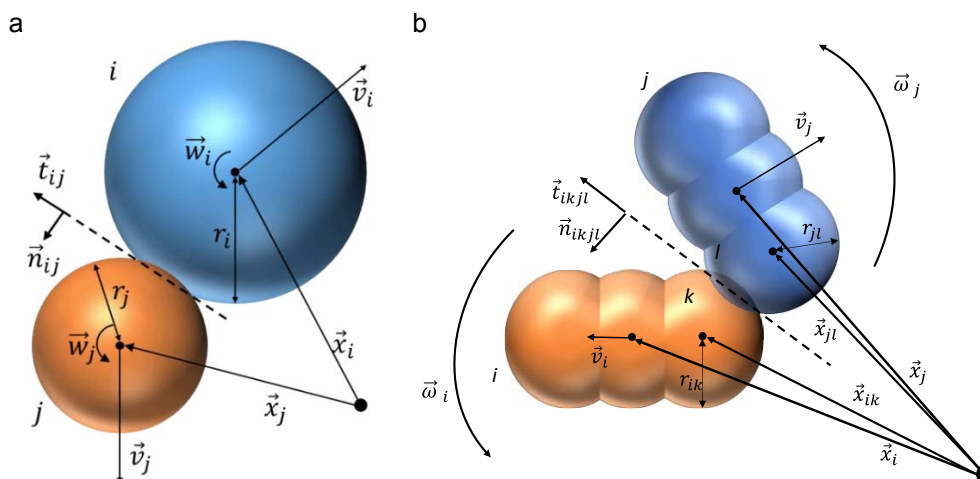


Fig. 19: A collision of two (a) spherical particles and (b) multi-sphere particles.

Fig. 19a shows a collision of two spherical particles i and j , whereas in Fig. 19b the two spheres l and k of two non-spherical (multi-sphere) particles i and j collide.

Normal force model

For the calculation of the normal force, several different models are available. According to the work by Kruggel-Emden et al. [92], where a detailed overview of normal force models is given, they can be grouped in continuous potential, linear viscoelastic, non-linear viscoelastic and hysteretic models depending on the overlap and displacement rate. The most common one is the linear viscoelastic spring damper model [92,93], which is also applied to obtain the normal component of the contact forces in all the publications which are part of this thesis. The normal force is exemplarily given for the contacting spheres i and j in Fig. 20a with an elastic and a dissipative component as

$$\vec{F}_{ij}^n = \vec{F}_{el}^n + \vec{F}_{diss}^n = k^n \delta_{ij} \vec{n}_{ij} + \gamma^n \vec{v}_{ij}^n, \quad (12)$$

where k^n is the spring stiffness, δ_{ij} is the virtual overlap, \vec{n}_{ij} is a normal vector, γ^n is a damping coefficient and $\vec{v}_{ij}^n = ((\vec{v}_i - \vec{v}_j) \cdot \vec{n}_{ij}) \vec{n}_{ij}$ is the relative normal velocity at the contact point with the velocities \vec{v}_i and \vec{v}_j [92]. Note that in case of the multi-sphere particles in Fig. 19b the force is calculated analogously between the contacting spheres k and l of particles i and j . The damping coefficient γ^n is obtained by

$$\gamma^n = -(2 \ln(e^n) m_{eff}) / t^n, \quad (13)$$

with the coefficient of restitution e^n , which has to be experimentally determined or obtained from literature, the duration of a collision

$$t^n = \pi / \left(\sqrt{\left(k^n / m_{eff} - (\gamma^n / (2m_{eff}))^2 \right)} \right) \quad (14)$$

and the effective mass $m_{eff} = m_i m_j / (m_i + m_j)$.

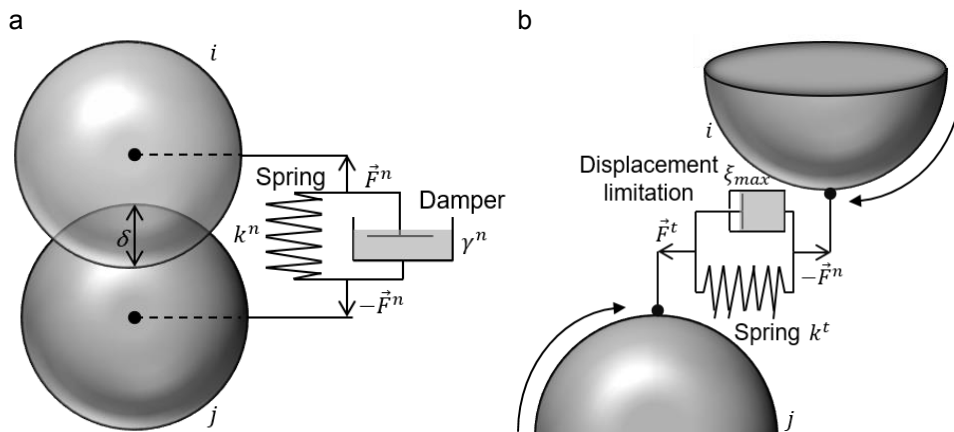


Fig. 20: Linear force model in (a) normal direction and (b) tangential direction.

Tangential force model

In addition to the normal force, a force component in the tangential direction for modeling occurring friction effects to prevent the sliding apart of particles in a particle bed is considered. Also for the tangential force, various models are applicable, whereby an extensive review is provided by Kruggel-Emden et al. [94]. Similar to the normal force, the most common tangential models are linear ones (comp. e.g. [95–97]). In this thesis, the tangential forces are calculated by applying a linear spring limited by the Coulomb condition, which is exemplarily shown for the two spheres i and j in Fig. 20b and calculated as

$$\vec{F}_{ij}^t = -\min(\vec{F}_{spring}^t, \vec{F}_{coul}^t) = -\min(k^t |\vec{\xi}_{ij}|, \mu_c |\vec{F}_{ij}^n|) \vec{t}_{ij}, \quad (15)$$

where k^t is the tangential stiffness of a linear spring, μ_c is the friction coefficient, $\vec{\xi}_{ij}$ is the relative tangential displacement and \vec{t}_{ij} is the tangential unit vector [94]. For the contact of two spheres k and l of two multi-sphere particles i and j (comp. Fig. 19b), only the indices are changed in eq. (15). The tangential spring stiffness k^t is obtained as

$$k^t = \kappa m_{eff} (\pi/t^n)^2, \quad (16)$$

where κ is given through the mechanical properties as

$$\kappa = ((1 - \nu_i)/G_i + (1 - \nu_j)/G_j) / ((1 - 0.5\nu_i)/G_i + (1 - 0.5\nu_j)/G_j), \quad (17)$$

where ν is the Poisson's ratio and $G = E/(2 + 2\nu)$ with Young's modulus E is the shear modulus of the two interacting materials i and j [98].

Rolling friction

Research has shown that the dissipation of energy due to particle rotation has a significant impact on the behavior of bulk solids [99], resulting in the incapability of the DEM to reproduce real static angles of repose of heaps with spherical particles if only the force models described above are applied. For simulating spherical particles in the DEM and thereby, reproducing the rolling resistance between the contact partners, a model for rolling friction is required to oppose the rolling motion of the spheres with a decelerating moment \vec{M}_{roll} . In all the publications which are part of this thesis, the model by Zhou et al. [100] is applied for spherical particles, where the decelerating moment is calculated as

$$\vec{M}_{roll} = -\mu_{roll} |\vec{F}_N| r_{eff} \frac{\vec{\omega}}{|\vec{\omega}|}, \quad (18)$$

with the coefficient of rolling motion μ_{roll} , the absolute value of the normal force $|\vec{F}_N|$ and the reduced effective radius $r_{eff} = r_i r_j / (r_i + r_j)$ of the contact partners i and j .

3.3.5 Liquid bridge forces

In addition to non-cohesive particle contacts, the DEM requires fine-particle or wet-particle forces for the simulation of cohesive particles, depending on the particle properties according to Ge et al. [101]. Interactions between fine particles are mostly described by the Johnson-Kendall-Roberts [102] or the Derjaguin-Muller-Toporov model [103], whereby the former is used for large surface energies and the latter for low surface energies and smaller particles. In contrast, for slightly wet or moist particles, liquid bridge forces have to be considered [101]. A lot of theoretical work has been done in this field and several researchers have proposed various expressions for the determination of capillary forces (comp. e.g. [104–106]), viscous forces (comp. e.g. [107–110]) as well as for the formation, the shape, the liquid volume and the redistribution of liquid due the rupture of a liquid bridge [111,112]. Furthermore, some closed form expressions for the accurate calculation of liquid bridges were proposed [113,114] and the derived models were applied in DEM simulations (comp. e.g. [115–119]). All these models are limited on calculating forces in pendular regimes, whereas only a few researchers also investigated the funicular state [120–122].

Further information concerning liquid bridge research can be found in the investigations in this thesis, where particles under the influence of moisture are considered (publications IX-X). Therein, only the pendular state (comp. section 3.1.1) with small amounts of liquid is considered. Accordingly, individual liquid bridges exist only between pairs of particles, resulting in several adhering forces. In the DEM model used for this thesis, only the capillary force \vec{F}_{ij}^{cap} as well as the viscous forces in normal \vec{F}_{ij}^{nvis} and tangential direction \vec{F}_{ij}^{tvis} are applied, resulting in the total liquid bridge force

$$\vec{F}_{ij}^l = \vec{F}_{ij}^{cap} + \vec{F}_{ij}^{nvis} + \vec{F}_{ij}^{tvis}, \quad (19)$$

which is calculated in addition to the contact force in eq. (9). The external moment \vec{M}_i in eq. (10) is also extended and is now the sum of the moments due to a contact $\vec{M}_{C,i}$ and a liquid bridge $\vec{M}_{L,i} = \vec{r}_i \times \vec{F}_i^{tvis}$.

When two particles i and j or a particle and a wall get into contact in a moist system, a liquid bridge forms out between them. A respective amount of water of both contact partners contributes in the liquid bridge which is assumed to be constant until its rupture, which occurs according to Willett et al. [105] when the distance S between two contact partners with $r_i \geq r_j$ is larger than

$$S_{rup} = 2r_{reff} \left(1 + (0.25\theta_{ij}) \left(1 + \frac{r_j}{r_i} \right) \right) \left(\left(\frac{V_{lb}}{8r_{reff}^3} \right)^{1/3} + \left(\frac{r_j}{2r_i} - \frac{2}{5} \right) \left(\frac{V_{lb}}{8r_{reff}^3} \right)^{2/3} \right). \quad (20)$$

During the liquid bridge contact, the capillary forces between two particles as well as between a particle and a wall are obtained according to Rabinovich et al. [104] and Pitois et al. [109] as

$$\vec{F}_{ijpp}^{cap} = \left(\begin{array}{c} -\frac{2\pi\sigma r_{eff}(\cos\theta_i + \cos\theta_j)}{1 + 1/\left(\sqrt{1 + \frac{2V_{liq}}{(\pi r_{eff} S^2)} - 1}}\right)} - 4\pi\sigma r_{eff} \sin(\theta_{ij}) \sin(\theta_{ij} + \varphi_{ij}) \end{array} \right) \vec{n}_{ij}, \quad (21)$$

$$\vec{F}_{ipw}^{cap} = \left(\begin{array}{c} -\frac{2\pi\sigma r_i(\cos\theta_i + \cos\theta_w)}{1 + S\sqrt{\pi r_i/V_{lb}}} - 2\pi\sigma r_i \sin(\theta_{iw}) \sin(\theta_{iw} + \varphi_{iw}) \end{array} \right) \vec{n}_{iw}, \quad (22)$$

with the surface tension coefficient σ , the static contact angles θ_i , θ_j and θ_w of the particles i , j and a wall, respectively as well as their mean values θ_{ij} and θ_{iw} (comp. [123]), the separation distance S and the half filling angles

$$\varphi_{ij} = \sqrt{S/r_{eff} \left(-1 + \sqrt{1 + V_{lb}/(\pi r_{eff} S^2)} \right)} \quad (23)$$

and

$$\varphi_{iw} = \sqrt{2S/r_i \sqrt{1 + V_{lb}/(\pi r_i S^2)}}. \quad (24)$$

Furthermore, viscous forces are considered, calculated in normal direction according to Pitois et al. [109] as

$$\vec{F}_{ij}^{nvis} = -\frac{6\pi\eta r_{eff}^2 \vec{v}_{ij}^n}{S} \left(1 - 1/\sqrt{(1 + V_{lb}/(\pi r_{eff} S^2))} \right)^2, \quad (25)$$

with the liquid dynamic viscosity η . In tangential direction, Goldman et al. [108] introduced the following correlations

$$\vec{F}_{ij}^{tvis} = -6\pi\eta r_{eff} \left(\frac{8}{15} \ln \frac{r_{eff}}{S} + 0.9588 \right) \vec{v}_{ij}^t - 6\pi\eta r_{eff} \left(\frac{2}{15} \ln \frac{r_{eff}}{S} - 0.2526 \right) \vec{\omega}_{ij} \times \vec{n}_{ij}, \quad (26)$$

$$\begin{aligned} \vec{F}_{ij}^{tvis} = & -6\pi\eta r_{eff} \left(\frac{8}{15} \ln \frac{r_{eff}}{S} + 0.9588 \right) \vec{v}_{ij}^t \\ & - \frac{6\pi\eta r_{eff}}{8} \left(\frac{r_{eff}}{S + r_{eff}} \right)^4 \left(1 - \frac{3r_{eff}}{8(S + r_{eff})} \right) \vec{\omega}_{ij} \times \vec{n}_{ij}, \end{aligned} \quad (27)$$

valid for $S < 0.1r_{eff}$ and $S \geq 0.1r_{eff}$, respectively, with $\vec{v}_{ij}^t = \vec{v}_i - \vec{v}_j - \vec{v}_{ij}^n$ as the tangential relative velocity and $\vec{\omega}_{ij} = r_i \vec{\omega}_i + r_j \vec{\omega}_j$ as relative rotational velocity of the spheres.

A detailed explanation and derivation of the equations concerning the formation of a liquid bridge and the liquid distribution after the rupture as well as different force models can be found in publication IX.

3.4 Determination of DEM parameters

In order to perform DEM simulations suitably and reliably, several material parameters like particle size, shape, density, stiffness as well as the coefficients of friction and restitution are required, which are often only assumed or taken from literature, with and without validations but should be ideally obtained by various own measurements [124–126]. However, respective small scale experiments for the calibration of DEM parameters of bulk material can be time consuming, leading to the need of efficient and robust calibration procedures [125,127]. Therein, it must be differentiated between the material properties, which can be measured on a single particle or at a bulk level and DEM parameters that have to be stated for single particles to obtain the same bulk behavior in simulations as for the physical material [126]. Different procedures and methods to obtain DEM parameters experimentally were introduced and applied in investigations in the past, from which some are described in the following.

Very recently, a comprehensive review including the presentation of various methods is provided by Coetzee [126] and a complete strategy to determine DEM parameters is given in publication VII, where several of these methods are applied. According to these works, a researcher can choose between two overarching methods or a combination of both to determine the DEM parameters. In the first one, bulk experiments and simulations with the same setup are performed, whereby the simulation parameters are iteratively adjusted to match the experimentally obtained data exactly, independent of the accurate representation of each single property. Disadvantages of this method are the potential limitation to the investigated application and the used DEM code as well as the partial loss of the physical meaning of the DEM parameters [125]. In contrast, these disadvantages are not present when applying the second method in which the single particle properties are directly measured. Difficult in this approach is the parameter determination for small and arbitrarily shaped non-spherical particles [125,126]. Even if the values are measured with a high accuracy, the results in bulk experiments and simulations can differ, because of a low accuracy in modeling the size and shape of the particles in the simulations due to computational limitations [128–130]. The last option is to combine both overarching methods by first determining the parameters with the second method followed by an adjustment to small scale experiments according to the first method and a later validation against the real application (comp. publication VII).

Single particle characteristics

Two of the most important parameters for DEM simulations are the particle size and shape, which have to be determined in advance of other parameters. Particle size distributions were already described in section 3.1.3. However, for some large scale applications, the real size distribution is not applicable, due to large computational costs. To overcome this problem, particle sizes can be increased or scaled up [81, 131–133]. This method is not further discussed due to being not sufficiently investigated for the applicability in classification processes and in particular for screening. Another method is to group particles with a size below a certain value into one particle size class in relation to this value [134–136], which is applied in this thesis for all validations between simulations and experiments involving non-spherical particles (publications I, VI-VIII). Thereby, only particles, which are much smaller than the aperture or cut size without a noticeable influence on the other particles, are considered as one size class. For more details on both methods including laws, tests and opportunities, it is referred to the work by Coetzee [126].

Several approaches to form shapes of non-spherical particles were shown in section 3.3.1, but one main challenge is how to approximate real shapes with these approaches. Some researchers represented simple model shapes, by manually putting some spheres together to approximate these geometries. Among others, Markauskas et al. [137] used between 3 and 50 different sized spheres to represent ellipsoidal particles, whereas Caulkin et al. [138] represented cylindrical particles with several different sized spheres in eight different arrangements. Particles with a slightly more complex shape were modeled by Pasha et al. [139] who represent corn grains with a clump of several spherical particles generated by an automated optimization process based on a 3D x-ray tomography model. In contrast, Williams et al. [140] evaluate descriptions for the irregular particle shapes of iron ore by a digital image segmentation technique and generate corresponding non-spherical DEM particles out of it. Mollon and Zhao [141] introduced a method to generate 3D non-spherical particles based on three 2D contours of the cross-sections of random realistic sand grains. A similar method is shown in publication VII for gravel particles using an automated algorithm. Furthermore, Lu and McDowell [142] developed an automated method to model various shaped non-spherical ballast particles comprising of a various amount of randomly positioned and sized spherical particles (comp. Fig. 21a). In addition, Coetzee [127] represents gravel particles with the multi-sphere approach using different amounts of particles and two different methods (comp. Fig. 21b). He compared the automatic approach also used by Pasha et al. [139], where particles are automatically created and optimized in size and shape based on scanned 3D models with a manual approach, where visual observations are used to identify distinct shapes.

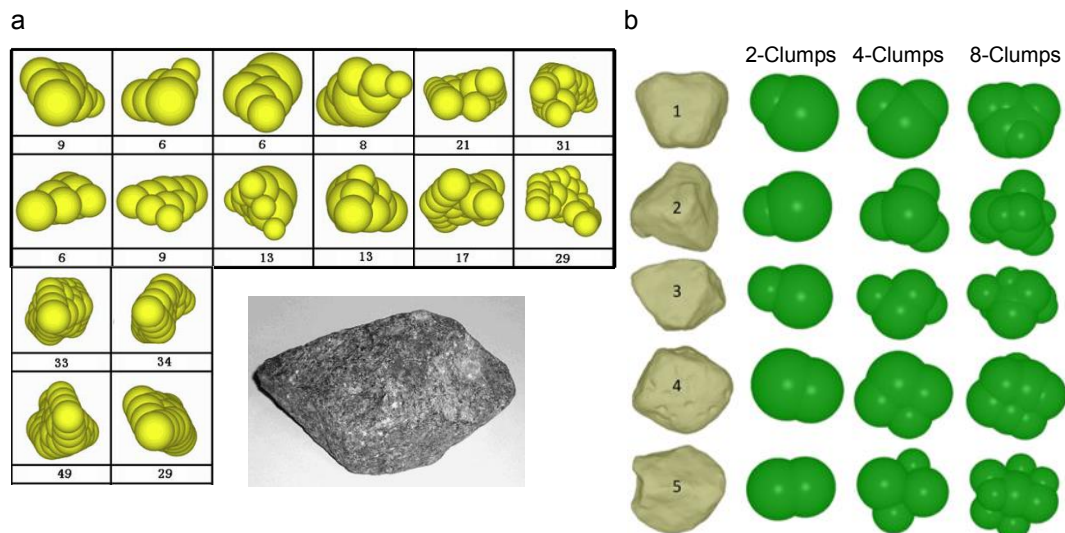


Fig. 21: Particle shape approximation with the multi-sphere approach by automated optimization processes (a) for ballast particles with 6 to 49 spheres (comp. [142]) and (b) gravel consisting of two to eight spheres (comp. [127]).

Further important parameters for DEM simulations, which can be determined by direct measuring approaches, are the particle density, the stiffness, the Young's and shear modulus, the sliding and rolling friction as well as the damping and the restitution coefficient. The particle density is mostly obtained by the pycnometer method, in which the volume of a respective amount of particles with known weight is determined by submerging it in a vessel with water [97,143].

If a linear contact model is applied, like in this thesis, the particle stiffness is specified based on an appropriate calibration with various small scale experiments (e.g. shear tests) or by sensitivity analyzes. Therein, based on the particle overlap, the contact stiffness can be reduced to increase the time step and to save computational time to some extent without a significant deficit in accuracy [125,144–147]. Note that usually, average overlaps should not be larger than 0.5 % of the particle diameter (comp. e.g. [148]).

In contrast, researchers who use Hertz-Mindlin models, calculate the contact stiffness based on the Young's modulus, the shear modulus and the Poisson's ratio. Thereby, the Young's modulus is obtained by uniaxial compression tests in which single particles are compressed [143,149,150]. Note that the particle stiffness can also be reduced with appropriate calibration procedures when Hertz-Mindlin models are applied.

Several researchers obtained the particle-wall sliding friction with different approaches. A method to obtain the sliding friction between two particles was developed by Senetakis et al. [151], who designed an apparatus to perform shearing tests for small displacements, loads and particles of non-spherical shape. Barrios et al. [130] measured the contact sliding friction coefficient with a pin-on-disc rotating tribometer. This apparatus is capable of determining the particle-wall coefficient between one fixed particle and a rotating disc out of the wall material or the particle-particle coefficient with several small particles on the disc representing the

particle surface. Similar measurements can be performed with a modified pin-on-disc rheometer [149,152]. Furthermore, the sliding friction coefficient can be obtained by using a direct shear box (e.g. Jenike shear cell), where one wall is replaced with the desired wall material and the particles are sheared over it (comp. e.g. [132,153–155]).

The static particle-wall friction can be measured by placing single particles or particles glued under a plate on a tiltable plate, which is inclined until the particles start to slide (comp. Fig. 22a). Then the inclination angle can be measured to obtain the static particle-wall friction coefficient $\mu_{s,pW} = \tan(\varphi)$ [143,156,157] (not applied in the investigations in this thesis). A similar method was also applied to determine the friction between particles, in which the plate consists out of the same material as the respective particle [158]. In addition, this method can be used for an adjustment to DEM simulations, where the friction parameter is changed iteratively until the particles start to slide under the same inclination angle in experiment and simulation [159].

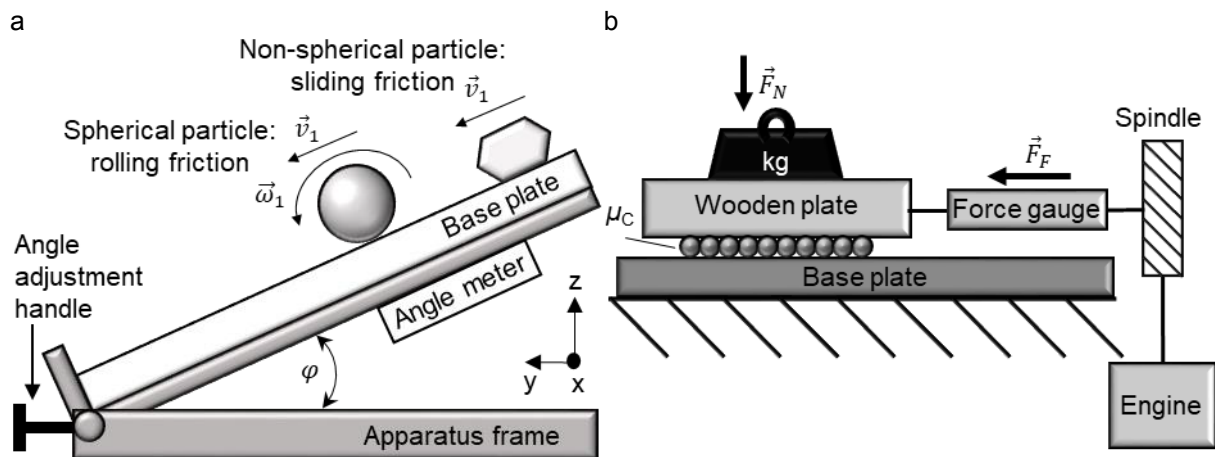


Fig. 22: Determination of (a) the static or rolling friction with an inclined plate [130,143,157] and (b) the sliding friction by dragging one contact partner over another [97,160].

For the investigations in this thesis, the sliding friction between two contact partners is adopted from literature data (publications I-VI) or obtained with the experimental setup shown in Fig. 22b (comp. [97,160], publications VII-X). Therein, samples of particles consisting of the material of the first contact partner are glued under a wooden plate, which is stabilized by a weight and pulled by an engine connected with a string. Then a force gauge measures the constant force, which is required to drag the particles uniformly over a plate consisting of the material of the second contact partner. If the effect of the contact area is ignored, a point-point contact can be assumed. As a consequence, the classical friction theory can be applied, where the coefficient of sliding friction is $\mu_c = |\vec{F}_F|/|\vec{F}_N|$, with the frictional force \vec{F}_F and the normal force \vec{F}_N . A similar experiment without the spindle (comp. Fig. 22b) is used to obtain the static friction coefficient at the moment when the plate with the particles starts to move [97,160].

With a known sliding friction, the rolling friction can be obtained with the same method used for the sliding friction (comp. Fig. 22a), directly applicable for a particle-wall and by using the

particle's material as surface for particle-particle contacts. Therein, the rolling friction coefficient in the simulation is iteratively adjusted so that the inclination angle is the same as in the experiment when the particle starts to roll (comp. [130]). Dependent on the applied model for the rolling friction, the coefficient of rolling friction between a sphere and a wall can also be obtained directly (not applied in this thesis). The inclination angle when the sphere starts to roll φ must be measured to calculate $\mu_{roll} = \tan(\varphi)$ [99,132,153].

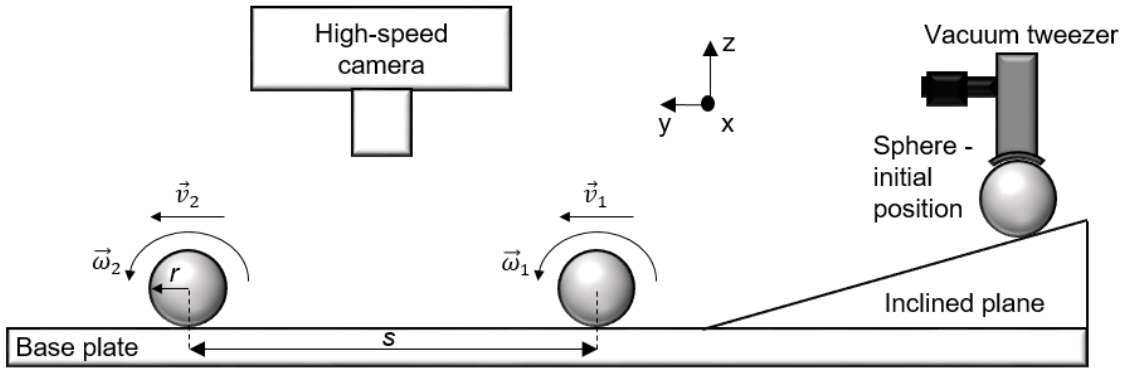


Fig. 23: Determination of rolling friction by measuring the alteration in velocity (comp. [161]).

In order to obtain the rolling friction coefficient experimentally in this thesis (comp. Fig. 23, publications VII-X), the velocity of a rolling sphere at the beginning (v_1) and at the end (v_2) of a flat surface with the length s is detected by image analysis of records taken with a high-speed camera from the top [161]. To ensure the same conditions for every attempt, the sphere is placed at its initial position on an inclined plane with a vacuum tweezer, before it is released. The measuring starts and ends always at the same positions on the base plate.

If the normal force \vec{F}_N is equal to the weight force of free rolling spherical particles, eq. (18) can be simplified and the coefficient of rolling friction can be calculated as

$$\mu_{roll} = |\vec{M}_{roll}|/|\vec{F}_N|. \quad (28)$$

The moment \vec{M}_{roll} is then determined by

$$|\vec{M}_{roll}| = \left(1/2 m(v_1^2 - v_2^2) + 1/2 \theta(\omega_1^2 - \omega_2^2)\right) d/(2s), \quad (29)$$

with the sphere's mass moment of inertia θ , its angular velocity at both time steps ω_1 and ω_2 and its half diameter $d/2$. If the sphere does not slip or bounce and moves slowly on the applied plane surface, the angular velocity ω can be obtained through the translational velocity v [161].

In the investigations in this thesis, several methods to experimentally obtain the coefficient of restitution are applied (comp. Fig. 24, publications VII-X). In all cases, one particle consisting of the material of one contact partner is hold tight in a respective position. This is first ensured by a small removable border and later by a vacuum tweezer to minimize external influences. In the method shown in Fig. 24a, the restitution coefficient between two particles is obtained according to Wong et al. [162], González-Montellano et al. [143] and Alonso-Marroquín et al.

[157]. Therein, a particle, which is connected to the end of a pendulum, is released from the vacuum tweezer to drop down, leading to a particle motion of a circular path until it bounces against another motionless particle consisting of the material of the second contact partner. Then, the restitution coefficient for this particle-particle contact is determined by

$$e_{pp}^n = -(v_1 - v_2)/u_1 = (\sqrt{H_2} - \sqrt{H_1})/\sqrt{H_0}, \quad (30)$$

where u_1 and v_1 as well as H_0 and H_1 are the velocities and the heights of particle P_1 before and after the collision, respectively. In addition, the velocity of particle P_2 after the collision with P_1 is v_2 and its height is H_2 .

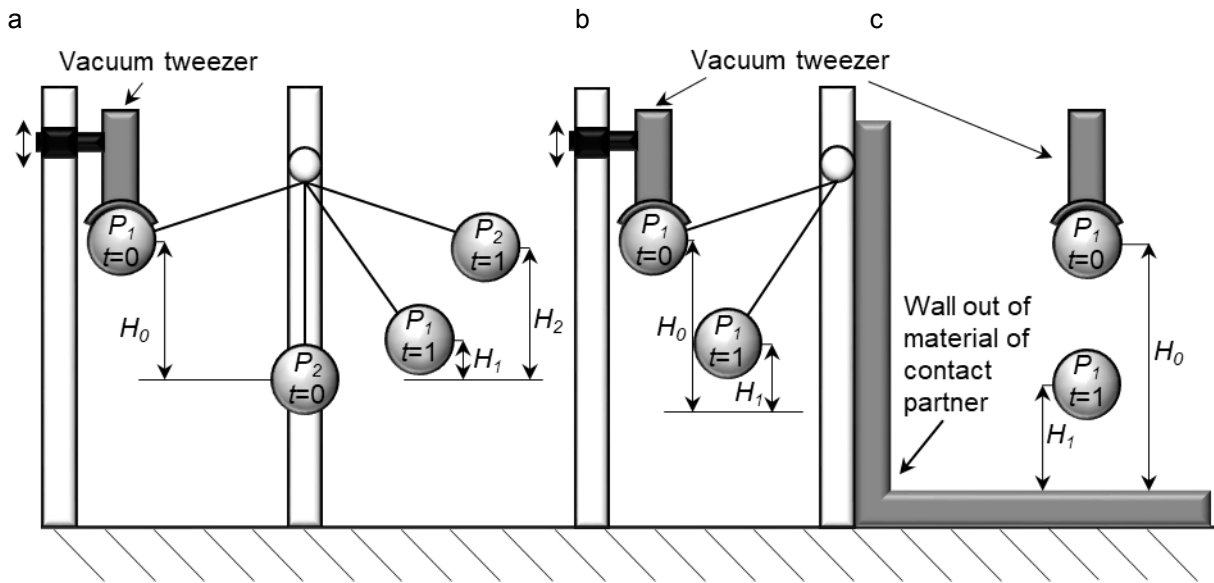


Fig. 24: Determination of the restitution coefficient for (a) particle-particle contacts with the double pendulum method [143,157,162] and particle-wall contacts with (b) the pendulum method and (c) the drop test [143,157,163,164].

If the same external effects in both experiments are important, the particle wall collisions are performed according to Fig. 24b, in which the second particle is replaced with a wall of the desired material. A second applied method to obtain the restitution coefficient between a particle and a wall, which is less influenced from external effects, is the common drop test (comp. e.g. [143,144,149,157,163,164]) shown in Fig. 24c. Therein, one particle is dropped vertically without a pendulum on the wall. It can be applied for spherical and non-spherical particles by taking the angle of travel and the angular velocity into account [156,165,166]. Note that the drop test can directly be used to measure the restitution coefficient for particle-wall contacts (comp. e.g. [143,144,149,157,163,164]). By fixing a second particle on the ground [156] or by taking a wall out of the particle's material, it can also be applied for particle-particle contacts [144]. In both cases, the velocities before (u_1) and after the rebound (v_1) or the heights before the particle drop (H_0) and at the highest point after the rebound (H_1) are measured, resulting in a restitution coefficient of

$$e_{pW}^n = -v_1/u_1 = \sqrt{H_1/H_0}. \quad (31)$$

Adjustment of DEM parameters of particles as bulk material

For the other overarching method on a bulk material level, various small scale experiments are carried out, whereby one or more parameters of respective DEM simulations are iteratively adjusted to fit the experimental results. To adjust the bulk density, simple box filling experiments can be performed with a container of known volume, where the same particle bed height should be achieved in experiments and simulations (comp. e.g. [127,167–169]).

A very common method to account for the sliding and rolling friction, particularly between particles but also between particles and walls, is to measure the static angle of repose in a slump or pile formation test (comp. e.g. [70,81,125,129,130,153,155], publication VII). Therein, a various formed container filled with the particles used in the real application is lifted from a plate or opened at the bottom, leading to the release of the particles and to the formation of a pile from which the angle to the horizontal can be measured. The material of the container and the base plate consists of the same material as the wall elements in the simulations.

Another approach for adjusting the sliding and rolling friction coefficients is based on measuring the dynamic angle of repose, which forms out by bulk particles in a rotating drum. This angle is compared to the results of respective simulations, where the same particle and wall properties like in the experiment are applied (comp. e.g. [130,149,170–173], publication VII).

Furthermore, hopper or silo experiments are performed, where the discharge time or rate as well as the velocity of particles flowing out of the hopper can be compared to simulation results (comp. e.g. [81,174–177]). This experiment is mainly influenced by the sliding and rolling friction, but was also applied to adjust the contact stiffness [175,178].

In addition, several researchers used direct or ring shear tests to measure the bulk friction angle. Subsequently, various parameters like the stiffness (e.g. [128,167,179]), the sliding (e.g. [127,128,180–182]) and the rolling friction (e.g. [128,181]) are iteratively adjusted to obtain similar results in simulations and experiments. These tests were also rarely applied to adjust damping coefficients [128]. Other researchers prefer in-situ penetration tests for the same purposes to account for uninfluenced particles [124,132,153].

In order to adjust the stiffness and the friction independently of each other, a confined uniaxial compression test with a bulk of particles can be performed to obtain the bulk stiffness in advance of the shear test. This approach is only influenced by the particle stiffness, which is gained from the determined bulk stiffness due to a linear relationship (e.g. [127,167–169,182]).

The coefficient of restitution or the damping can also be adjusted by the experimental and numerical comparison of the particle behavior and the average particle height in vibrated beds (e.g. [183], publication VII) as well as by reverse calibration applying the drop test [130].

In addition, most of the calibration procedures like hopper discharge [184], rotating drums [144] as well as shear [146] and compression tests [185–187] are also used to validate the applied particle shapes. More details on the approximation algorithm for non-spherical particles as well as the determination and adjustment of DEM parameters can be found in publication VII.

3.5 DEM screening validations and investigations

Batch sieving DEM simulations were rarely considered in literature, due to its lower relevance for large scale industrial applications. However, this process mode provides an easier access to the relevant sieving subprocesses, stratification and passage and is ideally suited for the derivation of process models (comp. section 3.6). Its advantages were first taken by Shimosaka et al. [46], who modeled a small scale sieve with a low amount of spherical particles. A similar setup was later applied by Yoshida et al. [5] for studies on the sieving rate and process models. Further small scale batch sieving simulations were carried out by Tung et al. [188].

For this thesis, DEM batch sieving investigations and sensitivity studies are performed and presented in publication II. A comparison between batch sieving experiments and simulations is also performed and visualized in Fig. 25.

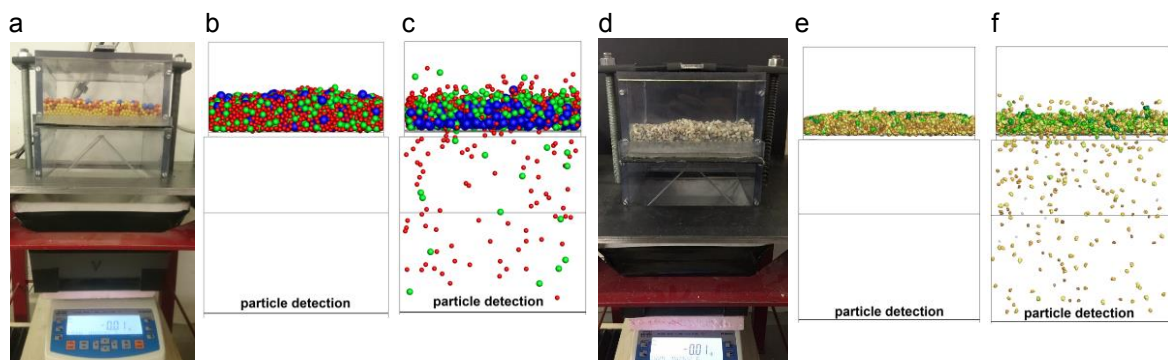


Fig. 25: (a) Experimental batch sieving setup applying POM spheres at $t = 0$ s and the corresponding DEM approximation at (b) $t = 0$ s and (c) $t = 3$ s as well as (d) the experimental batch sieving setup applying quartz gravel at $t = 0$ s and the corresponding DEM approximation at (e) $t = 0$ s and (f) $t = 3$ s.

In the corresponding investigations (publications VI, VII), POM spheres with three different particle sizes of $d_1 > a > d_2 > d_3$ (Fig. 25a-c) and quartz gravel (Fig. 25d-f) with a specified particle size distribution (comp. Fig. 84) and approximated as complex multi-sphere particles are applied. The experiments are shown at $t = 0$ s in Fig. 25a,d and the DEM simulations are represented at $t = 0$ s in Fig. 25b,e as well as at $t = 3$ s in Fig. 25c,f, respectively. The particles are filled into the screen box well mixed and pass the apertures supported by a nearly vertical vibration. The passage is detected below the screen with a balance in the experiments and by a position check of the particles in the simulations.

One of the first researchers, who simulated continuously operated throwing screens in 2D were Li et al. [50,189], who studied the effect of the bed depth and the influence of near mesh and

oversize particles. Batch and continuous screening were studied by Alkhaldi and Eberhard [190] on a multi-level tumbling screen. Based on this setup, a comparison between two different mesh descriptions on the continuously operated tumbling screen was carried out by Alkhaldi et al. [191].

Delaney et al. [20] applied spherical particles in the DEM to simulate a continuous screening process on a horizontal aligned throwing screen and to validate it against experiments with quarry rock particles. Based on these results, the first validation of DEM screening simulations in this thesis with various non-spherical particles is performed in publication I. Zhao et al. [192] used the DEM to simulate the screening process of spherical particles on an inclined screen with a circular vibration, followed by a study on the influence of vibration mode of Dong et al. [35] with otherwise identical conditions. The analyzed circularly operated screening process was later validated against experiments [193] and optimized in terms of screening efficiency [36]. The particle flow on an elliptical vibrated screen was numerically investigated by Yin et al. [194].

Furthermore, Dong et al. [195] and Liu et al. [196] studied the flow of spherical particles on simulated single deck banana screens, whereas Jahani et al. [197] additionally investigated the screening performance on double deck banana screens. Large scale research was carried out by Cleary et al. [6,198], who analyzed the separation performance and the particle flow on double deck banana screens applying superquadrics. A suitable method to decrease computational effort when simulating such complex screening processes is to apply periodic boundaries (comp. [199]). Therein, only a narrow sector of the screen with a lower amount of discrete elements need to be simulated and the particles, which protrude beyond the computational domain on one side influence the particles on the other side. If the center of a particle cross the domain boundary, it is transferred to the other side.

Besides the investigation in publication I, a similar configuration is applied in publications III-V, where also inclined and banana screens are studied (comp. Fig. 26). Therein, three particle size classes with $d_1 > a > d_2 > d_3$ are applied, continuously fed at the feed end and classified under various operational conditions, whereby the undersized particles pass the apertures and the oversized particles are transported to the discharge end. The snapshots from the side and the top in Fig. 26 clearly reveal the advantages and disadvantages of the three different screen apparatuses. The horizontal screen (Fig. 26a) has the spatially earliest passage, but accumulations occur close to the feed end, demonstrating the unsuitability for larger mass streams. By inclining the screen (Fig. 26b), all particles are transported faster without retardations, but with the drawback of several small particles classified in the overflow. The curvature of the banana screen (Fig. 26c) combines the sharp separation of the horizontal screen spread over the whole screen length with a sufficient transport velocity.

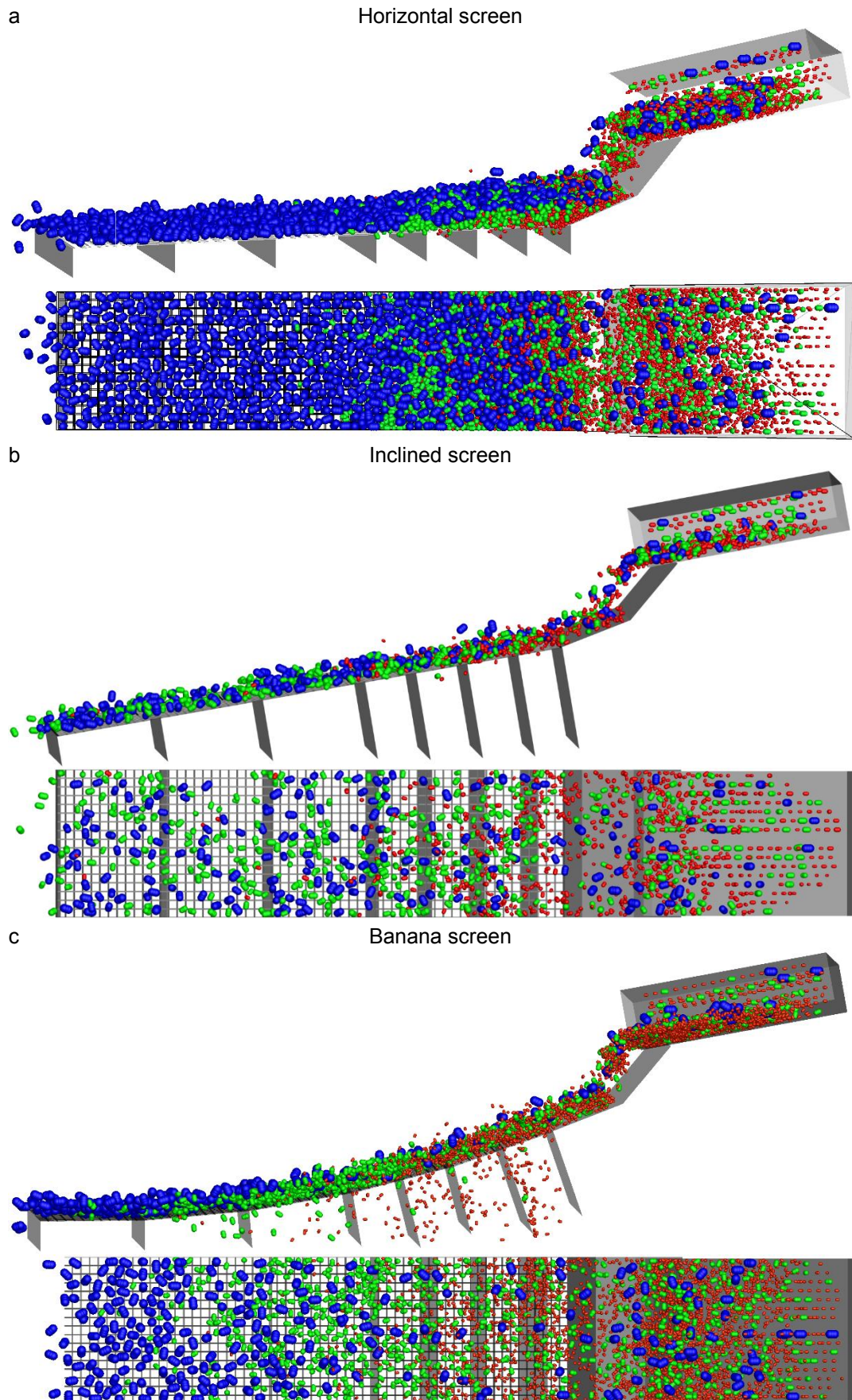


Fig. 26: Comparison of the three different vibrated throwing screens presented from the side and the top: (a) horizontal screen, (b) inclined screen and (c) banana screen.

A direct validation against own experiments is carried out in publication VIII on an inclined screen applying quartz gravel as material approximated with simple multi-sphere particles.

Numerical simulations of screening under the influence of fluids have rarely been performed until now. The DEM coupled with computational fluid dynamics (CFD) was used by Li et al. [200] to simulate an air-and-screen cleaning device, whereby the motion of the material was studied. Fernandez et al. [9] modeled wet banana screening by considering the coarse particles approximated as superquadrics and their influence on a slurry flow consisting of a fluid and small particles through a one-way coupling of the DEM with the smoothed particle hydrodynamics (SPH). Further investigations concerning wet screening by a two-way coupling of DEM and SPH were carried out by Sinnott et al. [148] for a drum screen attached to the outlet of a ball mill as well as by Sinnott and Cleary [201], who studied the mixing in the feed box for a screen.

In addition, Dong and Yu [202] simulated the particle flow and screening behavior by using the DEM for the particles and the CFD for the water flow. Very recently, Cleary et al. [203] investigated the screening process under the influence of particle cohesion with a similar configuration as Fernandez et al. [9]. Barbabela e Silva et al. [204] also applied the DEM extended by a model for considering the particle cohesion of spheres on a single deck roller screen and compared it to experimental results of green iron ore pellets with a moisture content of 9.6 %. Note that a validation of batch sieving simulations under the influence of liquid based on corresponding experiments is shown in publication IX. The validated simulations are analyzed in publications IX and X.

Additionally, with regard to the approximation of the screen surface geometry, the accuracy has to be weighed against the computational demand. Due to the comparatively low calculation costs, most researchers (comp. e.g. [6,49,192]) applied screen wires with a rectangular profile (comp. Fig. 27a).

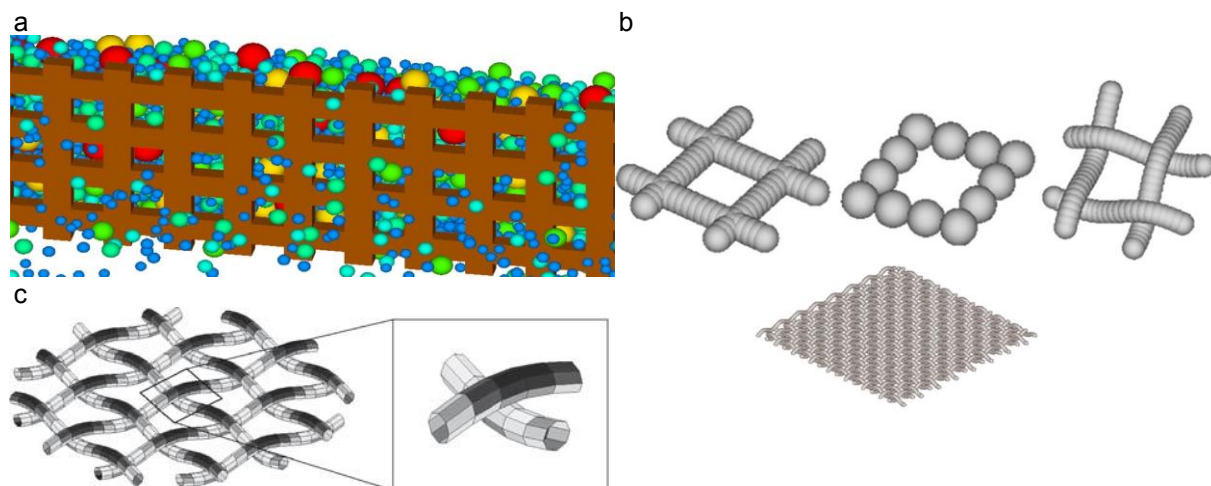


Fig. 27: Representation of the screen surface geometry as (a) grid with a rectangular wire profile [49], (b) various approximations by applying several rigid spherical bodies close to each other [188] and (c) woven mesh with several small wall elements [191].

However, Tung et al. [188] studied different approximations for the woven mesh structure on a batch sieve by applying several rigid spherical bodies close to each other (comp. Fig. 27b). The relevant geometry of the sieve wires has also been analyzed by Alkhaldi et al. [191], who applied a woven mesh structure with several small rectangular wall elements (comp. Fig. 27c). The geometry of the screen mesh is also analyzed numerically in publication I and the outcome concerning the approximation of the screen wires is used for considerations in the following publications.

3.6 Process models

In this section, flowsheet simulations of solids processes and in particular, phenomenological process models for screening are introduced and briefly discussed.

3.6.1 Flowsheet simulations of solids processes

A large amount of parameters has to be considered when solids production processes should be developed or optimized. These processes are often very complex and comprise of several separated subprocesses, which are connected over energy or mass streams. Therefore, it is important to study the steady and dynamic behavior of these processes [205].

A granulation process including a grinding classification circuit including two screens and a crusher as exemplary solids production process is shown as a flowsheet in Fig. 28. The challenge of modeling such flowsheet simulations increases for complex interconnections between the subprocesses as well as for different time-dependencies and dynamics, leading to the condition to solve the entire process at once and not each unit separated [205]. Therein, a differentiation can be made between steady state and dynamic modeling [206]. In the first stated, all processes are calculated under steady operation conditions including time constant process variables and a fulfilled mass and energy balance without accumulations. In contrast, in a dynamic modeling, accumulations and unbalanced systems can be considered to cover a large number of additional problems like oscillations, batch or semi-batch processes, load changes as well as startup and shutdown procedures [205]. Besides direct dynamic behavior in one process unit, dynamic effects can also be a result of changes in upstream process steps and additionally, they are able to influence subsequent downstream processes. To prevent interruptions or mechanical breakdowns in industrial processes in the worst case, the understanding of transient processes and the development of transient process models are essential [207]. In order to study the dynamic behavior of entire solids process chains without performing extensive experimental investigations, these models must be connected by a robust and efficient dynamic process simulation framework [208]. Note that such a framework for solids processes must satisfy very different requirements than a similar one for fluid processes [209] due to the complexity and disparity of the solid phase with sets of distributed

parameters, which can even be dependent on each other [210]. Therefore, most of the current dynamic simulation tools are designed for fluid processes with some limited extensions for the solid phase.

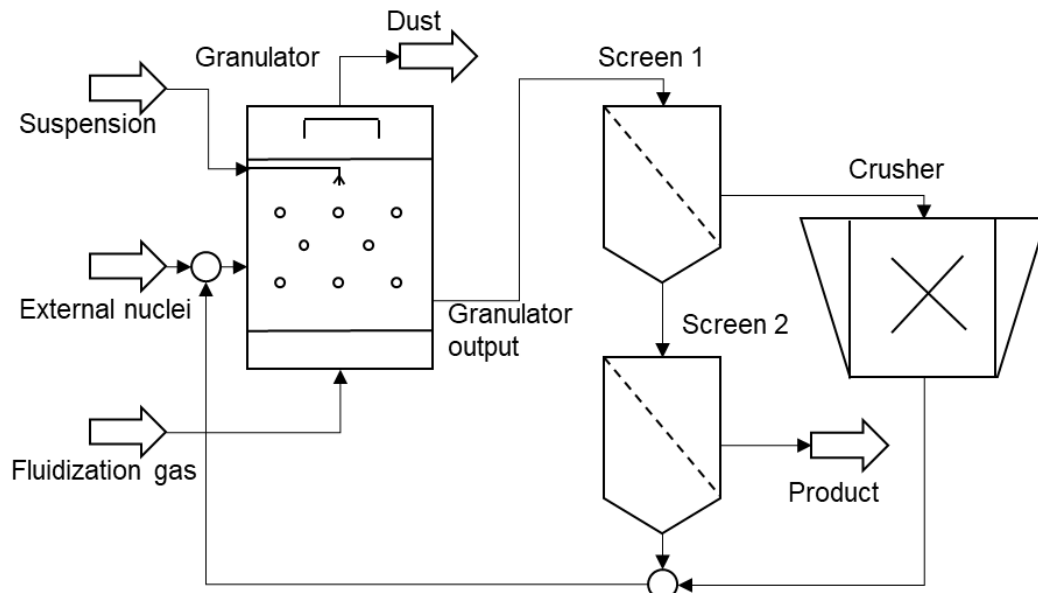


Fig. 28: Granulation process including a comminution classification circuit as an example of a solids production process [205].

At present, some commercial dynamic simulators like Aspen Plus Dynamics exist, which is applied in the chemical and petrochemical industry for fluid processes with a limitation in the solid phase [205,211]. In addition, gSOLIDS is used for dynamic simulations of solids processes and for the development and optimization of related operations with the drawback of not taking multidimensional distributed solid parameters into account [205,212]. Further dynamic process simulation tools for fluids are Apros, which is applied in the nuclear and thermal power plant sector [213] as well as PRO/II and DYNsIM, both used in the field of oil and gas plants [214]. Moreover, an extension to the steady state solids process simulation tool SolidSim allows for modeling dynamic effects [215], which was successfully tested in studies concerning the transient behavior of fluidized bed granulation plants [207].

From these examples, the necessity of developing methods, models and respective simulation frameworks for simulating dynamic connected solids processes with complex structures and parameters arises. Besides the study of the dynamics of solids processes and the development of various dynamic process models, a new framework for dynamic simulations of solids processes (Dyssol) was designed as part of the DFG priority program SPP 1679. Further information concerning the Dyssol system can be found in the work by Skorych et al. [205], where this novel tool for dynamic flowsheet simulations of solids processes is introduced. The Dyssol framework has already been tested for a chemical looping combustion process by Haus et al. [216] and will be further applied for connected solids processes like a combination of multiple classification and comminution units in the future.

3.6.2 Phenomenological process models for screening

In order to analyze entire process chains of interconnected solids processes, the understanding of the individual processes and their modeling as process models is inevitable. Until now, these models are often empirical to some extent, their parameters need to be adjusted to measured data to obtain reliable results and thus, they are dependent on material properties and apparatus geometries [215,217]. In particular, a predictive process model for screening including the consideration of its inherent transient nature as well as directly induced or resulting dynamic effects would be significant for industrial process design, monitoring and optimization [207].

For the representation of the particle size separation during a screening process without performing extensive experiments, several phenomenological screening process models are available. One type of representation of process models are the already described separation curves, which are limited to represent the steady state operation of continuous screening. Several researchers introduced empirical equations to estimate separation curves in order to provide integral results of the particle size separation. A common applied separation function is proposed in the work by Plitt [218] as

$$T(d) = (1 - a_s) \cdot \left(1 - \exp\left(-\ln 2 \cdot \left(\frac{d}{d_{cut}}\right)^{\alpha_s}\right)\right) + a_s, \quad (32)$$

where a_s considers the bypass of fine material in the overflow without getting into contact with the screen surface and α_s is the separation sharpness. Further equations concerning separation curves were suggested by Dehghani et al. [52] and Rogers [219], which are both based on the model by Hatch and Mular [220]. Another possibility to describe the screen partition number is the Rosin-Rammler function applied by King [221]. In addition, Molerus and Hoffmann [222] introduced a model equation for air separators, which is also applicable for screening processes. Further work in this field was accomplished by Trawinski [223], who gave a mathematical formulation of separation curves and provided a method for the systematic derivation of such functions. This method was recently used for deriving the equations proposed by Hennig and Teipel [27], who extended earlier equations by a second separation sharpness parameter. Further details on separation curve screening model equations and their application can be found in publications III and VIII.

In contrast, other process models are able to represent the particle size separation time-resolved for batch sieving or spatially resolved for continuous screening, whereby the particle size separation proceeds with the position along the screen. Some of the process models were only applied for discontinuous [45] or continuous screening processes [224], while others are applicable for both [225]. Note that most screening models can be used for representing the

two operation modes by changing the length l with the time t in the model equations [224,225] and vice versa.

One type of phenomenological models used to describe the screening process is based on a kinetic process consideration [3,45,47,224,226,227]. Therein, the passage rate is dependent on the properties of the screen apparatus and of the material, whereby varying passage rates are mainly caused by the particle size in relation to the aperture size [221]. The kinetic models are based on the “first-order rate law” [3,47,224] which is presented as the time dependent change in the mass m of the undersized particles remaining on the screen

$$dm/dt = -km, \quad (33)$$

where the screening rate constant k is an adjustable parameter. Based on this, an explicit equation for the fraction retained can be derived as

$$Y = Y(t) = m/m_0 = \exp(-kt), \quad (34)$$

where m_0 is the initial undersize mass at $t = 0$ and m is the remaining mass of the undersize material at time t . The fraction retained is related to the particle density distribution and the cumulative distribution (comp. sections 3.1.3 and 3.2.1) as follows

$$Y = Y(t) = \frac{m_c(t) \int_{d_{min}}^{d_{cut}} q_c(d, t) dd}{m_{in} \int_{d_{min}}^{d_{cut}} q_c(d, 0) dd} = \frac{m_c(t) Q_c(d_{cut}, t)}{m_{in} Q_c(d_{cut}, 0)}. \quad (35)$$

The fraction retained can also be stated per particle size class i if the undersize particles are considered as different fractions and is calculated as

$$Y_i = Y_i(t) = m_i/m_{i,0} = \exp(-k_i t), \quad (36)$$

where $m_{i,0}$ is the initial and m_i is the actual fractional undersize mass. The relation between both values is given by $Y = \sum_{i=1}^n (Y_i \cdot m_{i,0}/m_0)$, with n as number of undersized particle classes.

Besides kinetic models, several probabilistic theoretical models are available [3,52,225,228,229], which are based on the probability of passage p (comp. eq. (5) and eq. (6)) and the number of contacts between the screen surface and the particles. For instance, eq. (5) was used for the first probabilistic model proposed by Gaudin [24]. A probabilistic approach, which is commonly applied and used as basis to represent screening processes was introduced by Subasinghe et al. [228].

Simple kinetic and probabilistic models have in common, that the screening process under crowded conditions is not presented very well [221]. Such conditions occur at the feed end of continuous operated screens and at the beginning of a batch sieving process. Therefore, Ferrara and Preti [230] developed a model, which was later reviewed and validated by Ferrara

et al. [231], where crowded and separated screening is considered and the local passage of one size class under crowded conditions is assumed to be proportional to the mass fraction of this size class on the screen. One simple kinetic model that considers the stratification process in addition to the passage rate was introduced by Subasinghe et al. [227], who described screening as a conjugate rate process

Another screening model, where crowded regions and the interrelations of the two subprocesses stratification and passage are taken into account is the complex time step based model by Soldinger [7], which was later extended to additionally consider the particle size and the bed thickness in the screening process [8]. Based on these models, Asbjörnsson et al. [39] developed a process model for multi deck banana screens.

In addition to these different model groups, capacity models exist, which are used by screen manufacturers to determine the required screen geometry of a given screen type (comp. [48]).

All the previous discussed phenomenological models have in common that they were derived and verified based on data obtained from experiments. With the aim to avoid performing extensive experiments, Shimosaka et al. [46] were the first who showed the capability of the DEM for this purpose. They simulated a small batch-operated sieve and used this data for the development of a phenomenological sieving model. Following this approach, researchers developed and applied screening process models based on DEM simulations in the last years (comp. [5]), which is also done in the publications II, III and VIII. Furthermore, process models are extended for the representation of induced dynamic behavior in publication VI. In addition, the predictability of process models for continuous screening of a thin particle bed was increased by Dong et al. [49,51]. This investigation is used as basis in publication X, in which models are extended for the prediction of batch sieving results under dry and moist conditions by applying parameters adjusted for different operational parameters and liquid amounts. Very recently, Mabote [232] introduced a phenomenological model for wet fine screening processes based on experimental data. Further information on process models for screening and overviews of relevant equations can be found in publications II, III, VI and X or in the respective literature. Together with other models, a dynamic screening process model can be integrated in the context of a modeling framework like Dyssol [205] to simulate connected solids processes under the consideration of dynamic effects. In the following, the results relating the project “Development of a dynamic-physical process model for sieving” are presented in the respective publications.

4. Results and publications

I. Modeling of screening processes with the discrete element method involving non-spherical particles

Harald Kruggel-Emden¹, Frederik Elskamp²

Ruhr-Universität Bochum, Universitätsstraße 150, 44801 Bochum, Germany

¹Email: kruggel-emden@leat.ruhr-uni-bochum.de

²Email: elskamp@leat.ruhr-uni-bochum.de

The following accepted manuscript appeared as journal version in Kruggel-Emden H., Elskamp F., 2014, Modeling of Screening Processes with the Discrete Element Method Involving Non-Spherical Particles, Chemical Engineering & Technology 37 (5), 847-856 and may be found at <https://doi.org/10.1002/ceat.201300649>. Copyright Wiley-VCH Verlag GmbH & Co. KGaA. Reproduced with permission.

Abstract

Phenomena related to sieving of non-spherical particles are investigated numerically in two batch apparatuses and on a horizontally aligned continuous sieve by particle based simulation approaches in the framework of the discrete element method. The feed material is approximated by complex shaped particles composed of clustered spheres. Comparisons are made with regard to the passage through the screen as well as the segregation and transportation on the screen. Results for passage are compared to data from literature, where simulations with spherical particles were performed of a laboratory scale sieve operated with non-spherical quarry rock particles [20]. Additionally, variations in screen inclination are investigated. Experimental results [20] are matched by the simulations. A distinctive influence of particle shape on flow rates and residency times is identified.

Keywords: Simulation, Sieving, Discrete element method, Non-spherical particles

1. Introduction

In mechanical process engineering, but also in energy technology, it is often required to separate bulk materials according to their particle sizes. In typical processes particles are often of non-spherical shape and broad size distribution [2,3] depending on the preceding process steps and the type of bulk solid considered. A technical simple approach for the separation of solid mixtures is sieving. Despite its wide usage in industry, a satisfactory understanding of this process operation is currently still not fully gained.

For the design of sieving processes different complex phenomenological models as well as particle-based simulation approaches such as the discrete element method are available. For phenomenological models a distinction is made between kinetic [3,45,47,224] and probabilistic

theoretical models [3,52,228,233], which both allow time-resolved representation of the screening process. Kinetic models are often based on first-order kinetics; they find their application for discontinuous [45] and continuous screening processes [224] and need to be calibrated by experimental investigations. Some kinetic models were extended by the probability of particle passage [47] and tested for continuous screening processes. The model extensions increase the model complexity insignificantly. In case that a thicker particle layer forms out on the sieve the applicability of kinetic models is limited [50]. In contrast to kinetic approaches probabilistic models require a larger number of parameters [47]. Similarly, they can be applied to continuous screening processes considering operational parameters like mechanical agitation, particle composition and screen size [3,52,228,233]. Probabilistic models lack the representation of phenomena related to particle motion and are therefore constricted to represent motion triggered macroscopic bulk material behavior [50].

Some phenomenological models consider the interacting processes of segregation and actual passage of the particles through the screen surface [7,8,233,234]. Screening efficiency is handled as a function of time, taking into consideration the transport speed of the bulk material in dependence on the position on the screen. Input parameters of the models are parameters that represent segregation and passage rates [7]. Extensions for the model [7] were proposed addressing the influence of the particle layer thickness and the composition of the bulk material [8]. Further extensions were derived allowing for a prediction of the transport speed of the bulk material on the screen [234]; for simplification it was assumed that the particle shape and layer thickness does not affect the conveyance speed. In probabilistic models segregation and the passage of the particles through the screen surface and their interaction can also be taken into account by appropriate model assumptions [233].

Despite many modeling advances, phenomenological models still lack the ability to represent dynamic processes within the unit operation sieving. Additionally they require appropriate calibration by experimental investigations – predictive phenomenological models are currently not available. In contrast to phenomenological models particle-based simulation approaches such as the discrete element method dating back to Cundall and Strack [10] provide a detailed insight into the process of sieving and thereby allow, after appropriate validation, the optimization of equipment and operating parameters without performing extensive experiments in advance. Dynamic processes such as segregation, passage and transport of the particle system are represented automatically since the discrete element method is a transient simulation approach. Time-dependent external changes in the operational parameters or the particle composition can be inherently considered which makes particle based methods such as discrete element simulations a powerful predictive numerical tool for the process step sieving [195].

The first investigations in which particle based simulation approaches based on the discrete element method were used for sieving date back to Shimosaka et al. [46]. In three-dimensional simulations a small number of particles (400 particles) were considered on a batch-operated screen. Further investigations were carried out for two-dimensional continuous screening processes [50,189]. Here, the influence of the thickness of the bulk particle layer and the impact of the particle sizes on sieving efficiency were considered. Special attention was given to the influence of particles with sizes larger and equal to the aperture size dimensions. A small scale, three-dimensional sieve with periodic boundary conditions was considered by Cleary [62]. Large scale sieves were addressed in the works of Dong et al. [195], Alkhaldi and Eberhard [190] and Chen et al. [42]. The accuracy that is needed to represent the screen lining was investigated by Alkhaldi et al. [191]. Significant savings in computation time are realizable by application of stochastic models; at the same time, accuracy is lost. Screening processes in which fluids are present and modeled for in discrete element simulations were considered by Dong and Yu [202] as well as Fernandez et al. [9]. In addition to the contact parameters, no further input is required to perform simulations - thus the discrete element method is suited for optimization of equipment and operating parameters or applicable for deriving and verifying simpler phenomenological models [46].

Up to now only few numerical investigations on sieving involving the discrete element method addressed particles of complex shape [6,198]. In particular, the work of Delaney et al. [20] comes to the conclusion that bulk materials consisting of complex shaped particles must be modeled by complex-shaped particles in simulations, otherwise deviations for the transport and segregation behavior are evident and thus no reliable conclusions can be drawn from the simulations.

In the present work the investigation by Delaney et al. [20] is extended, applying a number of non-spherical particle shapes. Phenomena such as particle passage and segregation are investigated in detail. These investigations form the basis to later use discrete element simulations reliably for the derivation of phenomenological dynamic process models. The article is structured as follows. In section 2 the numerical method is described, followed by the numerical setup and the applied simulation parameters in section 3. Results in section 4 address different batch systems and a horizontally aligned continuous sieve in accordance to [20].

2. Numerical method

The discrete element method is routinely utilized for the modeling of systems of particles with spherical shape [60,61]. When the discrete element method is used to represent non-spherical particles, the translational and rotational motion is obtained by integrating Newton's and Euler's equations of each particle

$$m_i \frac{d^2 \vec{x}_i}{dt^2} = \vec{F}_i + m_i \vec{g}, \quad (37)$$

$$\hat{I}_i \frac{d\vec{W}_i}{dt} + \vec{W}_i \times (\hat{I}_i \vec{W}_i) = \Lambda_i^{-1} \vec{M}_i, \quad (38)$$

with particle mass m_i , particle acceleration $d^2 \vec{x}_i / dt^2$, contact force \vec{F}_i , gravitational force $m_i \vec{g}$, angular acceleration $d\vec{W}_i / dt$, angular velocity \vec{W}_i , external moments resulting out of contact forces \vec{M}_i , the inertia tensor along the principal axis \hat{I}_i and the rotation matrix converting a vector from the inertial into the body fixed frame Λ_i^{-1} . The equations for translational and rotational motion are solved by explicit integration schemes [82].

A flexible approach to model complex shaped particles in the discrete element method is the multi-sphere method where arbitrary sized spheres are clustered to resemble the desired complex particle shape [69]. In this method contact force laws are applied as used for spherical particles [65]. Further details on the contact scheme involving clustered spheres can be found in [90,91]. A sketch of two simple colliding particles ik and jl is shown in Fig. 29.

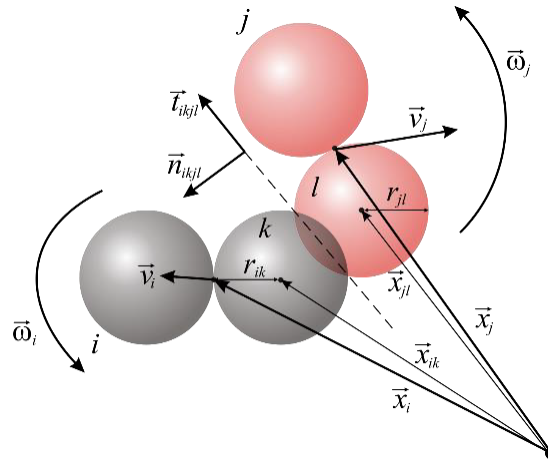


Fig. 29: A collision of two multi-sphere particles.

The normal component of the contact forces is obtained from a linear spring damper model

$$\vec{F}_{ikjl}^n = k^n \delta_{ikjl} \vec{n}_{ikjl} + \gamma^n \vec{v}_{ikjl}^n, \quad (39)$$

where subscripts i, j, k and l represent the four different spheres of the two particles ik and jl , k^n is the spring stiffness, δ_{ikjl} the virtual overlap, \vec{n}_{ikjl} a normal vector, γ^n a damping coefficient and \vec{v}_{ikjl}^n the normal velocity in the contact point. Both k^n and γ^n determine the coefficient of normal restitution between particles e_{pp}^n as well as particles and walls e_{pw}^n [92]. For the calculation of the tangential forces a linear spring limited by the Coulomb condition is used

$$\vec{F}_{ikjl}^t = -\min(k^t |\xi_{ikjl}^t|, \mu_c |\vec{F}_{ikjl}^n|) \vec{t}_{ikjl}, \quad (40)$$

where k^t is the stiffness of a linear spring, μ_C is the friction coefficient, $\vec{\xi}_{ijkl}$ is the relative tangential displacement and \vec{t}_{ijkl} is the tangential unit vector [94].

3. Numerical setup and simulation parameters

Sieving of a polydisperse feed material is investigated numerically by the discrete element method in two batch apparatuses and a horizontally aligned continuously operated sieve as shown in Fig. 30.

The first batch sieve (Fig. 30a) comprises of 14 inserts designed as wire screens put atop of each other at a distance of 10 mm. The screen size is 7.5 cm x 7.5 cm. The wire diameter is 0.71 mm. The aperture size is decreasing from the top downwards in alignment with the size classes of the feed material. The screen is vibrated with 27.55 Hz with an alternating stroke angle of 50° and 130° to the horizontal at an amplitude of 1.76 mm.

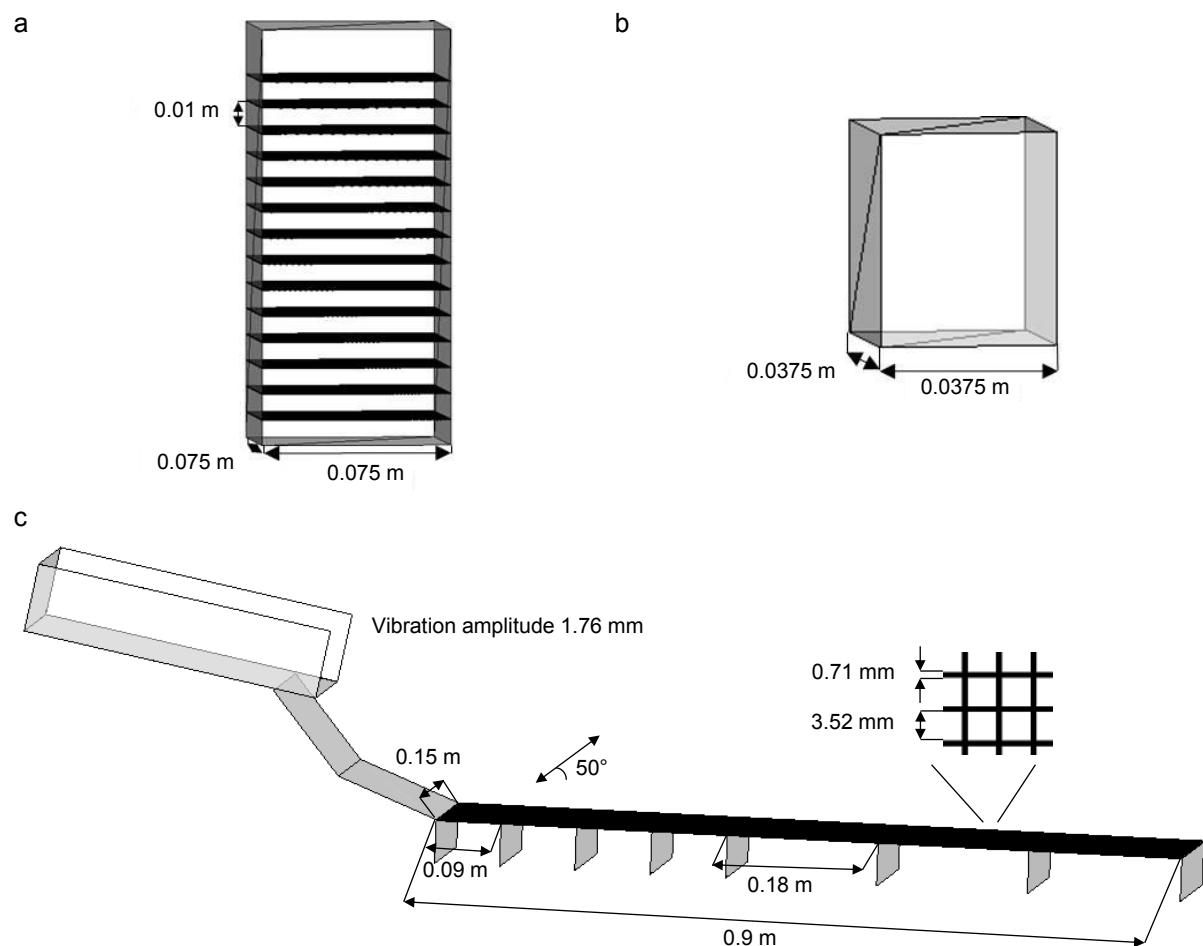


Fig. 30: Screen geometry of (a) first and (b) second batch apparatus and (c) continuously operated sieve.

The second batch apparatus (Fig. 30b) has neither apertures nor inserts and its floor area is 3.75 cm x 3.75 cm. It is vibrated with 27.55 Hz at previously used amplitude and motion.

As continuous setup (Fig. 30c) a horizontal sieve as investigated by Delaney et al. [20] is used. It is 90 cm long and 15 cm wide and equipped with a wire screen. The aperture size is 3.52 mm

and the wire diameter is 0.71 mm. The screen is initially vibrated with 27.55 Hz with a stroke angle of 50° to the horizontal at an amplitude of 1.76 mm. Besides the horizontal alignment, the inclination angle of the screen is later varied by 5° and 10° , respectively. To get information about the particles passing through the screen, the setup is equipped with a series of bins (first four 9 cm long; last three 18 cm long).

The particles used in the simulations are chosen in accordance with the investigation [20] and have a density of 2700 kg/m^3 . From a sieve analysis the particle size distribution is available. Sizes range from below 0.60 mm up to 5.00 mm split into 14 size classes as outlined in Table 1. Particle size distributions vary for the different mass flow rates applied.

For the simulations, near aperture size class 3 ranging from 3.35 mm to 4.00 mm is divided into 3 subclasses (3.1, 3.2 and 3.3), where their proportions are calculated from the overall particle distribution.

The stiffnesses k^n and k^t , the coefficients of normal restitution between particles e_{PP}^n and particles and walls e_{PW}^n and the Coulomb friction coefficient μ_C are adjusted according to [20]: $k^n = 1000 \text{ N/m}$, $k^t = 500 \text{ N/m}$, $e_{PP}^n = 0.4$, $e_{PW}^n = 0.5$, $\mu_C = 0.5$.

Table 1: Particle size distribution for the feed material used in the simulations for mass flow rates of 49 g/s (Case A) and 250 g/s (Case B) in accordance to [20].

| Class ID | Mean size (mm) | Case A (mass-%) | Case B (mass-%) |
|----------|----------------|-----------------|-----------------|
| 1 | 4.875 | 3.1 | 3.1 |
| 2 | 4.375 | 5.6 | 6.0 |
| 3.1 | 3.76 | 6.8 | 8.3 |
| 3.2 | 3.4633 | 1.4 | 2 |
| 3.3 | 3.4067 | 1.6 | 2.3 |
| 4 | 3.075 | 11.1 | 19.8 |
| 5 | 2.58 | 7.7 | 11.8 |
| 6 | 2.18 | 12.0 | 12.5 |
| 7 | 1.85 | 8.6 | 10.0 |
| 8 | 1.55 | 6.4 | 6.5 |
| 9 | 1.29 | 5.3 | 4.7 |
| 10 | 1.09 | 6.8 | 4.5 |
| 11 | 0.925 | 5.4 | 3.2 |
| 12 | 0.78 | 4.2 | 2.2 |
| 13 | 0.655 | 3.6 | 1.2 |
| 14 | 0.55 | 10.4 | 1.9 |

The sieve wire is approximated by triangular surface elements within the simulations. The total number of elements is significantly affecting the runtime of the simulations. Therefore, it is desired to have a small number of elements involved and to keep the approximation of the sieve wire as simple as possible (neglecting a possible woven structure). Different approximations with varying complexity are tested (Fig. 31) and the feed rate fraction passing is monitored (Fig. 31a). The mass flow rate is 49 g/s and only size class 3 with its subclasses (Table 1) is applied to the continuously operated sieve (Fig. 30c) using spherical particles. In

general, a higher complexity yields to an increased particle passage (feed rate fraction: 42 % for 10-edge approximation), but causes more computational effort. In the present investigation, a plane-shape approximation (marked in red in Fig. 31b) leads to acceptable passage (feed rate fraction: 36 %) at reasonable computational load.

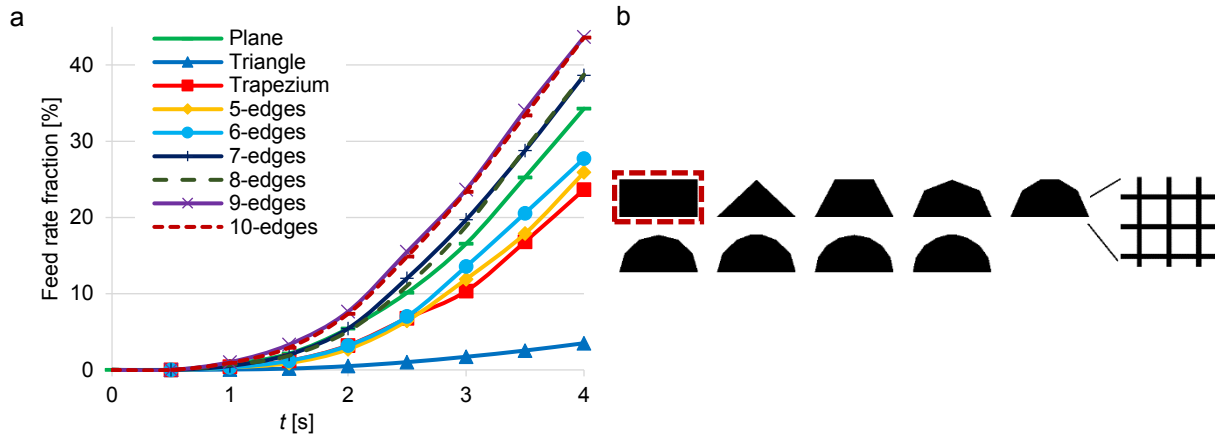


Fig. 31: (a) Mass percentage of spherical particles of class 3 passing through the screen at a feed rate of 49 g/s for (b) different sieve wire structures.

Besides spheres, which were intensively investigated in [20], differently sized cylinders as well as cones, double cones and double frustums are considered as particle shapes in the investigation here (Fig. 32a). The non-spherical particles (ii)-(vi) are chosen to have an aspect ratio of 1.55 which was calculated as average value from a particle sample provided in [20]. The aspect ratio distribution is shown in Fig. 32b. The small cylinders (shape (ii)) are volume equivalent to the spherical particles. The other shapes ((shapes (iii)-(vii)) have the same minor axis as the spheres. This gives them the same long-term separation characteristics in a sieve analysis; their separation rates however differ.

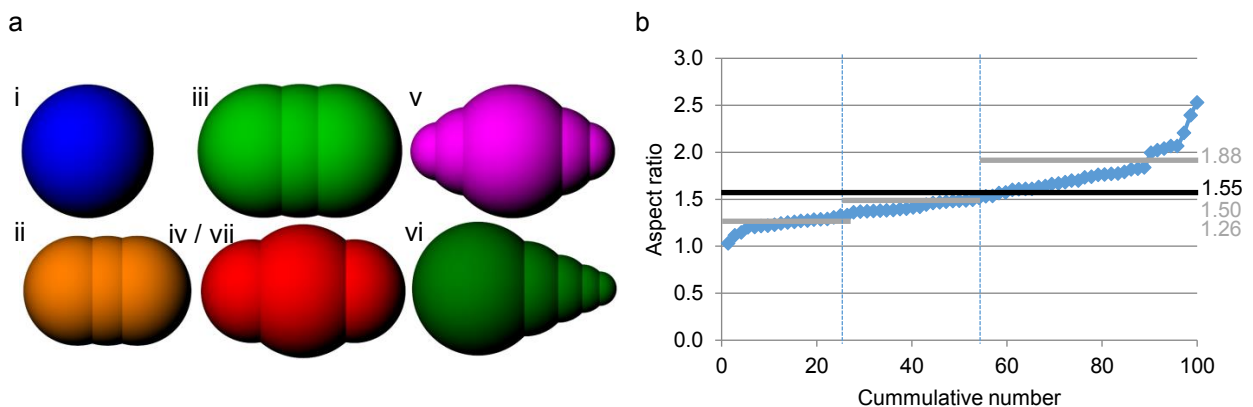


Fig. 32: (a) Modeled particle shapes: sphere (i), small cylinder (ii), big cylinder (iii), double frustum (iv,vii), double cone (v) and cone (vi) and particle aspect ratio distribution according to [20] and (b) its approximation.

Additionally, to address the influence of the aspect ratio distribution, the double frustum (shape (v)) is exemplarily approximated by a simplified aspect ratio distribution consisting of three ratios of 1.26, 1.50 and 1.88, respectively. For details, see Fig. 32b. In the following, shape (vii) is referred to in the figures as double frustum ARD.

4. Results and discussion

Three types of simulations are performed. Firstly, screen surface passage is examined in a batch sieving investigation. Secondly, batch simulations addressing segregation are performed. Finally, the continuous sieving apparatus is modeled for analyzing the interaction of particle passage, segregation and transport. In all investigations, the feed stream consists of one of the particle shapes outlined in Fig. 32 at a time. Results obtained for the continuously operated setup are compared to results provided in [20].

4.1 Batch sieving investigations

In the first batch sieving investigation particles with shapes according to Fig. 32 and a size distribution matching case A in Table 1 with a fixed aspect ratio of 1.55 in case of non-spherical particles are fed onto the uppermost insert of apparatus 1 (Fig. 30a) for $t = 2$ s at a feed rate of $\dot{m} = 9.8$ g/s. Due to the oscillating motion of the sieve, particles start to move downwards through the apertures in the inserts. Particles come to a rest at latest on a sieve insert with an aperture size smaller than the particle's minor axis. Screening is performed for $t = 20$ s in total; after $t = 10$ s spherical sieving aids are added on each insert to support the screening process. The diameter of the spherical screening aids is 1.25-times the largest sphere diameter.

In the second batch sieving investigation 49 g of particles with shapes according to Fig. 32 and a size distribution as stated for case A (Table 1) are placed in a cuboidal box (Fig. 30b) which is vibrated for 10 s. All particle sizes are charged into the box at a time in layers to prevent premature segregation. Aspect ratios of 1.55 for non-spherical particles (ii)-(vi) as well as double frustums with an aspect ratio distribution (vii) are considered. With the onset of vibration particles start to segregate according to their sizes.

4.1.1 Final mass distribution

In Fig. 33a, the final distribution of the overall particle mass on the sieve inserts is shown after $t = 20$ s for the first batch sieving investigation. In black the reference values according to the particle size distribution (Table 1) are given. Mass attributed to insert 0 results from particles charged on the uppermost sieve insert which have not passed through any apertures.

A significant number of particles remains on insert 0 after $t = 20$ s, although their sizes (minor axis ≤ 4.875 mm) allow them to pass through the uppermost sieve insert (aperture size = 5.00 mm). This behavior can be attributed to the very limited number of large particles in the feed stream. For the lowermost insert, reference values are not exactly matched for any of the particle shapes, not even spheres. The separation process is mostly not terminated at $t = 20$ s; with additional time particles would pass further through the apertures of the sieve inserts.

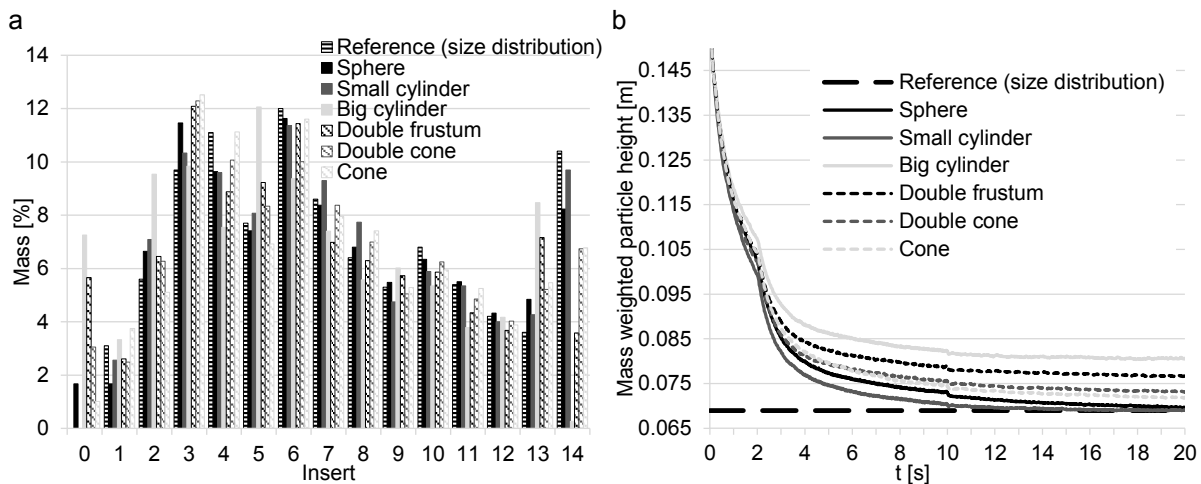


Fig. 33: (a) Distribution of the overall particle mass after $t = 20$ s and (b) progression of the average mass weighted particle height for batch sieving investigation 1 – feed rate: 9.8 g/s, inflow period: $t = 2$ s, size distribution: case A, aspect ratio of non-spherical particles: 1.55.

Particle shape has a strong influence on the separation characteristics. The large cylinders pass through the inserts much harder than the spheres. A peak-shaped appearance enhances the ability to pass. The sphere volume equivalent cylinders pass more easily than spheres due to their minor axis, which is smaller than the sphere diameter.

4.1.2 Progression of the mass weighted particle height

The progression of the mass weighted average particle height over time t is shown in Fig. 33b. For the first second the progression of the particle height is well aligned for the different particle shapes. Particles are charged at the topmost insert where the aperture size, the particles are facing, is much larger than the particle dimensions. Here, particle passage is unaffected by particle shape. At $t = 2$ s the interruption of the feed gets apparent by an accelerated decrease in the average particle height. Another instantaneous drop results from the addition of the spherical sieving aids at $t = 10$ s. This drop is not strongly pronounced and thereafter the sieving aids alter the passage rate only insignificantly.

Although the decrease in particle height has mostly not reached its final value at $t = 20$ s significant differences between the considered particle shapes are apparent. As a reference the black line in Fig. 33b represents the limiting value theoretically reachable for all shapes with a sphere diameter equivalent minor axis. The passage ability decreases in the following order: small cylinders, spheres, cones, double cones, double frustums and big cylinders. The small cylinders obtain a mass weighted particle height smaller than the spheres and also slightly smaller than the limiting value due to their minor axis which is smaller than the corresponding sphere diameter.

Some further insights into the passage behavior give the mean dwell times on each insert, which are given in Table 2. The listed values were obtained during the first 10 seconds of operation of apparatus 1. Good passage of a particular particle shape results in a short dwell time. On the uppermost inserts (insert 0 - insert 4) particle shape does not affect the dwell

times significantly. On the lower inserts (5-13) shape influences the dwell times strongly. Double cones are attributed to a larger ability to pass through the apertures than big cylinders or double frustums. An accumulation of particles on a particular insert can influence dwell times on subsequent lower inserts and alter general dwell time tendencies as noticeable for big cylinders on inserts 12 and 13.

Table 2: Derived mean dwell times of the considered particle shapes on each insert during the initial 10 seconds of operation of the first batch sieving apparatus.

| Insert | t [s] | t [s] | t [s] | t [s] | t [s] | t [s] |
|--------|---------|----------------|--------------|-------------|---------|----------------|
| | Sphere | Double frustum | Big cylinder | Double cone | Cone | Small cylinder |
| 0 | 0.1 | 0.1 | 0.1 | 0.09 | 0.1 | 0.09 |
| 1 | 0.08 | 0.07 | 0.08 | 0.07 | 0.07 | 0.06 |
| 2 | 0.08 | 0.08 | 0.08 | 0.07 | 0.08 | 0.07 |
| 3 | 0.11 | 0.11 | 0.11 | 0.1 | 0.11 | 0.1 |
| 4 | 0.14 | 0.14 | 0.17 | 0.12 | 0.14 | 0.12 |
| 5 | 0.19 | 0.2 | 0.23 | 0.19 | 0.19 | 0.16 |
| 6 | 0.25 | 0.26 | 0.29 | 0.24 | 0.26 | 0.22 |
| 7 | 0.29 | 0.31 | 0.34 | 0.29 | 0.3 | 0.27 |
| 8 | 0.43 | 0.46 | 0.59 | 0.43 | 0.46 | 0.39 |
| 9 | 0.59 | 0.69 | 0.81 | 0.61 | 0.63 | 0.54 |
| 10 | 0.9 | 0.99 | 1.18 | 0.91 | 0.94 | 0.8 |
| 11 | 1.21 | 1.44 | 1.86 | 1.27 | 1.36 | 1.15 |
| 12 | 1.99 | 2.79 | 3.98 | 2.29 | 2.4 | 1.89 |
| 13 | 3.78 | 4.33 | 3.43 | 4.28 | 3.89 | 3.7 |

4.1.3. Particle segregation

As a parameter to evaluate particle segregation the accumulated deviation of the average particle height per particle class from the total average particle height over time t is calculated, which is given as

$$h^* = \sum_{j=1}^{n_{class}} \left| \left(\sum_{i=1}^{n_{part,j}} z_{i,j} / n_{part,j} \right) - \left(\sum_{i=1}^{n_{part}} z_i / n_{part} \right) \right|, \quad (41)$$

where n_{class} is the number of size classes, n_{part} is the total number of particles, $n_{part,j}$ is the number of particles in the respective size class j , z_i is the height of a particle i and $z_{i,j}$ is the height of particle i belonging to size class j in the system. In Fig. 34 the accumulated deviation h^* is plotted for the different particle shapes over time t . For an unsegregated system h^* is zero; increasing segregation results in an inclined value for h^* . The results obtained indicate, that spheres segregate well because of their circular shape related mobility. They obtain a final value for h^* of 0.037 m, whereas elongated particles reveal a less pronounced degree of segregation with values of h^* between 0.026 m and 0.03 m. Elongated particles have the characteristics to take up preferred horizontal orientations which hinder particle motion and thereby segregation.

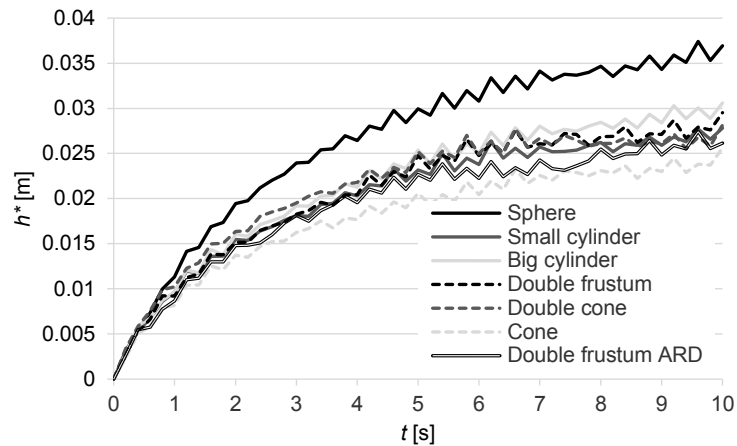


Fig. 34: Accumulated deviation of the average particle height per size class from the total average particle height h^* for the different particle shapes over time t in the second batch apparatus - applied mass: 49 g.

4.2 Continuous sieving investigations

In the continuous sieving investigations the setup examined in [20] is modeled at feed rates of 49 g/s and 250 g/s. Additionally variations of the screen inclination are performed. Prior to that, simulations of a screen with narrowed width (0.05 m) with a randomly varying inflow of 16.3 g/s but besides the same conditions as the 49 g/s case are carried out to test the repeatability of the model results. The flow rates in the first three collection bins and the residence time on screen of all particle size classes are quantified and compared to each other which is shown in Table 3. Concerning the flow rate, the average standard deviation per size class is 0.004 g/s and for the near aperture size classes 3 and 4 0.004 g/s and 0.03 g/s, respectively. Similar results, namely 0.04 s for the average standard deviation and 0.13 s and 0.03 s for the deviation of classes 3 and 4, respectively, come up for the residence time. Therefore, a good reproducibility is given and later obtained results are of statistical significance.

Table 3: Derived standard deviation per particle size class for the flow rates in collection bins 1-3 and the dwell times on the screen.

| Standard deviation of flow rates in collection bins 1-3 [g/s] | | | Standard deviation of dwell times on the screen [s] | | |
|---|---------|---------|---|---------|---------|
| Averaged | Class 3 | Class 4 | Averaged | Class 3 | Class 4 |
| 0.004 | 0.004 | 0.03 | 0.04 | 0.13 | 0.03 |

4.2.1 Continuous sieving investigations with a feed rate of 49 g/s

Fig. 35a shows results on the derived flow rates through the screen for the first three collection bins obtained for different particle shapes in comparison to data obtained in [20] for a particle inflow rate of 49 g/s. Results indicate differences for the larger undersized particles with $d > 2.36$ mm (classes 3-5). For the small particles with $d < 2.36$ mm (classes 6-14) shape does not relevantly affect the sieving. Flow rates obtained for spherical particles by own simulations vary from results obtained for spheres in [20]. Own results match the experimental data derived in [20] better. A dependence of the passing behavior on the initial charging of the particles on the sieving apparatus is a possible explanation. The usage of small cylinders increases

whereas all other shapes lower the passage through the screen in comparison to [20]. The passage ability decreases in the following order: small cylinders, spheres, cones, double cones, double frustums with aspect ratio distribution, double frustums and big cylinders.

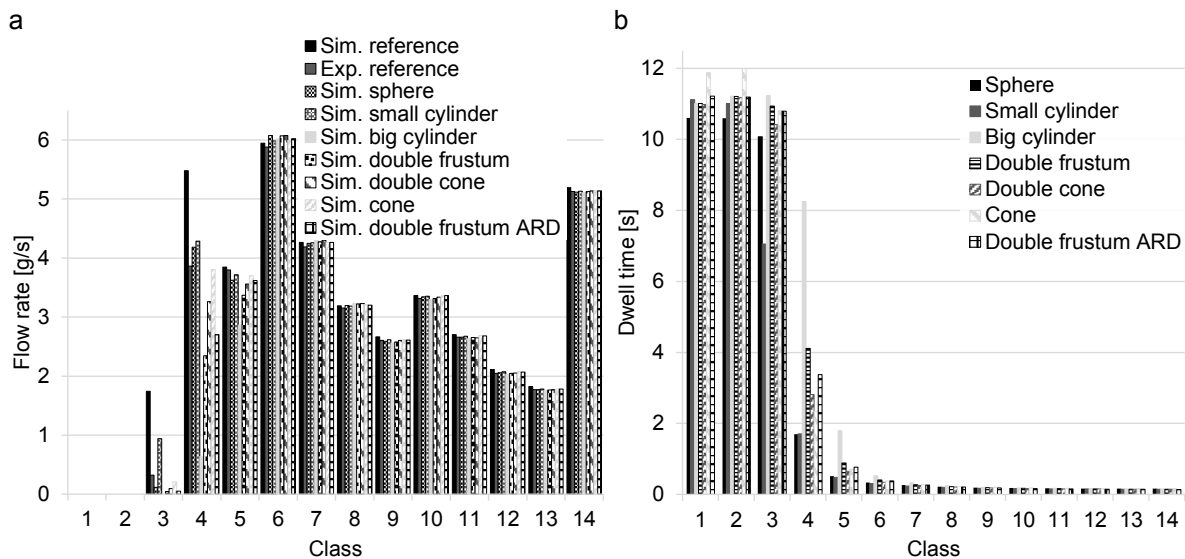


Fig. 35: (a) Flow rates through the screen for the first 3 collection bins and (b) dwell times of particles on the screen – feed rate: 49 g/s.

In Fig. 35b, the dwell time on the screen for each considered particle shape is outlined. As dwell time the time period is considered where particles enter the screen surface until either a particle is discharged at the end of the screen or it passes through an aperture. Shape mainly affects the near aperture (classes 3-5) and oversized (classes 1-2) but not the smaller particles (classes 6-14). Among the oversized particles spheres are the fastest and cones are the slowest shapes on the screen due to their differing rolling ability. For the near aperture size classes, spheres and small cylinder reside shortest and big cylinder longest on the screen in accordance to their passage ability. For a particle feed rate of 49 g/s, flow rates through the screen form out constant over time t for all considered particle shapes (not shown in any of the figures). Only some near aperture size particle classes lead to oscillating flow rates for non-spherical shapes due to their orientation dependent ability to pass through the apertures. For a feed rate of 49 g/s pegging, which is the clogging of apertures with near aperture size particles, has no relevant influence.

4.2.2 Continuous sieving investigations with a feed rate of 250 g/s

Fig. 36a shows results on the derived flow rates obtained for the first three collection bins with a feed rate of 250 g/s after $t = 25$ s. Here, shape affects the near aperture size particles (classes 3-4), but not the smaller particles (classes 5-14) in a comparable way as for the feed rate of 49 g/s (compare Fig. 35a).

The screening efficiency for the near aperture size classes, particularly class 3 (Fig. 36b), increases for a feed rate of 250 g/s in contrast to 49 g/s for all investigated particle shapes due to the higher share of coarse material (comp. Table 1) which supports passage and due to the

feed rate related larger mass on the screen surface. The flow rates for near aperture size classes at $t = 25$ s (Fig. 36a) are larger than in the investigation by Delaney et al. [20] obtained at $t = 50$ s, particularly for spheres (not shown here). In the investigation [20] flow rates summed up over the first three collection bins start to decline approximately at $t = 20$ s, which is also apparent from the investigation carried out here. This decline in flow rates is a result of pegging of apertures by oversized and near aperture size particles of class 3 and 4.

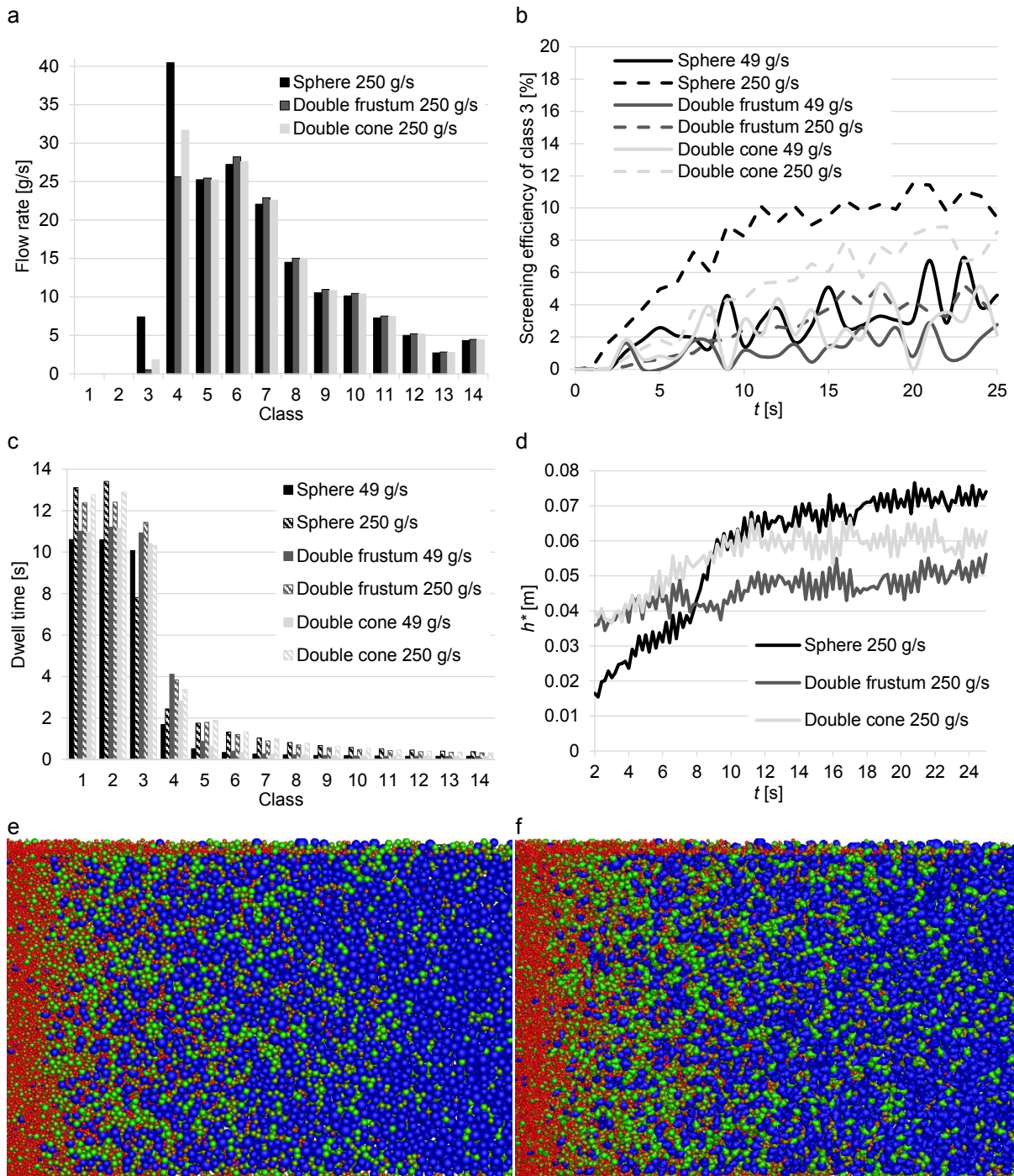


Fig. 36: (a) Flow rates through the screen for the first 3 collection bins, (b) screening efficiency of particle class 3, (c) dwell times of particles on the screen, (d) accumulated deviation of the average particle height per size class from the total average particle height h^* , pegging of apertures for (e) spheres and for (f) non-spherical particles - feed rate: 250 g/s.

In Fig. 36c, the effect of the feed rate on the dwell times is outlined. At an increased feed rate, oversized particles are discharged from the screen delayed. Additionally, smaller particles

require an increased amount of time to segregate through the oversized particles before being capable of passing through the screen apertures. At a feed rate of 250 g/s the dwell times of near aperture size particles (classes 3-4) are variously affected. Slower transport on the screen enhances the dwell times and thereby increases the probability to pass through the screen apertures. This effect is more pronounced for spheres than for elongated shaped particles.

Changing the feed rate from 49 g/s to 250 g/s leads to a buildup of particles on the screen. Due to segregation effects the average particle size is decreasing when getting closer to the screen surface. The progression of the accumulated deviation of the average particle height per size class from the total average particle height h^* is shown in Fig. 36d. Spheres segregate delayed but much more pronounced than double cones and double frustums.

A view from below the screen surface in Figs. 36e,f reveals the phenomena of pegging. Slightly oversized and near mesh particles marked in blue clog apertures, hence near mesh and smaller particles are interfered to pass. This phenomenon is less pronounced when using non-spherical particles (Fig. 36f) instead of spheres (Fig. 36e).

4.2.3 Continuous sieving investigations with varying screen inclinations

In Fig. 37 results on flow rates (Fig. 37a) and dwell times (Fig. 37b) at a feed rate of 49 g/s on a horizontally aligned screen are compared to screen setups with an inclination of 5° and 10°.

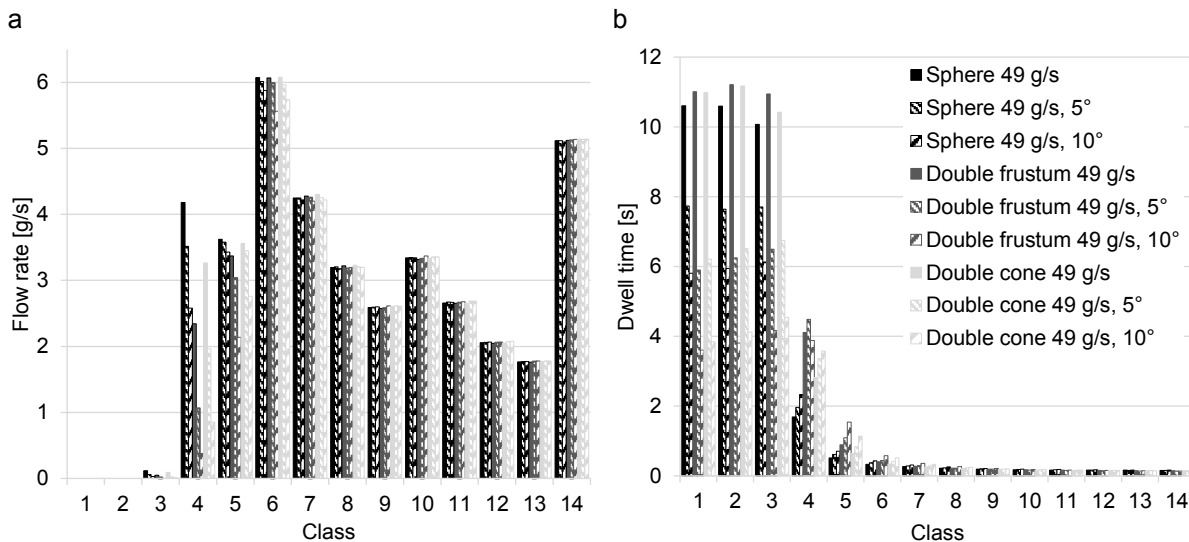


Fig. 37: (a) Flow rates through the screen for the first 3 collection bins and (b) dwell times on the screen for different screen inclinations – feed rate: 49 g/s.

The flow rates and thereby the screening efficiency decreases for larger inclinations due to the smaller effective aperture sizes. Consequently, the flow rate is lower for near mesh size particles (classes 3-6), particularly for non-spherical ones.

Oversized particles (classes 1-2) and class 3 are moving faster on a screen with a higher inclination and thus reside shorter. On average, all particles spend less time on the screen and

therefore have a lower probability to pass. Hence, the dwell times for classes 4 and 5 are increasing.

5. Conclusions

DEM simulations of complex shaped particles on two batch apparatuses and a continuously operated sieve have been performed. Experimental and numerical results in [20] are matched with some deviations. These deviations could result from differences in particle charging and the representation of the sieve wire structure [20,34]. Sieving is strongly affected by the particle size and shape as the passage probability of near aperture size particles is affected. In the present DEM investigations, the passage probability is decreasing in the following order: small cylinders, spheres, cones, double cones, double frustums with aspect ratio distribution, double frustums and big cylinders. Furthermore, transport and segregation tendency is declining in the following order: spheres, symmetrically shaped non-spherical particles and cones.

An increased feed rate supports particle passage by giving the near aperture size particles more possibilities to pass the screen apertures by lowering transport on the screen. Increasing the share of coarse material enables oversized particles to support near aperture size particles to pass the screen apertures.

The larger the inclination angle, the faster particles are transported, therefore oversized particles reside shorter on the screen. However, near aperture size particles dwell longer on the screen in consequence of the smaller effective aperture sizes as well as the faster movement and thus the lower possibility to pass before reaching the discharge zone of the screen.

Acknowledgments

The authors gratefully acknowledge the support by DFG within SPP 1679 through grant number KR3446/7-1. The discussion with G. W. Delaney and M.M. Hilden as well as with the project partners of SPP 1679 U. Teipel and M. Hennig is appreciated.

II. Review and benchmarking of process models for batch screening based on discrete element simulations

Frederik Elskamp, Harald Kruggel-Emden*

Ruhr-Universität Bochum, Universitätsstraße 150, D-44780 Bochum, Germany

*Corresponding author. E-mail address: kruggel-emden@leat.ruhr-uni-bochum.de

The following accepted manuscript appeared as journal version in Elskamp F., Kruggel-Emden H., 2015, Review and benchmarking of process models for batch screening based on discrete element simulations, Advanced Powder Technology 26 (3), 679-697 and may be found at <https://doi.org/10.1016/j.apt.2014.11.001>.

Abstract

In the recent past detailed particle-based simulation approaches such as the discrete element method (DEM) have become popular in addition to phenomenological models for the design and optimization of operating parameters of screening processes. As phenomenological process models, a large number of probabilistic and kinetic approaches of differing complexity are available which mostly provide information on the screening rate or efficiency. So far a review and comparative benchmarking of the various available screening process models has not been performed, although they are of high relevance, especially in industrial applications, due to their simplicity and easy use. To perform the benchmarking of batch screening process models, it is not relied on experimental investigations, but on detailed DEM simulations involving both spherical and non-spherical particles in the investigation here. The DEM simulations allow examining different particle characteristics such as size, shape, friction, as well as overall mass and size distribution. In addition, screen characteristics such as screen dimensions and surface as well as operational parameters including vibration frequency, stroke angle and amplitude are considered. On the basis of the DEM simulations screening efficiencies are obtained which allow the adjustment and thereon benchmarking of the process models through parameters such as the residual particle mass on the screen.

Keywords: Batch screening; Discrete element method (DEM); Arbitrary shaped particles; Process models

1. Introduction

In many processes in materials preparation technology, mechanical process engineering, mineral processing and energy technology individual particles of various bulk materials are often of non-spherical shape and broad size distribution [2,3]. Here, it is frequently required to separate a particulate solid into sub-products with different particle size ranges as e.g. in mineral processing when crushed material is separated into crushed rock, gravel and sand. Alternatively, it is sometimes essential to remove dust or abrasion products from coarser grained materials. If a multi component bulk solid mainly differs in particle size, it is regularly

required to split up its components by size as e.g. done in grain processing and food related processes. Furthermore, it is occasionally required to separate bulk solids comprising of similarly sized, but differently shaped particles. All these tasks can be performed by the simple process step screening which in industry is mostly regarded as mature. Nevertheless, scientifically screening and its sub-processes are currently still not satisfactorily understood, often complicating the design and optimization of screening processes in both small scale laboratory and industrial applications.

For the design and optimization of screening processes particle-based simulation approaches such as the discrete element method (DEM) dating back to Cundall and Strack [10] and Walton and Braun [59] as well as various phenomenological models are available. By providing a detailed insight into screening processes the DEM allows, after appropriate validation of its model parameters, the optimization of equipment and operating parameters without performing extensive experimental investigations. DEM simulations are predictive and due to their transient nature, dynamic processes associated with screening such as segregation, passage and transport are represented, inherently.

The first application of the DEM towards screening dates back to Shimosaka et al. [46], who performed three-dimensional simulations on a batch-operated screen with a small number of particles (400 particles) and used the simulations to derive a phenomenological screening model. In further continuous screening investigations the influence of the single particle size, particularly of larger or near aperture size particles and of the whole thickness of the bulk particle layer on the screening efficiency were considered [50,189]. Moreover, a small scale, three-dimensional screen with periodic boundary conditions was investigated by Cleary [62]. Large scale screens were addressed in the works of Dong et al. [195], Alkhaldi and Eberhard [190] and Chen et al. [235]. The accuracy that is needed to represent the complex screen surface was studied by Alkhaldi et al. [191]. For realization of significant savings in computation time stochastic models were applied, whereby accuracy is lost. Up to now, particles of complex shape were only addressed in few numerical investigations involving the DEM in the context of the process step screening [6,198]. In particular, Delaney et al. [20] concluded that deviations for the transport of the bulk material as well as for the segregation and passage behavior of the near aperture size particles are evident if complex-shaped material is not modeled by complex-shaped particles in simulations. Motivated by [20], the influence of particle shape on continuous screening was studied numerically by Kruggel-Emden and Elskamp corroborating this behavior [236].

Over the last years several investigations were performed of screening processes based on the DEM. Circularly vibrating screens have been studied by Zhao et al. [192] with regard to the vibration amplitude, throwing index and screen inclination; based on the simulations recommendations towards optimal operational parameters were proposed. Extending

investigations by Alkhalidi et al. [191], Tung et al. [188] focused on the effect of the woven-mesh structure in batch screening investigations. Further studies addressed banana screens [196], or other continuous screening processes in which especially the screen agitation was varied [35,237,238]. Very recently, particle/fluid interaction as well as adhesive forces due to liquid bridges were considered in DEM simulations of screening processes [9,200,202].

The listed investigations clearly indicate that the DEM is capable of providing detailed insight into screening processes. The DEM was validated against experimental data [34] and proved successful and reliable [236]. In case that no interstitial fluid is of relevance [239], no further model parameters, besides the contact parameters, are required to perform meaningful simulations. The DEM is thereby suited for optimization of equipment and operating parameters [35,50,189,192,236–238] or applicable for deriving and verifying simpler and less computationally extensive phenomenological models without performing extensive experiments as demonstrated firstly by Shimosaka et al. [46].

In the present work addressing batch screening processes involving spherical and non-spherical particle shapes, phenomena such as particle passage and the residual mass over time are investigated in detail. These investigations form the basis to use DEM simulations reliably for a comparative study of phenomenological batch screening process models following the idea of Shimosaka et al. [46]. The article is structured as follows. In section 2 the numerical method is described, followed by a description of the considered screening process models in section 3. The numerical setup and the applied simulation parameters are outlined in section 4. Results in section 5 firstly address different batch simulations, before the particle passage behavior is compared to the outcome of various phenomenological screening process models.

2. Numerical method

The DEM can be applied to systems of particles with non-spherical shape [60,61] by obtaining the translational and rotational motion of each particle. For this purpose the Newton's and Euler's equations are integrated

$$m_i \frac{d^2 \vec{x}_i}{dt^2} = \vec{F}_i + m_i \vec{g}, \quad (42)$$

$$\hat{I}_i \frac{d\vec{W}_i}{dt} + \vec{W}_i \times (\hat{I}_i \vec{W}_i) = \Lambda_i^{-1} \vec{M}_i, \quad (43)$$

with particle mass m_i , particle acceleration $d^2 \vec{x}_i / dt^2$, contact force \vec{F}_i , gravitational force $m_i \vec{g}$, angular acceleration $d\vec{W}_i / dt$, angular velocity \vec{W}_i , external moments resulting out of contact forces \vec{M}_i , the inertia tensor along the principal axis \hat{I}_i and the rotation matrix converting a

vector from the inertial into the body fixed frame Λ_i^{-1} . Both equations (eq. (42) and eq. (43)) are solved by explicit integration schemes [82].

A flexible approach to model complex shaped particles in the DEM is the multi-sphere method where arbitrary sized spheres are clustered to resemble the desired complex particle shape [69]. In this method contact force laws as used for spherical particles are applied [65]. Further details on the contact scheme involving clustered spheres can be found in [90,91]. A sketch of two simple colliding particles ik and jl is shown in Fig. 38.

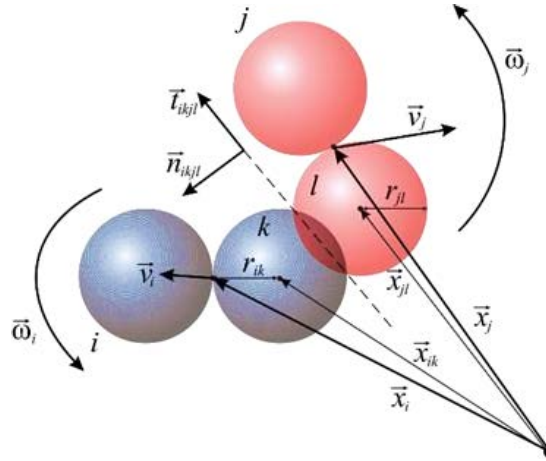


Fig. 38: A collision of two multi-sphere particles.

The normal component of the contact forces is obtained from a linear spring damper model

$$\vec{F}_{ikjl}^n = k^n \cdot \delta_{ikjl} \cdot \vec{n}_{ikjl} + \gamma^n \cdot \vec{v}_{ikjl}^n, \quad (44)$$

where subscripts i, j, k and l represent the four different spheres of the two particles ik and jl , k^n is the spring stiffness, δ_{ikjl} the virtual overlap, \vec{n}_{ikjl} a normal vector, γ^n a damping coefficient and \vec{v}_{ikjl}^n the normal velocity in the contact point. Both k^n and γ^n determine the coefficient of normal restitution between particles e_{pp}^n as well as particles and walls e_{pw}^n [92]. For the calculation of the tangential forces a linear spring limited by the Coulomb condition is applied

$$\vec{F}_{ikjl}^t = -\min(k^t \cdot |\vec{\xi}_{ikjl}|, \mu_c \cdot |\vec{F}_{ikjl}^n|) \cdot \vec{t}_{ikjl}, \quad (45)$$

where k^t is the stiffness of a linear spring, μ_c is the friction coefficient, $\vec{\xi}_{ikjl}$ is the relative tangential displacement and \vec{t}_{ikjl} is the tangential unit vector [94].

3. Phenomenological screening models

Available phenomenological models are divided into kinetic [3,45,47,224,226,227] and probabilistic theoretical models [3,46,52,225,228,229], which both allow a time-resolved representation of the screening process. Among them, several models are applicable for either discontinuous [45] or continuous screening processes [224] or else for both of them [225].

Usually continuous screening models can be adapted for discontinuous screening by replacing length l by time t in the model equations [224,225] and vice versa.

Kinetic models are mostly based on first-order kinetics and often further extended by the probability of particle passage [47] without increasing the model complexity significantly. Tests for continuous screening processes revealed their limited applicability if a thicker particle layer forms out on the screen [50]. In contrast to kinetic approaches, probabilistic models require a larger number of parameters [47] such as the probability for undersized particle passage (comp. Gaudin [24]). They can be applied to screening processes considering operational parameters like mechanical agitation, screen size and particle composition [3,52,228]. Simple probabilistic models lack the representation of phenomena related to particle motion and are therefore constricted to represent motion triggered macroscopic bulk material behavior [50].

In contrast, more complex phenomenological models with additional input parameters consider the interacting processes of segregation and actual particle passage through the screen surface [5,7,8]. Extensions for the model [7] were proposed addressing the composition of the bulk material and the influence of the particle layer thickness [8]. Further extensions were derived allowing for a prediction of the transport speed of the bulk material on the screen whereby assuming that the particle shape and layer thickness do not affect the conveyance speed [234].

Prior to a more detailed description, an overview of all investigated screening process models is given in Table 4 including the governing equations as well as the adjustable model parameters used. Phenomenological screening models are referred to by the author's names and a model number in the following and mostly require just a few major equations (comp. Table 4).

All phenomenological screening models allow the calculation of the overall screening efficiency E which is a time dependent variable during batch screening given as

$$E = E(t) = (m_0 - m)/m_0, \quad (46)$$

where m_0 is the initial undersize mass at $t = t_0$ and m is the actual mass of the undersize material on the screen at time t . Often the screening efficiency is stated per particle size class i as

$$E_i = E_i(t) = (m_{i,0} - m_i)/m_{i,0}, \quad (47)$$

which is related to the overall screening efficiency by $E = \sum_{i=1}^n (E_i \cdot m_{i,0}/m_0)$, where n is the number of undersize particle classes. The screening efficiency for each particle size class (eq. (47)) is calculated based on the fractional initial undersize mass $m_{i,0}$ and fractional actual undersize mass m_i .

Table 4: Governing equations of the studied phenomenological screening process models.

| Model number and origin | Major equations | Adjustable parameters |
|---|--|--|
| 1. Standish and others [45,47,225] | $E = 1 - \exp(-kt)$ | k |
| 2. Andreev et al. [226] | $E = 1 - \exp(-kt^n)$ | k, n |
| 3. Trumic/Magdalinovic [47] | $E = 1 - 1/(1 + kt)$ | k |
| 4. Standish [45] | $E = \sum_{i=1}^n \left((1 - \exp(-Ak_i t)) \cdot m_{i,0}/m_0 \right)$ A : screen area; n : number of undersize fractions | k_1, \dots, k_n |
| 5. Grozubinsky et al.; deterministic [3] | $E = 1 - \exp(-(a - d)(1 - \exp(-\beta t))tq/\beta)$ | q, β |
| 6. Subasinghe et al. [227] | $E_i = 1 - [k_{si} \exp(-k_{pi} t) - k_{pi} \exp(-k_{si} t)] / (k_{si} - k_{pi})$; $E = \sum_{i=1}^n (E_i \cdot m_{i,0}/m_0)$ k_{si} : rate constant of segregation and k_{pi} : rate constant of passage | k_{s1}, \dots, k_{sn} k_{d1}, \dots, k_{dn} |
| 7. Grozubinsky et al.; probabilistic [3] | $E = 1 - \exp(-q(a - d)(1 - \exp(-\beta t))t/\beta)$ $\cdot (1 + 0.5(qt/\beta)^2(a_D - d_{d0})(1 - \exp(-\beta t))^2)$ $a_D = \frac{1}{h-1} \sum_{i=1}^h (a_i - \bar{a})^2$; $d_{d0} = \frac{1}{n-1} \sum_{i=1}^n (d_i - \bar{d})^2$ a_D, d_{d0} : dispersion index of a (aperture size) and d (particle diameter) n : number of undersized particles; h : number of apertures \bar{d} : average undersized particle diameter; \bar{a} : average aperture size | q, β |
| 8. Subasinghe et al. [228] | $E = 1 - (1 - P)^N$; $P = (a - d)^2 / (a + w)^2$ for screen incl. $\varphi = 0^\circ$ $N = \begin{cases} c_1 \cdot t^{\tau_1} \cdot (d/a) & \text{for } (d/a) < c_2 \cdot t^{\tau_2} / (c_1 \cdot t^{\tau_1} + c_2 \cdot t^{\tau_2}) \\ c_2 \cdot t^{\tau_2} \cdot (1 - d/a) & \text{for } (d/a) > c_2 \cdot t^{\tau_2} / (c_1 \cdot t^{\tau_1} + c_2 \cdot t^{\tau_2}) \end{cases}$ | c_1, c_2, τ_1, τ_2 |
| 9. Shimosaka et al. [46] | $E = 1 - \exp(-Pt)$; $P = kP_g P_e P_f C_p$; P_e : initial undersized particle ratio $P_f = H/H_{50}$; $C_p = 0.1463 \cdot v_{frq} \cdot v_{amp}$; P_g : passage probability [24] v_{frq} : vibration frequency; v_{amp} : vibration amplitude H : max. height of initial position of particles; H_{50} : height of 50 % of particles | k |
| 10. Nakajima/Whiten [229] | $E = 1 - \exp(-NP)$; $N = kt$ $P = \cos^4(\theta - \pi/8) \alpha \left(1 - \left(\frac{d}{a_0} \right) \times \left(\left(\frac{a_1}{a_2} \right)^2 \sin^2 \theta + \cos^2 \theta \right)^{0.5} \right)^2$ $\theta = \tan^{-1}(d_t/d_w)$; d_t, d_w : particle thickness/width; $a_0 = \sqrt{a_1^2 + a_2^2}$ | k |
| 11. Dehghani et al. [52] | $E = 1 - \exp(-NP)$; $N = kt$ $P = \alpha \left((a_1 - \sqrt{2}d \cos \theta)(a_2 - \sqrt{2}d \sin \theta) / (a_1 a_2) \right)$ $\theta = \tan^{-1}(d_t/d_w)$; d_t, d_w : particle thickness/width; α : fraction open area | k |
| 12. Ferrara et al. [225] | $m_0 \left(\sum_{j=1}^n y_{j,0} \left(\frac{1}{X_{ji}} \right) (E_i(t)^{X_{ji}} - 1) + \ln E_i(t) \sum_{j=n+1}^r y_{j,0} \right) = -k2^\sigma \left(1 - \frac{d_i}{a} \right)^\sigma t$ $y_{j,0}$: initial weight fraction of particle fraction j $X_{ji} = \left((a - d_j) / (a - d_i) \right)^\sigma$ d_i, d_j : studied / other present particle diameters n, r : number of undersized / undersized + oversized particle classes | k σ (screen mesh dependent) |
| 13. Soldinger; without undersized fractions [7] | $E_{j+1} = k_j B_j (t_{j+1} - t_j) + E_j$ $B_{j+1} = B_j + (c_j(1 - S_j) - k_j B_j)(t_{j+1} - t_j)$ j : time index $k_j = b(1 - E_j)$; $c_j = f(w_q, w_d)$ B : fractional mass of undersized particles in bottom layer S : fractional mass of undersized particles stratified into bottom layer E : fractional mass of undersized particles passed through apertures | w_q (dependent on proportion of undersize material) w_d (dependent on width of particle size distribution) b (dependent on particle size) |
| 14. Soldinger; with undersized fractions [8] | $E_{i,j+1} = k_{i,j} B_{i,j} (t_{j+1} - t_j) + E_{i,j}$; i : particle class; j : time index $E_j = \sum_{i=1}^n E_{i,j}$; $B_j = \sum_{i=1}^n B_{i,j}$; n : number of undersized particle classes $B_{i,j+1} = B_{i,j} + (c_{i,j}(S_{i,\infty} - S_{i,j}) - k_{i,j} B_{i,j})(t_{j+1} - t_j)$ $k_{i,j} = b_i(1 - E_{i,j})$; $c_{i,j} = f(w_q, c_{d,i})$ B_i : fractional mass of undersized particles in bottom layer S_i : fractional mass of undersized particles stratified into bottom layer E_i : fractional mass of undersized particles passed through apertures | w_q (dependent on proportion of undersize material) $c_{d,1}, \dots, c_{d,n}$ (dependent on particle size distribution) b_1, \dots, b_n (dependent on particle diameter and aperture size) |
| 15. Yoshida et al. [5] | $E_j = 1 - 1/m_0(1 - P_j) \cdot m_{j-1}$ $P_j = P_r P_{p,j-1,n_L}$; j : trial index with $j = f \cdot t$; $P_r = P_b B + P_s(1 - B)$ P_b, P_s : probability of particles passing screen boundary / screen openings B : area ratio of the boundary on the screen surface P_p : probability of particles existing at a certain vertical position in the bed $P_{p,j,n_L} = P_{pe,n_L} P_{p,j-1,n_L-1} + (1 - P_r)(1 - P_{pe,n_L}) P_{p,j-1,n_L}$; n_L : bottom layer $P_{pe} = f(c)$: probability of undersized particles passing through a particle layer | $c = \{0, \dots, 1\}$ |

3.1 Kinetic screening process models

The basis for many batch screening process models, particularly for the kinetic ones, is the “first-order rate law” [45,47,225] referred to as model No. 1

$$dm/dt = -km, \quad (48)$$

which describes the change in mass of undersized particles remaining on the screen, m , as a function of the screening time t . Here, the adjustable parameter k is the screening rate constant. For the screening efficiency the explicit equation

$$E = 1 - \exp(-kt) \quad (49)$$

can be easily derived. An extension to model No. 1 was proposed by Andreev et al. [226] obtaining the screening efficiency as

$$E = 1 - \exp(-kt^n), \quad (50)$$

where the adjustable parameter n is additionally introduced. The model by Andreev et al. [226] referred to as model No. 2 reduces to model No. 1 for $n = 1$.

Further investigations were carried out by Trumic and Magdalinovic [47] in order to use only one adjustable parameter, resulting in an extension of the first order rate law

$$dm/dt = -kmk_p \quad (51)$$

by the coefficient of change of probability of screening $k_p = m/m_0$. This leads to

$$dm/dt = -km^2/m_0 \quad (52)$$

and after integrating, rearranging and substituting to the explicit equation

$$E = 1 - 1/(1 + kt), \quad (53)$$

referred to as model No. 3.

Screening process models Nos. 1-3 determine the screening rate and efficiency based on the passage of the whole undersized mass, thereby requiring only one set of model parameters. In case that information on the composition of the passed material is available, Standish [45] proposed a “first-order rate law” based model applicable for each undersized particle size class and its respective mass by including the screen area A , where the overall screening rate is given as

$$dm/dt = -A \cdot \sum_{i=1}^n (k_i m_i / m). \quad (54)$$

The overall undersized mass is calculated based on the fractional masses $m = m_1 + m_2 +$

... + m_n . The overall screening efficiency of this model referred to as model No. 4 is obtained as

$$E = \sum_{i=1}^n \left((1 - \exp(-Ak_i t)) \cdot m_{i,0}/m_0 \right). \quad (55)$$

Another screening process model was suggested by Grozubinsky et al. [3] following the idea of a deterministic rate law where the screening efficiency is given as

$$E = 1 - \exp(-(a - d)(1 - \exp(-\beta t))tq/\beta), \quad (56)$$

where the difference between the aperture size a and particle size d is taken into account. In this model, referred to as model No. 5, in addition to the adjustable screening intensity β , a coefficient of proportionality q is used as second adjustable parameter. For $\beta \gg 1$ model No. 5 reduces to the same functional form as model No. 1 as $\exp(-\beta t)$ becomes zero.

Subasinghe et al. [227] proposed a deterministic, kinetic model, referred to as model No. 6, in which both particle passage through the apertures as well as segregation are considered by independent rate laws per particle fraction i . The screening efficiency per fraction i is obtained as

$$E_i = 1 - [k_{si} \exp(-k_{pi} t) - k_{pi} \exp(-k_{si} t)] / (k_{si} - k_{pi}), \quad (57)$$

where k_{si} is the rate constant of segregation and k_{pi} is the rate constant of passage which are both treated as adjustable parameters. The overall screening efficiency can be obtained by $E = \sum_{i=1}^n (E_i \cdot m_{i,0}/m_0)$.

3.2 Probabilistic screening process models

The deterministic model No. 5 was extended to a probabilistic screening model referred to as model No. 7 by the same authors [3]

$$E = 1 - \exp\left(-q(a - d)(1 - \exp(-\beta t))\frac{t}{\beta}\right) \left(1 + 0.5\left(\frac{qt}{\beta}\right)^2 (a_D - d_{d0})(1 - \exp(-\beta t))^2\right), \quad (58)$$

where the dispersion indices of a and d are $a_D = 1/(h - 1) \sum_{i=1}^h (a_i - \bar{a})^2$ and $d_{d0} = 1/(n - 1) \sum_{i=1}^n (d_i - \bar{d})^2$, respectively. In the model h specifies the number of apertures, n is the number of undersized particles, \bar{d} the average undersized particle diameter and \bar{a} the average aperture size. In model No. 7 β and q are adjustable parameters.

Motivated by limitations of "first-order rate law" models, Subasinghe et al. [228] proposed a probabilistic model referred to as model No. 8 for continuous screening processes in supplement to the kinetic model No. 6. By replacing length l by time t it is made applicable to

batch screening [224]. The model calculates the screening efficiency based on the number of attempts N given by eq. (60) and the passage probability P given by eq. (61) as

$$E = 1 - (1 - P)^N, \quad (59)$$

where the number of attempts N is obtained for batch screening as

$$N = \begin{cases} c_1 \cdot t^{\tau_1} \cdot (d/a) & \text{for } (d/a) < c_2 \cdot t^{\tau_2} / (c_1 \cdot t^{\tau_1} + c_2 \cdot t^{\tau_2}) \\ c_2 \cdot t^{\tau_2} \cdot (1 - d/a) & \text{for } (d/a) > c_2 \cdot t^{\tau_2} / (c_1 \cdot t^{\tau_1} + c_2 \cdot t^{\tau_2}) \end{cases} \quad (60)$$

involving the ratio between the particle size d and the aperture size a . The model requires four adjustable parameters c_1 , c_2 , τ_1 and τ_2 . In this model the passage probability P is given by

$$P = \left(((a + w) \cos \varphi - w - d)(a - d) \right) / ((a + w)^2 \cos \varphi), \quad (61)$$

where φ is the inclination of the screen surface to the horizontal. For screens without inclination ($\varphi = 0^\circ$), eq. (61) can be simplified to

$$P = (a - d)^2 / (a + w)^2. \quad (62)$$

Shimosaka et al. [46] developed a rate law based model for the screening rate and screening efficiency which is referred to as model No. 9 in the following:

$$dm/dt = -Pm_0 \exp(-Pt), \quad (63)$$

$$E = 1 - \exp(-Pt) \quad (64)$$

It can be seen that it is equivalent to model No.1 from its functional form (comp. eq. (49) and eq. (64)), however its model parameter k is derived differently. The passage probability P is obtained as

$$P = kP_g P_e P_f C_p, \quad (65)$$

where P_g is the passage probability defined by Gaudin [24] given as

$$P_g = \alpha(1 - d/a)^2 \quad (66)$$

with aperture size a , for non-quadratic screens consisting of aperture width a_1 and length a_2 , and the particle size

$$d = \sqrt{(d_1^2 + d_2^2)/2}, \quad (67)$$

where d_1 and d_2 are particle width and length, respectively. The parameter α in eq. (66) is the fraction open area defined as

$$\alpha = a^2 / (a + w)^2 \quad (68)$$

with aperture size a and wire diameter w .

Besides P_g , the probability of existence of screening particles P_e , representing the ratio of undersized particles in the height of the initial particle layer H at $t = 0$ and all undersized particles initially on the screen is used to calculate the passage probability P . Moreover, the coefficient of dispersion of screening particles $P_f = H/H_{50}$ with the maximum height of the initial positions of the particles H and H_{50} as height of 50 % of the particles is needed. Additionally, the coefficient of velocity

$$C_p = 0.1463 \cdot v_{frq} \cdot v_{amp} \quad (69)$$

with vibration frequency v_{frq} and amplitude v_{amp} is added to the passage probability. The product $P_e P_f C_p$ expresses the collision probability of undersized particles with the screen surface. The product of $P_e P_f C_p$ and P_g represents the probability of undersized particles passing through the screen per time.

Nakajima and Whiten [229] used the following equation for the screening efficiency E in case of continuous screening processes

$$E = 1 - \exp(-NP), \quad (70)$$

where N is the number of attempts related to the specific screening conditions applied. The screening efficiency E thereby is an integral value independent of length l along the screen. To make N dependent on l and in our case on time t as suggested by [224] a linear relation $N = kt$ is introduced, where the attempts to pass are linearly related to time t which is required to describe batch screening. The probability P in eq. (70) can be calculated according to eq. (66) with $P = P_g$ and leads to accurate values in case of spherical particles and square-aperture screens [52]. In order to additionally describe the behavior of non-spherical particles on arbitrary slotted screens an empirical probability function was proposed by Nakajima and Whiten [229] which in combination with eq. (70) is referred to as model No. 10 in the following with

$$P = \cos^4(\theta - \pi/8) \alpha (1 - (d/a_0) \times ((a_1/a_2)^2 \sin^2 \theta + \cos^2 \theta)^{0.5})^2 \text{ or} \quad (71)$$

$$P = 0 \text{ for } d > a_0 / ((a_1/a_2)^2 \sin^2 \theta + \cos^2 \theta)^{0.5},$$

where α is the fraction open area (eq. (68)) and θ , the angle of a non-spherical particle, is defined by

$$\theta = \tan^{-1}(d_t/d_w) \quad (72)$$

with d_t the particle thickness and d_w the particle width. Besides, the non-square mesh is given through

$$a_0 = \sqrt{(a_1^2 + a_2^2)}, \quad (73)$$

where a_1 is the longer side of the rectangular aperture and a_2 is the shorter side. Model No. 10 requires one adjustable parameter k .

Based on the empirical probability function (eq. (71)) by Nakajima and Whiten [229], Dehghani et al. [52] proposed a probability function for rectangular-aperture screens in alignment with P_g by Gaudin [24] which is also applicable for non-spherical particles. The resulting probability equation reads

$$P = \alpha((a_1 - \sqrt{2}d \cos \theta)(a_2 - \sqrt{2}d \sin \theta)/(a_1 a_2)) \text{ or} \quad (74)$$

$$P = 0 \text{ for } d > a_0 / ((a_1/a_2)^2 \sin^2 d_t + \cos^2 d_t)^{0.5},$$

where α is the fraction open area again as defined by eq. (68). Eq. (74) can be combined with eq. (70) to form model No. 11, where k is an adjustable parameter.

Ferrara et al. [225] developed a probabilistic model based on the kinetic first order rate law and combined it with the probability function proposed by Gaudin (eq. (66)). The model is referred to as model No. 12. The following expression was proposed to take the influence of surrounding particles into account

$$X_{ji} = ((a - d_j)/(a - d_i))^\sigma, \quad (75)$$

where d_i is the diameter of the i -th particle size class studied and d_j is the diameter of the j -th surrounding size class affecting the behavior of the size class i ; σ is a screen mesh dependent adjustable parameter, which usually obtains values close to 2 for square meshes [225]. The expression (eq. (75)) was inserted into model equations for crowded, separated and mixed condition screening. For the batch screening investigations in this work, the crowded screening model equation

$$m_0 \left(\sum_{j=1}^n y_{j,0} (1/X_{ji}) (E_i(t)^{X_{ji}} - 1) + \ln E_i(t) \sum_{j=n+1}^r y_{j,0} \right) = -k2^\sigma (1 - d_i/a)^\sigma t \quad (76)$$

is used, where $y_{j,0}$ is the weight fraction of particle fraction j with $y_{j,0} = m_{j,0}/m_0$. $E_i(t)$ is the time dependent screening efficiency per particle class i as defined in eq. (47). The parameters n and r represent the number of undersized and the number of undersized plus oversized particle classes, respectively. Note, that $E_i(t) = 1$ for $n + 1 \leq i \leq r$. The model No. 12 must be

solved iteratively in order to obtain a result for the screening efficiency E_i and thus requires more time for its solution than the previously discussed models.

3.3 Complex phenomena based screening process models

In contrast to the models Nos. 1-12 discussed so far, the following screening models Nos. 13-15 do not provide parameters like the screening rate and efficiency in a single equation or in explicit form. Instead, they provide sets of equations which are discretized in time making available detailed information on the screening process such as segregation or passage.

One of these models is the model proposed by Solding [7], referred to as model No. 13 in the following, where all undersized particles are regarded as one lumped particle class. Before passing the apertures, the undersized particles have to stratify to the screen surface. To describe this process Solding [7] introduced a control volume referred to as bottom layer of the thickness of the diameter of the coarsest particles in the system. The fractional mass B of undersized particles in the bottom layer changes over time due to the fractional mass stream \dot{S} of particles stratifying into the bottom layer and due to the fractional mass stream \dot{E} of particles leaving the system when passing through the apertures. This process is described by

$$\dot{B} = \dot{S} - \dot{E} = \frac{B_{j+1} - B_j}{t_{j+1} - t_j} = \frac{S_{j+1} - S_j}{t_{j+1} - t_j} - \frac{E_{j+1} - E_j}{t_{j+1} - t_j}, \quad (77)$$

where $\Delta t = t_{j+1} - t_j$ represents a fixed, discrete time step and $E = m_0 - m/m_0$ is the fractional mass passed through the apertures with m the mass of the undersized material retained on the screen. Note, that E is the screening efficiency as defined in eq. (46). S_j is the fractional mass of undersized particles stratified into the bottom layer at time step j .

The fractional mass stream of stratified particles \dot{S} is proportional to the unstratified material outside the bottom layer $(1 - S_j)$ and can be calculated as

$$\dot{S} = (S_{j+1} - S_j)/(t_{j+1} - t_j) = c_j(1 - S_j), \quad (78)$$

where c_j is a time dependent parameter determining the rate of stratification (comp. eq. (82)). The rate of passage \dot{E} is dependent on the fractional mass in the bottom layer and determined by

$$\dot{E} = (E_{j+1} - E_j)/(t_{j+1} - t_j) = k_j B_j \quad (79)$$

with a parameter k_j that determines the rate of passage (comp. eq. (81)). Eqs. (75)-(77) can be combined to calculate the fractional mass of undersized particles in the bottom layer in an upcoming time step $j+1$ as

$$B_{j+1} = B_j + (c_j(1 - S_j) - k_j B_j)(t_{j+1} - t_j), \quad (80)$$

when S_0 and B_0 for $j = 0$ are provided. Note that $S_0 = B_0$ and $E_0 = 0$ in eq. (79). The rate of passage in eq. (77), eq. (79) and eq. (80) obtains a maximum value in case that the whole screen surface is covered with undersized particles. Therefore, B_j is limited by $B_p = B_{mP}/m_0$ with B_{mP} the mass of the bottom layer when the whole screen surface is covered with a single-particle layer of undersized material and m_0 the initial mass of undersized material on the screen.

To obtain the rate of passage, the passage parameter

$$k_j = b(1 - E_j) \quad (81)$$

is needed, where b is influenced by the average size of the undersized particles on the screen and used as adjustable parameter in model No. 13.

The stratification parameter is obtained through

$$c_j = c_{q,j} \cdot c_{d,j}, \quad (82)$$

with one part determined by the proportion of undersized material

$$c_{q,j} = w_q \cdot \exp(-(x \cdot q_j)^y), \quad (83)$$

where w_q is considered as a second adjustable parameter and used to take the influence of the proportion of undersized material and its shape into account. The constants x and y have to be adjusted before using the model and were set to $x = 2$ and $y = 5$ in the work of Soldinger [7]. The parameter q_j is the proportion of undersized material gathered above the bottom layer:

$$q_j = \left(Q_0 \cdot (1 - (E_j + B_j)) \right) / \left(1 - Q_0(E_j + B_j) \right), \quad (84)$$

with Q_0 as ratio of the undersized and the total applied particle mass above the bottom layer.

The other part of c_j is determined by the ratio of the size of the particles as

$$c_{d,j} = w_d \cdot q_j, \quad (85)$$

where w_d is dependent on the width of the particle size distribution and used as a third adjustable parameter in model No. 13.

In further studies Soldinger [8] refined model No. 13 by taking into account the different undersized particle fractions instead of regarding the undersized particles as one lumped fraction. This model is referred to as model No. 14 in the following. The equations governing

model No. 14 are similar to those of model No. 13. The fractional mass stream of undersized particles of class i passed into the bottom layer read analogously to eq. (78)

$$\dot{S}_i = (S_{i,j+1} - S_{i,j}) / (t_{j+1} - t_j) = c_{i,j}(S_{i,\infty} - S_{i,j}), \quad (86)$$

with the total proportion of undersized material in each fraction $S_{i,\infty} = m_{i,0}/m_0$ instead of the value 1 in model No. 13. The fractional and summed up passage rate are

$$\dot{E}_i = (E_{i,j+1} - E_{i,j}) / (t_{j+1} - t_j) = k_{i,j}B_{i,j}, \quad (87)$$

$$\dot{E} = \sum_{i=1}^n \dot{E}_i, \quad (88)$$

with n as number of undersized particle classes. The amount of material in the bottom layer is obtained by

$$B_{i,j+1} = B_{i,j} + (c_{i,j}(S_{i,\infty} - S_{i,j}) - k_{i,j}B_{i,j})(t_{j+1} - t_j) \quad (89)$$

when $S_{i,0}$ and $B_{i,0}$ for $j = 0$ are provided. Note that $S_{i,0} = B_{i,0}$ and $E_{i,0} = 0$ in eq. (87).

The passage rate in model No. 14 increases with an increasing amount of undersized particles in the bottom layer until a maximum value is reached when the complete screen surface is filled up by undersized particles [7,8]. To account for this, $B_{i,j}$ in eq. (89) is replaced by $B_p B_{i,j} / B_j$ when $B_j > B_p$ with $B_p = B_{mP} / m_0$. Here B_{mP} is the mass of the bottom layer when the whole screen surface is covered with a single-particle layer of undersized material and m_0 is the initial mass of undersized material on the screen. Note that as height of the single particle layer the average diameter of the undersized particle fractions is used. The total fraction of undersized material in the bottom layer is calculated as $B_j = \sum_{i=1}^n B_{i,j}$.

The passage parameter $k_{i,j}$ is not set constant for all undersized particle fractions as proposed in [8], but set dependent on passage as suggested by Soldinger [7] earlier as

$$k_{i,j} = b_i(S_{i,\infty} - E_{i,j}), \quad (90)$$

where b_i is influenced by the size of the respective undersized fraction on the screen. The parameters b_i are used as adjustable parameters in model No. 14.

The stratification parameter $c_{i,j}$ is calculated differently in model No. 14 in contrast to model No. 13 as it takes the bed thickness additionally into account as

$$c_{i,j} = (c_{q,j} \cdot c_{d,i}) / (H_{t,j} / d_{av,c}), \quad (91)$$

with $d_{av,c}$ as average diameter of the coarse particles and $H_{t,j}$ the thickness of the layer above the bottom layer at time step j . The part of $c_{i,j}$ determined by the proportion of undersized material atop the bottom layer

$$c_{q,j} = w_q \cdot \exp\left(-(2 \cdot q_j)^5\right) \quad (92)$$

is calculated like in Solding [7] with w_q considered as a further adjustable model parameter. The proportion of fine material is now obtained with

$$q_j = \left(m_0 \cdot \sum_{i=1}^n (S_{i,\infty} - S_{i,j})\right) / \left(M_0(1 - Q_0) + m_0 \cdot \sum_{i=1}^n (S_{i,\infty} - S_{i,j})\right), \quad (93)$$

where m_0 is the initial mass of the undersized material on the screen, M_0 is the total initial mass on the screen and Q_0 is the ratio of the undersized mass outside the bottom layer and the total applied particle mass.

The part of $c_{i,j}$ that is determined by the ratio of the size of the particles $c_{d,i}$ changes in model No. 14 with time. It is calculated by

$$c_{d,i} = \exp\left(-2.5 \cdot V_{i,part} / V_{av,t}\right) \quad (94)$$

where $V_{i,part}$ is the size of the respective particle and $V_{av,t}$ is the average volume of particles in the layer atop the bottom layer. The value of 2.5 was obtained by Solding [8] by fitting eq. (94) to experimental data.

The thickness of the layer atop the bottom layer needed in eq. (91) is calculated as

$$H_{t,j} = M_{t,j} / (W^2 \cdot \rho), \quad (95)$$

where W is the length and width of a quadratic screen, ρ is the bulk density which is assumed constant. The mass of material in the layer atop the bottom layer is

$$M_{t,j} = M_0 - m_0 \cdot (E_j + B_j), \quad (96)$$

where $E_j = \sum_{i=1}^n E_{i,j}$ and M_0 and m_0 are defined as in eq. (93).

Yoshida et al. [5] proposed a batch screening model, referred to as model No. 15 in the following, optimized for a specific setup in which a few undersized particles are placed atop several layers of oversized particles. It considers particle passage through the vibrated bed, through the boundary between oversized particles and the screen surface and through the screen apertures. The oversized particles are agitated due to the screen movement not leaving the system; hence the particle bed is undergoing cyclic expansion and compaction. The trajectories of the oversized particles can be calculated in the model as

$$z_p = z_{p,0} + z_{L,sn g} + k_y \cdot \sin \theta_y \cdot v_{L,sn g} (t - t_\phi) - 0.5g(t - t_\phi)^2, \quad (97)$$

where $z_{p,0}$ is the initial vertical position of the oversized particles, $z_{L,sn g} = r \cdot \sin \omega t_\phi$ is the vertical position of a single particle at the takeoff point, $v_{L,sn g} = r \cdot \omega \cdot \cos \omega t_\phi$ is the takeoff velocity of a single particle dependent on the half amplitude r and the angular velocity ω , $t_\phi = 1/\omega \sin^{-1} g/r\omega^2$ is the time after particle takeoff with g the gravitational acceleration, θ_y is the takeoff angle of the oversized particles from the screen surface and k_y is the decreasing ratio of the upward particle velocity which is 1 in the top layer and decreasing with more covering particles towards the bottom layer. Data on k_y as well as on θ_y has to be provided from experiments or detailed simulations. In contrast to the setup considered by Yoshida et al. [5] (many oversized particles) the overall bed height and thereby $z_{p,0}$ in the investigations here, decreases over time during screening due to undersized particles passing through the screen apertures. Therefore, $z_{p,0}$ needs to be obtained time dependent from experimental or other numerical data or model extensions have to be proposed where $z_{p,0}$ in eq. (97) is made dependent on the bed height as e.g. in the model by Soldinger [8]. Here, the first approach is used.

The thickness of one particle layer L is equal to the oversized particle diameter d_o . The height of the particle bed H is computed through the maximum value of z_p . The number of particle layers is varying over time when significant particle mass is passing the apertures. It is required to calculate the resistance of undersized particles stratifying through the bed and is obtained as

$$n_L = n_{L,ini} + \Delta n_L, \quad (98)$$

where $n_{L,ini} = H/L$ is the initial number of particle layers and Δn_L is the variation of particle layers over time due to passage and particle trajectories. The bottom layer is referred to as layer n_L , the layer above the bottom layer as n_{L-1} . The uppermost layer is defined as layer 0.

The number of oversized particles existing in the l -th layer is expressed as

$$\begin{aligned} N_{p,o,l} &= N_{p,o} / (n_L \cdot (\Delta n_L + 1)), \quad l < \Delta n_L + 1, \\ N_{p,o,l} &= N_{p,o} / n_L, \quad l > \Delta n_L + 1, \end{aligned} \quad (99)$$

with $N_{p,o}$ the total number of oversized particles. The number of undersized particles in the l -th layer is calculated likewise with the total number of undersized particles $N_{p,u}$.

The probability of undersized particles passing through a particle layer P_{pe} , is defined as

$$P_{pe} = 1 - P_c(d_o/L_e)^2, N_{p,u,l} \leq N_e \cdot m_e, \quad (100)$$

$$P_{pe} = (1 - P_c(d_o/L_e)^2) \cdot (N_e \cdot m_e) / N_{p,u,l}, N_{p,u,l} > N_e \cdot m_e,$$

where N_e is the number of unit elements (for a detailed definition it is referred to [5]) and $N_{p,u,l}$ is the number of undersized particles in a certain particle layer l . The maximum number of undersized particles approaching a unit element in a unit trial is

$$m_e = (4(L_e - d_u)^2) / (\pi d_u^2), \quad (101)$$

with d_u as the undersized particle diameter and the size of a unit element in a particle layer given by

$$L_e = L \sqrt{\pi / (6(1 - \varepsilon_l))}. \quad (102)$$

The porosity of the l -th layer needed in eq. (102) is calculated as

$$\varepsilon_l = \left(((\pi d_u^3) / 6) \cdot N_{p,o,l} \right) / V, \quad (103)$$

where V is the volume of a particle layer and $N_{p,o,l}$ is the number of oversized particles in the l -th layer as defined by eq. (99). Also required for P_{pe} (eq. (100)) is the possibility that the undersized particles will collide with the oversized particles

$$P_c = \left(L_e(L_e + d_u) \sin \left(\cos^{-1} \left(\frac{L_e}{L_e + d_u} \right) \right) + (L_e + d_u)^2 \left(\frac{\pi}{4} - \cos^{-1} \left(\frac{L_e}{L_e + d_u} \right) \right) \right) / L_e^2. \quad (104)$$

Due to considering the particle movement as only vertically, P_{pe} is multiplied with a compensation coefficient $c = \{0 \dots 1\}$ which is used as the only adjustable parameter in model No. 15. The modified probability P'_{pe} is obtained as

$$P'_{pe} = c \cdot P_{pe} \quad (105)$$

and can be used alternatively to P_{pe} in the following equations.

The probability of particles passing through screen openings is based on the equation of Gaudin (eq. (66)) which is modified, because of the passage limitation in a unit trial to

$$P_s = P_g, m_s \cdot N_s \geq N_{p,u} \cdot P_{p,j,n_L}, \quad (106)$$

$$P_s = P_g \cdot (m_s \cdot N_s) / (N_{p,u} \cdot P_{p,j,n_L}), m_s \cdot N_s < N_{p,u} \cdot P_{p,j,n_L},$$

where N_s is the number of screen openings and m_s the maximum number of undersized particles passing through one screen opening in a unit trial given as

$$m_s = (4(a - d_u)^2)/(\pi d_u^2). \quad (107)$$

For P_s it is necessary to know P_p , which is the probability of undersized particles existing at a certain vertical position in the bed in layer l at a certain trial j . For P_s particularly the bottom layer n_L is of relevance.

The equations for P_p in the l -th ($0 < l < n_{L-1}$), 0-th, (n_{L-1}) -th and n_L -th particle layer at the j -th trial are given as

$$P_{p,j,l} = P_{pe,l}P_{p,j-1,l-1} + (1 - P_{pe,l+1})(1 - P_{pe,l})P_{p,j-1,l} + (1 - P_{pe,l+2})P_{pe,l+1}P_{p,j-1,l+1}, \quad (108)$$

$$P_{p,j,0} = (1 - P_{pe,l})P_{p,j-1,0} + (1 - P_{pe,2})P_{pe,l}P_{p,j-1,l}, \quad (109)$$

$$P_{p,j,n_{L-1}} = P_{pe,n_{L-1}}P_{p,j-1,n_{L-2}} + (1 - P_{pe,n_L})(1 - P_{pe,n_{L-1}})P_{p,j-1,n_{L-1}} + (1 - P_r)P_{pe,n_L}P_{p,j-1,n_L}, \quad (110)$$

$$P_{p,j,n_L} = P_{pe,n_L}P_{p,j-1,n_{L-1}} + (1 - P_r)(1 - P_{pe,n_L})P_{p,j-1,n_L}, \quad (111)$$

with the trial index j which is related to the time t by $j = f \cdot t$, where f is the frequency of the vibration. At the beginning of a sieving investigation, particles are compacted and equally distributed over the layers giving $P_{p,0,0} = P_{p,0,l} = P_{p,0,n_{L-1}} = P_{p,0,n_L} = 1/n_L$ as starting values. Initial values for eqs. (104)-(107) at $j = 0$ for beds in which particles are not equally distributed can be obtained from other detailed numerical methods such as the DEM or from experiments. Note that eq. (99) which implies an equal particle distribution has to be altered accordingly. For eq. (110) and eq. (111) the combined probability

$$P_r = P_b B + P_s(1 - B) \quad (112)$$

is needed, where P_b is the probability of particles passing the boundary between the particle bed and the screen surface and P_s (comp. eq. (106)) is the probability of particles passing the screen openings, respectively. The probability of undersized particles passing through the boundary is calculated as

$$P_b = \frac{1}{t^*} \int_{t_1}^{t_1+t^*} \frac{h - d_u}{h} dt \cdot \frac{t^*}{T}, \quad (113)$$

where t^* is the time during which the undersized particles can pass through the boundary, t_1 is the time when the height of the boundary becomes larger than the undersized particle diameter and T is the time period of oversized particles bouncing on the screen surface which is the inverse frequency f . The boundary height $h_j = z_{p,btm,j} - z_{s,j}$ is the difference between the vertical position of the oversized particles in the bottom layer and the vertical position of the screen surface at trial index j .

The area ratio of the boundary formed on the screen surface is

$$B = \left(\frac{1}{t^*} \int_{t_1}^{t_1+t^*} N_{btm} dt (\pi d_o^2 / 4) \right) / S, \quad (114)$$

where N_{btm} is the number of oversized particles in the bottom layer and S is the screen area.

Therefore, the probability of undersized particles passing through the screen openings is

$$P_j = P_r P_{p,j-1,n_L} \quad (115)$$

which can finally be used to derive the screening efficiency as

$$E_j = 1 - \frac{(1-P_j) \cdot m_{j-1}}{m_0}. \quad (116)$$

Further information, particularly for the more complex models by Ferrara et al. [225], Soldinger [7,8] and Yoshida et al. [5], can be found in their respective publications.

4. Numerical setup and simulation parameters

Screening of a polydisperse feed material is investigated by the DEM in a batch screen apparatus as shown in Fig. 39a. The batch apparatus is initially equipped with a wire screen comprising 34 x 34 apertures on a floor area of 0.2 m x 0.2 m. The aperture size a is 4.9 mm and the wire diameter w is 1 mm. In initial configuration, the apparatus is vibrated with 27.6 Hz with a stroke angle of 90° to the horizontal at an amplitude of 3.52 mm (Fig. 39). The screen wire is approximated by triangular surface elements initially forming a rectangular profile in the simulations that is later compared to a semicircular one.

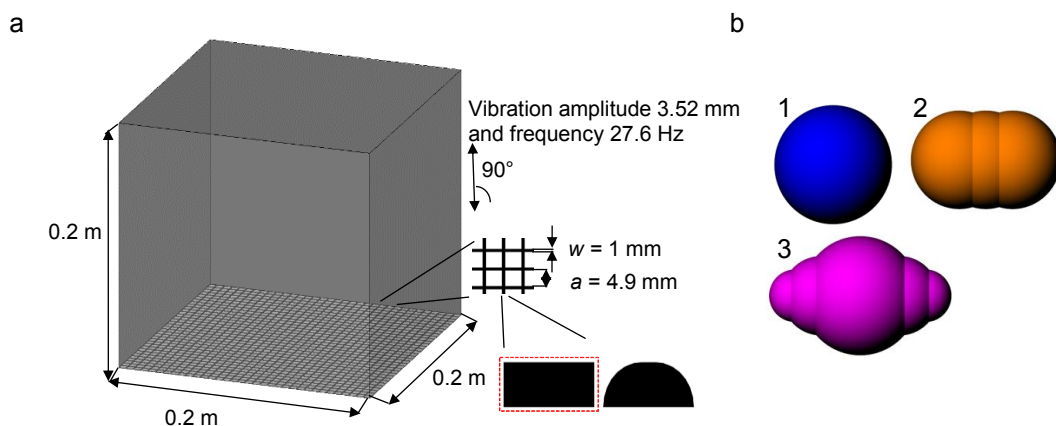


Fig. 39: (a) Batch screening apparatus with wire structure. (b) Considered particle shapes.

The polydisperse feed material comprises of particles with a density of 2700 kg/m³ subdivided into three relevant size classes consisting of coarse, near mesh and fine material represented by particles with average diameters of 7.35 mm (1.5a), 4.2875 mm (0.875a) and 2.45 mm (0.5a) in case of spheres, respectively. The initial mass amounts to 4 kg, divided equally into

the examined particle classes. The applied DEM parameters are adjusted according to the work by Delaney et al. [20] and Cleary [62] applicable for standard industrial quarry rock, where the tangential spring constant is $k^t = 0.5 \cdot k^n$. Accordingly, the stiffnesses k^n and k^t are set to $k^n = 1000 \text{ N/m}$ and $k^t = 500 \text{ N/m}$, resulting in average particle overlaps of around 0.5%, which leads to accurate outcomes independent of the spring stiffness. The coefficients of normal restitution between particles e_{PP}^n and particles and walls e_{PW}^n and the Coulomb friction coefficient μ_C between particles and the screen wire as well as between particles and particles are adjusted to: $e_{PP}^n = 0.4$, $e_{PW}^n = 0.5$, $\mu_C = 0.5$. To minimize boundary effects, there is no friction between the side walls and the particles considered ($\mu_C = 0$). Besides spheres, differently sized cylinders and double cones are studied in this investigation (Fig. 39b). The non-spherical particles (shapes (2) and (3)) are selected to have an aspect ratio of 1.55. The cylindrical particles with a hemispherical termination at both ends (shape (2)) are volume equivalent to the spherical particles. The double cones (shape (3)) have the same minor axis as the spheres. This gives them the same long-term separation characteristics in a screening analysis; their time dependent separation rates however differ.

Starting from the initial setup (base case), variations of the vibration amplitude and frequency, stroke angle and overall particle mass are performed for all three particle shapes varying one of the parameters at a time (Table 5).

Table 5: Initial setup and performed variations of the batch screening investigations.

| Parameter | Initial | Var. 1 | Var. 2 | Var. 3 | Var. 4 | Var. 5 | Var. 6 | Var. 7 | Var. 8 |
|--|---------------|---------------|------------------|------------------|-----------|--------|--------|--------|--------|
| Amplitude [mm] | 3.52 | 0.88 | 1.76 | 2.64 | 4.4 | 5.28 | 6.16 | 7.04 | 10.56 |
| Frequency [Hz] | 27.6 | 6.9 | 13.8 | 20.7 | 34.5 | 41.4 | 48.3 | 55.2 | - |
| Stroke angle [°] | 90 | 60/120 | 45/135 | 30/150 | - | - | - | - | - |
| Particle mass [kg] | 4 | 1 | 2 | 3 | 5 | 6 | - | - | - |
| Friction coefficient PP [-] / PW [-] | 0.5 / 0.5 | 0.3 / 0.5 | 0.7 / 0.5 | 0.5 / 0.3 | 0.5 / 0.7 | - | - | - | - |
| No. of particle classes [-] | 3 | 6 | 9 | - | - | - | - | - | - |
| Screen dimensions [m] / No. of apertures [-] | 0.2x0.2 34 | 0.1x0.1 17 | 0.047x0.047 8 | 0.023x0.023 4 | - | - | - | - | - |
| Scree wire profile | rectangular | semicircular | - | - | - | - | - | - | - |

Furthermore, the particle-particle as well as the particle-wall friction coefficient and the number of particle classes are changed. In the latter variation the number of subclasses per size class (coarse, near mesh and fine) is altered. Resulting particle diameters are 8.575 mm, 6.125 mm, 4.594 mm, 3.981 mm, 3.063 mm and 1.838 mm in case of 6 particle classes and 8.575 mm, 7.35 mm, 6.125 mm, 4.594 mm, 4.2875 mm, 3.981 mm, 3.063 mm, 2.45 mm and 1.838 mm in case of 9 particle classes. Additionally, the screen dimensions and thereby the number of apertures are changed. Note, that the overall particle mass is adjusted accordingly to maintain

the same fill level in the investigations. Last but not least, the screen wire approximation is changed to a semicircular profile (Fig. 39a).

5. Results and discussions

In all performed investigations, the feed consists of one of the particle shapes outlined in Fig. 39b. For each particle shape the influence of the parameter modifications outlined in Table 5 is examined, where only one parameter is varied at a time. The outcome obtained for the simulations is subsequently compared to results attained by phenomenological screening process models (Table 4) whose adjustable parameters are fitted by genetic algorithms to the retained mass on the screen obtained from the DEM [240].

5.1 Numerical investigations

Particles are filled into the screen apparatus well mixed which is then vibrated for $t = 40$ s. Due to the motion of the screen, fine and near mesh size particles stratify downwards through the gaps between the oversized particles towards the screen surface. By reaching the bottom layer of the box, whose thickness is defined by the diameter of the respective coarse sized particles, especially the fine particles gain the possibility to pass through the apertures in the bottom plate. Due to the smallest ratio between the fine particle's minor axis and the oversized particles or else the screen apertures, the possibility of passing through interstices between particles and screen openings is highest for them. Accordingly, the average residence time for the finest particles in the particle bed excluding the bottom layer as well as the bottom layer itself is shorter than for near mesh size particles (comp. Fig. 40).

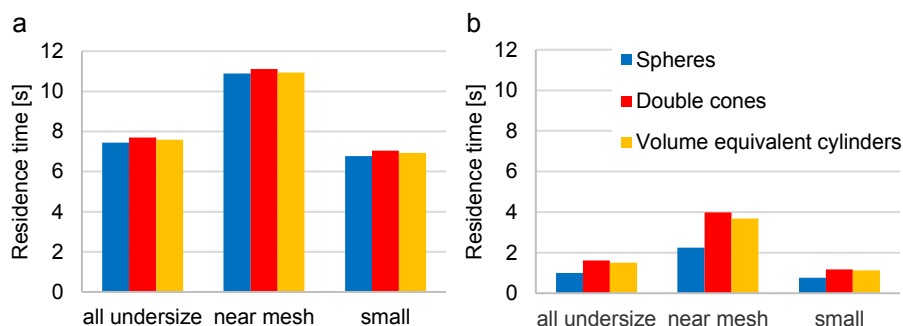


Fig. 40: Average residence time of fine, near mesh and all undersize particles in the base case: (a) in the particle bed above the bottom layer and (b) in the bottom layer.

Likewise, the decline of the residual mass and the particle passage over time are more pronounced for the finest material. Details on the average residence time in the particle bed above the bottom layer and the bottom layer for fine and near mesh particles are shown in Fig. 40 for the base case operational parameters. It can be seen that fine particles have a shorter residence time in the particle bed than the near mesh particles due to their better stratification ability (Fig. 40a). Furthermore, fine particles reside less time in the bottom layer than the near mesh particles which underlines their higher ability to pass the apertures in the

bottom plate (Fig. 40b). Particle shape has some influence on both stratification and passage. Stratification is not differing much for the considered particle shapes. It is fastest for spheres closely followed by volume equivalent cylinders and double cones. Likewise, passage is fastest for spheres as they stay shortest in the bottom layer followed by volume equivalent cylinders and double cones. In contrast to stratification, there is strong difference between spherical and non-spherical shapes for passage particularly for the near mesh particles (Fig. 40b).

To achieve a better comparability for the analysis of the time-resolved overall particle passage within the screen apparatus which is investigated in the following, the passed mass is summed up and normalized for all particle classes with diameters smaller than the apertures. Among the considered particle shapes the highest passage ability is exposed by spheres followed by the non-spherical shapes in all investigations (comp. Figs. 41 – 44). One reason for this order is the slightly longer residence time of complex shaped particles in the particle bed (comp. Fig. 40a) and particularly in the bottom layer (comp. Fig. 40b).

In the first study (Fig. 41a) the initial amplitude of 3.52 mm is varied according to Table 5. Looking at the results for the smallest amplitude of 0.88 mm where approximately 50 % residuals remain on the screen, the particle passage significantly increases for larger amplitudes independent of the particle shape. The passage is enhanced up to a critical amplitude of 6.16 mm (5.28 mm for double cones) and then stagnates or slightly decreases, respectively. A larger amplitude enhances the porosity in the particle bed and thus leads to larger gaps between the oversized particles resulting in an improved stratification of smaller particles. In contrast, larger amplitudes beyond a critical amplitude lead to an elevation of the particle bed and therefore to larger distances between particles and the screen surface reducing overall passage. Additionally, impacts are of higher velocity and thereby characterized by a strong rebound which is also affecting the passage through the apertures.

This behavior can be confirmed by Fig. 41c where the simulations with an amplitude of 4.4 mm show the shortest residence time in the bottom layer for undersized particles independent of shape. At this amplitude the possibility to pass the apertures is highest. Nevertheless, larger amplitudes provide a better overall passage rate, because overall passage is affected by both stratification and the ability to pass the apertures. Therefore, highest overall passage is shifted to amplitudes larger than 4.4 mm where stratification is enhanced and residence time in the bottom layer is yet not extended. For double cones it can be recognized exemplarily that residence times are enhanced in the bottom layer for larger amplitudes (Fig. 41c) which reduces overall particle passage as a consequence (Fig. 41a).

The second investigation (Fig. 41b) addresses the variation of the frequency (Table 5). Again the two lowest frequencies yield the least particle passage with under 50 % after $t = 40$ s, due to a low stratification. Additionally, the particles are in an immobile state which leaves them

few possibilities to get in direct contact with apertures, forcing them to reside an extended period of time in the bottom layer independent of particle shape (Fig. 41d). All the other settings reveal similar results for the overall passage throughout the first 10 s of the investigation, but with final residual mass on the screen varying between 0 % - 20 % at the end of the screening time. The initial frequency value of 27.6 Hz displays the best passage ability over more than half of the simulation time, before being outperformed by the frequency of 34.5 Hz. Despite a higher porosity in the bed and therefore theoretically more possibilities to stratify, all higher frequencies lead to lower passage rates, particularly for spheres. This can be explained by the chaotic particle motion caused by the difference between the oscillation frequency of the screen and the overall movement of the particles.

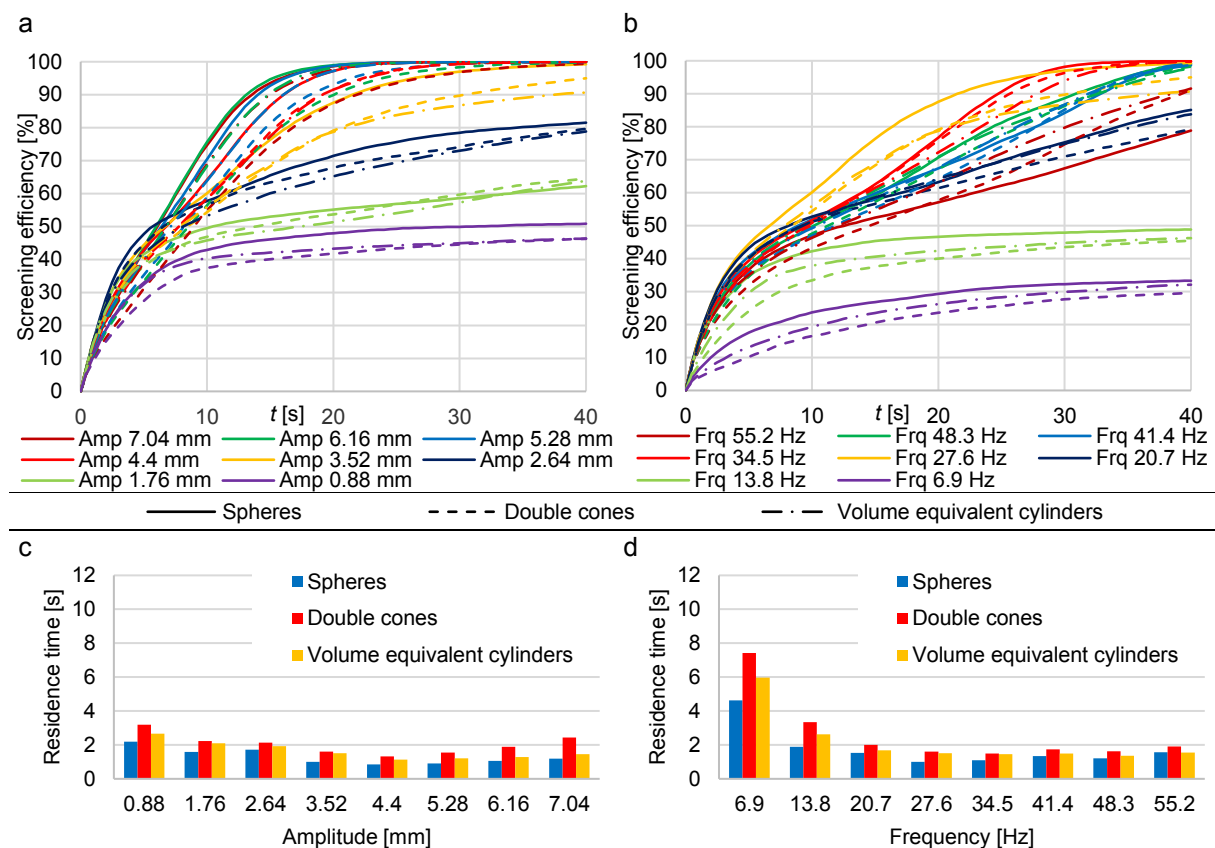


Fig. 41: (a,b) Particle passage through the screen openings for the three considered particle shapes for (a) varying amplitudes and (b) frequencies and (c,d) corresponding average residence times in the bottom layer for (c) varying amplitudes and (d) frequencies.

Initially, a stroke angle of 90° to the horizontal, is used in the simulations (Table 5) which is changed to an oscillating movement consisting of two stroke angles with varying horizontal and vertical components in the third investigation (Fig. 42a). While improving the particle passage significantly for spheres, an alternating stroke angle of $45^\circ/135^\circ$ reduces the passage of complex shaped particles. In contrast, a stroke angle of $30^\circ/150^\circ$ increases the screening efficiency of all particle shapes intensively as particles have enhanced chances to initially enter an aperture under trajectories allowing a quick passage due to a pronounced downwards motion before and after screen contact. Using a $60^\circ/120^\circ$ angle significantly reduces the passage only for cylinders. The above mentioned observations can also be affirmed by the

enhanced residence times of non-spherical particles in the case of $60^\circ/120^\circ$ and $45^\circ/135^\circ$ stroke angles as well as by the reduced residence times in the bottom layer for spheres for stroke angles of $45^\circ/135^\circ$ and for all particle shapes for stroke angles of $30^\circ/150^\circ$, respectively (Fig. 42c). Generally a combination of a stronger horizontal with a less intense vertical motion component as e.g. for $30^\circ/150^\circ$ facilitates more possibilities to pass the screen openings for all undersized particle shapes, whereas a combination of a stronger vertical with a weaker horizontal motion forces the oversized elongated non-spherical particles to vertically align with the bottom plate thus leading to pronounced pegging of the apertures.

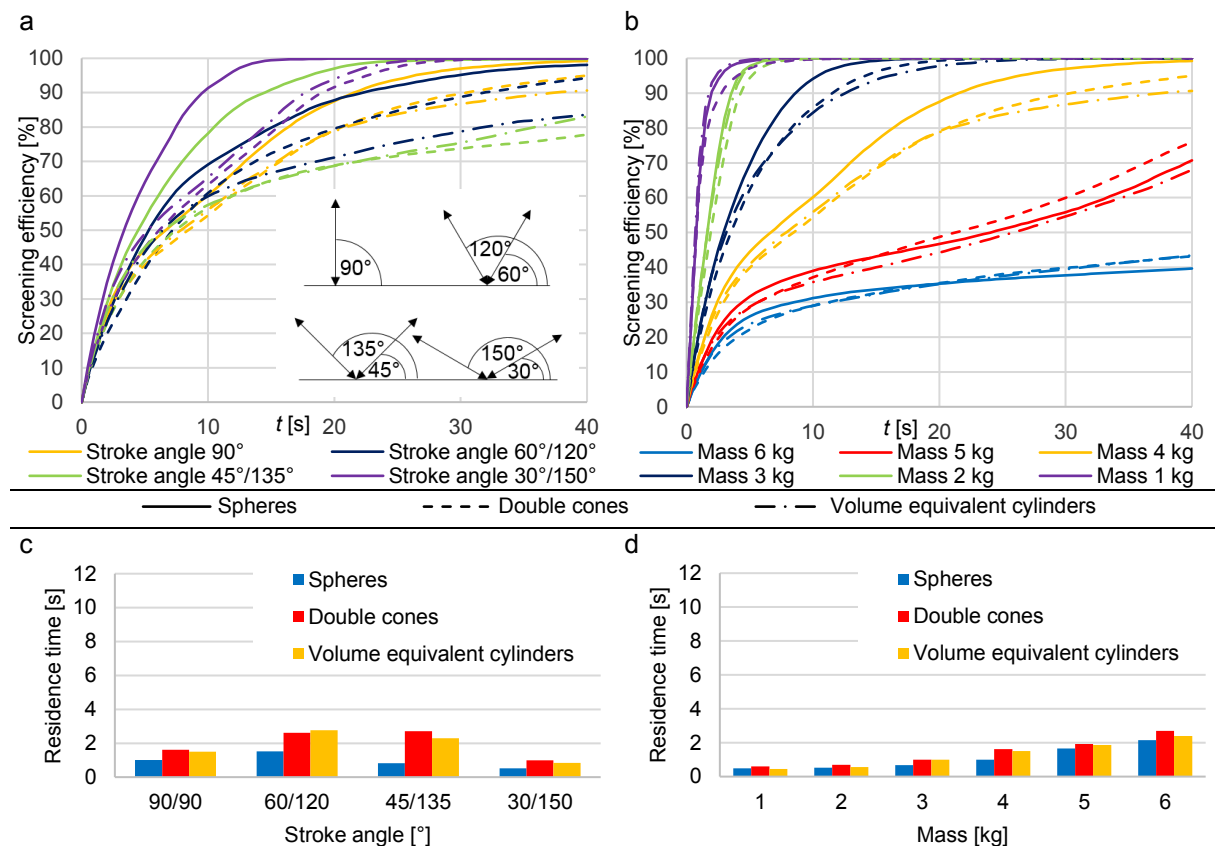


Fig. 42: (a,b) Particle passage through the screen openings for the three considered particle shapes for (a) varying stroke angles and (b) bulk masses and (c,d) corresponding average residence times in the bottom layer for (c) varying stroke angles and (d) bulk masses.

The fourth investigation addresses a variation of total particle mass (Fig. 42b). Due to a lower bed height and therefore faster stratification, applying a lower mass results in faster particle passage. In comparison, particles in a thicker bed layer caused by a larger particle mass require additional time to stratify and thus for passing likewise. The probability of pegging is enhanced for larger particle masses with more oversized particles being present. As a consequence, the undersized particles stay longer in the bottom layer when more mass is applied to the screen (Fig. 42d).

Due to a comparatively large mass applied in the base case of 4 kg, a change in friction, studied in the fifth investigation, has little effect on the overall particle passage (Fig. 43a). As driving force the bulk particle mass causes the undersize particles to pass through the

apertures regardless of particle/wall (PW) or particle/particle (PP) friction coefficients considered here. Solely, a reduction of friction among particles leads to an accelerated passage in the first 20 seconds. Nevertheless, after $t = 40$ s, approximately the same amount of particles has passed through the apertures independent of particle shape. Well in accordance to these results, residence times in the bottom layer shown in Fig. 43c are merely unaffected.

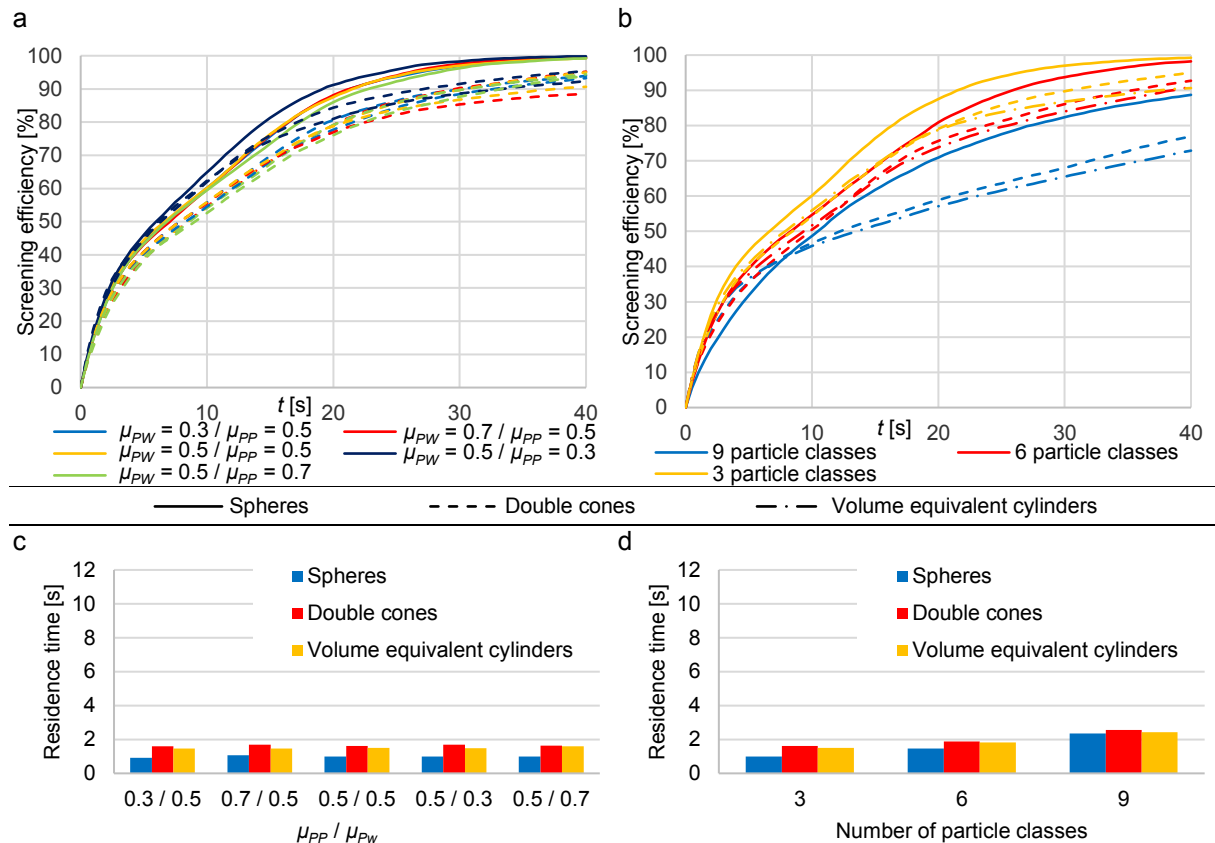


Fig. 43: (a,b) Particle passage through the screen openings for the three considered particle shapes for (a) varying particle/particle (PP) and particle/wall (PW) friction coefficients and (b) number of particle classes and (c,d) corresponding average residence times in the bottom layer for (c) varying particle/particle (PP) and particle/wall (PW) friction coefficients and (d) number of particle classes.

In the sixth investigation illustrated in Fig. 43b the original three particle classes are divided into further two and three subclasses, respectively. By increasing the number of subclasses without varying the average particle size of each of the coarse, near mesh and fine main classes the differences between the particle sizes are homogenized. Thereby, the porosity of the particle bed as well as the stratification ability in the system decreases.

By dividing the near mesh size particles into subclasses one originated class comprises of particles with dimensions even closer to the aperture size. These particles have a greater impact on the residence time in the bottom layer than the simultaneously downsized particles of the other subclasses (Fig. 43d). Accordingly, the particle passage is decelerated for simulations with more particle subclasses or generally for cases with a broader size distribution.

In the seventh investigation (Fig. 44a) a reduction of the screen dimensions is studied which allows the verification of the reliability of possibly smaller and computationally less extensive simulations where only a part of a screen is modeled for. While using the same contact parameters for the boundaries, the number of apertures of the screen surface and thereby the screen dimensions are decreased. For obtaining an equal initial bed height for all variations the bulk mass is changed proportionally to the screen dimensions. After quartering the dimensions the first time (17 x 17 apertures), results for the percentage passage are similar to the initial ones. Further reductions in size (8 x 8, 4 x 4) lead to similar final results after $t = 40$ s but to significantly volatile particle passage in the meantime. This effect is caused by the increase of passage interfering boundary effects and concurrent reduction of lateral particle motions when scaling down screen dimensions. Residence times on the down scaled screen (Fig. 44c) are similar to those on the screen with initial dimensions. Variations on the smallest screen might be a result of the lower number of particles in the calculation and stronger boundary effects although the friction between the side walls and the particles was set to $\mu_c = 0$.

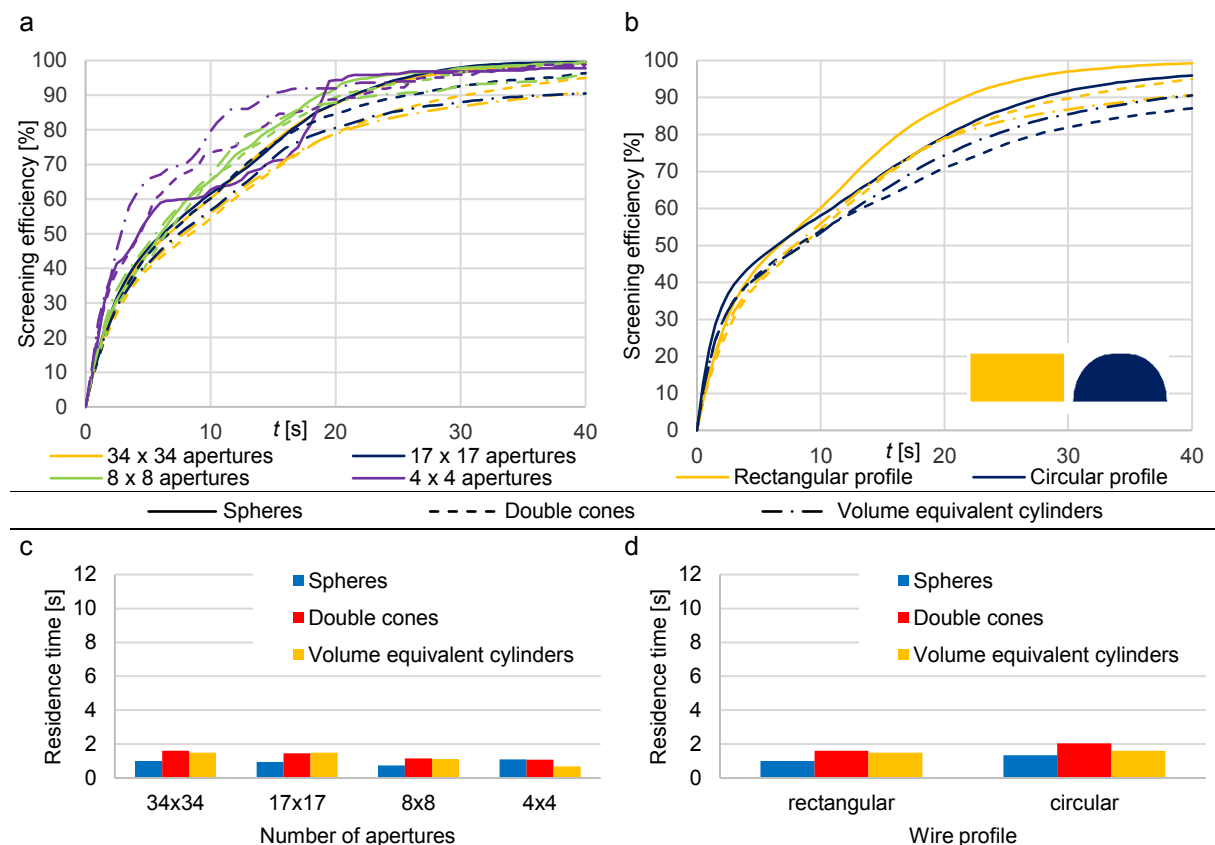


Fig. 44: (a,b) Particle passage through the screen openings for the three considered particle shapes for (a) varying screen dimensions/aperture numbers and (b) wire profiles as well as (c,d) corresponding average residence times in the bottom layer for (c) varying screen dimensions/aperture numbers and (d) wire profiles.

In the last investigation the particle passage through apertures generated by screen wires of rectangular and circular profiles is compared (Fig. 44b). The passage for spheres and double cones is reduced for a circular profile due to oversized particles intensively pegging the

rounded apertures. Besides stronger pegging of spherical particles, using a circular profile for the screen wires can increase the possibility of particles to contact apertures as they can be guided by the curvature of the screen wire towards the opening. These two microscopic phenomena compensate each other in case of volume equivalent cylinders which reveal the same percentage passage at the end of the screening investigation independent of the wire approximation applied. The dominance of pegging in case of spheres and double cones is also underlined by the illustration of the residence time in the bottom layer in Fig. 44d.

5.2 Comparison of phenomenological screening process models

The simulation results as described in section 5.1 covering a broad range of operational parameters are used to benchmark the phenomenological screening models as outlined in Table 4 in the following. The residual mass in the batch screening apparatus over time obtained from the DEM is compared with data obtained by phenomenological models which were fitted to the DEM by adjusting their respective model parameters. The obtainable accuracy of the adjustment is exemplarily shown in Fig. 45 for spheres that are screened with a vibration frequency of 20.7 Hz and apart from that with initial (base case) operational parameters. For models that account for the division of undersized particle fractions (Nos. 4, 6, 12, 14) the sum of all undersized fractions is shown.

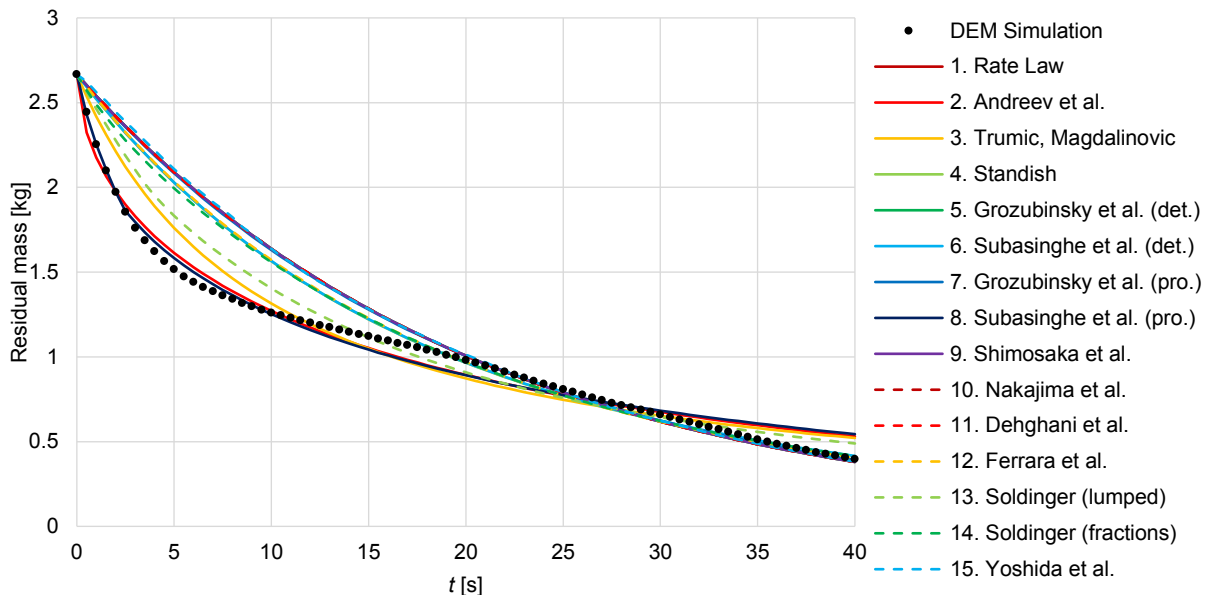


Fig. 45: Progression of the residual mass on the screen over time for various process models and the DEM simulations for an investigation with a screen vibration frequency of 20.7 Hz.

A good match of the DEM results is obtained with the models by Andreev et al. (No. 2) and Subasinghe et al. (No. 8) which both reveal some deviation for $t > 30$ s. Both the models by Soldinger (No. 13) and the model by Trumic and Magdalinovic (No. 3) also obtain an acceptable match. Although the models by Standish (No. 4), Subasinghe et al. (No. 6), Ferrara et al. (No. 12), Soldinger (No. 14) and Yoshida et al. (No. 15) reveal larger deviations in the first 10 seconds of the investigation they attain a good overall result due to a nearly perfect match with

the DEM results for $t > 20$ s. Already from this exemplarily selected data set it can be concluded that screening process model accuracy is not necessarily correlated with the model complexity (number of governing equations), the number of adjustable model parameters and the aspect if undersized material is considered as lumped or in fractions.

For the benchmarking over a larger number of investigations an average deviation of the simulated and model predicted mass is calculated for models considering the whole fine material as one lumped undersized fraction by $(\sum_{k=1}^j |m_{sim}(k) - m_{mod}(k)|)/j$, where j is the total number of considered time steps k . For models considering the different undersized particle classes i as fractions (Nos. 4, 6, 12, 14) the average of the obtained fractional deviations is calculated by $(\sum_{i=1}^l (\sum_{k=1}^j |m_{sim}(i, k) - m_{mod}(i, k)|))/ (j \cdot l)$, where l is the total number of undersized fractions.

In Fig. 46 the summed up deviations of all performed simulations using spherical particles (Figs. 46a,b), double cones (Figs. 46c,d) and volume equivalent cylinders (Figs. 46e,f) for varying amplitudes (Figs. 46a,c,e) and frequencies (Figs. 46b,d,f) for all considered screening process models are presented.

Nearly all models reveal problems for representing flat residual mass curves caused by small amplitudes or low and high vibration frequencies, respectively. The kinetic models by Andreev et al. (No. 2), Standish (No. 4) and Subasinghe et al. (No. 6) as well as the probabilistic models by Subasinghe et al. (No. 8) and Ferrara et al. (No. 12) as well as the fractional complex model by Soldinger (No. 14) attain the best overall results. However, they are relying on empirical model parameters (No. 2) or are requiring long adjustment times during fitting (No. 12) due to the non-explicit functional form used.

In case of varied amplitudes the models Nos. 2 and 8 show particularly suitable results. The functional forms with an additional adjustable parameter as exponent of the time t used in these models are able to compensate well for the variations in residual mass on the screen caused by different amplitudes. Due to being optimized for continuous screening and due to a simple parameter structure, deviations from the model by Trumic and Magdalinovic (No. 3) are largest, although obtaining acceptable results for some small amplitudes and frequencies of e.g. 6.9 Hz, 20.7 Hz and 55.2 Hz. However, model No. 3 has problems representing simulations with strong residual mass decrease and complete depletion of material caused by large amplitudes and passage optimized frequencies, respectively.

In all investigated cases (Fig. 46) the models Nos. 1, 5, 7, 9, 10 and 11 indicate deviations of the same order of magnitude. As shown in section 3 models Nos. 5 and 7 could be easily reduced to the rate law (No. 1). In both models the additionally introduced parameter q offers no significant improvement in accuracy while β being similar to k . Models Nos. 9, 10 and 11

directly rely on the screening efficiency of the rate law (No. 1), whereby only the parameter ranges of the model parameters are altered. These shifted ranges possibly affect the adjustment of the model parameters (easier guess of initial values and quicker convergence) or enhance their physical meaning as e.g. in model No. 9, where passage probabilities are introduced, but total model accuracy is unaffected.

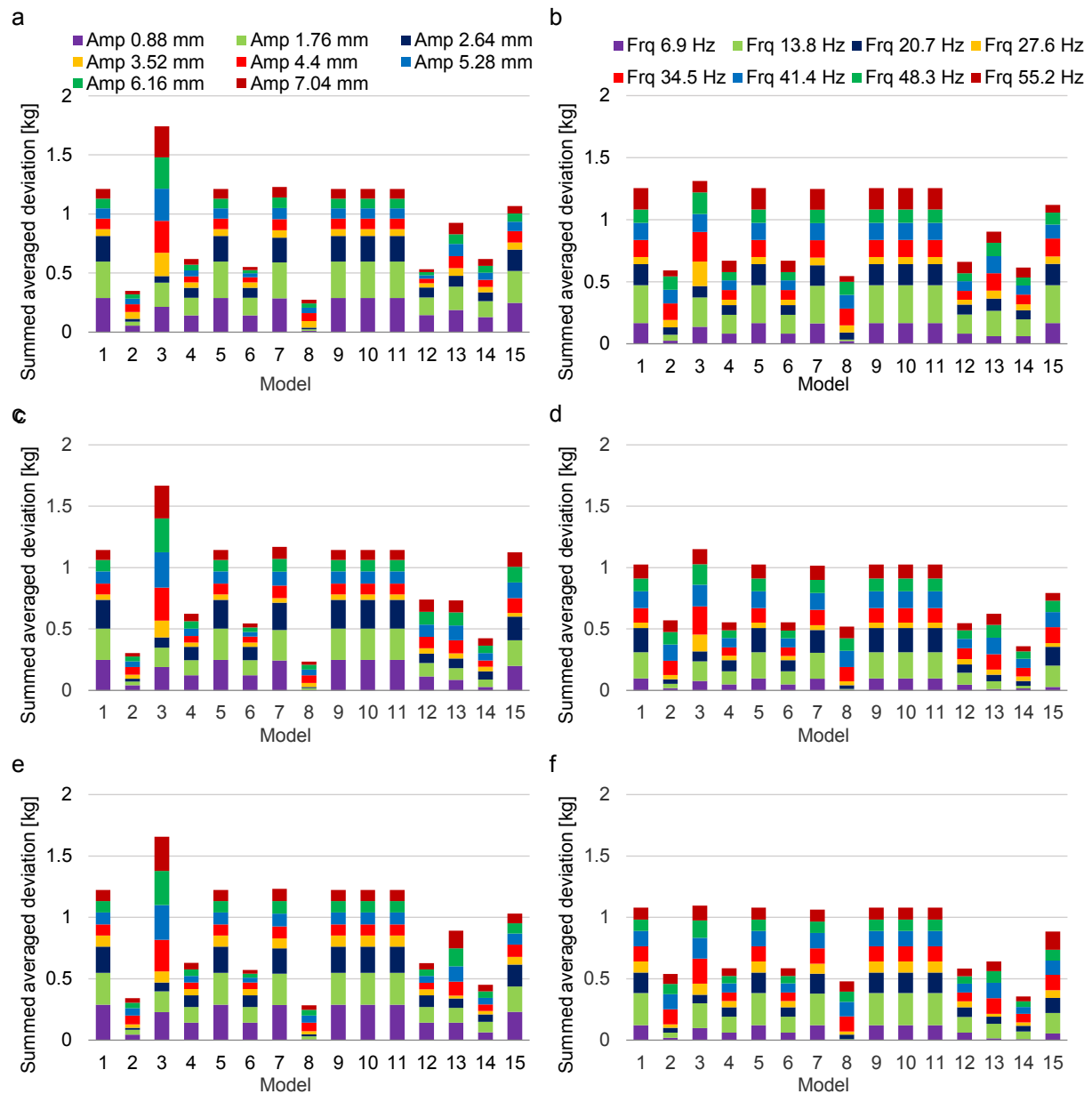


Fig. 46: Particle passage deviation between phenomenological models sorted according to Table 4 and discrete element simulations summed up for various (a, c, e) amplitudes (spheres, double cones, volume equivalent cylinders); (b, d, f) frequencies (spheres, double cones, volume equivalent cylinders).

Besides obtaining quantitative slightly better results, nearly all models represent the simulations with complex shaped particles qualitatively similar to those with spheres. Overall deviations are smaller for double cones than for volume equivalent cylinders. Model No. 15 by Yoshida et al. reveals comparatively big deviances despite its complexity due to being derived for a batch simulation setup differing from the setup here. The model No. 15 does not account for mass loss, as in the setup by Yoshida et al. [5] a large number of oversized particles is

considered so that the passing of undersized particles does not affect the particle mass on the screen significantly. Additionally only one type of undersized spherical particles is present which has to be considered later on in the model; in contrast multiple undersized fractions are considered in the setup here which have to be modeled in a lumped way in model No. 15. From the comparison of the two models by Soldinger (No. 13 and No. 14) it can be concluded that a representation of varying fractions in a lumped way could reduce model accuracy especially in case of complex models where stratification is accounted for in detail. As a consequence, model No. 14 is the most accurate model for representing cases with varying frequencies and complex shaped particles. Additionally, despite providing the best time averaged results the models by Andreev et al. (No. 2) and Subasinghe et al. (No. 8) reveal large maximum divergences when applying them for screening of spheres or cylinders with very low amplitudes and frequencies (not shown in Fig. 46). In these cases, the retained mass is perfectly matched for $t > 5$ s; however, the decrease of residual mass in the first 5 seconds is reproduced exaggerated compared to the DEM simulations.

In Fig. 47 the summed up deviations for simulations performed with spheres (Figs. 47a,b), double cones (Figs. 47c,d) and volume equivalent cylinders (Figs. 47e,f) for varying stroke angles (Figs. 47a,c,e) and masses (Figs. 47b,d,f) are shown.

The results for various mechanical agitations differ from the previously discussed results by obtaining much better results for spheres than for non-spherical particles except if using model No. 3 revealing a better accuracy for complex shaped particles due to not reaching a final screening efficiency of 100 %, which is easier to represent for this model. Several models struggle when representing complex shaped particles agitated by an oscillating movement especially for combinations of $45^\circ/135^\circ$ and to some extent also for $60^\circ/120^\circ$ (comp. Figs. 47c,e). As discussed in section 5.1 strong pegging of apertures is reported for these agitation modes in case of non-spherical particles. Of course, screening process models are not capable of representing these phenomena, which are reported in the DEM, where particle orientations of all particles are tracked.

A variation in mass affects all three investigated particle types similarly as the variation of amplitudes (comp. Figs. 46a,c,e) - deviations increase in case of a larger initial particle mass applied to the screen. Although model No. 2 shows good time averaged behavior, high maximum deviations are apparent for simulations with very low mass (not shown in Fig. 47), especially towards the beginning of the simulations. Using a lower bulk mass, undersized particles are less interfered by oversized particles during screening, resulting in a more steadily decreasing retained mass on the screen which allows more accurate modeling by the screening process models as a consequence. For both cases, a varying stroke angle and a variation in mass, models Nos. 2 and 8 show particularly suitable results due to their functional forms which are able to take varying mass depletions into account.

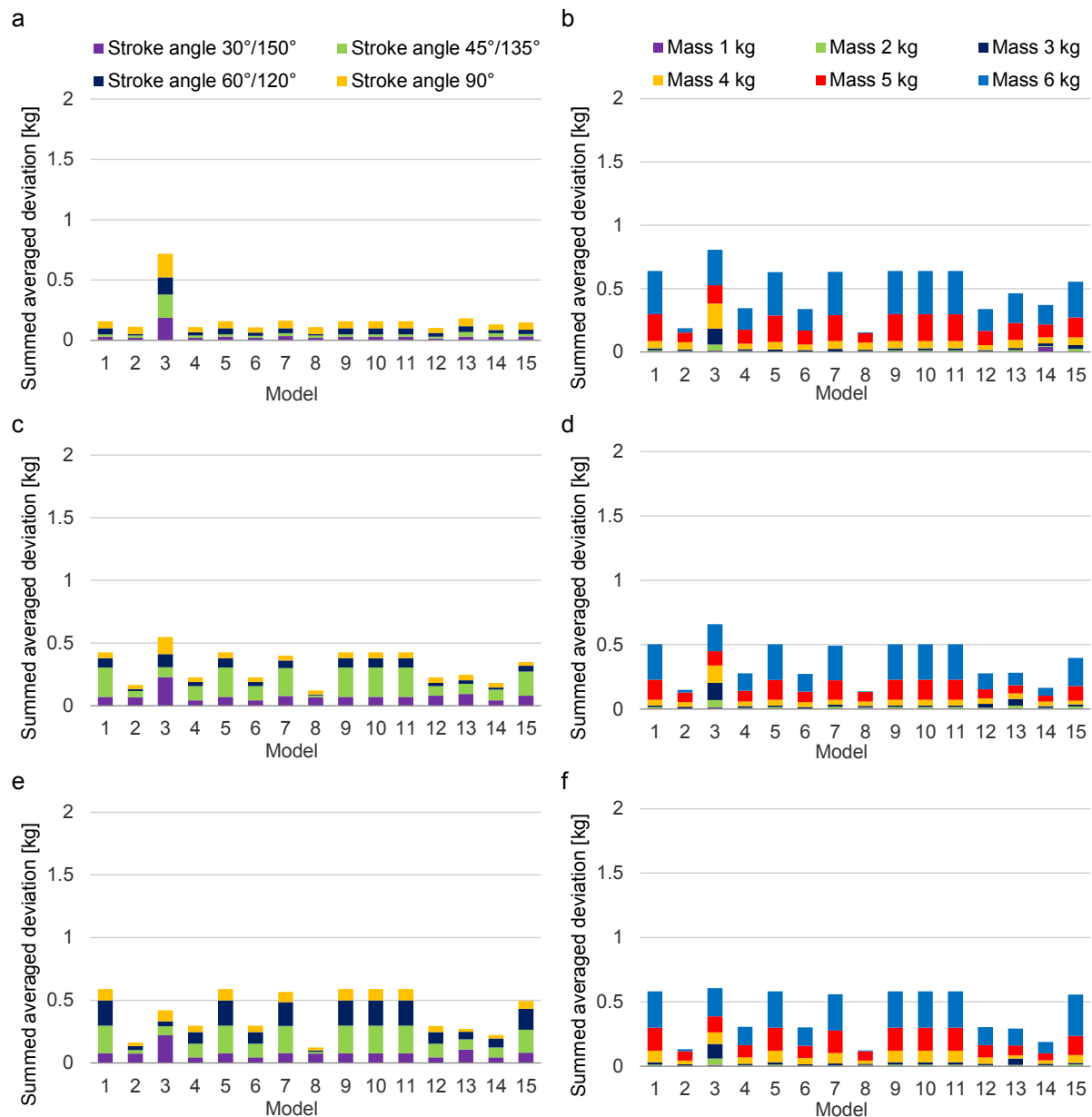


Fig. 47: Particle passage deviation between phenomenological models sorted according to Table 4 and discrete element simulations summed up for various (a, c, e) stroke angles (spheres, double cones, volume equivalent cylinders); (b, d, f) masses (spheres, double cones, volume equivalent cylinders).

In Fig. 48 the summed up deviations for simulations performed with spheres (Figs. 48a,b), double cones (Figs. 48c,d) and volume equivalent cylinders (Figs. 48e,f) for varying particle-wall and particle-particle friction coefficients (Figs. 48a,c,e) and different subdivisions into particle classes (Figs. 48b,d,f) are visualized.

Although, only a few differences in particle passage occur when changing the friction coefficients (Fig. 43a), the quality of the model results are quite different (Figs. 48a,c,e). Model No. 3 shows inaccurate outcomes for spheres and double cones, but acceptable results for volume equivalent cylinders in comparison to all other models, respectively. Due to its optimization for continuous screening this model is more accurate if the residual mass is not approaching zero, which is the case for non-spherical particles in contrast to spheres. Models No. 4 and No. 12 obtain the best accuracy for spheres because of the representation of

undersize particles in fractions. Models No. 2 and No. 8 perform well for non-spherical particles due to their adjustable parameter in the exponent of the model equation. Both models No. 2 and 8 are followed in accuracy by model No. 14 which offers good overall results. Similar findings can be made by analyzing the diagrams of the subdivisions of particle classes. In contrast, model No. 3 gives acceptable results for complex shaped particles in comparison to models Nos. 1, 5, 7, 9-11 and 15. One reason is again the screening efficiency not converging towards 100 % at the end of the investigation thereby supporting model No. 3. Another reason is that the other models have problems with representing 9 classes of complex shaped particles while not taking the different passing possibilities into account. Particularly, models No. 2 and No. 8 are able to represent these cases very well due to their additional adjustable parameter as exponent of the time.

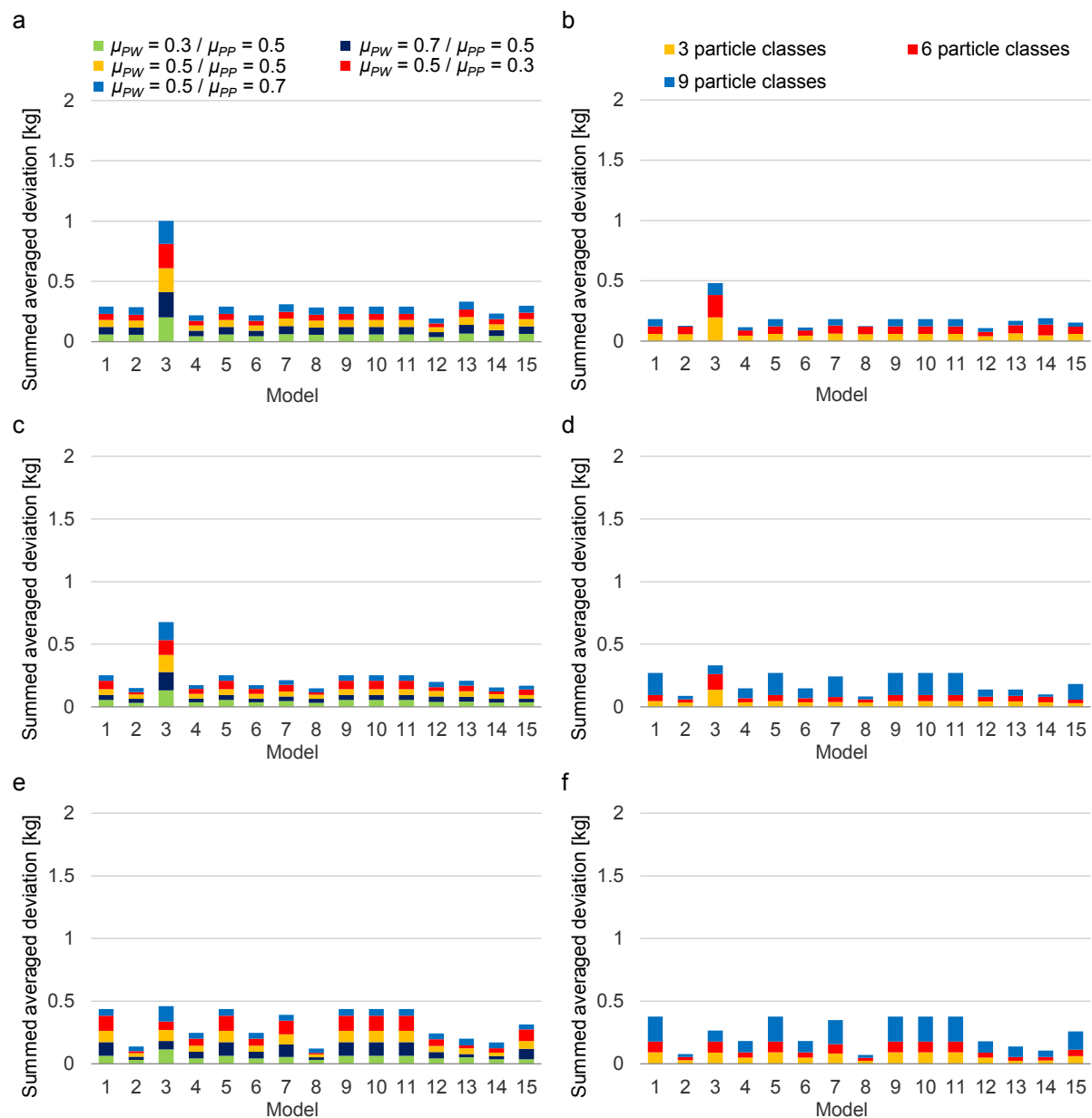


Fig. 48: Particle passage deviation between phenomenological models sorted according to Table 4 and discrete element simulations summed up for various (a, c, e) friction coefficients (spheres, double cones, volume equivalent cylinders); (b, d, f) subdivisions into particle classes (spheres, double cones, volume equivalent cylinders).

Fig. 49 presents the summed up deviations for simulations performed with spheres (Figs. 49a,b), double cones (Figs. 49c,d) and volume equivalent cylinders (Figs. 49e,f) for varying number of apertures (Figs. 49a,c,e) and screen wire profiles (Figs. 49b,d,f).

When reducing the number of apertures, the screen apparatus contains less bulk mass, but the percentage passage remains approximately on the same level (Fig. 49a). Due to this lower mass the deviations for cases with a reduced number of apertures are less intensive. Nevertheless, the same models like before reveal accurate (No. 2, No. 4, No. 8, No. 6, No. 12, No. 13, No. 14) and partial inaccurate results (No. 3, No. 15), respectively.

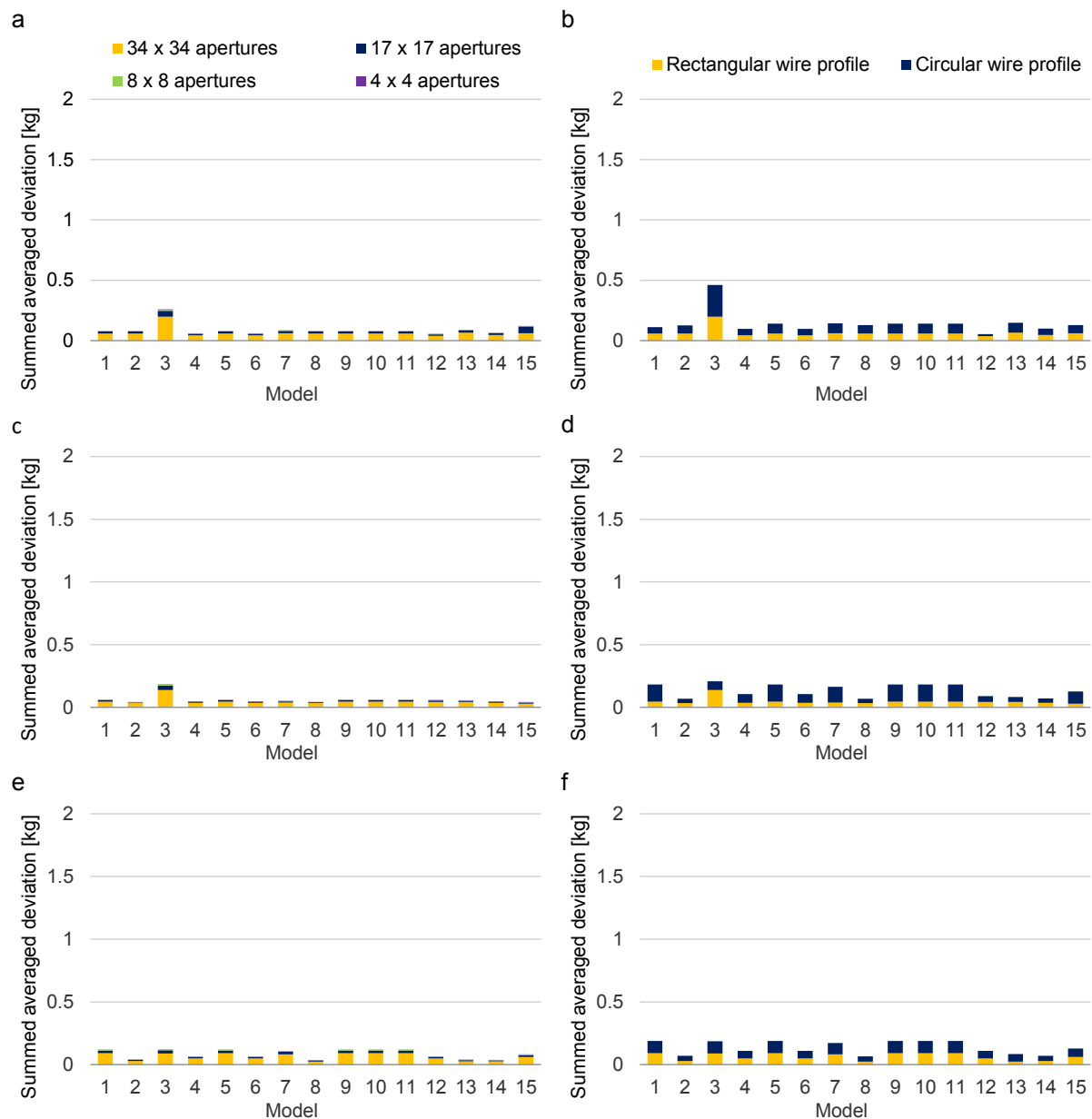


Fig. 49: Particle passage deviation between phenomenological models sorted according to Table 4 and discrete element simulations summed up for various (a, c, e) number of apertures (spheres, double cones, volume equivalent cylinders); (b, d, f) screen wire profiles (spheres, double cones, volume equivalent cylinders).

Using a circular profile for the screen wires can lead to more pegging of spherical particles, but then a higher passage rate is provided due to a higher possibility of getting into contact with the screen openings. This phenomenon supports the application of model No. 12 for spheres

and in case of complex shaped particles the application of models Nos. 2 and 8 and of model No. 3 in contrast to the previous results. However, particularly model No. 3 and model No. 13 for spheres, Nos. 1, 5, 7, 9-11, 15 for double cones and model No. 13 for volume equivalent cylinders reveal stronger deviations when representing screening with a circular wire profile. All the other models show approximately the same deviations for both wire approximations.

6. Conclusions

The discrete element method (DEM) has been used to perform batch screening investigations of varying particle characteristics such as size (coarse, near mesh, fine), shape (spheres, double cones and volume equivalent cylinders), friction (particle / particle and particle / wall), overall mass and size distribution (3, 6, 9 subclasses). Additionally, screening parameters such as screen dimensions (smaller screens) and the surface representation (rectangular / semi-circular wire) as well as operational parameters including vibration frequency, stroke angle and amplitude have been varied. The investigations are transient by nature and automatically include the startup phase of the equipment which is often not considered in models for continuous screening.

Results obtained by the DEM clearly unveil that the screening rate is higher for spheres than for volume equivalent cylinders and double cones due to their respective stratification and passage possibilities. The screening efficiency can be increased by enlarging the vibration amplitude and frequency in batch screening. However, in case of exceeding a critical amplitude or frequency this can lead to stagnating or even declining screening rates. Moreover an oscillating motion supports the screening while the amount of material should be adapted to the size of the screening apparatus with a non-linear influence of total mass on the screening rate. Changing the friction coefficients has no remarkable influence on the sieving efficiency except for a slightly faster stratification in case of lower particle-particle friction. However, a division of particle size classes in more subclasses diminishes the stratification and therefore the passage of particles, whereas a reduction of the size of the screening apparatus with simultaneously reduced mass leads to the same end results but causes volatile particle passage in the meantime. Using semicircular wires supports the contact probability of particles with sieve openings; but also the phenomenon of pegging is more pronounced which leads to declining sieving efficiencies particularly for spherical and cone shaped particles.

The models by Andreev et al. [47], Standish [45], Subasinghe et al. [228], Ferrara et al. [225] and Soldinger [8] attain the overall best results in modeling batch screening simulations. Nearly all models reveal problems with representing low screening rates resulting in flat residual mass curves. Although requiring more time for fitting and calculation, complex models such as [7,8] or [5] not necessarily offer better results than simpler models but have the advantage that model parameters are calculated within known intervals instead of obtaining arbitrary values

with neither a physical meaning nor the possibility to extrapolate parameters for unconsidered operational situations.

The model by Yoshida et al. [5] (No. 15), although being the most advanced batch screening model, needs to be extended to use it more flexibly. Currently it does not account for declining bed heights due to passage of undersize particles, equal initial particle distributions are assumed throughout the particle bed and only one undersized fraction is realized. All screening process models currently existing are not predictive; they are apparatus and screening material dependent and rely on adjustable parameters. To apply them reliably for screening situations where they are not adjusted for is currently not possible. An approach to overcome this problem is the use of complex screening models [7,8] or [5] providing additional information on the particle bed such as the bed height, the vertical particle distribution and their dependence on operational parameters. With help of this information the complex models try to describe the screening process more detailed however currently still needing adjustable parameters. Thus, they are not predictive neither, but associated with more computational cost.

As further steps it is planned to apply the screening models for dynamic simulations in which process parameters are altered during operation. Additionally, continuous screening is planned to be investigated. Note, that the DEM simulations were not benchmarked against experimental investigations in this study. The DEM was used to derive a qualitatively realistic parameter space as could also be obtained from experimental investigations. To apply the models towards real screening investigations involving experimental equipment requires a benchmarking of the DEM against experiments. Such benchmarking has been done to some extend for the DEM applied here for continuous screening for literature data [236]; similar benchmarking is planned for batch screening in the near future.

Acknowledgements

The authors gratefully acknowledge the support by DFG within project SPP 1679 through grant number KR3446/7-1.

III. Benchmarking of process models for continuous screening based on discrete element simulations

Frederik Elskamp¹, Harald Kruggel-Emden^{1*}, Manuel Hennig², Ulrich Teipel²

¹Ruhr-Universität Bochum, Universitätsstraße 150, D-44780 Bochum, Germany

²Technische Hochschule Nürnberg Georg Simon Ohm, Wassertorstrasse 10, D-90489 Nuremberg, Germany

*Corresponding author. E-mail address: kruggel-emden@leat.ruhr-uni-bochum.de

The following accepted manuscript appeared as journal version in Elskamp F., Kruggel-Emden H., Hennig M., Teipel U., 2015, Benchmarking of process models for continuous screening based on discrete element simulations, Minerals Engineering 83, 78-96 and may be found at <https://doi.org/10.1016/j.mineng.2015.08.011>.

Abstract

For the design and the scale-up of screening processes and the optimization of operating parameters the particle-based discrete element method (DEM) as well as classic phenomenological screening models are available. Phenomenological screening process models are simple to use and require only sparse computational resources, hence providing the possibility to use them efficiently in industrial applications. In this context, a comparative benchmark of numerous kinetic and probabilistic screening models of various complexities has been performed for discontinuous screening, recently. Following the approach of this study, in the investigation here, DEM simulations applying spherical and non-spherical particles are used to benchmark process models for continuous screening. In the DEM simulations different particle characteristics such as size, shape and size distribution are taken into account. Screen characteristics such as aperture size, wire shape and inclination angles as well as operational parameters including vibration frequency, amplitude, stroke angle and mass flow rate are varied. Based on the data obtained from the simulations, the overall fraction retained on the screen as well as the selectivity in terms of overflow partition number, the transport velocity and the residence time all in dependence on particle size are investigated. Finally, phenomenological screening process models are adjusted to the outcome of the DEM simulations in terms of the fraction retained on the screen and overflow separation curves, respectively. The resulting deviations are evaluated and thereby allowing the comparative benchmarking of available process models for continuous screening. Obtained DEM results indicate a strong dependence of screening on operational parameters and particle shape. Screening process models vary intensively in their ability to represent DEM results.

Keywords: Continuous screening; Discrete element method (DEM); Arbitrary shaped particles; Process models

1. Introduction

Screening or sieving is a technical simple, but important process step widely used in industry for the classification of particles. In mechanical process engineering, materials preparation technology or energy technology it is routinely used to separate various bulk materials consisting of particles with sometimes broad size distribution according to desired size class specifications. Such particles are usually of non-spherical shape complicating the separation into homogeneous classes [2,3]. Besides separating crushed material into sub-products in minerals engineering, screening is applied for a wide range of tasks including e.g. the removal of dust or wear debris from coarser grained materials, splitting up components in grain processing or in other food related processes according to particle sizes or the separation of similarly sized particles by their shapes. Despite its widespread usage in industry, the scientific understanding of screening is still not completely matured, often leading to complications when designing, optimizing or scaling-up screening processes.

To overcome current limitations in the understanding of screening without performing extensive experimental investigations, the discrete element method (DEM) dating back to Cundall and Strack [10] and Walton and Braun [59] as a particle-based simulation approach is applicable. DEM simulations are predictive and provide detailed insights into screening processes, giving the possibility to study the governing dynamic sub-processes such as particle transport, stratification and passage. This knowledge is essential when optimizing equipment and operating parameters.

Documented experimental studies of screening date back to the first part of the last century [24]. However, the first DEM screening investigations addressing small scaled batch-operated screens are reported for the beginning of this century [46]. The influence of the particle layer thickness on screening efficiency for continuous screening was analyzed by Li et al. [189] followed by investigations of the differing behavior of near mesh sized and oversized particles [50]. In the works of Alkhalidi and Eberhard [190] and Chen et al. [235] large scale screens were studied, whereas Cleary [199] diminished the effort required to simulate a screen with the help of periodic boundary conditions. The required accuracy for modeling the sieve wire structure was addressed by Alkhalidi et al. [191], Tung et al. [188] and Kruggel-Emden and Elskamp [236]. Investigations addressing the particle excitation on the screen induced by various stroke orientations, amplitudes and inclination angles were performed by Zhao et al. [192], Dong et al. [35] and Xiao and Tong [237,238]. Further studies addressed banana screens operated with dry particles [195,196], particle/fluid interaction as well as adhesive forces due to liquid bridges on screens [200,202] and banana screens simulated under wet conditions [6,9,198].

Evident deviations for the stratification and the passage of near mesh sized particles as well as for the particle transport occur if non-spherical bulk material is modeled by spherical particles in simulations [20]. Nevertheless, up to now, only a few numerical investigations of screening processes involving complex shaped particles were carried out [6,198,236,241].

For screening processes with dry particles, the DEM was validated against experimental data [34] and proved successful and reliable [236]. Therefore, the DEM is an appropriate tool to optimize operating parameters and appliances [35,50,189,192,236–238]. Additionally, the derivation and verification of simpler and less computational demanding phenomenological models without performing extensive experiments is feasible. First, this was demonstrated by Shimosaka et al. [46] for batch screening processes and very recently by Dong et al. [49] for continuous screening.

In a former publication by the authors [241] batch screening processes were investigated in detail and a benchmarking of applicable phenomenological screening process models was performed. In the present study continuous screening involving spherical and non-spherical particle shapes is addressed. Therein, phenomena such as particle passage, average transport velocity in dependence on particle size and the residual mass flow over the screen length are investigated in detail. These investigations form the basis to use DEM simulations reliably for a comparative study of phenomenological continuous screening process models as previously performed for discontinuous screening [241].

The article is divided into five sections. Section 2 and 3 are the description of the numerical method and of the considered steady state screening process models, respectively. Section 4 addresses the numerical setup and the applied simulation parameters. Besides particle transport velocities, residence times and results of the particle passage behavior for continuous screening are shown in section 5.1. Afterwards, a comparison is made between the passage in dependence on screen length and particle size, respectively, to the outcome of various phenomenological screening process models in parts 5.2 (spatially resolved models) and 5.3 (separation curve models). Finally, conclusions are drawn in section 6.

2. Numerical method

Besides spherical particles, the DEM can be applied to systems with non-spherical shaped particles [60,61]. For this purpose the translational and rotational motion of each particle are tracked by integrating the Newton's and Euler's equations

$$m_i \frac{d^2 \vec{x}_i}{dt^2} = \vec{F}_i + m_i \vec{g}, \quad (117)$$

$$\hat{I}_i \frac{d\vec{W}_i}{dt} + \vec{W}_i \times (\hat{I}_i \vec{W}_i) = \Lambda_i^{-1} \vec{M}_i, \quad (118)$$

with particle mass m_i , particle acceleration $d^2 \vec{x}_i / dt^2$, contact force \vec{F}_i , gravitational force $m_i \vec{g}$, angular acceleration $d\vec{W}_i / dt$, angular velocity \vec{W}_i , external moments resulting out of contact forces \vec{M}_i , the inertia tensor along the principal axis \hat{I}_i and the rotation matrix converting a vector from the inertial into the body fixed frame Λ_i^{-1} . Both equations (eq. (117) and eq. (118)) are solved by explicit integration schemes (comp. e.g. [82]).

The multi-sphere method is a flexible approach to model complex shaped particles in the DEM. Thereby, the desired complex particle shape is resembled with clustered arbitrary sized spheres [69] applying similar contact force laws as used for spherical particles [65].

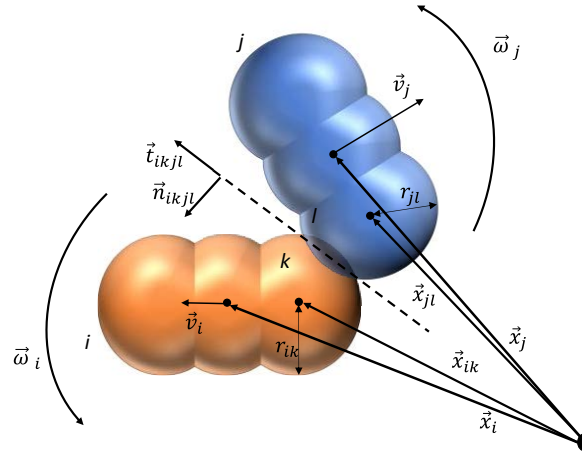


Fig. 50: A collision of two multi-sphere particles.

Fig. 50 shows a sketch of two simple colliding complex particles i and j , where the spheres l and k got into contact. Further details on the contact scheme involving clustered spheres are provided in Kruggel-Emden and Kačianauskas and Kruggel-Emden et al. [90,91].

The normal component of the contact forces is obtained from a linear spring damper model which is exemplarily given for the contacting spheres k and l of particle i and j as

$$\vec{F}_{ikjl}^n = k^n \cdot \delta_{ikjl} \cdot \vec{n}_{ikjl} + \gamma^n \cdot \vec{v}_{ikjl}^n, \quad (119)$$

where k^n is the spring stiffness, δ_{ikjl} the virtual overlap, \vec{n}_{ikjl} a normal vector, γ^n a damping coefficient and \vec{v}_{ikjl}^n the normal velocity at the contact point. Both k^n and γ^n determine the coefficient of normal restitution between particles e_{pp}^n as well as between particles and walls e_{pW}^n [92]. For the calculation of the tangential forces a linear spring limited by the Coulomb condition is applied

$$\vec{F}_{ikjl}^t = -\min(k^t \cdot |\vec{\xi}_{ikjl}|, \mu_c \cdot |\vec{F}_{ikjl}^n|) \cdot \vec{t}_{ikjl}, \quad (120)$$

where k^t is the stiffness of a linear spring, μ_C is the friction coefficient, $\vec{\xi}_{ijkl}$ is the relative tangential displacement and \vec{t}_{ijkl} is the tangential unit vector [94].

3. Phenomenological screening models

Phenomenological screening process models aim for representing the particle size separation during a screening process. Some process models represent this time-resolved while other models do it spatially resolved, dependent on the position along the screen. Separation curves, a second applicable model class (comp. [218]), are restricted to the steady state operation of continuous screens. They provide integral results on the attained separation by particle size.

3.1 Steady state spatially resolved screening models

Available phenomenological continuous screening models are divided into kinetic [3,45,47,224,226,227] and probabilistic theoretical models [3,46,52,225,228,229]. Both model groups allow a spatially resolved representation of a screening process when it runs in steady state. Listed phenomenological screening models are applicable to discontinuous [45] or continuous screening processes [224] or else to both of them (comp. [225]). Usually, discontinuous screening models can be applied for continuous screening by replacing time t by length l in the model equations [224,225] and vice versa. This characteristic was exploited for the benchmark of the models investigated in Elskamp and Kruggel-Emden [241] and is utilized in the investigation here. Note, that a discontinuous screening process is transient by definition, whereas a continuous screening process can be transient (e.g. during start-up and for load or operational changes), but usually adopts a steady state after some while. This allows the application of screening process models which provide spatially resolved information on passage along the screen at the obtained state (currently transient, spatially resolved screening process models are not available).

The first order kinetics provides the basis for kinetic models which can be extended further by a particle passage probability [47] without needing more computational effort to solve the underlying equations. Thereby, obtained models are restricted to shallow particle beds on continuously operated screens [50] which was also confirmed for discontinuous screening processes [241]. In contrast, probabilistic approaches require a larger number of parameters [47] usually involving the probability of undersized particles to pass an aperture as derived e.g. by Gaudin [24]. Operational parameters of screening processes like mechanical agitation, screen size and characteristics (e.g. aperture shape) and particle composition (e.g. particle elongation) can be considered when applying probabilistic models [3,52,228]. Nevertheless, probabilistic models usually consider only the particle passage itself during the screening process and thereby no further insight into other concurrent subprocesses is given [50].

In contrast, some phenomenological screening models take concurrent subprocesses into consideration by providing additional input parameters which address e.g. the opposing processes of stratification and particle passage through the sieve openings [5,7,8]. The initial model by Soldinger [7] was further extended by the influence of the particle layer thickness and the consideration of the bulk material composition [8]. The prediction of the conveyance speed of the bulk material on the screen as a further extension of this model was addressed in a further work by the same author [234] without taking the particle shape and bed depths into account in detail.

Table 6 gives an overview of all investigated screening process models titled by the author's names and a model number (Arabic numerals) including the major equations as well as the used adjustable model parameters. A more detailed description of all investigated models can be found in Elskamp and Kruggel-Emden [241] or in the respective publications.

The overall screening efficiency E is a screen length dependent variable during continuous screening and the prime output parameter of all spatially resolved screening models. It is given as

$$E = E(l) = (\dot{m}_0 - \dot{m})/\dot{m}_0, \quad (121)$$

where \dot{m}_0 is the initial undersized mass flow at $l = 0$ and \dot{m} is the remaining mass flow of the undersized material at the screen position l . If the undersized particles are considered as different fractions, the screening efficiency is stated per particle size class i

$$E_i = E_i(l) = (\dot{m}_{i,0} - \dot{m}_i)/\dot{m}_{i,0}, \quad (122)$$

where $\dot{m}_{i,0}$ is the initial fractional and \dot{m}_i is the actual fractional undersized mass flow. It is related to the overall screening efficiency by $E = \sum_{i=1}^n (E_i \cdot \dot{m}_{i,0}/\dot{m}_0)$, where n is the number of undersized particle classes.

The "first-order rate law" [45,47,225] referred to as model No. 1 is the basis for most continuous screening process models, particularly for the kinetic ones, given as

$$d\dot{m}/dl = -k\dot{m}. \quad (123)$$

It describes the change of mass flow of undersized particles on the screen \dot{m} as a function of the screen length l . Here, the adjustable parameter k is the screening rate constant. From eq. (123) the derivation of the explicit equation for the screening efficiency leads to

$$E = 1 - \exp(-kl). \quad (124)$$

Table 6: Governing equations of the studied phenomenological screening process models.

| Model number and origin | Major equations | Adjustable parameters | Features |
|---|---|--|---|
| 1. Standish and others [45,47,225] | $E = 1 - \exp(-kl)$ | k | kinetic |
| 2. Andreev et al. [226] | $E = 1 - \exp(-kl^n)$ | k, n | kinetic |
| 3. Trumic/Magdalinovic [47] | $E = 1 - 1/(1 + kl)$ | k | kinetic |
| 4. Standish [45] | $E = \sum_{i=1}^n \left((1 - \exp(-Ak_i l)) \hat{m}_{i,0} / \hat{m}_0 \right)$ A : screen area; n : number of undersized fractions | k_1, \dots, k_n | kinetic, fractioned |
| 5. Grozubinsky et al.; deterministic [3] | $E = 1 - \exp(-(a - d)(1 - \exp(-\beta l))lq/\beta)$ | q, β | kinetic |
| 6. Subasinghe et al.; deterministic [227] | $E = 1 - [k_s \exp(-k_p l) - k_p \exp(-k_s l)] / (k_s - k_p)$ k_s : rate constant of stratification and k_p : rate constant of passage | k_s, k_d | kinetic, stratification |
| 7. Grozubinsky et al.; probabilistic [3] | $E = 1 - \exp(-q(a - d)(1 - \exp(-\beta l))l/\beta) \cdot \left(1 + 0.5(q/\beta)^2 (a_D - d_{d0})(1 - \exp(-\beta l))^2 \right)$ $a_D = \frac{1}{h-1} \sum_{i=1}^h (a_i - \bar{a})^2$; $d_{d0} = \frac{1}{n-1} \sum_{i=1}^n (d_i - \bar{d})^2$ a_D, d_{d0} : dispersion index of a (aperture size) and d (particle diameter) n : number of undersized particles; h : number of apertures \bar{d} : average undersized particle diameter, \bar{a} : average aperture size | q, β | probabilistic, |
| 8. Subasinghe et al.; probabilistic [228] | $E = 1 - (1 - P)^N$; $P = \left(((a + w) \cos \varphi - w - d)(a - d) \right) / ((a + w)^2 \cos \varphi)$ w : wire diameter; φ : screen inclination angle $N = \begin{cases} c_1 \cdot l^{\tau_1} \cdot (d/a) & \text{for } (d/a) < c_2 \cdot l^{\tau_2} / (c_1 \cdot l^{\tau_1} + c_2 \cdot l^{\tau_2}) \\ c_2 \cdot l^{\tau_2} \cdot (1 - d/a) & \text{for } (d/a) > c_2 \cdot l^{\tau_2} / (c_1 \cdot l^{\tau_1} + c_2 \cdot l^{\tau_2}) \end{cases}$ $E = 1 - \exp(-NP)$; $N = kl$ | c_1, c_2, τ_1, τ_2 | probabilistic, fractioned, inclination angle |
| 9. Nakajima/Whiten [229] | $P = \cos^4(\theta - \pi/8) \alpha \left(1 - \left(\frac{d}{a_0} \right) \times \left(\left(\frac{a_1}{a_2} \right)^2 \sin^2 \theta + \cos^2 \theta \right)^{0.5} \right)^2$ $P = 0$ for $d > a_0 / ((a_1/a_2)^2 \sin^2 \theta + \cos^2 \theta)^{0.5}$ $\theta = \tan^{-1}(d_t/d_w)$; $d = \sqrt{(d_t^2 + d_w^2)/2}$; $a_0 = \sqrt{(a_1^2 + a_2^2)}$ with $a_1 > a_2$ d_t, d_w : particle thickness, width | k | probabilistic, fractioned, complex shape |
| 10. Dehghani et al. [52] | $E = 1 - \exp(-NP)$; $N = kl$ $P = \alpha((a_1 - \sqrt{2d} \cos \theta)(a_2 - \sqrt{2d} \sin \theta) / (a_1 a_2))$ $\theta = \tan^{-1}(d_t/d_w)$; d_t, d_w : particle thickness/width; α : fraction open area | k | probabilistic, fractioned, complex shape |
| 11. Ferrara et al. [225] | Crowded $l \leq l_c$: $m_0 \left(\sum_{j=1}^n y_{j,0} \left(\frac{1}{X_{ji}} \right) (E_i(l)^{X_{ji}} - 1) + \ln E_i(l) \sum_{j=n+1}^r y_{j,0} \right) = -k2^\sigma \left(1 - \frac{d_i}{a} \right)^\sigma l$ Separated $l > l_c$: $E_i(l) = \exp(-(k/m(l))2^\sigma(1 - d_i/a)^\sigma l)$ $y_{j,0}$: initial weight fraction of particle fraction j ; $X_{ji} = ((a - d_j)/(a - d_i))^\sigma$ d_i, d_j : studied / other present particle diameters n, r : number of undersized / undersized + oversized particle classes | k , l_c (length related to the mode of operation) σ (screen mesh dependent) | probabilistic, fractioned, iterative, bed depth, stratification |
| 12. Solderger; not resolving undersized fractions [7] | $E_{j+1} = k_j B_j (t_{j+1} - t_j) + E_j$ $t_j = l_j/v$ $B_{j+1} = B_j + (c_j(1 - S_j) - k_j B_j)(t_{j+1} - t_j)$ j : time index $k_j = b(1 - E_j)$; $c_j = f(w_q, w_d)$ B : fractional mass of undersized particles in bottom layer S : fractional mass of undersized particles stratified into bottom layer E : fractional mass of undersized particles passed through apertures | v (transport velocity) w_q (dependent on proportion of undersized material) w_d (dependent on width of particle size distribution) b (dependent on particle size) | history dependent, bed depth, stratification |
| 13. Solderger; resolving undersized fractions [8] | $E_{i,j+1} = k_{i,j} B_{i,j} (t_{j+1} - t_j) + E_{i,j}$; $t_j = l_j/v$; i : particle class; j : time index $E_j = \sum_{i=1}^n E_{i,j}$; $B_j = \sum_{i=1}^n B_{i,j}$; n : number of undersized particle classes $B_{i,j+1} = B_{i,j} + (c_{i,j}(S_{i,\infty} - S_{i,j}) - k_{i,j} B_{i,j})(t_{j+1} - t_j)$ $k_{i,j} = b_i(1 - E_{i,j})$; $c_{i,j} = f(w_q, c_{d,i})$ B_i : fractional mass of undersized particles in bottom layer S_i : fractional mass of undersized particles stratified into bottom layer E_i : fractional mass of undersized particles passed through apertures | v (transport velocity) w_q (dependent on proportion of undersized material) b_1, \dots, b_n (dependent on particle diameter and aperture size) | history dependent, fractioned, bed depth, stratification |

Besides replacing time t by length l in the model equations, the models Nos. 1-8 and 10 are used analogously as in Elskamp and Kruggel-Emden [241].

Model 9 is used in its original form (as stated in Table 6) and in a revised form. In model No. 9 the behavior of non-spherical particles on arbitrary slotted screens is described by an empirical probability function [229] given as

$$P = \cos^4(\theta - \pi/8)\alpha(1 - (d/a_0) \times ((a_1/a_2)^2 \sin^2 \theta + \cos^2 \theta)^{0.5})^2 \text{ or} \quad (125)$$

$$P = 0 \text{ for } d > a_0/((a_1/a_2)^2 \sin^2 d_t + \cos^2 d_t)^{0.5}.$$

Therein, the particle diameter is calculated as $d = \sqrt{(d_t^2 + d_w^2)}/2$, where d_t is the minor axis of the particle and d_w is the major axis. For particles with an equivalent diameter larger than the apertures, but with the possibility to pass the apertures due to $d_t < a_2$ with $a_1 \geq a_2$, the condition $(d > a_0/((a_1/a_2)^2 \sin^2 d_t + \cos^2 d_t)^{0.5})$ of the probability function (eq. (125)) enforces $P = 0$. As this is incorrect, the model was modified with the following condition for the probability function

$$P = \cos^4(\theta - \pi/8)\alpha(1 - (d/a_0) \times ((a_1/a_2)^2 \sin^2 \theta + \cos^2 \theta)^{0.5})^2 \text{ or} \quad (126)$$

$$P = 0 \text{ for } d_t > a_0/((a_1/a_2)^2 \sin^2 d_t + \cos^2 d_t)^{0.5}.$$

The probabilistic model No. 11 by Ferrara et al. [225] which is based on the kinetic first order rate law in combination with the probability function proposed by Gaudin (comp. [24]) is applied differently than for discontinuous screening (comp. [241]), due to possibly varying conditions over the screen length.

For the continuous screening investigations in this work, the crowded and the separated screening model equations

$$\dot{m}_0 \left(\sum_{j=1}^n y_{j,0} (1/X_{ji}) (E_i(l)^{X_{ji}} - 1) + \ln E_i(l) \sum_{j=n+1}^r y_{j,0} \right) = -k2^\sigma \left(1 - \frac{d_i}{a}\right)^\sigma l \text{ for } l \leq l_c, \quad (127)$$

$$E_i(l) = \exp(-(k/\dot{m}(l)) 2^\sigma (1 - d_i/a)^\sigma l) \text{ for } l > l_c, \quad (128)$$

are used, where $y_{j,0}$ is the weight fraction of particle class j with $y_{j,0} = \dot{m}_{j,0}/\dot{m}_0$. $E_i(l)$ is the length dependent screening efficiency per particle class i as defined in eq. (122). The parameters n and r represent the number of undersized and the number of undersized plus oversized particle classes, respectively. Note, that $E_i(l) = 1$ for $n + 1 \leq i \leq r$. The transition position along the screen from crowded to separate screening is determined by an additional adjustable parameter l_c . In case of crowded screening, the model No. 11 must be solved iteratively in order to obtain a result for the screening efficiency E_i and thus requires more time for its solution than the other screening process models discussed.

Both more complex models by Solding [7,8] can be used for continuous screening in the same manner as for discontinuous screening besides modeling for a mass flow instead of an overall mass on the screen. Since the fraction retained is determined and modeled over screen length l instead of time t , the time step $\Delta t = t_{j+1} - t_j$ has to be calculated with

$$\Delta t = t_{j+1} - t_j = l_{j+1}/v - l_j/v, \quad (129)$$

where l_j is the current position, l_{j+1} is a subsequent position on the screen and v is an adjustable, constant transport velocity. Due to the transport velocity in continuous screening, all the equations proposed by Solding [7,8] can be applied in their original form.

Further information, particularly on the more complex models by Ferrara et al. [225] and Solding [7,8], can be found in the respective publications.

3.2 Steady state separation curve screening models

For screening processes in steady state, separation curves provide information on the separation as a function of the particle size summed up over the whole screen length in a spatially non-resolved form. For known fractional flow rates in the feed and in the overflow which can be obtained from experiments or simulations, overflow separation curves can be derived with

$$T_i = T(d) = \frac{\dot{m}_{i,overflow}}{\dot{m}_{i,feed}}. \quad (130)$$

In literature, several authors proposed equations to estimate separation curves without performing extensive experiments. Most of these model equations rely on the parameter a_s , representing the fine material which is not getting into contact with the screen surface and leaving as overflow, the cut size d_{cut} , which is the particle size where $T_i = 0.5$ and the separation sharpness α_s which is an adjustable parameter. In this context, Dehghani et al. [52] proposed the following equation based on the model by Hatch and Mular [220] referred to as model No. I (all separation curve models are referred to by Roman numerals)

$$T(d)_{Dehghani} = 1 / \left(1 + \exp \left(\theta \left(d_{cut}^3 - (d_t \sqrt{2} d \cos \theta - \sqrt{2} d \sin \theta) \right) / \alpha_s \right) \right), \quad (131)$$

where $\theta = \tan^{-1}(d_t/d_w)$ and d_t , d_w and d_l are the thickness, width and length of the particle, respectively. The particle diameter d in eq. (131) is obtained as $d = \sqrt{(d_t^2 + d_w^2)}/2$.

Plitt [218] described the classification with the following separation function

$$T(d)_{Plitt} = (1 - a_s) \cdot \left(1 - \exp \left(-\ln 2 \cdot \left(\frac{d}{d_{cut}} \right)^{\alpha_s} \right) \right) + a_s, \quad (132)$$

referred to as model No. II in the following.

Based on the model by Hatch and Mular [220], Rogers [219] proposed a refined separation equation referred to as No. III

$$T(d)_{Rogers} = \frac{(1 - a_S)}{1 + \left(\frac{d_{cut}}{d}\right) \cdot \exp\left(\alpha_S \cdot \left(1 - \left(\frac{d}{d_{cut}}\right)^3\right)\right)} + a_S. \quad (133)$$

Another model equation normally used for air separators, but also applicable for screening processes was derived by Molerus and Hoffmann [222]. It is referred to as model No. IV in the following, including the possible bypassing of fines (comp. [219])

$$T(d)_{Molerus} = \frac{(1 - a_S)}{1 + \left(\frac{d_{cut}}{d}\right)^2 \cdot \exp\left(\alpha_S \cdot \left(1 - \left(\frac{d}{d_{cut}}\right)^2\right)\right)} + a_S. \quad (134)$$

In order to provide a better adaptability, based on the model structure by Trawinski [223], three other separation functions are considered here

$$T(d)_{Trawinski_1} = \left(1 - \left(1 + \left(\alpha_S \sqrt{2} - 1\right) \left(\frac{d}{d_{cut}}\right)^{\alpha_S \beta_S}\right)^{-\alpha_S}\right) \cdot (1 - a_S) + a_S, \quad (135)$$

$$T(d)_{Trawinski_2} = \left(1 - \left(1 + 3 \cdot \left(\frac{d}{d_{cut}}\right)^{\left(\left(\frac{d}{d_{cut}} + \alpha_S\right) \cdot \beta_S\right)}\right)^{-0.5}\right) \cdot (1 - a_S) + a_S, \quad (136)$$

$$T(d)_{Trawinski_3} = \frac{\left(\frac{d}{d_{cut}}\right)^{\alpha_S \left(\frac{d}{d_{cut}} + \beta_S\right)}}{1 + \left(\frac{d}{d_{cut}}\right)^{\alpha_S \left(\frac{d}{d_{cut}} + \beta_S\right)}} \cdot (1 - a_S) + a_S. \quad (137)$$

Their additional adjustable parameter β_S conduces to represent the asymmetry of the separation curve. In the following they are referred to as models Nos. V-VII.

4. Numerical setup and simulation parameters

Screening of a polydisperse feed material is investigated by the DEM in a continuous screen apparatus as shown in Fig. 51a. The apparatus is equipped with a wire screen on a floor area of 0.35 m x 0.1 m. The initial aperture size a is 4.9 mm and the wire diameter w is 1 mm. In the initial configuration, the apparatus is vibrated with 27.6 Hz with a stroke angle of 45° to the horizontal at an amplitude of 1.76 mm (Fig. 51). The screen wire is approximated by triangular surface elements initially forming a rectangular profile in the simulations that is later compared to a semicircular one.

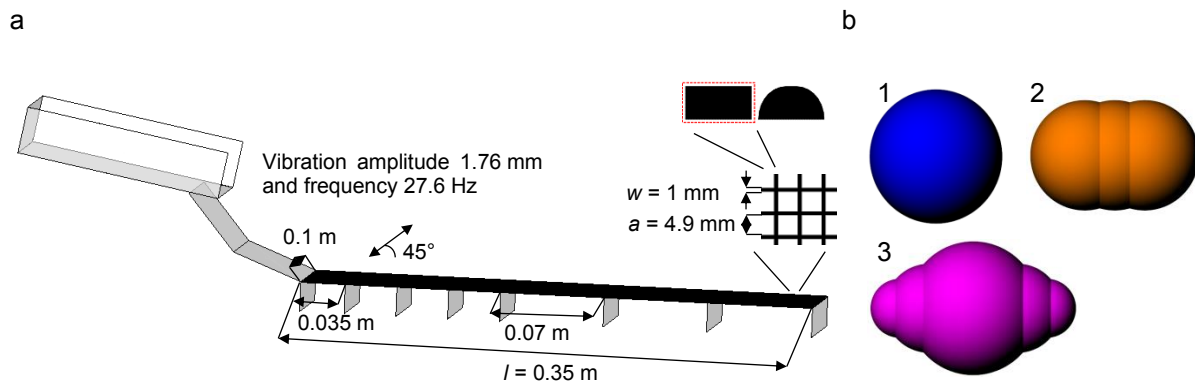


Fig. 51: (a) Continuous screening apparatus with wire structure; (b) Considered particle shapes.

The initial mass flow of the polydisperse feed material amounts to 0.1 kg/s. The material comprises of particles with a density of 2700 kg/m³ subdivided equally into 100 size classes as outlined in Table 7 for the cases with spheres.

Table 7: Particle size distribution of spheres.

| | d_{vol} [mm] | d_{vol}/a |
|----------------------|----------------|-------------|
| Fine | 2.40 - 3.60 | 0.49 - 0.73 |
| Undersized near mesh | 3.65 - 4.85 | 0.74 - 0.99 |
| Oversized near mesh | 4.90 - 6.10 | 1.00 - 1.24 |
| Coarse | 6.15 - 7.35 | 1.25 - 1.50 |

Due to the fact that results obtained from DEM simulations largely depend on the used parameters [242], continuous sieving simulations were validated with data from literature in a previous work [236]. According to the work by Delaney et al. [20] and Cleary [199], DEM parameters were used which are applicable for standard industrial quarry rock. In the present work, the same parameters are applied as outlined in Table 8.

Table 8: DEM parameters and material properties.

| Parameter | Density | Spring stiffness (normal) | Spring stiffness (tangential) | Coefficient of normal restitution (particle/particle) | Coefficient of normal restitution (particle/wall) | Coulomb friction coefficient (particle/particle) | Coulomb friction coefficient (particle/wall) |
|-----------|----------------------|---------------------------|-------------------------------|---|---|--|--|
| Symbol | ρ | k^n | k^t | e_{PP}^n | e_{PW}^n | $\mu_{c,PP}$ | $\mu_{c,PW}$ |
| Unit | [kg/m ³] | [N/m] | [N/m] | [-] | [-] | [-] | [-] |
| Value | 2700 | 1000 | 500 | 0.4 | 0.5 | 0.5 | 0.5 |

The stiffnesses $k^n = 1000$ N/m and $k^t = 500$ N/m lead to an accurate representation of particle/particle and particle/wall interactions due to an average particle overlap of around 0.5% of the particle diameter at maximum.

Besides spheres, cylinders and double cones are studied in this investigation (comp. Fig. 51b). The non-spherical particles (shapes (2) and (3)) have an aspect ratio of 1.55. The cylindrical particles (shape (2)) are volume equivalent to the spherical particles and have a hemispherical termination at both ends. The double cones (shape (3)) have the same minor axis as the spheres. This gives the double cones the same long-term separation characteristics in a batch screening analysis. However, their separation rates over screen length differ from that of

spheres. If needed for analysis or as a parameter for a screening model, the diameter of a complex shaped particle is calculated volume equivalent to a spherical particle in this investigation as

$$d_{vol} = \sqrt[3]{6 \cdot V / \pi}, \quad (138)$$

where V is the volume of the complex shaped particle. Note that some screening process models specify other definitions for the equivalent diameter which are then applied accordingly.

Table 9: Initial setup and performed variations of the continuous screening investigations.

| Parameter | Initial | Var. 1 | Var. 2 | Var. 3 | Var. 4 |
|---|-------------|--------------|--------|--------|--------|
| Amplitude [mm] | 1.76 | 1.32 | 2.2 | 2.64 | - |
| Frequency [Hz] | 27.6 | 20.7 | 34.5 | 41.4 | - |
| Stroke angle [°] | 45 | 30 | 60 | - | - |
| Particle mass flow [kg/s] | 0.1 | 0.05 | 0.15 | 0.2 | - |
| Scree wire profile [-] | rectangular | semicircular | - | - | - |
| Inclination angle [°] | 0 | 4.75 | 9.5 | 14.25 | 19 |
| Aperture size [m] (particle size adjusted) | 0.0049 | 0.00245 | - | - | - |

The following variations in operational and screen design parameters (comp. Table 9) are considered in the investigation here, applying the particle shapes shown in Fig. 51b. Starting from the initial setup (base case), variations of the vibration amplitude and frequency, stroke angle and particle mass flow are performed. In further investigations the screen wire approximation is changed to a semicircular profile (comp. Fig. 51a). Additionally, the inclination angle of the screen is varied from 0° to 19° to the horizontal. Last but not least the aperture size is reduced to $a = 2.45$ mm with an according reduction of the wire diameter to $w = w_{initial}/2$ and of the equivalent particle diameter to $d = d_{initial}/2$.

5. Results and discussions

In all performed investigations, the feed consists of one of the particle shapes outlined in Fig. 51b. For each particle shape, the influence of the parameter modifications outlined in Table 9 is examined, whereby only one parameter is varied at a time. The outcome obtained for the simulations is subsequently compared to results attained by phenomenological screening process and separation curve models (comp. Table 6, section 3.1 and section 3.2) whose adjustable parameters are fitted by genetic algorithms [240] to the fraction/fractions retained on the screen or the separation curves obtained from the DEM, respectively.

5.1 Numerical investigations

Particles are continuously fed onto the vibrated screen in the DEM simulations well mixed until a steady state is reached in which the inlet flow rate is equal to the sum of overflow and underflow which is then maintained for at least $\Delta t = 10$ s, thereafter. All analysis presented in

the following is based on this time period of $\Delta t = 10$ s in the steady state. Due to the oscillating motion of the screen and its inclination, particles are transported along it. The finest particles nearly instantly pass the apertures after getting in contact with the screen surface. Larger undersized particles need more attempts to pass and hence travel along the screen for some distance before being able to pass the screen apertures. After a while a bottom layer of particles larger than the aperture size forms out on the screen surface which hinders the passage of the smaller particles. Dependent on the screen configuration, the operational parameters and the particle shape, the bottom layer is whether dilute or dense and covered with multiple layers of coarse material. Now, fine and near mesh sized particles have to stratify downwards through the gaps between the oversized particles to approach the screen surface. By reaching the bottom layer of the screen, whose thickness is defined by the diameter of the respective coarse sized particles (comp. [7]), the fine particles regain the possibility to pass through the screen apertures. The ratio between the minor axis of the finest particles and the oversized particles or else the screen apertures is significant in the simulations. Therefore, the passing probability through interstices between particles and screen openings is highest for them. Accordingly, the average residence time for the finest particles in the particle bed is shorter than for undersized particles with a diameter closer to the aperture size (comp. Fig. 52a). Note, that the residence time considered here is the time particles need from the instance of getting onto the screen until whether passing through an aperture or leaving the screen in the overflow. Details on the average residence time in the particle bed for fine, undersized and oversized near mesh particles as well as the accumulated residence time of all particle sizes are shown in Fig. 52a for a screen operated with an amplitude of 2.2 mm. Besides the altered amplitude, initial base case operational parameters are applied in this example (comp. Table 9). Due to having no possibilities to pass the screen apertures, the residence time of the oversized material is much longer than the residence time of the undersized material. It can be seen that fine particles have a shorter residence time in the particle bed than the near mesh particles due to their higher stratification and passage ability (comp. Fig. 52a). Particle shape influences the transportation, the stratification and the passage which is reflected in the integral parameter residence time. Oversized spheres remain on the screen for the longest time because they have the highest possibility to get stuck in the sieve openings (pegging). Non-spherical particles also have the possibility to peg apertures, if they obtain vertical orientations. However, they can be released more easily as they preferably obtain horizontal orientations and therefore penetrate into the apertures less deeply. Note, that in the definition of the particle diameter used here (a diameter volume equivalent to a sphere), complex shaped particles with a diameter equivalent to the threshold diameter of an oversized sphere are still able to pass the apertures even though the passing probability is low. Undersized near mesh double cones remain on the screen longer than the other shapes due

to their reduced passage ability. In consequence of their small minor axis which easily faces the aperture diameter, volume equivalent cylinders pass the apertures faster than the other shapes.

In Fig. 52b the average transport velocity of oversized, near mesh and small undersized as well as of all particles is shown. The average transport velocity is based on the respective distance a particle has traveled along the screen divided by the average of the particle residence time. Small particles generally travel faster than larger ones due to less pegging if embedded in layers close to the screen surface or due to a chaotic motion which propels them to large distances in free flight when they remain on top of the bulk material. The other particle sizes have approximately the same average transport velocity. For the considered operational parameters, spheres are slower than double cones and volume equivalent cylinders due to their more pronounced pegging.

It can be concluded, that the increased residence time of oversized particles is caused by a slower transport velocity. Primarily for cases in which a thick layer of particles forms out on the screen surface, stratification influences the residence time of the considered particle shapes. The more particles pile up, the longer is the residence time of all particles.

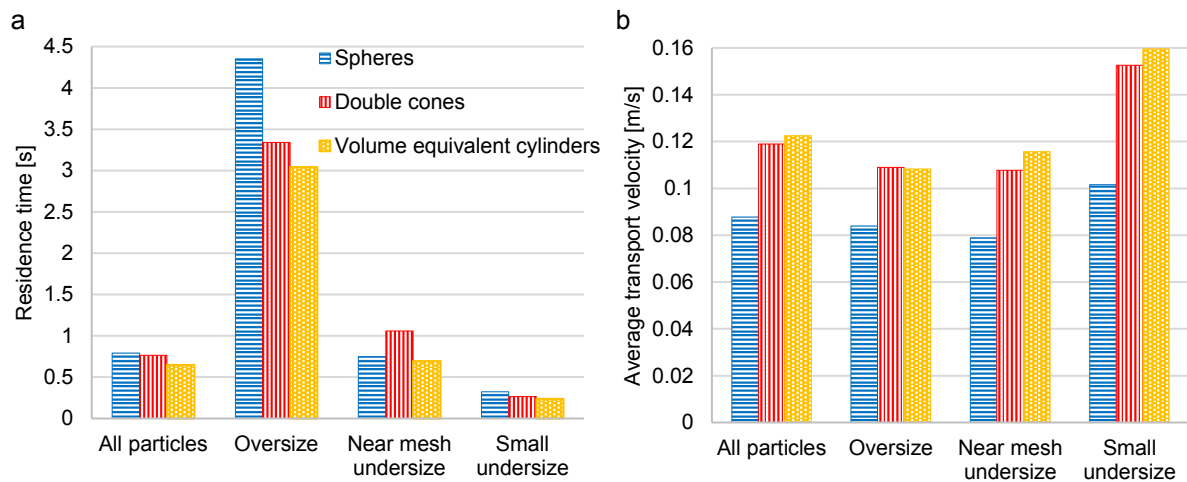


Fig. 52: (a) Average residence time and (b) average transport velocity of fine, undersized near mesh, oversized and all particles on the screen for an amplitude of 2.2 mm applied to the screen along with other parameters used as in the base case.

To achieve a better comparability for the analysis of the particle passage investigated in the following, the passed mass flow rate is summed up and normalized by the feed mass flow rate for all particle classes with diameters smaller than the apertures. For all shapes the threshold diameter $d = d_{vol}$ is a . Thereby, the fraction retained over the screen length is obtained which is related to the screening efficiency by $1-E$. The fraction retained is outlined in Figs. 53a,b-56a. Among the considered particle shapes, the highest passage ability is exposed by volume equivalent cylinders followed by double cones and then spheres in most investigations. This order is in alignment with the residence times, whereby spheres and double cones remain longer on the screen, which is mostly caused by pegging of apertures (comp. e.g. Fig. 52a).

In the base case configuration using spheres (shown in Figs. 53-56), the steady state is not reached before $t = 65$ s. In the start-up phase, particles pass the apertures at the beginning of the screen, but over time particles pile up as a consequence of pegged apertures. This causes particle passage to shift towards the end of the screen over time accompanied by long residence times, particularly for near mesh particles. Parts of the screen surface get completely blocked by near mesh sized particles and therefore, the fraction retained curves in Figs. 53a,b-56a show a flat, nearly linear decline instead of an initial rapid decline followed by a flattening as observed usually for non-spherical particles. Due to the thick particle layer, especially very small particles need more time to stratify and thereby travel along the screen, which causes a delayed/shifted transition into the underflow or they even remain on the screen and get discharged into the overflow. In the base case, some of the undersized particles pass the apertures close to the end of the screen, as larger particles previously pegging the apertures get aerated when being discharged into the overflow. The overall transport velocity is very low due to the high amount of blocking particles resulting from the low amplitude and frequency the screen is agitated with and due to a zero screen inclination (Figs. 53c,d-56b). This phenomenon is particle shape independent, although the tendency of its occurrence is stronger for spheres.

Additionally, data for the overflow separation curves depicted as partition number over the ratio of particle size (d_{vol}) and aperture size is shown in Figs. 53e,f-56c. If applying spheres, particles with a particle to aperture size ratio larger than 1 are not able to pass the apertures, since apertures and particles have exactly matching dimensions. This results in separation curves with 100 % oversized particles ($d > a$) in the overflow. In contrary, non-spherical particles with an equivalent diameter larger than the apertures still have the possibility to pass the sieve openings. This leads to separation curves with cut sizes d_{cut} shifted to values larger than 1. In the base case with spheres, many larger and even very small undersized particles are mistakenly discharged into the overflow resulting in a directly increasing separation curve at particle/aperture size ratios much smaller than 1. Thereby, separation curves deviate from the S-shape, which is usually encountered.

In the first variation performed (Figs. 53a,c,e), the initial amplitude of 1.76 mm is varied according to Table 9. A reduction of the amplitude is not realizable for spheres due to too excessive accumulation of particles on the screen, whereas an amplitude of 1.32 mm for complex shaped particles is applicable. However, this results in an intensive accumulation of particles and hence, slow particle transport, long residence times and shifted/delayed particle passage, particularly for double cones. Here, the steady state is reached after $t = 50$ s. An increase of the amplitude to 2.2 mm fixes the problems for spheres, improves their particle passage, enlarges their transport velocity and shortens their residence time on the screen. The

separation curve shifts closer to the ideal form of a unit step function with only a few undersized near mesh particles in the overflow (Fig. 53e).

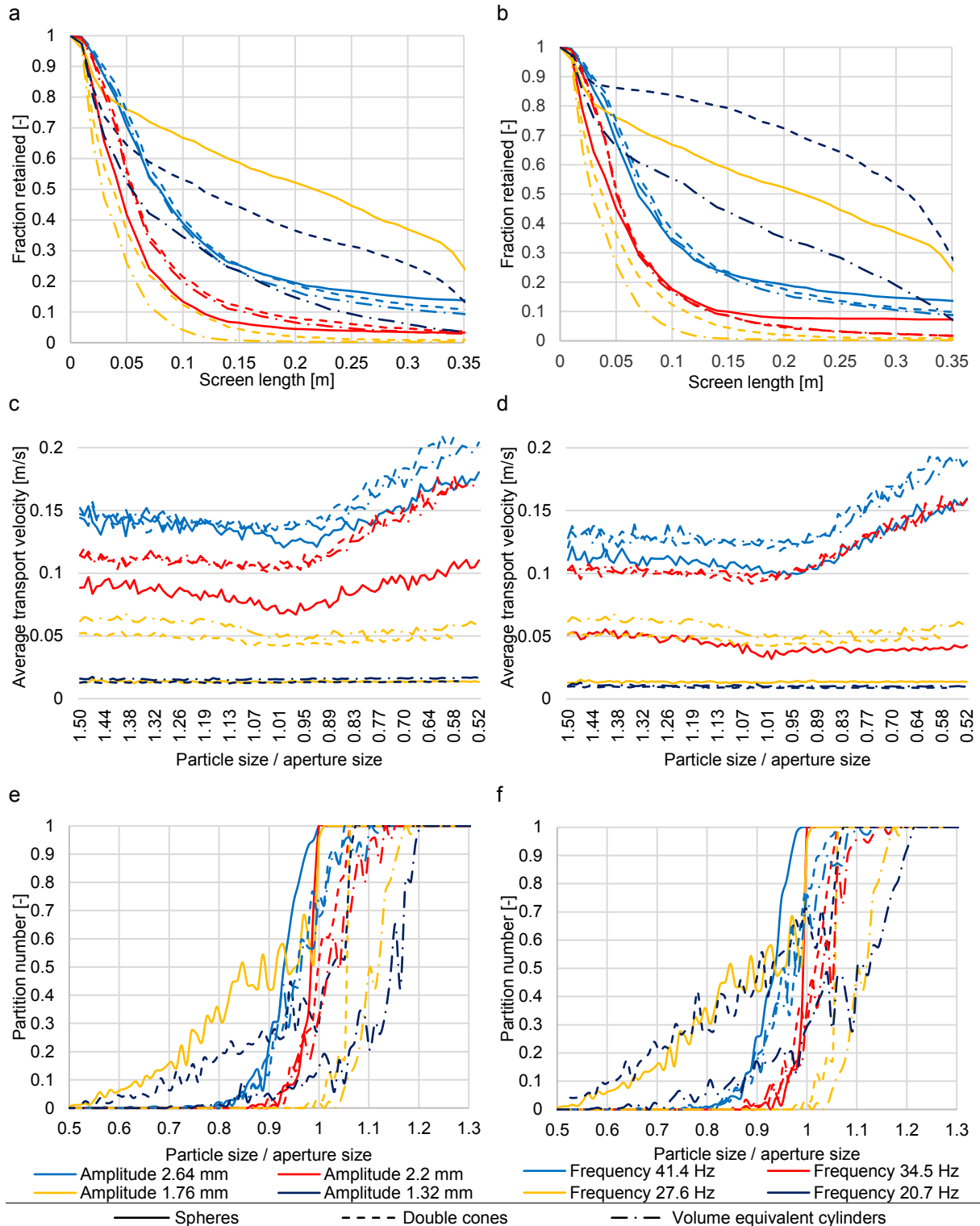


Fig. 53: (a,b) Particle passage through the screen openings for the three considered particle shapes over screen length for varying amplitudes (a) and frequencies (b) and (c,d) corresponding particle transport velocities over particle size per aperture size on the screen for varying amplitudes (c) and frequencies (d) as well as (e,f) partition number over particle size per aperture size for varying amplitudes (e) and frequencies (f).

Both non-spherical particle shapes obtain the sharpest classification for the initial operational configuration (comp. Table 9). In case of double cones, the separation curve is nearly ideal with only some undersized near mesh particles in the overflow, whereas the separation curve

of volume equivalent cylinders reveals an evenly distributed presence of near mesh sized particles in the overflow and in the underflow (typical S-shape).

An increased amplitude results in shorter residence times for oversized particles (increased transport velocity), but also in a much stronger reduction of undersized particle residence times and a pronounced increase of respective transport velocities (comp. Fig. 53c). For a certain threshold amplitude this can result in reduced undersized particle passage due to a higher transport velocity, which can be observed for all shapes (comp. e.g. Figs. 53a,e). The smallest particles have the highest average transport velocity, which is decreasing with increasing particle size until it reaches the aperture size, where pegging induces a minimum in the transport velocity. A further increase in particle size leads to less pegging and therefore, to a higher transport velocity.

When applying a larger amplitude beyond a threshold (amplitude > 2.2 mm) undersized near mesh particles reside longer on the screen because of an extended free flight period resulting in less particle screen contacts and thus less available attempts to pass (not shown in Fig. 53). The elevated transport velocity of small undersized particles (Fig. 53c) is compensated by a reduced particle passage (Fig. 53a). As a consequence, the residence time for small particles is not much influenced by a larger amplitude. The separation curves reveal more undersized near mesh particles classified in the overflow for enlarged screening amplitudes beyond the threshold amplitude (Fig. 53e).

The second parameter variation (Figs. 53b,d,f) addresses the change of the frequency (comp. Table 9). The results agree qualitatively with those from the first investigation. In case of a reduced frequency for non-spherical particles, the steady state is not reached before $t = 70$ s. Accordingly, a lower frequency leads to an intensively retarded particle passage, reduced transport velocity and longer residence times for all particle classes, whereas a higher frequency has slightly lower influence on all shapes compared to the case where an enhanced amplitude is being applied (Figs. 53a-d). The overall particle velocity is a bit slower when increasing the frequency instead of the amplitude for all shapes. A frequency of 34.5 Hz in case of spheres results in quicker particle passage, a higher transport velocity and shorter residence times for all size classes. A further increase above a threshold frequency diminishes the passage rates and increases the residence time for near mesh sized particles. Note, that the separation curves obtained for varying frequencies (Fig. 53f) are alike to the respective curves for varied amplitudes. They deviate only minimally.

Initially, a stroke angle of 45° to the horizontal is used in the simulations which is changed according to Table 9 in the third investigation (Figs. 54a,c,e). In case of spheres a lower vertical stroke component (vibration plane tilted by 30°) results in a pronounced piling of particles already on the first parts of the screen because it is less probable for pegged spheres to leave

blocked sieve openings. Therefore, the undersized material passes the apertures delayed/shifted along the screen towards its end or it is discharged from the screen as part of the overflow. 60 % of the undersized material is released in this way. This additionally results in slower particle transport velocities and longer residence times. Due to the stronger horizontal motion component, oversized particles still need approximately the same time to travel along the screen. Although the support for horizontal transport is lower, a stronger vertical motion component (vibration plane tilted by 60°) accelerates the transport velocity of spheres. It also enhances the particle passage due to a faster removal of pegged particles which leads to shorter residence times for all particles (comp. Fig. 54c).

In case of double cones, changing the stroke angle in both directions leads to slower transport velocities, longer residence times and delayed particle passage. Here, a stroke angle of 30° leads to particle piling and therefore slower particle transport and longer residence times. In contrast, a stroke angle of 60° results in delayed/shifted passage due to particle trajectories with an elevated vertex and an overall lower transport velocity, particularly for oversized particles. In case of volume equivalent cylinders, a decreased stroke angle has only minor effects on the passage of particles even though particle accumulation is observed. Therefore, the transport velocity of undersized particles is lower and approximately the same number of undersized near mesh particles is discharged in the overflow (Figs. 54c,e). An increased stroke angle leads to a lower transport velocity, delayed particle passage and less oversized near mesh particles in the overflow.

The fourth variation takes the particle mass flow rate into account (Figs. 54b,d,f). The probability of pegging for spheres is enhanced for larger particle mass flows with more near mesh sized particles being present. Due to a larger bed height and therefore a stronger necessity for stratification, applying a higher mass flow results in delayed/shifted particle passage and flat fraction retained curves (Fig. 54b). In comparison, spheres in a shallower bed caused by a lower particle mass flow require less time to stratify and thus for passing especially when so few near mesh sized particles are present that pegging is a rare event. If the mass flow is further increased from $\dot{m} = 150$ g/s to $\dot{m} = 200$ g/s the percentage of undersized particles remaining on the screen is not changing apparently for spheres (Fig. 54b).

As a consequence of the higher mass flow $\dot{m} \geq 100$ g/s, the undersized particles, but also the oversized particles entrained in the bed layer reside longer on the screen with a marginally increased transport velocity (Fig. 54d). Increasing the mass flow in case of complex shaped particles also leads to a delayed/shifted particle passage (comp. Fig. 54b). However, the fraction retained curves remain steep compared to spheres as no pegging of particles or blocking on the screen occurs (comp. Fig. 54b). Also due to no pegging, the transport velocity

for low mass flow rates (e.g. for $\dot{m} = 50$ g/s), but also for elevated mass flow rates of $\dot{m} = 100$ g/s - 200 g/s is larger (comp. Fig. 54d).

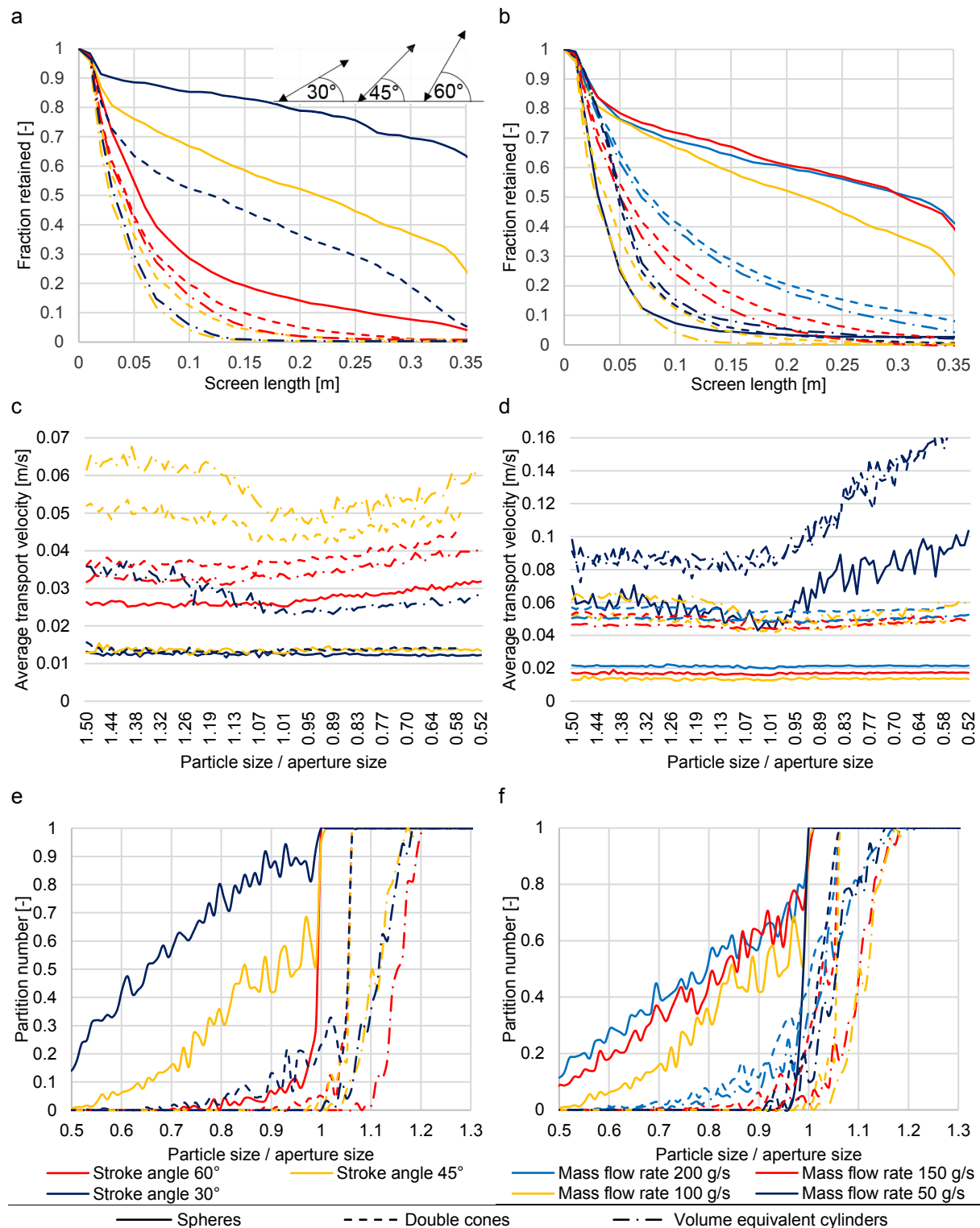


Fig. 54: (a,b) Particle passage through the screen openings for the three considered particle shapes over screen length for (a) varying stroke angles and (b) mass flows and (c,d) corresponding particle transport velocities over particle size per aperture size on the screen for (c) varying stroke angles and (d) mass flows as well as (e,f) partition number over particle size per aperture size for (e) varying stroke angles and (f) mass flows.

For an elevated mass flow rate the separation curves shift away from the ideal unit step function for all particle shapes which means that the separation becomes less sharp. In case

of spheres this is extremely pronounced, as a significant amount of all undersized particle classes can be found in the overflow, which is increasing with larger mass flow rates (Fig. 54f).

In the fifth investigation the particle passage through apertures generated by screen wires of rectangular and semicircular profiles is compared (Figs. 55a,c,e). In case of semi cylindrical wires the passage rate of spheres is higher in the start-up phase than in the base case where cuboidal wires are used. Nevertheless, particles still pile up due to pegging of near mesh sized particles (not shown in Fig. 55). When the steady state is reached ($t > 75$ s), the fraction retained over screen length is decreasing in the same manner as in the base case, but with even more particles passing the apertures at the end of the screen (Fig. 55a). The transport velocity of spheres is unchanged by altering the wire shape (Fig. 55c). In contrast to the initial case, undersized particles are found in the overflow to a slightly lower extent making the separation much sharper. In case of double cones, a semicircular wire profile can lead to pegging and piling of particles. Accordingly, the particles pass the apertures delayed/shifted (comp. Fig. 55a), particles travel slower over the screen (com. Fig. 55c) and all particle classes reside longer on the screen (not shown in Fig. 55). The evolution of the partition number plotted over the particle to aperture size ratio reveals a higher amount of near mesh sized double cones in the overflow when applying a semicircular wire profile (comp. Fig. 55e). In contrast to the other shapes, the fraction retained over screen length for volume equivalent cylinders is not much influenced by the shape of the wires. A semicircular profile results in slightly quicker passage and a lower transport velocity for all size classes (Figs. 55a,c). For a semicircular wire profile the cut size d_{cut} shifts to larger particle sizes (Fig. 55e).

In the sixth variation the inclination angle of the screen surface is changed from 0° to 19° to the horizontal according to Table 9 (Figs. 55b,d,f). A larger inclination angle leads to a faster particle transport independent of shape (Fig. 55d). This results in shorter residence times for oversized particles on the screen. In case of double cones and volume equivalent cylinders a larger inclination angle causes a delayed/shifted passage of particles because of the faster particle transport velocity forcing the particles to move with lengthened trajectories along the screen. This leads to less particle screen contacts and therefore fewer possibilities to pass the apertures. However, the residence time of undersized particles is nearly uninfluenced due to the compensation of the high particle transport velocity and the low passage rates (not shown in Fig. 55).

In case of the two considered non-spherical particle shapes the separation curves shift away from the ideal unit step function with a higher inclination angle. At larger inclination angles ($\gg 10^\circ$) even smaller non-spherical particles are in the overflow (Fig. 55f). In conclusion, an effective screening process for these two particle shapes should be operated only with a small inclination angle. In contrary, spheres pile up due to pegging in the base case, revealing the

necessity for a higher transport velocity to prevent this. Besides a higher amplitude or frequency (Fig. 53), this can be achieved by enhancing the inclination angle.

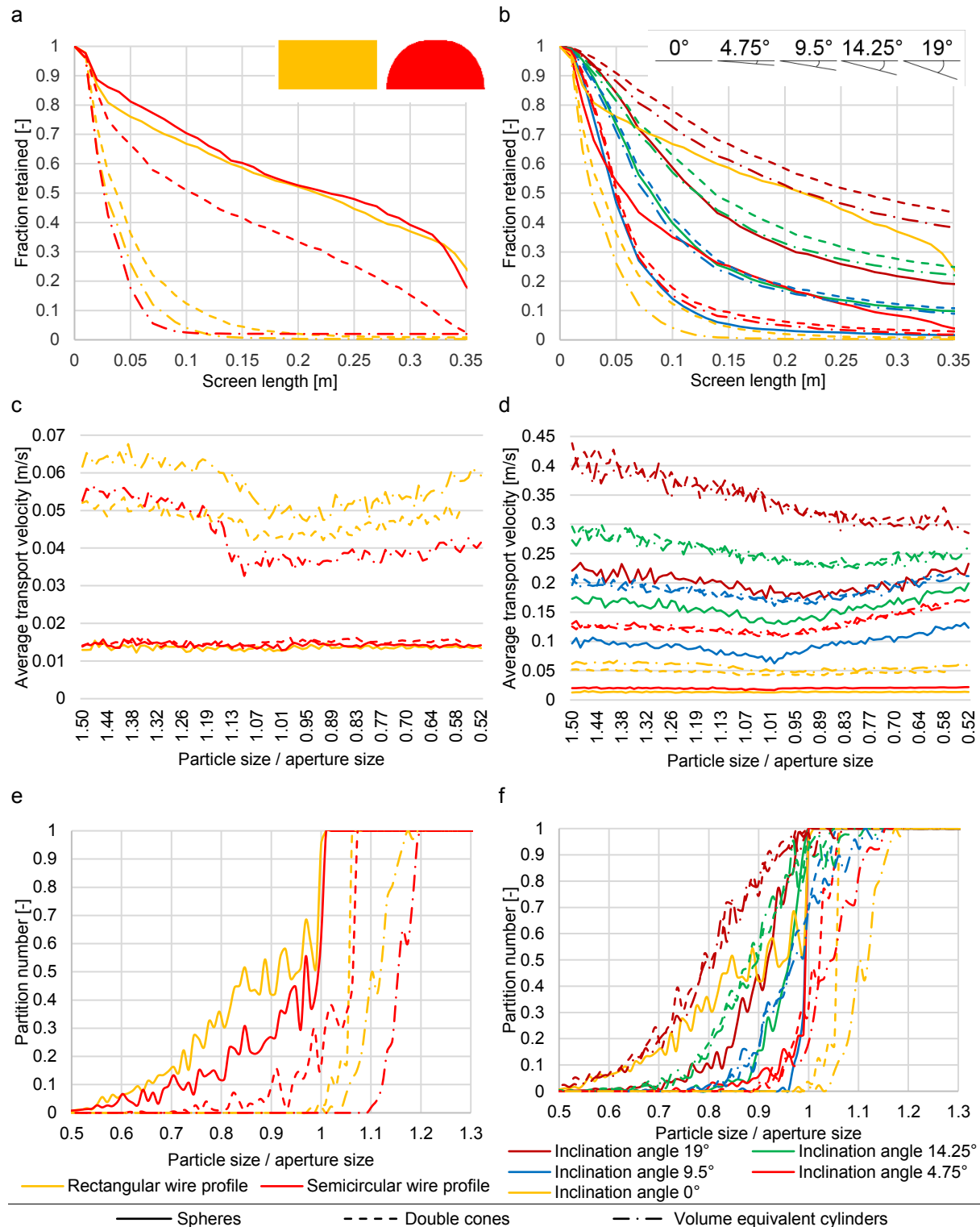


Fig. 55: (a,b) Particle passage through the screen openings for the three considered particle shapes for (a) varying wire profiles and (b) screen inclination angles as well as (c,d) corresponding particle transport velocities over particle size per aperture size on the screen for (c) varying wire profiles and (d) screen inclination angles as well as (e,f) partition number over particle size per aperture size for (e) varying wire profiles and (f) screen inclination angles.

In these investigations, an inclination angle of around 10° to the horizontal is required to avoid intensive pegging of spheres and to provide an instant particle passage close to the front of the screen with most of the near mesh sized particles being classified into the underflow. A

further increase of the inclination angle results in less particle passage with more near mesh sized particles getting in the overflow as similarly observed for non-spherical particles.

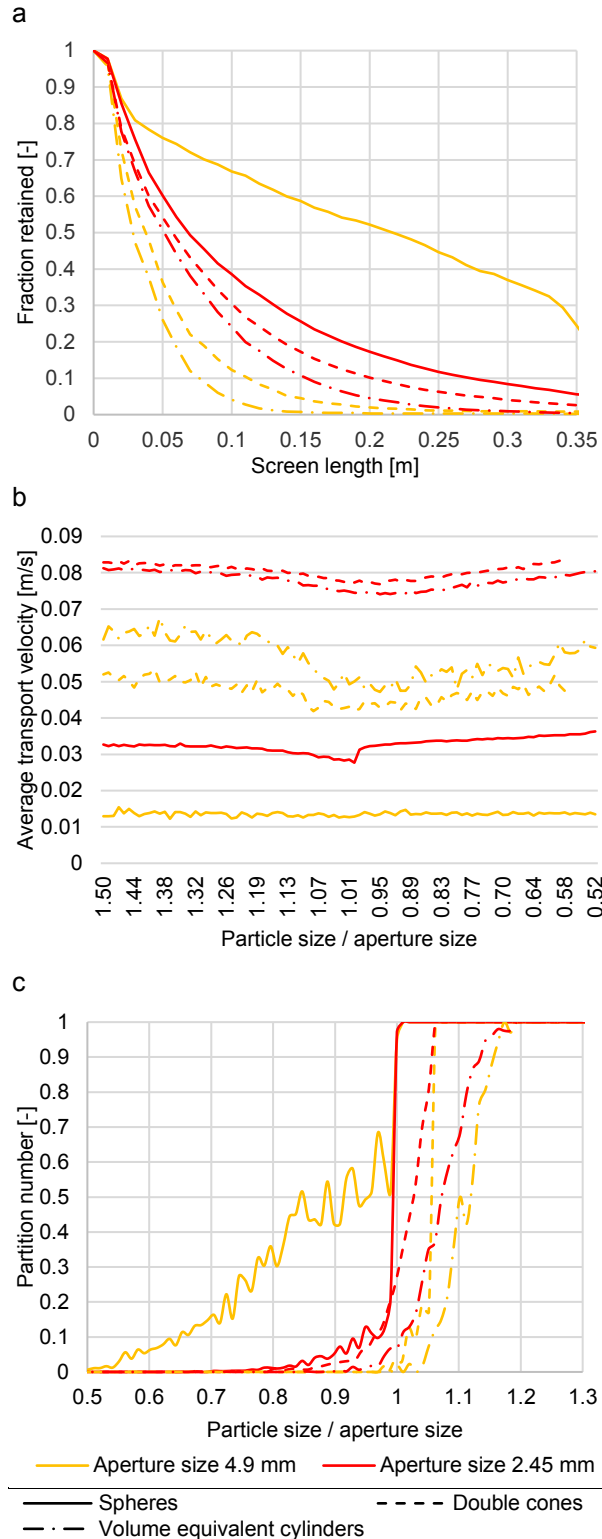


Fig. 56: (a) Particle passage through the screen openings, (b) transport velocities and (c) partition number for the three considered particle shapes for varying screen aperture sizes.

In the last investigation, a decrease of the equivalent particle diameter to $d = d_{initial}/2$ and an according reduction of aperture and wire sizes is carried out (geometrical scaling by a factor of 2) and compared to the base case in Fig. 56. Note, that the particle mass, which is not

directly altered here, scales differently than size (with d^3). The reduction of particle and aperture size results in less pegging of spherical particles, improving their passage rates intensively (Fig. 56a). Due to the differently to size scaled mass, pegged spheres are more easily removed from the sieve openings. Thereby, the overall transport velocity is increased and the residence time for undersized spheres is shortened. The amount of undersized spheres in the overflow is very low. Only some near mesh sized particles are classified incorrectly (Fig. 56c). In case of volume equivalent cylinders and double cones, the downscaled configuration results in delayed particle passage due to more chaotic particle motion (Fig. 56a). The overall particle transport velocity is enhanced (Fig. 56b), therefore oversized particles reside shorter on the screen whereas near mesh sized particles have less possibilities to pass, leading to a larger residence time (not shown in Fig. 56). Additionally, a higher amount of near mesh sized non-spherical particles is counted in the overflow resulting in less ideal separation curves (Fig. 56c). The obtained results from geometrical scaling are qualitatively in alignment with results obtained for increased amplitudes or frequencies.

5.2 Benchmarking of steady state spatially resolved screening models

The simulation results as outlined in section 5.1 covering a broad range of operational parameters are used to benchmark the steady state spatially resolved screening process models as outlined in Table 6 in the following. The fraction retained on the continuous screening apparatus in dependence on screen length obtained from the DEM simulations is compared with data from spatially resolved phenomenological models which are fitted to the DEM results by adjusting their respective model parameters. The obtainable accuracy of the adjustment is exemplarily shown in Fig. 57 for spheres on a screen with an inclination angle of 19° to the horizontal and apart from that with initial (base case) operational parameters. For models that account for the division of undersized particle fractions (Nos. 4, 8, 9, 10, 11, 13) the average of all undersized fractions is shown.

The best match of the DEM results is obtained with the model by Soldinger (No. 12) followed by the two models of Grozubinsky et al. (Nos. 5, 7). This is due to the fact that all of them use more than one adjustable parameter to calculate only the lumped undersized fraction in dependence on the screen length. In contrast, a model that accounts for the different particle fractions has to provide information on each fraction which is a far more difficult task. In the latter case, the ratio of the number of model parameters and information provided is less favorable. The best result for such a model is obtained by the model of Standish (No. 4) because each particle class is represented by a single parameter.

The model by Ferrara et al. (No. 11) has problems with representing the fraction retained on the first part of the screen (note the discontinuity between crowded and separated screening), but reveals a good match for the middle and end section of the screen. It reaches an overall

good result for a model that accounts for the division of undersized particle fractions by only a few adjustable parameters. A comparable model which is easier to adjust, because no iterative procedure is required as in model No. 11, is the one by Subasinghe et al. (No. 8). The models by Nakajima et al. (No. 9) and Deghani et al. (No. 10) reveal larger deviations, however, needing only one adjustable parameter for all particle fractions. Already from this exemplarily selected data set, it can be concluded that spatially resolved screening process model accuracy is not necessarily correlated with the model complexity (number of governing equations), the number of adjustable model parameters and the aspect if undersized material is considered as lumped or in fractions.

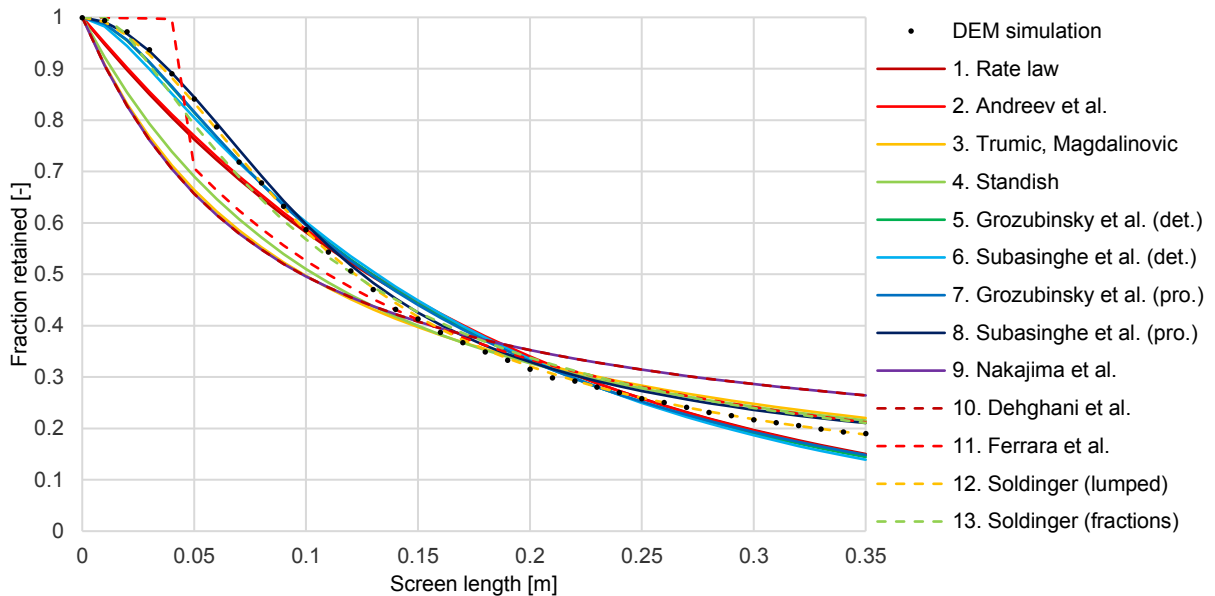


Fig. 57: Fraction retained on the screen over screen length for various steady state spatially resolved screening process models and the DEM simulations for an investigation with spheres and a screen inclination angle of 19° to the horizontal.

For the benchmarking of a larger number of investigations an average deviation of the simulated and model predicted fraction retained is calculated for models considering the whole fine material as one lumped undersized fraction by $(\sum_{k=1}^j |E_{mod}(k) - E_{sim}(k)|) / j$, where j is the total number of considered positions along the screen k . For models considering the different undersized particle classes i as fractions (Nos. 4, 8, 9, 10, 11, 13) the average of the obtained fractional deviations is calculated by $(\sum_{i=1}^l (\sum_{k=1}^j |E_{mod}(i, k) - E_{sim}(i, k)|)) / (j \cdot r)$, where r is the total number of undersized fractions. Note, that the screen of length 0.35 m is divided into intervals of 0.01 m.

In Fig. 58 the summed up particle passage deviations between steady state spatially resolved screening models sorted according to Table 6 and discrete element simulations performed with spheres (Fig. 58a), double cones (Fig. 58b) and volume equivalent cylinders (Fig. 58c) for all investigated variations (comp. Table 9) are shown.

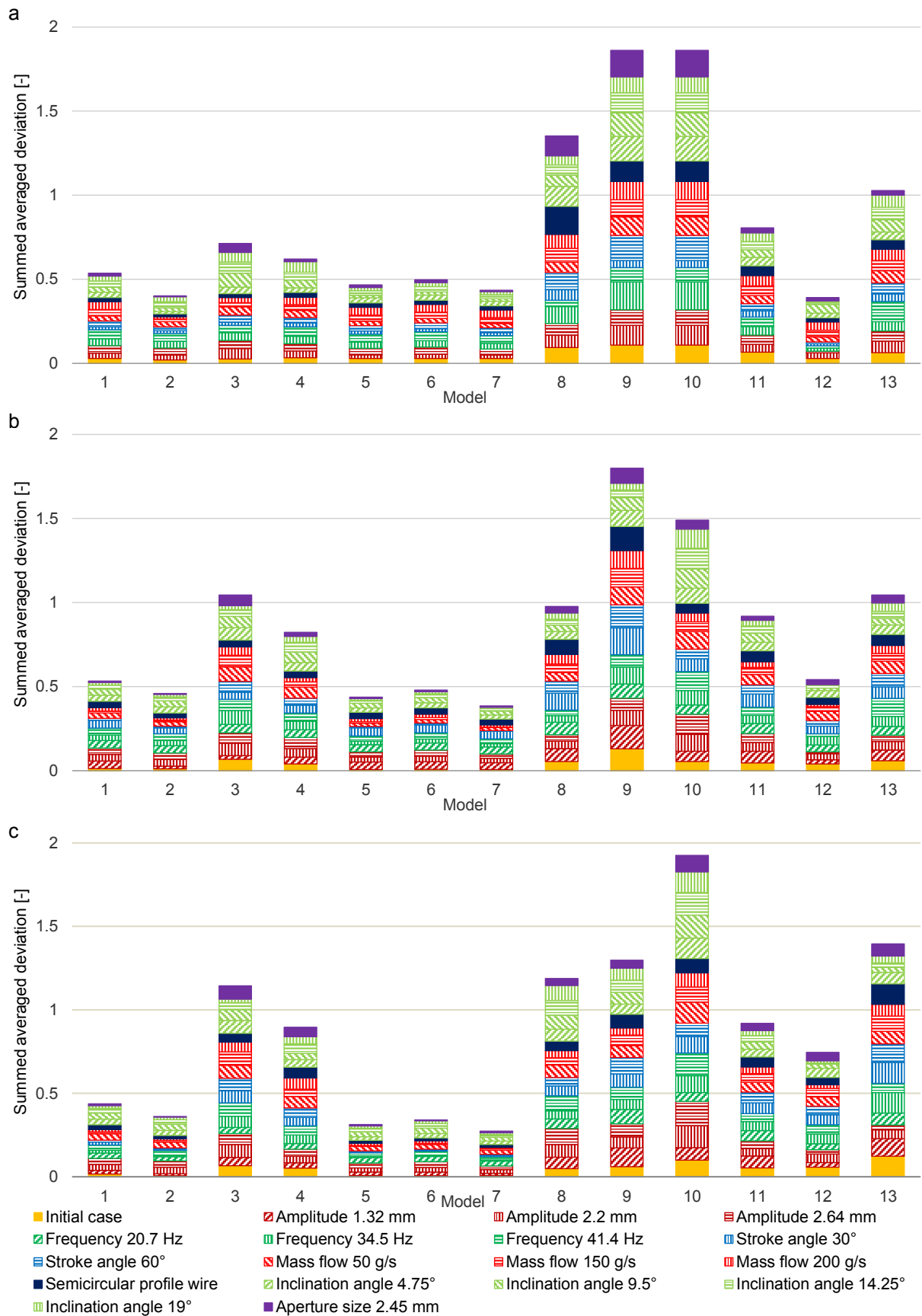


Fig. 58: Particle passage deviations between steady state spatial resolved screening models sorted according to Table 6 and discrete element simulations summed up for all investigated variations according to Table 9 for (a) spheres, (b) double cones and (c) volume equivalent cylinders.

Independent of shape, the models that do not account for the division of undersized particle fractions (Nos. 1, 2, 3, 5, 6, 7 and 12) are quickest to adjust and obtain low deviations because only the lumped fraction retained curve has to fit to the simulation results (36 data points) instead of the fraction retained curves of all undersized particle classes (36×100 data points). Among these models, the one by Soldinger (No. 12) followed by Andreev et al. (No. 2), Subasinghe et al. (No. 6) and Grozubinsky et al. (Nos. 5, 7) show the least overall deviations when spheres are used in the simulations (Fig. 58a). All these models use more than one adjustable parameter. The functional forms with additional adjustable parameters for instance as exponent of the screen length l used in the model No. 2 are able to compensate well for the variations in the fraction retained on the screen caused by different screen agitations or mass flows. The models Nos. 5 and 7 can be easily reduced to the rate law (model No. 1); for the screening intensity $\beta \gg 1$ the term $\exp(-\beta t)$ becomes zero (comp. [241]). In both models the additionally introduced coefficient of proportionality q offers an improvement in accuracy for continuous screening when many different size classes are considered. The model by Trumic and Magdalinovic (No. 3) reveals the largest deviations of the models that do not account for the division of undersized particle fractions due to using only one adjustable parameter. For a model that accounts for the division of undersized particle fractions, relatively low deviations are obtained by the one of Standish (No. 4). However, this is achieved by using one adjustable parameter per size class. Although accounting for different particle size classes and using only a few adjustable parameters, the model by Ferrara et al. (No. 11) exhibits overall minor deviance, but with the disadvantage of a long adjustment time as it has to be fitted iteratively. A bit larger deviations are visible for the fractioned model by Soldinger (No. 13) with the advantage of a shorter adjustment time. The probabilistic model by Subasinghe et al. (No. 8) is adjusted and applied even faster, but leads to larger deviations in return. The models by Nakajima et al. (No. 9) and Deghani et al. (No. 10) obtain the largest overall deviations for the simulations with spheres. This is mainly caused by the fact that they model particle size class resolved results of a screening process with the help of only one adjustable parameter. Note, that these models (No. 9 and No. 10) are identical if spheres are used. The differences only become present for non-spherical particles.

The initial (base) case with delayed/shifted particle passage and a resulting flat fraction retained curve is comparatively easy to model. This leads to low deviations for most of the investigated models. Furthermore, cases with instant particle passage and strongly decreasing fraction retained curves reveal not much deviation between models and DEM results, likewise. Stronger differences occur if the fraction retained curves are decreasing unevenly or if they stagnate over a certain length of the screen. The models that account for the division of undersized particle fractions, particularly models Nos. 8-10, have more problems if the differences between the passage rates of undersized particles are erratic or if the curves of

different particle size classes intersect each other. This could be the case, if the particles have a high transport velocity on the screen when e.g. a large amplitude, frequency or inclination angle is applied.

In the investigations with double cones (Fig. 58b) the models by Grozubinsky et al. (Nos. 5, 7) and Andreev et al. (No. 2) followed by the model by Subasinghe et al. (No. 6) are adjusted to the simulation results with the least deviations. Although needing many adjustable parameters, model No. 4 reveals comparatively large deviations as it is not considering the shape of the particles. Again, model No. 11 is the model with least deviations that accounts for the division of undersized particle fractions without needing an adjustable parameter for each size class. However, in case of double cones, it leads to larger deviations and model No. 8 by Subasinghe et al. achieves nearly the same result with less computational effort. The models by Nakajima et al. (No. 9) and Deghani et al. (No. 10) obtain the largest deviations again, but in case of double cones, the condition for the probability function of model No. 10 leads to lower deviations. The original model No. 9 (comp. eq. (125)) reveals even larger deviations which are twice as large for some cases. Similar cases as for spheres are easy to model and reveal low deviations. Large deviations occur if the passage in dependence on the screen length is unequal. Here, this is primarily caused by pegging of apertures, for instance when the screen is operated with a low amplitude or frequency.

The models by Grozubinsky et al. (Nos. 5, 7) reveal the least deviations for volume equivalent cylinders (Fig. 58c). Here, the probabilistic model No. 7 obtains slightly better results than the deterministic model due to taking the dispersion of the particles into account. In contrast to the two former investigated shapes (spheres and double cones), model No. 12 by Soldingier does not obtain the lowest deviations caused by arbitrarily passing particles with an equivalent diameter larger than the aperture size. Due to the same reason, model No. 13 by Soldingier reveals more deviations than for the other shapes. Again, model No. 3 by Trumic and Magdalinovic shows comparatively large deviations due to its simplicity of offering only one adjustable parameter and not considering the particle shape. In the case of volume equivalent cylinders, model No. 11 by Ferrara et al. obtains only slightly larger deviations than model No. 4 by Standish, which needs a lot more adjustable parameters. Additionally, model No. 11 has much lower deviations than model No. 3 that accounts only for the undersized fraction as a lumped entity. Requiring a shorter time for the adjustment than model No. 11, model No. 8 by Subasinghe et al. obtains the second lowest deviations for a model that takes the probability of passage for each single size class into account. This is of high relevance in case of non-spherical particles. In case of volume equivalent cylinders, model No. 10 by Deghani et al. reveals the largest deviations due to its condition for the probability function and the use of only one parameter for all particle classes. Here, the revised model No. 9 with a similar model structure and the same number of model parameters obtains comparatively lower deviations,

because of taking the passage probability of particles with a larger equivalent diameter than the apertures with the help of the modified condition for the probability function (eq. (126)) into account. The use of the original model No. 9 by Nakajima et al. results in twice as large deviations as the use of the modified one due to giving all particle classes with an equivalent diameter larger than the apertures a probability of $p=0$ to pass.

Some of the investigated models show fewer deviations for simulations with spherical particles. This is easy to explain for kinetic models (Nos. 1-6) without a passage probability and the models by Soldinger (Nos. 12, 13) which all do not take the particle shape into account. Models Nos. 7 and 11 calculate the particle passage probability, but do not account for the particle shape. In contrast, models Nos. 9 and 10 consider the particle shape in the functions for the passage probability (comp. Table 6) leading to lower deviations depending on the conditions for these functions. Overall larger deviations in case of spheres are a result of stronger pegging. Many investigated configurations lead to particle pegging, whereby two configurations are even not viable as they do not reach the steady state. Of course, screening process models are not capable of representing all the phenomena which are reported in the DEM, where the particle orientation of all particles is tracked transiently at much higher computational cost.

5.3 Benchmarking of steady state separation curve screening models

In a second step, the steady state separation curve screening models are benchmarked based on the data shown in section 5.1. The overflow separation curves obtained from the DEM simulations for the continuous screening apparatus are compared with data from steady state separation curve screening models which are fitted to the DEM results by adjusting their respective model parameters. The obtainable accuracy of the adjustment is exemplarily shown in Fig. 59 for spheres on a screen with an inclination angle of 19° to the horizontal and apart from that with initial (base case) operational parameters.

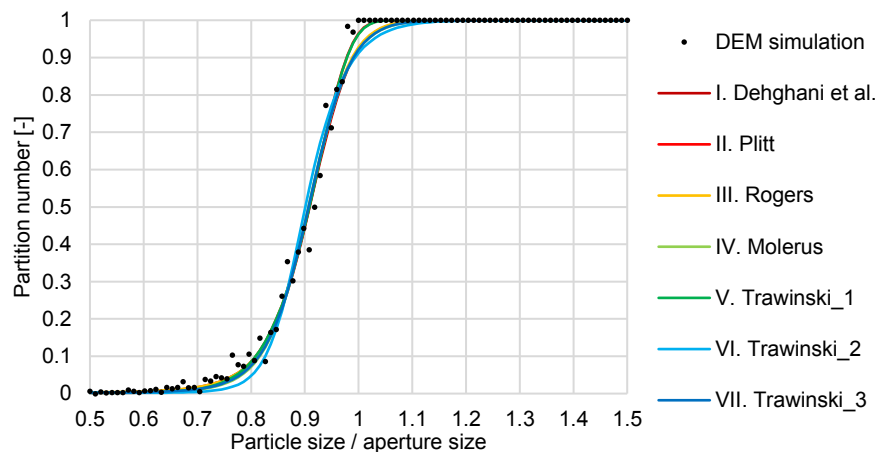


Fig. 59: Separation curves for various process models and the DEM simulations for an investigation with spheres and a screen inclination angle of 19° to the horizontal.

All models reveal acceptable results with little deviations. There are some differences due to the scattering of the simulation results and for the representation of oversized near mesh particles. Besides the second revised model of Trawinski (No. VI) and the one by Plitt (No. II), the adjusted separation curves are not able to properly represent the values of the partition number slightly above a particle to aperture size ratio of 1. The overall best results in Fig. 59 are obtained by the models of Plitt (No. II) and the first revised model of Trawinski (No. V).

For the benchmarking over a larger number of investigations in case of separation curve models an average deviation of the simulated and model predicted separation curves is calculated by $\left(\sum_{i_S=1}^{r_S} |T_{sim}(i_S) - T_{mod}(i_S)|\right)/r_S$ where r_S is the total number of considered particle classes i_S . In Fig. 60 the summed up deviations between steady state separation curve screening models according to section 3.2 and discrete element simulations performed with spheres (Fig. 60a), double cones (Fig. 60b) and volume equivalent cylinders (Fig. 60c) according to Table 9 are visualized for all investigated variations.

Besides model No. I by Dehghani et al., the investigated steady state separation curve screening models do not consider the particle shape. Nevertheless, deviations between the adjusted models and the DEM results remain low due to the fact that the separation curve models are adjusted to each simulation separately as they do not have any predictive capabilities. Separation curve screening models are able to easily represent partition numbers forming an ideal separation curve (unit step function) or a symmetric S-shaped curve. In case of spheres (Fig. 60a), the closest result to an ideal separation curve can be obtained when applying either an amplitude, a frequency, a stroke angle or an inclination angle slightly larger than in the base case configuration. Therefore, pegging is prevented, but the particle transport is still slow enough to ensure good passage. The very low deviations are caused by undersized near mesh particles that do not pass the apertures and thereby lead to symmetric separation curves. Geometric scaling (size reduction) or a lower mass flow rate also result in nearly ideal separation curves, leading to low deviations between DEM results and separation curve models.

For cases with a larger transport velocity induced by larger amplitudes, frequencies or inclination angles, the amount of small particles in the overflow increases. The simulation results do not lead to symmetric S-shaped curves due to undersized near mesh particles not passing the screen. This ends up in larger deviations between the separation curve screening models and the simulation results.

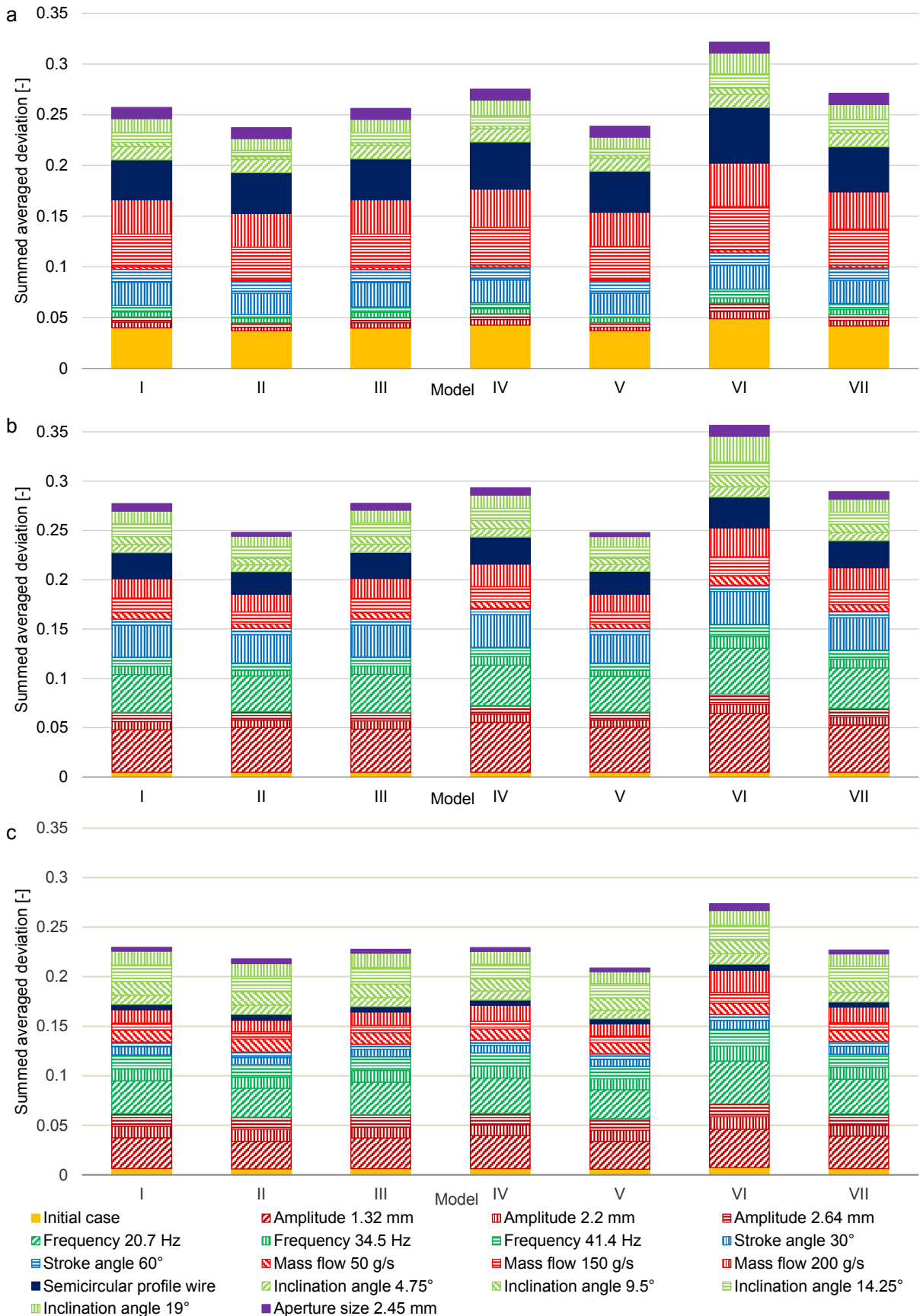


Fig. 60: Deviations between steady state separation curve screening models (section 3.2) and discrete element simulations summed up for all investigated variations (Table 9) for (a) spheres, (b) double cones and (c) volume equivalent cylinders.

For the base case configuration or if a semicircular wire profile, a higher mass flow or a stroke angle with a larger horizontal motion component is applied, the near mesh sized particles are

intensively pegging the apertures. Therefore, many small and even very small particles are discharged into the overflow. As a consequence, separation curve screening models reveal larger deviations when being adjusted to these simulation results.

Non-spherical particles (Figs. 60b, c) with an equivalent diameter larger than the aperture size can pass the sieve openings into the underflow if their minor-axis is smaller than the aperture size. In return, undersized near mesh particles are discharged into the overflow. As a consequence, the simulation results form symmetric S-shaped curves which are readily represented by separation curve screening models. However, the passing rates of near mesh sized non-spherical particles are more sensitive than for spherical particles, particularly if a higher mass flow is applied or if particles accumulate on the screen when the screen is operated with a small amplitude or frequency. In these cases, the separation curves increase unevenly and therefore, much larger deviations occur. A faster particle transport velocity, which is attained by applying a larger amplitude, frequency or inclination angle, also leads to a few more small and oversized near mesh particles in the overflow amounting to larger deviations.

Lower deviations for separation curve models are obtained in some cases if double cones are screened instead of spheres (Fig. 60b) due to a lower pegging probability. Here, the largest deviations result from applying lower amplitudes and frequencies followed by stroke angles with low vertical motion components. The lowest deviations for double cones are obtained for the base case configuration.

The summed up deviations for volume equivalent cylinders (Fig. 60c) reveal the lowest deviations of the investigated shapes due to the lowest pegging probability. The largest deviations for volume equivalent cylinders occur for low amplitudes and frequencies due to the formation of unsymmetrical separation curves. In contrast, good results are attained for the base case configuration independent of wire profile and stroke angle as well as for cases with a slightly enlarged mass flow and for a reduction of particle and aperture dimensions (geometric scaling).

The overall lowest deviations summed up over all investigations can be obtained by the model No. II by Plitt and the first revised model by Trawinski (No. V). In both models, the term (d/d_{cut}) which is increasing with particle diameter is influenced by one or even two adjustable parameters in the exponent independent of additional parameters (comp. eq. (132) and eq. (135)) giving both models a good adaptability. The largest deviations are obtained by the second revised model of Trawinski (No. VI). Here, both adjustable parameters are in the exponent of the term (d/d_{cut}) , but both parameters are dependent on the particle size d (comp. eq. (136)).

Compared with spatially resolved models that do not account for the representation of undersized fractions, the deviations of separation curve models are in the same order of

magnitude, because both model classes have to adjust to a set of relevant values of roughly similar number (number of positions on the screen and number of particle size classes). In contrast, the fractioned spatially resolved models which are adjusted to the product of both, positions and particle size classes, obtain much larger deviations.

6. Conclusions

The discrete element method (DEM) has been used to perform continuous screening investigations of a polydisperse particle mixture with particles of predefined shapes (spheres, double cones and volume equivalent cylinders). The particles have been subdivided into 100 size classes consisting of coarse, oversized near mesh, undersized near mesh and fine material represented by particles with diameters of 7.35 mm (1.5a) to 6.15 mm (1.255a), 6.1 mm (1.245a) to 4.9 mm (1a), 4.85 mm (0.99a) to 3.65 mm (0.745a) and 3.6 mm (0.735a) to 2.4 mm (0.49a) in case of spheres, respectively (comp. Table 7). Screening parameters such as the inclination angle, a geometric scaling and the surface representation (rectangular / semicircular wire) as well as operational parameters including vibration frequency, amplitude, stroke angle and mass flow rate have been varied.

Results obtained by the DEM clearly unveil that the screening efficiency in case of a broad particle size distribution including particle sizes close to the aperture dimensions is higher for non-spherical particles than for spheres due to the strong pegging of the latter. The screening efficiency for spheres, but also for non-spherical particles can be increased by enlarging the vibration amplitude and frequency as well as the inclination angle in continuous screening until a threshold is reached. In case of exceeding this threshold amplitude, frequency or inclination angle screening efficiencies decrease. In the investigation here, the initially applied operating configuration (for amplitude, frequency, inclination angle) results in the highest screening efficiency for non-spherical particles. Moreover, a stroke angle with approximately evenly distributed horizontal and vertical motion components leads to the highest screening efficiency for non-spherical particles. This is due to the low pegging tendency of these particles and a sufficiently induced particle transport. In case of spheres, a stroke angle with a larger vertical motion component supports both, the screening efficiency and the particle transport by removing pegged particles from the apertures. The amount of material charged to the screen needs to be adapted to the size of the screening apparatus. Note, that a strongly non-linear relation exists between screening efficiency and the mass flow rate. In case of spheres with the configuration applied here, a reduction of mass flow can prevent the strong accumulation of particles, which is observed for enhanced mass flow rates which strongly deteriorates particle passage. In contrast, a larger mass flow rate of non-spherical particles is easily realizable. Using semicircular wires in case of double cones increases the risk of pegging whereas spherical particles and cylinders are nearly unaffected by the chosen wire profile. A

reduction of particle and aperture size (geometric scaling) leads to more dynamic particle motion, resulting in less particle passage for non-spherical particles, but in a prevention of pegging and therefore, in a higher screening efficiency for spheres.

The screening models by Grozubinsky et al. [3], Andreev et al. [226], Subasinghe et al. [227] and Soldinger [7] attain the overall least deviations in modeling spatially resolved continuous screening simulations if the undersized mass flow is considered as one lumped fraction. The model by Standish [45] obtains the lowest deviations if the undersized fractions are handled separately, with the drawback of needing one adjustable parameter per size class. Almost the same accuracy can be achieved with less adjustable parameters with the model by Ferrara et al. [225]. However, it requires more time for adjusting. Although obtaining the largest deviations, the models by Deghani et al. [52] and Nakajima et al. [229] have the advantage of needing only one adjustable parameter and low computational effort despite of taking the division of undersized particle fractions into account. Complex models such as the one by Soldinger [8] have the advantage of obtaining the adjustable parameters within known intervals. However, they require more time for adjusting and calculation and do not necessarily provide lower deviations than models with less computational effort. Their model parameters have a physical meaning and offer the possibility to extrapolate parameters for unconsidered operational situations.

In case of steady state separation curve screening models, the most accurate adjustment can be obtained with the model by Plitt [218] and the first model by Trawinski [223]. They use one or even two adjustable parameters, which influence the term (d/d_{cut}) in the exponent independent of additional parameters. They reveal less deviations than the fractioned spatially resolved models due to being time or length independent. The obtained deviations are in the same order of magnitude as for spatially resolved models that do not account for the undersized fractions.

All screening models (spatially resolved and separation curve models) are dependent on the screening material and apparatus and rely on one or more adjustable parameters. Therefore, they cannot predict screening processes where they are not adjusted for. Complex screening models [7,8] which provide additional information on the particle bed such as the bed height, the vertical particle distribution and their dependence on operational parameters are an approach to overcome this situation. Although describing the screening process more detailed, the complex models still need adjustable parameters and are not predictive, neither.

The DEM simulations performed here, automatically include the startup phase of the screening process which is not considered in models for continuous screening only modeling the steady state. In further investigations, dynamic changes like the startup or the shutdown phase

needing a time-resolved representation will be addressed and process parameters like the mass flow rate, the particle distribution or the frequency will be varied during the simulations.

Note, that the DEM simulations were not directly benchmarked against experimental investigations in this study. A benchmarking has been exemplarily done for the DEM approach applied here to literature data [236]. The purpose of the DEM was to derive a qualitatively realistic parameter space as could also be derived by experimental investigations. A benchmarking of the DEM against experiments is currently ongoing in order to apply the screening models (spatially resolved and separation curve models) towards real screening investigations involving experimental equipment in the future.

In this work here, complex shaped particles are represented by a small number of clustered spheres. In future work, the shape will be taken into account more accurately by a larger number of clustered spheres and particles represented by polyhedra, respectively. Another task in the future will be the study of screen performance linked to moisture content. The resulting liquid bridges will influence the transport velocity and behavior of particles along the screen. Therefore, the residence time and passage of particles through the particle bed and apertures will be influenced.

Acknowledgements

The authors gratefully acknowledge the support by DFG within project SPP 1679 through grant numbers KR3446/7-1 and KR3446/7-2.

IV. Numerical investigation of a continuous screening process by the discrete element method

Harald Kruggel-Emden^a, Frederik Elskamp^a

^aDepartment of Energy Plant Technology, Ruhr-Universität Bochum, Bochum, Germany

This article may be downloaded for personal use only. Any other use requires prior permission of the author and AIP Publishing. The following article appeared in Kruggel-Emden H., Elskamp F., 2015, Numerical Investigation of a Continuous Screening Process by the Discrete Element Method, AIP Conference Proceedings 1648, 400004 and may be found at <https://doi.org/10.1063/1.4912624>

Abstract

Continuous screening processes are of high relevance in industrial applications in case that a bulk solid is separated based on particle sizes. Besides experimental investigations, process models or discrete element simulations can be applied for the numerical modeling of screening. In the investigation here a sensitivity analysis is performed for varying amplitudes, frequencies, stroke angles and feed rates of a continuous lab scale screening process. Thereby, a selection of representative particle shapes is considered and its influence on the throughput is analyzed.

Keywords: Continuous screening; Discrete element method; Complex shaped particles

1. Introduction

Screening is an important process in bulk solids handling and mineral processing with large industrial relevance. Screening can be used for a wide range of applications. In case of a bulk solid with a wide particle size distribution screening can be applied to separate the original particulate solid into several sub products with different particle size ranges. This is e.g. done in mineral processing when crushed material is separated into crushed rock, gravel and sand. Often screening is also used in mineral processing as a protective measure to prevent downstream equipment and machinery from handling too large sized particles resulting in possible damage. In other applications screening is used to remove dust or abrasion products from coarse grained materials. In case that a multi component bulk solid mainly differs in particle size, screening can be used to split up its components as e.g. done in grain processing and many other food related processes. Last but not least screening can be applied to separate bulk solids comprising of similarly sized but differently shaped particles. Note that in all listed applications batch or mostly continuous screening apparatuses are used depending on the amount of material to be handled.

As it is the case for many processes, optimal process parameters for screening strongly depend on the used apparatus and on the material and amount of material to be handled. Depending on the intended screening application a high selectivity, a high throughput or the

removal of oversized or undersized particles can be desired. The search for optimal process parameters usually requires extensive experimental testing. Instead of experiments screening process models such as [7,45,47] or detailed discrete element simulations [6,20,190,202] are applicable for the screening apparatus design and optimization of process parameters. In the latter approach, the discrete element method, each individual particle which may be of non-spherical shape is tracked over time. Based on this data integral quantities can be derived on the system scale required for process optimization.

In the investigation here a continuous lab scale screening process is analyzed numerically, based on the discrete element method. A sensitivity analysis is performed for varying amplitudes, frequencies, stroke angles and feed rates. Thereby, a selection of representative particle shapes is considered.

2. Numerical method

In the discrete element method the translational and rotational motion of particles of non-spherical shape is obtained by integrating Newton's and Euler's equations of each particle

$$m_i \frac{d^2 \vec{x}_i}{dt^2} = \vec{F}_i + m_i \vec{g}, \quad (139)$$

$$\hat{I}_i \frac{d\vec{W}_i}{dt} + \vec{W}_i \times (\hat{I}_i \vec{W}_i) = \Lambda_i^{-1} \vec{M}_i, \quad (140)$$

with particle mass m_i , particle acceleration $d^2 \vec{x}_i / dt^2$, contact force \vec{F}_i , gravitational force $m_i \vec{g}$, angular acceleration $d\vec{W}_i / dt$, angular velocity \vec{W}_i , external moments resulting out of contact forces \vec{M}_i , the inertia tensor along the principal axis \hat{I}_i and the rotation matrix converting a vector from the inertial into the body fixed frame Λ_i^{-1} .

A flexible approach to model complex shaped particles in the discrete element method is the multi-sphere method where arbitrary sized spheres are clustered to resemble the desired complex particle shape. In this method contact force laws as used for spherical particles are applied. The normal component of the contact forces is obtained from a linear spring damper model [92]

$$\vec{F}_{ij}^n = k^n \delta_{ij} \vec{n}_{ij} + \gamma^n \vec{v}_{ij}^n, \quad (141)$$

where subscripts i and j represent two interacting particles, k^n is the spring stiffness, δ_{ij} the virtual overlap between the two particles, \vec{n}_{ij} a normal vector, γ^n a damping coefficient and \vec{v}_{ij}^n the normal velocity in the contact point. Both k^n and γ^n determine the coefficient of normal restitution. For the calculation of the tangential forces and resulting moments a linear spring limited by the Coulomb condition is used [94]

$$\vec{F}_{ij}^t = -\min(k^t |\vec{\xi}_{ij}|, \mu_c |\vec{F}_{ij}^n|) \vec{t}_{ij}, \quad (142)$$

where k^t is the stiffness of a linear spring, μ_c is the friction coefficient, $\vec{\xi}_{ij}$ is the relative tangential displacement and \vec{t}_{ij} is the tangential unit vector.

3. Numerical setup and simulation parameters

The feed material is charge onto the continuous screen as outlined in Fig. 61a. The screen is horizontally aligned and of 0.35 m length and 0.1 m width. It is equipped with a wire screen. The aperture size is 4.9 mm and the rectangular shaped wire is of 1 mm diameter. In the base case configuration the apparatus is vibrated with 27.6 Hz with a stroke angle of 45° to the horizontal at an amplitude of 1.76 mm. The material passing the screen is captured in segments along the screen where the first four have a length of 0.035 m and the last three of 0.07 m.

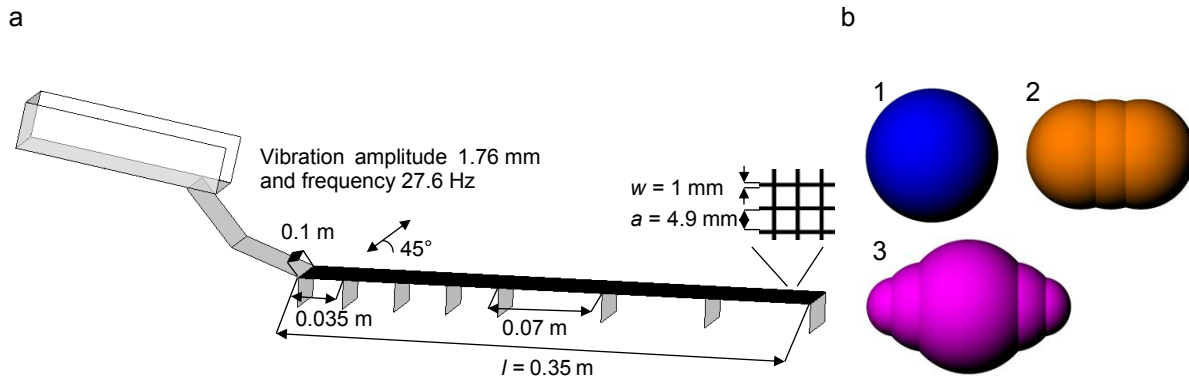


Fig. 61: (a) Continuous screening apparatus; (b) Considered particle shapes.

The particles in the feed material have a density of 2700 kg/m³ and are equally divided into three size classes made up of coarse, near mesh and fine material with average diameters of 7.35 mm, 4.2875 mm and 2.45 mm. The feed material is supplied at a mass flow rate of 0.1 kg/s for $t = 25$ s. The stiffnesses k^n and k^t , the coefficients of normal restitution between particles e_{pp}^n and particles and walls e_{pW}^n and the Coulomb friction coefficient μ_c between particles and the screen wire as well as between particles and particles are adjusted to: $k^n = 1000$ N/m, $k^t = 500$ N/m, $e_{pp}^n = 0.4$, $e_{pW}^n = 0.5$, $\mu_c = 0.5$. There is no friction between the side walls and the particles considered ($\mu_c = 0$). Besides spheres (shape No. 1), two other non-spherical shapes are investigated (Fig. 61b). Shape No. 2 is a sphere volume equivalent cylinder and shape No. 3 is referred to as double cone with the same minor axis diameter as spheres in the following.

4. Results and discussions

Results for the percentage passage over time for varying amplitudes and frequencies are shown in Fig. 62. As outlined before the feed rate is chosen with 0.1 kg/s in the base case configuration. A passage of 100% is therefore related to the passing of the entire near mesh and fine material charged during the simulation until $t = 25$ s which is calculated as $m = \frac{2}{3} \dot{m}_{feed} \cdot 25 \text{ s} \approx 1.67 \text{ kg}$. In case of an altered feed rate m obtains values differing from 1.67 kg as later investigated and shown in Fig. 63. The selected base case values for the amplitude and frequency induce the most complete passing through the screen of around 95%. Amplitudes of 0.88 mm and frequencies of 13.8 Hz lead to significantly reduced passage for all considered particle shapes; frequencies of 20.7 Hz lead to a lower passage at least for spheres. Reduced frequencies and amplitudes result in the pile up of feed material on the screen and related pegging of apertures. Elevated amplitudes of 3.52 mm reduce the passage for all shapes and amplitudes of 2.64 mm significantly reduce particle passage at least for double cones. At an elevated frequency of 41.4 Hz as for the listed enlarged amplitudes particles do get in contact with the screen surface only occasionally. This results in a strong decrease of the chance that particles can pass through the apertures. Therefore, many of the near mesh and fine particles become outside material.

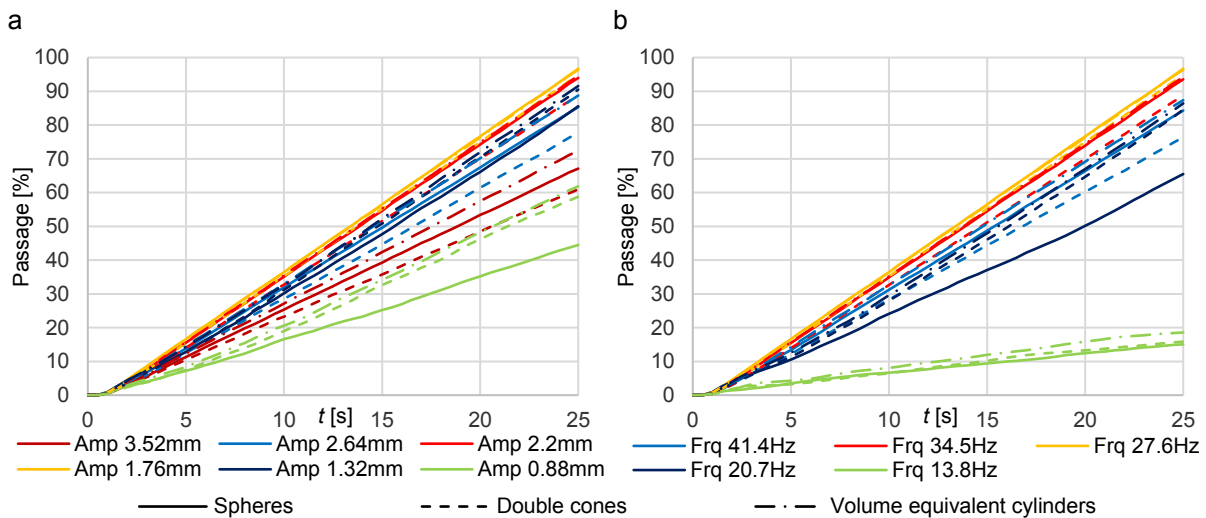


Fig. 62: Particle passage through the sieve openings for the three considered particle shapes for (a) varying amplitudes and (b) vibration frequencies.

Results for percentage passage over time for varying stroke angles to the horizontal as well as varying feed rates are shown in Fig. 63. As it is the case for the amplitude and frequency the base case stroke angle of 45° results in the best passage. The circular stroke is too slow and not effective to aerate the particle system on the screen. As a result, pile up of feed material as well as pegging results. The best percentage passage is achieved for stroke angles which guarantee for a balance between vertical and horizontal movement (45°). In case of a more vertical movement the particle transport is slowed down; a more horizontal movement leads to a significantly reduced aeration of particles on the screen (comp. Fig. 63).

A varying feed rate in the range considered in the investigation here (25 g/s – 200 g/s) has low influence on the passage rate. A larger mass leads to a stronger blocking among the particles. On the other hand, more of the small particles can be pushed through the screen apertures thereby. Therefore, overall residence times (not shown in Fig. 63) increase slightly in case of an enlarged feed rate.

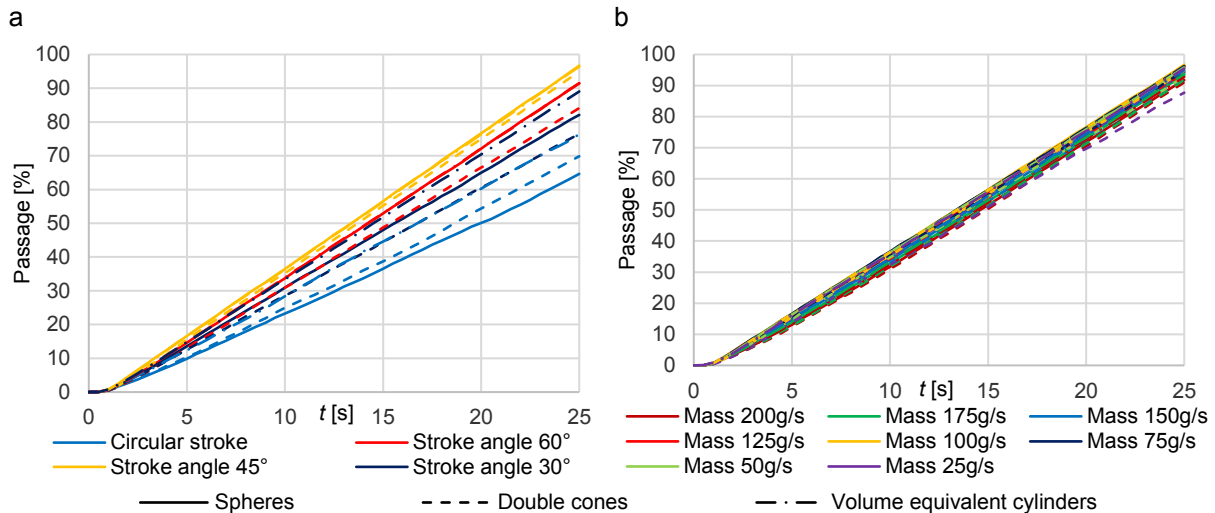


Fig. 63: Particle passage through the sieve openings for the three considered particle shapes for (a) varying stroke angles and (b) bulk mass flow rates.

5. Conclusions

Numerical discrete element simulations of a continuous screening process indicate that the passage can be enlarged by increasing the amplitude and frequency. However in case that amplitudes and frequencies are enlarged too much the contact with the screen is reduced and therefore passage is decreased again. A stroke angle of 45° is most optimal as it forms a compromise between transport and aeration of the particle packing on the screen. A variation of mass flow rates in the range of values studied here has no large influence on the percentage passage.

Acknowledgments

The authors gratefully acknowledge the support by DFG within project SPP 1679 through grant number KR3446/7-1.

V. Numerical investigation of banana screens involving non-spherical particles by the discrete element method

Frederik Elskamp^{1*}, Harald Kruggel-Emden¹, Manuel Hennig², Ulrich Teipel²

¹Department of Energy Plant Technology, Ruhr-University Bochum, Bochum, Germany

²Department of Process Engineering, Nuremberg Institute of Technology, Nuremberg, Germany

*elskamp@leat.rub.de

The 8th International Conference for Conveying and Handling of Particulate Solids, Tel-Aviv, Israel, May 2015

Abstract

In order to improve the screen capacity without compromising the screening efficiency the banana screen is increasingly employed for separation processes. By giving a detailed insight into the process of sieving, the discrete element method allows the optimization of equipment and operating parameters. In this investigation continuous banana screening processes are modeled by using detailed discrete element simulations involving complex shaped particles. First, the needed approximation accuracy of the screen surface in terms of deck divisions is tested. The results are primarily compared to non-curved screens before varying additional parameters. Different particle characteristics such as size, shape and mass flow rate are examined. In addition, screen characteristics such as the number of screen increments and the inclination angles at the discharge as well as operational parameters including vibration frequency and amplitude are considered. A comparison of the considered cases is performed based on the residence time of particles and the particle fractions retained on the screen. The comparative study will provide numerical data required for the benchmarking and extension of phenomenological screening models that are able to represent dynamic processes during screening in the future.

Keywords: Screening; Banana screen; Discrete element method; Complex shaped particles

1. Introduction

In mechanical process engineering and energy technology it is often required to separate bulk materials according to their particle sizes. In typical processes particles are often of non-spherical shape and broad size distribution. A technical simple approach for the separation of solid mixtures is screening which is widely used in industry. In order to improve the screen capacity without compromising the screening efficiency the banana screen is increasingly employed for separation processes [195]. These screens consist of one or more curved decks providing varying inclination angles and thereby differing support of particle acceleration. For

the design of screening processes particle-based simulation approaches such as the discrete element method provide a detailed insight into the process of sieving and thereby allow, after appropriate validation, the optimization of equipment and operating parameters.

So far discrete element simulations have been used by Liu et al. [196] to study the motion characteristics, penetrating mechanisms and geometric parameters on a single deck banana screen. Preceding this, a dynamic model of the screen was developed [38]. Operational conditions and geometries of multi-deck banana screens were investigated by Dong et al. [195] and Cleary et al. [6,198]. In other studies, banana screens were simulated under wet conditions by Fernandez et al. [9]. Within discrete element simulations of screening processes the limitations of shape approximations solely relying on spheres are well known [20]. Despite of this, up to now only few numerical investigations on sieving, particularly on banana screens, addressed particles of complex shape [6,198]. Therefore, in this investigation continuous banana screening processes are modeled by performing detailed discrete element simulations involving complex shaped, dry particles [236].

2. Numerical method

Besides spherical particles, the DEM can be applied to systems with non-spherical shaped particles [60,61] by obtaining the translational and rotational motion of each particle. For this purpose the Newton's and Euler's equations are integrated

$$m_i \frac{d^2 \vec{x}_i}{dt^2} = \vec{F}_i + m_i \vec{g}, \quad (143)$$

$$\hat{I}_i \frac{d\vec{W}_i}{dt} + \vec{W}_i \times (\hat{I}_i \vec{W}_i) = \Lambda_i^{-1} \vec{M}_i, \quad (144)$$

with particle mass m_i , particle acceleration $d^2 \vec{x}_i / dt^2$, contact force \vec{F}_i , gravitational force $m_i \vec{g}$, angular acceleration $d\vec{W}_i / dt$, angular velocity \vec{W}_i , external moments resulting out of contact forces \vec{M}_i , the inertia tensor along the principal axis \hat{I}_i and the rotation matrix converting a vector from the inertial into the body fixed frame Λ_i^{-1} . Both equations (eq. (143) and eq. (144)) are solved by explicit integration schemes [82].

The multi-sphere method is a flexible approach to model complex shaped particles in the DEM. Thereby, the desired complex particle shape is resembled with clustered arbitrary sized spheres [69] applying the same contact force laws as used for spherical particles [65]. Fig. 64 shows a sketch of two simple colliding complex particles i and j , where the spheres l and k got into contact. Further details on the contact scheme involving clustered spheres are provided in [90,91].

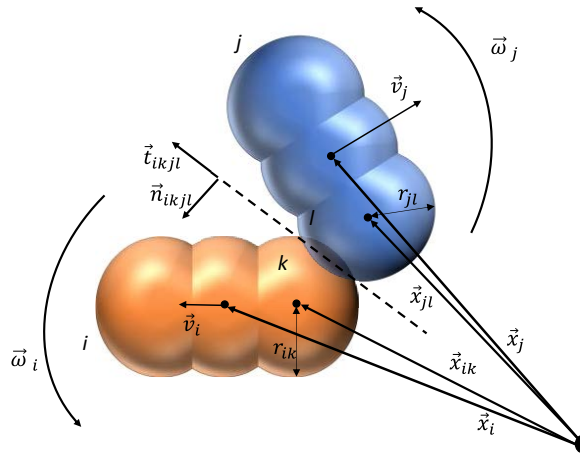


Fig. 64: A collision of two multi-sphere particles.

The normal component of the contact forces is obtained from a linear spring damper model which is exemplarily given for the contacting spheres k and l of particle i and j as

$$\vec{F}_{ikjl}^n = k^n \cdot \delta_{ikjl} \cdot \vec{n}_{ikjl} + \gamma^n \cdot \vec{v}_{ikjl}^n, \quad (145)$$

where k^n is the spring stiffness, δ_{ikjl} the virtual overlap, \vec{n}_{ikjl} a normal vector, γ^n a damping coefficient and \vec{v}_{ikjl}^n the normal velocity in the contact point. Both k^n and γ^n determine the coefficient of normal restitution between particles e_{pp}^n as well as particles and walls e_{pW}^n [92]. For the calculation of the tangential forces a linear spring limited by the Coulomb condition is applied

$$\vec{F}_{ikjl}^t = -\min(k^t \cdot |\vec{\xi}_{ikjl}|, \mu_C \cdot |\vec{F}_{ikjl}^n|) \cdot \vec{t}_{ikjl}, \quad (146)$$

where k^t is the stiffness of a linear spring, μ_C is the friction coefficient, $\vec{\xi}_{ikjl}$ is the relative tangential displacement and \vec{t}_{ikjl} is the tangential unit vector [94].

3. Numerical setup and simulation parameters

Screening of a polydisperse feed material is investigated by the DEM in continuous horizontal, inclined and banana screen apparatuses (the latter is shown in Fig. 65a). The apparatuses are equipped with a wire screen whose floor area is always of approx. 0.35 m x 0.1 m; their respective projection lengths l and projection floor areas however differ. The inclination angle at the inlet (19° if not otherwise stated), and at the discharge at the end of the screen (0° if not otherwise stated) determine among other parameters the banana screen shape (comp. Fig. 65). A change of height of about 0.0588 m is experienced by the granular material when passing along the screen.

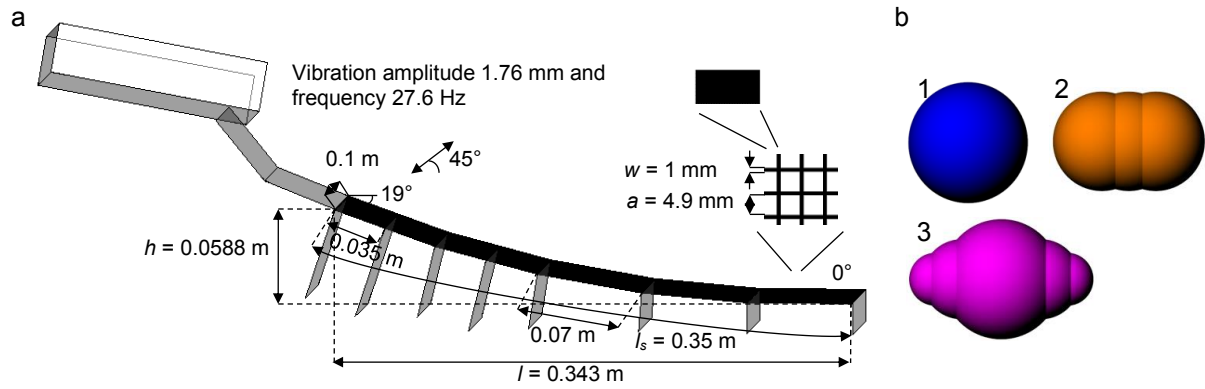


Fig. 65: (a) Continuous banana screening apparatus with wire structure and collection bins whose separating side walls are oriented normal to the screen surface; (b) Considered particle shapes.

The screen position as a function of the horizontal position is given as

$$h(l) = 0.0588 - 0.5 \cdot l^2. \quad (147)$$

The projected length l of the horizontal screen exactly matches the screen length l_s of 0.35 m by definition. Two inclined screens with 9.5° and 19° are investigated for comparison with the banana screen. The screen with an inclination of 9.5° was chosen to have the average between the inlet and outlet inclination of the banana screen as constant inclination. The screen with an inclination of 19° has the same constant inclination as the banana screen has initially at the inlet.

The aperture size a is chosen with 4.9 mm and the wire diameter w is set to 1 mm. In initial configuration, the apparatuses are vibrated with 27.6 Hz with a stroke angle of 45° to the horizontal at an amplitude of 1.76 mm (comp. Fig. 65). The screen wire is approximated by triangular surface elements forming a rectangular profile in the simulations. Note that in case of a continuously changing inclination every small division of a longitudinal wire is approximated with one set of triangular surface elements resulting in many wall elements and thus huge computational effort. By dividing the screen into several divisions with constant inclinations the amount of wall elements is reduced and thereby the computational cost declines. As a consequence, the change of height over screen length h and the projection of the screen length l are varying to a minor extent.

The polydisperse feed material comprises of particles with a density of 2700 kg/m^3 subdivided into 3 size classes consisting of coarse, near mesh size particles and fine material represented by particles with average diameters of 7.35 mm ($1.5a$), 4.2875 mm ($0.875a$) and 2.45 mm ($0.5a$) in case of spheres, respectively. The initial mass flow amounts to 0.1 kg/s, divided equally into the examined particle classes. The applied DEM parameters are adjusted according to the work by Delaney et al. [20] and Cleary [199] applicable for standard industrial quarry rock, where the tangential spring constant is $k^t = 0.5 \cdot k^n$. Accordingly, the stiffnesses k^n and k^t are set to $k^n = 1000 \text{ N/m}$ and $k^t = 500 \text{ N/m}$, resulting in average particle overlaps

of around 0.5% of the particle diameter, which leads to accurate simulation outcomes independent of the spring stiffness. The coefficients of normal restitution between particles e_{PP}^n and particles and walls e_{PW}^n and the Coulomb friction coefficient μ_C between particles and the screen wire as well as between particles and particles are adjusted to: $e_{PP}^n = 0.4$, $e_{PW}^n = 0.5$, $\mu_C = 0.5$. Besides spheres, cylinders and double cones are studied in this investigation (comp. Fig. 65b). The non-spherical particles (shapes (2) and (3)) have an aspect ratio of 1.55. The cylindrical particles (shape (2)) are volume equivalent to the spherical particles and have a hemispherical termination at both ends. The double cones (shape (3)) have the same minor axis as the spheres. This gives the double cones the same long-term separation characteristics in a batch screening analysis. However, their separation rates over screen length differ.

The following variations (comp. Table 10) are considered in the investigation here addressing the particle shapes shown in Fig. 65b.

Table 10: Initial setup and performed variations of the continuous screening investigations.

| Parameter | Initial | Var. 1 | Var. 2 | Var. 3 |
|--|---------|------------|---------------|--------------|
| Number of deck divisions [-] | 5 | 3 | continuous | - |
| Screen type [-] | banana | horizontal | inclined 9.5° | inclined 19° |
| Amplitude [mm] | 1.76 | 1.32 | 2.2 | - |
| Frequency [Hz] | 27.6 | 20.7 | 41.4 | - |
| Particle mass flow [kg/s] | 0.1 | 0.05 | 0.15 | - |
| Inclination angle at the discharge [°] | 0 | 5 | 10 | - |

First of all, different approximations of the banana screen surface starting with 3 deck divisions and low computational costs up to a continuously changing inclination along the screen (after each aperture) with long calculation times are investigated. The screen with the lowest computational effort and under 5 % deviation of the total screening efficiency for all shapes and different frequencies is used as base case for the further investigations (5 deck divisions). Next, the banana screen is compared to a horizontally aligned and two differently inclined screens (9.5° and 19°). Afterwards, starting from this initial banana screen setup, variations of the vibration amplitude and frequency as well as particle mass flow are performed varying one of the parameters at a time. Finally, the inclination angle at the discharge of the banana screen is varied from 0° to 10°. The inclination angles of the other four deck divisions are increased accordingly giving an inclination angle at the inlet of 24° and 29°, respectively. Note that in this case the particles are experiencing a larger change of height when passing along the screen.

4. Results and discussions

In all performed investigations, the feed consists of one of the particle shapes outlined in Fig. 65b. For each particle shape the influence of the parameter modifications outlined in

Table 10 is examined, where only one parameter is varied at a time. Particles are continuously fed on the vibrated screen well mixed for $t = 25$ s. Due to the motion of the screen and its inclination, particles are transported along the screen. The finest particles nearly instantly pass the apertures after getting in contact with the screen surface. Larger undersize particles need more attempts to pass and hence travel along the screen for some distance before being able to pass the screen apertures. All oversize and some undersize particles are discharged at the end of the screen.

To achieve a better comparability for the analysis of the overall particle passage investigated in the following, the passed mass is summed up and normalized for all particle classes with diameters smaller than the apertures. Thereby, the fraction retained over screen length is calculated with

$$Y = Y(l_s) = 1 - ((\dot{m}_0 - \dot{m})/\dot{m}_0), \quad (148)$$

where \dot{m}_0 is the initial undersize mass flow at $l_s = 0$ and \dot{m} is the remaining mass flow of the undersize material at the screen position l_s which can be visually accessed in Figs. 66a,b - Figs. 68a,b. Additionally, the average residence times of the three investigated particle shapes are presented in Figs. 66c,d - Figs. 68c,d.

Note that in case of only three different particle classes with the diameter of the near mesh size particles being small enough, only temporal pegging of apertures with spherical particles occurs. Therefore, spheres have the obviously best passage rates in all investigated cases followed by volume equivalent cylinders and double cones. In contrast, the residence times of volume equivalent cylinders are in average slightly shorter than for spheres mainly caused by coarse spheres remaining longer in the flat part of the banana screen due to temporal pegging.

In the first investigation (Figs. 66a,c) the needed accuracy for the banana screen approximation is tested. The overall fraction retained over screen length is well aligned for all particle shapes, besides that the passage rates are increasing for an increasing number of deck divisions used. Note that major differences in the fraction retained are apparent particularly for the approximation with 3 divisions at the beginning of the third panel. Especially for non-spherical particles, a sudden decrease in the fraction retained occurs due to many particles passing the apertures at the beginning of the flat part of the screen at $l_s \approx 0.25$ m hindering themselves. As a consequence, the average residence time incline compared to cases with a larger number of divisions independent of shape. Besides some deviances at the end of the screen in case of double cones and slightly different residence times, the 5 division approximation obtains fairly accurate results, which allows using it as base case configuration for further banana screen investigations.

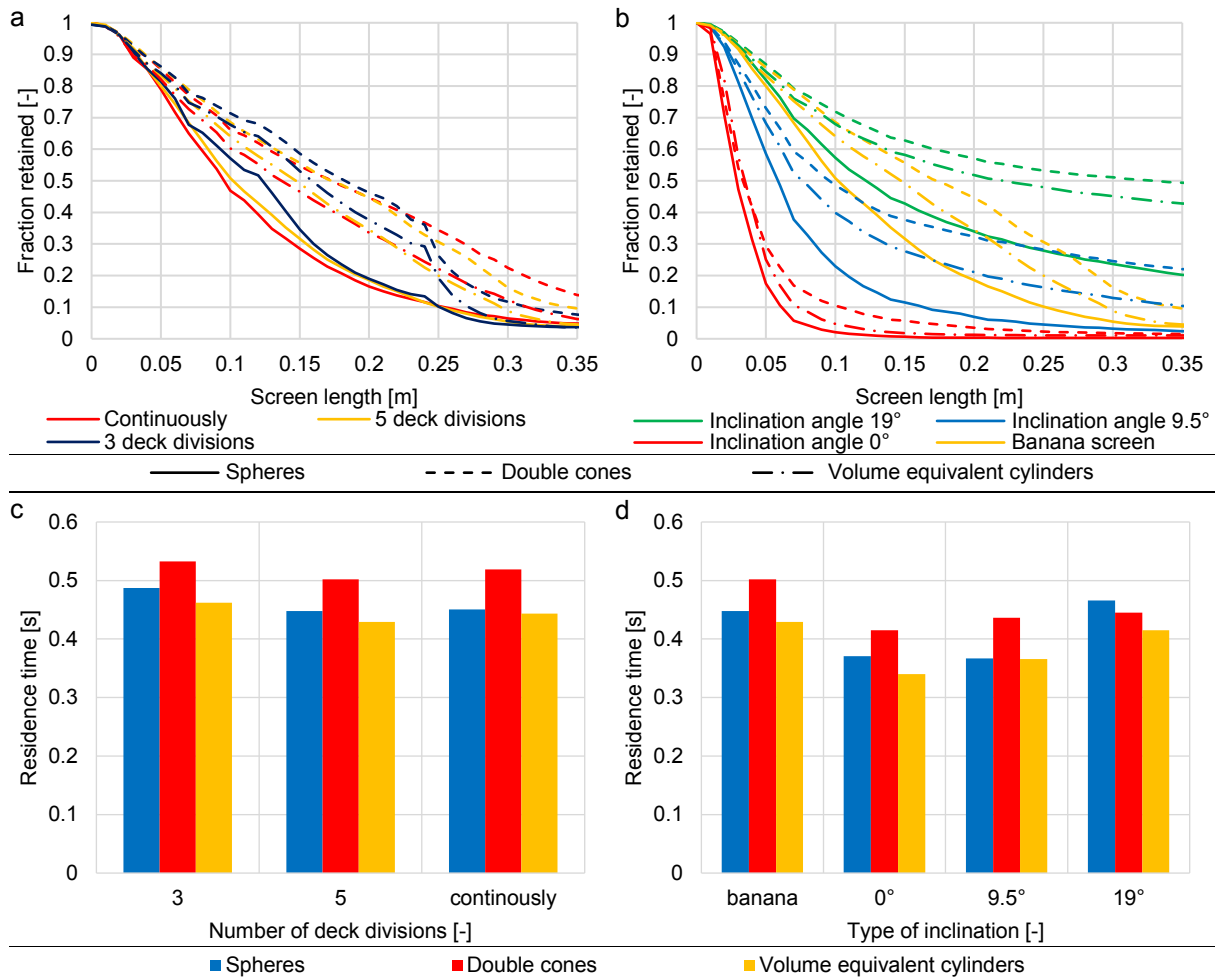


Fig. 66: Particle passage through the screen openings for the three considered particle shapes over screen length for varying banana screen deck approximations (a) and types of inclinations (b) as well as corresponding particle residence times for the considered particle shapes on the screen for varying banana screen deck approximations (c) and types of inclinations (d).

In the second investigation (Figs. 66b,d) the banana screen is compared to a horizontal and two inclined screens. As already described, the inclination of 19° to the horizontal is chosen to represent the largest inclination encountered with the banana screen and the other with 9.5° represents the average inclination of the banana screen. In contrast to all inclined cases, the particle shape influences the passage rates only to a minor extent on the horizontal screen. The fraction retained over screen length is directly decreasing due to the passage of most of the undersize particles in the first part of the screen giving the shortest overall residence times of all screen types. The coarse material however, resides longest on the screen. At the end of the screen, nearly all of the undersize material is classified in the underflow. In these investigations, with only temporary pegging, a horizontal screen reveals the best passage rates. Nevertheless, horizontal screens exhibit the highest risk of intensive pegging of very near mesh size particles, which can be attributed to the long residence times of the coarse material on the screen. In combination with other particle size distributions, a larger mass flow or less particle agitation this leads to damming of particles and therefore declining passage rates and longer residence times. To prevent this, inclined screens are used in real world

applications and the study here. Inclined screens result in a delayed particle passage, longer overall residence times but in shorter residence times of oversize particles. Applying a screen with an inclination of 9.5° additionally leads to a certain amount of undersize non-spherical particles in the overflow. For spheres, the fraction retained at the end of the screen and the overall residence times are very alike for both 0° and 9.5° inclination. An inclination of 19° to the horizontal forces many undersize particles into the overflow and additionally results in longer residence times for all shapes. The banana screen has the same low particle passage at the beginning of the screen but it is increasing with decreasing inclination angle resulting in more than 90% undersize double cones and over 95% cylinders and spheres classified in the underflow. The overall residence time is comparatively long due to the strongly decreased passage rate in the first part of the screen. In conclusion, the risk of pegging is reduced but the right particle classification is still effective.

In the third study (Figs. 67a,c) the initial amplitude of 1.76 mm is varied according to Table 10. A reduction leads to a quicker particle passage for all shapes, due to a slower transport velocity along the screen and therefore shorter throws and more particle sieve contacts. In case of an amplitude of 1.32 mm coarse particles pile up on the flat parts of the banana screen slowing down the undersize material. In this context, a further decrease of the amplitude would cause an intensive damming of particles, thereby preventing particles from getting in contact with the screen apertures and thus lowering passage. Increasing the amplitude generally results in a delayed passage as the transport velocity is increased and the ability for particles to pass the screen apertures decreases. Although the overall transport velocity is larger and the residence time for oversize particles is shorter, the overall residence time is not decreasing but increasing for larger amplitudes due to a lower passage probability of undersize particles needing more time on the screen to pass the apertures.

In the fourth study (Figs. 67b,d) the initial frequency of 27.6 Hz is varied according to Table 10. The obtained curves for the fraction retained on the screen are very alike to those for the change of amplitude, besides more pronounced effects in both directions. However, the obtained residence times reveal differences. An increase in frequency leads to an enlarged residence time for spheres due to a declining passage probability of near mesh size material. Note that also the non-spherical particles are affected, but to a lower extent. With a reduction in frequency, spheres and volume equivalent cylinders remain longer on the screen, because of a longer residence time of the coarse and comparatively not much shorter residence time of the undersize material. In contrast in case of double cones, the improvement due to the reduced particle passage of near mesh size particles prevails giving an overall shorter residence time.

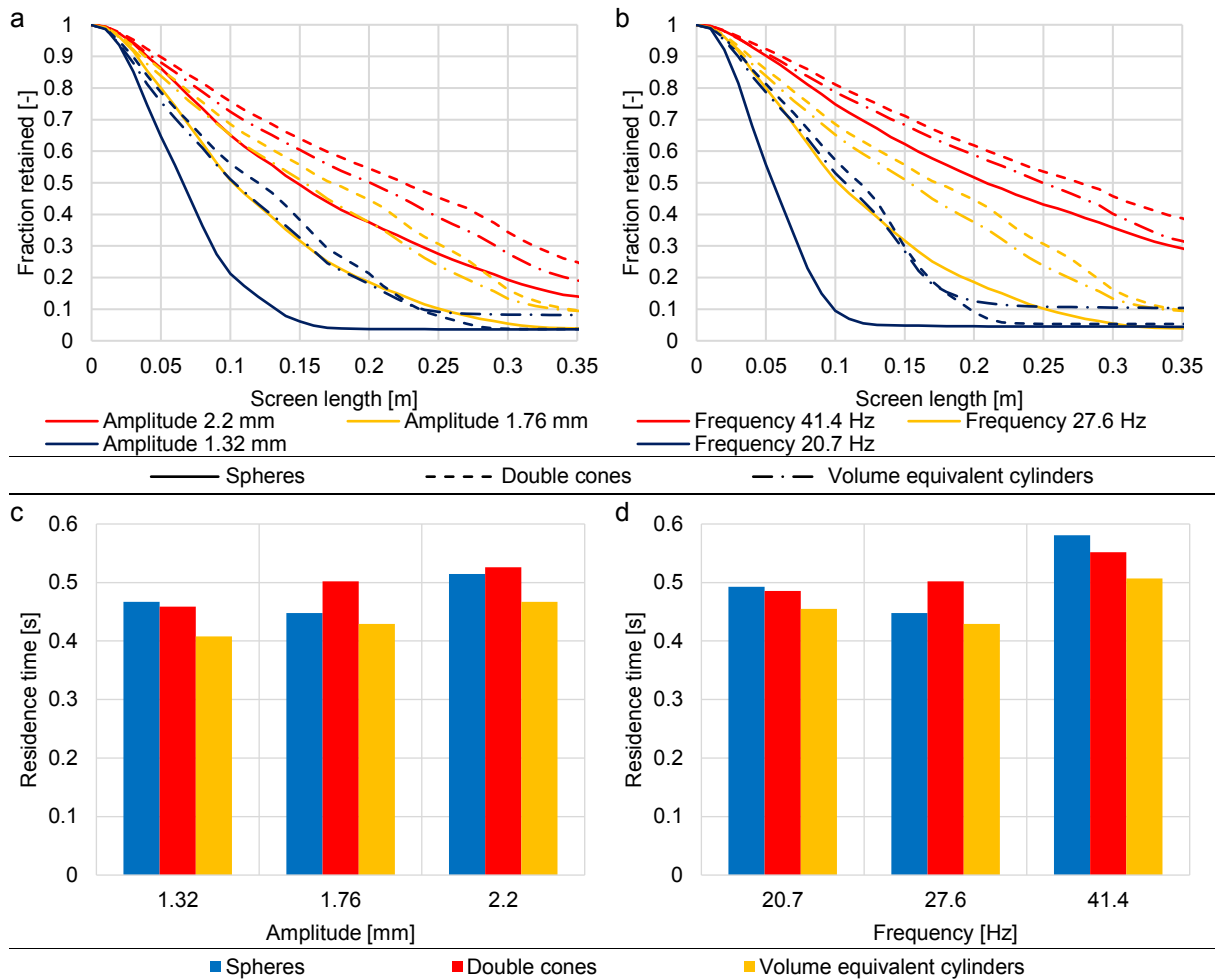


Fig. 67: Particle passage through the screen openings for the three considered particle shapes over screen length for varying amplitudes (a) and frequencies (b) as well as corresponding particle residence times for the considered particle shapes on the screen for varying amplitudes (c) and frequencies (d).

The fifth investigation (Figs. 68a,c) addresses a variation of particle mass flow (comp. Table 10). An increased mass flow results in an accelerated particle passage and thereby shorter residence times, whereas a lower mass flow leads to the opposite for all shapes. Particles are slowed down by the presence of other particles giving more particles sieve contact and allowing for a faster particle passage. This underlines the ability of banana screens to cope with enlarged flow rates.

In the last investigation (Figs. 68b,d) the inclination angle of the screen at the discharge position is increased from 0° to 10° according to Table 10 resulting in an increase of the inclination angle of the same value for all deck divisions. This measure can prevent damming of particles in the area of the discharge zone, but leads to an overall enhanced transport velocity. Therefore, the fraction retained over screen length is decreasing slower and much of the undersize material which is not slowed down by other coarse particles gets into the overflow. As a result, only in case of spheres, a discharge angle of 5° leads to results of less than 10 % wrongly classified undersize material in the overflow. The residence times in case of spheres and volume equivalent cylinders are only slightly enlarged by adjusting the

inclination angle and in case of double cones even shorter for a larger inclination angle. The shorter residence time of oversize particles caused by the larger transport velocity equals out the enhanced passage of undersize particles occurring later.

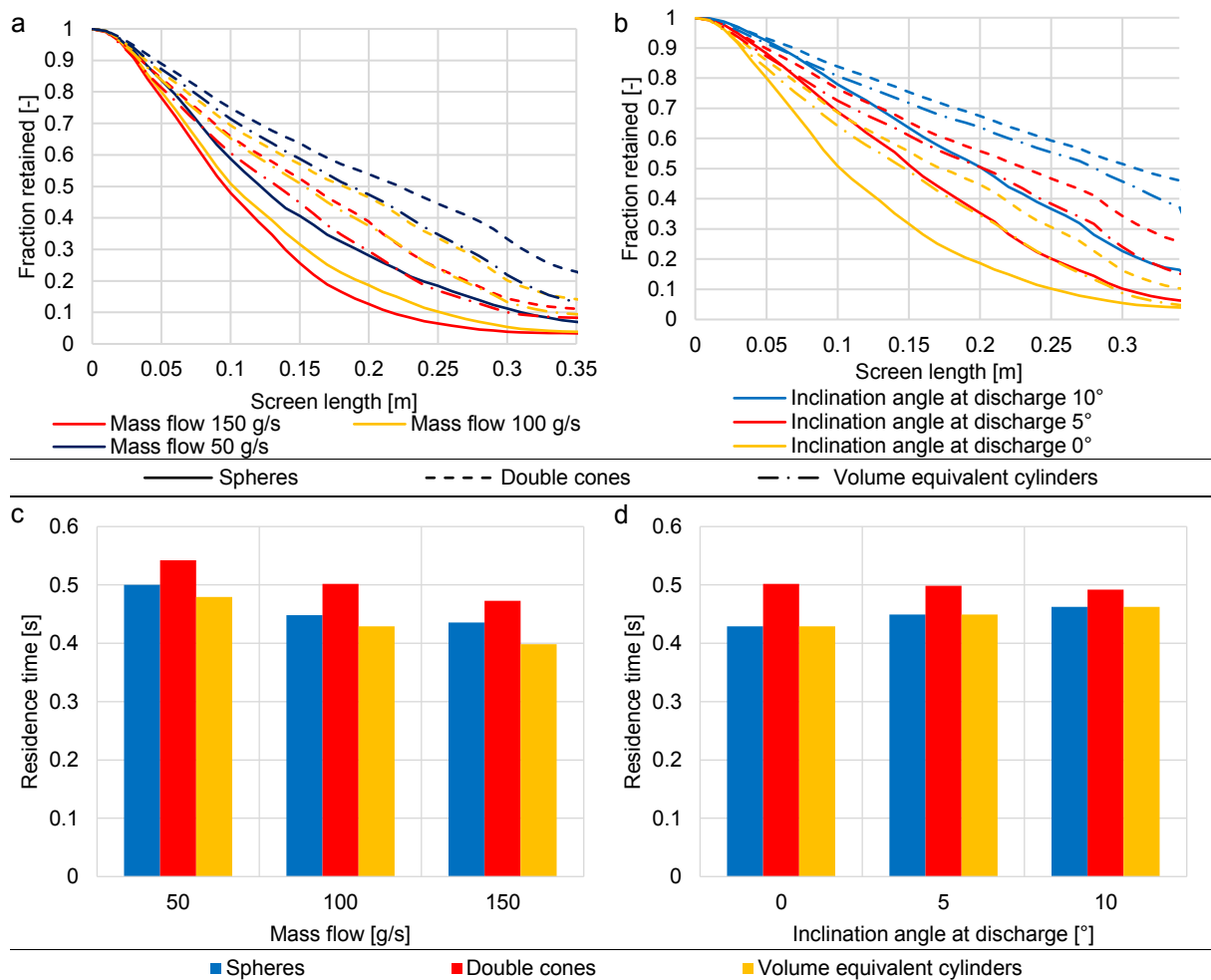


Fig. 68: Particle passage through the screen openings for the three considered particle shapes over the screen length for varying mass flows (a) and inclination angles of the discharge end (b) as well as corresponding particle residence times for the considered particle shapes on the screen for varying mass flows (c) and inclination angles at the discharge at the screen end (d).

5. Conclusions

The discrete element method (DEM) has been used to compare different banana screen approximations with a horizontal as well as two inclined screens. Thereby, the influence of varying particle characteristics such as size (coarse, near mesh and fine particles) and shape (spheres, double cones and volume equivalent cylinders) as well as the mass flow were studied. Additionally, screening parameters such as the inclination angle at discharge as well as operational parameters including vibration frequency and amplitude were varied.

Results obtained by the DEM clearly unveil that the screening rate is higher for spherical than for non-spherical particles, due to lower pegging tendencies of the material. An approximation with 5 deck divisions is fairly enough to represent a banana screen with a continuously changing inclination. Such an approximation is characterized by a delayed particle passage than a horizontal screen, but is less vulnerable to damming of particles. A larger amplitude or

frequency leads to an increased transport velocity and therefore lower passage rates, whereas a reduced amplitude or frequency results in earlier passage but with the tendency of intensive blocking. The investigations with different mass flows reveal obviously that banana screens are capable of handling larger flow rates. An increase of the screen inclination angle at discharge can prevent damming at the end of the screen. In the investigations here, the risk of pegging is low and therefore, increasing the screen inclination angle at discharge only results in decreased passage rates.

In upcoming studies, a benchmarking of phenomenological screening models based on the obtained data as in [241] for batch screening will be performed, in order to extend phenomenological models to represent dynamic processes during screening in the future.

Acknowledgement

The authors gratefully acknowledge the support by DFG within project SPP 1679 through grant number KR3446/7-1.

VI. Discrete element investigation of process models for batch screening under altered operational conditions

Frederik Elskamp^{1*}, Harald Kruggel-Emden¹, Manuel Hennig², Ulrich Teipel²

¹Department of Energy Plant Technology, Ruhr-University Bochum, Universitätsstraße 150, D-44780 Bochum, Germany

²Department of Particle Technology, Technical University Nürnberg, Wassertorstrasse 10, D-90489 Nuremberg, Germany

*Corresponding author. E-mail address: elskamp@leat.ruhr-uni-bochum.de

The following accepted manuscript appeared as journal version in Elskamp F., Kruggel-Emden H., Hennig M., Teipel U., 2016, Discrete element investigation of process models for batch screening under altered operational conditions, Powder Technology 301, 78-95 and may be found at <https://doi.org/10.1016/j.powtec.2016.05.039>.

Abstract

For the design and improvement of operational parameters of screening processes the particle-based discrete element method (DEM), as well as phenomenological screening models are available. Due to their simplicity and low calculation costs, the latter can be applied efficiently for industrial applications. So far, both DEM and phenomenological screening models were only used to provide information about screening processes with constant operational parameters neglecting transient changes. To overcome this, in the investigation here, DEM simulations applying spherical and non-spherical particles are used to benchmark process models extended for batch screening under altered operational conditions. For this purpose, different particle characteristics such as size, shape and size distribution are taken into account in the DEM simulations. Operational parameters including vibration frequency, amplitude and stroke angle are permanently changed after a specific time. Based on the data obtained from the simulations, the overall fraction retained on the screen over time is analyzed and compared to DEM results of screening under constant operational conditions. Predictions of phenomenological screening process models, which were adjusted to the outcome of DEM simulations under constant operational conditions in terms of the fraction retained on the screen over time, are taken to predict the outcome of batch screening simulations under unsteady operational conditions. The resulting deviations to simulations with a change in operational parameters are evaluated, thereby allowing the comparative benchmarking of process models for screening in transient operation. Obtained DEM results of batch screening indicate a strong dependence on operational parameters and particle shape. Process models vary intensively in their ability to represent DEM results of screening in unsteady operation.

Keywords: Unsteady operation; Screening; Discrete element method (DEM); Arbitrary shaped particles; Process models

1. Introduction

In mechanical process engineering, materials preparation and energy technology, the process step screening is important for the separation of bulk materials. By screening, particles, which are often of non-spherical shape and broad size distribution [2,3] are classified according to desired size class specifications. Although being used extensively in industry, scientifically screening and its sub-processes are not completely understood, complicating the design, improvement and scale-up of screening processes. Screening gains further complexity, if operational changes are applied through interval mode in batch screening as well as by variations in frequency or stroke direction on an elliptically vibrating screen to intensify the process or when bulk solids properties change. Alternatively, such dynamic changes may result from upstream process steps and might influence subsequent downstream processes. Until now, a satisfying transient description of screening is not gained, but would be of great significance to industry [207], particularly to prevent operational disruption of processes in the worst case.

In order to learn more about transient operation of particulate processes without performing extensive experimental tests, developing a robust and efficient dynamic process simulation framework is an important, state-of-the-art task [208]. Therein, the realization of a dynamic screening model for batch screening constitutes a first step, due to greater simplicity. In a second step, through the acquired knowledge, this framework could be extended for continuous screening under transient operational conditions, to meet the requirements of industrial applications.

With the help of carefully validated particle-based simulation approaches like the discrete element method (DEM) dating back to Cundall and Strack [10] and Walton and Braun [59] open aspects associated with screening can be addressed without performing extensive experiments. DEM simulations are predictive, transient and provide detailed insights into screening processes, whereby dynamic sub-processes such as particle transport, stratification and passage can be studied conveniently even though operational parameters transiently change.

Screening as one of the central process operations in mechanical process engineering has been studied broadly under steady state operational conditions in scientific literature. One of the first reported experimental studies of screening was carried out by Gaudin already in 1939 [24], whereas the first small scaled batch screening investigations applying the DEM were performed at the beginning of this century [46]. In order to analyze phenomena particularly relevant for screening, further studies by Li et al. addressed the influence of the particle layer thickness [189] and of near mesh size and oversize particles [50] on screening efficiency. The influence of the sieve wire structure on screening behavior was addressed by Alkhaldi et al.

[191], Tung et al. [188] and Kruggel-Emden and Elskamp [236]. In the works by Zhao et al. [192], Dong et al. [35], Xiao and Tong [237,238] and Ma et al. [243] various stroke orientations, amplitudes and inclination angles were considered for different screens to analyze the induced particle excitation.

In screening process simulations, it is important to model complex shaped particles by appropriate non-spherical shapes due to the large influence of shape on stratification and passage, particularly for near mesh size particles, as well as on particle transport [20]. Nevertheless, complex shaped particles are considered in only a few numerical investigations of screening processes [6,198,236,241,243,244].

In order to optimize operating parameters and screen designs by the DEM [35,50,189,192,236–238], the particle based DEM approach was validated against experimental data [34] and proved successful and reliable [236]. The DEM also provides the ability to derivate and verify simpler and less computational demanding phenomenological screening process models without performing extensive experiments, which was firstly utilized by Shimosaka et al. [46]. Note that all DEM screening investigations referred to so far, have in common that operational parameters are not altered during the screening process.

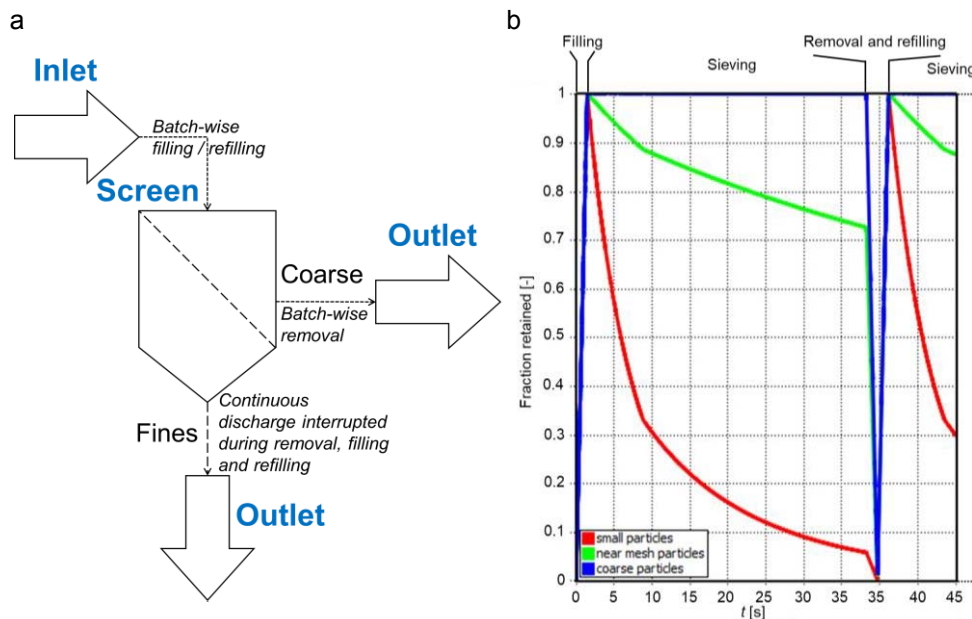


Fig. 69: (a) Exemplary flowsheet of batch screening and (b) progression of the fractions retained on a batch screen as calculated in Dyssol for a material consisting out of three size classes.

In a former publication by the authors [241], batch screening processes were investigated in detail and a benchmarking of applicable phenomenological screening process models was performed. In the present study, batch screening under varying operational conditions involving spherical and non-spherical particle shapes is addressed. Phenomena such as the particle passage and the fractional residual mass over time are investigated in detail. These investigations form the basis to use DEM simulations reliably for a comparative study of selected phenomenological screening process models [241] extended for the representation

of discontinuous screening under altered operational conditions. Combined with other process models, suitable batch screening models will be made available in the context of a modeling framework for the dynamic flowsheet simulation of solids processes (Dyssol) in the near future [245].

In order to illustrate the process step addressed in the investigation here, a flowsheet outlining batch screening is shown in Fig. 69. Therein, the semi-continuous outlet flow only consists of fine particles, whereas the coarse particles accumulate on the screen until they are removed as a bulk and new material is refilled batch-wise to continue the screening process.

The article is divided into five sections. Section 2 is the description of the discrete element method (DEM) used as numerical approach and its validation. In section 3 the analysis of accessible integral quantities such as the fraction retained in transient operation and the outline of considered screening process models are presented. Section 4 addresses the numerical setup for the DEM and the applied simulation parameters. Results of the particle passage behavior for discontinuous screening under altered operational conditions and attempts to represent the respective summed fraction retained based on the outcome of DEM batch screening simulations with constant operational parameters are discussed in section 5.1. Afterwards, a comparison is made between the passage over time for the DEM results of batch screening under altered operational conditions to the outcome of various extended phenomenological screening process models in part 5.2. Finally, conclusions are drawn in section 6.

2. Numerical method and validation

In this section the discrete element method and the applied force laws are described briefly. A validation of the used DEM code is conducted by a comparison of results obtained from batch screening experiments and simulations, respectively.

2.1 The discrete element method

Besides spherical particles, the DEM can be applied to systems with non-spherical shaped particles [60,61], by tracking the translational and rotational motion of each particle. For this purpose the Newton's and Euler's equations are integrated

$$m_i \frac{d^2 \vec{x}_i}{dt^2} = \vec{F}_i + m_i \vec{g}, \quad (149)$$

$$\hat{I}_i \frac{d\vec{W}_i}{dt} + \vec{W}_i \times (\hat{I}_i \vec{W}_i) = \Lambda_i^{-1} \vec{M}_i, \quad (150)$$

with particle mass m_i , particle acceleration $d^2\vec{x}_i/dt^2$, contact force \vec{F}_i , gravitational force $m_i\vec{g}$, angular acceleration $d\vec{W}_i/dt$, angular velocity \vec{W}_i , external moments resulting out of contact forces \vec{M}_i , the inertia tensor along the principal axis \hat{I}_i and the rotation matrix converting a vector from the inertial into the body fixed frame Λ_i^{-1} . Explicit integration schemes (comp. e.g. [82]) are used to solve both equations (eq. (149) and eq. (150)).

A flexible approach to model complex shaped particles in the DEM is the multi-sphere method. Thereby, spheres of arbitrary size are clustered to resemble the desired complex particle shape [69] and similar contact force laws as used for spherical particles are applied [65].

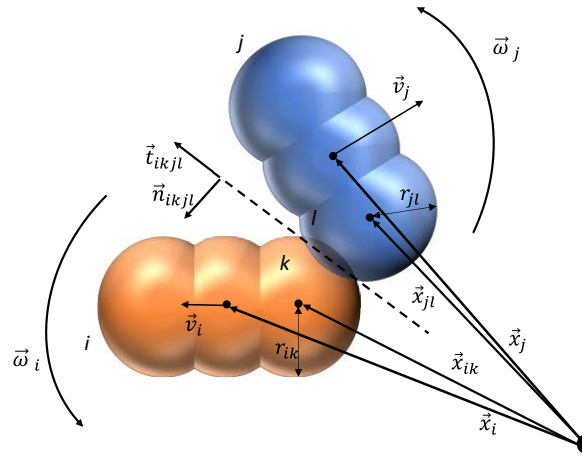


Fig. 70: A collision of two multi-sphere particles.

In Fig. 70 a sketch of two complex shaped particles i and j is shown, where the spheres l and k collide. For further details on the contact scheme involving clustered spheres the works by Kruggel-Emden and Kačianauskas and Kruggel-Emden et al. [90,91] are recommended.

The normal component of the contact forces is obtained from a linear spring damper model which is exemplarily given for the contacting spheres k and l of particle i and j as

$$\vec{F}_{ikjl}^n = k^n \cdot \delta_{ikjl} \cdot \vec{n}_{ikjl} + \gamma^n \cdot \vec{v}_{ikjl}^n, \quad (151)$$

where k^n is the spring stiffness, δ_{ikjl} the virtual overlap, \vec{n}_{ikjl} a normal vector, γ^n a damping coefficient and \vec{v}_{ikjl}^n the normal velocity at the contact point. The coefficient of normal restitution between particles e_{pp}^n as well as between particles and walls e_{pw}^n are determined by k^n and γ^n [92]. The tangential forces are calculated by applying a linear spring limited by the Coulomb condition

$$\vec{F}_{ikjl}^t = -\min(k^t \cdot |\vec{\xi}_{ikjl}|, \mu_c \cdot |\vec{F}_{ikjl}^n|) \cdot \vec{t}_{ikjl}, \quad (152)$$

where k^t is the stiffness of a linear spring, μ_c is the friction coefficient, $\vec{\xi}_{ikjl}$ is the relative tangential displacement and \vec{t}_{ikjl} is the tangential unit vector [94].

2.2 Validation of the used DEM code

In order to validate the applied DEM code, batch screening of well mixed spheres (POM) with three different size classes was carried out experimentally and compared to the undersize fraction retained obtained from DEM simulations in Fig. 71 with the following parameters applied (comp. Table 11).

Table 11: Applied DEM and process parameter.

| Screen parameter | Value | Particle parameter | Value | Vibration parameter | Value | DEM parameter | Value |
|-------------------------|---------------|------------------------------|--------------------------|------------------------------------|--------------|------------------------------------|--------|
| Floor area [m] | 0.185 x 0.185 | Particle diameter [mm] | 10 / 7 / 5 ± 0.1 | Amplitude [mm] | 1.2± 0.01 | Normal stiffness PP / PW [N/m] | 100000 |
| Aperture size [mm] | 8± 0.02 | Density [kg/m ³] | 1377 / 1369 / 1429 | Frequency [Hz] | 50 / 60 | Tangential stiffness PP / PW [N/m] | 88888 |
| Wire Diameter [mm] | 1.5± 0.01 | Mass of particles [kg] | 1 | Stroke angle to the horizontal [°] | ~90 | Restitution coefficient PP [-] | 0.85 |
| Screen wire profile [-] | rectangular | | | | | Restitution coefficient PW [-] | 0.89 |
| | | | | | | Friction PP [-] | 0.39 |
| | | | | | | Friction PW [-] | 0.51 |

*PP: particle – particle contact
PW: particle – wall contact

Therein, the vibration parameters are obtained by an accelerometer which measures an amplitude of around 1.2 ± 0.04 mm in z-direction and only minor amplitudes in the horizontal (x- / y-stroke < 0.1mm). A transient period of the screen motion before $t = 0.61$ s is also measured and applied to the simulation as well as the removal of the retaining plate below the apertures ($t = 0.1 \pm 0.02$ s). The DEM parameters are first obtained by the determination of single particle characteristics [157,160]. These values are used as initial values to adjust respective simulations to small scale experiments [130,158] which leads to the DEM parameters in Table 11.

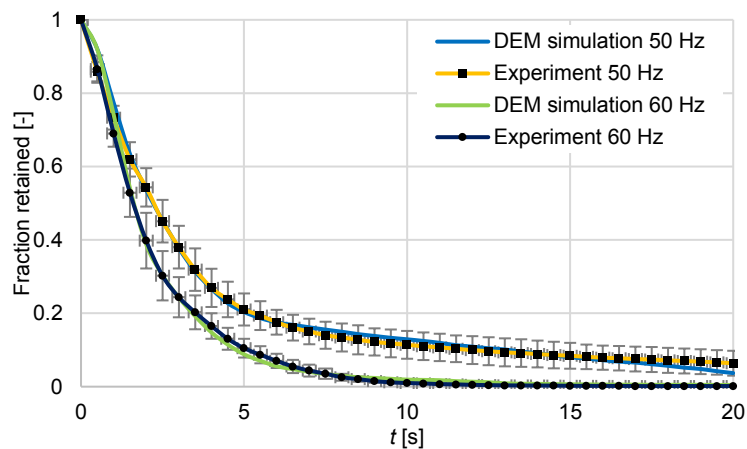


Fig. 71: Fraction retained on the screen over time applying spheres for two different frequencies obtained by experimental investigations (both graphs are averaged over 10 experiments) and DEM simulations, respectively.

Investigations are performed for two different frequencies and the results (Fig. 71) averaged over a sufficient number of experiments (standard deviation represented by the vertical error bars) reveal a good agreement with only a few deviations between simulations and

experiments in both cases. The mean and maximum deviations are for 50 Hz 0.0164 and 0.0572, respectively and for 60 Hz 0.0083 and 0.0534, respectively.

Slight offsets can only be recognized for the frequency of 60 Hz at the beginning of the screening process and around $t = 5$ s and for the frequency of 50 Hz between $t = 7$ s and $t = 13$ s and after $t = 17$ s. The discrepancy at the beginning is mainly due to the response time of the balance which is up to 0.2 s (represented by the horizontal error bars), whereas deviations due to repeatability (standard deviation < 0.01) and eccentricity (± 0.015 g) of the balance are negligible. Additionally, deviations between experiments and simulations can occur due to inaccuracies in the production of the screen mesh and the POM particles (comp. Table 11). The main reason for the scattering of the measured experimental values is the minor difference in the mixture of the feed material. Furthermore, the time of removing the retaining plate below the apertures ($t = 0.1 \pm 0.02$ s) and the amplitude of the screen can differ slightly (comp. Table 11). In conclusion, the used DEM code is applicable to represent batch screening processes.

3. Methods to model batch screening under altered operational conditions

In a former study by the authors [241], batch screening under steady operational parameters was examined in detail. Starting from an initial simulation, several parameter variations were performed. Afterwards, a comparative study of existing phenomenological screening process models on representing the simulation outcome was carried out based on the mass retained on the screen over time.

In the investigation here, the same setup and initial operational parameters are used as in the previous study, but operational parameters are not kept constant but altered during the simulation process one at a time. In this context the question arises if it is possible to represent operational changes based on integral quantities such as the fraction retained available for operation under steady operational parameters or from process models adjusted for latter processes. It will be investigated to which extent it is possible to predict the mass retained on the screen in unsteady operation without performing new DEM simulations just from the outcome of simulations and screening process models applied under steady operational conditions [241]. Different methods are proposed to use DEM data obtained under constant operational parameters in the first sub-section and thereafter for process models in the next subsection. Note that results not only apply to DEM simulations, but also to possible experimental investigations, from which the mass retained on the screen over time is known for different constant operational parameters. However, the DEM is beneficial in the determination of the actual mass and particle distribution.

The overall undersize fraction retained, which is a time dependent variable during batch screening, is used here similar to the investigation with constant operational parameters [241] to assess screening results. It is given as

$$Y = Y(t) = m/m_0, \quad (153)$$

where m_0 is the initial undersize mass at $t = 0$ and m is the remaining mass of the undersize material at time t .

If the undersize particles are considered as different fractions, the fraction retained is stated per particle size class i

$$Y_i = Y_i(t) = m_i/m_{i,0}, \quad (154)$$

where $m_{i,0}$ is the initial and m_i is the actual fractional undersize mass. It is related to the overall fraction retained by $Y = \sum_{i=1}^n (Y_i \cdot m_{i,0}/m_0)$, where n is the number of undersize particle classes.

Various approaches to predict/model screening under altered operational parameters are introduced in the following.

3.1 DEM results used to predict screening under altered operational conditions

The first method to represent screening under altered operational conditions is to use existing DEM results of screening under constant operational conditions available for the fraction retained over time $Y(t)$ for the set of initial and the altered operational parameters, where various approaches are conceivable. Note that only instant changes of one operational parameter are considered in the following. However, the approach is also applicable to changes of multiple parameters like in interval operation of a batch screening apparatus as long as the operational change is applied instantaneously. The change of operational parameters is introduced at $t = t_c$, where the initial are changed to the altered operational parameters. A sketch of $Y(t)$ obtained for such a situation is shown in Fig. 72. As yellow line, the fraction retained $Y_{init}(t)$ is shown if the initial operational parameters are maintained throughout the whole simulation from $t = 0$ up to $t = t_{end}$. In contrast, if the altered operational parameters are applied from $t = 0$ up to $t = t_{end}$, $Y_{alt}(t)$ follows the blue line. Both curves represent operations with constant parameters. If a change of one operational parameter is applied at $t = t_c$ from the initial parameters to the altered parameters, $Y_{init \rightarrow alt}(t)$ follows the yellow line up to $t = t_c$ and then the green line afterwards up to $t = t_{end}$. $Y_{init}(t)$, $Y_{alt}(t)$ and $Y_{init \rightarrow alt}(t)$ given as yellow, blue and green lines are obtained by DEM simulations.

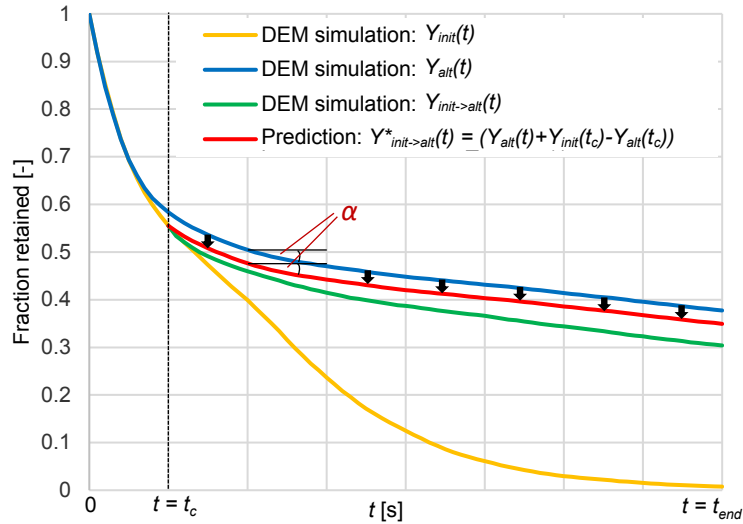


Fig. 72: Fraction retained Y as a function of time. Operational parameters are instantaneously altered at $t = t_c$. Initial operational parameters applied for $t = 0..t_{end}$ ($Y_{init}(t)$ - yellow line), altered operational parameters applied for $t = 0..t_{end}$ ($Y_{alt}(t)$ - blue line), altered operational parameters applied after $t = t_c$ ($Y_{init \rightarrow alt}(t)$ - green line) and prediction of $Y(t)$ after $t = t_c$ according to eq. (155) ($Y_{init \rightarrow alt}^*(t)$ - red line).

When $Y(t)$ needs to be evaluated for screening investigations involving operational changes (Fig. 72 - green line) the question comes up, if this is possible solely based on results obtained with steady operational parameters (Fig. 72 - yellow and blue lines). Such an approach would strongly reduce the required number of DEM or corresponding experimental investigations. Different approaches are applicable how to use $Y(t)$ obtained from steady state.

The first approach shown in Fig. 72 by the red line is based on the assumption, that the influence of the past of a batch screening process can be neglected for the proceeding screening process in terms of $Y(t)$. Following this idea, the material on the screen at $t = t_c$ with the mass $m = m_c$ is only influenced by the screening operation parameters applied after $t = t_c$. Therefore, the change in fraction retained in the simulation under altered operational conditions is equal to the change in fraction retained in the corresponding simulation under steady operational conditions in the same time period (equal inclination α of the fraction retained in Fig. 72). That implies the following equations for the predicted fraction retained

$$Y_{init \rightarrow alt}^*(t) = Y_{init}(t) \text{ for } t \leq t_c, \quad (155)$$

$$Y_{init \rightarrow alt}^*(t) = Y_{alt}(t) + Y_{init}(t_c) - Y_{alt}(t_c) \text{ for } t > t_c,$$

where the difference between the fraction retained Y_{init} for the initial operational parameters and the fraction retained for the altered parameters Y_{alt} at the time $t = t_c$ is added to the fraction retained of the latter (Y_{alt}) at each point in time for $t > t_c$. From Fig. 72 it can be seen that the proposed approach leads to deviations between the result obtained from DEM simulations (green line) and the predicted value for $1 - Y_{init \rightarrow alt}^*$ (red line). If the fraction retained should be stated per particle size class i , the equation reads accordingly

$$Y_{init \rightarrow alt, i}^*(t) = Y_{init, i}(t) \text{ for } t \leq t_c, \quad (156)$$

$$Y_{init \rightarrow alt,i}^*(t) = Y_{alt,i}(t) + Y_{init,i}(t_c) - Y_{alt,i}(t_c) \text{ for } t > t_c,$$

$$Y = \sum_{i=1}^n (Y_i \cdot m_{i,0}/m_0),$$

where $m_{i,0}$ is the initial fractional mass, m_0 is the initial undersize mass and n is the number of undersize particle classes. For the following approach the fraction retained per particle size class i is calculated in a similar way and is therefore not stated again.

In the second approach (Fig. 73) the past of the screening process is taken into account by using the progression of the fraction retained for the altered parameters from the time instance $t = t_s$ when the same amount of particles as in the initial case is found on the screen. Following this approach, the decline in fraction retained from this point of intersection at $t = t_s$ (blue line) is equal to the decline in fraction retained at $t = t_c$ (red line) if the operational parameters are changed (inclination α of the fraction retained in Fig. 73). This leads to

$$Y_{init \rightarrow alt}^*(t) = Y_{init}(t) \text{ for } t \leq t_c, \tag{157}$$

$$Y_{init \rightarrow alt}^*(t) = Y_{alt}(t_s + t - t_c) \text{ for } t > t_c,$$

and allows to calculate the new fraction retained after t_c based on the remaining particles at $t = t_c$ and on the new operational parameters applied. Exemplarily given results indicate a good match by the corresponding curves (red and green lines) as can be seen in Fig. 73.

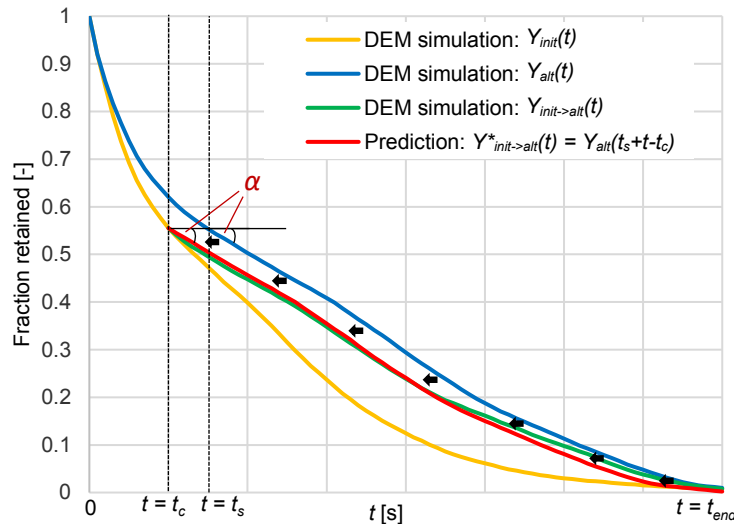


Fig. 73: Fraction retained Y as a function of time. Operational parameters are instantaneously altered at $t = t_c$. Initial operational parameters applied for $t = 0..t_{end}$ ($Y_{init}(t)$ - yellow line), altered operational parameters applied for $t = 0..t_{end}$ ($Y_{alt}(t)$ - blue line), altered operational parameters applied after $t = t_c$ ($Y_{init \rightarrow alt}(t)$ - green line) and prediction of $Y(t)$ after $t = t_c$ according to eq. (157) ($Y_{init \rightarrow alt}^*(t)$ - red line).

3.2 Extended models for screening under altered operational conditions

Phenomenological screening process models aim for representing the particle size separation during a screening process, which is done time-resolved in batch screening.

Investigated phenomenological screening models are divided into kinetic [45,226] and probabilistic theoretical models [225,228]. These phenomenological screening models are

directly applicable to discontinuous screening [45] or they can be applied for discontinuous screening by replacing length l by time t in the model equations [225]. This characteristic was exploited for the benchmark of the models investigated in Elskamp and Kruggel-Emden [241] and is utilized in the investigation here.

The basis for kinetic models is the first order kinetics. Models are restricted to shallow particle beds on screens [50,241]. In contrast, probabilistic approaches require a larger number of parameters [47] as e.g. the probability of undersize particles to pass an aperture e.g. by Gaudin [24]. By using probabilistic models, the mechanical agitation, screen size and characteristics (e.g. aperture shape) as well as the particle composition and shape (e.g. particle elongation) can be considered [49,52,225,228]. Some phenomenological screening models take concurrent subprocesses into account by providing additional parameters like the stratification and the particle passage [7,8].

Note that a discontinuous screening process is transient by definition, due to a continuous loss of bulk mass. Additionally, operational parameters can be altered during the process to intensify the screening process like in interval operation of batch screens, which is currently not represented in screening process models. In the following, possibilities to apply selected models for screening under altered operational conditions are analyzed.

Table 12 gives an overview of all investigated screening process models titled by the author's names and a model number, including the major equations extended for screening under altered operational conditions as well as the used model parameters. A more detailed description of all investigated models for screening under constant operational parameters can be found in Elskamp and Kruggel-Emden [241] or in the respective publications.

The "first-order rate law" [45,47,225] referred to as model No. 1 is the basis for most screening process models, particularly for the kinetic ones, given as

$$dm/dt = -km. \quad (158)$$

It describes the change of mass of undersize particles on the screen m as a function of the time t . Here, the adjustable parameter k is the screening rate constant. From eq. (158) the derivation of the explicit equation for the fraction retained leads to

$$Y(t) = \frac{m}{m_0} = \exp(-k(t - t_0)), \quad (159)$$

if $m(t_0) = m_0$. With $t_0 = 0$, eq. (159) becomes

$$Y(t) = \exp(-kt). \quad (160)$$

To model a change in operational parameters at $t = t_c$, eq. (158) would be valid up to t_c with $k = k_{init}$. For $t > t_c$ the screening is governed by the screening rate constant $k = k_{alt}$ leading to the set of equations

$$Y(t) = \exp(-k_{init}t) \text{ for } t \leq t_c, \quad (161)$$

$$Y(t) = \exp(-k_{init}t_c + k_{alt}t_c - k_{alt}t) \text{ for } t > t_c.$$

A similar approach can be used for all investigated kinetic models (Nos. 1-3).

Table 12: Governing equations of the studied phenomenological screening process models.

| Model number and origin | Major equations | Adjustable parameters |
|---|--|--|
| 1. Standish and others [45,47,225] | $Y = \exp(-k_{init}t) \text{ for } t \leq t_c$ $Y = \exp(-k_{alt}t - k_{init}t_c + k_{alt}t_c) \text{ for } t > t_c$ | k_{init}, k_{alt} |
| 2. Andreev et al. [226] | $Y = \exp(-k_{init}t^{n_{init}}) \text{ for } t \leq t_c$ $Y = \exp(-k_{alt}t^{n_{alt}} - k_{init}t_c^{n_{init}} + k_{alt}t_c^{n_{alt}}) \text{ for } t > t_c$ | $k_{init}, k_{alt}, n_{init}, n_{alt}$ |
| 3. Standish [45] | $Y = \sum_{i=1}^n \left((\exp(-Ak_{i,init}t)) \cdot m_{i,0}/m_0 \right) \text{ for } t \leq t_c$ $Y = \sum_{i=1}^n \left((\exp(-Ak_{i,alt}t + Ak_{i,alt}t_c - Ak_{i,init}t_c)) \cdot m_{i,0}/m_0 \right) \text{ for } t > t_c$ <i>A: screen area; n: number of undersize fractions</i> $Y_i = (1 - P_i)^{N_i(t)}$ $P_i = \left(((a+w) \cdot \cos \varphi - w - d_i) \cdot (a - d_i) \right) / ((a+w)^2 \cdot \cos \varphi)$ <i>w: wire diameter; φ: screen inclination angle</i> $N_i(t) = \begin{cases} K_{1,init}(t) \cdot (d_i/a) \\ \text{for } (d_i/a) < K_{2,init}(t) / (K_{1,init}(t) + K_{2,init}(t)) \\ K_{2,init}(t) \cdot (1 - d_i/a) \\ \text{for } (d_i/a) > K_{2,init}(t) / (K_{1,init}(t) + K_{2,init}(t)) \end{cases} \text{ for } t \leq t_c$ $K_{1,init}(t) = c_{1,init} \cdot t^{\tau_{1,init}}$ $K_{2,init}(t) = c_{2,init} \cdot t^{\tau_{2,init}}$ | $k_{1,init}, \dots, k_{n,init}$ $k_{1,alt}, \dots, k_{n,alt}$ $c_{1,init}, c_{2,init}, \tau_{1,init}, \tau_{2,init}$ $c_{1,alt}, c_{2,alt}, \tau_{1,alt}, \tau_{2,alt}$ |
| 4. Subasinghe et al. [228] | $Y_{j+1} = Y_j - k_{j,init}B_j(t_{j+1} - t_j) \text{ for } t \leq t_c$ $Y_{j+1} = Y_j - k_{j,alt}B_j(t_{j+1} - t_j) \text{ for } t > t_c$ $B_{j+1} = B_j + (c_{j,init}(1 - S_j) - k_{j,init}B_j)(t_{j+1} - t_j) \text{ for } t \leq t_c$ $B_{j+1} = B_j + (c_{j,alt}(1 - S_j) - k_{j,alt}B_j)(t_{j+1} - t_j) \text{ for } t > t_c$ <i>j: time index</i> $k_{j,init} = b_{init}Y_j; c_{j,init} = f(w_{q,init}, w_{d,init})$ $k_{j,alt} = b_{alt}Y_j; c_{j,alt} = f(w_{q,alt}, w_{d,alt})$ <i>B: fractional mass of undersize particles in bottom layer</i> <i>S: fractional mass of undersize particles stratified into bottom layer</i> | $W_{q,init}, W_{q,alt}$ (dependent on proportion of undersize material) $W_{d,init}, W_{d,alt}$ (dependent on width of particle size distribution) b_{init}, b_{alt} (dependent on particle size) |
| 5. Soldering; not resolving undersize fractions [7] | $Y_{i,j+1} = Y_{i,j} - k_{i,j,init}B_{i,j}(t_{j+1} - t_j); i \text{ particle class; } j \text{ time index}$ $B_{i,j+1} = B_{i,j} + (c_{i,j,init}(S_{i,\infty} - S_{i,j}) - k_{i,j,init}B_{i,j})(t_{j+1} - t_j) \text{ for } t \leq t_c$ | $W_{q,init}, W_{q,alt}$ (dependent on proportion of undersize material) |
| 6. Soldering; resolving undersize fractions [8] | $Y_{i,j+1} = Y_{i,j} - k_{i,j,alt}B_{i,j}(t_{j+1} - t_j); i \text{ particle class; } j \text{ time index}$ $B_{i,j+1} = B_{i,j} + (c_{i,j,alt}(S_{i,\infty} - S_{i,j}) - k_{i,j,alt}B_{i,j})(t_{j+1} - t_j) \text{ for } t > t_c$ $Y_j = \sum_{i=1}^n Y_{i,j}; B_j = \sum_{i=1}^n B_{i,j}; n: \text{ number of undersize particle classes}$ $k_{i,j,init} = b_{i,init}Y_{i,j}; c_{i,j,init} = f(w_{q,init}, c_{d,i})$ $k_{i,j,alt} = b_{i,alt}Y_{i,j}; c_{i,j,alt} = f(w_{q,alt}, c_{d,i})$ <i>B_i: fractional mass of undersize particles in bottom layer</i> <i>S_i: fractional mass of undersize particles stratified into bottom layer</i> | $b_{1,init}, \dots, b_{n,init}$ $b_{1,alt}, \dots, b_{n,alt}$ (dependent on particle diameter and aperture size) |

In a former publication [241], the applicability of the probabilistic model by Subasinghe et al. [228] to batch screening under constant operational parameters by replacing length l by time t

was shown. This model takes the different undersize particle fractions into account by using one set of adjustable parameters. For batch screening where a load change is applied at $t = t_c$, the fraction retained can be still obtained as

$$Y_i = (1 - P_i)^{N_i(t)}, \quad (162)$$

where the passage probability P_i , which is not affected by the motion of the screen, reads

$$P_i = \left(\frac{((a + w) \cdot \cos \varphi - w - d_i) \cdot (a - d_i)}{((a + w)^2 \cdot \cos \varphi)} \right), \quad (163)$$

with the wire diameter w , the respective particle diameter d_i , the aperture size a and the inclination angle of the screen surface to the horizontal φ . For batch screens without inclination ($\varphi = 0^\circ$), eq. (163) can be simplified to

$$P_i = (a - d_i)^2 / (a + w)^2. \quad (164)$$

In contrast, the number of attempts for the respective particles to pass the apertures N_i is dependent on the motion of the screen. Therefore, it has to be calculated differently before and after $t = t_c$. Due to applying initial conditions up to t_c , the number of attempts N_i before $t = t_c$ are calculated as in Subasinghe et al. [228]

$$N_i(t) = \begin{cases} K_{1,init}(t) \cdot (d_i/a) \\ \text{for } (d/a) < K_{2,init}(t)/(K_{1,init}(t) + K_{2,init}(t)) \\ K_{2,init}(t) \cdot (1 - d_i/a) \\ \text{for } (d/a) > K_{2,init}(t)/(K_{1,init}(t) + K_{2,init}(t)) \end{cases} \quad \text{for } t \leq t_c, \quad (165)$$

with $K_{1,init}(t) = c_{1,init} \cdot t^{\tau_{1,init}}$ and $K_{2,init}(t) = c_{2,init} \cdot t^{\tau_{2,init}}$ where $c_{1,init}$, $\tau_{1,init}$, $c_{2,init}$ and $\tau_{2,init}$ are adjustable parameters. The change of operational parameters leads to the following equation for N_i after t_c

$$N_i(t) = \begin{cases} N_i(t_c) + K_{1,alt}(t) \cdot (d_i/a) \\ \text{for } (d_i/a) < K_{2,alt}(t)/(K_{1,alt}(t) + K_{2,alt}(t)) \\ N_i(t_c) + K_{2,alt}(t) \cdot (1 - d_i/a) \\ \text{for } (d_i/a) > K_{2,alt}(t)/(K_{1,alt}(t) + K_{2,alt}(t)) \end{cases} \quad \text{for } t > t_c, \quad (166)$$

with $K_{1,alt}(t) = c_{1,alt} \cdot (t - t_c)^{\tau_{1,alt}}$ and $K_{2,alt}(t) = c_{2,alt} \cdot (t - t_c)^{\tau_{2,alt}}$ where $c_{1,alt}$, $\tau_{1,alt}$, $c_{2,alt}$ and $\tau_{2,alt}$. The number of attempts $N_i(t_c)$ in eq. (166) is calculated with eq. (165) and then added to the number of attempts after $t = t_c$. Four model parameters have to be provided for the timespan before t_c and additional four for $t > t_c$. The model is referred to as model No. 4 in the following.

In contrast to the models discussed so far, the screening models by Soldinger [7,8] provide sets of equations with detailed information on the screening process such as stratification or passage which are discretized in time.

In the first model by Solding [7], which is here referred to as model No. 5, all undersize particles, which have to stratify to the bottom of the screen before passing the apertures, are regarded as one lumped particle class. Besides the stratification and the passage, Solding [7] introduced the bottom layer of fine material, which contains all undersize particles above the screen surface that are either in direct contact with the screen surface or those stratifying to the surface without coarse particles in their way. Through the mass stream of undersize particles stratifying into the bottom layer \dot{S} and the mass stream of undersize particles passing the apertures \dot{R} and thus leaving the bottom layer, the fractional mass B of undersize particles is changing over time which is described by

$$\dot{B} = \dot{S} - \dot{R} = \frac{B_{j+1} - B_j}{t_{j+1} - t_j} = \frac{S_{j+1} - S_j}{t_{j+1} - t_j} - \frac{Y_j - Y_{j+1}}{t_{j+1} - t_j}, \quad (167)$$

where $\Delta t = t_{j+1} - t_j$ is a fixed, discrete time step (comp. Fig. 74a).

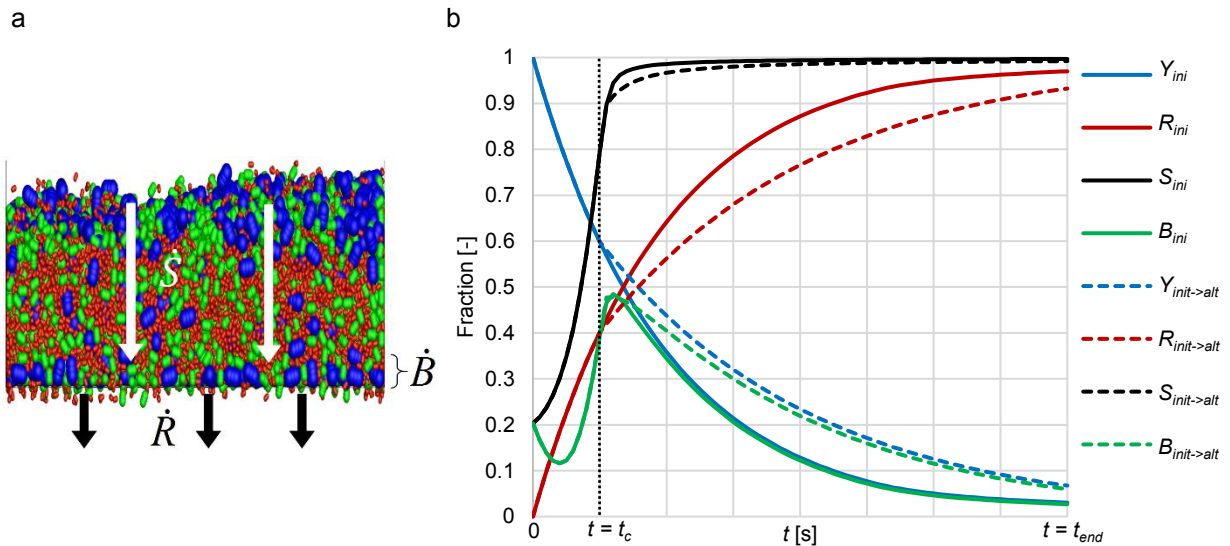


Fig. 74: (a) Model by Solding [7] with S : share of fine particles passed and fine particles in the bottom layer (stratified particles), R : share of fine particles passed, B : share of fine particles in the bottom layer and (b) exemplary progression of these values and the fraction retained $Y = 1 - R$ over time for batch screening with initial operational parameters applied for $t = 0..t_{end}$ (solid lines) and a variation of operational parameters at $t = t_c$ (dashed lines).

The fractional mass stream of stratified particles \dot{S} can be calculated as

$$\dot{S} = (S_{j+1} - S_j)/(t_{j+1} - t_j) = c_j(1 - S_j), \quad (168)$$

where $(1 - S_j)$ represents the unstratified material, which remains above the bottom layer, thus in the top layer. The rate of stratification is determined by the time dependent parameter $c_j = c_{q,j} \cdot c_{d,j}$, where $c_{q,j}$ and $c_{d,j}$ are both dependent on the proportion of undersize material gathered above the bottom layer q_j which is determined by

$$q_j = (Q_0 \cdot (Y_j - B_j)) / (1 - Q_0(1 - Y_j + B_j)), \quad (169)$$

with Q_0 as ratio of the undersize and the total applied particle mass M_0 . The parameter $c_{q,j}$ is calculated by $c_{q,j} = w_q \exp(-(2q_j)^5)$ where w_q is an adjustable parameter, which takes the influence of the proportion of undersize material as well as its shape into account. $c_{d,j}$ is calculated as $c_{d,j} = w_d q_j$ with the adjustable parameter w_d dependent on the width of the particle size distribution.

The rate of passage of undersize material \dot{R} is dependent on the fractional mass in the bottom layer and is calculated as

$$\dot{R} = (Y_j - Y_{j+1}) / (t_{j+1} - t_j) = k_j B_j \quad (170)$$

with $k_j = b Y_j$ determining the rate of passage, where b is an adjustable parameter influenced by the average size of the undersize particles on the screen.

If the initial values $S_0 = B_0$ and $Y_0 = 1$ for $j = 0$ are provided at $t = 0$, the fractional mass of undersize particles in the bottom layer can be calculated as a combination of eq. (167), eq. (168) and eq. (170) as

$$B_{j+1} = B_j + (c_j(1 - S_j) - k_j B_j)(t_{j+1} - t_j). \quad (171)$$

If the whole screen surface is covered with undersize particles, the rate of passage k_j obtains a maximum value. Therefore, \dot{R} is limited by $B_p = B_{mP} / m_0$ where B_{mP} is the mass of the bottom layer in this case. If $B_j > B_p$, $k_j B_j$ is replaced by $k_j B_p$ in eq. (170) and eq. (171), reducing the amount of particles that leaves the bottom layer due to passage.

Due to calculating each new time step based on properties (Y , S , B) from the previous one, the model by Soldinger [7] can be used easily to represent batch screening under altered operational conditions. At $t = t_c$, only the adjustable parameters need to be updated according to the new operational parameters. The change of the governing properties (Y , S , B) is exemplarily shown for model No. 5 in Fig. 74b for an operation without any operational change (solid lines) and for an operation with the initiation of a load change at $t = t_c$ (dashed lines).

If the initial operating parameters are applied for $t = 0 \dots t_{end}$ the undersize particles are passing the apertures at a high rate at the beginning of the simulation whereas this rate dR/dt is decreasing throughout the simulation (red solid line). Inversely to R the fraction retained Y is decreasing accordingly (blue solid line). At $t = 0$, approximately one fifth of the undersize material is present in the bottom layer, resulting in $S_0 = B_0 = 0.2029$. The stratification S is quickly progressing which leaves only few material unstratified ($1 - S \ll 0.1$) already at $t = t_c$ (black line). The material in the bottom layer is increasing to a maximum roughly at $t = t_c$ (green solid line), because of the limitation in the rate of passage. This amount at $t \approx t_c$ is then decreasing with no further material being added to the bottom layer due to further stratification.

The change in operational parameters applied at $t = t_c$ outlined in Fig. 74b is the result of an instantaneous reduction of agitation e.g. of frequency or amplitude. Clearly, the passing of undersize material is slowed down (red and blue dashed lines). This is accompanied by a reduction in stratification (black dashed curve) and a slower reduction of solid mass in the bottom layer (green dashed line). As can be seen in Fig. 74b the behavior of the integral parameters on a screen is qualitatively correctly modeled for by the model of Soldinger [7] even if an operational change is applied. Note that a detailed analysis of the accuracy gained, is given later when results are compared to detailed DEM simulations.

To further improve its model [7], Soldinger later considered the different undersize particle fractions separately, instead of regarding them as one lumped fraction [8], here referred to as model No. 6. Besides this refinement, the governing equations remained similar to those from model No. 5. Thereby, the ability to apply it to transient operational conditions is maintained. The stratified fractional mass stream of undersize particles of class i reads analogously to eq. (168)

$$\dot{S}_i = (S_{i,j+1} - S_{i,j}) / (t_{j+1} - t_j) = c_{i,j}(S_{i,\infty} - S_{i,j}), \quad (172)$$

with $S_{i,\infty} = m_{i,0}/m_0$ as total proportion of undersize material in each fraction. The fractional and summed up passage rate and the amount of material in the bottom layer are obtained by

$$\dot{R}_i = (Y_{i,j} - Y_{i,j+1}) / (t_{j+1} - t_j) = k_{i,j}B_{i,j}, \quad \dot{R} = \sum_{i=1}^n \dot{R}_i, \quad (173)$$

and

$$B_{i,j+1} = B_{i,j} + (c_{i,j}(S_{i,\infty} - S_{i,j}) - k_{i,j}B_{i,j})(t_{j+1} - t_j), \quad \dot{B} = \sum_{i=1}^n \dot{B}_i, \quad (174)$$

respectively. Again $B_{i,j}$ is limited by $B_p = B_{mP}/m_0$, but here $k_{i,j}B_{i,j}$ is replaced by $B_p \cdot k_{i,j} \cdot B_{i,j}/B_j$ when $B_j > B_p$. In the investigation here, the passage parameter $k_{i,j} = b_i (S_{i,\infty} - (1 - Y_{i,j}))$ is set dependent on the passage with the adjustable parameter b_i as suggested in the previous model [7]. In contrast to model No. 5, the stratification parameter $c_{i,j}$ additionally takes the bed thickness into account leading to

$$c_{i,j} = (c_{q,j} \cdot c_{d,i}) / (H_{t,j}/d_{av,c}), \quad (175)$$

with the average diameter of the coarse particles $d_{av,c}$. Therein, $c_{q,j}$ is calculated according to model No. 5 with the adjustable parameter w_q and the proportion of fine material in the top layer which is now obtained by

$$q_j = \left(m_0 \cdot \sum_{i=1}^n (S_{i,\infty} - S_{i,j}) \right) / \left(M_0(1 - Q_0) + m_0 \cdot \sum_{i=1}^n (S_{i,\infty} - S_{i,j}) \right). \quad (176)$$

In contrast to model No. 5, $c_{d,i} = \exp(-2.5 \cdot V_{i,part}/V_{av,t,j})$ is now dependent on the volume of the respective particle $V_{i,part}$ and the average volume of particles in the top layer $V_{av,t,j}$ which is changing over time, instead of being dependent on an adjustable parameter.

The thickness of the top layer in eq. (175) $H_{t,j}$ is calculated as

$$H_{t,j} = M_{t,j}/(W^2 \cdot \rho), \quad (177)$$

where $M_{t,j}$ is the mass of material in the top layer, W is the length and width of a quadratic screen and ρ is the bulk density which is assumed constant.

Note that parameters for the models Nos. 1-6 need to be adjusted to experimental data or data from detailed simulations with predictive capabilities like the DEM. For screening investigations performed with operational changes the question arises if model parameters necessarily need to be adjusted individually to the time periods $t = 0 \dots t_c$ and $t = t_c \dots t_{end}$ where operational parameters are altered at $t = t_c$. As an alternative, screening investigations can be considered which are performed under constant operational parameters without applying load changes; such an approach would significantly simplify the model adjustment. To which extent such an approach is applicable should be of investigation here.

4. Numerical setup and simulation parameters

To address the applicability of screening process models under altered operational conditions and to clarify the issue of screening model parameter adjustment, screening of a polydisperse feed material is investigated by the DEM in a discontinuously operated screen apparatus (Fig. 75a). The apparatus is equipped with a wire screen on a floor area of 0.2 m x 0.2 m. The aperture size a is 4.9 mm and the wire diameter w is 1 mm. In the initial configuration, the screen is vibrated sinusoidal with 27.6 Hz with a stroke angle of 90° to the horizontal at an amplitude of 3.52 mm (Fig. 75a). The screen wire is approximated by triangular surface elements forming a rectangular profile in the simulations. No inclination angle to the horizontal is applied.

The polydisperse feed material comprises of particles with a density of 2700 kg/m³ subdivided into 3 size classes consisting of coarse, near mesh, and fine material represented by particles with diameters of 7.35 mm ($1.5a$), 4.2875 mm ($0.875a$) and 2.45 mm ($0.5a$) in case of spheres, respectively. The mass of 4 kg is divided equally into the examined particle classes. According to the works by Delaney et al. [20] and Cleary [199], DEM parameters are applied in the investigation here, which are applicable for standard industrial quarry rock. The tangential spring constant is $k^t = 0.5 \cdot k^n$. Accordingly, the stiffnesses k^n and k^t are set to $k^n = 100000$ N/m and $k^t = 50000$ N/m, leading to an accurate representation of particle/particle and particle/wall interactions due to an average particle overlap of less than

0.5 % of the particle diameter at maximum. The coefficients of normal restitution between particles e_{pp}^n and particles and walls e_{pW}^n and the Coulomb friction coefficient μ_C between particles and the screen wire as well as between particles and particles are adjusted to: $e_{pp}^n = 0.4$, $e_{pW}^n = 0.5$, $\mu_C = 0.5$. The friction between the side walls and the particles is set to $\mu_C = 0$, in order to minimize boundary effects. Therefore, the scaling of the results is possible until the floor size of the screen is chosen smaller than 0.25 % of the size used in the investigation here (comp. [241]).

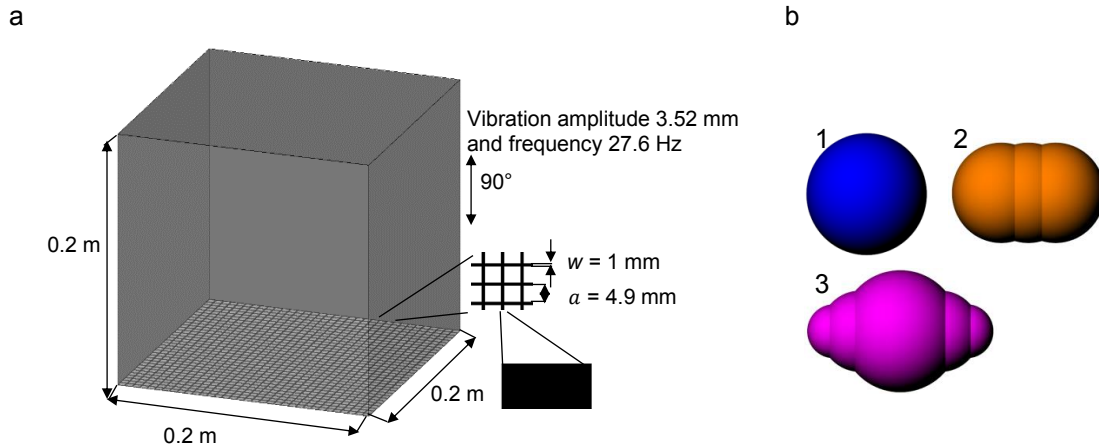


Fig. 75: (a) Discontinuous screening apparatus with wire structure; (b) Considered particle shapes.

Besides spheres, cylinders and double cones are studied in this investigation (comp. Fig. 75b). The non-spherical particles (shapes (2) and (3)) have an aspect ratio of 1.55. The cylindrical particles (shape (2)) are volume equivalent to the spherical particles and have a hemispherical termination at both ends. The double cones (shape (3)) have the same minor axis as the spheres. This gives the double cones the same long-term separation characteristics in a batch screening analysis. However, their separation rates over screen length differ from that of spheres. If needed for analysis or as a parameter for a screening model, the diameter of a complex shaped particle is calculated volume equivalent to a spherical particle in this investigation as

$$d_{vol} = \sqrt[3]{6 \cdot V / \pi}, \quad (178)$$

where V is the volume of the complex shaped particle. Note that some screening process models specify other definitions for the equivalent diameter which are then applied accordingly.

Table 13: Initial setup and performed changes during the discontinuous screening process.

| Parameter | Initial | Var. 1 | Var. 2 | Var. 3 | Var. 4 | Var. 5 | Var. 6 | Var. 7 |
|------------------|---------|--------|--------|--------|--------|--------|--------|--------|
| Amplitude [mm] | 3.52 | 0.88 | 1.76 | 2.64 | 4.4 | 5.28 | 6.16 | 7.04 |
| Frequency [Hz] | 27.6 | 6.9 | 13.8 | 20.7 | 34.5 | 41.4 | 48.3 | 55.2 |
| Stroke angle [°] | 90 | 60/120 | 45/135 | 30/150 | - | - | - | - |

The following variations in operational parameters during the process (comp. Table 13) are considered in the investigation here, applying the particle shapes shown in Fig. 75b. Starting with the initial setup (base case) until $t = t_c = 5$ s, a change of the vibration amplitude, frequency and stroke angle is applied at $t = 5$ s, whereby only one parameter is varied.

5. Results and discussions

Firstly, a general analysis of the transient behavior is given in the next sub-section 5.1 followed by a study on the applicability of the approaches introduced in section 3.1 to predict fractions retained for screening with operational changes based on investigations performed with steady operational parameters. Then in sub-section 5.2, the outcome obtained by DEM simulations is subsequently compared to results attained by the phenomenological screening process models extended / used for batch screening under altered operational conditions (comp. Table 12 and section 3.2.). The required adjustable parameters were fitted by genetic algorithms [240] to the fraction/fractions retained on the screen obtained from DEM simulations performed with no operational changes applied.

5.1 Numerical investigations

In the initial case, particles are filled into the screen apparatus well mixed which is then vibrated for $t = 40$ s without changing any parameters. In all the other cases (comp. Table 13), one parameter of the initial case is changed at $t_c = 5$ s (solid lines in Figs. 76-78) and the simulation is continued until $t = 40$ s. The motion of the screen causes smaller particles to stratify downwards through gaps between larger particles towards the screen surface of the box. By reaching the bottom layer of the box (comp. [7]), smaller particles gain the possibility to pass through the apertures in the bottom plate. Thereby, the finest particles have the highest probability to pass through interstices between particles and screen openings, due to the small ratio between their minor axis and the oversize particles or else the screen apertures. Accordingly, the decline of the residual mass over time is most pronounced for the finest material.

To achieve a better comparability for the analysis of the time-resolved overall particle passage within the screen apparatus and the two different approaches from section 3.1, the passed mass is summed up and normalized for all particle classes with diameters smaller than the apertures. Thereby, the undersize fraction retained over time $Y(t)$ is obtained (Figs. 76-78). Among the considered particle shapes, the highest passage ability is exposed by spheres followed by the non-spherical shapes in all investigations before and after the parameter change (comp. Figs. 76-78). One reason for this order is the slightly longer residence time of complex shaped particles in the particle bed and particularly in the bottom layer (comp. [241]). The change of an operational parameter results in a different progression of the fraction

retained on the screen after $t_c = 5$ s. The ability of particles to stratify is directly influenced by the variation of the motion of the screen. Although the theoretical passage probability is constant following e.g. Gaudin [24], in reality the ability to pass an aperture is affected strongly by the particle motion and the particle distribution in the bottom layer.

Besides the results from the DEM simulations for the fraction retained, results obtained for the two different approaches introduced in section 3.1 to predict the outcome under altered operational conditions from results obtained with steady operational parameters are graphically outlined in Figs. 76-78. Additionally, averaged deviations are later stated in Table 14.

In the first study (Fig. 76) the initial amplitude of 3.52 mm is changed at $t_c = 5$ s according to Table 13, whereby only a selection of amplitude variations is shown in the figure for clarity. For an amplitude of 0.88 mm, the change in the fraction retained after the parameter variation is very low for all shapes ending up in slightly under and above 50 % remaining undersize particles in case of spheres and non-spherical particles, respectively. Independent of particle shape, the fraction retained significantly declines for larger amplitudes, due to larger gaps between the oversize particles and thus an improved stratification. Note when a certain threshold amplitude is reached, the passage of particles stagnates or slightly decreases due to larger distances between particles and the screen surface, which is discussed in detail in Elskamp and Kruggel-Emden [241].

Looking at the results of the approaches discussed in section 3.1 (Fig. 76), starting from the lowest amplitude of 0.88 mm applied after $t = t_c$, the approach No. 1, where $Y_{init \rightarrow alt}^*(t) = Y_{alt}(t) + Y_{init}(t_c) - Y_{alt}(t_c)$, significantly underpredicts the outcome independent of shape. The passage rate in the DEM simulation with a constant amplitude of 0.88 mm after $t_c = 5$ s is low [241], but still on a higher level than the passage after a change from the initial amplitude of 3.52 mm to 0.88 mm. This is caused by a lower amount of small particles remaining on the screen after applying the larger initial amplitude in the first five seconds of the simulation. This phenomenon is more pronounced for double cones and spheres than for volume equivalent cylinders, because the difference of the particle passage under initial operational conditions to the altered conditions with an amplitude of 0.88 mm is larger.

In contrast to approach No. 1, the approach No. 2, which is given as $Y_{init \rightarrow alt}^*(t) = Y_{alt}(t_s + t - t_c)$, slightly overpredicts the fraction retained of double cones and clearly overpredicts $Y(t)$ for the other shapes. This overprediction is a result of a different composition of the particle system due to differences in stratification when $Y_{alt}(t)$ is taken from t_s onwards in approach No. 2 to predict $Y_{init \rightarrow alt}^*(t)$. For an amplitude of 7.04 mm, both approaches represent the simulation results well after $t_c = 5$ s for all particle shapes investigated, especially

for spheres and cylinders. Fractions retained of double cones are represented well with only minor deviations at medium simulation times for approach No. 2.

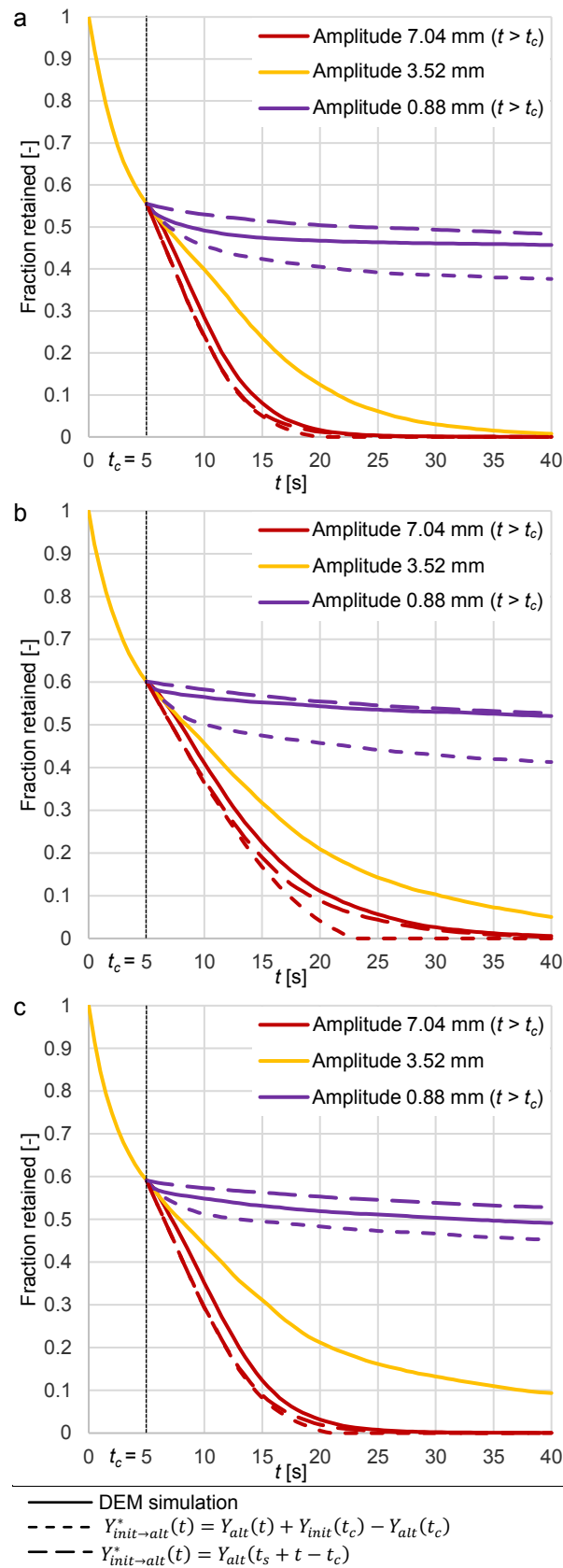


Fig. 76: Fraction retained on the screen over time for (a) spheres, (b) double cones and (c) volume equivalent cylinders for varying amplitudes.

In contrast, approach No.1 predicts the complete discharge of undersize particles to early, because the passage rate in the simulation with double cones at a constant amplitude of 7.04 mm is very low in the first five seconds and larger thereafter (comp. [241]). This is then used to predict $Y(t)$ in approach No. 1 resulting in an overprediction of the passage rate compared to what is obtained from the DEM simulations.

The second investigation (Fig. 77) addresses a change of the vibration frequency of the screen which is applied at $t_c = 5$ s (Table 13). Note that again only a selection of variations is shown in Fig. 77 to enhance clarity. The lowest frequency (6.9 Hz) yields the least particle passage for all shapes with less than 5 % undersize particles passed between $t_c = 5$ s and $t_{end} = 40$ s. This results out of a low stratification and the immobile state of the particle system as a whole preventing the direct contact of undersize particles with the apertures. Obtained results indicate that particle passage is generally enhanced with increasing frequency until a limiting value is reached. Here, this limiting value is reached for a frequency of 34.5 Hz. Thereafter, passage is declining with increasing frequency resulting in an incomplete discharge of undersize particle fractions at the next considered frequency of 55.2 Hz.

The approaches proposed in section 3.1 to predict $Y(t)$ for operational changes based on operation with constant parameters show stronger deviations for the lowest frequency of 6.9 Hz independent of particle shape than for the lowest amplitude (0.88 mm) due to an even smaller passage rate reached after the parameter change. Thereby, approach No. 1 reveals large deviations. The passage rate of the DEM simulation with a constant frequency of 6.9 Hz is too low to obtain a value for the fraction retained according to $Y_{init \rightarrow alt}^*(t) = Y_{alt}(t_s + t - t_c)$. For this reason, the approach No. 2 is not calculable for this simulation. As simplification it is assumed that $Y_{init \rightarrow alt}^*(t) = Y_{init}(t_c)$. With this assumption, this approach slightly overpredicts the simulation results for a frequency of 6.9 Hz after $t_c = 5$ s.

Good accuracy for both approaches is obtained for the frequency of 34.5 Hz. The results up to $t = t_c$ of $Y_{alt}(t)$ are very close to the results obtained when applying a frequency of 27.6 Hz (comp. [241]) and after $t = 5$ s, $Y_{alt}(t)$ and $Y_{init \rightarrow alt}(t)$ are similar in this case (34.5 Hz). Minor deviations can also be stated for a frequency of 55.2 Hz, especially in the case of volume equivalent cylinders (Fig. 77c). The passage of spheres is significantly reduced applying a frequency of 55.2 Hz compared to 34.5 Hz, resulting in a good representation of $Y(t)$ in case of approach No. 1 and in more deviations for No. 2.

The passage rate at 55.2 Hz is nearly uninfluenced of the remaining spheres on top of the screen, leading to the same passage rates after t_c independent of a possible operational change being applied (comp. [241]). In case of double cones, a good agreement is reached if approach No. 2 is applied. Here particularly, approach No. 1 leads to larger deviations. For volume equivalent cylinders both approaches are equally suited.

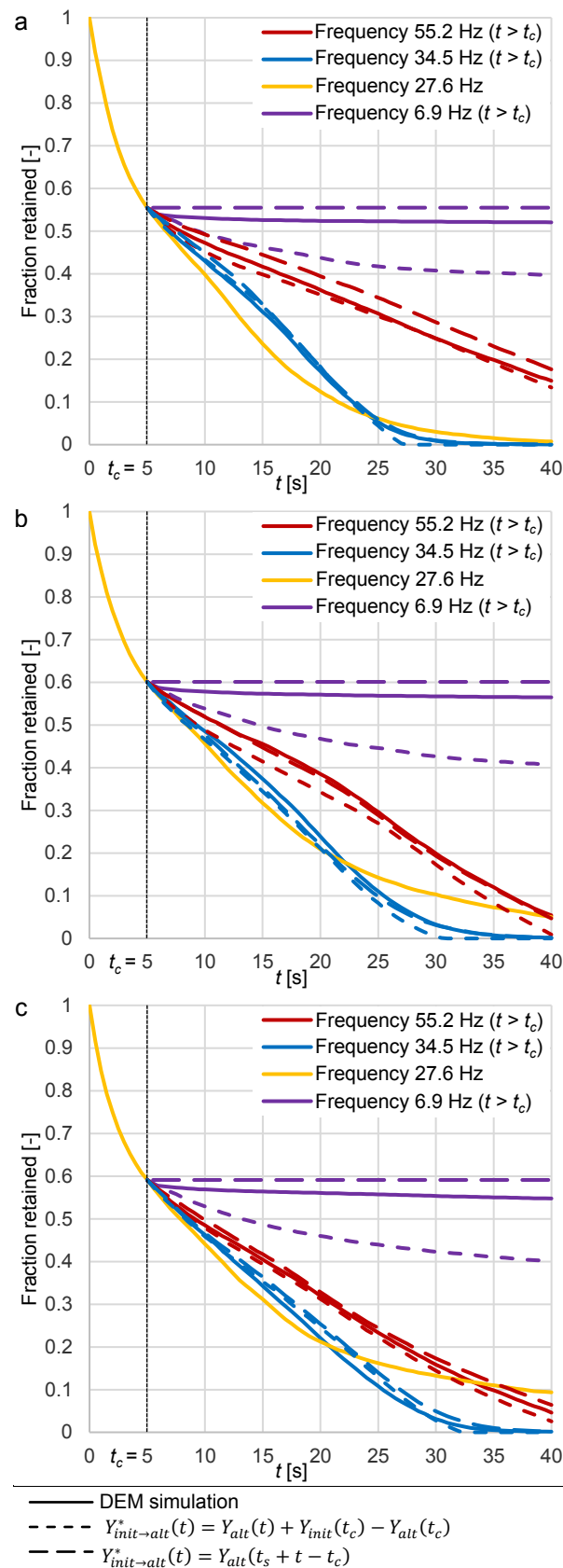


Fig. 77: Fraction retained on the screen over time for (a) spheres, (b) double cones and (c) volume equivalent cylinders for varying frequencies.

In the simulations of the third investigation (Fig. 78), a stroke angle of 90° to the horizontal is used initially, which is changed at $t_c = 5$ s to an oscillating movement consisting of two stroke angles with varying horizontal and vertical components (Table 13).

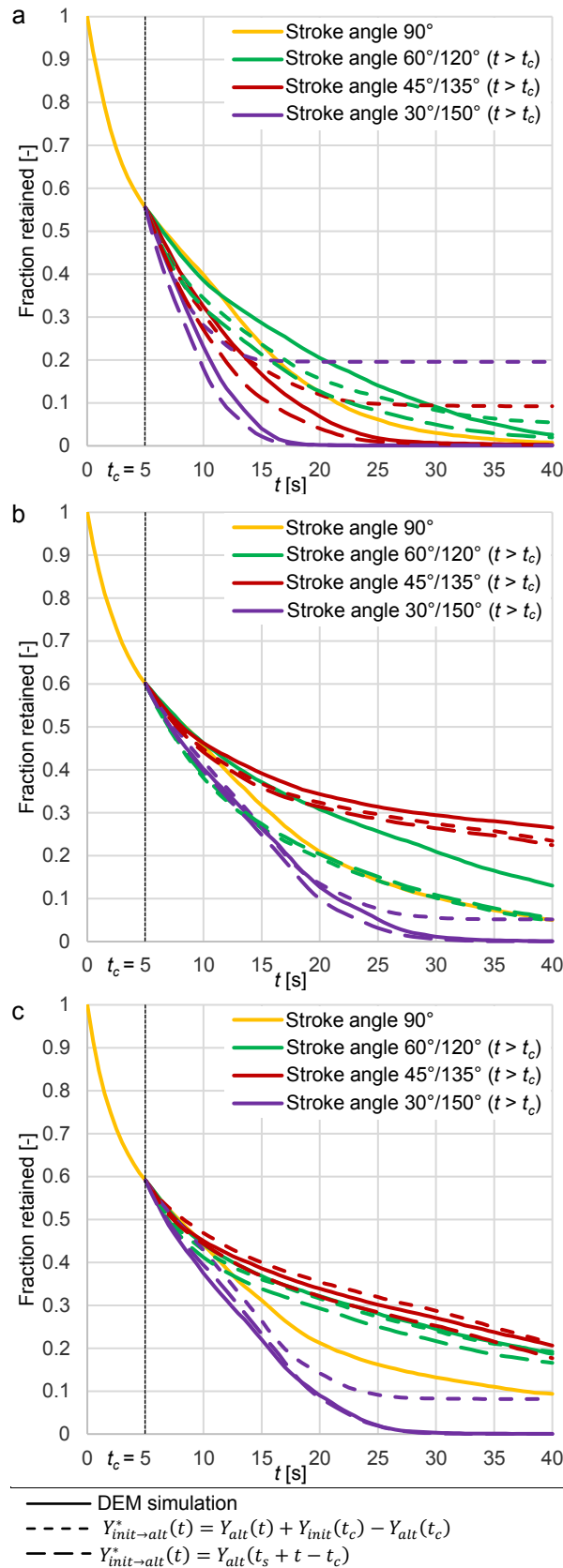


Fig. 78: Fraction retained on the screen over time for (a) spheres, (b) double cones and (c) volume equivalent cylinders for varying stroke angles.

Independent of shape, an alternating stroke angle of 30°/150° after $t_c = 5$ s increases the passage rate intensively resulting in the fastest depletion of undersize particles of all simulations performed. In contrast, a stroke angle of 60°/120° leads to a significant amount of

final particles remaining on the screen. Interestingly, a stroke angle of $45^\circ/135^\circ$ increases the passage for spheres, but reduces the passage for volume equivalent cylinders and double cones which was already observed for constant stroke angles for $1 - Y_{alt}(t)$ [241].

The fast depletion of undersize particles for a stroke angle of $30^\circ/150^\circ$ independent of shape and for spheres applying a stroke angle of $45^\circ/135^\circ$ results in large deviations for approach No. 1, whereas approach No. 2 represents the results for the fraction retained with minor deviations.

The predictions of the DEM simulations applying an alternating stroke angle of $60^\circ/120^\circ$ after $t_c = 5$ s reveal low deviations for cylinders but large deviations for spheres and double cones. Both approaches underpredict the fraction retained of spheres and double cones after $t_c = 5$ s, but in case of spheres, $Y_{init \rightarrow alt}^*(t)$ approaches the results obtained by the DEM simulations towards $t_{end} = 40$ s. Deviations occur for these shapes, due to the differences of $Y_{init \rightarrow alt}(t)$ and $Y_{alt}(t)$ (comp. [241]).

Besides a compilation of the deviations of all investigations (comp. Table 14) averaged over time for the two approaches by $(\sum_{k=1}^j |Y_{init \rightarrow alt}^*(k) - Y_{init \rightarrow alt}(k)|) / j$, where j is the total number of considered time steps k and the time step interval is $\Delta t = 0.5$ s, Table 14 lists the average of these deviations for each approach categorized by shape. In order to assess the size of the deviations it has to be kept in mind, that $Y(t)$ varies in-between 0 and 1 by definition. A calculation of relative deviations, although favorable to evaluate deviances was not possible as $Y(t)$ obtains 0 for $t \rightarrow \infty$.

Averaged over all investigations, approach No. 2 has the lowest deviations of around 0.02 with the best results in case of volume equivalent cylinders ($\varnothing = 0.018$), followed by double cones ($\varnothing = 0.021$) and spheres ($\varnothing = 0.022$). By taking the past of the screening process into account, this approach reveals larger deviations only in a few cases. The disadvantage is, that the fraction retained for cases with very low passage rates can only be assumed as $Y_{init \rightarrow alt}^*(t) = Y_{init}(t_c)$ after $t = t_c$. The predictions of approach No. 1 differ more from the DEM simulation results ($\varnothing = 0.034$) due to not taking the amount of remaining particles into account. Large deviations occur when the DEM simulation with constant parameters reveals a lower amount of particles remaining on the screen in the first five seconds than the DEM simulation with initial parameters ($Y_{alt}(t_c) < Y_{init}(t_c)$) and $Y_{alt}(t_{end}) = 0$, due to the resulting limitation of the predicted fraction retained ($\min(Y_{init \rightarrow alt}(t)) = Y_{init}(t_c) - Y_{alt}(t_c)$). In conclusion, a prediction of operational changes based on the fractions retained available for operation with constant parameters is possible if the past of the screening process is taken into account as in approach No. 2.

Table 14: Deviations between the results obtained by DEM simulation with an instant parameter change at $t_c = 5$ s and the approaches to predict $Y(t)$ by $Y_{init \rightarrow alt}^*(t) = Y_{alt}(t) + Y_{init}(t_c) - Y_{alt}(t_c)$ (No. 1) and by $Y_{init \rightarrow alt}^*(t) = Y_{alt}(t_s + t - t_c)$ (No. 2).

| Shape | Spheres | | | | | | | | | | | | | | | | | |
|--------------------|-----------------------------|-------|-------|-------|-------|-------|-------|----------------|-------|-------|-------|-------|-------|------------------|-------|------------|------------|------------|
| Parameter | Amplitude [mm] | | | | | | | Frequency [Hz] | | | | | | Stroke angle [°] | ∅ | | | |
| Parameter value | 0.88 | 1.76 | 2.64 | 4.4 | 5.28 | 6.16 | 7.04 | 6.9 | 13.8 | 20.7 | 34.5 | 41.4 | 48.3 | 55.2 | | 30/ 150 | 45/ 135 | 60/ 120 |
| Approach No. 1 [-] | 0.060 | 0.034 | 0.028 | 0.007 | 0.012 | 0.014 | 0.016 | 0.085 | 0.046 | 0.025 | 0.007 | 0.024 | 0.023 | 0.011 | 0.157 | 0.056 | 0.031 | 0.037 |
| Approach No. 2 [-] | 0.034 | 0.055 | 0.004 | 0.004 | 0.009 | 0.013 | 0.013 | 0.030 | 0.034 | 0.032 | 0.008 | 0.010 | 0.010 | 0.030 | 0.012 | 0.023 | 0.051 | 0.022 |
| Shape | Double cones | | | | | | | | | | | | | | | | | |
| Parameter | Amplitude [mm] | | | | | | | Frequency [Hz] | | | | | | Stroke angle [°] | ∅ | | | |
| Parameter value | 0.88 | 1.76 | 2.64 | 4.4 | 5.28 | 6.16 | 7.04 | 6.9 | 13.8 | 20.7 | 34.5 | 41.4 | 48.3 | 55.2 | | 30/ 150 | 45/ 135 | 60/ 120 |
| Approach No. 1 [-] | 0.085 | 0.006 | 0.025 | 0.021 | 0.027 | 0.025 | 0.040 | 0.103 | 0.094 | 0.029 | 0.021 | 0.018 | 0.047 | 0.033 | 0.025 | 0.020 | 0.097 | 0.042 |
| Approach No. 2 [-] | 0.011 | 0.014 | 0.015 | 0.017 | 0.018 | 0.010 | 0.019 | 0.030 | 0.015 | 0.028 | 0.010 | 0.003 | 0.025 | 0.005 | 0.011 | 0.029 | 0.089 | 0.021 |
| Shape | Volume equivalent cylinders | | | | | | | | | | | | | | | | | |
| Parameter | Amplitude [mm] | | | | | | | Frequency [Hz] | | | | | | Stroke angle [°] | ∅ | | | |
| Parameter value | 0.88 | 1.76 | 2.64 | 4.4 | 5.28 | 6.16 | 7.04 | 6.9 | 13.8 | 20.7 | 34.5 | 41.4 | 48.3 | 55.2 | | 30/ 150 | 45/ 135 | 60/ 120 |
| Approach No. 1 [-] | 0.035 | 0.019 | 0.010 | 0.010 | 0.013 | 0.016 | 0.021 | 0.098 | 0.048 | 0.013 | 0.010 | 0.010 | 0.008 | 0.012 | 0.061 | 0.014 | 0.007 | 0.024 |
| Approach No. 2 [-] | 0.032 | 0.032 | 0.017 | 0.007 | 0.010 | 0.014 | 0.017 | 0.032 | 0.037 | 0.015 | 0.016 | 0.004 | 0.005 | 0.013 | 0.006 | 0.017 | 0.028 | 0.018 |

The passage rate in the simulation with constant parameters is too low to obtain a value for the fraction retained according to $Y_{init \rightarrow alt}^(t) = Y_{alt}(t_s + t - t_c)$. For this reason, the approach No. 2 is not calculable for this simulation. Therefore, it is assumed that $Y_{init \rightarrow alt}^*(t) = Y_{init}(t_c)$.

5.2 Benchmarking of screening models extended for screening under altered operational conditions

In the following, a benchmarking of the selected phenomenological models as outlined in Table 12 is carried out by using the DEM simulation results of batch screening under altered operational conditions as described in section 5.1. The fraction retained over time from DEM simulations is compared with data obtained by phenomenological screening models which are extended for batch screening under altered operational conditions as described in detail in section 3.2. Note that the models are all adjusted to the fraction retained for screening under constant operational parameters available in between $t = 0 \dots t_{end}$, whereby respective sub-parameters are inherently calculated and not adjusted independently. The obtainable accuracy of using the latter steady parameters to an operation with changes during the process is analyzed in this section.

In Fig. 79 and Fig. 80, the lumped fraction retained over time is shown for all selected phenomenological screening models in comparison to the outcome of the DEM simulations. Just exemplarily, in Fig. 81 the results obtained by screening models that account for the division of undersize particle fractions (Nos. 3, 4, 6), resolved in near mesh and fine undersize fractions, are exemplarily compared with DEM results.

In Figs. 79a-c the comparison is shown for spheres (Fig. 79a), double cones (Fig. 79b) and cylinders (Fig. 79c) applying amplitudes of 1.76 mm and 6.16 mm after $t_c = 5$ s; while before $t_c = 5$ s initial (base case) operational parameters are applied. Nearly all models reveal good results when initial operational parameters are applied independent of shape, resulting in low deviations before $t_c = 5$ s. Only model No. 4 is an exception, which reveals large deviations for spheres and double cones at $t_c = 5$ s. This model takes the division of undersize particle fractions with different passage probabilities P_i (comp. Eq. (163)) into account, whereby using only one set of adjustable parameters. This approach can result in large deviations for the summed up fraction retained (Figs. 79a,b) if the passage rates of two fractions are similar (comp. Figs. 81a,b), although their particle diameters and thereby the passage probabilities P_i differ strongly from each other. In this case, large deviations occur between the particle passage rates of the two fractions predicted by model No. 4 and the DEM results which is also true if the fractions retained per size class are considered (comp Figs. 81a,b).

An increase of the amplitude at $t_c = 5$ s (in Figs. 79a-c and Figs. 81a-c shown for an amplitude of 6.16 mm) results in a stronger decrease of the fraction/fractions retained independent of particle shape. All selected models are able to represent this change in operational parameters with minor deviations, which can also be observed for the two different fractions shown in Figs. 81a-c. Although revealing large deviations at $t_c = 5$ s in case of spheres and double cones, the fraction retained curves of model No. 4 better fit the DEM simulation results at progressed time, especially after one fraction has fully passed.

Decreasing the amplitude at $t_c = 5$ s (in Figs. 79a-c shown for an amplitude of 1.76 mm) leads to a larger amount of remaining particles on the screen independent of shape. With respect to the DEM results, all models reveal larger deviations than for an increase in amplitude, due to various reasons. The adjustment of the models Nos. 1, 3, 5 and 6 to the data of screening under constant operational parameters $Y_{alt}(t)$ already led to significant deviations (comp. [241]) which were of the same order as the deviations after $t = 5$ s shown here (Figs. 79a-c). This is especially the case for the simple rate law equation with one lumped parameter (model No. 1) or with one parameter per fraction (model No. 3) which has the consequence that both models lack the ability to represent the progressions of the fraction retained curves well (see details in [241]). The models Nos. 5 and 6 are not prone to these limitations (comp. [241]). However, the amount of particles in the bottom layer (comp. [7,8]) at $t_c = 5$ s can easily get overpredicted in the initial operation with an amplitude of 3.52 mm, due to adjusting the models only for the fraction/fractions retained and not for each sub-parameter.

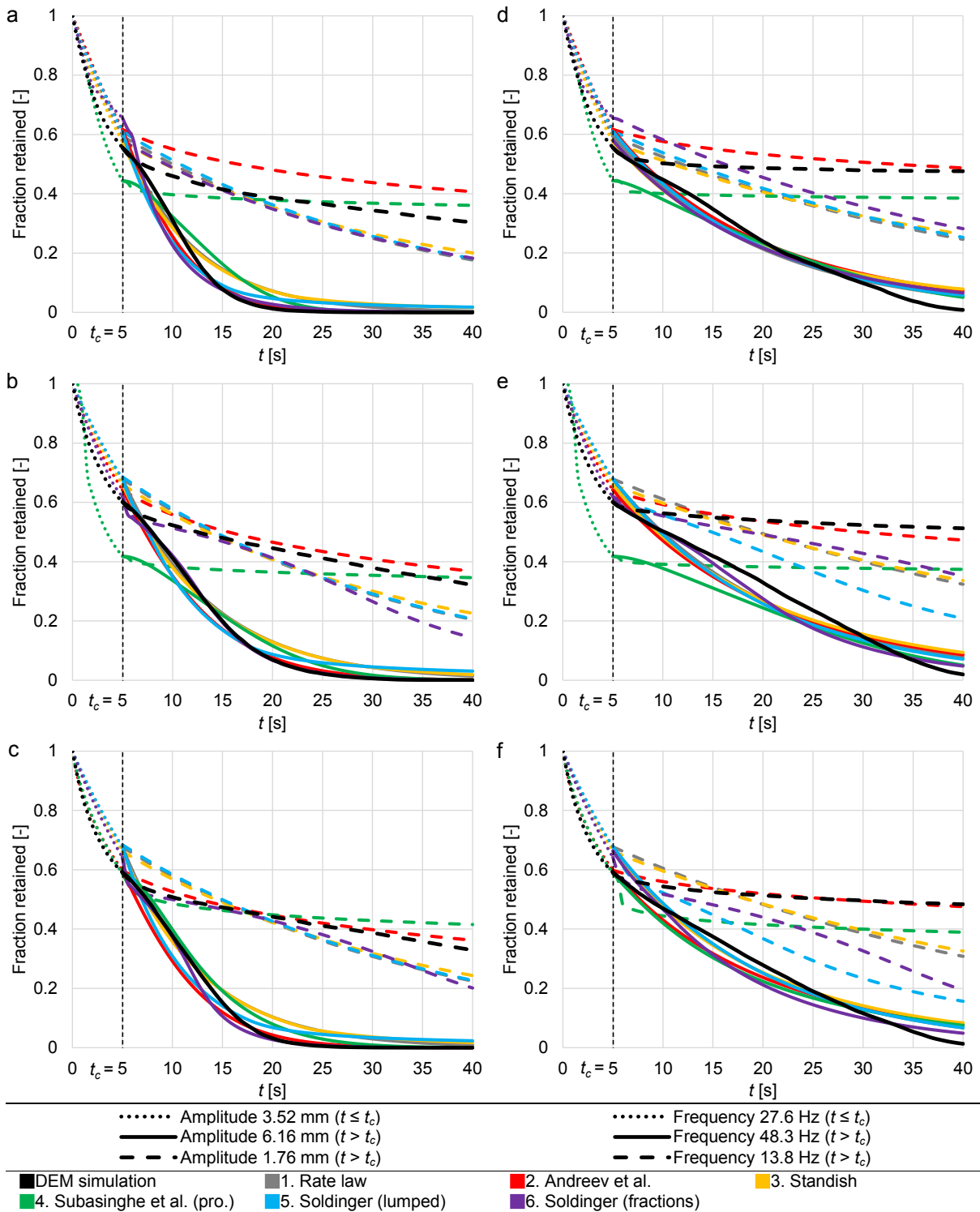


Fig. 79: Fraction retained on the screen over time for various phenomenological screening process models and the DEM simulations for (a,d) spheres, (b,e) double cones and (c,f) volume equivalent cylinders for (a-c) varying amplitudes and (d-f) frequencies.

In contrary to the initial amplitude, the operation with the constantly small amplitude (1.76 mm) assumes only weak stratification but strong passage for models Nos. 5 and 6. The combination of both parameter sets from operation with constant parameters to represent the passage after $t_c = 5$ s when initiating the change to a lower amplitude leads to a prevailing intensive passage of particles over time which are available to a large amount in the bottom layer. Thereby, DEM results are undercut by models Nos. 5 and 6. Model No. 2 was adjusted very accurately to

$Y_{alt}(t)$ independent of particle shape (comp. [241]), also resulting in low deviations for non-spherical particles when the amplitude is reduced at $t_c = 5$ s and constant operational model parameters are used to calculate $Y_{init \rightarrow alt}^*(t)$. In contrast, the representation of spheres reveals significant but nearly constant deviations after the parameter change, due to an already existing deviation at $t_c = 5$ s. Model No. 4 reveals low deviations for cylinders but larger ones if one of the other shapes is applied, because of the strong underprediction of the fraction retained at $t_c = 5$ s.

The results for a change in frequency at $t_c = 5$ s are shown in Figs. 79d-f. In the investigations here, a further increase of the frequency at $t_c = 5$ s from initially 27.6 Hz (here shown exemplarily for a frequency of 48.3 Hz) firstly leads to a decelerated passage of particles (see slope of $Y(t)$ at $t = t_c$ for the DEM), but ends up with lower values of fractions retained at $t_{end} = 40$ s independent of particle shape (Figs. 79d-f). Anyway, besides model No. 4 addressing spheres or double cones, all selected models are able to represent the DEM simulation results very accurately. Again, model No. 4 reveals large deviations at $t_c = 5$ s for spheres and double cones, but the differences decrease over time after $t_c = 5$ s.

A reduction of the frequency at $t_c = 5$ s (in Figs. 79d-f shown for a frequency of 13.8 Hz) leads to a very low amount of particles passing the apertures. As a result, relatively large deviations occur for the models Nos. 1, 3, 5 and 6 independent of shape. The reasons are similar to the ones stated before for the change to a lower amplitude. Model No. 2 reveals good results, particularly for cylinders, due to the additional parameter as exponent of the time t in the model equation, already leading to an accurate adjustment for $Y_{alt}(t)$ (comp. [241]). In addition, the similar decrease of the fraction retained of the DEM simulations with altered parameters $Y_{alt}(t)$ and those under altered operational conditions $Y_{init \rightarrow alt}(t)$ after $t_c = 5$ s supports the accuracy of the model prediction. In contrast, larger deviations occur again at $t_c = 5$ s for model No. 4, whereby the difference of the predicted ($Y_{init \rightarrow alt}^*(t)$) and the simulated fraction retained from the DEM ($Y_{init \rightarrow alt}(t)$) are reduced or stay constant over time.

In Fig. 80 the results for the representation of the DEM simulations with an instant change of the stroke angle orientation at $t_c = 5$ s are shown for spheres (Fig. 80a), double cones (Fig. 80b) and volume equivalent cylinders (Fig. 80c). A change to an alternating stroke angle with a large horizontal component ($30^\circ/150^\circ$) at $t_c = 5$ s from initially a completely vertical motion leads to higher passage rates independent of particle shape. Nearly all investigated models predict the stronger decrease of the fraction retained after $t_c = 5$ s with low deviations from the results obtained by DEM simulations. Only model No. 4 reveals differences for spheres and double cones at $t_c = 5$ s as already stated before; however, they significantly reduce after $t_c = 5$ s.

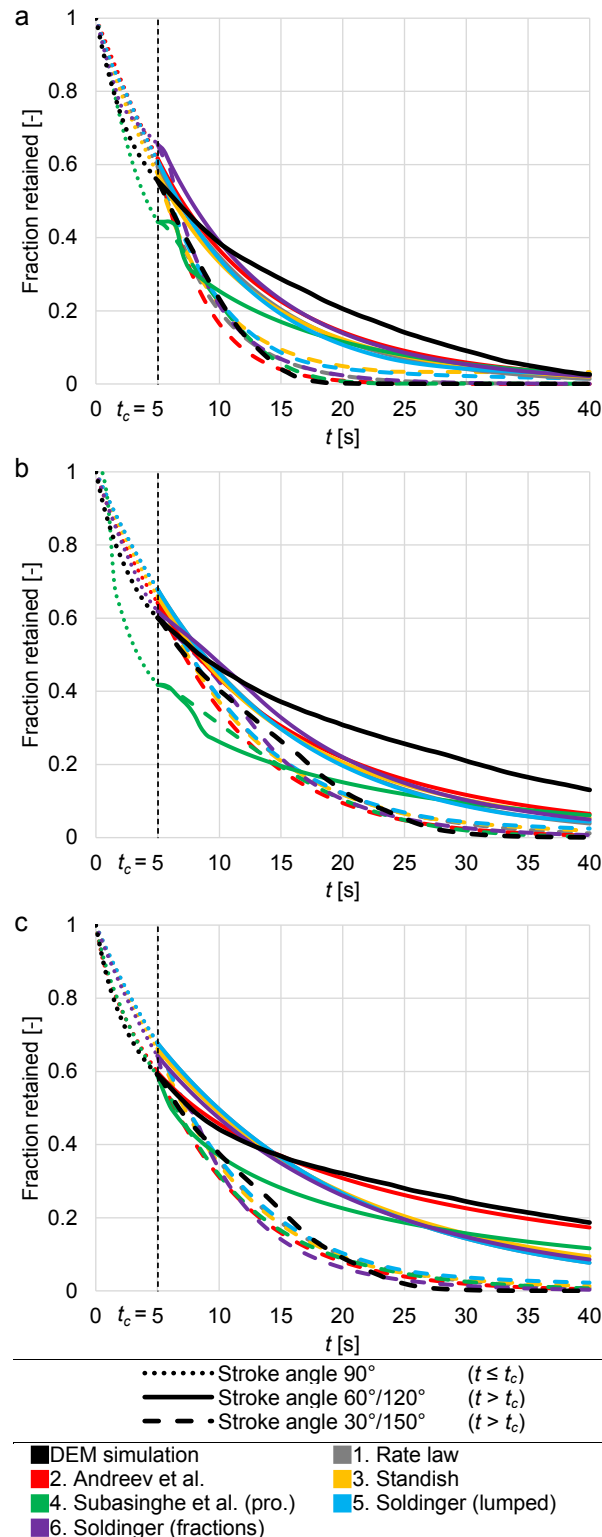


Fig. 80: Fraction retained on the screen over time for various phenomenological screening process models and the DEM simulations for (a) spheres, (b) double cones and (c) volume equivalent cylinders for varying stroke angles.

The change of the stroke angle to an oscillating motion with a larger vertical component ($60^\circ/120^\circ$) at $t_c = 5$ s results in more remaining material on the screen after $t_c = 5$ s, particularly for non-spherical particles. In contrast, the fraction retained of the DEM simulations with altered parameters $Y_{alt}(t)$ is lower than in the initial case $Y_{init}(t)$ (comp. [241]).

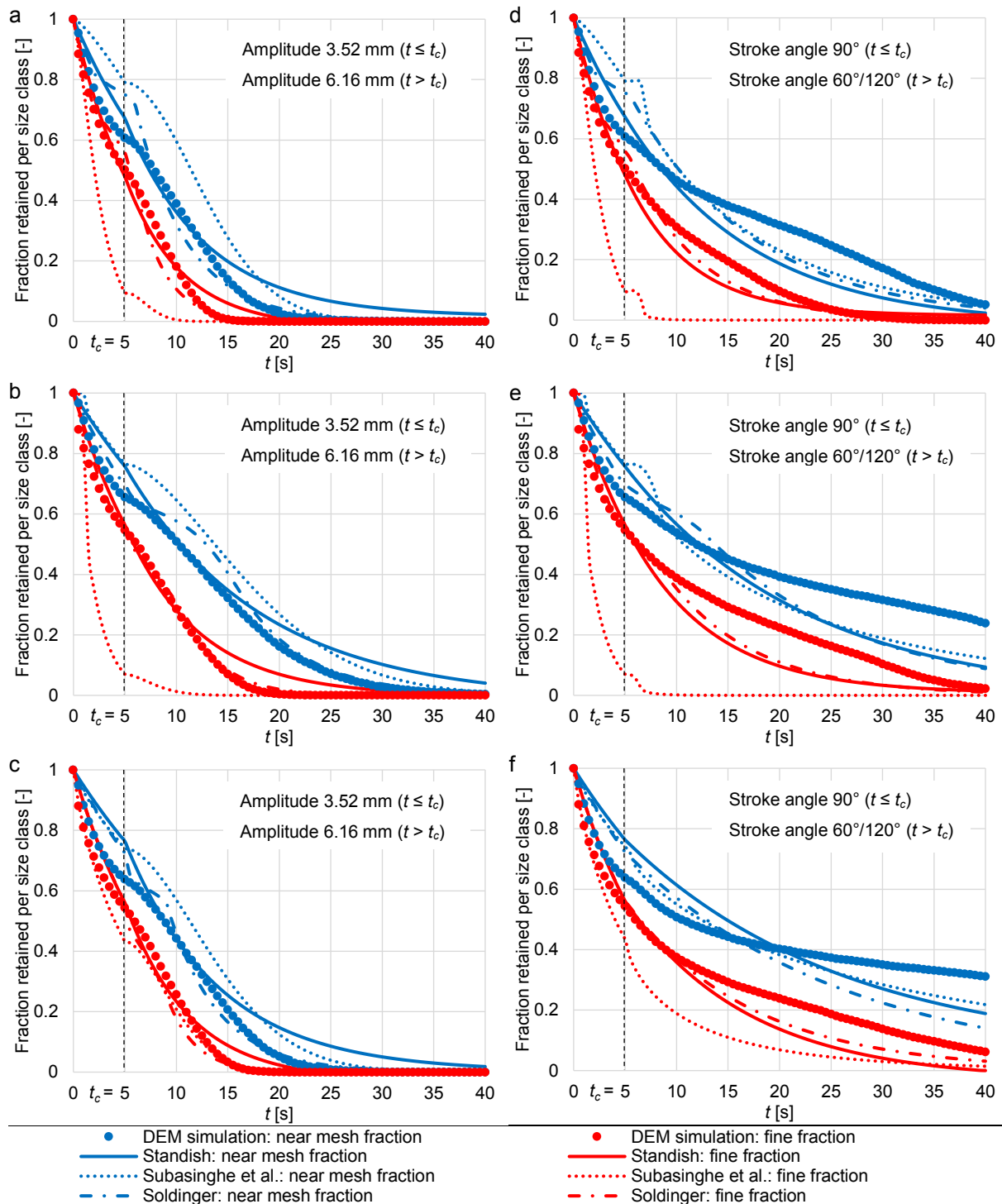


Fig. 81: Fraction retained resolved for the two undersize fractions on the screen over time for various phenomenological screening process models and the DEM simulations for spheres (a,d), double cones (b,e) and volume equivalent cylinders (c,f) for a change to an amplitude of 6.16 mm (a-c) and a stroke angle of 60°/120° (d-f) at $t = t_c$.

By using the parameters which were adjusted for these operations with constant operational parameters, the selected process models underpredict the results for the fraction retained obtained by DEM simulations after $t_c = 5$ s until $t_{end} = 40$ s for all shapes, particularly for non-spherical particles (Figs. 80b,c). The deviations of the model predicted fractions retained for complex shaped particles are mainly caused by the overpredicted passage rate of the near mesh size particles after $t = 20$ s and in case of model No. 4 by a strong underprediction of the

remaining amount of the smallest fraction (comp. Figs. 81e,f). Interestingly, if cylinders are applied, model No. 2 represents the simulation results nearly exactly.

For the benchmarking over a larger number of investigations, an average deviation of the simulated and model predicted fraction retained is calculated for models considering the whole fine material as one lumped undersize fraction by $(\sum_{k=1}^j |Y_{mod}(k) - Y_{sim}(k)|) / j$, where j is the total number of considered time steps k . For models considering the different undersize particle classes i as fractions (Nos. 3, 4, 6) the average of the obtained fractional deviations is calculated by $(\sum_{i=1}^l (\sum_{k=1}^j |Y_{mod}(i, k) - Y_{sim}(i, k)|)) / (j \cdot r)$, where r is the total number of undersize fractions (here $r = 2$). Note that the time of the screening process $t = 40$ s is divided into intervals of $\Delta t = 0.5$ s.

The averaged deviations between models and DEM results of all investigated cases with an instant change in operational parameters during the screening process at $t = t_c$ are shown in Fig. 82. Note that the left bar indicates the deviations obtained for each model being adjusted to the data obtained with constant operational parameters ($Y_{init}(t)$ and $Y_{alt}(t)$) which is analyzed in the following. In contrast, the right bar reveals the lowest deviations that are possible for each model through a direct adjustment to the altered operational conditions $Y_{init \rightarrow alt}(t)$. In total 17 simulations / parameter variations are considered per particle shape. Deviations are summed up per parameter variation forming the bars in Fig. 82. Note that the accuracy of adjusting models directly to DEM results is discussed in detail in Elskamp and Kruggel-Emden [241].

In this investigation, the rate law (model No. 1) which is the basis for most screening models is used to provide a better assessment of the prediction quality of the other models. The model No. 2 reveals the overall lowest deviations, particularly for volume equivalent cylinders (Fig. 82c). This model was adjusted very accurately to nearly all simulations with constant operational parameters and particularly, it benefits from the similar passage rates of cylinders in the DEM simulations under constant and altered operational parameters after $t_c = 5$ s. The models Nos. 3 and 6 obtain the lowest deviations for models that take the undersize fractions into account (Fig. 82). The Model No. 3 was adjusted accurately to the simulations with constant operational parameters by using one parameter for each particle size class. In the investigation here, similar low deviations occur. Some larger deviations are caused by the functional form of the model (similar to model No. 1) which lacks the ability to predict an abrupt deceleration of the particle passage. Model No. 6 obtains good results without requiring one parameter per size class, but by taking the size of the particles and the particle distribution into account.

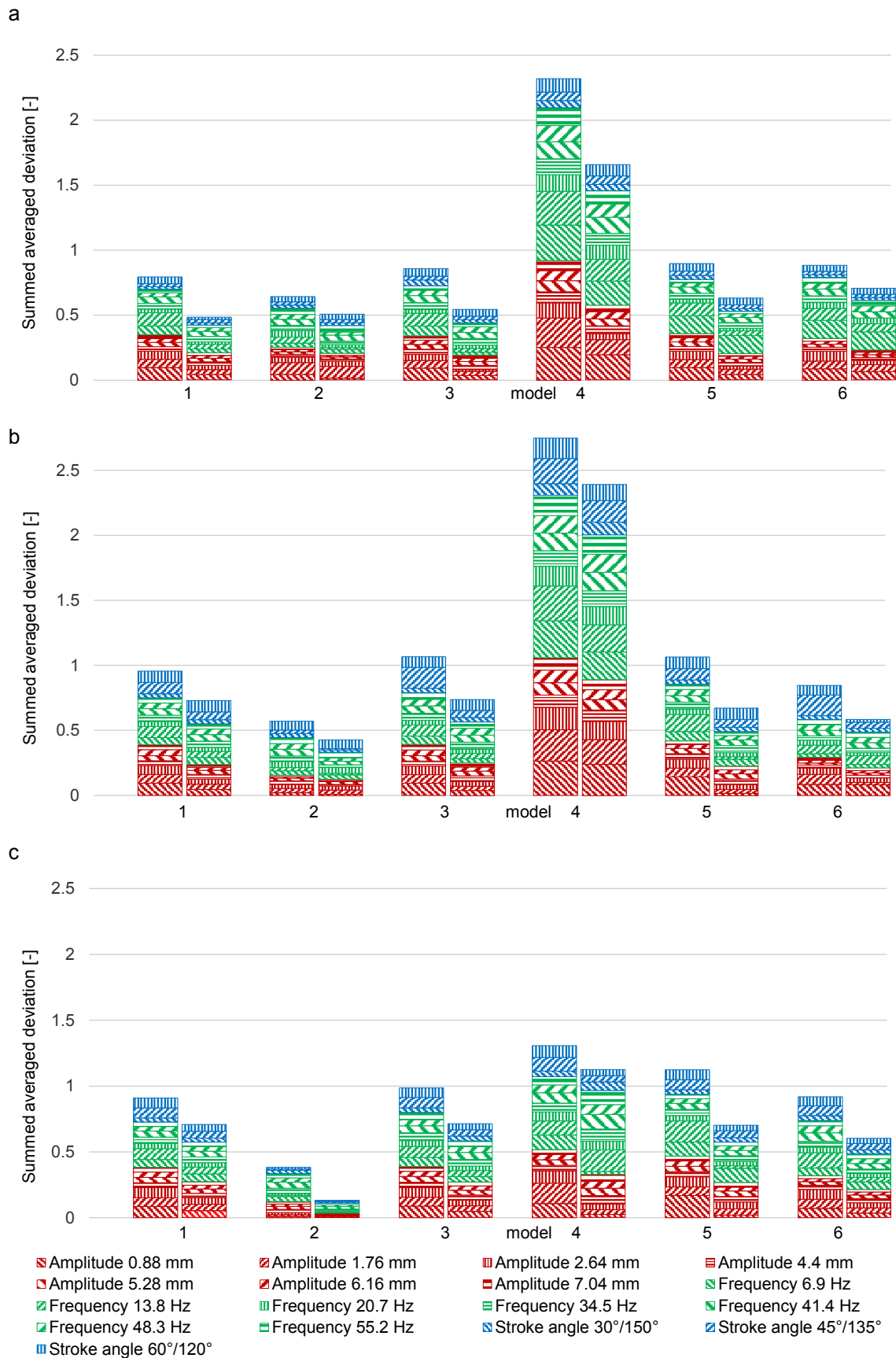


Fig. 82: Deviations between the fraction retained obtained by phenomenological screening models sorted according to Table 12 and discrete element simulations summed up for all investigated changes during the screening process at $t = t_c$ according to Table 13 for spheres (a), double cones (b) and volume equivalent cylinders (c) based on an adjustment to screening under constant operational conditions $Y_{init}(t)$ and $Y_{alt}(t)$ (left bar) and the changed operational conditions $Y_{init \rightarrow alt}(t)$ (right bar) for $t > t_c$.

In contrast, model No. 4 reveals large deviations for spheres and double cones (Figs. 82a,b) due to using only one set of adjustable parameters for the adjustment of $Y_i(t)$ while considering the different undersize particle classes as fractions. This leads to large deviations for $Y_{init}^*(t)$ and hence for $Y_{init \rightarrow alt}^*(t)$ until $t_c = 5$ s. However, they are reduced after $t_c = 5$ s up to $t_{end} = 40$ s when the new set of parameters is applied. In contrast to the predictions for spheres and double cones, model No. 4 reveals overall lower averaged deviations for volume equivalent cylinders (Fig. 82c). The deviations for this model under base case operation at $t_c = 5$ s applying cylinders are lower, due to predicting the difference in the passage rates of the two undersize fractions almost as in the DEM simulations. Therefore, the ability to match the results of the DEM simulations under altered operational conditions after $t_c = 5$ s is also larger. The deviations of models Nos. 5 and 6, independent of particle shape, are mainly caused by an overpredicted amount of particles in the bottom layer at $t_c = 5$ s resulting from initial operation, due to adjusting the models for the integral value of the fraction/fractions retained and not for sub-phenomena like e.g. the stratification to the bottom layer. Therefore, the predicted particle passage after $t_c = 5$ s is still large, leading to large deviations for the representation of simulations where an operational parameter change results in a sudden deceleration of the passage rate.

Compared to the approaches that predict the fraction retained of operation under altered conditions based on unaltered operation evaluated in section 5.1, the phenomenological models adjusted for screening under constant operational conditions are prone to slightly larger deviations. Note that in order to assess the size of the deviations in the following, it has to be kept in mind that $Y(t)$ varies in-between 0 and 1. For instance, the approach No. 2, which takes the past of the screening process into account, averagely obtains deviations of 0.02.

Compared to this, the deviations obtained as a consequence of an adjustment of parameters to the operation under altered conditions are slightly lower with 0.021. In contrast to model No. 2, the model with the lowest differences to the DEM results that takes the various particle fractions into account is model No. 6 with 0.052 mean average deviations, while a direct adjustment to the operation under altered conditions results in mean deviations of 0.038 per operational parameter change. Although revealing slightly larger deviations than the approaches introduced in section 5.1 requiring fractions retained over time from steady operational conditions, phenomenological screening models, particularly the ones by Andreev et al. [226] and Soldinger [8] clearly offer the possibility to predict most operational changes based on parameters available for steady operational conditions.

6. Conclusions

Batch screening investigations under altered operational conditions have been performed taking different particle sizes (coarse, near mesh, fine) and particle shapes (spheres, double

cones and volume equivalent cylinders) into account by using the discrete element method (DEM). During batch screening, which is already transient by nature due to a time dependent mass loss, an instant change of operational parameters such as vibration amplitude, frequency and stroke angle has been exemplarily considered.

Results obtained by the DEM show the potential to increase the particle passage by enlarging the vibration amplitude and frequency during batch screening up to a critical value. Furthermore, a change from a vertical motion to an oscillating motion can support the screening efficiency if the horizontal motion component is larger than the vertical motion component. In contrast to batch screening with a constant oscillating motion, a change to a motion with a larger vertical component during the process leads to reduced passage rates in the investigation here.

The results of batch screening simulations under altered operational conditions are predictable based on integral quantities of DEM simulations such as the fraction retained available for steady operational conditions without performing new DEM simulations directly realizing for the operational change. For this purpose, one possibility is to apply the passage rate of the operation with constant operational parameters after $t = t_c$ for the time after the change of operational parameters (approach No.1). The approach No. 2 uses the passage rate of the operation under constant parameters from $t = t_s$ when the same amount of particles as in the initial case is encountered on the screen.

Besides few exceptions, approach No. 2 obtains the most accurate results with 0.02 average deviations to the simulated fraction retained Y (Y varies in-between 0 and 1), which takes the past of the screening process into account. Accuracy decreases if the particle passage rates of the DEM simulations with constantly altered parameters and those under altered operational conditions differ strongly after $t = t_c$ or $t = t_s$ due to differences in the particle composition.

Additionally, phenomenological screening process models have been extended to represent batch screening simulations under altered operational conditions. Instead of a new adjustment to the operation under altered operational conditions, parameters, which were adjusted for unchanged operations, were applied. For the kinetic models by Andreev et al. [226] and Standish [45] the parameters adjusted for the initial and the altered unchanged operation have to be applied at $t = t_c$ to take the difference in the fraction/fractions retained at this time into account. Additionally, the parameters adjusted for the altered operation under constant conditions have to be applied for the time period after $t = t_c$ where the screening process is governed by the latter parameters. For the probabilistic model by Subasinghe et al. [228] the attempts of particles to pass the apertures after $t = t_c$ have to be added to the attempts needed until $t = t_c$ if a change of operational conditions is performed. These values are obtained with the sets of adjustable parameters applied for the altered and the initial unchanged operation,

respectively. In contrast, the more complex models by Soldinger [7,8] require only the different sets of parameters, due to calculating each new time step based on properties (Y , S , B) from the previous one.

The extended model by Andreev et al. [226] reveals the overall lowest deviations, particularly if cylinders are applied as particle shape. The second model by Soldinger [8] and the one by Standish [45] obtain the best results for models that take the different particle fractions into account, whereby the latter requires a set of parameters for each particle fraction. Large deviations occur for the model by Subasinghe et al. [228] if the fractional particle passage rates obtained by the DEM simulations are similar for different particle sizes (and passage probabilities P_i) which is the case when spheres or double cones are applied. The models by Soldinger [7,8] obtain large deviations if the passage rate is reduced abruptly by changing to a very low frequency or amplitude. This is caused by an overpredicted amount of particles in the bottom layer at $t = t_c$, resulting from adjusting the models only for the fraction/fractions retained and not for sub-processes like the stratification into the bottom layer. The adjustment was carried out in accordance to the investigation by Soldinger [7,8], where such parameters were barely obtainable during the experimental investigation. However, in order to increase the accuracy for the prediction of transient operations in further investigations, the adjustment will be based on sub-processes such as stratification and passage determined from DEM simulations.

Overall, the extended phenomenological screening process models Nos. 2 and 6 [8,226] are suited for representing batch screening simulations under altered operational conditions in most cases without being adjusted to new DEM simulations (0.021 and 0.038 mean deviations), but by applying model parameters that were previously adjusted for DEM simulations under constant operational conditions (0.031 and 0.052 mean deviations to the simulated fraction retained Y , which varies in-between 0 and 1). Besides no new adjustment to existing data, an advantage of using model parameters adjusted for operations under constant operational parameters is the omission of further simulations or experiments to investigate the repercussions and possible process intensifications of changes in operational parameters during the screening process.

As a next step, the suitable batch screening models ([8,226]) will be made available for the modeling framework Dyssol. In further investigations, the applicability of screening process models to represent continuous screening under transient operational conditions will be investigated to extent the modeling framework. Based on this, a dynamic screening model for a dynamic process simulation framework will be realized.

Note that the DEM simulations in this study were not directly benchmarked against experimental investigations under altered operational conditions. However, the DEM applied

here was validated against discontinuous screening processes with constant operational parameters. Additionally, a large benchmarking has previously been done for continuous screening against literature data [236]. The purpose of the DEM was to derive a qualitatively realistic parameter space as could also be obtained from experimental investigations. A benchmarking of the DEM against batch screening experiments under altered operational conditions is currently ongoing to apply the screening models towards real batch screening investigations involving experimental equipment.

Acknowledgements

The authors gratefully acknowledge the support by DFG within project SPP 1679 through grant number KR3446/7-2.

VII. A strategy to determine DEM parameters for spherical and non-spherical particles

Frederik Elskamp^{1*}, Harald Kruggel-Emden¹, Manuel Hennig², Ulrich Teipel²

¹Mechanical Process Engineering and Solids Processing, Technische Universität Berlin, Ernst-Reuter-Platz 1, D-10587 Berlin, Germany

²Department of Particle Technology, Technical University Nürnberg, Wassertorstrasse 10, D-90489 Nuremberg, Germany

*Corresponding author. E-mail address: frederik.elskamp@tu-berlin.de

The following accepted manuscript appeared as journal version in Elskamp F., Kruggel-Emden H., Hennig M., Teipel U., 2017, A strategy to determine DEM parameters for spherical and non-spherical particles, Granular Matter 19:46 and may be found at <https://doi.org/10.1007/s10035-017-0710-0>.

Abstract

In discrete element method (DEM) simulations the choice of appropriate contact parameters is significant to obtain reasonable results. Particularly, for the determination of DEM parameters for non-spherical particles a general straightforward procedure is not available. Therefore, in a first step of the investigation here, methods to obtain the friction and restitution coefficients experimentally for single particles (Polyoxymethylene (POM) spheres and quartz gravel) will be introduced. In the following, these predetermined DEM coefficients are used as initial values for the adjustment of bulk simulations to respective experiments. In the DEM simulations, the quartz gravel particles are represented by non-spherical particles approximated by clustered spheres. The best fit approximation of the non-spherical particles is performed automatically by a genetic algorithm. In order to optimize the sliding and rolling friction coefficients for DEM simulations, the static and dynamic angle of repose are determined from granular piles obtained by slump tests and rotating drum experiments, respectively. Additionally, a vibrating plate is used to obtain the dynamic bed height which is mainly influenced by the coefficient of restitution. The adjustment of the results of the bulk simulations to the experiments is conducted automatically by an optimization tool based on a genetic algorithm. The obtained contact parameters are later used to perform batch screening DEM simulations and lead to accurate results. This underlines the applicability of the in parts automated strategy to obtain DEM parameters for particulate processes like screening.

Keywords: Discrete element method (DEM); Parameter determination; Automatic adjustment of DEM parameters; Arbitrary shaped particles; Screening

1. Introduction

The process step screening is important to separate bulk material in a wide range of industrial applications, where particles of non-spherical shape are classified according to desired size

class specifications [2,3]. In the interest of studying screening and its sub-processes in detail without performing extensive experimental tests the discrete element method (DEM) dating back to Cundall and Strack [10] has been proved as a suitable tool [5,6,20,198,236]. To apply the DEM for complex processes like screening a proper calibration of DEM parameters and particle shape approximation has to be carried out. Several methods to calibrate DEM parameters have been proposed but particularly, for non-spherical particles general straightforward procedures with a high degree of automation are hardly available.

The first investigations published, addressing DEM parameter calibration, mostly concentrate on spherical particles without automated procedures. In one of them [160] Li et al. measured the coefficient of sliding friction in simple drag tests applying spheres and confirmed the DEM parameters by comparing quasi-two-dimensional hopper discharge and conical pile experiments with simulations. Based on this, Gryma and Wypych [129] as well as Chen et al. [158] applied particle clusters consisting of two spheres to measure the static angle of repose in a slump test to confirm and adjust the DEM parameters which had been determined in single particle tests before. Coetzee and Els [168] also applied clusters of two spheres and determined the DEM parameters in shear and compression tests before measuring the static angle of repose. The obtained values were later applied successfully to hopper discharge and bucket filling processes. Natsui et al. [246] determined the contact friction and used rolling friction to consider the irregular shape of coke in simulations where the angle of repose was measured. They stated that the choice of the Young's modulus is important to accelerate the calculation time in DEM simulations as long as the results are not influenced. Alonso-Marroquín et al. [157] determined the DEM parameters stiffness, the friction and restitution coefficients for polygonal wood particles with several single particle experiments, including sliding, triaxial and pendulum collision tests, respectively. They applied the obtained parameters to hopper discharge simulations and compared the results with respective experiments. Similar single particle tests are carried out by Barrios et al. [130] applying particle clusters consisting of four different sized spheres to approximate iron ore pellets. The validation of the DEM parameters by slump and tumbling tests clarified the significance of particle shape and the need of adjusting the DEM parameters after simple single particle tests. A review for DEM parameters and contact models for granular material has been done by Horabik and Molenda [247] who highlighted the importance of material and interaction properties for obtaining reliable information out of DEM simulations. Recently, Coetzee [127] investigated the influence of particle shape approximation with particle clusters created manually and by an automated optimization process with the multi-sphere method of up to eight spheres as main part of a DEM parameter calibration. Additionally, Dobrohotoff et al. [248] used spheropolygons to describe two-dimensional complex-shaped objects like pebbles, gravel and crushed shells where only a few iteration steps were needed to get good results. The significant optimization

of the shape was confirmed by comparing anchor pull-out and hopper discharge simulations with respective experiments. Höhner et al. [184,249] investigated the influence of the multi-sphere and the polyhedral method on the mechanical behavior of particles during hopper discharge. Only minor differences were obtained between both methods for complex shaped particles. However, the computational time increased significantly if the polyhedral method was used for real particles like quartz gravel. Accordingly, Li et al. [250] approximated real particles with the multi-sphere method automatically by a greedy heuristic algorithm obtaining very accurate results. In order to determine adequate DEM parameters automatically, Benvenuti et al. [251] developed a neural network which can be trained by dedicated DEM simulations to predict granular bulk behavior for a large number of DEM parameter sets.

Based on these previous investigations, the strategy to determine DEM parameters in this investigation is as follows. First, DEM parameters and physical properties of single particles are determined. Additionally, non-spherical particles are clustered with the multi-sphere method automatically. Afterwards, the physical properties and the DEM parameters are applied to bulk simulations where the DEM parameters are adjusted automatically with an optimization tool to fit the results of corresponding experiments. To confirm the adjustment procedure, initial and adjusted parameter values are compared against each other. The adjusted DEM parameters are then applied to screening processes as example for a more complex particulate process.

2. Numerical method

The DEM can be applied to systems with spherical and non-spherical shaped particles [60,61], by tracking the translational and rotational motion of each particle. For this purpose the Newton's and Euler's equations are integrated

$$m_i \frac{d^2 \vec{x}_i}{dt^2} = \vec{F}_i + m_i \vec{g}, \quad (179)$$

$$\hat{I}_i \frac{d\vec{W}_i}{dt} + \vec{W}_i \times (\hat{I}_i \vec{W}_i) = \Lambda_i^{-1} \vec{M}_i, \quad (180)$$

with particle mass m_i , particle acceleration $d^2 \vec{x}_i / dt^2$, contact force \vec{F}_i , gravitational force $m_i \vec{g}$, angular acceleration $d\vec{W}_i / dt$, angular velocity \vec{W}_i , external moments resulting out of contact forces \vec{M}_i , the inertia tensor along the principal axis \hat{I}_i and the rotation matrix converting a vector from the inertial into the body fixed frame Λ_i^{-1} . Explicit integration schemes (comp. e.g. [82]) are used to solve both equations (eq. (179) and eq. (180)).

To model complex shaped particles in the DEM the multi-sphere method is used. Thereby, the desired complex particle shape is represented by clustered spheres of arbitrary size [69] and similar contact force laws as used for spherical particles are applied [65].

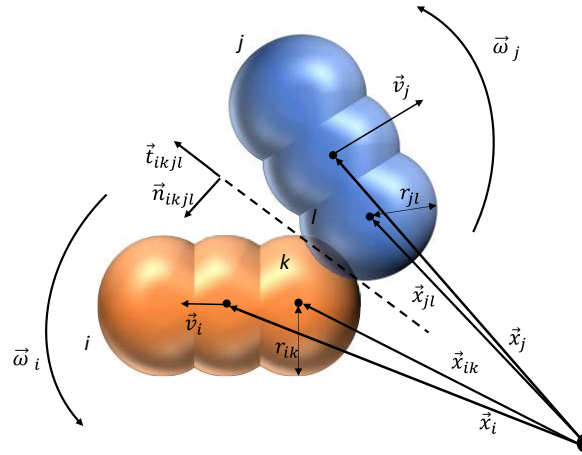


Fig. 83: A collision of two multi-sphere particles.

In Fig. 83 a sketch of two complex shaped particles i and j is shown, where the spheres l and k collide. For further details on the contact scheme involving clustered spheres the works by Kruggel-Emden and Kačianauskas and Kruggel-Emden et al. [90,91] are recommended.

The normal component of the contact forces is obtained from a linear spring damper model which is exemplarily given for the contacting spheres k and l of particle i and j as

$$\vec{F}_{ikjl}^n = k^n \delta_{ikjl} \vec{n}_{ikjl} + \gamma^n \vec{v}_{ikjl}^n \quad (181)$$

where k^n is the spring stiffness, δ_{ikjl} the virtual overlap, \vec{n}_{ikjl} a normal vector, γ^n a damping coefficient and \vec{v}_{ikjl}^n the normal velocity at the contact point [92]. The damping coefficient γ^n is calculated as

$$\gamma^n = - (2 \ln(e^n) m_{eff}) / t^n \quad (182)$$

with the experimentally determined coefficient of restitution e^n (comp. section 3.5), the duration of a collision

$$t^n = \pi / \left(\sqrt{(k_n / m_{eff} - (\gamma_n / (2m_{eff}))^2)} \right) \quad (183)$$

and the effective mass $m_{eff} = m_i m_j / (m_i + m_j)$. The tangential forces are calculated by applying a linear spring limited by the Coulomb condition

$$\vec{F}_{ikjl}^t = -\min(k^t |\vec{\xi}_{ikjl}|, \mu_C |\vec{F}_{ikjl}^n|) \vec{t}_{ikjl} \quad (184)$$

where k^t is the tangential stiffness of a linear spring, μ_c is the friction coefficient, $\vec{\xi}_{ikjl}$ is the relative tangential displacement and \vec{t}_{ikjl} is the tangential unit vector [94]. The tangential spring stiffness k^t is obtained from

$$k^t = \kappa m_{eff} (\pi/t^n)^2, \quad (185)$$

where κ is given through the mechanical properties as

$$\kappa = ((1 - \nu_i)/G_i + (1 - \nu_j)/G_j) / ((1 - 0.5\nu_i)/G_i + (1 - 0.5\nu_j)/G_j), \quad (186)$$

where ν is the Poisson's ratio and $G = E/(2 + 2\nu)$ with Young's modulus E is the shear modulus of the two interacting materials i and j [98].

3. Determination of DEM parameters and physical properties of single particles

In this section, the material and physical properties, the particle shapes, the sliding and rolling friction coefficients and the coefficient of restitution are obtained by single particle characterization. In case of the coefficients of friction and restitution the calibration at the particle level is done to get a first approximation. These parameters can be used as initial values for the parameter adjustment so that the calibration converges quickly; additionally they are used as comparison for the values reached after the adjustment. If these values are already accurate enough, the adjustment is very fast or is not necessary at all.

3.1 Determination of material and physical properties

In a first step, material and physical properties like the size distribution, mass, volume and density of the particles are determined and listed in Table 15. Polyoxymethylene (POM) spheres are applied in three different discrete size classes which are equally distributed in each investigated case.

Table 15: Mechanical particle and wall properties.

| Mechanical particle property | Particle | | Wall | |
|---|---|---------------|----------|----------|
| | POM | Gravel | Metal | Acryl |
| Diameter d [mm] | 5 / 7 / 10 \pm 0.1 | 3.15-5.60 | - | - |
| Mass m [g] | 0.0935 / 0.2459 / 0.7210 \pm 0.02 | 0.0316-0.4440 | - | - |
| Density ρ [kg/m ³] | 1.43E+03 / 1.37E+03 / 1.38E+03 \pm 1.50E+03 | 2.76E+03 | 7.85E+03 | 1.20E+03 |
| Young's modulus E [N/m ²] | 2.84E+09 | 6.00E+10 | 2.08E+11 | 2.20E+09 |
| Poisson's ratio ν [-] | 0.35 | 0.25 | 0.30 | 0.37 |
| Stiffness k_{PP}^n / k_{PW}^n [N/m] | 1.00E+05 | 1.00E+05 | - | - |

For the quartz gravel the cumulative particle size distribution as outlined in Fig. 84, which is obtained by an image analysis of a CAMSIZER®, is used. Note that the dots represent one size class in the DEM simulations.

The mass m_i of each POM particle size class is measured as average of 20 POM spheres and the density ρ_i is determined with $\rho_i = m/(1/(6\pi d^3))$. The average volume V_i of the gravel is obtained by water displacement of around 500 particles which are weighed before to obtain an average density of $\rho = 2755\text{kg/m}^3$. The normal spring stiffness is set to $k^n = 1.00\text{E}+05$ N/m for both materials after carrying out test simulations of granular piles (comp. section 4.2) applying values of $k^n = 1.00\text{E}+03$ N/m up to $k^n = 1.00\text{E}+06$ N/m and measuring no changes for values larger than $1.00\text{E}+05$ N/m. Additionally, the particle overlap is consistently below 0.5 % of the particle diameter according to Cleary [199].

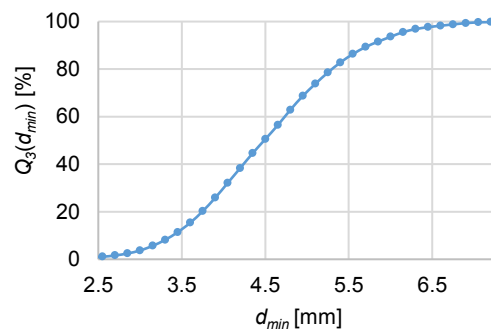


Fig. 84: Cumulative particle size distribution of quartz gravel.

3.2 Shape approximation

As stated before, the POM particles are assumed to be ideal spheres of 5 mm, 7 mm and 10 mm which are applied in the DEM simulations accordingly. The gravel consists of non-spherical particles with a sphericity between 0.35 and 0.87 (average: 0.75) and an aspect ratio between 1.06 and 2.49 (average: 1.49) which is both obtained by an image analysis. To represent such particles, various methods can be applied [127,248,250]. For this approximation a genetic algorithm which is part of Matlab® is used. This algorithm is very flexible and allows adjusting many features such as population size, generation, mutation and crossover functions as well as initial values (comp. [240]). It was already applied successfully in the work by Kruggel-Emden et al. [252] for the adjustment of coefficients as part of multi-parameter models describing reaction kinetics in the context of chemical looping where details on the algorithm and possible settings can be found.

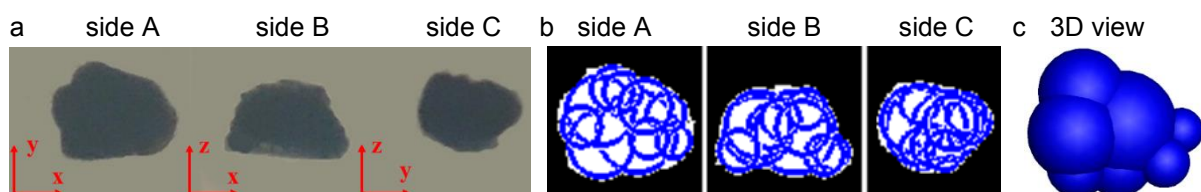


Fig. 85: (a) Cross sectional areas and (b) areas filled with circles to (c) approximate the shape of gravel particles (example).

Instead of modeling the gravel with a polyhedral shape, the particles are approximated by clustered spheres like in Coetzee [127] to save computational time in the DEM simulation, which is important for an efficient adjustment algorithm. Therefore, in a first step, a sample of gravel particles is filled into cast resin cubes and images are taken from three sides giving the

three cross sectional areas (Fig. 85a). With the help of an optimization tool, arbitrary sized circles, which represent spheres, are placed one after the other into these three areas to obtain the best fit for all areas while receiving penalty points for not included pixels in or for overlaps over a projected zone (Fig. 85b). The number of applied spheres determines the accuracy of the approximation but in contrary influences the simulation time. One method to terminate the optimization is to specify the amount of clustered spheres before the optimization, whereas another method is to automatically stop the tool if no further improvement is detected when applying more spheres (decrease in deviation is lower than defined). For the placing of each single sphere, the maximum number of iterations or a specified change in deviations to the previous iteration can be defined. The whole algorithm is presented in the flow chart in Fig. 86.

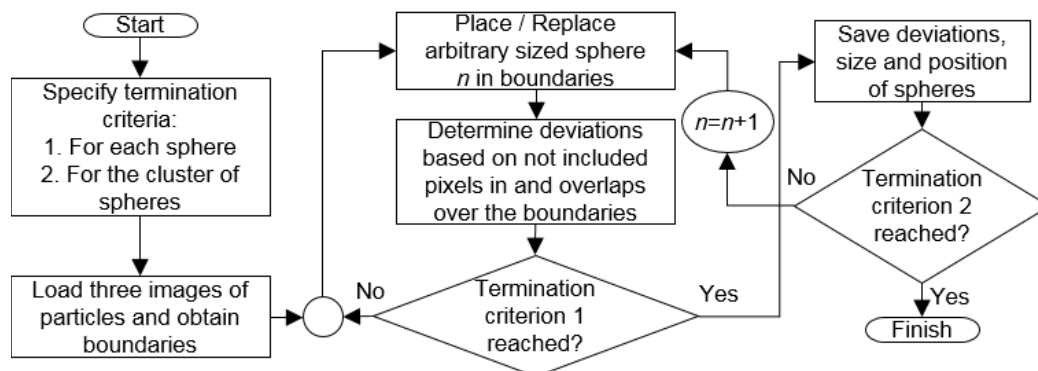


Fig. 86: Algorithm to best fit the representation of gravel particles with clustered spheres on the basis of cross-sectional areas.

One of the created gravel particles which is applied in the following simulations is shown in Fig. 85c. It consists of 10 spheres which is sufficient enough to represent the gravel particles (no further improvement by applying more spheres) and is still computationally efficient. It is accomplished in less than 10 minutes requiring less than 100 generations where a population consisting of 200 individuals was used. For the simulations, several different shapes for each size class can be applied. A particle can be classified in one particle size class by measuring its volume equivalent sphere diameter if the particle size distribution is based on this equivalent diameter. Due to applying the particles for a screening process in the following, the approximated particle is classified based on the minor axis diameter in this investigation (comp. Fig. 84). The other particle size classes are created by scaling the approximated cluster with respective scaling factors obtained through the ratio of the equivalent diameters of two size classes.

3.3 Coefficient of sliding friction

To determine the sliding friction of the particles, samples of POM spheres of each size class and gravel particles of each fraction are glued under a wooden plate and the force which is necessary to drag these particles over a plate consisting of the material of one contact partner is measured (comp. Fig. 87). Thereby, the evenness of the particle layer influences the quality

of the measurement. To stabilize the wooden plate a weight is placed on it. The value of the weight is changed to test its influence resulting in deviations of below 1 %.

In this investigation, the classical friction theory is applied, which states that $\mu_c = |\vec{F}_F|/|\vec{F}_N|$, with the frictional force \vec{F}_F and the normal force \vec{F}_N . This is suitable for a point-point contact when ignoring the effect of the contact area [160]. Due to having a very small contact area between a particle and a plane wall like between two particles, a plate of the particle material (POM spheres with a POM plate and quartz gravel with a gravel plate) is used as approximation for the particle-particle friction.

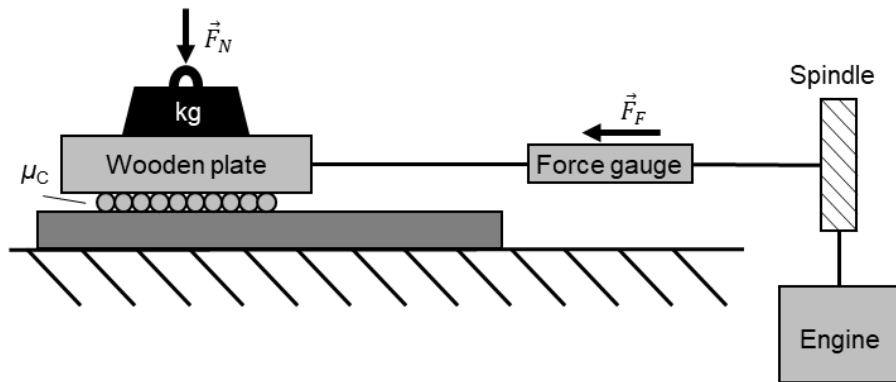


Fig. 87: Determination of sliding friction.

Results for the sliding friction coefficient between particles and the same material for the particle-particle contacts and between particles and the wall materials (acryl, metal) for the particle-wall contacts each averaged over 10 experiments are listed in Table 16. For two different sized POM spheres the average of the respective values is applied.

Table 16: Coefficient of sliding friction.

| Contact partner | POM 5 mm | POM 7 mm | POM 10 mm | Gravel |
|---------------------------------|-----------------|-----------------|-----------------|-----------------|
| | μ_c [-] | μ_c [-] | μ_c [-] | μ_c [-] |
| Acryl (side walls) | 0.16 ± 0.01 | 0.19 ± 0.01 | 0.21 ± 0.01 | 0.19 ± 0.01 |
| Metal (screen wire) | 0.17 ± 0.01 | 0.16 ± 0.01 | 0.17 ± 0.02 | 0.31 ± 0.02 |
| POM / quartz gravel (particles) | 0.23 ± 0.01 | 0.30 ± 0.02 | 0.28 ± 0.02 | 0.57 ± 0.03 |

3.4 Coefficient of rolling friction

For simulating spherical particles in the DEM (here for POM spheres) it is necessary to use a model for rolling friction to oppose the rolling motion of the spheres with a decelerating moment \vec{M}_{roll} . Here, the model by Zhou et al. [100] is used which can be simplified for free rolling spherical particles where the normal force \vec{F}_N is equal to the weight force. Therefore, the coefficient of rolling friction can be calculated as

$$\mu_{roll} = |\vec{M}_{roll}|/|\vec{F}_N|. \quad (187)$$

To determine the coefficient of rolling friction experimentally, the rolling motion of a sphere on a plane wall is recorded [161]. The moment \vec{M}_{roll} is then obtained as

$$|\vec{M}_{roll}| = \left(1/2 m(v_1^2 - v_2^2) + 1/2 \theta(\omega_1^2 - \omega_2^2) \right) d/(2s) \quad (188)$$

with the velocities of the sphere at the beginning (v_1) and at the end (v_2) of the surface, the sphere's mass moment of inertia θ , its angular velocity at both time steps ω_1 and ω_2 , the distance travelled by the sphere s and its half diameter $d/2$. The velocities of the sphere v_1 and v_2 as well as the distance travelled are measured by image analysis of records taken from above with a high speed camera. It can be assumed that the spheres do not slip or bounce on the applied plane surface and have low velocities. Therefore, the angular velocity ω can be obtained through the translational velocity v .

Table 17: Coefficient of rolling friction.

| Contact partner | POM 5 mm | POM 7 mm | POM 10 mm |
|---------------------|------------------------|------------------------|------------------------|
| | $\mu_{roll} [10^{-5}]$ | $\mu_{roll} [10^{-5}]$ | $\mu_{roll} [10^{-5}]$ |
| Acryl (side walls) | 5.44 ± 1.1 | 7.76 ± 2.7 | 6.41 ± 3.3 |
| Metal (screen wire) | 7.22 ± 2.2 | 8.13 ± 3.6 | 7.07 ± 3.7 |
| POM (particles) | 5.94 ± 1.4 | 8.63 ± 1.6 | 7.76 ± 3.1 |

Results for the coefficient of rolling friction between POM spheres and a POM plate for the particle-particle contacts and between particles and the wall materials (acryl, metal) for the particle-wall contacts each averaged over 10 experiments are listed in Table 17. For two different sized POM spheres the average of the respective values is applied. The large standard deviations indicate the need of a further adjustment of these initial values.

3.5 Coefficient of restitution

In order to determine the coefficient of restitution, a particle which is on the end of a pendulum is dropped so that it bounces against a wall (comp. Fig. 88a) or another particle which has a velocity of $v_2 = 0$ before the collision according to Alonso-Marroquín et al. [157] (comp. Fig. 88b).

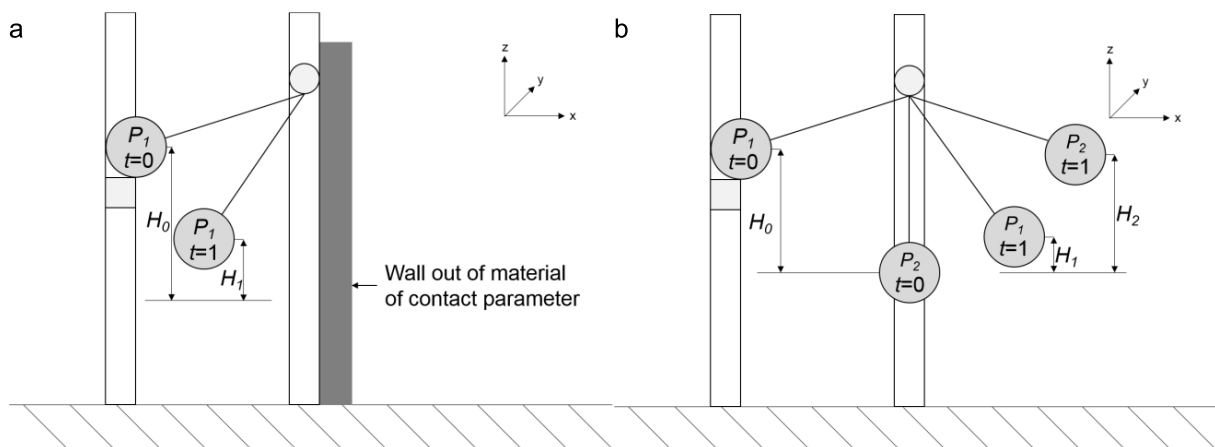


Fig. 88: Determination of the restitution coefficient for (a) particle-wall and (b) particle-particle contacts according to Alonso-Marroquín et al. [157].

For the particle wall collisions this experimental setup was chosen instead of a drop test to have the same external effects in both experiments. Note that the procedure in Fig. 88b is only applied for POM spheres, whereas for quartz gravel particles the setup in Fig. 88a is used with a wall of the same material due to their arbitrary shapes, resulting in rotations or skewed rebounds. Furthermore, it should be mentioned, that these experiments are more difficult if smaller particles with a low mass compared to the mass of the thread are applied.

For the particle-wall contact, the velocities before (u_1) and after the rebound (v_1) are measured. Alternatively, the heights before the particle drop (H_0) and at the highest point after the rebound (H_1) could be measured. Thus, the particle-wall restitution coefficient is obtained by

$$e_{PW}^n = -v_1/u_1 = \sqrt{H_1/H_0}. \quad (189)$$

The restitution coefficient for a particle-particle contact is determined by

$$e_{PP}^n = -(v_1 - v_2)/u_1 = (\sqrt{H_2} - \sqrt{H_1})/\sqrt{H_0}, \quad (190)$$

where u_1 and v_1 are the velocities and H_0 and H_1 the heights of particle P_1 before and after the collision, respectively. Furthermore, v_2 is the velocity and H_2 the height of particle P_2 after the collision with particle P_1 .

Results for the coefficient of restitution between particles and the same material (each size of POM sphere with itself and the other sizes and quartz gravel with a gravel plate) for the particle-particle contact and between particles and the wall materials (acryl, metal) for the particle-wall contacts are listed in Table 18.

Table 18: Coefficient of restitution.

| Contact partner | | POM 5 mm | POM 7 mm | POM 10 | Contact partner | | Gravel |
|----------------------|----------------|-------------|-------------|-------------|--|----------------|-------------|
| Acryl (side walls) | e_{PW}^n [-] | 0.88 ± 0.01 | 0.76 ± 0.01 | 0.81 ± 0.05 | Acryl (side walls) | e_{PW}^n [-] | 0.81 ± 0.01 |
| Metal (screen wire) | e_{PW}^n [-] | 0.80 ± 0.01 | 0.83 ± 0.01 | 0.74 ± 0.04 | Metal (screen wire) | e_{PW}^n [-] | 0.48 ± 0.02 |
| POM (5 mm particle) | e_{PP}^n [-] | 0.84 ± 0.02 | 0.81 ± 0.04 | 0.85 ± 0.03 | Quartz gravel plate (gravel particle) | e_{PP}^n [-] | 0.77 ± 0.01 |
| POM (7 mm particle) | e_{PP}^n [-] | 0.81 ± 0.04 | 0.82 ± 0.02 | 0.86 ± 0.03 | | | |
| POM (10 mm particle) | e_{PP}^n [-] | 0.85 ± 0.03 | 0.86 ± 0.03 | 0.87 ± 0.03 | | | |

4. Adjustment of DEM parameters of particles as bulk material

After the calibration at the particle level in section 3 the parameters have to be adjusted based on the bulk behavior due to two reasons. Firstly, it could be possible, that due to particle size or shape it is not possible to perform an accurate calibration at the single particle level where assumptions have to be made. A second aspect is that parameter sets obtained at the single particle level and at the bulk level differ from each other. This is a result of inaccuracies related to the single particle measurements for which it is compensated for in the bulk calibration or of the models (e.g. insufficient approximation of shape or of contact models). In a first step before

the adjustment, three different bulk experiments with several settings are conducted. They are later compared with respective simulations to test the DEM parameters obtained by the single particle experiments before adjusting the DEM parameters to minimize the differences between the results of simulations and experiments. In the bulk experiments the static and dynamic angles of repose which are mainly influenced by the friction coefficients between particles (static) and particles and walls (dynamic) are measured. Furthermore, the bed height on a vibrating plate is determined, where the restitution coefficient is the crucial parameter. Note that in all investigations with POM spheres the same mass for each fraction and for gravel the particle size distribution from Fig. 84 is applied. In all investigations the appliances are filled according to a defined filling degree or level. Due to different bulk densities in case of POM spheres, the resulting average particle mass varies slightly dependent on the applied particle size classes.

4.1 Adjustment of DEM parameters by a genetic algorithm

For obtaining the best fit between simulations and experiments for all investigated bulk experiments, an optimization tool based on a genetic algorithm [240] like the one used for the shape approximation in section 3.2 is used. The whole adjustment procedure for one particle distribution and an arbitrary number of bulk calibration processes is outlined in Fig. 89.

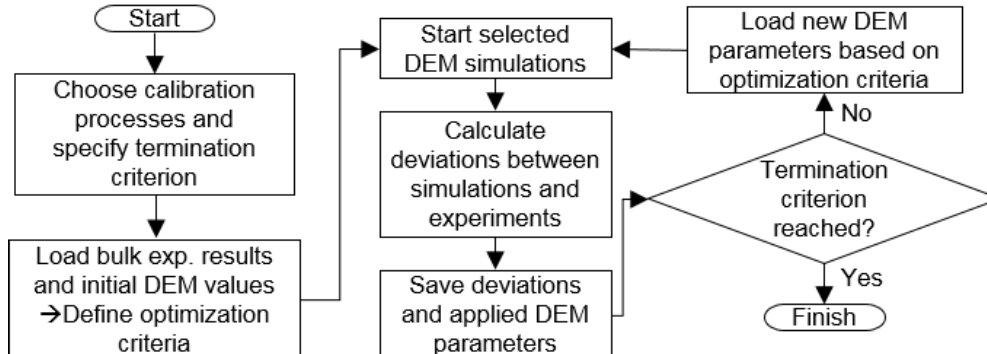


Fig. 89: Algorithm to adjust the DEM parameters for the best fit between simulations and experiments.

Therein, the termination criterion can be a defined number of generations or a specified change in deviations between two generations. The algorithm is fed with the results shown in Fig. 91, Table 21 and Table 23 and the initial DEM parameters listed in Table 15, Table 16 and Table 18. The DEM parameters are changed in defined physical boundaries, supporting a quick convergence of the optimization. As DEM simulations are dependent on input parameters in a complex way the generations required for convergence are varying. It depends on the quality of the initial values, their difference to the values after optimization and if the initial values lead to consistent results. At the most, 100 generations were enough to get good results, which were not further improved in consecutive generations; often 50 generations were sufficient. Due to calculating up to 100 generations for each adjustment, one main criterion is

the time needed for one simulation. Thus, the dimensions of the bulk tests are chosen as small as possible while still obtaining suitable results.

In case of the gravel particles the procedure is performed one time for all size classes due to the simplification of using the same friction and restitution coefficients for each particle. In case of the POM spheres with three discrete size classes, one possible method would be to directly fit the DEM parameters for all size classes. However, in this investigation, all monodisperse cases are fitted before the bidisperse cases to reduce the amount of adjustable parameters in one adjustment procedure and thereby, to enhance the quality of the optimization. The obtained parameters are then applied for the case with three different particle size classes.

4.2 Static angle of repose

Static angle of repose measurements were conducted in a slump test by releasing POM spheres and gravel particles contained in a hollow acrylic cylinder onto an acrylic and a steel surface (Fig. 90a). To prevent excessive spreading of spheres, an acrylic ring as boundary is used for both materials. The static angle of repose α_{sta} is measured after reaching a steady state. The experimental and simulative properties (Figs. 90b,c) are listed in Table 19.

Table 19: Experimental and simulative properties for measuring the static angle of repose.

| Properties | POM | Gravel |
|-------------------------|-------------|--------|
| Bed height [m] | 0.065 | 0.040 |
| Cylinder velocity [m/s] | 0.011 | 0.011 |
| Cylinder diameter [m] | 0.070 | 0.035 |
| Ring diameter [m] | 0.125 | 0.072 |
| Particle mass [kg] | 0.195-0.221 | 0.060 |

For the simulations, DEM parameters obtained in section 3 are applied in the first step of the adjustment. Therein, the angle of repose is mainly influenced by the rolling (in case of spheres) and sliding friction coefficient between particles. This simulation is time-determining for the whole adjustment procedure, due to needing the longest time for reaching the steady state. Therefore, it should be calculated with a larger number of processors n_{proc} as used for the other simulations ($n_{proc}/2$ for the tumbling and approx. $n_{proc}/4$ for the vibrating plate simulation). Note, that the DEM code used is parallelized using domain decomposition.

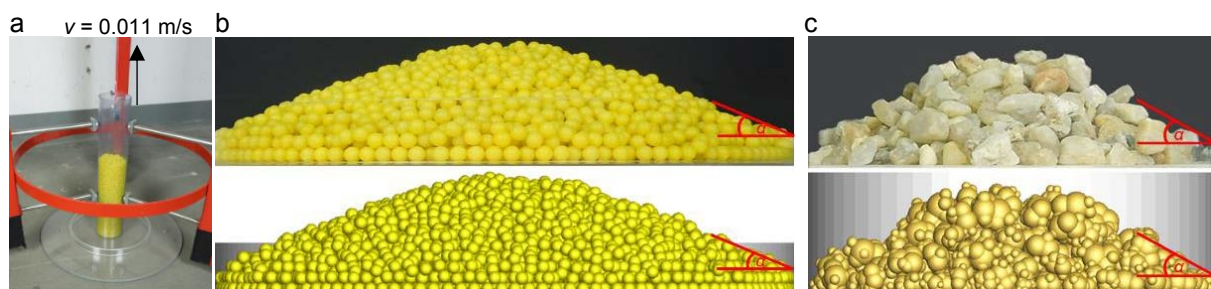


Fig. 90: (a) Experimental set-up to measure the static angle of repose and (b) resulting piles of 5mm POM spheres as well as (c) piles of gravel in the experiments (top) and the simulations (bottom).

Most of the results for POM spheres and for gravel particles applying the initial DEM parameters reveal a good agreement between simulations and experiments with deviations below the standard deviations (comp. Fig. 91). In contrast, the simulations with 7 mm and 10 mm POM spheres (not shown in Fig. 91) and with 3 size classes applying an acryl surface form out too flat static angles of repose.

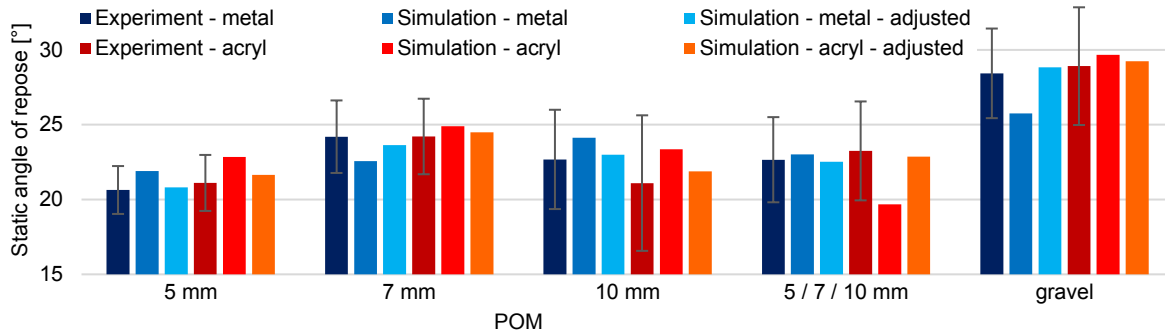


Fig. 91: Experimental results of measuring the static angle of repose α_{sta} and comparison to simulations applying DEM parameters determined in section 3 as well as after the adjustment.

By adjusting the DEM parameters (comp. Table 24), the deviations are reduced for all cases but particularly for the polydisperse simulations where 7 mm and 10 mm spheres are in contact (averagely from 9.59 % to 2.15 %).

4.3 Dynamic angle of repose

For determining the dynamic angle of repose α_{dyn} , tumbling tests with a hollow acrylic and a metal cylinder (Fig. 92a) are conducted for POM spheres (Figs. 92b,c) and gravel particles (Figs. 92d,e) with three different velocities and 30 % filling (comp. Table 20).

Table 20: Experimental and simulative properties for measuring the dynamic angle of repose.

| Properties | POM | Gravel |
|-------------------------|--------------|--------|
| Cylinder velocity [rpm] | 10 / 15 / 20 | |
| Cylinder diameter [m] | 0.085 | |
| Cylinder depth [m] | 0.050 | |
| Filling degree [%] | 30 | |
| Particle mass [kg] | 0.061-0.069 | 0.130 |

The dynamic angle of repose was measured at 10 different points in time after a transient period of one second.

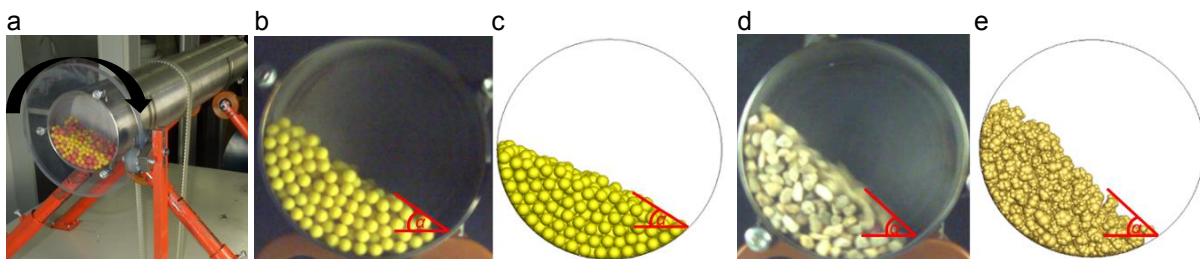


Fig. 92: (a) Experimental set-up to measure the dynamic angle of repose as well as resulting piles of (b,c) 5mm POM spheres and (d,e) gravel in (b,d) the experiments and (c,e) the simulations.

The results, which are mainly influenced by the friction coefficients between particles and walls are presented in Table 21. All investigations for POM spheres and for gravel with the initial DEM parameters for an acrylic cylinder obtained in section 3 reveal a much lower dynamic angle of repose in the simulations than in the experiments (average deviations of 26.39 %). The simulations with the metallic cylinder also reveal lower angles which are however closer to the experimental ones (average deviations of 18 %). The low initial friction coefficient between particles and acrylic walls leads to slip which is prevented to some extent by the larger coefficient in case of metallic walls.

Table 21: Experimental results of measuring the dynamic angle of repose α_{dyn} and comparison to simulations applying DEM parameters determined in section 3 as well as after the adjustment.

| Dynamic angle of repose α_{dyn} [°] | POM | | | | Gravel |
|--|--------------|--------------|--------------|---------------|---------------|
| | 5 mm | 7 mm | 10 mm | 5 / 7 / 10 mm | 3.15 - 5.6 mm |
| Experiment - metal - 10 rpm | 28.26 ± 2.15 | 31.73 ± 4.06 | 23.26 ± 2.74 | 32.03 ± 3.76 | 40.81 ± 1.98 |
| Simulation - metal - 10 rpm | 25.39 | 23.92 | 20.65 | 23.76 | 39.49 |
| Simulation - metal - 10 rpm - adjusted | 29.79 | 32.92 | 23.15 | 30.64 | 41.49 |
| Experiment - acryl - 10 rpm | 33.40 ± 2.14 | 38.81 ± 1.34 | 32.25 ± 3.37 | 33.91 ± 2.61 | 42.82 ± 1.68 |
| Simulation - acryl - 10 rpm | 24.01 | 27.87 | 22.81 | 25.68 | 28.97 |
| Simulation - acryl - 10 rpm - adjusted | 33.01 | 37.87 | 29.81 | 32.25 | 42.54 |
| Experiment - metal - 15 rpm | 29.80 ± 1.73 | 32.16 ± 4.32 | 24.70 ± 4.74 | 31.31 ± 3.51 | 40.99 ± 1.28 |
| Simulation - metal - 15 rpm | 25.06 | 24.58 | 22.8 | 24.93 | 38.96 |
| Simulation - metal - 15 rpm - adjusted | 29.49 | 33.91 | 25.49 | 31.17 | 41.16 |
| Experiment - acryl - 15 rpm | 32.82 ± 1.31 | 35.75 ± 3.88 | 32.59 ± 3.52 | 34.85 ± 2.53 | 42.95 ± 1.73 |
| Simulation - acryl - 15 rpm | 23.5 | 25.6 | 22.6 | 26.82 | 29.23 |
| Simulation - acryl - 15 rpm - adjusted | 32.5 | 35.35 | 29.68 | 33.58 | 43.89 |
| Experiment - metal - 20 rpm | 30.33 ± 2.31 | 29.87 ± 2.89 | 26.42 ± 2.55 | 32.58 ± 2.38 | 40.39 ± 1.61 |
| Simulation - metal - 20 rpm | 24.62 | 21.7 | 21.28 | 25.02 | 41.19 |
| Simulation - metal - 20 rpm - adjusted | 29.06 | 30.7 | 24.78 | 32.39 | 41.59 |
| Experiment - acryl - 20 rpm | 33.93 ± 2.77 | 35.29 ± 2.56 | 33.72 ± 2.71 | 34.29 ± 2.33 | 42.57 ± 1.87 |
| Simulation - acryl - 20 rpm | 23.3 | 25.38 | 24.99 | 25.8 | 29.44 |
| Simulation - acryl - 20 rpm - adjusted | 32.3 | 34.38 | 31.99 | 32.56 | 43.13 |

After adjusting the DEM parameters (comp. Table 24) and particularly by increasing the friction coefficient between particles and walls, the deviations of the dynamic angle of repose are all minimized significantly and below the standard deviation (average deviations of 3.18 %).

4.4 Bed heights on a vibrating plate

In order to obtain the dynamic bed height, tests on a vibrating metal plate with three different degrees of filling are conducted (comp. Fig. 93; here with one particle layer of 5 mm spheres or 5 % filling) for POM spheres (Figs. 93b,c) and gravel particles (Figs. 93d,e). The average maximum bed height (referred to as “Top”) and the average distance between the lowest particles and the bottom plate (referred to as “Bottom”) at different points in time are measured using the properties listed in Table 22. Therein, the vibration parameters are obtained by an

accelerometer which measures an amplitude of around 1.2 ± 0.04 mm in z-direction and only minor amplitudes in the horizontal (x- / y-stroke < 0.1mm) at a frequency of 54 Hz. Note that the bed height is analyzed after one second when a continuous motion of the plate is ensured.

Table 22: Experimental and simulative properties for measuring the dynamic bed height.

| Properties | POM | Gravel |
|------------------------------|---|-----------------------|
| Length, width and height [m] | 0.045 x 0.045 x 0.100 | |
| Amplitude [mm] | 1.2 ± 0.04 | |
| Frequency [Hz] | 54 | |
| Stroke angle [°] | ~90 | |
| Filling degree [%] | 1 Layer (5-10) / 20 / 50 | |
| Particle mass [kg] | 0.007-0.013 / 0.029-0.033 / 0.076-0.083 | 0.013 / 0.065 / 0.162 |

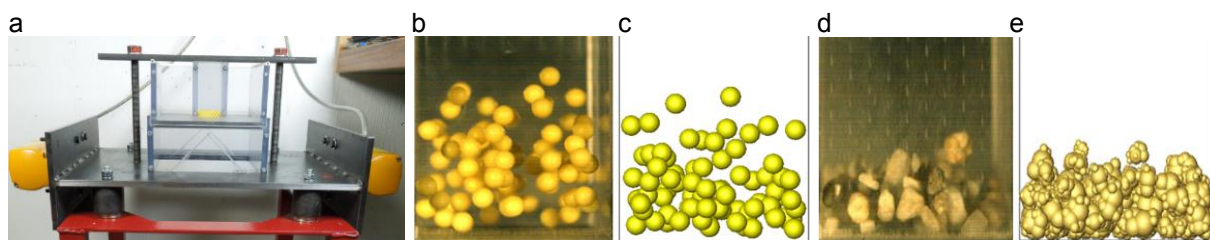


Fig. 93: (a) Experimental set-up to measure the bed height on a vibrating plate as well as resulting particle beds for a filling of one layer of (b,c) 5 mm POM spheres and (d,e) gravel in (b,d) the experiments and (c,e) the simulations.

Table 23: Experimental results of measuring the dynamic bed height on a vibrating plate and comparison to simulations applying DEM parameters determined in section 3 as well as after the adjustment.

| Average bed height [mm] | POM | | | | Gravel |
|--|-------|-------|-------|---------------|---------------|
| | 5 mm | 7 mm | 10 mm | 5 / 7 / 10 mm | 3.15 - 5.6 mm |
| Experiment - 1 Layer - Top | 41.40 | 35.70 | 35.50 | 49.90 | 20.70 |
| Simulation - 1 Layer - Top | 39.80 | 42.10 | 38.86 | 43.64 | 21.54 |
| Simulation - 1 Layer - Top - adjusted | 41.20 | 37.31 | 36.87 | 49.64 | 20.88 |
| Experiment - 1 Layer - Bottom | 3.81 | 3.99 | 6.26 | 8.07 | 2.74 |
| Simulation - 1 Layer - Bottom | 2.69 | 4.09 | 6.83 | 3.58 | 1.14 |
| Simulation - 1 Layer - Bottom - adjusted | 4.20 | 4.05 | 6.45 | 4.62 | 1.97 |
| Experiment - 20 % - Top | 35.90 | 37.10 | 46.00 | 40.90 | 29.00 |
| Simulation - 20 % - Top | 30.85 | 36.55 | 46.46 | 34.12 | 26.40 |
| Simulation - 20 % - Top - adjusted | 35.77 | 37.29 | 46.44 | 40.38 | 27.50 |
| Experiment - 20 % - Bottom | 1.39 | 1.82 | 4.07 | 3.46 | 2.44 |
| Simulation - 20 % - Bottom | 0.74 | 1.24 | 2.50 | 0.87 | 0.80 |
| Simulation - 20 % - Bottom - adjusted | 1.35 | 1.34 | 2.69 | 1.21 | 0.95 |
| Experiment - 50 % - Top | 56.20 | 54.10 | 58.60 | 59.30 | 58.22 |
| Simulation - 50 % - Top | 53.15 | 53.69 | 54.41 | 54.53 | 59.97 |
| Simulation - 50 % - Top - adjusted | 55.90 | 54.4 | 57.80 | 57.24 | 59.00 |
| Experiment - 50 % - Bottom | 1.17 | 1.29 | 1.18 | 0.98 | 2.42 |
| Simulation - 50 % - Bottom | 0.81 | 0.92 | 0.73 | 0.64 | 1.20 |
| Simulation - 50 % - Bottom - adjusted | 1.90 | 2.10 | 2.50 | 1.93 | 1.23 |

The experimental results presented in Table 23, which are mainly influenced by the coefficient of restitution, are compared to simulations applying the same properties (comp. Table 22).

They are initially obtained with the DEM parameters determined in section 3 and thereafter, with the best fit of the adjustment.

Applying the initial DEM parameters, the results reveal some good agreements between simulations and experiments but also deviations up to 17 % between the “Top” values in some cases. The “Bottom” values are mostly lower in the simulations than in the experiments but the absolute deviations are less than one respective particle in all cases. After the adjustment, the deviations of the “Top” values are minimized significantly (all below 10 %), whereas the “Bottom” values in the simulations are only slightly adjusted and still reveal a few deviations.

5. Application of the adjusted DEM parameters for batch screening

The DEM parameters after the adjustment of section 4 are listed in Table 24.

Table 24: DEM parameters after the adjustment for POM spheres and quartz gravel particles. For gravel, the rolling friction is neglected.

| Contact partner 1 | Contact partner 2 | μ_c [-] | μ_{roll} [m] | e^n [-] |
|-------------------|--|--------------------------|--------------------------------|--------------------------|
| 5 mm POM | Acryl (side walls) / metal (screen wire) | 0.6649 / 0.4074 | 4.30E-05 / 6.99E-05 | 0.8145 / 0.8412 |
| 7 mm POM | | 0.4415 / 0.3561 | 8.66E-05 / 6.01E-05 | 0.7531 / 0.8013 |
| 10 mm POM | | 0.5330 / 0.2816 | 5.16E-05 / 4.91E-05 | 0.8195 / 0.8055 |
| Gravel particle | | 0.3710 / 0.5461 | - / - | 0.5334 / 0.3966 |
| 5 mm POM | 5 mm POM / 7 mm POM / 10 mm POM | 0.2395 / 0.3237 / 0.2935 | 3.83E-05 / 4.00E-05 / 3.30E-05 | 0.8676 / 0.8686 / 0.7701 |
| 7 mm POM | 7 mm POM / 10 mm POM | 0.4882 / 0.4673 | 3.89E-05 / 8.92E-05 | 0.7303 / 0.8209 |
| 10 mm POM | 10 mm POM | 0.4229 | 3.844E-05 | 0.7653 |
| Gravel particle | Gravel particle | 0.5381 | - | 0.8676 |

Particularly, the sliding friction coefficients between particles and walls have to be increased by an average factor of 2.68 and 1.96 for acryl and metal, respectively. Additionally, the sliding friction between particles is increased by an average factor of 1.27 whereas the rolling friction and the restitution coefficients are adjusted in both directions. All these parameters are applied for batch screening of well mixed POM spheres with three different size classes and gravel particles with the particle size distribution outlined in Fig. 84. The particle and experimental properties as outlined in Table 15 and Table 25 are used in the simulations.

Table 25: Experimental properties for batch screening experiments.

| Properties | POM / gravel |
|------------------------|---|
| Floor area [m] | 0.185 x 0.185 |
| Aperture size [mm] | 8.00 ± 0.02 / 5.80 ± 0.01 and 4.00 ± 0.01 |
| Wire diameter [mm] | 1.5 ± 0.01 |
| Scree wire profile [-] | rectangular |
| Particle mass [kg] | 1 |
| Amplitude [mm] | 1.20 ± 0.04 |
| Frequency [Hz] | 44 and 54 |
| Stroke angle [°] | ~90 |

The vibration parameters are obtained like in section 4.4, but here the transient period of the screen motion before $t = 0.61$ s is also measured and applied to the simulations as well as the removal of the retaining plate below the apertures which lasts $t = 0.1 \pm 0.02$ s.

Investigations for POM spheres are performed for two different frequencies and the results averaged over a sufficient number of experiments (standard deviation represented by the vertical error bars) and simulations reveal a good agreement with only a few deviations between simulations and experiments (comp. Fig. 94a). The horizontal error bars represent the response time of the balance. The average deviations are for 44 Hz 0.0164 and for 54 Hz 0.0083. In case of quartz gravel, a frequency of 54 Hz and two different mesh sizes are applied resulting in a fast particle depletion for the aperture size of 5.8 mm and in a low passage rate for the aperture size of 4 mm.

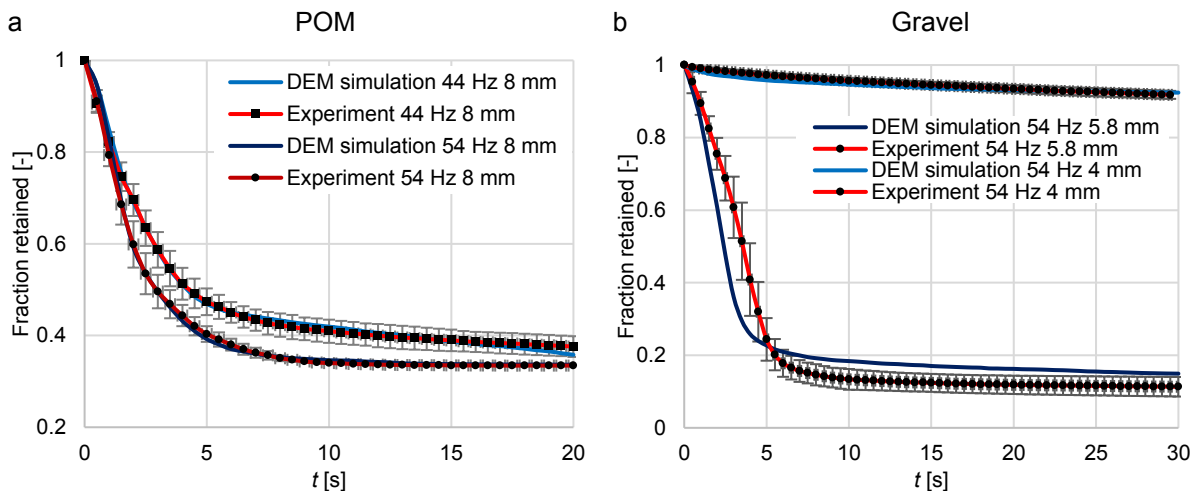


Fig. 94: Fraction retained on the screen over time applying (a) POM spheres for two different frequencies with a mesh size of 8 mm and (b) gravel for one frequency with mesh sizes of 5.8 mm and 4 mm all obtained by experimental investigations (results are averaged over 10 experiments) and DEM simulations, respectively.

The results for the latter also reveal low deviations (average: 0.0074). In contrast, the results with an aperture size of 5.8 mm reveal larger deviations (average: 0.0554) particularly in the first five seconds, where the particles in the simulations pass faster than in the experiment. Thereafter, the passage rate is reduced and too many particles remain on the screen. Reasons for the deviations can be the rounded shape of the particles increasing the stratification and passing possibility, the scaling in the particle size classes based on pixels of images or the low number of different shapes per size class used in the simulations. To overcome these discrepancies will be focused on in further investigations.

6. Conclusions

DEM parameters for POM spheres of three different size classes and quartz gravel particles with a realistic size distribution have first been determined by single particle tests and later applied to simulations representing three small bulk experiments. The static and dynamic angle of repose as well as the dynamic bed height are measured and particularly, the measurement

of the dynamic angle of repose reveals large deviations between simulations and experiments. Motivated to reduce these discrepancies, the DEM parameters are automatically adjusted with an optimization tool, whereby the deviations between simulations and experiments are minimized significantly. The deviations averaged over all bulk tests are reduced from 9.59 % to 2.15 % for the static angle of repose, from 22.19 % to 3.18 % for the dynamic angle of repose and from 7.25 % to 4.15 % for the dynamic bed height (only the “Top” value). The adjusted DEM parameters are then applied to batch screening simulations and reveal a good agreement with respective experiments in case of POM spheres and for quartz gravel with a low passage rate. In contrast, in case of the quartz gravel particles applying a large aperture size, the simulation overpredicts the passage rate in the first five seconds but more particles remain on the screen afterwards which indicates that the screening simulation needs further improvement. Investigations with another less rounded particle shape are currently ongoing and more different shapes will be applied for each size class. Nevertheless, it could be shown that the results of single particle tests can only be used as initial values for DEM parameters, which have to be further adjusted to minimize deviations between simulations and bulk experiments. After an appropriate automatic adjustment of the DEM parameters, the results of bulk experiments applying spherical and non-spherical particles and the results of more complex processes applying spheres are represented well. In further studies, the batch screening will be integrated in the adjustment process to enhance the accuracy.

Acknowledgements

The authors gratefully acknowledge the support by DFG within project SPP 1679 through grant number KR3446/7-2. The original form of the DEM code “DEM-Calc” applied is based on a development of LEAT, Ruhr-Universität Bochum, Germany. The code “DEM-Calc” has then been continuously extended both at Ruhr-Universität Bochum and Technische Universität Berlin, Germany. We thank all who have contributed.

VIII. Trennkurven in Siebung und Gegenstromsichtung bei geringen Gutbeladungen

Christian Spötter, Frederik Elskamp, Manuel Hennig, Ulrich Teipel, Alfred P. Weber, Harald Kruggel-Emden

Das folgende akzeptierte Manuskript erschien als Zeitschriftenversion in Spötter C., Elskamp F., Hennig M., Teipel U., Weber A.P., Kruggel-Emden H., 2016, DEM-Simulation der Trennkurven in Siebung und Gegenstromsichtung bei geringen Gutbeladungen, Chemie Ingenieur Technik 89, 1726–1738 und kann unter <https://doi.org/10.1002/cite.201600156> gefunden werden. Copyright Wiley-VCH Verlag GmbH & Co. KGaA. Reproduced with permission.

Zur Abtrennung unterschiedlich großer Partikeln sind in der Feststoffverfahrenstechnik trockene Klassierprozesse zur Herstellung enger Fraktionen von großer Bedeutung. Um das Trennverhalten von Strömungs- und Siebklassierprozessen genauer vorhersagen zu können, wurden experimentelle Resultate mit DEM-Simulationen verglichen. Bei der Siebklassierung wurde der Einfluss der Partikelform auf den Trennprozess betrachtet, während das Partikelverhalten zwischen den Schaufeln eines Abweiseradsichters mit der DEM simuliert wurde. Die Kombination aus DEM und Experiment ermöglicht es, Modellvorhersagen durch Ermittlung prozessspezifischer Parameter zu verbessern und Klassiermodelle abzuleiten, die in dynamischen Feststofffließschemasimulationen verwendet werden.

Schlagwörter: Sichtluftströmung, Partikelbewegung, DEM-Simulation, Trennprozess, Siebung, Windsichtung

Separation curves of screening and air classifying processes at low material loadings

For the separation of particles with different sizes, dry classification processes are of great importance for the production of narrow fractions in the solid processing technology. To be able to more accurately predict the separation behavior of flow and sieve classifying processes, experimental results were compared with DEM simulations. In screening, the influence of the particle shape on the separation process was considered while the particle behavior between the paddles of a deflector wheel classifier was simulated with the DEM. The combination of DEM simulation and experiment makes it possible to improve model predictions by identifying process-specific parameters and to develop classification models, which are applicable in dynamic flowsheet simulations of solids processes.

Keywords: airflow, particle movement, DEM simulation, separation process, sieving, air sifting

1. Einleitung

Trockene Klassierprozesse sind in der Feststoffverfahrenstechnik sowohl zur Abtrennung von Fehlkorn, z.B. hinter einer Mühle, als auch zur Herstellung enger Fraktionen von großer Bedeutung. Sie lassen sich prinzipiell in Strömungs- und Siebklassierung unterteilen. Für beide Klassierverfahren werden Trennfunktionen T_i verwendet, die auf die gleiche Prozessgleichung zurückgehen. Das erste Modell, das auf der Lösung dieser Prozessgleichung basiert, stammt von Molerus (Gl. (191)) [53]. Es wurde ursprünglich für die Windsichtung entwickelt, aber später auch für den Abweiseradsichter und für die Siebung eingesetzt. In der Formel von Molerus ist x_t die Trenngrenze, x die Laufvariable des Partikeldurchmessers einer Kugel mit gleicher Sinkgeschwindigkeit gegenüber der Trenngrenze sowie k ein dimensionsloser Faktor für die Trennschärfe und somit die Steilheit der Trennfunktion. Die Formel des Molerus-Modells für den Abweiseradsichter lautet:

$$T_i = \frac{1}{1 + \left(\frac{x_t}{x}\right)^2 \cdot \exp\left(k \cdot \left(1 - \left(\frac{x}{x_t}\right)^2\right)\right)} \quad (191)$$

Nach mehreren Verbesserungen des Modells durch Rumpf [54], Senden [55,56] und Schubert [12] stellte Husemann eine erweiterte Modellvorstellung vor, die erstmals geometrische Daten des Sichters sowie Betriebsparameter berücksichtigte [57]. Alle diese Modelle für den stationären Betrieb eines Abweiseradsichters gehen aber von einer Gegenstromklassierung der ungestörten Einzelpartikel aus. Dabei werden weder Stöße zwischen den Partikeln noch mit den Schaufeln berücksichtigt, die erheblichen Einfluss auf die Partikelbahnen nehmen können. Neuere Untersuchungen zur Partikelbewegung im Abweiseradsichter haben jedoch gezeigt, dass sogar die bisher benutzten Vorstellungen über den Zusammenhang zwischen Partikelbewegung und resultierendem Trenngrad nicht korrekt sind [253]. Insbesondere erfahren die einströmenden Partikel erst nach der Kollision mit der nacheilenden Schaufel eine nennenswerte absolute tangentielle Geschwindigkeitskomponente und damit eine Zentrifugalkraft. Als erster Ansatz soll hier aufgezeigt werden, wie diesem Sachverhalt durch die Ermittlung der effektiven Sinkgeschwindigkeit aus den gemessenen Partikelumfangsgeschwindigkeiten nach dem Stoß mit der nacheilenden Schaufel und unter Berücksichtigung der Strömungseinschnürung zwischen den Schaufeln Rechnung getragen werden kann. Für die Siebung schlugen Dong et al. [49] eine Gleichung für die Vorhersage des Durchtritts in Gewichtsprozent nach Partikelgröße vor, die sich nach erfolgreicher Anpassung in eine Trennfunktion umrechnen lässt:

$$W_p = 1 - (1 - p)^N \quad (192)$$

mit

$$p = \frac{(w - x)(w \cos(\theta) - x)}{(w + b)^2 \cos(\theta)} \quad (193)$$

und

$$N = k \left(\frac{Af}{\sqrt{xg}} \right)^\alpha \left(\frac{x}{L^*} \right)^\beta \theta^\gamma \quad (194)$$

Dabei ist die Wahrscheinlichkeit des Durchtritts p abhängig vom Maschendurchmesser w , der Partikelgröße x , dem Stabdurchmesser b und dem Siebneigungswinkel θ . Die Anzahl der Versuche N , die jedes Partikel für einen Durchtritt hat, wird durch die Amplitude A , die Frequenz f , den Partikeldurchmesser x , die Gravitationskraft g , die Siebdecklänge L^* , den Siebneigungswinkel θ und die anpassbaren Parameter k , α , β und γ beeinflusst. Neben den probabilistischen Modellen [225,228] wie dem Modell von Dong [49] existieren für den stationären Siebprozess auch kinetische Ansätze [45,226] (vergl. [241]). In der Literatur finden sich ebenfalls Arbeiten von Dehghani [52] sowie Nakajima und Whiten [229,254], bei denen zusätzlich zum zeitlichen oder örtlichen Durchtritt die Partikelform berücksichtigt wird und die Ergebnisse leicht in Trennkurven umgesetzt werden können. Für die Siebung wurde die Diskrete-Elemente-Methode (DEM) seit den ersten kleineren diskontinuierlichen Untersuchungen zu Beginn dieses Jahrhunderts durch Shimosaka [46] schon in verschiedenen Fällen genutzt, um einen besseren Einblick in den Prozess zu erhalten. So studierten Li et al. den Einfluss der Partikelschichtdicke [189] und der maschennahen Partikeln [50] bei kontinuierlichen Siebprozessen. Weitere Studien beschäftigten sich mit der Siebmaschenstruktur [188,191,236] und den Betriebseinstellungen [35,192,237,238,243]. Die für das Durchtreten durch die Siebmaschen relevante Form der Partikeln wurde erst in den letzten Jahren stärker berücksichtigt [6,198,236,241,243,244].

Um die komplexen Teilprozesse besser verstehen zu können, werden in diesem Beitrag experimentelle Ergebnisse zur Strömungs- und Siebklassierung mit Resultaten der DEM verglichen, welche die Partikelbewegung unter Berücksichtigung von Partikel/Partikel- und Partikel/Wand-Stößen berechnet. Während bei der Siebung speziell der Einfluss der Partikelform auf das Trennverhalten untersucht wird, steht beim Abweiseradsichter die Erfassung der Partikelbewegung mittels Hochgeschwindigkeitskamera bei geringen Gutbeladungen, bei denen die Partikel/Partikel-Stöße mittels DEM erfasst werden, im Vordergrund. Beim Abweiseradsichter wird die Strömung zwischen den Sichtschaufeln aus der Visualisierung mittels Tracer-Partikeln übernommen. Schließlich werden aus den berechneten Partikelbahnen Trennfunktionen abgeleitet und mit den gemessenen Trennkurven verglichen, wobei auch die Grenzen der Anwendbarkeit eines Modellansatz basierend auf dem an der Trenngrenze x_t (Gl. (204)) angreifendem Kräftegleichgewicht erörtert werden.

2. Material und Methoden

2.1 Partikelbewegung und Trennkurven bei der Siebung

Bei der Siebklassierung wird das Aufgabegut entsprechend des charakteristischen Merkmals, der Partikelgröße x , mittels Sieb in eine Grobgut- und in eine Feingutfraktion getrennt. Als Trennkorngröße gilt bei Siebvorgängen die Maschenweite w . Bei einer idealen Trennung sind alle Partikel im Feingut kleiner als die Maschenweite und alle Partikel im Grobgut größer als die Maschenweite. Im Fall von realen, nicht sphärischen Partikelformen können Partikel, welche größer als die Trennkorngröße sind, ins Feingut gelangen. Ebenso können sich nach der Klassierung feine Partikel im Grobgut befinden. Diese Anteile werden als Fehlkorn bezeichnet. Um die Güte des Trennvorganges darstellen zu können, wird die Trennfunktion $T(x)$ ermittelt, welche den Anteil des Aufgabegutes wiedergibt, der nach der Klassierung dem Grobgut zugeordnet ist.

Für den experimentellen Teil der Siebung wurde ein Kreisschwingsieb im halbindustriellen Maßstab verwendet, mit dem Änderungen der Trennkurven im stationären Zustand [255] und bei zeitlichen Änderungen der Betriebsparameter im instationären Betrieb untersucht werden können. Außerdem ist für beide Betriebszustände eine Erfassung der Trennfunktion entlang der Sieblänge möglich, wozu das Feingut entlang der Siebfläche in Behältern gesammelt wird. Eingesetzt wird ein Kreisschwingsieb der Fa. Siebtechnik GmbH, Mühlheim, V 3/10/I L (Abb. 95a).

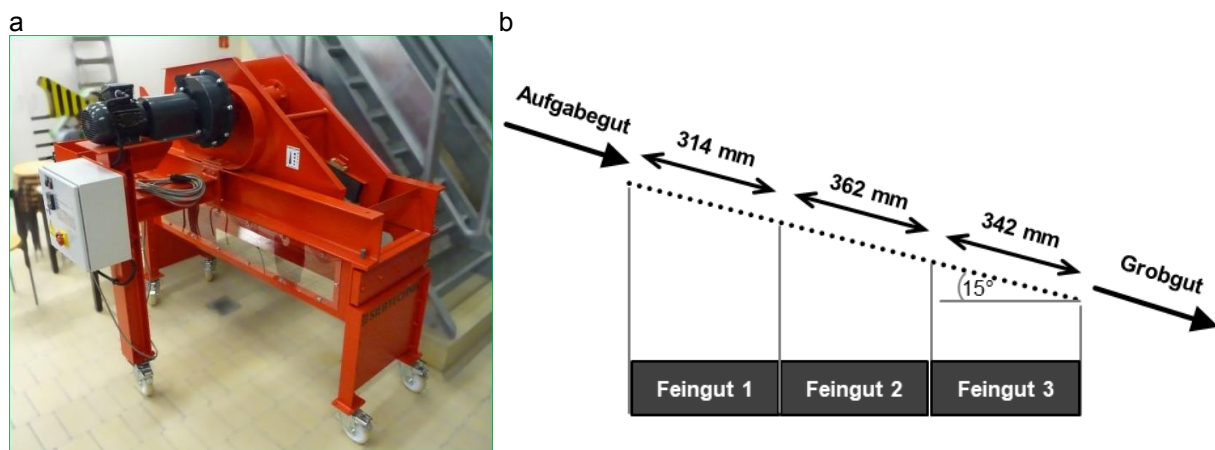


Abb. 95: (a) Kreisschwingsieb der Fa. Siebtechnik GmbH und (b) Auffangbehälter entlang der Siebfläche.

Die Siebfläche beträgt $0,3 \text{ m}^2$ (Nutzlänge = 1000 mm ; Nutzbreite = 300 mm). Unter der Siebfläche ist ein Deck für Siebhilfen zur Abreinigung der Siebmaschen angebracht. Die Schwingung wird mittels einer Erregerwelle durch zwei Unwuchten links und rechts des Siebkastens erzeugt, die in Gewicht und Dimension variierbar sind. Ein Unwuchtmotor erzeugt in Kombination mit O-Federn eine ellipsenförmige Schwingung des Siebdecks. Folgende Betriebsparameter sind an der Siebmaschine einstellbar: Siebkasteneigung (von 0° bis 40°), Drehzahl (zwischen 880 min^{-1} und 1860 min^{-1}) und Amplitude, wobei die Minimal- und

Maximalwerte von Drehzahl und Amplitude gekoppelt sind. Für die Siebeläge stehen Maschenweiten von $w = 0,125$ mm, $w = 0,25$ mm, $w = 0,5$ mm und $w = 1$ mm zur Verfügung.

Der Trenngrad $T(x)$ kann mittels mehrerer Behälter unter dem Siebboden zeitabhängig aufgelöst ermittelt werden (Abb. 95b). Das Feingut kann entlang der Sieblänge separiert betrachtet werden. Unter dem Siebboden sind drei Auffangbehälter angebracht, welche den Feingutmassenstrom in drei analysierbare Fraktionen aufteilen. Das Partikelkollektiv der Aufgabe sowie das Feingut und das Grobgut werden mittels dynamischer Bildanalyse mit einem CAMSIZER® der Firma Retsch GmbH hinsichtlich ihrer Partikelgröße und Form analysiert. Als Aufgabegut wird Quarzsand mit der Partikelgrößenverteilung aus Abb. 96 verwendet.

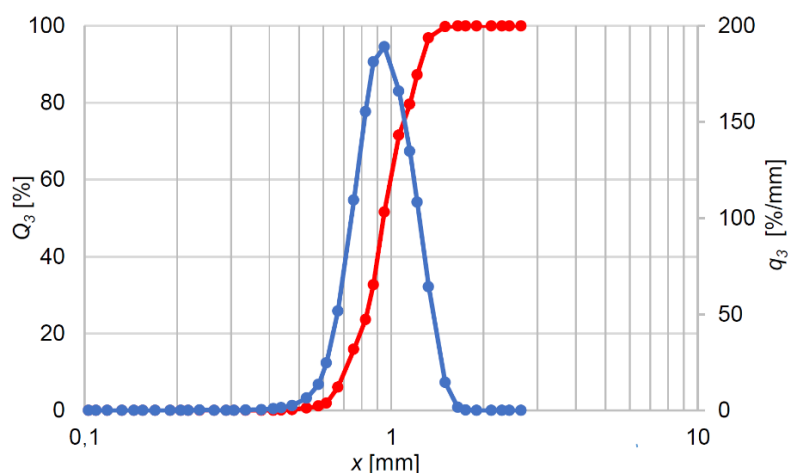


Abb. 96: Partikelgrößenverteilung des Quarzsandaufgabegutes.

2.2 Abweiseradsichter

Im Abweiseradsichter wird das Aufgabegut an einem rotierenden Sichtrad in Grob- und Feingut getrennt [58,256], wobei die Partikel in der Zone zwischen den Sichtschaufeln Schleppkräfte nach innen und Zentrifugalkräfte nach außen erfahren (Abb. 97a). Im Modell von Husemann werden Fein- und Grobgutstrom getrennt betrachtet, wobei angenommen wird, dass der Feingutstrom proportional zur Fluidgeschwindigkeit und der Grobgutstrom proportional zur Sinkgeschwindigkeit im Zentrifugalfeld sind [257]. Insbesondere erweiterte Husemann das Modell um Geometrie- und Betriebsparameter des Sichters. Mit vier Anpassungsparametern bedarf das theoretisch begründete Husemann-Modell zwar immer noch einer Kalibrierung, liefert dann aber gute Werte für das Trennkorn und die Trennschärfe des betrachteten Klassierprozesses. Allerdings lassen sich die Abhängigkeiten der Anpassungsparameter nicht aus physikalischen Überlegungen ableiten. Alle bisher diskutierten Modelle vernachlässigen zudem die Partikel/Partikel- und die Partikel/Wand-Wechselwirkungen (d.h. mit den Sichtradschaufeln). Im traditionellen Ansatz wird die Partikelbewegung zwischen den Schaufeln durch die entgegengesetzt wirkenden Kräfte, nämlich Zentrifugalkraft F_Z und Widerstandskraft F_W , bestimmt (Abb. 97a):

$$F_z = \rho_P V_P (u_\varphi^2 / r) \quad (195)$$

$$F_w = c_w (Re) A_P (\rho_F / 2) |v_{rel}| v_{rel} \quad (196)$$

wobei r der Abstand zur Rotationsachse, ρ_P die Partikeldichte, ρ_F die Fluidichte, V_P das Partikelvolumen, A_P die Partikelprojektionsfläche, u_φ die Umfangsgeschwindigkeit, c_w der Widerstandsbeiwert und v_{rel} die relative Geschwindigkeit zwischen Trägergas und Partikel darstellt.

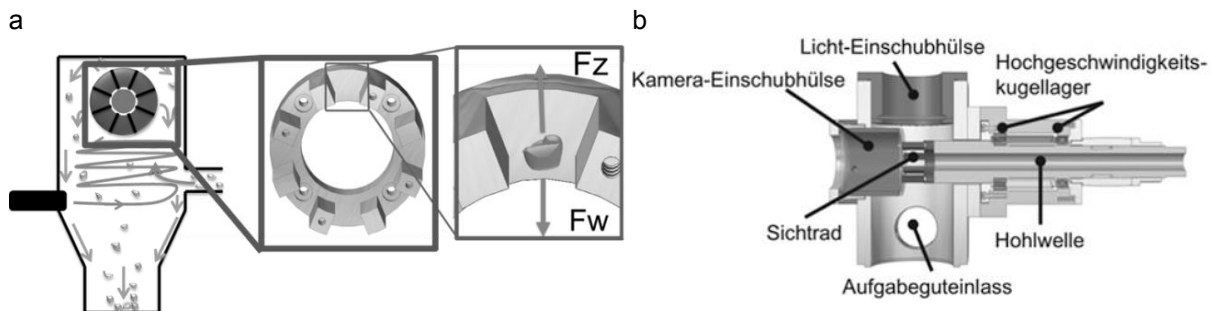


Abb. 97: (a) Schematische Darstellung eines Abweiseradsichters mit vergrößerter Darstellung des Siehtrades und der an einem Partikel in der Sichtzone angreifenden Kräfte (Schleppkraft F_w und Zentrifugalkraft F_z) [258]; (b) CAD-Schnittdarstellung des von Stender et al. [253] umgebauten Turboplex-Feinstsichters ATP 50.

Zur Bestimmung der Trenncharakteristik des Abweiseradsichters wurde im Rahmen dieser Arbeit der von Stender et al. [253] umgebaute Abweiseradsichter des Typs „Turboplex-Feinstsichter ATP 50“ der Firma Hosokawa Alpine, mit eingebauten Einschubhülsen für einen optischen Zugang zum Siehträd verwendet (Abb. 97b) [259]. Als Aufgabegut wurde Kalkstein (CaCO_3) mit einer Gutbeladung von 0,33 bis 1,00 Gew.-% verwendet ($x_{10,3} = 5,86 \mu\text{m}$, $x_{50,3} = 59,86 \mu\text{m}$, $x_{90,3} = 179,54 \mu\text{m}$). Über einen Frequenzumrichter wurde die Drehzahl des horizontal gelagerten Siehtrades ($\varnothing = 50 \text{ mm}$) von 3000 min^{-1} bis 15000 min^{-1} variiert. Der Sichtluftstrom von $75 \text{ m}^3\text{h}^{-1}$ wurde durch ein Radialgebläse gefördert. Nach der Klassierung am Siehträd strömt das Feingut in einen Zyklon und wird in einem nachgeschalteten Schlauchfilter abgeschieden [253,258,259]. Um die Bewegung der Sichtluftströmung und der zu trennenden Partikel sichtbar zu machen, wurde eine Hochgeschwindigkeitskamera des Typs Keyence VW-600M an die Stirnseite des Siehtrades platziert, während das benötigte Licht über die in der Decke des Gehäuses eingebaute Einschubhülse eingebracht wurde (Abb. 97b). Die Partikelbewegung außerhalb des Siehtrades sowie im Bereich zwischen zwei Schaufeln (Sichtzone) konnte somit aufgenommen und mittels der Software Motion Analyzer VW 9000 ausgewertet werden.

2.3 Numerische Methode

2.3.1 Diskrete-Elemente-Methode (DEM)

Die DEM eignet sich für Anwendungsfälle mit sphärischen und nicht-sphärischen Partikeln [60,61], wobei die translatorische und rotatorische Bewegung der Partikel verfolgt wird. Dafür werden die Newtonschen und Eulerschen Gleichungen integriert:

$$m_i \frac{d^2 \vec{x}_i}{dt^2} = \vec{F}_{k,i} + \vec{F}_{pf,i} + \vec{F}_{z,i} + m_i \vec{g}, \quad (197)$$

$$\hat{I}_i \frac{d\vec{W}_i}{dt} + \vec{W}_i \times (\hat{I}_i \vec{W}_i) = \Lambda_i^{-1} \vec{M}_i, \quad (198)$$

mit der Partikelmasse m_i , der Partikelbeschleunigung $d^2 \vec{x}_i / dt^2$, der Kontaktkraft $\vec{F}_{k,i}$, der Zentrifugalkraft $\vec{F}_{z,i}$, der Partikel/Fluidkraft $\vec{F}_{pf,i}$, der Gravitationskraft $m_i \vec{g}$, der Winkelbeschleunigung $d\vec{W}_i / dt$, der Winkelgeschwindigkeit \vec{W}_i , den aus Kontaktkräften resultierenden externen Momenten \vec{M}_i , dem Trägheitstensor entlang der Hauptachse \hat{I}_i und der Rotationsmatrix Λ_i^{-1} . Zur Lösung beider Gleichungen werden explizite Integrationsschemas (vgl. z.B. [82]) benutzt.

Um komplex geformte Partikel in der DEM darzustellen, kann die Multi-Sphere-Methode Verwendung finden, bei der die gewünschte Form durch beliebig große, zusammenhängende Kugeln repräsentiert wird [69]. Dabei werden die gleichen Kontaktkraftgesetze wie für Kugeln verwendet [65].

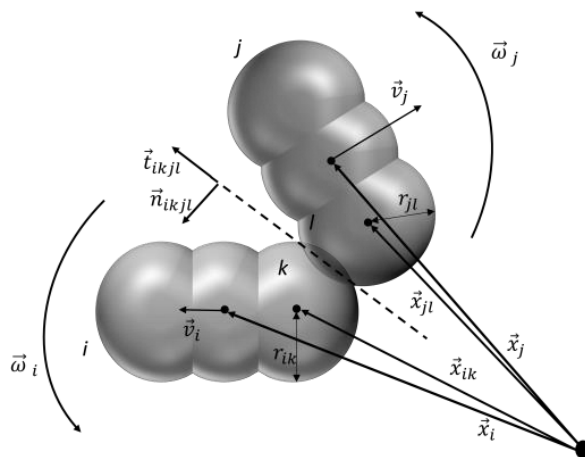


Abb. 98: Eine Kollision von zwei Kugelclustern nach dem "Multisphere"-Verfahren.

In Abb. 98 sind zwei komplex geformte Partikel i und j zu sehen, bei denen die Kugeln i und k kollidieren. Für weitere Details zu dem Kontaktschema bei Kugelclustern werden die Arbeiten von Kruggel-Emden und Kačianauskas sowie Kruggel-Emden et al. [90,91] empfohlen. Die normale Komponente der Kontaktkraft wird über ein lineares Feder-Dämpfer-Model ermittelt,

welche beispielhaft für die in Kontakt stehenden Kugeln k und l der Partikel i und j gegeben ist als

$$\vec{F}_{ikjl}^n = k^n \delta_{ikjl} \vec{n}_{ikjl} + \gamma^n \vec{v}_{ikjl}^n, \quad (199)$$

wobei k^n die Federsteifigkeit, δ_{ikjl} die virtuelle Überlappung, \vec{n}_{ikjl} ein Normalenvektor, γ^n ein Dämpfungskoeffizient und \vec{v}_{ikjl}^n die Normalengeschwindigkeit im Kontaktpunkt ist [92].

Die tangentialen Kräfte werden mit Hilfe einer linearen Feder, welche durch die Coulombsche Bedingung limitiert ist, folgendermaßen berechnet

$$\vec{F}_{ikjl}^t = -\min(k^t |\vec{\xi}_{ikjl}|, \mu_c |\vec{F}_{ikjl}^n|) \vec{t}_{ikjl}, \quad (200)$$

Dabei ist k^t die tangentielle Steifigkeit einer linearen Feder, μ_c der Reibungskoeffizient, $\vec{\xi}_{ikjl}$ die relative tangentielle Verschiebung und \vec{t}_{ikjl} der tangentielle Einheitsvektor [94].

Die Partikel/Fluidkraft berechnet sich unter der Annahme, dass eine parallele Strömung herrscht und somit die Rotationsbewegung und die Partikel-Fluid-Spannung vernachlässigt werden können nach dem Ansatz von Di Felice [260] aus einer Kombination der Widerstandskraft $\vec{F}_{w,i}$ und der Druckgradientkraft $\vec{F}_{\nabla p,i}$ folgendermaßen

$$\vec{F}_{pf,i} = \vec{F}_{w,i} + \vec{F}_{\nabla p,i} = \frac{\rho_F}{2} |\vec{u}_F - \vec{v}_i| A_{\perp} \varepsilon_F^{1-\chi} (\vec{u}_F - \vec{v}_i) C_w. \quad (201)$$

Hierbei ist \vec{u}_F die Fluidgeschwindigkeit, \vec{v}_i die Partikelgeschwindigkeit, A_{\perp} die Querschnittsfläche orthogonal zur Strömung, ε_F die lokale Fluidporosität und χ ein Korrekturfaktor als Funktion der Partikel-Reynoldszahl gegeben durch

$$\chi = 3,7 - 0,65 \exp(-(1,5 - \log(Re))^2 / 2), \quad (202)$$

mit $Re = \varepsilon_F \rho_F x_p |\vec{u}_F - \vec{v}_i| / \mu_F$, wobei x_p der Durchmesser eines volumengleichen sphärischen Partikels und μ_F die Fluidviskosität darstellen. Für den Widerstandsbeiwert C_w wurde in dieser Arbeit das einfache und allgemein anwendbare Modell von Hölzer und Sommerfeld [261] verwendet

$$C_w = \frac{8}{Re} \frac{1}{\sqrt{\phi_{\perp}}} + \frac{16}{Re} \frac{1}{\sqrt{\phi}} + \frac{3}{Re} \frac{1}{\phi^{3/4}} + 0,42 \times 10^{0,4(-\log(\phi))^{0,2}} \frac{1}{\phi_{\perp}}, \quad (203)$$

wobei ϕ_{\perp} die Quersphärizität als Verhältnis der Querschnittsfläche der volumengleichen Kugel zur projizierten Querschnittsfläche des Partikels senkrecht zur Strömung und ϕ die Sphärizität ist. Im Fall von sphärischen Partikeln gilt $\phi_{\perp} = \phi = 1$. Detailliertere Informationen zur Partikel/Fluidkraft sind u.a. in der Arbeit von Oschmann et al. [262] zu finden.

2.3.2 DEM-Simulationen des Kreisschwingsiebes

Für die DEM-Simulationen des Kreisschwingsiebes werden auf Grund des hohen Rechenaufwandes einige Vereinfachungen getroffen. Die Rechnungen werden nur für den ersten Feingutbereich F1 (vgl. Abb. 95) durchgeführt. F2, F3 und G sind hierbei als Grobgut G* zusammengefasst. Periodische Randbedingungen werden nicht verwendet, da die Schüttdichte des Partikelmassenstroms nach außen hin abnimmt (Abb. 99). Die Siebmaschen werden mit der vorgegebenen Maschenweite von $w = 1 \text{ mm}$ als gerade, starre und nur durch die Siebanregung bewegte Stäbe angenommen (Abb. 99 Vergrößerung), sowie die Siebhilfen vernachlässigt. Die Partikelverteilung ist entsprechend Abb. 99, wobei 8 diskrete Klassen mit den Partikeldurchmessern der jeweiligen Klassenmitte zwischen $0,55 \text{ mm} < x < 1,85 \text{ mm}$ (Punkte in Abb. 99) und einer einheitlichen Dichte von $\rho = 2500 \text{ kg/m}^3$ verwendet werden.

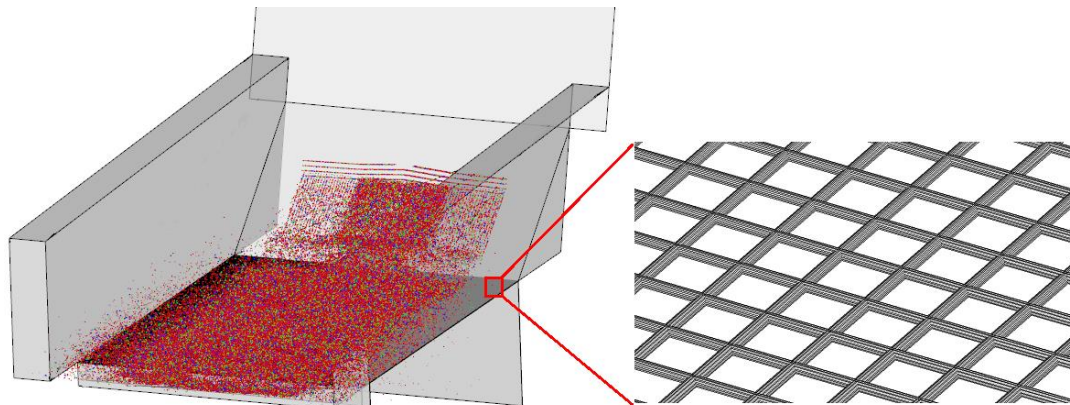


Abb. 99: Darstellung des ersten Siebabschnittes in der DEM

Gemäß der Arbeiten von Delaney et al. [20] und Cleary [62] wurden DEM-Parameter, die sich für industriellen Quarzkies eignen, verwendet. Die tangentielle Federkonstante ist $k^t = 0,5k^n$. Daher sind die Steifigkeiten auf $k^n = 100.000 \text{ N/m}$ und $k^t = 50.000 \text{ N/m}$ gesetzt worden, was zu maximalen Partikelüberlappungen von weniger als 0,5 % des Durchmessers und somit zu einer akkuraten Darstellung von Partikel/Partikel und Partikel/Wand Interaktionen führt. Die Reibungskoeffizienten wurden als etwa $\mu_c = 0,5$ für Partikel/Partikel und Partikel/Wand-Kontakte ermittelt. Dafür wurden die Partikel möglichst gleichmäßig und dicht aneinanderliegend unter einen Waagen geklebt und über Flächen, die aus dem gleichen Material wie die Siebmaschen bzw. die Partikel bestehen, gezogen. Dabei wurde die benötigte Kraft \vec{F}_R mit einem Kraftmessgerät bestimmt und durch Division mit der Normalkraft \vec{F}_N der Reibungskoeffizient $\mu_c = |\vec{F}_R|/|\vec{F}_N|$ berechnet [263]. Bei Kugeln wurde die Rollreibung für Partikel/Partikel und für Partikel/Wand Kontakte auf $\mu_{roll} = 0,00008$ gesetzt, was sich bei repräsentativen Simulation als geeignet erwiesen hat um entgegen der Rollbewegung zu wirken und somit teilweise die Formvereinfachung, welche sich stark auf das Bewegungsverhalten auswirkt, auszugleichen [263]. Für den Restitutionskoeffizienten zwischen Partikeln wird $e_{pp}^n = 0,3$ und für Stöße zwischen Partikeln mit den nachgebenden

Siebmaschen $e_{pW}^n = 0,15$ verwendet. Zur Ermittlung werden die Partikel an einem Pendel gegen das entsprechende Material prallen gelassen und die Geschwindigkeit vor (u_1) und nach (v_1) dem Stoß bestimmt. Damit lässt sich $e^n = -v_1/u_1$ berechnen [263]. Für die Siebmaschen wurde dieser Wert auf Basis von visuellen Vergleichen reduziert, da diese nur als starr und nicht nachgebend simuliert werden konnten.

In einem ersten Ansatz werden die verwendeten Quarzpartikel in allen Simulationen als Kugeln dargestellt. Da dadurch neben Unterschieden im Transportverhalten alle Partikel mit $x > w$ nicht ins Feingut gelangen können, wird in einem zweiten Ansatz für eine repräsentative Drehzahl auf eine einfache Darstellung mit nicht-sphärischen Partikeln, bestehend aus drei gleichgroßen Kugeln mit einem Seitenverhältnis von 1,5 (Durchschnittliches Seitenverhältnis der CAMSIZER® Messungen) bei äquivalentem Kugelvolumen, zurückgegriffen (vgl. Abb. 98) [244]. Diese sind nicht den exakten Körpern nachempfunden, sondern weisen nur ein vergleichbares Seitenverhältnis auf.

2.3.3 DEM-Simulationen des Abweiseradsichters

Für die DEM-Simulationen des Abweiseradsichters werden ebenfalls aufgrund des hohen Rechenaufwandes einige Vereinfachungen getroffen. Es wird nur das Verhalten innerhalb einer Schaufel des Sichtrades betrachtet (vgl. Abb. 97 und Abb. 108), das sich in der Simulation nicht bewegt. Das verwendete Strömungsprofil wurde durch Leerrohr-Messungen ermittelt und in der Simulation als stationär angenommen. Die Einflüsse der Zentrifugalkraft (vgl. Abb. 97a), der Schleppkraft und des Wandimpulses werden in der Simulation berechnet. Die Partikelbewegung wird relativ zur Schaufelbewegung angesetzt. Die geometrischen Abmaße der Schaufel und deren Drehung um die eigene Achse werden exakt wie im Experiment nachgebildet. Partikel mit einer einheitlichen Dichte von $\rho = 2700 \text{ kg m}^{-3}$ treten gleichverteilt über die gesamte Breite der Schaufel mit Geschwindigkeiten von $4 - 6 \text{ m s}^{-1}$ in Winkeln von $10 - 20^\circ$ ein und werden, wenn sie diese nach außen verlassen, direkt als Grobgut betrachtet. Es werden 19 verschiedene Partikelklassen als Kugeln mit Partikeldurchmessern von $14,25 \mu\text{m} < x < 335 \mu\text{m}$ betrachtet, welche den mittleren Durchmessern der relevanten Partikelklassen des Aufgabeguts (s. Abschnitt 2.2) entsprechen. Bei allen kleineren und größeren Partikeln kann vereinfachend angenommen werden, dass sie sicher ins Feingut bzw. Grobgut gelangen. Eine sphärische Form kann angenommen werden, da dadurch das gesamte Trennergebnis nicht weiter beeinflusst wird und nur die Streuung des Abprallverhaltens etwas niedriger ist.

3. Ergebnisse und Diskussion

3.1 Trennverhalten bei der Siebung

3.1.1 DEM-Simulation

Der Siebvorgang des Kreisschwingsiebes wird wie in Abb. 99 zu sehen, für die drei Drehzahlen $n = 1000 \text{ min}^{-1}$, $n = 1200 \text{ min}^{-1}$, und $n = 1550 \text{ min}^{-1}$, einem Massenstrom von 150 kg h^{-1} und ansonsten gleichen Betriebsparametern mit der DEM nachsimuliert. Dabei befinden sich zeitgleich maximal etwa 10.000 Partikel auf dem Sieb und insgesamt werden ungefähr 140.000 Partikel gesiebt.

Wenn bei der DEM-Simulation des Siebvorgangs die Quarzpartikel als Kugeln dargestellt werden, ist eine relativ gute Übereinstimmung der Partikelklassen mit $x < 0,7 w$ und $x > w$ zwischen allen untersuchten Experimenten und Simulationen für Summenkurven (s. Abb. 100a) zu erkennen. Nur bei den Partikelklassen mit $0,7 w < x < w$ sind leichte Abweichungen in den Summenkurven unabhängig von der verwendeten Drehzahl festzustellen.

Bei Verwendung der einfachen, nicht sphärischen Partikeln für eine repräsentative Drehzahl von $n = 1200 \text{ min}^{-1}$ kann für die Feingutsummenverteilung ebenfalls keine exakte Übereinstimmung erreicht werden, jedoch liegen die Ergebnisse der Simulation wesentlich näher an den experimentellen Werten (s. Abb. 100b). Die Kurven der Grobgutsummenverteilung weisen so gut wie keine Unterschiede auf. Durch diese positive Auswirkung wird die Notwendigkeit, die Partikelform exakter abzubilden, wie dies schon in kleinerem Maßstab in Elskamp et al. [263] durchgeführt wurde, bestätigt.

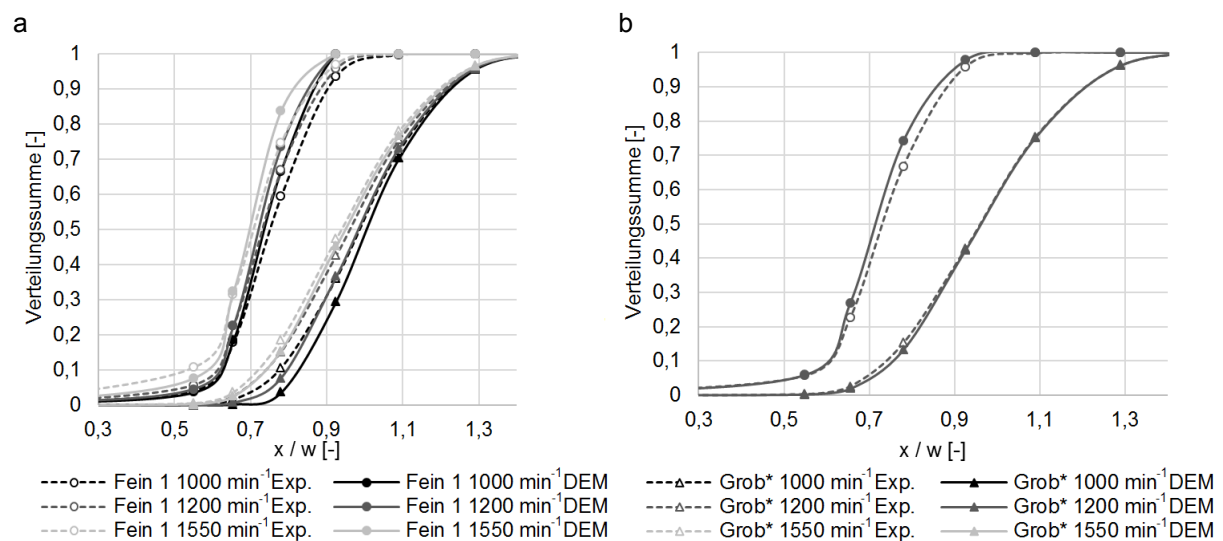


Abb. 100: Experimentelle (Exp.) und numerische (DEM) Durchtrittssummenkurven ins Fein- (Fein 1) und Grobgut (Grob*) für (a) $n = 1000 \text{ min}^{-1}$, $n = 1200 \text{ min}^{-1}$ und $n = 1550 \text{ min}^{-1}$ mit einer sphärischen Partikelapproximation in der DEM und für (b) $n = 1200 \text{ min}^{-1}$ mit einer nicht-sphärischen Partikelapproximation in der DEM.

3.1.2 Vergleich der Trennkurven: Experiment - DEM - Trennmodell

In einem weiteren Schritt wird überprüft, wie gut Siebmodelle im Vergleich zu DEM-Simulationen experimentelle Daten wiedergeben können. Im Fall der DEM-Simulation kann auch bei den Trennkurven eine relativ gute Übereinstimmung zwischen allen untersuchten Experimenten und Simulationen erreicht werden, wenn die Quarzpartikel als Kugeln dargestellt werden (s. Abb. 101)). Hierbei sind jedoch vor allem bei höheren Drehzahlen Abweichungen bei den Partikelklassen mit $x < 0,9 w$ zu sehen, da die kleineren Partikel durch ihre nicht sphärische Form im Experiment eher in das Grobgut gelangen können.

Für die Darstellung mit Siebmodellen wurde hier beispielhaft das durch Dong et al. [49] prädiktiv erweiterte Modell von Subasinghe et al. [228] an die Ergebnisse des Experiments mit einer Frequenz von $n = 1200 \text{ min}^{-1}$ angepasst. Für die Fälle der höheren und niedrigeren Frequenz wurden die zuvor angepassten Parameter ohne weitere Anpassung verwendet. Dabei kann neben der Frequenz von $n = 1200 \text{ min}^{-1}$ auch für $n = 1550 \text{ min}^{-1}$ eine gute Übereinstimmung erreicht werden. Eine niedrigere Frequenz von $n = 1000 \text{ min}^{-1}$ weist hierbei größere Abweichungen auf, da neben der Nichtberücksichtigung von nicht-sphärischen Formen auch der Einfluss des Partikelkontakts untereinander, z.B. in Partikelschichten auf dem Sieb, nicht berücksichtigt wird. Diese Schichten entstehen bei geringen Frequenzen, was hier der Fall ist.

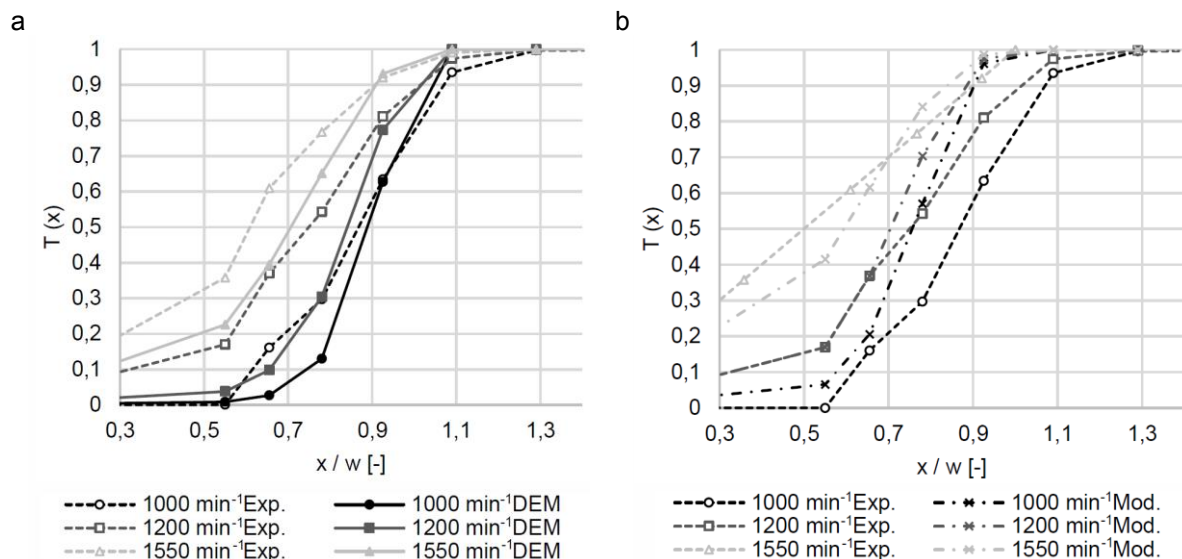


Abb. 101: (a) Vergleich der experimentellen (Exp.) und numerischen (DEM) Trennkurven für $n = 1000 \text{ min}^{-1}$, $n = 1200 \text{ min}^{-1}$ und $n = 1550 \text{ min}^{-1}$ mit einer sphärischen Partikelapproximation in der DEM. (b) Vergleich der experimentellen (Exp.) und mittels Modell (Mod.) erstellten Trennkurven für $n = 1000 \text{ min}^{-1}$, $n = 1200 \text{ min}^{-1}$ und $n = 1550 \text{ min}^{-1}$ mit einer sphärischen Partikelannahme im Modell.

Durch Verwendung von nicht sphärischen Partikeln in der DEM-Simulation können die Abweichungen für alle Partikelgrößen wesentlich verringert werden, weil dadurch der Durchtritt der kleinen Partikel erschwert und ihr Durchtritts- und Transportverhalten ähnlicher zu dem im Experiment ist. Dies ist in Abb. 102 beispielhaft für eine Drehzahl von $n = 1200 \text{ min}^{-1}$ gezeigt. Aufgrund dieser positiven Effekte wird bei zukünftigen Untersuchungen versucht, die komplexe

Partikelform exakter abzubilden (vgl. [263]). Ebenso wird in der Modellentwicklung auf Modelle zurückgegriffen, bzw. Modelle so erweitert, dass auch verschiedene Partikelformen und Gutmengen berücksichtigt werden können.

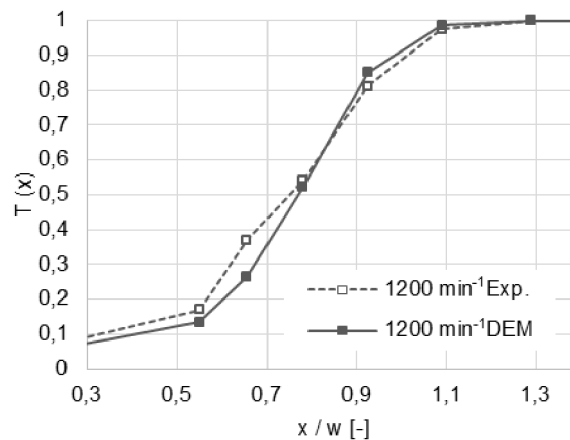


Abb. 102 Vergleich der experimentellen (Exp.) und numerischen (DEM) Trennkurven für $n = 1200 \text{ min}^{-1}$ mit einer nicht-sphärischen Partikelapproximation in der DEM.

3.2 Trennverhalten beim Abweiseradsichter

3.2.1 Die Partikelbewegung außerhalb des Sichtrades

Während sich im Außenbereich des Sichtrades ein umlaufender Gutring bildet, der kaum von der Drehzahl des Sichtrades beeinflusst wird, ist im sichtradenahen Außenbereich der Einfluss des zwischen zwei Sichtschaufeln auftretenden Sichtluftströmungsprofils auf die Partikelbewegung deutlich zu erkennen. Während bei einer Drehzahl von $n = 3000 \text{ min}^{-1}$ die Partikel der nahezu senkrecht in die Sichtzone einströmenden Sichtluft folgen (Abb. 103a), wird der Einzugswinkel der Partikel bei steigender Drehzahl deutlich spitzer (Abb. 103b-d).

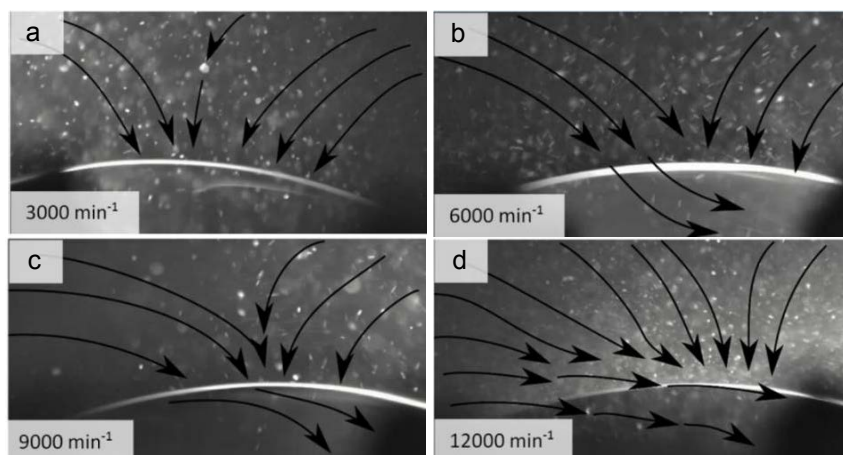


Abb. 103: Visualisierung der Partikelbewegung in der Peripherie des Sichtrades. Die Sichtraddrehrichtung ist entgegen dem Uhrzeigersinn.

Die absoluten Geschwindigkeiten der anfliegenden Partikel variieren allerdings kaum mit der Drehzahl. Das Anflugverhalten der Aufgabegutpartikel zum Schaufelzwischenraum, mit relativ konstanter Geschwindigkeit und einem mit ansteigender Drehzahl zunehmend spitzer

werdendem Einflugwinkel, wurde für die DEM-Simulationen der Partikelflugbahnen als Eingangsparameter verwendet.

3.2.2 Visualisierung der Sichtluftströmung und der Partikelbewegung in der Sichtzone des Sichtrades

Für die Visualisierung der Luftströmung in der Sichtzone wurden sehr feine Kalkstein-Tracer-Partikel verwendet ($x_{50,3} = 2,15 \mu\text{m}$), während die Partikelbewegung mit größeren Kalksteinpartikeln ($x_{50,3} = 59,86 \mu\text{m}$) sichtbar gemacht wurde. Die Bewegung der feinen Partikelansammlungen ist in Abb. 104 durch Pfeile dargestellt [253,258,259]. Bei einer Drehzahl von $n = 3000 \text{ min}^{-1}$ passieren die Tracer-Partikel die gesamte Sichtzone in einer bogenförmigen Strömung (Abb. 104a). Die groben Kalksteinpartikel folgen der Luftströmung zu Beginn in die Sichtzone (Abb. 105a), wobei sie aufgrund ihrer höheren Trägheit langsamer radial nach innen getragen werden, so dass sie scheinbar auf die nacheilende Schaufel fokussiert werden. Aufgrund der nur wenig abgelenkt einfliegenden Partikel ist die Verteilung der Partikel über die Sichtzone bei dieser langsamen Drehzahl zumindest für kleinere Partikel noch relativ homogen [253,258,259].

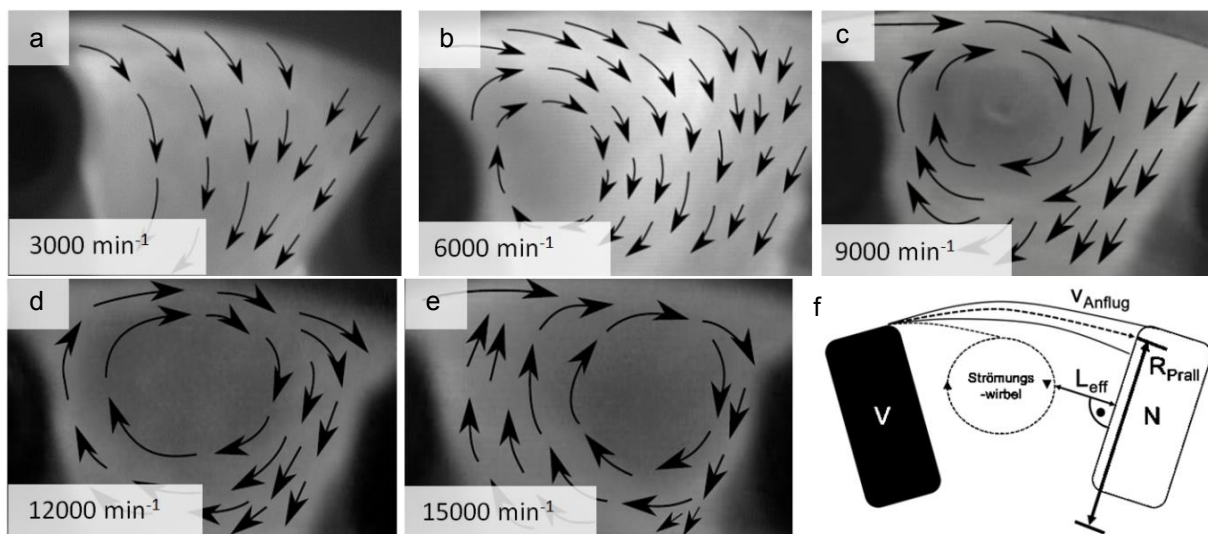


Abb. 104: Visualisierung der Sichtluftbewegung zwischen zwei Sichtradschaufeln für eine zunehmende Drehzahl von (a) bis (e) (vorauselende Schaufel (V) jeweils links im Bild und nacheilende Schaufel (N) rechts). Das Sichtrad bewegt sich entgegen dem Uhrzeigersinn [253,258,259]. Die Parameter zur Beschreibung des Wirbels L_{eff} (effektiver Abstand zur Prallplatte) und der Partikelfokussierung A_{prall} (Prallfläche) sind unter (f) definiert [258,259].

Bei höheren Drehzahlen wird ein Sichtluftwirbel zwischen den Schaufeln ausgebildet (Abb. 104b-e). Zur Parametrisierung der Position des Wirbels und seiner Wirkung auf die Bewegung der größeren Partikel wurden die beiden Größen L_{eff} , welche den kürzesten Abstand des Wirbels von der nacheilenden Schaufel angibt, und R_{prall} eingeführt, die den Abstand von der Sichtradachse zum Mittelpunkt der Partikelaufrallfläche beschreibt (Abb. 104f). Mit steigender Drehzahl nähert sich der Trennwirbel zunehmend der nacheilenden Schaufel an [258,259].

Dieses führt zu einer Einschnürung der Luftströmung und somit zu einer erhöhten Strömungsgeschwindigkeit radial nach innen, was die Schleppkraft vergrößert. Des Weiteren führt die Einschnürung der Sichtluft zu einer zunehmenden Fokussierung des Partikelstroms auf eine sich drehzahlabhängig verkleinernde Aufprallfläche, wobei sich der Mittelpunkt der Aufprallfläche mit zunehmender Drehzahl zur Sichttradaußenkante verschiebt (Abb. 105b-e und Abb. 104f) [253,258,259].

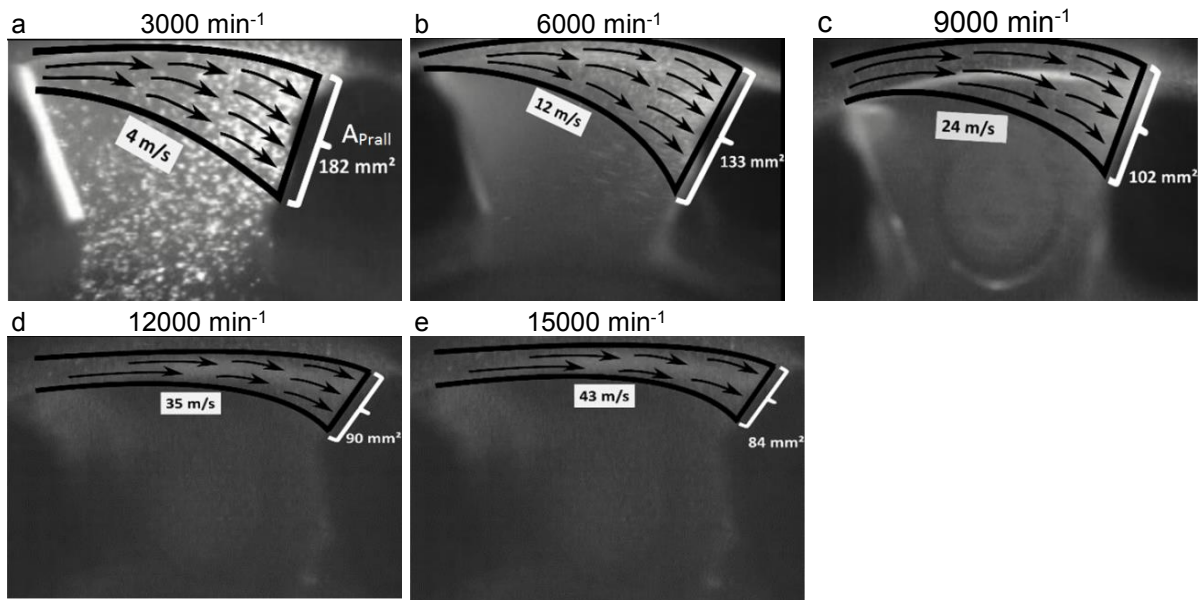


Abb. 105: Visualisierung der Partikelbewegung zwischen zwei Sichttradschaufeln für eine zunehmende Drehzahl von (a) bis (e). Das Sichtrad bewegt sich entgegen dem Uhrzeigersinn [253,258,259].

Der Einfluss der Drehzahl auf die Geschwindigkeiten für Anflug und Reflexion sowie auf die effektiv durchströmte Länge L_{eff} und den Aufprallradius R_{prall} ist in Abb. 106 dargestellt. Aus den gemessenen Anflugs- und Rücksprunggeschwindigkeiten der Partikel (Abb. 106a) ergibt sich ein gemittelter Restitutionskoeffizient von 1,39, d.h. im absoluten Koordinatensystem erfahren die Partikel durch den Schlag bei der Kollision mit der Schaufel einen Impulsübertrag, so dass sie sich absolut gesehen nachher schneller bewegen als vorher.

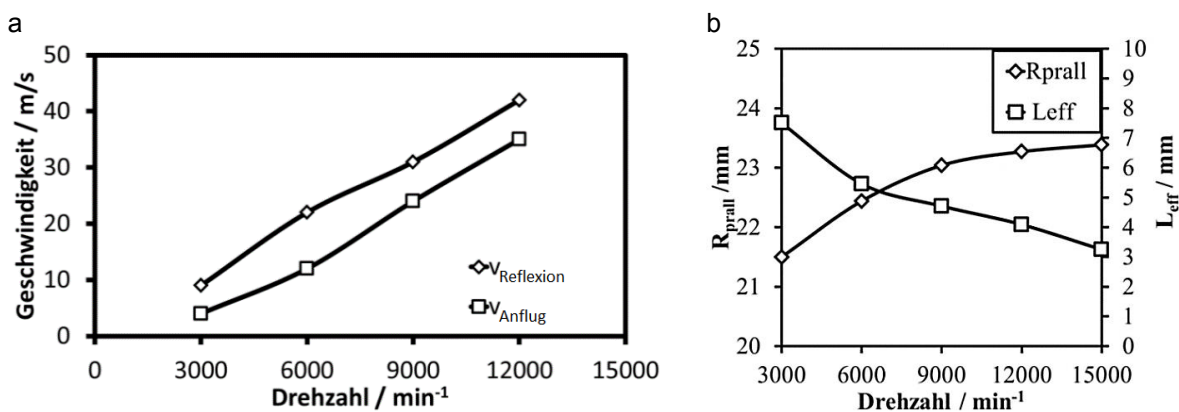


Abb. 106: (a) Zusammenhang zwischen Anfluggeschwindigkeit v_{Anflug} und Reflexionsgeschwindigkeit $v_{Reflexion}$. (b) Aufprallradius R_{prall} und effektive Länge L_{eff} in Abhängigkeit der Sichttraddrehzahl.

Bei geringen Drehzahlen folgen die Partikel der weit gefächerten Strömung weiter in das Innere der Sichtzone, bevor sie mit der nacheilenden Schaufel in Wechselwirkung

(Partikel/Wand-Kollision) treten. Bei höheren Drehzahlen ist dies deutlich weniger der Fall [253,258,259].

3.2.3 Trennverhalten bei geringer Gutbeladung

In Abb. 107 sind die gemessenen Trenneffekte bei drei geringen Beladungen für verschiedene Drehzahlen dargestellt. Während eine Erhöhung der Drehzahl um den Faktor 3 (von $n = 3000 \text{ min}^{-1}$ auf $n = 9000 \text{ min}^{-1}$) zu einer Abnahme der Trenngrenze um 86 % führt (Abb. 107b), resultiert eine Steigerung der Gutbeladung um den Faktor 3 (von 0,33 Gew.-% auf 1,00 Gew.-%) nur in einer Reduzierung der Trenngrenze um wenige Prozent. Verglichen mit der Trenngrenze wird die Trennschärfe jedoch nur geringfügig von der Gutbeladung und Drehzahl beeinflusst. Für ein Kalksteinaufgabegut mit einer mittleren Partikelgröße von $59 \mu\text{m}$ schwankt die Trennschärfe bei Drehzahlen über $n = 3000 \text{ min}^{-1}$ nur um wenige Prozent mit einem Mittelwert von 60 %. Für eine Drehzahl von $n = 3000 \text{ min}^{-1}$, bei der sich noch kein Wirbel zwischen den Schaufeln ausgebildet hat, schwankt sie in einem Bereich von etwa 10 % um den Mittelwert von 60 %.

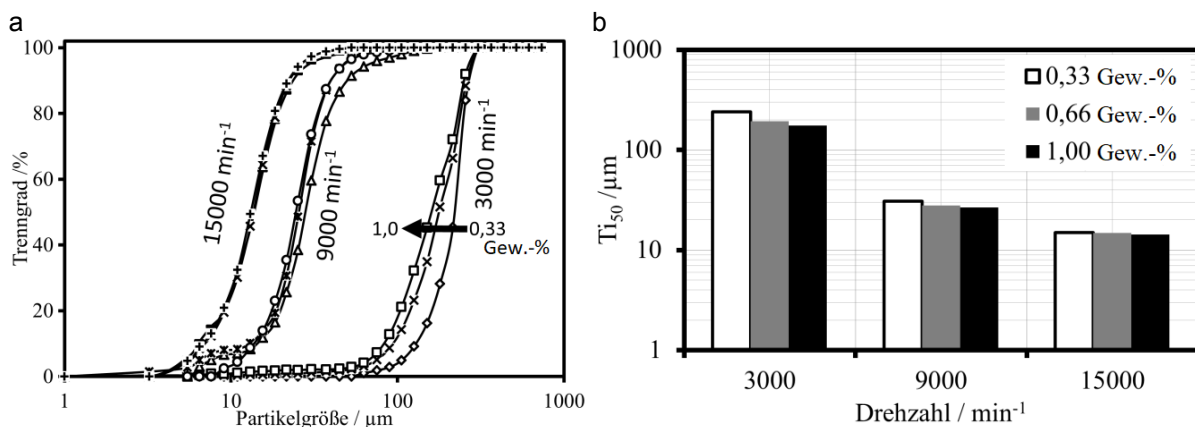


Abb. 107: (a) Trennkurven und (b) Trenngrenze in Abhängigkeit der Sichtraddrehzahl für drei geringe Beladungen.

3.2.4 DEM-Simulation des Abweiseradsichters

Der Trennvorgang beim Abweiseradsichter wird für die zwei Drehzahlen $n = 3000 \text{ min}^{-1}$ und $n = 9000 \text{ min}^{-1}$ mit jeweils 3 niedrigen Gutbeladungen (0,33 Gew.-%, 0,66 Gew.-%, 1,00 Gew.-%) und ansonsten gleichen Betriebsparametern mit der DEM nachsimuliert. In Abb. 108 ist die Darstellung der Sichtradschaufel in der DEM-Simulation beispielhaft nach einigen Millisekunden für eine Drehzahl von $n = 9000 \text{ min}^{-1}$ und einer Gutbeladung von 0,33 Gew.-% gezeigt. In Abb. 108a sind die verschiedenen Partikelgrößen gut zu erkennen, die auf der linken Seite noch gemischt und auf der rechten Seite und besonders nach dem Kontakt mit der Schaufel in feinere (unten) und gröbere Partikel (oben) getrennt werden.

In Abb. 108b sind die Bewegungsorientierungen der verschiedenen Partikel zu sehen, wobei vor allem die kleineren Partikel der Fluidströmung folgen. Dem sich zurückbewegenden Wirbel

(vgl. Abb. 104c, Abb. 105c) würden vor allem die hier vernachlässigten Partikel mit $x < 15 \mu\text{m}$ folgen.

a



b

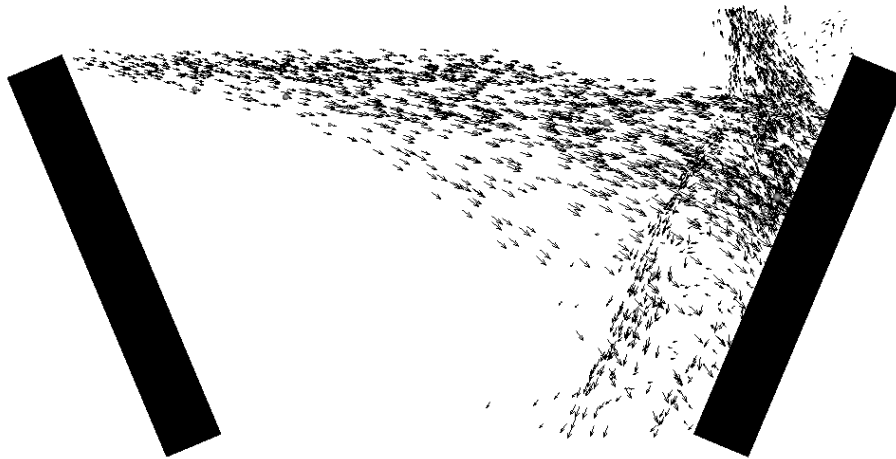


Abb. 108: Darstellung der Sichtradschaukel in der DEM mit (a) Partikeldarstellung und mit (b) Geschwindigkeitsprofil bei $n = 9000 \text{ min}^{-1}$ und einer Gutbeladung von 0,33 Gew.-%.

In Abb. 109 sind die Verteilungssummen des Fein- und Grobgutes für die Versuche mit einer Gutbeladung von 0,33 Gew.-% und 1,00 Gew.-% jeweils mit einer Drehzahl von $n = 3000 \text{ min}^{-1}$ und $n = 9000 \text{ min}^{-1}$ dargestellt.

Bei einer Drehzahl von $n = 3000 \text{ min}^{-1}$ (Abb. 109a) weichen die Verteilungssummenkurven der Simulation im kleineren Partikelbereich von denen des Experiments ab, da die kleinen Partikel in der Simulation mit einer sehr hohen Wahrscheinlichkeit im Feingut landen, was im Experiment durch deren stochastisch geprägte Bewegungen oft nicht der Fall ist. Im Bereich $x > 100 \mu\text{m}$ stimmen die Verteilungssummenkurven jedoch gut überein.

Für eine Drehzahl von $n = 9000 \text{ min}^{-1}$ (Abb. 109b) werden die experimentellen Verteilungssummen des Feingutes sehr gut wiedergegeben. Minimale Abweichungen sind im Bereich der kleinsten Partikel zu erkennen. Die Kurven für die Grobgutverteilung bei einer Gutbeladung von 0,33 Gew.-% liegen für die Simulationen etwas höher als die experimentellen Verteilungen. Dies liegt vor allem daran, dass bei dieser niedrigen Gutbeladung schon einige wenige, falsch klassierte Partikel nahe der Trenngrenze entscheidend sein können. Bei beiden Verteilungssummen liegt die Abweichung bei maximal 5 %.

Die unterschiedlichen Gutbeladungen zeigen ansonsten sehr ähnliche Ergebnisse für beide Drehzahlen, wobei die Versuche mit einer höheren Gutbeladung geringere Abweichungen zwischen Experimenten und Simulationen aufweisen. Dies gilt ebenso für die Simulationen mit einer Gutbeladung von 0,66 Gew.-%, die zwischen den jeweils anderen Versuchen liegen und aus Gründen der Übersichtlichkeit nicht in Abb. 109 dargestellt sind.

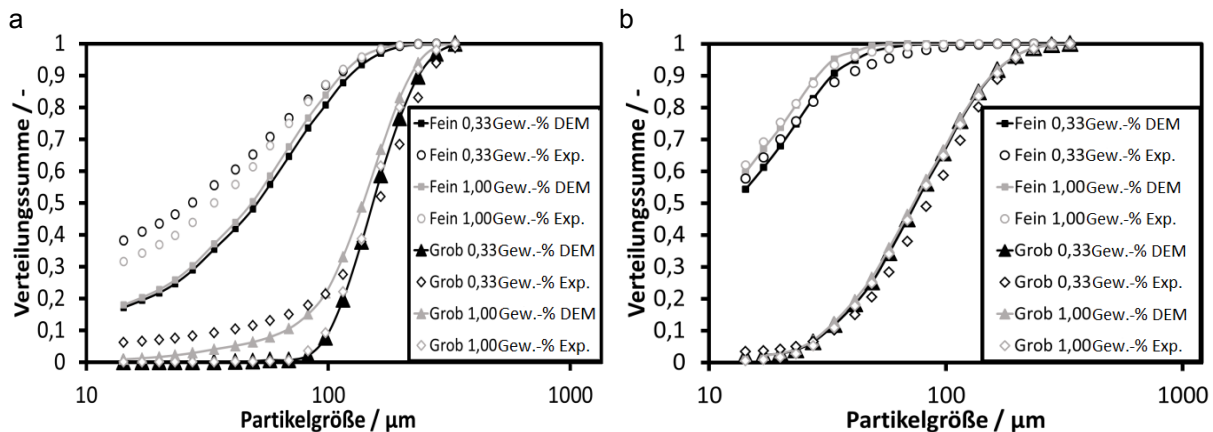


Abb. 109: Experimentelle (Exp.) und numerische (DEM) Durchtrittssummenkurven ins Fein- und Grobgut mit einer sphärischen Partikelapproximation in der DEM für Gutbeladungen von 0,33 Gew.-% und 1,00 Gew.-% und Drehzahlen von (a) $n = 3000 \text{ min}^{-1}$ sowie (b) $n = 9000 \text{ min}^{-1}$.

3.2.5 Vergleich der Trennkurven: Experiment - DEM - Trennmodelle

In Abb. 110 und Abb. 111 werden die mittels experimenteller Daten, DEM-Simulationen und dem vorgestellten Modellansatz ermittelten Partikelgrößenverteilungen sowie Trennkurven verglichen. Der verwendete Modellansatz berechnet, über die in Abb. 104f dargestellte Parametrisierung der Fluidströmung [258], die größenabhängige Flugbahn der Partikel und schlussendlich die Trenngrenze x_t (Gl. (204)) am Aufprallpunkt auf die Sichtradschaufel, aus dem angreifenden Kräftegleichgewicht aus Zentrifugal- und Widerstandskraft.

$$x_t = \sqrt{\frac{18\eta_{eff}R_{Prall}\dot{V}_{Luft}}{L_{eff}b\rho_P v_R^2 N}} \quad (204)$$

In der verwendeten Gleichung ist R_{Prall} der Aufprallradius (vgl. Abb. 106b), \dot{V}_{Luft} der Luftvolumenstrom von $75 \text{ m}^3 \text{ h}^{-1}$, L_{eff} die maximale Einschnürung der Sichtluft (vgl. Abb. 104 und Abb. 106), b die Schaufelbreite von $0,025 \text{ m}$, ρ_P die Partikeldichte von 2700 kg m^{-3} , N die Anzahl der Schaufeln, v_R die Reflexionsgeschwindigkeit und η_{eff} die effektive Viskosität. Die Werte wurden mit der Hochgeschwindigkeitskamera am realen Prozess erhoben (Abb. 106). Die effektive Viskosität η_{eff} wird wie in den Abschnitten 3.2.1. und 3.2.2. beschrieben, durch die drehzahlabhängige Einschnürung des Sichtluftstromes und der daraus entstehenden Fokussierung des Partikelstromes über Partikel/Partikel-Stöße beeinflusst. Da die Abhängigkeit der effektiven Viskosität von Beladung und Drehzahl nicht bekannt ist, dient sie im vorgestellten Modell als Fit-Parameter.

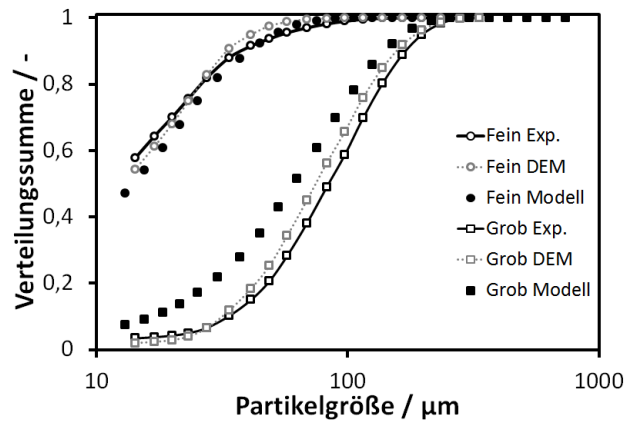


Abb. 110: Vergleich der experimentellen, numerischen (DEM) und mittels Modell ermittelten Verteilungssummenkurven bei $n = 9000 \text{ min}^{-1}$ und einer Gutbeladung von 0,33 Gew.-%.

Eine Gegenüberstellung der Fein- und Grobgutverteilungssummen des Modells mit den experimentell und numerisch (DEM) ermittelten Daten (Abb. 110) zeigt, dass die Modellverteilungssummen deutlich größere Abweichungen zu den experimentellen Werten aufzeigen, als es bei den numerischen Verteilungssummen der Fall ist. Der Vergleich der experimentellen und mittels DEM-Simulation erstellten Trennkurven zeigt, dass die DEM die experimentellen Daten bei verschiedenen Drehzahlen gut abbilden kann (Abb. 111a). Bei einer Drehzahl von $n = 3000 \text{ min}^{-1}$ zeigt Abb. 111a nur geringe Unterschiede zwischen der experimentell ermittelten Trennkurve und der DEM-Simulation. Für eine Drehzahl von $n = 9000 \text{ min}^{-1}$ (Abb. 111a) stimmt die experimentell ermittelte Kurve mit den mittels DEM-Simulation bestimmten Trennkurven sehr gut überein. Kleine Abweichungen in der DEM sind nur im Bereich von $50 \mu\text{m} < x < 100 \mu\text{m}$ festzustellen, da in der Simulation die Trennung etwas weniger scharf stattfindet. Grund sind vor allem Partikel knapp über der Trenngrenze, die in der Simulation noch ins Feingut gelangen. Hierbei weicht die DEM-Trennkurve nur in einem Partikelgrößenbereich zwischen $135 \mu\text{m} < x < 235 \mu\text{m}$ von den experimentellen Messwerten ab.

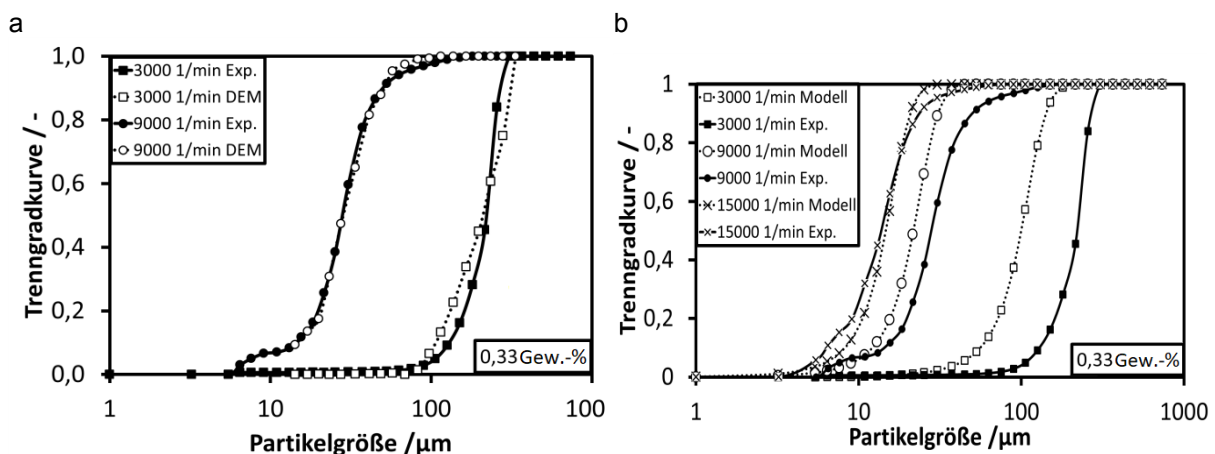


Abb. 111: (a) Vergleich der experimentellen und numerischen (DEM) Trennkurven; (b) Vergleich der experimentellen und mittels Modell erstellten Trennkurven.

Abb. 111b zeigt den Vergleich von Modellkurven mit den experimentellen Kurven, wobei die effektive Viskosität bei $n = 15000 \text{ min}^{-1}$ angepasst wurde und dann für die anderen Drehzahlen

übernommen wurde. Während sich die Trennkurven mit steigender Drehzahl in Richtung feiner Partikelgrößen verschieben, weichen die Modellkurven mit abnehmender Drehzahl zunehmend von den experimentellen Trennkurven ab. Betrachtet man Gl. (204), so müsste η_{eff} mit abnehmender Drehzahl zunehmen, um die experimentellen Resultate richtig wiederzugeben. Weitere experimentelle Untersuchungen und DEM-Simulationen zum Wechselspiel von Partikel/Partikel-Stößen und resultierender effektiver Viskosität sollen Aufschluss über die Anwendbarkeit des vorgestellten einfachen Trennmodells geben.

4. Zusammenfassung

Durch einen Vergleich von experimentellen Resultaten mit DEM-Simulationen, welche die Partikelbewegung unter Berücksichtigung von Partikel/Partikel- und Partikel/Wand-Stößen berechnet, wurden die Strömungs- und Siebklassierprozesse betrachtet. Für die Siebklassierung konnte sowohl für die Simulation von Feingut-Verteilungssummenkurven als auch Trennkurven gezeigt werden, dass bei der Verwendung einer nicht-sphärischen Partikelform die Modellergebnisse besser mit den experimentellen Resultaten übereinstimmen. Auch ein Vergleich mit dem Modell von Dong et al. [49] unterstreicht die Bedeutung der adäquaten Berücksichtigung der Partikelform sowie der Partikelkontakte für eine exakte Modellierung realer Siebprozesse.

Beim Abweiseradsichter wurden die Strömungsverhältnisse in der Sichtzone mittels Hochgeschwindigkeitskamera aufgenommen. Bei Drehzahlen über 6000 min^{-1} (15 m s^{-1}) bildete sich ein Wirbel in der Sichtzone, der zu einer Einschnürung der Strömung und zu einer Fokussierung der Partikel auf die nacheilende Schaufel führt. Die beobachteten Flugbahnkurven der Partikel sowie die experimentell ermittelten Trennkurven konnten erstmals in DEM-Simulationen sehr gut wiedergegeben werden. Aus den gemessenen Rücksprunggeschwindigkeiten wurde mit einem einfachen Modell unter Berücksichtigung der Tatsache, dass die Partikel erst beim Rückspringen von der Schaufel eine signifikante Zentrifugalkraft erfahren, die Trenngrenze abgeschätzt. Die Kombination aus DEM und Experiment eröffnet die Möglichkeit, die Parameter, die in dieses einfache Modell eingehen, z.B. die effektive Viskosität, fundierter zu bestimmen und somit die Genauigkeit der Modellvorhersagen zu verbessern.

Nach erfolgreicher Validierung kann die DEM für beide Klassierverfahren dazu verwendet werden, Prozesse mit verschiedenen Betriebseinstellungen sowie geometrischen Änderungen ohne aufwendigen Umbau durchzuführen und Parameter wie das Einzelpartikelbewegungsverhalten zu bestimmen und zu untersuchen, die experimentell nur schwer zugänglich wären. Vor allem ist es aber durch die DEM-Simulationen auch möglich, makroskopische Modelle zu generieren und entsprechende Parameter zu ermitteln, die in

Feststofffließschemasimulation [205] verwendet werden und dadurch zur effektiven Prozessoptimierung beitragen können.

Danksagung

Für die finanzielle Unterstützung der Projekte (WE 2331/16-2, KR 3446/7-2 und TE 361/3-2) im Rahmen des SPP 1679 bedanken wir uns bei der Deutschen Forschungsgemeinschaft (DFG). Die originale Form des verwendeten DEM-Codes „DEM-Calc“ basiert auf einer Entwicklung des LEAT, Ruhr-Universität Bochum, Deutschland. Der Code „DEM-Calc“ ist dann sowohl an der Ruhr-Universität Bochum als auch an der Technischen Universität Berlin, Deutschland kontinuierlich weiterentwickelt worden. Wir danken allen daran Beteiligten.

IX. DEM simulations of screening processes under the influence of moisture

Frederik Elskamp^{1*}, Harald Kruggel-Emden¹

¹Mechanical Process Engineering and Solids Processing, Technische Universität Berlin, Ernst-Reuter-Platz 1, D-10587 Berlin, Germany

*Corresponding author. E-mail address: frederik.elskamp@tu-berlin.de

The following accepted manuscript appeared as journal version in Elskamp F., Kruggel-Emden H., 2018, DEM simulations of screening processes under the influence of moisture, Chemical Engineering Research and Design 136, 593-609 and may be found at <https://doi.org/10.1016/j.cherd.2018.06.022>.

Abstract

In a wide field of applications, screening is required to separate bulk materials according to their particle sizes. Due to environmental, material or process related effects, particles frequently prevail in moist conditions, which is not preferred due to attractive forces altering the screening efficiency, but often not preventable. As for the design of dry screening processes detailed particle-based simulation approaches like the discrete element method (DEM) and phenomenological models are available, a step towards meeting the requirements for real particle systems under moist conditions is made. Therefore, batch screening under the influence of moisture is investigated experimentally and by using DEM simulations involving different sized polyoxymethylene and glass spheres. For this purpose, a DEM code is extended to calculate forces caused by liquid bridges, forming out between particles or walls close to each other under moist conditions. Thereby, the bridge formation and rupture and the liquid distribution are considered. First, the DEM framework is validated against experiments by monitoring the capillary and viscous force acting on two liquid bridge contact partners. Further extensive validations are performed by comparing the fraction retained over time and the final liquid distribution for discontinuous screening under the influence of various amounts of liquid for different mechanical agitations in experiments and simulations. Finally, the detailed liquid distribution over time in the DEM simulations is examined and general conclusions are drawn. The overall aim is to use the framework and the respective data, to extend phenomenological process models for screening under moist conditions in subsequent studies.

Keywords: Discrete element method (DEM); Capillary and viscous forces; Liquid bridge; Screening; Moisture

1. Introduction

In order to separate bulk material in many industrial applications, screening is a technical simple but important process step to classify particles according to requested size class specifications [2,3]. Until now, screening under the influence of a liquid phase has rarely been

investigated. Pure experimental investigations have been performed, e.g. by Guerreiro et al. [31], who focused on the optimization of the residual moisture content and the separation efficiency on the screen. Further research addressed the vibrating dewatering of bulk material on screens [264] or the effect of wet screening on particle size distribution [32]. The performance of wet and dry screening was exemplarily compared by Robertson et al. [33].

To avoid extensive experimental tests, the discrete element method (DEM), which was first introduced by Cundall and Strack [10], can be applied to study screening and its sub-processes in detail. It has been proven as a suitable tool in various investigations on screening [5,6,20,198,236]. However, the particles were assumed as dry or the influence of the fluid was omitted in these studies. In contrast, some researchers concentrated on wet screening applications. In the investigation by Dong and Yu [202], the particle flow and the complex screen geometry as well as a simplified description of the fluid flow modeled by computational fluid dynamics was taken into account. Other researchers coupled discrete element simulations with methods used for simulating the dynamics of continua like the smoothed particle hydrodynamics (SPH) for wet screening. In the work by Fernandez et al. [9], one-way coupled DEM-SPH simulations are performed to take the particle as well as the fluid flow into account. Therein, the particles are completely covered by the surrounding fluid, which reduces the bonding of particles, removes pile-ups on the screen and supports the transport of fine particles through the apertures resulting in an improvement of the screening efficiency. In contrast, a slight natural amount of water in the material can result in bonding of particles and in a lower screening efficiency [32]. Therefore, it is preferable to perform screening either completely under fully dry or wet conditions. Nevertheless, as fully dry or wet conditions cannot always be ensured, the screening behavior under the influence of moisture must be better understood to determine the impact in respective processes. Since discrete element simulations seem to be suitable also for this purpose, the contact forces in the DEM have to be extended by forces, which arise from the presence of liquid. An overview of theoretical developments of discrete particle simulations of dry and wet particulate systems is given by Zhu et al. [60]. Besides systems where the particles are completely surrounded by a liquid, most of the researches are limited on applying a small amount of liquid to ensure only individual capillary bridges without liquid in the pores in between the particles.

The forces acting on particles due to the formation of liquid bridges were studied in many investigations without (e.g. [104–106,265,266]) and with (e.g. [14,117,119,267,268]) using particle based simulation methods such as the DEM and by applying models for the forces, formation and rupture of the liquid bridges (first method) or by adjusting the restitution coefficient to account for the affected contacts (second method). The first method has the advantage of being more realistic when the resulting restitution coefficient is close to zero, due to taking the possible adhering of contact partners into account, which is not possible in the

second method. However, resulting lubrication forces have to be considered by additional models, whereas in the second method, these forces are directly considered in addition to the capillary forces [269]. Latter approach was used by several researchers, among them Fu et al. [270] who studied the impact behavior of wet granules on dry surfaces to obtain the contact behavior under such conditions. A lot of effort was put into measuring and investigating the restitution coefficient of various dry particles on different wet surfaces, first experimentally and numerically by Antonyuk et al. [271,272] and later experimentally complemented by Crüger et al. [273,274]. In addition, Sutkar et al. [275], developed expressions for the wet restitution coefficient by energy and dimensional analysis. The interaction between wet particles in a fluidized bed by considering a restitution coefficient which is varied in time and space depending on the moisture content was studied numerically by van Buijtenen et al. [276].

Some of the researchers, who modeled liquid bridges, only considered capillary forces while others also took the influence of viscous forces into account, which are more important for large liquid viscosities or in systems with particles under high velocities. Kralchevsky and Nagayama [277] give an overview and comparison about lateral capillary forces. One of the first expressions for the capillary force of a liquid bridge based on its total energy was given by Israelachvili [266]. Lambert et al. [265] and Gabrieli et al. [278] compared two different capillary force methods, namely the energetic method based on the derivation of the total interfacial energy and a method based on the Young-Laplace equation where the pressure and tension terms obtained from the meniscus profile are summed up. Therein, a further subdivision in gorge (e.g. [113]) and boundary (e.g. [279]) methods can be made. Soulié et al. [280] and Richefeu et al. [281] proposed an approximate exponential fitting of the Young-Laplace equation for unequal sized spheres and offered an equation for calculating the capillary force during and after a direct particle contact. A commonly used model for the capillary forces, based on the pressure difference across the liquid bridge, was later presented by Rabinovich et al. [104]. They proposed and validated equations for liquid bridge contacts between a sphere and a wall as well as between two unequal sized spheres with different wettability. Another capillary liquid bridge model was developed by Willett et al. [105], providing equations for the force acting between two unequal sized spheres and their rupture distance. Weigert and Ripperger [106] introduced a liquid bridge model, where besides the capillary force, the bridge volume is calculated from the half-filling angle. A comparison of the three aforementioned capillary bridge models in terms of their applicability in a DEM framework has been carried out by Gladkyy and Schwarze [115]. Furthermore, Lian et al. [113] developed a closed form equation for capillary bridges between spherical particles which was later extended by Lian and Seville [114] to calculate capillary bridges more accurately with general closed-form expressions also applicable for unequal sized spheres, differing wettability and varying liquid bridge volumes.

Adams and Perchard [107] derived a viscous force model in the normal direction, which was implemented by several other authors (e.g. [14,112,113]). Pitois et al. [109] investigated the viscosity effects between two moving spheres connected by a liquid bridge and extended the aforementioned model, which was also applied by Washino et al. [117]. A commonly used liquid bridge viscosity model in tangential direction is the extended model by Goldmann et al. [108], which was applied by many authors (e.g. [113,117,282,283]). In further studies, Pitois et al. [110] proposed a dynamic rupture distance and validated their liquid bridge viscosity model.

The formation, shape, liquid volume and liquid redistribution after rupture of a bridge was intensively studied by Pepin et al. [111] as well as by Shi and McCarthy [112]. Schmelzle and Nirschl [118] studied mixing of dry and wet granular material with the DEM and performed a regression analysis for the liquid bridge force which also gave information about the rupture distances and transfer ratios. All three studies assumed a constant liquid bridge volume between formation and rupture. To overcome this lack, Wu et al. [284] developed a dynamic liquid bridge formation model for equal sized particles, capable of predicting the actual liquid volume in the bridge and on the particles. In particular, this is relevant for highly viscous liquids and short collisions.

Although mostly small liquid amounts are applied to the particles, the liquid bridges between them can become big enough to overlap with other bridges nearby. To prevent this, Scholtès et al. [120] proposed a numerical procedure to identify such overlapping bridges. For the case when a larger amount of liquid is present in a process, Melnikov et al. [121] provided a model to combine capillary bridges, menisci and fully saturated pores to liquid clusters. Additionally, for the case of such a funicular state, Wu et al. [122] investigated the forces and the rupture of liquid bridges between three spherical particles.

One of the first studies of larger particulate systems with equal sized spheres in the DEM was conducted by Yang and Hsiau [285] who applied powders in a 2D vibrated bed under the influence of a small amount of liquid. An early 3D study of a packed bed with wet coarse uniform spheres was performed by Yang et al. [286]. The flow of dense cohesive granular materials in a homogeneous plane shear without interstitial fluid was investigated by Rognon et al. [287] with the help of the molecular dynamics method in 2D. Based on this, the major laws for modeling the flow of wet granular media in the pendular state and the influence of capillary effects were examined applying three dimensional simulations by Khamseh et al. [288]. Among further applications which were simulated and studied with the help of the DEM, Radl et al. [119] investigated the mixing of wet particles in a bladed mixer application. Rotating drums with wet material were studied by Liu et al. [268] and Tsunazawa [267], who applied capillary bridge models and took viscosity effects into account. Further studies on this application were done by Washino et al. [14] who developed a new liquid dispersion model to

take the partial wetting of particles into account. Heine et al. [289] investigated the droplet dynamics in the spray zone of a two-fluid nozzle and the single particle wetting with a coupled DEM-CFD approach. Furthermore, Lim et al. [290] studied mixtures under the influence of liquid in vibrated beds and He et al. [291] simulated wet cohesive particles in spout fluid bed applications. However, for screening such investigations are mostly lacking [202].

In addition to the liquid bridge models, an appropriate calibration of DEM parameters has to be performed to apply the DEM for complex processes like screening under the influence of moisture. A review for DEM parameters and contact models for granular material has been done by Horabik and Molenda [247] who highlighted the importance of material and interaction properties for obtaining reliable information out of DEM simulations. Several methods have been proposed to calibrate DEM parameters [126,127,130,157] and recently, a general straightforward procedure for spherical and non-spherical particles with a high degree of automation was proposed by Elskamp et al. [263].

2. Numerical method

In this section, the discrete element method and the applied force laws including the contact, the capillary and the viscous forces as well as the formation and rupture of liquid bridges are summarized.

2.1 The discrete element method

The DEM is capable of tracking the translational and rotational motion of particles in various systems [60,61]. For this purpose, the Newton's and Euler's equations are integrated

$$m_i \frac{d^2 \vec{x}_i}{dt^2} = \vec{F}_i^c + \vec{F}_i^l + m_i \vec{g}, \quad (205)$$

$$I_i \frac{d\vec{\omega}_i}{dt} = \vec{M}_i, \quad (206)$$

with particle mass m_i , particle acceleration $d^2 \vec{x}_i / dt^2$, contact force \vec{F}_i^c , liquid bridge force \vec{F}_i^l , gravitational force $m_i \vec{g}$, moment of inertia I_i , angular acceleration $d\vec{\omega}_i / dt$, angular velocity $\vec{\omega}_i$ and external moments resulting out of contact and liquid bridge forces \vec{M}_i . Explicit integration schemes (comp. e.g. [82]) are used to solve both equations (eq. (205) and eq. (206)).

A sketch of two colliding spheres of different sizes i and j is shown in Fig. 112. The contact forces consist of a normal component and the tangential forces

$$\vec{F}_{ij}^c = \vec{F}_{ij}^{cn} + \vec{F}_{ij}^{ct}, \quad (207)$$

where the normal component is obtained from a linear spring damper model as

$$\vec{F}_{ij}^{cn} = k^n \delta_{ij} \vec{n}_{ij} + \gamma^n \vec{v}_{ij}^n, \quad (208)$$

where k^n is the spring stiffness, δ_{ij} the virtual overlap, \vec{n}_{ij} a normal vector, γ^n a damping coefficient and \vec{v}_{ij}^n the normal velocity at the contact point [92].

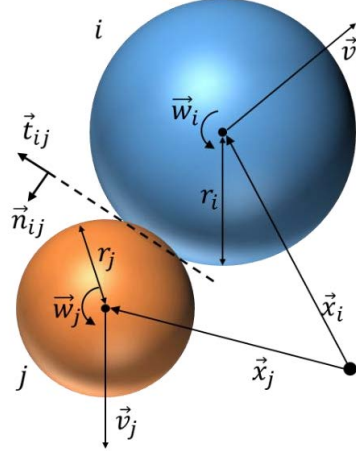


Fig. 112: A collision of two spherical particles.

The coefficient of normal restitution between dry particles e_{pp}^n as well as particles and walls e_{pw}^n is determined by k^n and γ^n . For the tangential forces a linear spring limited by the Coulomb condition is used, resulting in

$$\vec{F}_{ij}^{ct} = -\min(k^t |\vec{\xi}_{ij}|, \mu_c |\vec{F}_{ij}^n|) \vec{t}_{ij}, \quad (209)$$

where k^t is the tangential stiffness of a linear spring, μ_c is the friction coefficient, $\vec{\xi}_{ij}$ is the relative tangential displacement and \vec{t}_{ij} is the tangential unit vector [94].

2.2 Liquid bridges in the discrete element method

Liquid, which is added to dry material, can be in different states depending on the saturation of the pores between the particles. If only a small amount of liquid is present, it will form individual, pendular bridges between pairs of particles. In the funicular state more than two particles can share one liquid bridge due to the filling of some of the pores between the particles. In the capillary state all pores between the particles are filled with liquid [13]. In the investigation here, only a small amount of liquid is added and uniformly distributed on the particles to ensure the pendular state.

The presence of liquid results in the formation of liquid bridges, which evokes several bonding forces acting on the particles. In this investigation, only the capillary forces \vec{F}_{ij}^{cap} and the viscous forces in normal \vec{F}_{ij}^{nvis} and tangential \vec{F}_{ij}^{tvis} direction are taken into account as

$$\vec{F}_{ij}^l = \vec{F}_{ij}^{cap} + \vec{F}_{ij}^{nvis} + \vec{F}_{ij}^{tvis}. \quad (210)$$

Note that the tangential capillary force vanishes due to the assumption of a symmetric structure of the liquid bridge. Moreover, the particle motion is not affected by the small mass of liquid in the liquid bridges (comp. [14]) and the gravitational force of the liquid is neglected, which is valid to assume for sufficiently small capillary bridges in the pendular state [109,280]. The external moment \vec{M}_i (comp. eq. (206)) is extended and is now the sum of the moments due to a contact $\vec{M}_{C,i}$ and a liquid bridge $\vec{M}_{L,i} = \vec{r}_i \times \vec{F}_i^{tvis}$.

2.2.1 Liquid bridge formation and volume

When two particles i and j or a particle and a wall get into contact under the influence of moisture, a liquid bridge forms out between the contact partners (comp. Fig. 113).

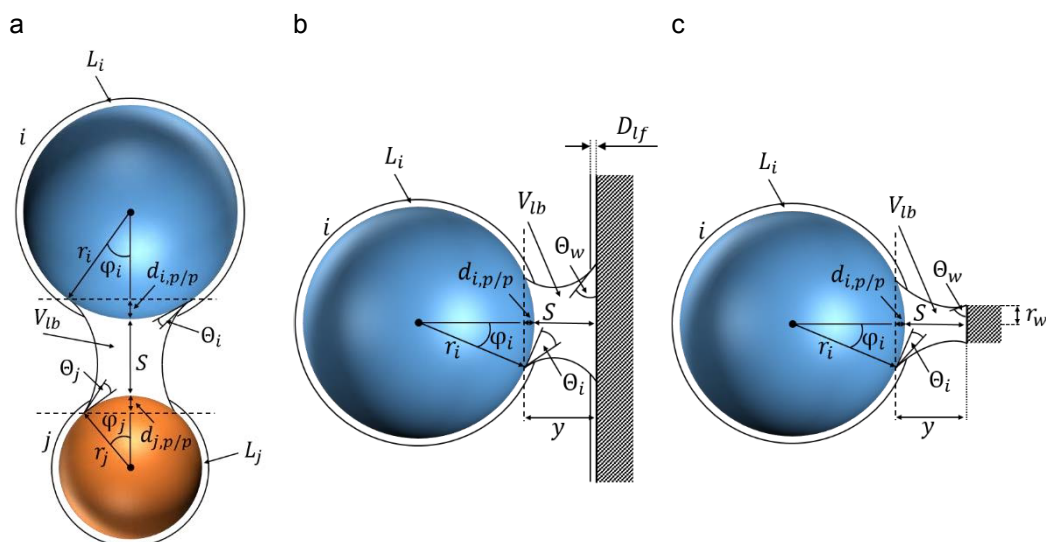


Fig. 113: Liquid bridges between (a) two different sized spherical particles, (b) a particle and a large wall (side wall, $r_w > r_i$) as well as (c) a particle and a small wall (screen wire, $r_w < r_i$).

In case of two particles, where a liquid with a low viscosity is equally distributed on their surfaces, the geometrical assumption is made, that the liquid on the spherical caps of the respective particles (dashed lines in Fig. 113) contributes in a liquid bridge (comp. [112]). The height of one of the spherical caps $d_{i,p/p}$ for particle i , also called immersion distance, is calculated as

$$d_{i,p/p} = r_i - \sqrt{r_i^2 - \left(\frac{r_i r_j}{r_i + r_j}\right)^2}, \quad (211)$$

with the radii r_i and r_j of the two particles i and j . $d_{j,p/p}$ is calculated analogously. The total volume of the liquid bridge V_{lb} is calculated for two spheres as proposed by Shi and McCarthy [112] as sum of the liquid volume contributed from each particle

$$V_{lb} = V_i + V_j = \frac{L_i}{2} \left(1 - \sqrt{1 - \frac{r_j^2}{(r_i + r_j)^2}} \right) + \frac{L_j}{2} \left(1 - \sqrt{1 - \frac{r_i^2}{(r_i + r_j)^2}} \right), \quad (212)$$

where L_i and L_j are the total liquid volumes present on particles i and j . Note that the dimensionless liquid volume of the liquid bridge is $V_{lb}^* = V_{lb}/r_{eff}^3$, where $r_{eff} = 2r_i r_j / (r_i + r_j)$ is the effective radius. The assumption of an equally distributed liquid can be made for low liquid viscosities and hydrophilic surfaces [14] and has been proven as a suitable assumption in case that it is not desired to track the spatial distribution of the liquid on particles and walls [118]. Thereby, it should be noted, that it results in a slightly higher number of liquid bridges with respective lower volumes for materials with a low wettability compared to considering the spatial distribution of the liquid.

For a particle i and a wall, the effective radius is $r_{eff} = r_i$ and the volume of the liquid bridge is $V_{lb} = V_i + V_w$. In case of a wall, where the half length of the sides (r_w) is larger than the radius r_i of the sphere ($r_w > r_i$, referred to as large wall) the liquid volume V_i contributed from the particle is assumed to be like when a particle gets in contact with another particle of the same size, calculated as

$$V_i = \frac{L_i}{2} (1 - \sqrt{0.75}). \quad (213)$$

The liquid contributed from the wall is assumed as

$$V_w = W_{lf} \frac{\pi}{4} r_i^2, \quad (214)$$

where W_{lf} is the liquid film thickness on the wall and $\frac{\pi}{4} r_i^2$ is the projection surface of the spherical cap of the particle on the wall (comp. Fig. 113).

For a wall, where one half side is shorter than the radius of the particle ($r_w < r_i$, referred to as small wall), which is e.g. the case for screen wires, the liquid bridge volume is calculated differently. These wires are approximated by several triangular elements (comp. [236]), giving a nearly cylindrical shape. Two neighboring elements with the same normal vector form a flat surface. If a particle is close to a screen wire, a direct contact between the particle and one of these surfaces is assumed. The liquid contributed from the particle is based on the calculation of a spherical ring with the area $A_{sr} = 2\pi r_i 2r_w$. The contact area of the sphere and a small wall is only the part $\frac{2\varphi}{360}$ of this area, where φ is the half filling angle, resulting in

$$A_{sw} = 2\pi r_i 2r_w \frac{2\varphi}{360}. \quad (215)$$

With proposed geometric considerations for equal sized spheres and a direct contact, it is $\varphi = \cos^{-1} \left(\frac{r_i - d_{i,p/p}}{r_i} \right) = 30^\circ$. To obtain the liquid that contributes from the particle, the area A_{sw} must be multiplied with the liquid film of the sphere which is $S_{lf} = \frac{L_i}{4\pi r_i^2}$, giving

$$V_i = \frac{L_i}{6r_i} r_w. \quad (216)$$

Under the same geometric considerations, the liquid contributed from the small wall can be calculated as

$$V_w = W_{lf} r_i 2r_w, \quad (217)$$

where $r_i 2r_w$ is the projection surface of the particle's spherical cap on the wall.

In this investigation, it is assumed that a liquid bridge between a particle and a wall is always located at the shortest distance of both contact partners. This means that the entire liquid bridge is moving with the particle and that it is not fixed at the first point of contact. Although a wall can be approximated by several triangular wall elements in the DEM, a particle is only able to have a liquid bridge contact with the closest element of this wall. If a particle is already in contact with another element of a wall, the existing contact information is transferred. Moreover, in this investigation the assumption is made, that the volume of the liquid bridge is constant from its formation until its rupture. The liquid volume from particles and walls contributing in liquid bridges is stored in temporary values until all liquid bridge formation processes of one time step are calculated. After that, the volume on the walls (proportional on each element of a wall) and on the particles is determined. This ensures that liquid bridge contacts of one contact partner with several other contact partners at the same time are all build up under the same conditions.

2.2.2 Capillary liquid bridge force

The capillary liquid bridge force can be calculated based on several different models. As described before, a classification can be made between the energetic method and a method based on the Young-Laplace equation. Additionally, the models can be subdivided into two groups the gorge (neck) and boundary (contact) methods. In the first group, the force is determined at the neck of the liquid bridge, whereas in the second group the force is calculated in the contact region of solid and liquid (comp. Fig. 113) [60]. A selection of models is briefly described in the following and later applied in DEM simulations.

Based on the models used by Rabinovich et al. [104] and Pitois et al. [109], which belong to the neck method, the capillary force between two particles i and j and between a particle i and a wall are calculated in this work as

$$\vec{F}_{ijpp}^{cap} = \left(-\frac{\pi\sigma r_{eff}(\cos\theta_i + \cos\theta_j)}{1 + 1/\left(\sqrt{1 + \frac{2V_{liq}}{(\pi r_{eff} S^2)}} - 1\right)} - 2\pi\sigma r_{eff} \sin(\theta_{ij}) \sin(\theta_{ij} + \varphi) \right) \vec{n}_{ij}, \quad (218)$$

$$\vec{F}_{ipw}^{cap} = \left(-\frac{2\pi\sigma r_i(\cos\theta_i + \cos\theta_w)}{1 + S\sqrt{\pi r_i/V_{lb}}} - 2\pi\sigma r_i \sin(\theta_{iw}) \sin(\theta_{iw} + \varphi) \right) \vec{n}_{iw}, \quad (219)$$

where σ is the surface tension coefficient, θ_i , θ_j and θ_w are the static contact angles of the particles i and j and a wall, respectively. $\theta_{ij} = (\theta_i + \theta_j)/2$ and $\theta_{iw} = (\theta_i + \theta_w)/2$ are the mean contact angles between two particles as well as between a particle and a wall, respectively (comp. [123]). Note that the contact angle is the angle formed by a drop of liquid on the surface of a solid to the surface of this solid. The size of the contact angle between liquid and solid depends on the interaction between solid, liquid and vapor at the three phase contact points. The smaller this interaction is, the larger the contact angle becomes [292]. Therein, a differentiation is made between the dynamic contact angle, which occurs in case of wetting and dewetting of a solid as well as the static contact angle, where the surrounding does not influence the contact area between liquid and solid during the measurement. Note that the static contact angle is used for the applied models. S is the separation distance between particles or between particles and a wall. In the second part of both equations, the attraction force due to the vertical component of the surface tension of the liquid bridge is taken into account. Therein, the half filling or “embracing” angle φ is calculated in case of two spheres as

$$\varphi = \sqrt{S/r_{eff} \left(-1 + \sqrt{1 + 2V_{lb}/(\pi r_{eff} S^2)} \right)}. \quad (220)$$

The relation between the volume and a given half filling angle φ is as follows

$$V_{lb} = \pi\varphi^2 r_{eff}^2 S + 0.5\pi\varphi^4 r_{eff}^3. \quad (221)$$

For a sphere and a plate with given V_{lb} , the relation is

$$\varphi = \sqrt{2S/r_i \sqrt{1 + V_{lb}/(\pi r_i S^2)}}. \quad (222)$$

In section 3, some other capillary bridge models, which are applicable for a liquid bridge between two spheres are applied to validate them against experimental results and compare them with the already introduced model by Rabinovich et al. [104]. Therefore, they are briefly outlined here. In the capillary bridge model by Willett et al. [105] the force is calculated as

$$\vec{F}_{ipp}^{cap} = 2\pi r_{eff} \sigma \exp(f_1 - f_2 \exp(f_3 \ln S^* + f_4 \ln^2 S^*)), \quad (223)$$

where the scaled dimensionless half-separation distance is

$$S^* = \frac{S}{2\sqrt{V_{lb}/r_{eff}}} \quad (224)$$

and f_1, f_2, f_3, f_4 are coefficients derived by curve-fitting to a numerical solution. They are functions of θ_{ij} and V_{lb}^* which is explained in detail in the work by Willett et al. [105]. The latter group of authors also proposed a simplified capillary bridge model where

$$\vec{F}_{ipp}^{cap} = \frac{2\pi r_{eff} \sigma (\cos \theta_i + \cos \theta_w)}{1 + 2.1S^* + 10 \cdot S^{*2}}. \quad (225)$$

In the capillary bridge model by Weigert and Ripperger [106], which is an example for the boundary method, the force is calculated as

$$\vec{F}_{ipp}^{cap} = \frac{\pi}{4} (2r_{eff})^2 p \sin^2 \varphi + 2\pi \sigma r_{eff} \sin(\theta_{ij}) \sin(\theta_{ij} + \varphi), \quad (226)$$

where the half filling angle can be obtained as

$$\varphi = \sin^{-1} \left(\frac{V_{lb}}{0.12(2r_{eff})^2 (1 + 6S/2r_{eff})(1 + 1.1 \sin(\theta_{ij}))} \right)^{0.25} \quad (227)$$

and the capillary pressure is

$$p = \sigma \left(\frac{\cos(\varphi + \theta_{ij})}{r_{eff}(1 - \cos \varphi) + S} + \frac{1}{r_{eff} \sin \varphi \frac{r_{eff}(1 - \cos \varphi) + S}{\cos(\varphi + \theta_{ij})} (\sin(\theta_{ij} + \varphi) - 1)} \right). \quad (228)$$

2.2.3 Viscous liquid bridge force

The importance of the viscous force increases with a high liquid viscosity or larger interparticle velocities [107]. Due to the high frequency motion of a screen apparatus, the latter is relevant and therefore, this force is important in the following investigations. The normal viscous force was derived by Adams and Perchard [107] and can be obtained by

$$\vec{F}_{ij}^{nvis} = -\frac{6\pi\eta r_{eff}^2 \vec{v}_r^n}{S}, \quad (229)$$

where η is the liquid viscosity, $r_{eff} = r_i r_j / (r_i + r_j)$ the reduced effective radius and $\vec{v}_r^n = ((\vec{v}_i - \vec{v}_j) \cdot \vec{n}_{ij}) \vec{n}_{ij}$ is the relative normal velocity of the spheres with the velocities \vec{v}_i and

\vec{v}_j . Pitois et al. [109] extended this formulation to make the normal viscous force dependent on the volume of the liquid bridge V_{lb} , which was also applied in the work by Liu et al. [268]. Here, it is calculated as

$$\vec{F}_{ij}^{nvis} = -\frac{6\pi\eta r_{reff}^2 \vec{v}_r^n}{S} \left(1 - 1/\sqrt{(1 + V_{lb}/(\pi r_{reff} S^2))}\right)^2. \quad (230)$$

The tangential viscous force is proportional to both the relative translational and rotational velocities and is obtained by several authors [14,112,113] as

$$\vec{F}_{ij}^{tvis} = -6\pi\eta r_{reff} \left(\frac{8}{15} \ln \frac{r_{reff}}{S} + 0.9588\right) (\vec{v}_r^t + \vec{\omega}_r \times \vec{n}_{ij}), \quad (231)$$

with $\vec{v}_r^t = \vec{v}_i - \vec{v}_j - \vec{v}_r^n$ as the relative translational and $\vec{\omega}_r = r_i \vec{\omega}_i + r_j \vec{\omega}_j$ as rotational velocity of the spheres. Based on the numerical solution of the stokes equation, Goldman et al. [108] proposed the following equation for the tangential viscous force

$$\vec{F}_{ij}^{tvis} = -6\pi\eta r_{reff} \left(\frac{8}{15} \ln \frac{r_{reff}}{S} + 0.9588\right) \vec{v}_r^t - 6\pi\eta r_{reff} \left(\frac{2}{15} \ln \frac{r_{reff}}{S} - 0.2526\right) \vec{\omega}_r \times \vec{n}_{ij}, \quad (232)$$

which has a slight change in the part of the rotational velocity and is valid for smaller S ($S < 0.1r_{reff}$). In case of large S ($S \geq 0.1r_{reff}$) the following equation is proposed by Goldmann et al. [108]

$$\begin{aligned} \vec{F}_{ij}^{tvis} = & -6\pi\eta r_{reff} \left(\frac{8}{15} \ln \frac{r_{reff}}{S} + 0.9588\right) \vec{v}_r^t \\ & - \frac{6\pi\eta r_{reff}}{8} \left(\frac{r_{reff}}{S + r_{reff}}\right)^4 \left(1 - \frac{3r_{reff}}{8(S + r_{reff})}\right) \vec{\omega}_r \times \vec{n}_{ij}. \end{aligned} \quad (233)$$

When the separation distance S approaches zero, the viscous forces tend to infinity. For this reason, a minimum separation distance $S_{min} = 0.001r_{reff}$ is introduced and added to S (comp. e.g. [283]).

2.2.4 Liquid bridge rupture and redistribution

At a respective distance between two particles or a particle and a wall, the liquid bridge ruptures. This rupture distance is calculated as follows by several authors [106,113,278,280,281]

$$S_{rup} = r_{eff} (1 + 0.5\theta_i) V_{lb}^{*1/3}, \quad (234)$$

which is valid for equal contact angles. Willett et al. [105] extended this equation and calculated the rupture distance as

$$S_{rup} = r_{eff}(1 + 0.5\theta_i) \left(V_{lb}^{*1/3} + 0.1V_{lb}^{*2/3} \right). \quad (235)$$

For different sized spheres and different contact angles, the rupture distance is dependent on the contact angles and radii of the particles $r_i > r_j$ (comp. [105]) as

$$S_{rup} = r_{eff} \left(1 + (0.125\theta_i + 0.125\theta_j) \left(1 + \frac{r_j}{r_i} \right) \right) \left(V_{lb}^{*1/3} + \left(\frac{r_j}{2r_i} - \frac{2}{5} \right) V_{lb}^{*2/3} \right). \quad (236)$$

In order to take into account the influence of the particle velocity on the rupture distance, Pitois et al. [110] introduced the dynamic rupture distance as

$$S_{rup,dyn} = S_{rup} \left(1 + \sqrt{\left(\frac{(\vec{v}_i - \vec{v}_j)\eta}{\sigma} \right)} \right). \quad (237)$$

When the bridge ruptures, it ruptures at its thinnest point and the liquid of the liquid bridge is redistributed on the contributing particles or the particle and the wall. Here, it is assumed, that the liquid is instantly added to the liquid amount of both contact partners without a local distribution. To ensure the same conditions for new liquid bridge contacts, the liquid amount of one time step is cumulated and added to the particle or wall at the end of the current time step (comp. section 2.2.1). The resulting liquid film thickness is calculated as

$$P_{lf,i} = \sqrt[3]{\left(\frac{3V_{lb}}{4\pi} + r_i^3 \right)} - r_i. \quad (238)$$

The liquid share, which is received by the particle or the wall, is dependent on the rupture location. This location is dependent on the particle size, the contact angle and the volume of the liquid bridge. Note that due to neglecting the gravitational force for the liquid bridge, the rupture location is not influenced by the vertical position of one particle to another one. If the contributing particles are of the same size and have the same contact angles, the rupture location is centered between them giving the same liquid amount for both contact partners. For different sized particles with the same contact angles, which is the case in this study, the rupture location is closer to the small particle resulting in a larger amount of liquid assigned to the large one. To obtain this amount, the transfer ratio between the two contact partners is determined. Therefore, the shape of the liquid bridge before its rupture must be known, which can be assumed with the parabolic equation

$$Y(x) = ax^2 + bx + c. \quad (239)$$

The location of the thinnest point of this bridge is where the derivation $Y'(x) = 0$ and is denoted with the coordinates (x_{min}, y_{min}) . To obtain this point of the liquid bridge before its rupture, the

following six equations must be solved numerically. The three phase contact points are located on the two spheres with the coordinates $(0, y(0))$ and $(d_{lb}, y(d_{lb}))$ and can be obtained by

$$y(0) = \sqrt{r_i^2 - (r_i - d_{i,p/p})^2}, \quad (240)$$

$$y(d_{lb}) = \sqrt{r_j^2 - (r_j - d_{j,p/p})^2}, \quad (241)$$

$$d_{lb} = d_{i,p/p} + d_{j,p/p} + S, \quad (242)$$

where d_{lb} is the shortest length of the liquid bridge plus both cap heights. The solid liquid contact angles are related to the previously described parameters as

$$\theta_i = \frac{\pi}{2} + \tan^{-1}(y'(0)) - \sin^{-1}\left(\frac{y(0)}{r_i}\right), \quad (243)$$

$$\theta_j = \frac{\pi}{2} + \tan^{-1}(y'(d_{lb})) - \sin^{-1}\left(\frac{y(d_{lb})}{r_j}\right). \quad (244)$$

The volume of the liquid bridge is

$$V_{lb} = V_{lb,i} + V_{lb,j}, \quad (245)$$

where the volumes of the two parts of the liquid bridge, which are redistributed to each particle after rupture, are given by

$$V_{lb,i} = \pi \int_0^{x_{min}} y^2(x) dx - \frac{\pi}{6} (3y^2(0)d_{i,p/p} + d_{i,p/p}^3), \quad (246)$$

$$V_{lb,j} = \pi \int_{x_{min}}^{d_{lb}} y^2(x) dx - \frac{\pi}{6} (3y^2(0)d_{j,p/p} + d_{j,p/p}^3). \quad (247)$$

More details can be found in the works by Shi and McCarthy [112], Pepin et al. [111] and Schmelzle and Nirschl [118].

In case of a particle and a large wall, similar equations have to be solved. It is assumed that the shape of the bridge is the same as for two equal sized particles. Besides, the wall has no spherical cap, so it is not subtracted from the liquid bridge volume, giving $V_{lb,w} = \pi \int_{x_{min}}^{d_{lb}} y^2(x) dx$ (comp. eq. (247)). For a particle and a small wall, the shape is assumed to be like in case of two different sized particles where only the spherical cap of the particle is subtracted from the liquid bridge volume.

2.3 “Intercell” liquid bridge particle contacts and parallelization in the DEM

In addition to the implementation of the aforementioned models, it must be ensured, that the liquid bridge contacts are identified correctly in the applied DEM code. The following procedures are visualized in Fig. 114. In the DEM, it is essential to detect contacts between particles as well as between particles and walls fast and reliably. In order to avoid checking all possible contact partners of a domain for a contact, various detection methods based on Cartesian grids have been introduced, where based on binning of the particles only the possible contact partners in one cell are checked for a contact (comp. e.g. [293]). In a frequently used method, the grid is adjusted so that cells are larger than the largest applied particle diameter (comp. Fig. 114, the 8 large red, blue and white cells surrounded by red lines), and a particle is assigned to the cell where its center is located. In this way, possible contact partners are only in the same or surrounding cells. In case of a polydisperse system, many small particles can be in one cell, resulting in a longer time for the identification of contacts, giving a reason for a different grid based contact detection method. When relying on this approach throughout a DEM code, a small contact grid (comp. Fig. 114, the 16 small cells in each large cell) is applied to faster identify new and existing contacts between different sized particles (comp. [293]). A particle is assigned to each cell that is covered by a part of this particle. Thereby, only cells with a particle assigned to it must be checked for a contact and the amount of particles in one cell is comparatively small.

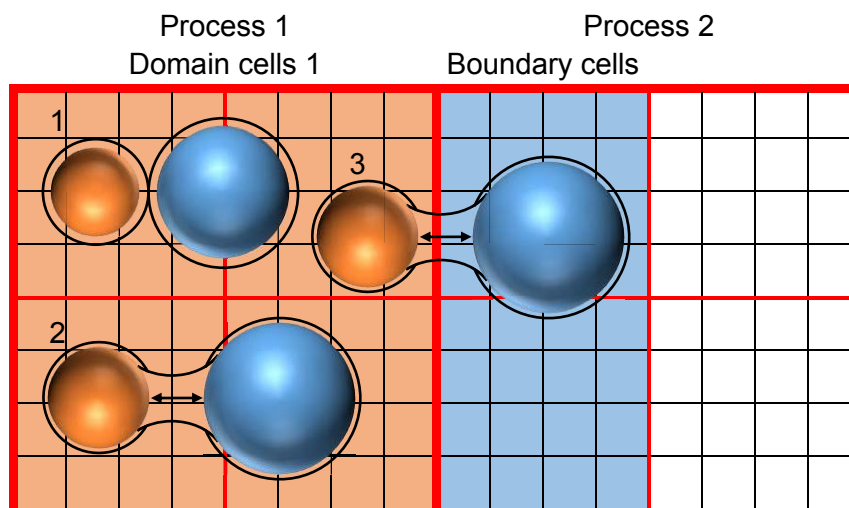


Fig. 114: “Intercell” liquid bridge particle contacts and parallelization by domain decomposition in the DEM.

In case of a liquid bridge contact, the localization of a new bridge is similar but with the liquid film added to the radius of the sphere as detection radius $r_d = P_{lf} + r_i$ (situation 1 in Fig. 114). Existing liquid bridges can become so large that they connect particles, which are not assigned to the same grid cell (situation 2 in Fig. 114). In order to detect these existing liquid bridges, a list containing the contact partners of each liquid bridge contact is created and checked each time step before the new liquid bridge contacts are identified. With the parameters V_{lb} and S_{rup} stored in a liquid bridge contact array, the liquid bridge forces, the rupture and the liquid

redistribution can be calculated at each time step for each liquid bridge contact even for “intercell” liquid bridge particle contacts.

In order to require less computational time to perform DEM simulations of complex process steps involving large numbers of particles like screening multiple processors can be used. The applied DEM code is parallelized using domain decomposition, where the computational domain is divided spatially in several smaller domains (comp. Fig. 114, Process 1 (red) and Process 2 (blue, white)), each assigned to one processor (comp. e.g. [294]). By applying a uniform or possibly even load based division, the calculation time can theoretically decrease linearly with applied processors. An exchange of information between two neighboring domains is performed with the help of boundary cells of the large DEM grid described previously (comp. Fig. 114, large blue cells surrounded by red lines). The boundary cells are one layer of cells around the domain. Particles exist in their domain and as boundary particles in the neighboring domain, so that properties assigned to the particles and contacts between particles are known in both domains e.g. for the calculation of forces. To avoid duplications in the subsequent exchange between the domains and in the visualization, this information is saved after the calculation procedure of one time step and the boundary particles including its contacts are removed. In the next time step, the particles are again inserted in the boundary cells and the information is restored before the particles are repositioned by integrating the equations of motion.

If parallel computing should be applied in the investigation here, the proper transfer of liquid bridge contact information and its history over the process boundaries must be ensured (situation 3 in Fig. 114). Therefore, the parts of the contact list containing liquid bridge contacts between boundary particles and their contact partners in the domain, are transferred between the processes. Additionally, the associated parts of the contact array with the stored liquid bridge contact data (V_{lb} and S_{rup}) and information about the boundary particles like the liquid volume on the particles L_i are exchanged. The same procedure can be utilized when periodic boundaries are applied. Note that the cells of the DEM grid (large cells in Fig. 114) should be large enough to detect an existing liquid bridge contact for the largest possible liquid bridge in the respective simulation.

3. Numerical validation

In order to validate the implementation of the capillary liquid bridge forces in the DEM code, various simulations of two particles comprising of one single sphere in presence of a liquid bridge are conducted (comp. Fig. 116c). The simulation setup is similar to the one used in the work by Gladkyy and Schwarze [115] which corresponds to the experiments performed by Willet et al. [105] and Rabinovich et al. [104].

In the simulations, two spheres are placed in direct contact to each other ($S = 0$ m), but without overlapping to prevent contact forces. This results in the formation of a liquid bridge. Gravitational forces are not taken into account. One particle is pulled away slowly to avoid viscous effects while the other one is fixed. The capillary liquid bridge force F_{cap} is tracked until the bridge brakes due to reaching the rupture distance S_{rup} . The implementation for a particle and a wall is validated similarly. Therefore, a particle is placed in direct contact to a wall to form out a liquid bridge before it is slowly pulled away from the wall.

In the work by Willet et al. [105] precision synthetic sapphire spheres and dimethylsiloxane as fluid with a surface tension of $\sigma = 20.6$ mN/m and a contact angle of $\theta_i = \theta_j = 0^\circ$ are used. Rabinovich et al. [104] used smaller silica particles, different oils with surface tensions of $\sigma = 24$ -28 mN/m and a contact angle between particles of $\theta_i = \theta_j = 10^\circ$ and between a particle and a wall of $\theta_i = \theta_w = 0$ - 10° .

In Fig. 115 exemplary results for the calculation of the capillary liquid bridge forces in the simulations for four different models [104–106] are compared to the corresponding experimental data by Willet et al. [105] (Fig. 115a) and Rabinovich et al. [104] (Fig. 115b). In Fig. 115a, the results for a liquid bridge of $V_{lb} = 13.6 \cdot 10^{-12}$ m³ between particles of $r_1 = r_2 = 2.381$ mm are presented. The models by Willet et al. [105] and Rabinovich et al. [104] fit the experimental results well over the whole distance and reveal only deviations for very small distances. In contrast, the model by Weigert and Ripperger [106] provides the best result for a very small distance but has large discrepancies for larger distances. Fig. 115b shows the results for a liquid bridge of $V_{lb} = 2 \cdot 10^{-19}$ m³ between smaller particles of $r_1 = 19$ μ m and $r_2 = 35$ μ m. The results are similar to those obtained for larger particles and volumes.

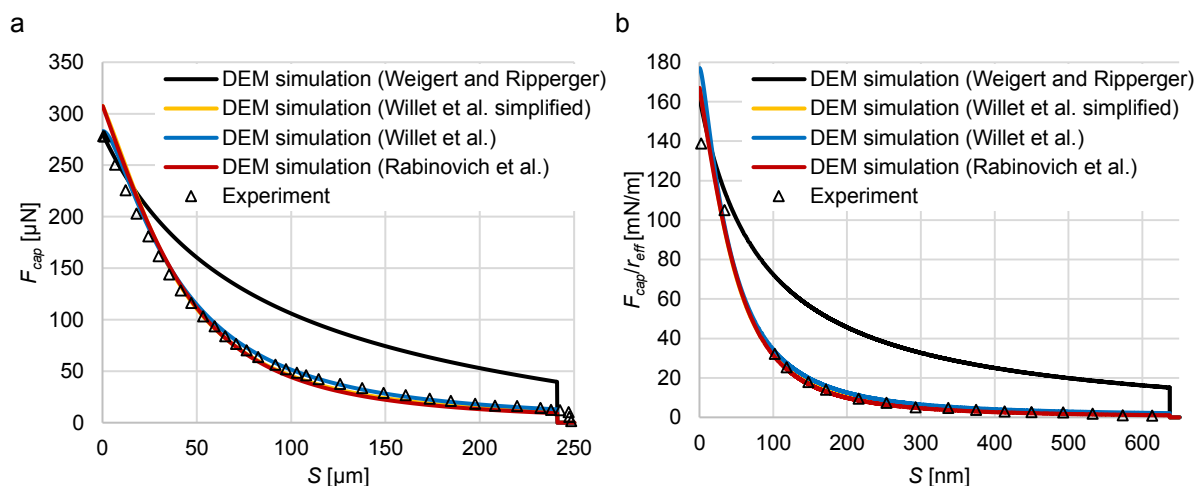


Fig. 115: Comparison of capillary liquid bridge forces of various models in DEM simulations to corresponding experimental data by (a) Willet et al. [105] for a liquid bridge of $V_{lb} = 13.6 \cdot 10^{-12}$ m³ between particles with $r_1 = r_2 = 2.381$ mm and $\theta_i = \theta_j = 0^\circ$ as well as by (b) Rabinovich et al. [104] for a liquid bridge of $V_{lb} = 2 \cdot 10^{-19}$ m³ between particles with $r_1 = 19$ μ m, $r_2 = 35$ μ m, and $\theta_i = \theta_j = 0^\circ$.

The results for a liquid bridge contact between a particle and a wall are presented in Fig. 116a only for the model by Rabinovich et al. [104] because the other models are not directly applicable for particle wall contacts. The applied parameters are $r_1 = 12$ μ m, $V_{lb} = 7 \cdot 10^{-19}$ m³,

$\theta_i = \theta_w = 0^\circ$ for the first configuration and $r_1 = 25 \mu\text{m}$, $V_{lb} = 170 \cdot 10^{-19} \text{m}^3$, $\theta_i = \theta_w = 10^\circ$ for the second configuration. The surface tension is $\sigma = 26 \text{mN/m}$ in both cases. Besides minor deviations at very small distances, the model by Rabinovich et al. [104] fits the experimental results very well in both cases. Therefore, this model is applied in the DEM simulations for the capillary forces.

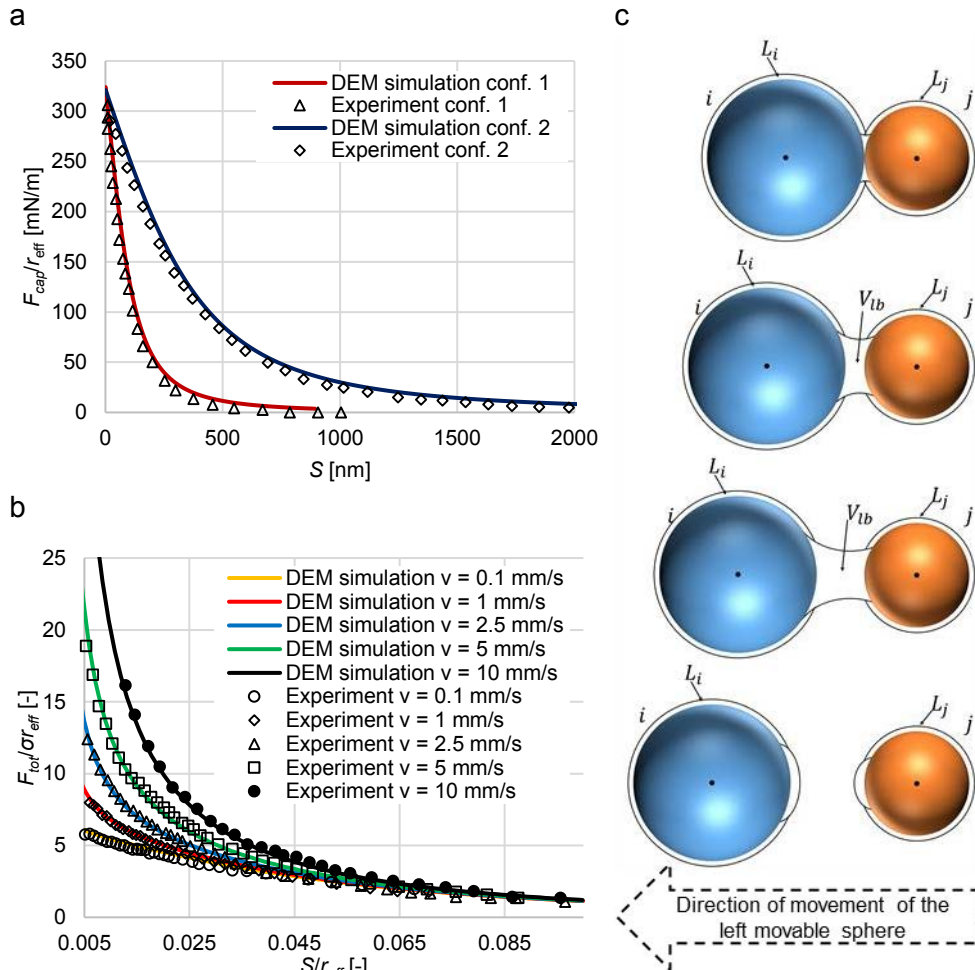


Fig. 116: (a) Comparison of capillary liquid bridge forces in DEM simulations to corresponding experimental data by Rabinovich et al. [104] for a liquid bridge between a wall and a particle with conf. 1: $r_i = 12 \mu\text{m}$, $V_{lb} = 7 \cdot 10^{-19} \text{m}^3$ and $\theta_i = \theta_w = 0^\circ$ as well as conf. 2: $r_i = 25 \mu\text{m}$, $V_{lb} = 170 \cdot 10^{-19} \text{m}^3$ and $\theta_i = \theta_w = 10^\circ$. (b) Comparison of liquid bridge forces (capillary and viscous) in DEM simulations to corresponding experimental data by Pitois et al. [110] for a liquid bridge of $V_{lb} = 5 \cdot 10^{-10} \text{m}^3$ between particles with $r_1 = r_2 = 4 \text{mm}$ and $\theta_i = \theta_j = 10^\circ$ as well as various constant particle velocities. (c) Schematic representation of the procedure until the bridge ruptures.

For the validation of the implementation of the viscous liquid bridge forces in the DEM code a similar setup as for the capillary forces is used, which corresponds to the experiments performed by Pitois et al. [110] (comp. Fig. 116c). In these experiments polished ruby spheres of $r_1 = r_2 = 4 \text{mm}$ with a contact angle of $\theta_i = \theta_j = 10^\circ$ are applied and one particle is pulled away with a constant velocity which is changed for the different experiments (here $v = 0.1\text{-}10 \text{mm/s}$). In the investigation here, a configuration with liquid properties of $V_{lb} = 5 \cdot 10^{-10} \text{m}^3$, $\sigma = 21 \text{mN/m}$ and $\eta = 0.1 \text{kg/ms}^2$ is simulated and compared to the experiments. In the simulations, the capillary and viscous liquid bridge forces are recorded as total liquid bridge force $F_{tot} = F_{cap} + F_{vis}$ until the bridge brakes due to reaching the rupture distance S_{rup} .

In Fig. 116b, the dimensionless force $F_{tot}/\sigma r_{eff}$ is plotted over the dimensionless distance S/r_{eff} . Note that the capillary model by Rabinovich et al. [104] is applied for calculating the capillary forces and the viscous models by Pitois et al. [109] and Goldmann et al. [108] are used for the viscous forces. In case of a low velocity of $v = 0.1$ mm/s, F_{tot} is nearly completely determined by the capillary force. For larger velocities, the influence of the viscous force increases for short distances between the particles. The simulation results fit the experimental ones very well for all applied velocities.

4. Determination of the contact angle and the transfer ratio

As previously described, larger contact angles reduce the capillary liquid bridge force and extend the rupture distance. In addition, a lower contact angle of one contact partner results in more liquid redistributed on this contact partner after the liquid bridge ruptures. Therefore, it is important to obtain the contact angle for the applied particles and walls with the respective liquid. In this work, polyoxymethylene (POM) and glass spheres are used for the particles as well as stainless steel and treated PVC (polyvinylchlorid) for the walls and water with a surface tension of $\sigma = 72.75$ mN/m as liquid.

In Fig. 117, the liquid bridges between two POM spheres, two glass spheres and a sphere and a steel plate are shown to visualize the different shapes of the bridges including the respective contact angles. To obtain this, one particle is pulled away from the other fixed particle or the wall, respectively.

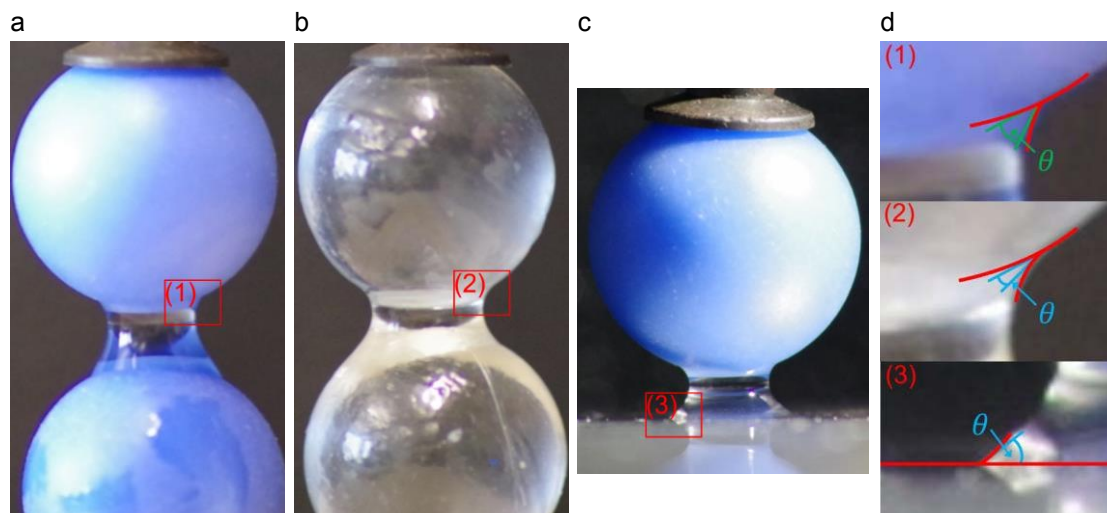


Fig. 117: Liquid bridges between (a) POM spheres, (b) glass spheres and (c) a sphere and a steel plate. (d) Close-up of the contact angles.

In the investigation here, an optical measurement tool is utilized to measure the angle between the slope of the liquid bridge and the tangent to the sphere at the three phase contact points (comp. Fig. 117). The average value of 10 experiments is determined. It can be seen in Fig. 117d that the contact angle between the POM spheres and water (1) is much larger than between the glass spheres and water (2). Furthermore, the bridge between the glass spheres

is wider, giving a smooth transition between sphere and liquid. Note that in this investigation the static contact angle is measured and applied in the DEM. In case of two spheres, the contact angle between each single spheres and the water was measured and the average value was taken to account for gravitational effects. This is due to reducing the complexity for processes with many particle and wall elements. In addition, the applied capillary force, rupture and redistribution models are based on the static contact angle (comp. e.g. [284]).

With the obtained contact angles (comp. Table 26), it is now possible to determine the liquid volumes $V_{lb,i}$ and $V_{lb,j}$ assigned to the particles i and j after the rupture of a liquid bridge by numerically solving the equations given in section 2.2.4. With these liquid volumes, the transfer ratio $T_{r,i} = V_{lb,i} / (V_{lb,i} + V_{lb,j})$ between contact partners can be obtained. Note that the transfer ratio is related to particle i , whereas the ratio for particle j is $T_{r,j} = 1 - T_{r,i}$.

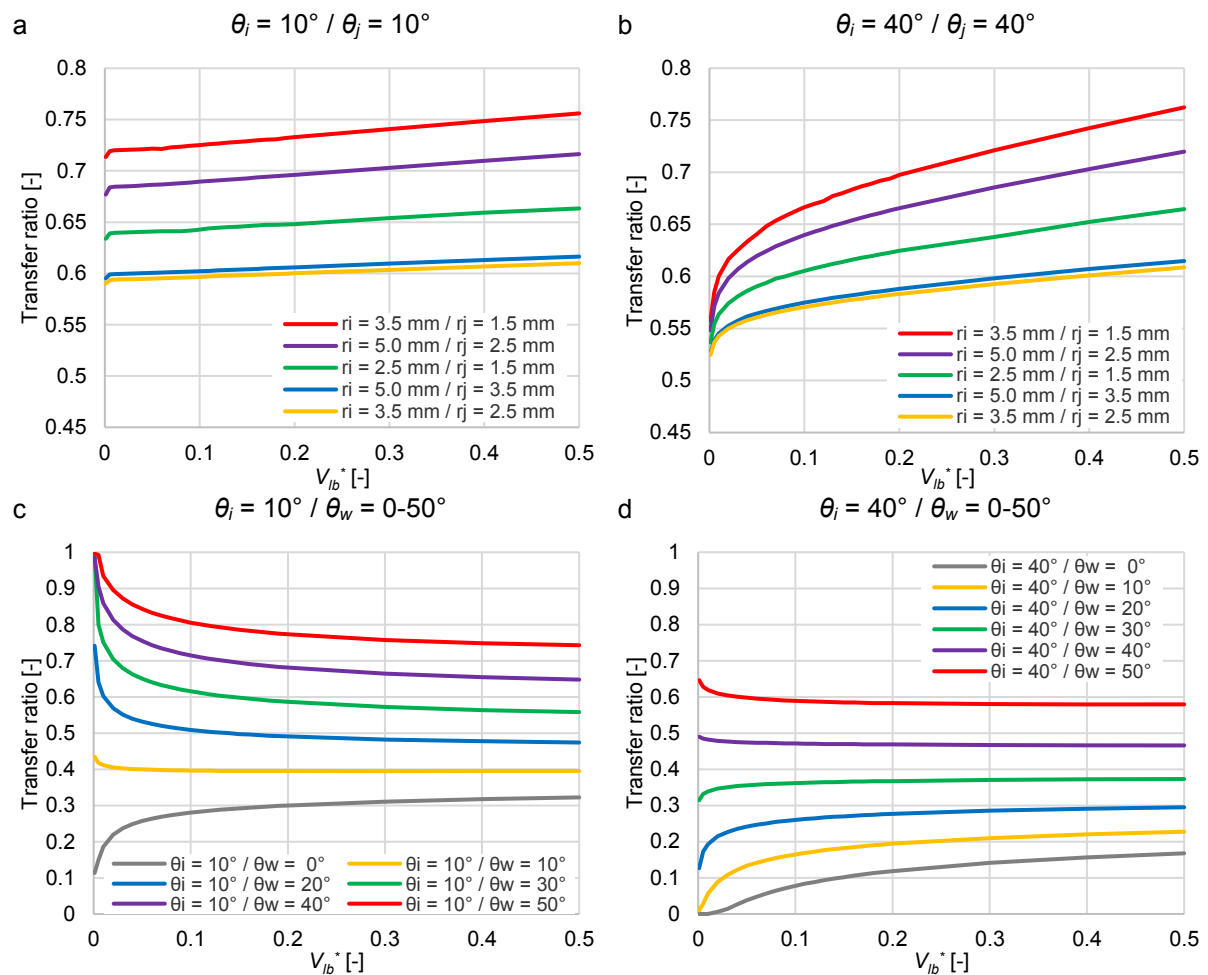


Fig. 118: Transfer ratio between spheres of different sizes and a contact angle of (a) $\theta_i = \theta_j = 10^\circ$ and (b) $\theta_i = \theta_j = 40^\circ$ as well as spheres of $r_i = 1.5$ mm with a contact angle of (c) $\theta_i = 10^\circ$ and (d) $\theta_i = 40^\circ$ and different walls with contact angles of $\theta_w = 0-50^\circ$.

In Fig. 118a,b the transfer ratios for several particle sizes and two contact angle combinations are shown for dimensionless liquid volumes of $V_{lb}^* \leq 0.5$. The transfer ratio increases for a larger particle size difference r_i/r_j and larger V_{lb}^* . For a low contact angle (comp. Fig. 118a), the transfer ratio inclines nearly linearly and slowly with V_{lb}^* , whereas a larger contact angle (comp. Fig. 118b) results in a steeper increase. Nevertheless, the transfer ratio for contact angles of

$\theta_i = \theta_w = 10^\circ$ is lower than for $\theta_i = \theta_w = 40^\circ$ for $V_{lb}^* \leq 0.4$. The transfer ratio between a particle and a wall is presented in Fig. 118c,d for several contact angle combinations. Here, the contact angle between a sphere and the water is chosen as before ($\theta_i = 10^\circ$ in Fig. 118c and $\theta_i = 40^\circ$ in Fig. 118d). As expected, a larger θ_w results in a higher transfer ratio $T_{r,i}$ and a larger θ_i causes a lower $T_{r,i}$. Additionally, if $\theta_i < \theta_w$ the transfer ratio increases with V_{lb}^* and if $\theta_i > \theta_w$ it declines.

An equation for the transfer ratio, which depends on the particle size and the liquid bridge volume, cannot be easily obtained to be applied in DEM simulations. Hence, for the DEM code, a look-up table is generated to include this data with minimal more computational effort. This look-up table is created in Matlab® for various possible contact partners before it is used in DEM simulations. Just one time in the initialization process of a DEM simulation this look-up table is read and only the required data (transfer ratios for all applied contact angle and contact partner combinations for liquid volumes of $V_{lb}^* \leq 0.5$) is written in a transfer ratio array. If necessary, non-existing values are obtained by linearly interpolating between available data. When a bridge ruptures during the DEM simulation, the transfer ratio for the respective contact angle and contact partner combination as well as the current liquid bridge volume (interpolation required) is obtained with the data stored in this transfer ratio array.

5. Experimental and numerical batch screening

A validation of the used DEM code and an in depth investigation of the related subprocesses during screening and their linkage to liquid bridge formation, stressing and rupture as well as liquid redistribution is performed by a comparison of results obtained from batch screening experiments and simulations under the influence of various liquid amounts.

5.1 Experimental and numerical setup

The mechanical and physical particle and wall properties are presented in Table 26.

Table 26: Mechanical and physical particle and wall properties.

| Mechanical particle property | Particle | | Wall | |
|---|--|--|----------|----------|
| | POM | Glass | Steel | PVC |
| Diameter d [mm] | 3 / 5 / 7 / 10 \pm 0.1 | 3 / 5 / 7 / 10 \pm 0.1 | - | - |
| Mass m [g] | 0.0192 / 0.0935 / 0.2459 / 0.7210 \pm 0.02 | 0.0353 / 0.1636 / 0.4490 / 1.3090 \pm 0.02 | - | - |
| Density ρ [kg/m ³] | 1.3570E+03 / 1.3580E+03 / 1.3356E+03 / 1.3425E+03 \pm 1.50 | 2.5240E+03 / 2.5351E+03 / 2.5373E+03 / 2.5300E+03 \pm 1.50 | 7.85E+03 | 1.30E+03 |
| Young's modulus E [N/m ²] | 2.84E+09 | 5.00E+10 | 2.08E+11 | 2.20E+09 |
| Poisson's ratio ν [-] | 0.35 | 0.2 | 0.30 | 0.4 |
| Stiffness k_{PP}^n / k_{PW}^n [N/m] | 1.00E+05 | 1.00E+05 | - | - |
| Contact angle θ [°] | 40 | 15 | 45 | 50 |

For the experiments in this study, a batch screening apparatus, which can be applied for dry and wet screening (comp. Fig. 119) is used. The screen apparatus is a modified "Haver and Boecker EML digital plus" batch screen tower with a circular screen surface, additionally

equipped with a feed bin on top of it to ensure that the particles in experiment and simulation reach the screen surface at the same time and that the screen excitation is already in a continuous motion. Additionally, an outlet is added below the screen to measure the particle passage through the apertures when they reach the collecting bin on a balance. Various screens with different aperture sizes can be staked over the outlet of the screen apparatus. In the investigation here, one screen surface is applied in each case with the aperture sizes in Table 27 adjusted to the particle sizes in Table 26.

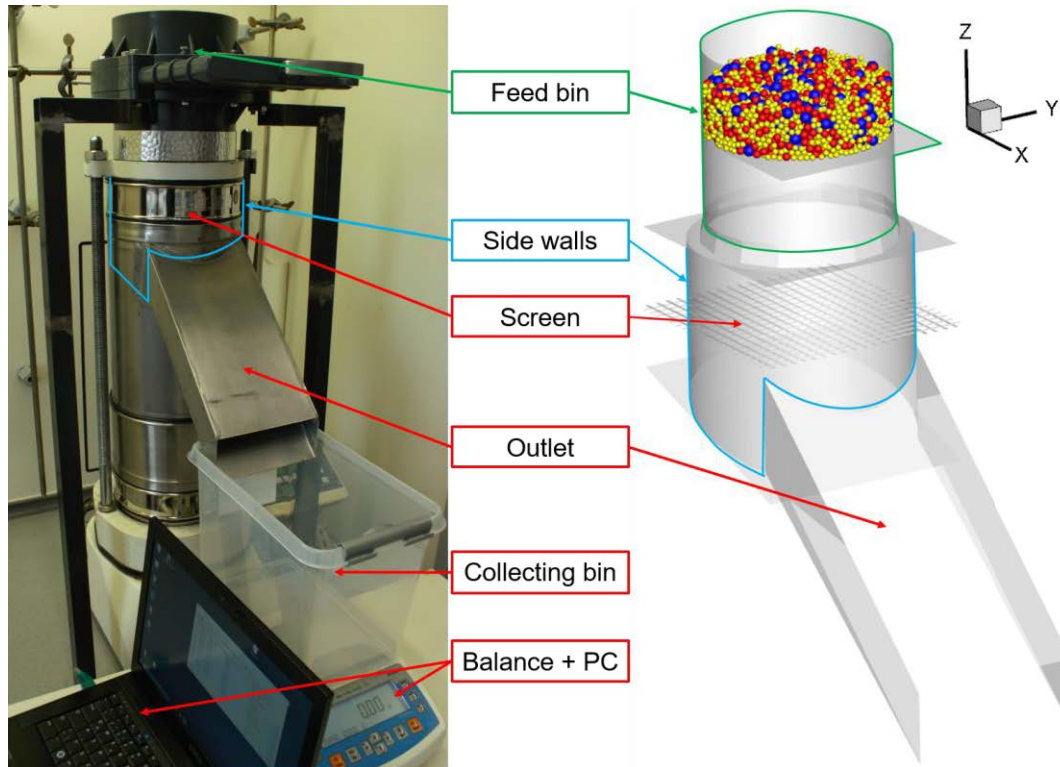


Fig. 119: (a) Experimental setup and (b) corresponding approximation in the DEM simulations of the batch screening apparatus.

In a first step, the weighted particles are filled well mixed with the respective already attached amount of water in the feed bin on a flat surface. After the screen reaches a steady motion, the surface in the feed bin is pulled out and all particles drop as bulk material on the screen surface. Some smaller particles directly pass through the apertures while others have to stratify through the gaps between larger ones until getting the possibility to pass through the apertures. After that, the particles drop on an inclined impact plate from where they get to the outlet and through it on a balance, which continuously weights the incoming material. In this way, the remaining mass over time can be compared between experiment and simulation for various configurations.

In this investigation, POM and glass spheres are applied in three different equally distributed discrete size classes. They are assumed to be ideal spheres of $d_1 = 5$ mm, $d_2 = 7$ mm, $d_3 = 10$ mm in the first configuration and $d_1 = 3$ mm, $d_2 = 5$ mm and $d_3 = 7$ mm in the second configuration. In all configurations, the particles and the aperture size are in the same relationship, $d_1 < d_2 < a < d_3$. In the following the particle classes are called small (d_1), near

mesh (d_2), which has the additional relationship $0.8a < d_2 < a$, and large (d_3). POM spheres are filled into the feed bin with a mass of $m_p = 3m_{pi} = 3 \times 250 \text{ g} = 750 \text{ g}$. The amount of glass spheres is chosen to be volume equivalent with the POM spheres giving a mass of $m_p \approx 1410 \text{ g}$ (comp. Table 27).

The experimental properties for the batch screening experiments can be found in Table 27. For both materials, three different liquid amounts in the range of $0 \% \leq M \leq 10 \%$ are applied. In the case of glass spheres, the percentage amount is lower in order to maintain a pendular regime. The applied liquid is distilled water. At the beginning of each simulation, the same liquid film thickness P_{lf} is assigned to each particle (comp. [267]). The walls are dry ($V^* = 0$). The screen profile is woven with cylindrical wires of $w = 2 \text{ mm}$ and $w = 1.6 \text{ mm}$ giving aperture sizes of $a = 8 \text{ mm}$ and $a = 5.6 \text{ mm}$, respectively. Note that the wires in the DEM simulation are approximated as horizontal bars (not woven) with a semicircular profile, which has proven to be a valid simplification (comp. [236]).

Table 27: Experimental properties for batch screening experiments.

| Properties | POM | Glass |
|------------------------|--|-------------|
| Particle mass [kg] | 0.75 | ~1.41 |
| Liquid amount [%] | 0 / 5 / 10 | 0 / 2.5 / 5 |
| Surface tension [N/m] | 0.07275 | |
| Aperture size [mm] | 8.00 ± 0.02 / 5.60 ± 0.01 | |
| Wire diameter [mm] | 2.00 ± 0.01 / 1.60 ± 0.01 | |
| Scree wire profile [-] | circular (woven) | |
| Set amplitude [mm] | 1 / 0.8 | |
| Frequency [Hz] | ~50.6 | |
| Stroke behavior | Elliptical, mainly vertical (comp. Fig. 120) | |

In Fig. 120, the screen motion in 3D obtained by measurements of an accelerometer (“Sequoia FastTracer PA”) fixed under the screen is presented.

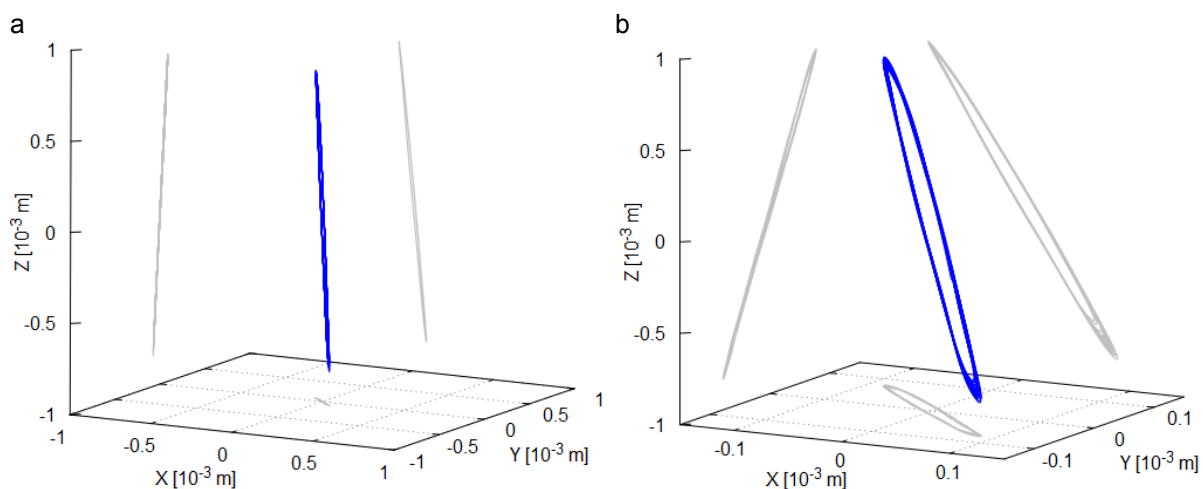


Fig. 120: Elliptical stroke behaviour of the batch screen apparatus applying an amplitude of $A = 1 \text{ mm}$ giving a frequency of approx. $f = 50,6 \text{ Hz}$ obtained by measurements of an accelerometer shown in (a) original scale and (b) with zoomed x- and y-axes.

The amplitude is set to $A = 1 \text{ mm}$ and to $A = 0.8 \text{ mm}$, respectively, resulting in a frequency of approximately $f = 50.6 \text{ Hz}$. The motion is elliptical but mainly in vertical direction (z- direction

of the screen of about 0.9 mm and 0.72 mm for the different configurations, respectively) while the motion in x- and y- directions is low with maximum amplitudes of $A < 0.1$ mm. In the following, the set amplitude is used to differentiate the cases.

In Table 28 the DEM parameters coulomb friction μ_c , rolling friction μ_{roll} and the coefficient of restitution e^n for POM and glass spheres with their respective contact partners are listed. Details according the determination can be found in a previous work by the authors [263]. Note that the coefficient of restitution for dry particles was obtained and applied in the simulations due to considering the adhering effects by implementing the liquid bridge models.

Table 28: DEM parameters for POM and glass spheres and various contact partners.

| Contact partner 1 | Contact partner 2 | μ_c [-] | μ_{roll} [m] | e^n_{dry} [-] |
|-------------------|--|-------------|------------------|-----------------|
| POM sphere | Steel (side walls, screen wires, bottom, outlet walls) | 0.3484 | 5.97E-05 | 0.8473 |
| POM sphere | POM sphere | 0.3725 | 4.63E-05 | 0.8038 |
| Glass sphere | Steel (side walls, screen wires, bottom, outlet walls) | 0.2866 | 1.09E-04 | 0.4351 |
| Glass sphere | Glass sphere | 0.1966 | 8.95E-05 | 0.7808 |

5.2 Fraction retained in experiments and DEM simulations

In the following, a comparison of the fraction retained between experiments and DEM simulations is carried out. An overview of all performed experiments and DEM simulations can be found in Table 29.

Table 29: Overview of performed simulations and experiments (averaged over 15 experiments).

| Simulation No. | Material | Particle size $d_{1/2/3}$ [mm] | Aperture size a [mm] | Amplitude A [mm] | Liquid amount M [%] |
|----------------|----------|--------------------------------|------------------------|--------------------|-----------------------|
| 1 | POM | 5/7/10 | 8 | 1 | 0 |
| 2 | POM | 5/7/10 | 8 | 1 | 5 |
| 3 | POM | 5/7/10 | 8 | 1 | 10 |
| 4 | POM | 5/7/10 | 8 | 0.8 | 0 |
| 5 | POM | 5/7/10 | 8 | 0.8 | 5 |
| 6 | POM | 5/7/10 | 8 | 0.8 | 10 |
| 7 | POM | 3/5/7 | 5.6 | 1 | 0 |
| 8 | POM | 3/5/7 | 5.6 | 1 | 5 |
| 9 | POM | 3/5/7 | 5.6 | 1 | 10 |
| 10 | Glass | 5/7/10 | 8 | 1 | 0 |
| 11 | Glass | 5/7/10 | 8 | 1 | 2.5 |
| 12 | Glass | 5/7/10 | 8 | 1 | 5 |
| 13 | Glass | 5/7/10 | 8 | 0.8 | 0 |
| 14 | Glass | 5/7/10 | 8 | 0.8 | 2.5 |
| 15 | Glass | 5/7/10 | 8 | 0.8 | 5 |
| 16 | Glass | 3/5/7 | 5.6 | 1 | 0 |
| 17 | Glass | 3/5/7 | 5.6 | 1 | 2.5 |
| 18 | Glass | 3/5/7 | 5.6 | 1 | 5 |

In Fig. 121 and Fig. 123, the results are presented as fraction retained over time which is

$$Y = Y(t) = m_{p,l}/m_{p,l,0}, \quad (248)$$

where $m_{p,l,0}$ is the initial mass at $t = 0$ s and $m_{p,l}$ is the remaining mass of the particles and the liquid which is not in the collecting bin at time t . The fraction retained can also be stated per particle size class i , if the undersized particles should be considered as different fractions in the DEM simulations which is exemplarily shown in Fig. 124. This resolved fraction retained can be calculated as

$$Y_i = Y_i(t) = m_{p,l,i}/m_{p,l,i,0}. \quad (249)$$

Here, $m_{p,l,i}$ and $m_{p,l,i,0}$ are the actual and initial fractional mass of the particles plus the liquid assigned to the particles.

In the first investigations, dry material with different size classes is screened (Simulation Nos. 1,4,7,10,13,16) and the experimental results for the fraction retained on the screen over time are compared to the ones obtained by DEM simulations in Fig. 121.

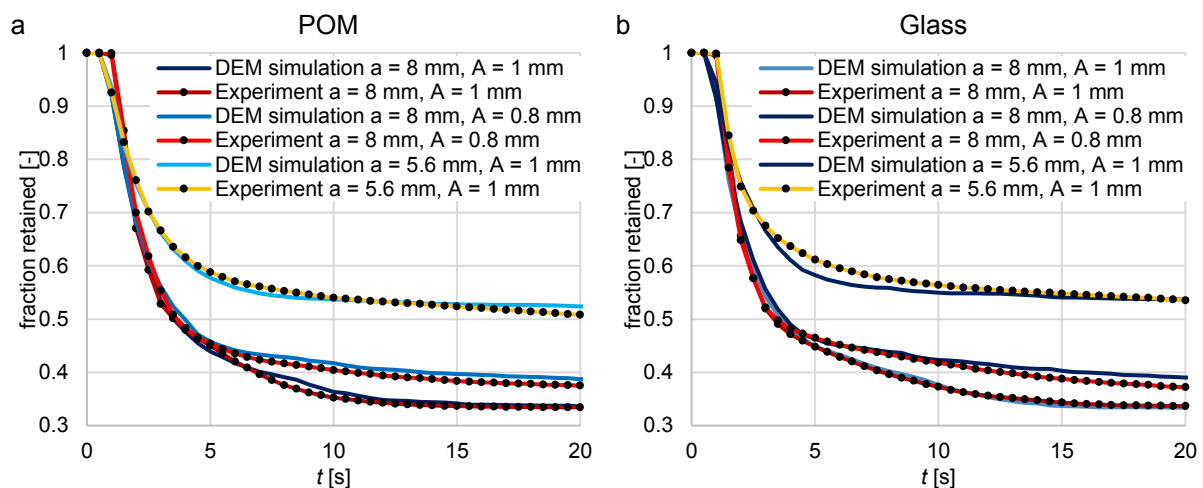


Fig. 121: Fraction retained on the screen over time applying (a) dry POM spheres with $a = 8$ mm ($d_{1/2/3} = 5/7/10$ mm) with $A = 0.8$ mm and $A = 1$ mm as well as $a = 5.6$ mm ($d_{1/2/3} = 3/5/7$ mm) with $A = 1$ mm and (b) dry glass spheres with $a = 8$ mm ($d_{1/2/3} = 5/7/10$ mm) with $A = 0.8$ mm and $A = 1$ mm as well as $a = 5.6$ mm ($d_{1/2/3} = 3/5/7$ mm) with $A = 1$ mm. All results are obtained by experimental investigations (results are averaged over 15 experiments) and DEM simulations, respectively.

Besides some minor deviations, the simulation results of POM spheres fit the experimental ones very well (comp. Fig. 121a). For an aperture size of $a = 8$ mm ($d_{1/2/3} = 5/7/10$ mm), an amplitude of $A = 1$ mm (now referred to as initial configuration, independent of M) results in a fast reduction of the fraction retained value until all particles are screened at $t \approx 15$ s. In contrast, an amplitude of $A = 0.8$ mm reduces the passing of particles after $t = 5$ s due to shorter particle throws resulting in less possibilities for the smaller particles to pass through gaps between coarse particles and the screen surface in the direction of the apertures. When an aperture size of $a = 5.6$ mm ($d_{1/2/3} = 3/5/7$ mm) is applied, the particles pass the apertures fast in the first seconds, but after $t = 2$ s the passing is reduced and takes longer than in the initial configuration, both in experiment and DEM simulation. After the first layers of undersized particles have passed the apertures, the larger particles peg the apertures more intensively

than in the initial configuration. Thereafter, the stratification through the coarse material to the screen surface is hindered. The results for dry glass spheres are very similar, but some larger deviations occur when applying a smaller aperture size (comp. Fig. 121b). The retardation is slightly more intensive, both in experiment and in DEM simulation.

In the next investigations, small liquid amounts are added to the particles. In Fig. 122 the visualization of the liquid distribution on the particles and walls as liquid film thickness is presented in ascending intensity of blue tones at $t = 3$ s. Some of the undersized particles have already passed the apertures and the remaining ones reveal thinner liquid films than the larger particles. Most of the large wall elements claim only thin liquid films.

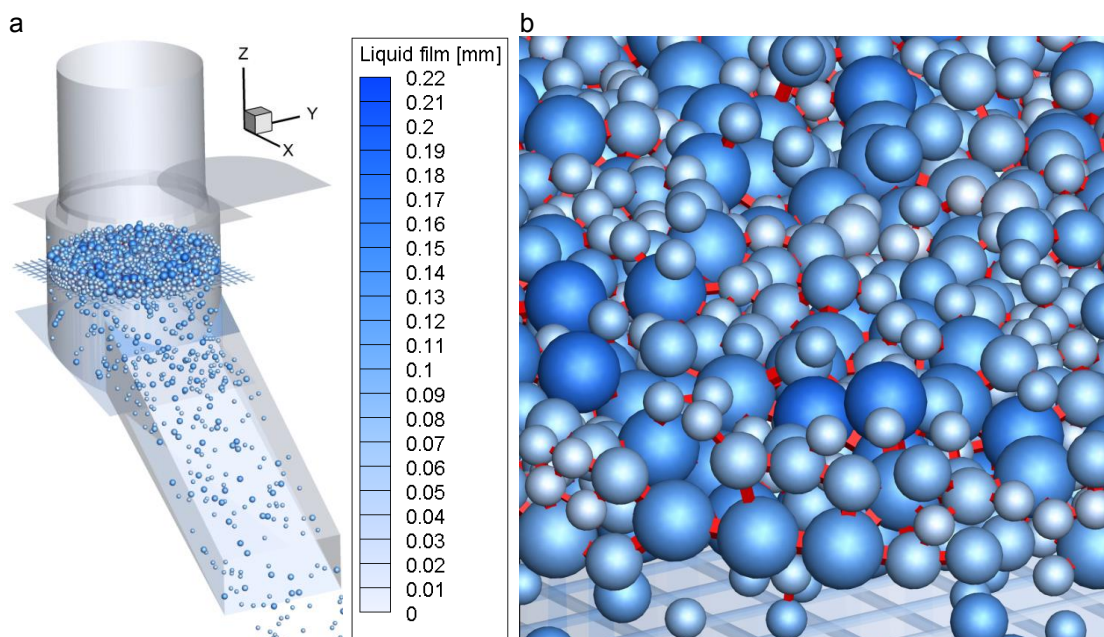


Fig. 122: Visualization of the liquid distribution on the particles and walls presented as liquid film thickness at $t = 3$ s for POM spheres ($a = 8$ mm, $d_{1/2/3} = 5/7/10$ mm) and a liquid amount of $M = 10\%$ for (a) the whole screen apparatus and (b) zoomed in to reveal the liquid bridge volume between particles presented as cuboids.

The close-up in Fig. 122b additionally reveals the liquid bridges between the particles and their respective volumes, presented as cuboids. The cuboids always have the length d_{lb} , hence, a part of them is inside the spherical caps of the two connected particles. The volume of the cuboids, which is visible outside the spheres, is equal to the volume of the liquid bridge. The cuboids are stretched when one particle move away from another until the liquid bridge ruptures. The screen wires also show relatively thin liquid films.

In Fig. 123, the experimental results for the fraction retained on the screen over time for dry particles and particles under the influence of different liquid amounts are compared to the ones obtained by DEM simulations. In the initial configuration (comp. Fig. 123a), a small liquid amount ($M = 5\%$) reduces the particle passage, whereas a larger amount ($M = 10\%$) does not further impair it, both in experiment and simulation. The influence of the water is comparatively low due to the large contact angles and particle sizes. Therefore, the capillary

force is low in comparison to the weight force. In the DEM simulations, slightly more particles remain on the screen between $t = 2.5-10$ s, but afterwards the results fit very well.

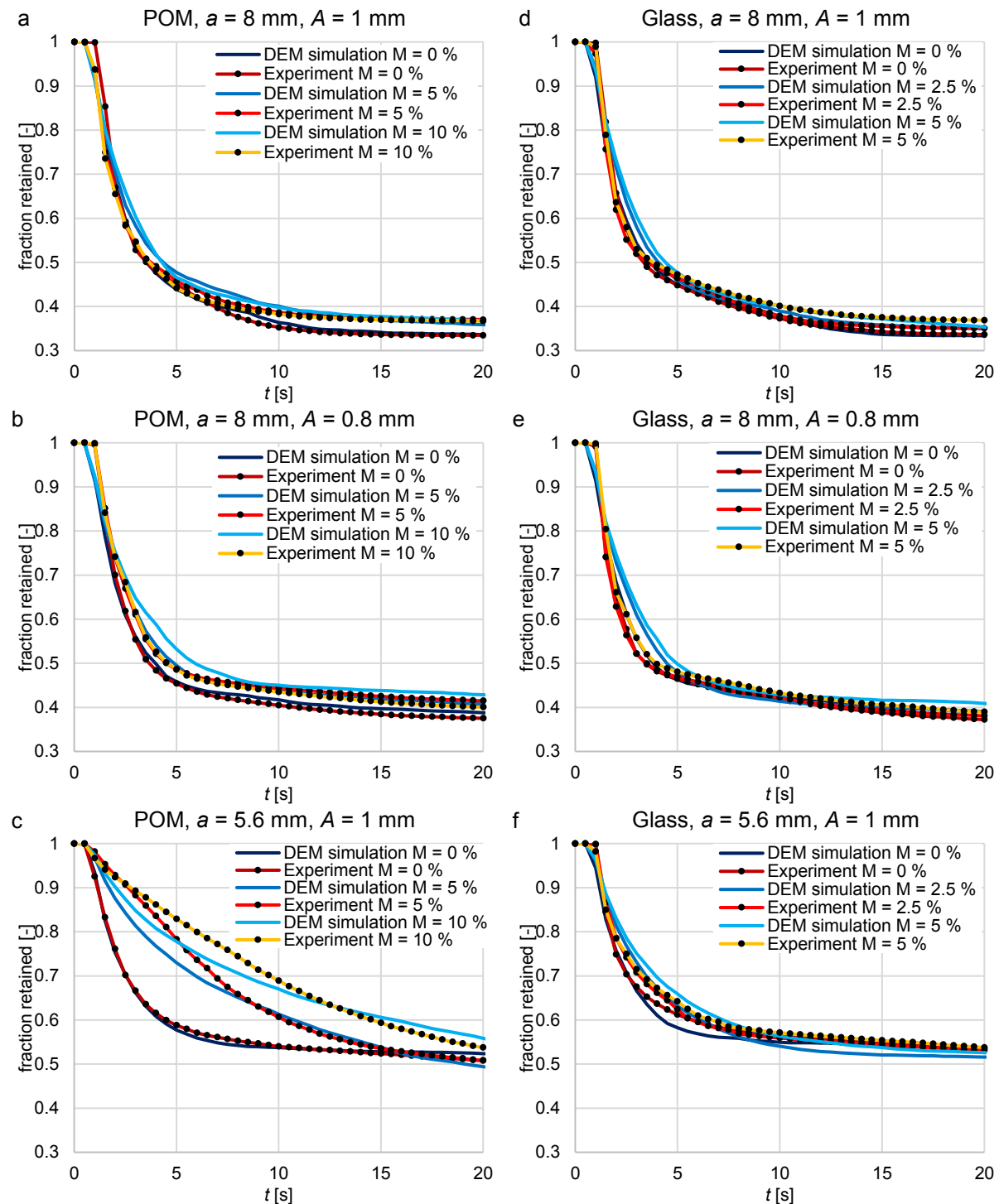


Fig. 123: Fraction retained on the screen over time applying (a,b,c) dry and wet ($M = 0/5/10\%$) POM spheres with $a = 8$ mm ($d_{1/2/3} = 5/7/10$ mm) with (a) $A = 1$ mm and (b) $A = 0.8$ mm as well as (c) $a = 5.6$ mm ($d_{1/2/3} = 3/5/7$ mm) with $A = 1$ mm as well as (d,e,f) dry and wet ($M = 0/2.5/5\%$) glass spheres with $a = 8$ mm ($d_{1/2/3} = 5/7/10$ mm) with (d) $A = 1$ mm and (e) $A = 0.8$ mm as well as (f) $a = 5.6$ mm ($d_{1/2/3} = 3/5/7$ mm) with $A = 1$ mm. All results are obtained by experimental investigations (results are averaged over 15 experiments) and DEM simulations, respectively.

When an amplitude of $A = 0.8$ mm is applied (comp. Fig. 123b), the fraction retained value is higher if water is added to the particles. The experimental and numerical results for a lower amount of water ($M = 5\%$) fit very well. However, in the DEM simulations, the fraction retained for a larger amount of water ($M = 10\%$) is slightly overpredicted. The influence of liquid is more

pronounced for the configuration with smaller particle diameters $d_{1/2/3} = 3/5/7$ mm (comp. Fig. 123c). Until $t = 20$ s the particle passage is reduced for $M = 5\%$ and even more retarded for $M = 10\%$. With smaller particle sizes applied in this investigation, the adhesive forces become larger relative to the weight force, which is relatively small due to the low density of POM. Due to the pegging of particles in the dry case, the fraction retained is similar after $t = 20$ s for $M = 0\%$ and $M = 5\%$ and only slightly larger for $M = 10\%$. The DEM simulations show the same trends but reveal some deviations between $t = 1-10$ s.

Applying the initial configuration with glass spheres as material (comp. Fig. 123d), a larger amount of water increases the experimentally and numerically obtained fraction retained. However, the influence of the water is relatively low due to the large particle size, density and the related masses. The simulation results under the influence of liquid both reveal some deviations between $t = 2-5$ s. Afterwards, the results fit very well. The same trends are recognizable for an amplitude of $A = 0.8$ mm (comp. Fig. 123e). Here, all the results are closer together.

The results for the glass spheres with smaller particle diameters of $d_{1/2/3} = 3/5/7$ mm (comp. Fig. 123f) are very different from those obtained with POM spheres. Particularly, the experimental results lie close to each other with slightly larger values if more water is added to the particles. Due to the larger density of glass spheres, the influence of the weight force compared to the capillary force is more intense than for POM. The simulation results reveal a bit more differences and slightly overpredict the fraction retained until $t \approx 7$ s and underpredict it afterwards. Due to the pegging of the dry particles, fewer particles remain on the screen at $t = 20$ s if water is added before the screening process. Overall, the simulation results fit the experimental ones quite good. The most deviations for the configurations with the larger diameters $d_{1/2/3} = 5/7/10$ mm are the result of overpredictions while in the other configurations under- and overpredictions occur.

The simulation results of the fraction retained resolved for the two undersized fractions (near mesh and small) are shown in Fig. 124 for various liquid amounts. In most of the configurations, the smaller particles with the diameter d_3 pass the apertures faster than the near mesh particles with the diameter d_2 . Besides one exception, this is also valid for the initial configuration. The smaller particles (d_3) at a liquid amount of $M = 10\%$ need more time to pass the apertures at the beginning (until $t = 7$ s), but then show expected results. Here, the water seems to have a large influence on the small particles (d_3). In the configuration with an aperture size of $a = 5.6$ mm (comp. Fig. 124b), the particles are more influenced by the water, but pass the apertures as estimated in terms of small and near mesh sized particles. Here, it is even more obvious, that after a while, the small and near mesh sized dry particles are hindered from passing the apertures. In both configurations where an amount of water is added to the

particles, the passage is slower in the beginning of the screening process, but it is not hindered and for $M = 5\%$ even less particles remain on the screen.

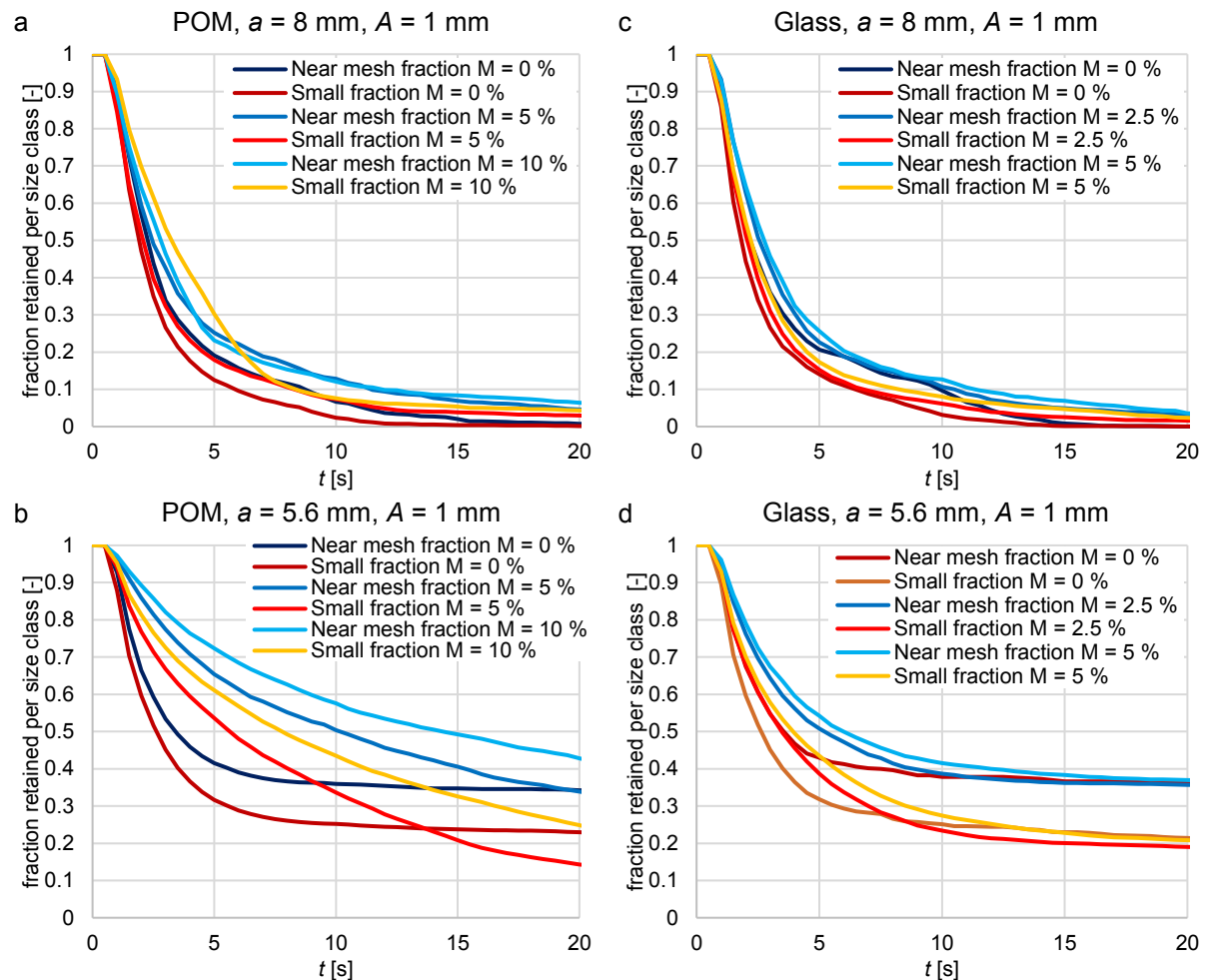


Fig. 124: Fraction retained on the screen over time presented for the small (d_3) and near mesh sized particle fractions (d_2) applying dry and wet ($M = 0/5/10\%$) POM spheres with (a) $a = 8\text{ mm}$ ($d_{1/2/3} = 5/7/10\text{ mm}$) and (b) $a = 5.6\text{ mm}$ ($d_{1/2/3} = 3/5/7\text{ mm}$) as well as dry and wet ($M = 0/2.5/5\%$) glass spheres with (c) $a = 8\text{ mm}$ ($d_{1/2/3} = 5/7/10\text{ mm}$) and (d) $a = 5.6\text{ mm}$ ($d_{1/2/3} = 3/5/7\text{ mm}$) all with $A = 1\text{ mm}$. All results are obtained by DEM simulations.

If glass spheres are applied in the initial configuration (comp. Fig. 124c), the resolved fraction retained values are as expected before. Interesting is that the small particles (d_3) under the influence of a liquid amount of $M = 5\%$ temporarily pass the apertures even slower than the dry near mesh sized particles (d_2). Besides the peculiarities mentioned about the not resolved fraction retained (comp. Fig. 123f), the configuration with small glass spheres (comp. Fig. 124d) shows expected results.

5.3 Liquid distribution in experiments and DEM simulations

In order to find out more about the reasons for the occurred deviations, a closer look should be taken at the liquid distribution. Hence, in Fig. 125 the liquid distribution at the end of the screening process is compared between experimental measurements and results obtained by DEM simulations for POM (Fig. 125a) and glass spheres (Fig. 125b). Note that the residuals (light blue contour, comp. Fig. 125c) are due to mixing, transferring, evaporation and slots in

the apparatus. This amount is subtracted from the liquid amount before the simulation. The other divisions (comp. Fig. 125c) are the feed bin, the side walls and the outlet (red contour), the coarse material and the screen wires plus the side walls of the screen (purple contour) and the fine particles plus the collecting bin (green contour). Note that the liquid of the currently existing liquid bridges is assigned by means of the transfer ratio (comp. section 4) to the particles or walls for the evaluations concerning the liquid distribution. When applying POM spheres in the DEM simulations (comp. Fig. 125a), the amount of water on the screen and on the coarse material as well as on the other wall elements is larger than in the experiments.

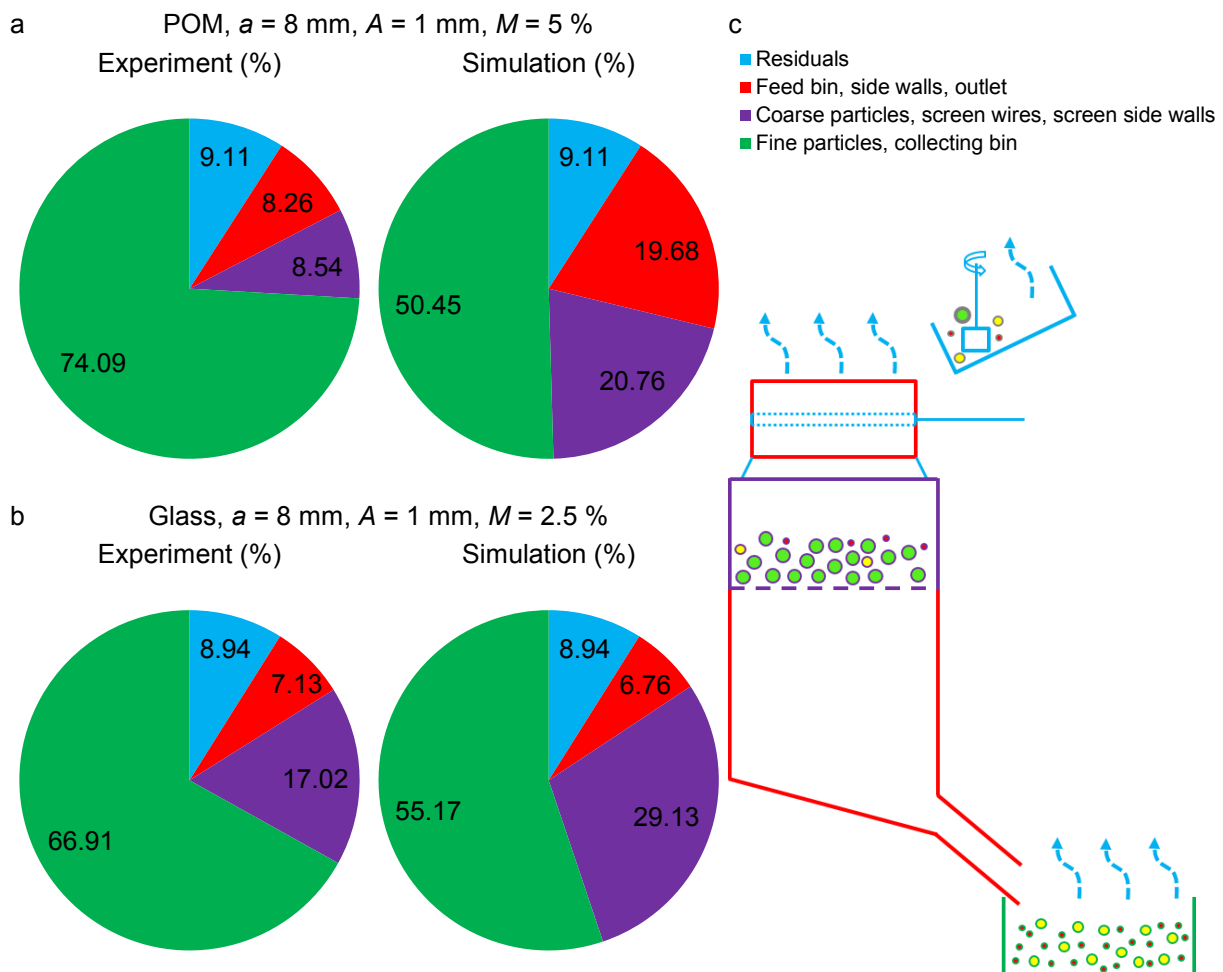


Fig. 125: Liquid distribution of the screening process at $t = 20 \text{ s}$ compared between experiments and simulations for (a) POM spheres with $M = 5 \%$ and (b) glass spheres with $M = 2.5 \%$ both with $a = 8 \text{ mm}$ ($d_{1/2/3} = 5/7/10 \text{ mm}$) and $A = 1 \text{ mm}$. (c) Visualization of the divisions of the screening apparatus and the applied material covered by liquid.

The liquid amount on the coarse particles and on the screen is also overpredicted in case of glass spheres (comp. Fig. 125b), but the other wall elements hold about the same amount of water in the experiments and the DEM simulations. Due to the large contact angle of POM, the liquid amount on the particles is lower in comparison to the glass spheres. When a liquid bridge between a wall and a POM sphere ruptures, the wall element takes a comparatively larger amount of liquid than after the rupture of a bridge with a glass sphere. After the liquid bridge between two glass spheres ruptures, relatively more water is assigned to the larger sphere in comparison to the configuration with POM spheres for a dimensionless liquid volume of

$V_{lb}^* < 0.4$, which is valid in the investigation here (comp. Fig. 118). Due to these reasons, the proportion of water on the coarse glass spheres is larger than on the coarse POM spheres.

The main reason for the underprediction of water on the fine particles and in the collecting bin is that the water in the simulations persists only on particles, walls and in liquid bridges. In contrast, the water in the experiments can also be separated from particles and walls in free motion. The liquid separation from particles due to vibrating dewatering is not realized in the DEM simulations until now and is required to be addressed in further investigations. First studies with the same configurations but with smaller apertures ($a < d_3$) reveal that the amount of water which pass through the outlet is approximately equal to the amount of water that is overpredicted on the coarse particles (and wall elements in case of POM) in the simulations. By considering this, the prediction of the amount of water, which adheres to the fine particles, might be correct, but the water accumulating in the collecting bin is not taken into account in the DEM simulations.

In Fig. 126, the liquid distribution over time during the screening process in the DEM simulations is shown. Here, it is possible to consider the various parts of the screen apparatus (all wall elements) separately (screen wires, feed bin, outlet, side walls) and only the liquid on and between the particles remaining on top of the screen is referred to as “coarse material”. Note that the liquid between two particles or particles and walls at time t is split up on the respective particle or wall like when the bridge would rupture at that point in time t (comp. section 4). The liquid on the particles that passed the outlet is referred to as “fines” in Fig. 126. To avoid confusions and redundancies, the division of the coarse material and fines into the particle fractions instead of the division of the screen apparatus is only shown for one case with glass spheres in Fig. 126c.

At $t = 0$ s, the water persists only on the particles above the screen (coarse material) in all simulations. The same liquid film thickness P_{lf} is applied for each particle (comp. section 5.1). Directly in the first time step, the first liquid bridges form out between particles as well as particles and walls. The amount of liquid of the coarse material decreases continuously, while the amount of liquid on the wall elements and particularly of the fines increases. Latter is not only due to the transfer of water between particles, but also due to small and near mesh particles passing through the apertures whereby they turn from coarse material to the fines. At the end of a screening process under investigated configurations (not necessarily $t = 20$ s), probably more liquid is assigned to the fines than to the coarse material which is already the case for the configurations shown in Figs. 126a,c. The increase of the amount of water on the wall elements is more pronounced in the simulations with POM spheres due to their lower wettability or rather their high contact angle. In Fig. 126a, the liquid amount on the screen apparatus is nearly equal to the liquid amount on the coarse particles at $t = 20$ s and still gets

closer. At this time, nearly all undersized particles have passed the apertures. Therefore, the change in the liquid amount is mainly due to the transfer between coarse particles and wall elements.

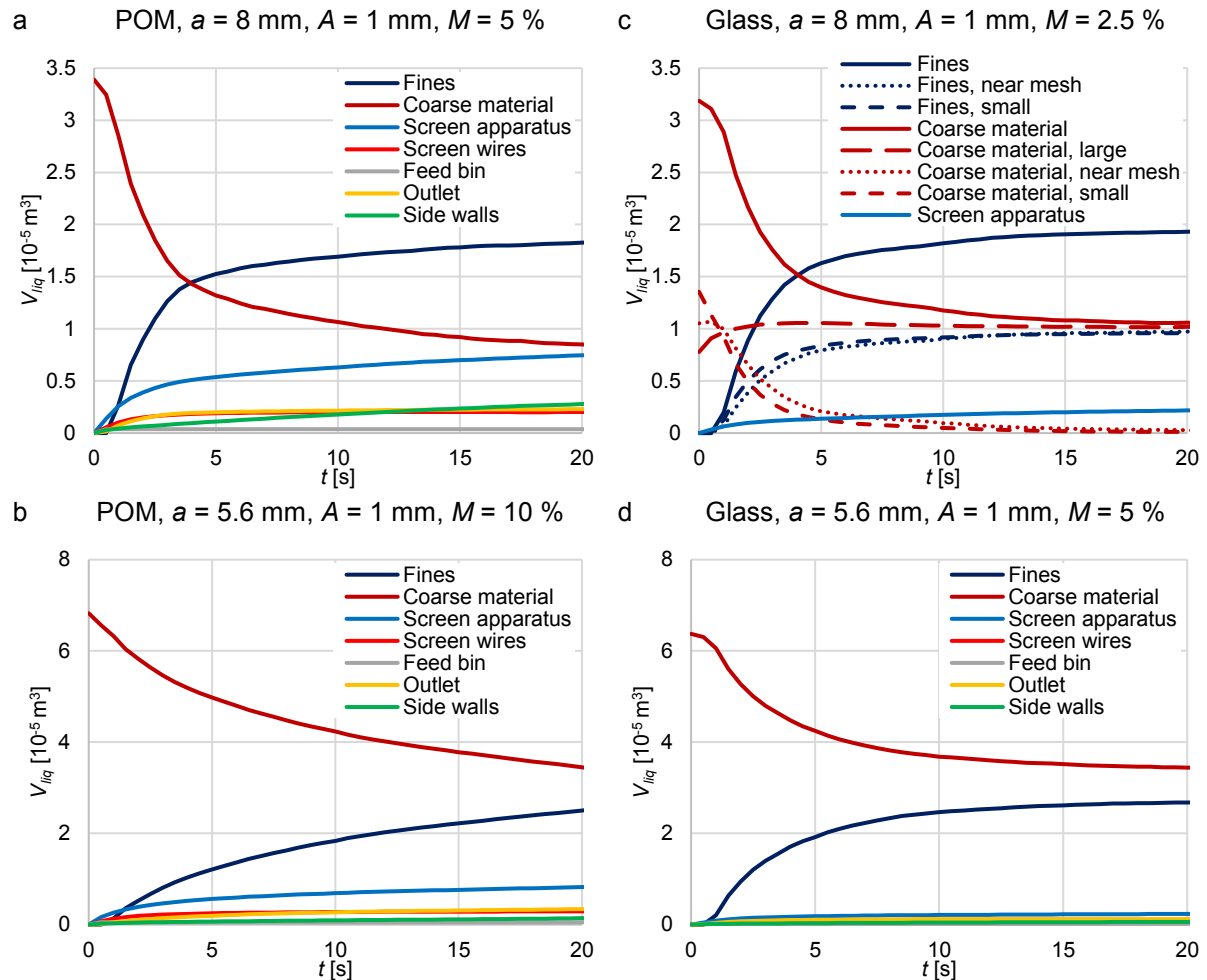


Fig. 126: Liquid distribution as liquid volume V_{liq} over time t during the screening process for POM spheres with $M = 5\%$ and (a) $a = 8\text{ mm}$ ($d_{1/2/3} = 5/7/10\text{ mm}$) as well as (b) $a = 5.6\text{ mm}$ ($d_{1/2/3} = 3/5/7\text{ mm}$) and glass spheres with $M = 2.5\%$ and (c) $a = 8\text{ mm}$ ($d_{1/2/3} = 5/7/10\text{ mm}$) as well as (d) $a = 5.6\text{ mm}$ ($d_{1/2/3} = 3/5/7\text{ mm}$) all with $A = 1\text{ mm}$. All results are obtained by DEM simulations.

In contrast to POM spheres, the liquid distribution in case of glass spheres (Figs. 126c,d) nearly reaches an equilibrium when the majority of the undersized particles are screened. In Fig. 126c it is also visible, that for the coarse material the amount of liquid on the near mesh and particularly on the large particles increases at the beginning of the screening process, whereas the amount of liquid on the small particles decreases at the same time. Both is mainly due to the transfer ratio between different sized spheres. Additionally, Fig. 126c provides the information, that slightly more water gets through the outlet on small than on near mesh particles. A larger amount of small particles passes the apertures, but each near mesh particle hold more water. In case of an aperture size of $a = 5.6\text{ mm}$ for both materials, some of the smaller particles are still ($t = 20\text{ s}$) on top of the screen resulting in a larger amount of water assigned to the coarse particles compared to the fines.

6. Conclusions

In this work, capillary and viscous force models for liquid bridge contacts as well as the formation and rupture of liquid bridges have been applied in DEM simulations. The implemented force models were successfully validated against data from literature and additionally, the capillary force models were compared with each other. The most appropriate capillary model, here the one by Rabinovich et al. [104], was applied in subsequent DEM simulations. In addition, the normal and tangential viscous force models by Pitois et al. [109] and Goldman et al. [108], respectively, were chosen. For the rupture distance, the model by Willett et al. [105] extended for dynamic behavior by Pitois et al. [110] was selected. The implemented formation and rupture process of the liquid bridge between two spheres is based on the geometrical considerations of the model by Shi and McCarthy [112]. For the formation and rupture between a particle and a wall, similar geometrical considerations were made and used for the DEM simulations. The required contact angles of glass ($\theta_i = 15^\circ$) and POM ($\theta_i = 40^\circ$) spheres as well as of steel ($\theta_w = 45^\circ$) and treated PVC ($\theta_w = 50^\circ$) with water and respective transfer ratios were obtained and implemented in the DEM by generating a look-up table. Furthermore, a method to detect existing liquid bridge contacts at large distances over different cells and to transfer liquid bridge contact information and history over process boundaries has been introduced.

Based on this, experimental and numerical batch screening has been performed. The applied DEM code is capable to simulate dry screening processes very well with only minor deviations. For the applied screen apparatus, a set amplitude of $A = 1$ mm and larger particles ($d_{1/2/3} = 5/7/10$ mm) accompanied by a larger aperture size ($a = 8$ mm) reveal a slightly lower fraction retained than an amplitude of $A = 0.8$ mm and a much lower fraction retained than smaller particles ($d_{1/2/3} = 3/5/7$ mm) accompanied by a smaller aperture size ($a = 5.6$ mm).

An addition of water slightly reduces the particle passage in most of the applied configurations, whereas blocking of apertures by particles can be reduced in some cases. The extended DEM code is able to simulate screening under the influence of a slight amount of water ($M \leq 10$ %). The results fit the experimental ones, while revealing slightly more deviations than for the dry configuration. Small particles mostly pass the apertures faster than near mesh sized particles independent of the amount of water. In some configurations, more small particles under the influence of moisture remain on the screen than dry near mesh sized particles.

The amount of water on particles, which are able to pass the apertures, during and at the end of the screening process, is underpredicted. If POM spheres are applied, too much water is predicted on the walls and coarse particles. In the case of glass spheres, the deviations are lower, due to their good wettability. Only the coarse material reveals to have more water attached in the simulation than in the experiment. Approximately the same amount of water is

associated to the fine particles in the experiment. The main reason for these deviations is that the liquid in the DEM simulations only persists on particles, walls and in liquid bridges, whereas in reality, the liquid is also separated from particles and walls in free motion. The liquid bridge models are not able to take this in account and no reliable and directly applicable correlations are available. The liquid separation due to vibrating dewatering will be addressed in further studies concerning wet screening applications. For this purpose, coupled discrete element simulations with methods used for simulating the dynamics of continua like the SPH can be applied (comp. e.g. [295]). By utilizing the SPH, the fluid flow and the interaction between fluid and solid as well as the local liquid amounts can be obtained. As long as the local liquid amount is small enough, the liquid bridge models are still applicable. Additionally, resolved liquid distribution models (comp. [14]) can be used in the DEM to account for partial wetting, particularly if large contact angles are applied.

Furthermore, in order to meet requirements for real particle systems such as encountered in industrial applications, the implemented liquid bridge models will be extended to be applied for non-spherical shaped particles under moist conditions in the DEM in the future. Therefore, the liquid bridge force calculation will be realized analogously and the liquid contact detection rules will be combined with already implemented routines for the detection of non-spherical particles. However, new methods for the liquid distribution on the individual spheres will be required. The data obtained from the DEM simulations in the investigation here will be used for extending phenomenological process models to represent screening processes under moist conditions in consecutive studies.

Acknowledgements

The authors gratefully acknowledge the support by DFG within project SPP 1679 through grant number KR3446/7-2 and KR3446/7-3. The original form of the DEM code "DEM-Calc" applied is based on a development of LEAT, Ruhr-Universität Bochum, Germany. The code "DEM-Calc" has then been continuously extended both at Ruhr-Universität Bochum and Technische Universität Berlin, Germany. We thank all who have contributed.

Compliance with ethical standards

The authors declare that there is no conflict of interest related to this manuscript.

X. Extension of process models to predict batch screening results under the influence of moisture based on DEM simulations

Frederik Elskamp^{1*}, Harald Kruggel-Emden¹

¹Mechanical Process Engineering and Solids Processing, Technische Universität Berlin, Ernst-Reuter-Platz 1, D-10587 Berlin, Germany

*Corresponding author. E-mail address: frederik.elskamp@tu-berlin.de

The following accepted manuscript appeared as journal version in Elskamp F., Kruggel-Emden H., 2019, Extension of process models to predict batch screening results under the influence of moisture based on DEM simulations, Powder Technology 342, 698-713 and may be found at <https://doi.org/10.1016/j.powtec.2018.10.039>.

Abstract

Screening is a technical simple but still not fully understood process step, which can be used in a wide field of applications to separate bulk materials according to their particle sizes. A severe issue in screening technologies is that particles frequently prevail in moist conditions, due to effects related to the environment, the material or the process. This is often not preventable, although it is not preferred due to attractive forces altering the screening efficiency. For the design of dry screening processes, phenomenological models and detailed particle-based simulation approaches like the discrete element method (DEM) are available. The latter method has recently been extended and validated against experiments to calculate forces caused by liquid bridges formed out between particles or walls close to each other to meet the requirements to tackle real particle systems under moist conditions. In the investigation here, batch screening under the influence of moisture involving different sized glass spheres is investigated numerically with DEM simulations and by using process models. Therein, the related subprocesses stratification and passage as well as the influence of the operating parameters and the liquid amount on the fraction retained per size class are examined. Existing phenomenological process models, which can be applied efficiently for industrial applications due to their short calculation time, are extended to represent batch screening processes under moist conditions for the first time. Therefore, a benchmark is realized in which the fraction retained per size class over time for discontinuous screening under the influence of various amounts of liquid and different mechanical agitations obtained by DEM simulations and process models is compared. In this context, the process models are first adjusted to fit related simulation results and later used in a novel method to predict the outcome of screening with different operating parameters and liquid amounts. Thereby, process models, which consider the subprocesses stratification and passage, predict screening results for process parameters requiring interpolation or extrapolation in the investigated range very well. As a consequence, newly derived process models can function as prototypes to be applied in dynamic process simulation frameworks.

Keywords: Discrete element method; Process model; Liquid bridges; Screening; Moisture

1. Introduction

Screening is a simple but major process step used in a wide field of industrial applications to perform a classification of bulk material into particles of requested size classes [2,3]. Most of performed investigations on screening only considered dry particles, whereas screening under the influence of liquid has rarely been studied until now. The only exception are a few pure experimental investigations considering different amounts of liquid [31–33] under process specific conditions for particular applications.

To study screening and its subprocesses under moist or wet conditions in detail without performing extensive experimental tests, the discrete element method (DEM) can be used. This method was first introduced by Cundall and Strack [10] and proved as a suitable tool in various investigations on screening [6,203,236]. In these studies, the fluid was omitted or the material was assumed as dry resulting in a mostly undisturbed transport, stratification and passage of the particles. In contrast, some researchers concentrated on wet screening applications and coupled the DEM with methods to model the fluid flow like cell-based computational fluid dynamics [202] or particle-based smoothed particle hydrodynamics [9]. In wet screening processes, the liquid can support the transport of fine particles through the apertures. For screening, dry or completely wet conditions are preferred over conditions where material is only influenced by a slight amount of water, where the particles can adhere to each other and the screening efficiency is reduced [32,296]. For more details on this, Zhu et al. [60] provide an overview of theoretical developments of discrete particle simulations of dry and wet particulate systems.

A small amount of water in the screening process conveyed from preceding process steps cannot always be prevented and consequently, the impact on the screening process has to be better understood and the consequences for following process steps should be made ascertainable. Therefore, a relevant state-of-the-art task is the development of an efficient and robust dynamic process simulation framework [208], where a dynamic screening model is an essential process step. In this framework, the results of a screening model can be influenced by liquid or material under moist conditions from other process steps. For this reason, the extension of an appropriate phenomenological process model for screening under the influence of moisture is inevitable. Besides the possibility to consider a small amount of water, this model should account for different particle sizes, various operational conditions and it should be able to represent batch screening with its inherent transient nature and a possibly thick particle bed with multiple layers at the beginning of the screening process. The DEM, extended by forces, which arise from the presence of liquid, seems to be suitable to study

screening under the influence of liquid as well as to provide data to adjust and to test respective process models.

Liquid bridges including their formation, the resulting forces and the rupture event were studied experimentally over decades by several researchers [104–106,265,266]. In other investigations in the recent past, the impact behavior of wet particles on dry surfaces or vice versa was studied to obtain the restitution coefficient under these conditions and to apply it in DEM simulations [270,273,297]. However, in many studies [14,119,267,268,298] and in the investigation here, the applied DEM is extended with respective force models to simulate screening under moist conditions.

The primarily studied forces arising from a liquid bridge contact are the capillary and the viscous forces. While capillary forces are dominant in systems with slow particle movements and low liquid viscosities, the importance of the viscous forces increases for fast moving particles involving liquids with high viscosities. The capillary forces can either be obtained by the energetic method based on the total interfacial energy or by summing up the pressure and tension terms from the meniscus profile based on the Young-Laplace equation [265,278]. Latter can be subdivided in the neck [113] and boundary method [279]. One example where the capillary force is calculated between two spherical bodies with the boundary method is the liquid bridge model by Weigert and Ripperger [106], where the bridge volume is related to the half-filling angle. In contrast, the frequently used models by Willett et al. [105] and Rabinovich et al. [104] both applicable for unequal sized spheres are representatives of the neck method. Rabinovich et al. [104] also introduced equations for different wettability of contact partners and for contacts between spherical particles and walls. Gladkyy and Schwarze [115] benchmarked these capillary bridge models by applying them in a DEM framework, whereby the latter two models (Willett et al. [105] and Rabinovich et al. [104]) reveal results close to the presented experimental data. In order to provide tractable calculations for the capillary forces, Lian and Seville [114] developed closed-form equations, which can be applied for capillary bridges containing varying amounts of liquid formed out between unequal sized spheres with different contact angles.

For particle systems with a high liquid viscosity or large interparticle velocities, the consideration of the viscous forces is necessary. A commonly used liquid bridge viscosity model in the normal direction was proposed by Adams and Perchard [107] and later extended and applied in a DEM framework by Pitois et al. [109], who studied the viscosity effects of a liquid bridge between two moving spheres. Furthermore, Goldmann et al. [108] introduced an often applied tangential viscosity model for liquid bridge contacts.

In addition to the acting forces, several researchers [111,112,118] studied the formation process of a liquid bridge including its shape and the containing liquid volume as well as the

liquid redistribution after rupture of a bridge. The rupture conditions were intensively addressed by Willett et al. [105] and several other researchers like Pitois et al. [110] who further developed the up to then static to a dynamic rupture model.

Several studies of larger particulate systems were performed for 2D [285] and 3D [286] like packed beds or rotating drums with uniform spheres [14,267,268] as well as mixing processes with unequal sized spheres [118,119,290]. Besides some exceptions [202], such investigations are mostly lacking for screening processes. In a previous investigation by the authors [298], an extension of the DEM including a validation for screening under the influence of moisture has been performed. Therein, only a small amount of liquid is applied to ensure individual capillary bridges without liquid in the pores in between the particles.

The derivation and verification of simpler and less computing-intensive phenomenological screening process models is also possible with the DEM. One of the first, who applied the DEM instead of performing extensive experiments for this purpose were Shimosaka et al. [46]. A comprehensive benchmark of phenomenological screening process models based on the results of batch screening processes modeled by the DEM was performed by Elskamp et al. [241]. These models were not applicable for screening under moist conditions and limited in predictability. In a very recent investigation, Dong et al. [49] introduced a model based on the work by Subasinghe et al. [228], which provides the ability to predict the outcome for continuous screening processes valid for a thin particle bed and square [49] as well as rectangular apertures [51]. In contrast to continuous screening, in batch screening investigation, the assumption of a thin particle bed is invalid. This results in the necessity of considering stratification arising from thicker particle beds in addition to the passage process according to the works by Subasinghe et al. [227] and Soldinger [7,8] in future investigations.

In the present study, first, batch screening under the influence of moisture and different operational conditions involving spherical particles is investigated numerically. Based on these DEM simulation results, a comparative study of selected phenomenological screening process models (comp. [4,241]) is conducted. As novelty, these models are extended for the representation and prediction of discontinuous screening under various amounts of liquid and different mechanical agitations. As a result, the extended batch screening models will be applied in dynamic flowsheet simulations of solids processes (Dyssl) together with other process models to simulate and predict the outcome of connected processes in further investigations [205].

2. Numerical method

In this section, the discrete element method including the applied contact and liquid bridge force laws as well as the liquid distribution are briefly described.

2.1 The discrete element method

The tracking of particles and the calculation of their translational and rotational motion in various systems can be realized by utilizing the DEM [60,61]. Therefore, the Newton's and Euler's equations are integrated

$$m_i \frac{d^2 \vec{x}_i}{dt^2} = \vec{F}_i^c + \vec{F}_i^l + m_i \vec{g}, \quad (250)$$

$$I_i \frac{d\vec{\omega}_i}{dt} = \vec{M}_i, \quad (251)$$

with particle mass m_i , particle acceleration $d^2 \vec{x}_i / dt^2$, contact force \vec{F}_i^c , liquid bridge force \vec{F}_i^l , gravitational force $m_i \vec{g}$, moment of inertia I_i , angular acceleration $d\vec{\omega}_i / dt$, angular velocity $\vec{\omega}_i$ and external moments resulting out of contact and liquid bridge forces \vec{M}_i . Both equations can be solved by using explicit integration schemes (comp. e.g. [82]). Fig. 127a shows a sketch of two colliding different sized spheres i and j .

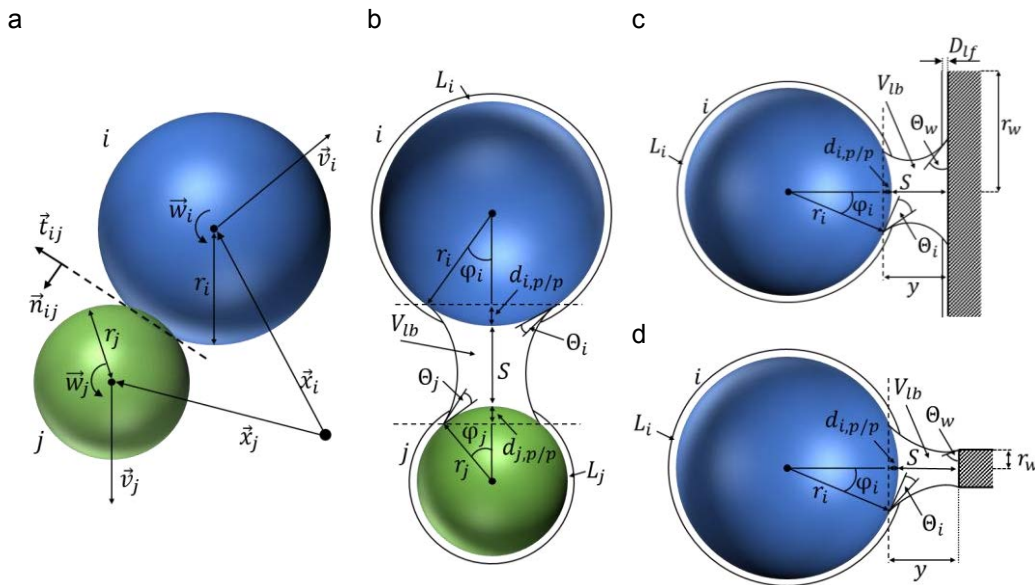


Fig. 127: (a) A collision of two spherical particles and liquid bridges having formed out between (b) spherical particles of different sizes, (c) a particle with a large wall with $r_w > r_i$ (side wall) as well as (d) with a small wall of $r_w < r_i$ (screen wire).

For such a contact, the resulting contact force consists of normal and tangential forces

$$\vec{F}_{ij}^c = \vec{F}_{ij}^{cn} + \vec{F}_{ij}^{ct}, \quad (252)$$

where a linear spring damper model is used to obtain the normal component as

$$\vec{F}_{ij}^{cn} = k^n \delta_{ij} \vec{n}_{ij} + \gamma^n \vec{v}_{ij}^n, \quad (253)$$

where k^n is the spring stiffness, δ_{ij} the virtual overlap, \vec{n}_{ij} a normal vector, γ^n a damping coefficient and \vec{v}_{ij}^n the normal velocity at the contact point [92]. The normal coefficient of restitution between particles e_{pp}^n as well as particles and walls e_{pw}^n under dry conditions is

determined by k^n and γ^n . A linear spring limited by the Coulomb condition is applied to obtain the tangential forces, leading to

$$\vec{F}_{ij}^{ct} = -\min(k^t |\vec{\xi}_{ij}|, \mu_c |\vec{F}_{ij}^n|) \vec{t}_{ij}, \quad (254)$$

where k^t is the tangential stiffness of a linear spring, μ_c is the friction coefficient, $\vec{\xi}_{ij}$ is the relative tangential displacement and \vec{t}_{ij} is the tangential unit vector [94].

2.2 Liquid bridges in the discrete element method

In this investigation, only a small and uniformly distributed amount of liquid is added to the particles to ensure the pendular state with individual liquid bridges between pairs of particles. Several adhering forces result out of the existence of these liquid bridges, of which the capillary and the viscous forces are applied in this work. The total liquid bridge force is obtained as

$$\vec{F}_{ij}^l = \vec{F}_{ij}^{cap} + \vec{F}_{ij}^{nvis} + \vec{F}_{ij}^{tvis}, \quad (255)$$

where \vec{F}_{ij}^{cap} is the capillary force and \vec{F}_{ij}^{nvis} as well as \vec{F}_{ij}^{tvis} are the viscous forces in normal and tangential direction, respectively. An extension is made for the external moment \vec{M}_i (comp. eq. (251)), which is now the sum of the moments due to a contact $\vec{M}_{C,i}$ and a liquid bridge $\vec{M}_{L,i} = \vec{r} \times \vec{F}_i^{tvis}$.

A liquid bridge forms out between two particles i and j or a particle and a wall when they get into contact under the influence of moisture (Figs. 127b-d). For two spherical particles (comp. Fig. 127b), the liquid volumes contributing from each particle are combined to the total volume of the liquid bridge V_{lb} as

$$V_{lb} = V_i + V_j = \frac{L_i}{2} \left(1 - \sqrt{1 - \frac{r_j^2}{(r_i + r_j)^2}} \right) + \frac{L_j}{2} \left(1 - \sqrt{1 - \frac{r_i^2}{(r_i + r_j)^2}} \right), \quad (256)$$

where L_i and L_j are the total liquid volumes present on particles i and j [112].

The volume of a liquid bridge between a particle i and a wall is $V_{lb} = V_i + V_w$. In case of a wall, which is extending larger than the diameter of the particles (comp. Fig. 127c), the liquid volume V_i contributed from the particle is assumed to be

$$V_i = \frac{L_i}{2} (1 - \sqrt{0.75}). \quad (257)$$

The liquid contributed from the wall is calculated as

$$V_w = W_{lf} \frac{\pi}{4} r_i^2, \quad (258)$$

where W_{lf} is the liquid film thickness on the wall.

For the case of a liquid bridge contact between a particle and a screen wire (comp. Fig. 127d) the liquid that contributes from the particle is calculated as

$$V_i = \frac{L_i}{6r_i} r_w. \quad (259)$$

The liquid contributed from the screen wire is assumed as

$$V_w = W_{lf} r_i 2r_w, \quad (260)$$

where $r_i 2r_w$ is the projection surface of the particle's spherical cap on the wall. Note that the liquid bridge volume is assumed as constant as long as it exists. A detailed explanation and derivation of the equations concerning the formation of a liquid bridge can be found in a previous work by the authors [298].

In the investigation here, the applied capillary force is based on the models used by Rabinovich et al. [104] and Pitois et al. [109], where the force is calculated at the neck of the liquid bridge (comp. Figs. 127b-d). Therein, the capillary forces for a liquid bridge between two particles i and j as well as between a particle and a wall are determined as

$$\vec{F}_{ijpp}^{cap} = \left(-\frac{\pi\sigma r_{eff}(\cos\theta_i + \cos\theta_j)}{1 + 1/\left(\sqrt{1 + \frac{2V_{liq}}{(\pi r_{eff} S^2)}} - 1\right)} - 2\pi\sigma r_{eff} \sin(\theta_{ij}) \sin(\theta_{ij} + \varphi) \right) \vec{n}_{ij}, \quad (261)$$

$$\vec{F}_{ipw}^{cap} = \left(-\frac{2\pi\sigma r_i(\cos\theta_i + \cos\theta_w)}{1 + S\sqrt{\pi r_i/V_{lb}}} - 2\pi\sigma r_i \sin(\theta_{iw}) \sin(\theta_{iw} + \varphi) \right) \vec{n}_{iw}, \quad (262)$$

where σ is the surface tension coefficient, $r_{eff} = 2r_i r_j / (r_i + r_j)$ is the effective radius, θ_i , θ_j and θ_w are the static contact angles of the particles i , j and a wall, respectively. The parameters $\theta_{ij} = (\theta_i + \theta_j)/2$ and $\theta_{iw} = (\theta_i + \theta_w)/2$ are the mean contact angles of two particles as well as of a particle and a wall, respectively (comp. [123]). S is the separation distance between two contact partners and φ is the half filling angle, obtained in the case of two spherical particles as

$$\varphi = \sqrt{S/r_{eff} \left(-1 + \sqrt{1 + 2V_{lb}/(\pi r_{eff} S^2)} \right)}. \quad (263)$$

For a particle and a wall, φ is given as

$$\varphi = \sqrt{2S/r_i \sqrt{1 + V_{lb}/(\pi r_i S^2)}}. \quad (264)$$

Additionally, viscous forces have to be taken into account in this investigation, because the applied screen apparatus induces a high frequency motion resulting in large interparticle velocities. Here, the normal viscous force model proposed by Pitois et al. [109] is used, which is given as

$$\vec{F}_{ij}^{nvis} = -\frac{6\pi\eta r_{reff}^2 \vec{v}_r^n}{S} \left(1 - 1/\sqrt{(1 + V_{lb}/(\pi r_{reff} S^2))}\right)^2, \quad (265)$$

where η is the liquid dynamic viscosity, $r_{reff} = r_i r_j / (r_i + r_j)$ is the reduced effective radius and $\vec{v}_r^n = ((\vec{v}_i - \vec{v}_j) \cdot \vec{n}_{ij}) \vec{n}_{ij}$ is the relative normal velocity of particles with the velocities \vec{v}_i and \vec{v}_j .

For the tangential viscous forces, Goldman et al. [108] proposed the following equations valid for $S < 0.1r_{reff}$ and $S \geq 0.1r_{reff}$, respectively, which can be calculated as

$$\vec{F}_{ij}^{tvis} = -6\pi\eta r_{reff} \left(\frac{8}{15} \ln \frac{r_{reff}}{S} + 0.9588\right) \vec{v}_r^t - 6\pi\eta r_{reff} \left(\frac{2}{15} \ln \frac{r_{reff}}{S} - 0.2526\right) \vec{\omega}_r \times \vec{n}_{ij}, \quad (266)$$

$$\begin{aligned} \vec{F}_{ij}^{tvis} = & -6\pi\eta r_{reff} \left(\frac{8}{15} \ln \frac{r_{reff}}{S} + 0.9588\right) \vec{v}_r^t \\ & - \frac{6\pi\eta r_{reff}}{8} \left(\frac{r_{reff}}{S + r_{reff}}\right)^4 \left(1 - \frac{3r_{reff}}{8(S + r_{reff})}\right) \vec{\omega}_r \times \vec{n}_{ij}, \end{aligned} \quad (267)$$

with $\vec{v}_r^t = \vec{v}_i - \vec{v}_j - \vec{v}_r^n$ as the tangential relative velocity from the translational motion and $\vec{\omega}_r = r_i \vec{\omega}_i + r_j \vec{\omega}_j$ as relative rotational velocity of the spheres. Note that a minimum separation distance $S_{min} = 0.001r_{reff}$ is added to S to prevent that the viscous forces tend to infinity when S approaches zero (comp. e.g. [283]).

When the distance S between two contact partners reaches a respective length, the liquid bridge ruptures. Based on the work by Willett et al. [105] the rupture distance is calculated as

$$S_{rup} = r_{reff} \left(1 + (0.125(\theta_i + \theta_j)) \left(1 + \frac{r_j}{r_i}\right)\right) \left(\left(\frac{V_{lb}}{r_{reff}^3}\right)^{1/3} + \left(\frac{r_j}{2r_i} - \frac{2}{5}\right) \left(\frac{V_{lb}}{r_{reff}^3}\right)^{2/3}\right), \quad (268)$$

with $r_i \geq r_j$. Additionally, in this work, the dynamic rupture distance

$$S_{rup,dyn} = S_{rup} \left(1 + \sqrt{\left(\frac{(\vec{v}_i - \vec{v}_j)\eta}{\sigma}\right)}\right) \quad (269)$$

proposed by Pitois et al. [110] is applied to account for the rupture distance dependency of the particle velocity.

Note that the rupture of a liquid bridge occurs at its thinnest point. This point is somewhere located between the contact partners depending on the particle size, the contact angles and the liquid bridge volume. This rupture location is decisive for the liquid share, which is received by each contact partner after a rupture event. More details on the liquid distribution, the transfer ratio and the contact angles as well as a numerical validation of the liquid bridge forces with data from literature can be found in a previous publication by the authors [298].

3. Extended phenomenological screening process models

Phenomenological screening process models can be used for the time-resolved representation of the particle size separation during a batch screening process. This can be achieved by probabilistic theoretical [49,52,228] and kinetic [45,47,227] models which are either directly applicable to discontinuous screening or they can be used for batch screening by replacing length l by time t in the equations of the respective models (comp. [241]).

Kinetic models are based on first order kinetics, whereas probabilistic models need additional parameters like the probability of particles to pass an aperture e.g. by Gaudin [24]. Several probabilistic models consider the screen motion, the aperture shape and size as well as the particle composition and shape [49,51,52,228]. In addition, some more complex phenomenological screening models take the opposing subprocesses stratification and particle passage into account by providing additional parameters [7,8,227]. However, besides some exceptions [49,51], most of the existing models lack the ability to predict the outcome of screening processes with different mechanical agitations or bulk characteristics satisfactorily.

Table 30 provides an overview of all applied screening process models in this investigation, which are extended for screening under the influence of moisture and for the prediction of screening results with different operational parameters and liquid amounts as novelty of this work. They are titled by the author's names and a model number and include the major equations as well as the used model parameters. A more detailed description of all investigated models for dry screening can be found in Elskamp and Kruggel-Emden [241] or in the respective publications. All investigated models should represent the fraction retained per particle size class i over time which is

$$Y_i = Y_i(t) = m_{p,l,i} / m_{p,l,i,0}, \quad (270)$$

where $m_{p,l,i,0}$ is the initial fractional mass of the particles at $t = 0$ s and $m_{p,l,i}$ is the remaining fractional mass of the particles at time t . Note that both masses include the particles plus the liquid assigned to the particles.

Table 30: Governing equations of the extended and applied phenomenological screening process models.

| Model number and origin | Major equations | Adjustable parameters |
|---|--|--|
| 1. Dong et al. [49] (based on Subasinghe et al. [228]) | $Y_i = (1 - P_i)^{N_i}$ $P_i = (a - d_i)^2 / (a + w)^2$ <p><i>a</i>: aperture size <i>w</i>: wire diameter; <i>d_i</i>: particle diameter</p> $N_i = k \left(\frac{Af(1-M)^\gamma}{\sqrt{d_i g}} \right)^\alpha \frac{t}{t_{end}}$ | <i>k</i> , α , γ |
| 2. Subasinghe et al. [227] | $Y_i = \left(k_{s,i} \exp(-k_{p,i}t) - k_{p,i} \exp(-k_{s,i}t) \right) / (k_{s,i} - k_{p,i})$ $k_{s,i} = k_s \left(\frac{Af(1-M)^\gamma}{\sqrt{d_i g} \frac{d_i}{d_{av}}} \right)^\alpha$ $k_{p,i} = k_p \left(\frac{Af(1-M)^\delta}{\sqrt{d_i g} \frac{d_i}{a}} \right)^\beta$ | <i>k_s</i> , <i>k_p</i> , α , β , γ , δ |
| 3. Soldingier [8] | $Y_{i,j+1} = Y_{i,j} - k_{i,j} B_{i,j} (t_{j+1} - t_j); \quad i: \text{particle class}; j: \text{time index}$ $B_{i,j+1} = B_{i,j} + (c_{i,j} (S_{i,\infty} - S_{i,j}) - k_{i,j} B_{i,j}) (t_{j+1} - t_j)$ $Y_j = \sum_{i=1}^n Y_{i,j}; B_j = \sum_{i=1}^n B_{i,j}; n: \text{number of undersized particle classes}$ $k_{i,j} = b_i Y_{i,j}; c_{i,j} = f(w_{q,i}, C_{a,i,j})^\alpha$ $w_{q,i} = k_s \left(\frac{Af(1-M)^\gamma}{\sqrt{d_i g} \frac{d_i}{d_{av}}} \right)^\alpha$ $b_i = k_p \left(\frac{Af(1-M)^\delta}{\sqrt{d_i g} \frac{d_i}{a}} \right)^\beta$ <p><i>B_i</i>: fractional mass of undersized particles in bottom layer <i>S_i</i>: fractional mass of undersized particles stratified into bottom layer</p> | <i>k_s</i> , <i>k_p</i> , α , β , γ , δ |

Subasinghe et al. [228] proposed a probabilistic screening model, where the probability P_i for a particle to remain on the screen after N_i attempts is

$$P_i(N_i) = (1 - p_i)^{N_i} \quad (271)$$

where p_i is the probability of the particle to pass the apertures in a single attempt, which is calculated as

$$p_i = \frac{(a - d_i)(a \cos(\tau) - d_i)}{(a + w)^2 \cos(\tau)}, \quad (272)$$

where a is the aperture size, d_i the particle diameter, w the wire diameter and τ the inclination of the screen. For a horizontal batch screen, this correlation is simplified to

$$p_i = \frac{(a - d_i)^2}{(a + w)^2}. \quad (273)$$

For a bulk of particles, the fraction retained per size class is calculated similar to eq. (270), by using the average probability p_i per size class. The probability is multiplied with the ratio of the mass of one particle to the total initial mass fraction leading to

$$Y_i = \left(1 - p_i \frac{m_{p,l,i}}{m_{p,l,i,0}}\right)^{N_i}. \quad (274)$$

The amplitude A and the frequency f influence the motion of the particles on the screen. The motion is also dependent on the particle diameter d_i . For a continuously operated screen with a thin particle bed, Dong et al. [49] found out that N_i is lower for larger $A \cdot f$ as well as for a larger τ and N_i decreases nearly linearly for an increasing particle size d_i . Based on these considerations and dimensional analysis, the number of attempts N_i is represented according to Dong et al. [49] by

$$N_i = k \left(\frac{Af}{\sqrt{d_i g}}\right)^\alpha \left(\frac{d_i}{L}\right)^\beta \tau^\delta, \quad (275)$$

with the fitting parameters k , α , β , δ , the gravitational force g and the total length of the deck L . In the investigation here, the last part of the equation has to be removed for a horizontal screen. In case of batch screening, the length L has to be replaced by the time t . To maintain a dimensionless value, the actual point in time t is set in relation to the total simulation time t_{end} resulting in

$$N_i = k \left(\frac{Af}{\sqrt{d_i g}}\right)^\alpha \frac{t}{t_{end}}. \quad (276)$$

In case of screening under the influence of moisture, the liquid amount M influences the motion of the particles on the screen by reducing their motion. Note that the term $1 - M$ is used to apply this equation under moist and dry conditions ($M = 0\%$). Since the influence of the liquid amount is not in advance quantifiable, a third fitting parameter γ has to be added, leading to

$$N_i = k \left(\frac{Af(1-M)^\gamma}{\sqrt{d_i g}}\right)^\alpha \frac{t}{t_{end}}, \quad (277)$$

which is used in combination with eq. (273) and eq. (274) and referred to as model No. 1 in the following.

The basis for kinetic screening models is the “first-order rate law” in which the explicit equation for the fraction retained per size class of particles remaining above the screen is

$$Y_i(t) = \exp(-k_i t), \quad (278)$$

where the screening rate constant k_i is an adjustable parameter.

Subasinghe et al. [227] also introduced a kinetic model, where besides the passage of the undersized particles, the stratification of the small particles through the coarse material is

considered. A detailed derivation can be found in their work, leading to the following equation for the fraction retained per particle size class i

$$Y_i(L) = \left(k_{s,i} \exp(-k_{p,i}L) - k_{p,i} \exp(-k_{s,i}L) \right) / (k_{s,i} - k_{p,i}). \quad (279)$$

Instead of the screening rate constant k_i , the adjustable parameters $k_{s,i}$ and $k_{p,i}$ were introduced. The parameter $k_{s,i}$ is used to describe the fraction retained of particles above the screen and not in contact with it, whereas $k_{p,i}$ is applied to consider the fraction retained of particles above the screen that are in contact with the screen. To apply eq. (279) for the representation of batch screening processes, the screen length L is exchanged by the time t , leading to

$$Y_i(t) = \left(k_{s,i} \exp(-k_{p,i}t) - k_{p,i} \exp(-k_{s,i}t) \right) / (k_{s,i} - k_{p,i}). \quad (280)$$

In order to make the model and its adjustable parameters $k_{s,i}$ and $k_{p,i}$ dependent on the screen motion and the particle sizes according to model No. 1, the following equations are introduced

$$k_{s,i} = k_s \left(\frac{Af}{\sqrt{d_i g} \frac{d_i}{d_{av}}} \right)^\alpha, \quad (281)$$

$$k_{p,i} = k_p \left(\frac{Af}{\sqrt{d_i g} \frac{d_i}{a}} \right)^\beta, \quad (282)$$

where $d_{av} = \frac{1}{n} \sum_{i=1}^n d_i$ is the average particle size. The relations $\frac{d_i}{d_{av}}$ and $\frac{d_i}{a}$ are additionally applied to consider the particle composition and to compensate for the lack of the particle passage probability.

For screening under the influence of moisture, the motion of the particles on the screen is influenced, which is realized similarly like in model No. 1, leading to

$$k_{s,i} = k_s \left(\frac{Af(1-M)^\gamma}{\sqrt{d_i g} \frac{d_i}{d_{av}}} \right)^\alpha, \quad (283)$$

$$k_{p,i} = k_p \left(\frac{Af(1-M)^\delta}{\sqrt{d_i g} \frac{d_i}{a}} \right)^\beta. \quad (284)$$

This model is referred to as model No. 2 in the following.

In the investigations by Soldinger [7,8], a bottom layer of fine material is introduced besides the subprocesses stratification and passage. This bottom layer consists of all undersized particles directly on the screen surface and those that have the possibility to reach the screen without being blocked by other particles in their way. In contrast to her first investigation [7], Soldinger subdivided the undersized particles in different size classes i in her following studies (comp. e.g. [8]). The fractional mass of undersized particles per size class in the bottom layer B_i changes over time due to the concurrent mass streams \dot{S}_i and \dot{R}_i , which are the particles stratifying to the bottom layer and those passing the apertures and thus leaving the bottom layer, respectively. This procedure is described by

$$\dot{B}_i = \dot{S}_i - \dot{R}_i = \frac{B_{i,j+1} - B_{i,j}}{t_{j+1} - t_j} = \frac{S_{i,j+1} - S_{i,j}}{t_{j+1} - t_j} - \frac{Y_{i,j} - Y_{i,j+1}}{t_{j+1} - t_j}, \quad (285)$$

where $\Delta t = t_{j+1} - t_j$ is a fixed, discrete time step.

The fractional mass stream of stratified particles of class i can be calculated as

$$\dot{S}_i = (S_{i,j+1} - S_{i,j}) / (t_{j+1} - t_j) = c_{i,j}(S_{i,\infty} - S_{i,j}), \quad (286)$$

with $S_{i,\infty} = m_{i,0}/m_0$ as total proportion of undersized material in each fraction. The amount of material in the bottom layer and the fractional and summed up passage rate are determined by

$$B_{i,j+1} = B_{i,j} + (c_{i,j}(S_{i,\infty} - S_{i,j}) - k_{i,j}B_{i,j})(t_{j+1} - t_j), \quad \dot{B} = \sum_{i=1}^n \dot{B}_i, \quad (287)$$

and

$$\dot{R}_i = (Y_{i,j} - Y_{i,j+1}) / (t_{j+1} - t_j) = k_{i,j}B_{i,j}, \quad \dot{R} = \sum_{i=1}^n \dot{R}_i, \quad (288)$$

respectively. $B_{i,j}$ is limited by $B_p = B_{mP}/m_0$, where B_{mP} is the mass of the bottom layer. Therein, $k_{i,j}B_{i,j}$ is exchanged by $B_p \cdot k_{i,j} \cdot B_{i,j}/B_j$ when $B_j > B_p$. In this investigation, the passage parameter $k_{i,j} = b_i(S_{i,\infty} - (1 - Y_{i,j}))$ is influenced by the parameter b_i similar to the first model by Soldinger [7]. To make the passage parameter additionally dependent on the screen motion and the liquid amount, b_i is determined according to model No. 2 as

$$b_i = k_p \left(\frac{Af(1-M)^\delta}{\sqrt{d_i g} \frac{d_i}{a}} \right)^\beta \quad (289)$$

in this investigation. The rate of stratification is obtained by the time dependent parameter

$$c_{i,j} = (c_{q,i,j} \cdot c_{d,i,j}) / (H_{t,j} / d_{av,c}), \quad (290)$$

where the average diameter of the coarse particles $d_{av,c}$ as well as the thickness of the top layers in the particle bed $H_{t,j} = M_{t,j}/(W^2 \cdot \rho_b)$, with the mass of material in the top layer $M_{t,j}$, the length and width of a quadratic screen W and the bulk density ρ_b assumed as constant are taken into account. In addition, $c_{q,i,j}$ and $c_{d,i,j}$ are both dependent on the proportion of fine material in the top layer which is obtained by

$$q_{i,j} = \left(m_0 \cdot \sum_{i=1}^n (S_{i,\infty} - S_{i,j}) \right) / \left(M_0(1 - Q_0) + m_0 \cdot \sum_{i=1}^n (S_{i,\infty} - S_{i,j}) \right). \quad (291)$$

The parameter $c_{d,i,j} = \exp(-2.5 \cdot V_{i,part}/V_{av,t,j})$ is obtained with $V_{i,part}$ and $V_{av,t,j}$ which are the volume of the respective particle and the average volume of particles in the top layer, respectively. The parameter $c_{q,i,j}$ is obtained by $c_{q,i,j} = w_{q,i} \exp(-(2q_{i,j})^5)$. Soldinger [8] expected that $w_{q,i}$ increases for an increase in screen motion due to a larger frequency or amplitude. In addition, it is assumed that a larger amount of liquid reduces $w_{q,i}$. Therefore, in the investigation here, this parameter is determined according to model No. 2 as

$$w_{q,i} = k_s \left(\frac{Af(1 - M)^\gamma}{\sqrt{d_i g} \frac{d_i}{d_{av}}} \right)^\alpha. \quad (292)$$

This model is referred to as model No. 3 in the following.

4. Numerical setup and simulation parameters

For the DEM simulations in this study, a batch screening apparatus is modeled according to a modified ‘‘Haver and Boecker EML digital plus’’ batch screen tower with a circular screen surface with a woven mesh and square apertures, which is applicable for dry and wet screening (comp. Fig. 128). A feed bin is placed over the screen apparatus without direct contact, to avoid being influenced by the screen motion. The particle passage is measured at the end of an outlet, which was added to a corresponding experimental screen apparatus for an easier measurement (comp. [298]). In each simulation in the investigation here, only one screen surface is used. Before the actual simulations, the desired quantity of particles with the attached amount of water is placed well mixed on a flat surface in the feed bin. At the beginning of each simulation, the flat surface under the particles is removed and the particles drop as bulk material down on the screen surface. While some smaller particles directly pass the apertures with their first attempt, others need more tries or have to stratify through the gaps between larger particles before reaching the screen surface. After passing the apertures, the particles drop on an inclined wall and move further to the outlet, where size and attached liquid amount as well as the time of passage are recorded and tracked. In this way, the fraction retained per size class over time for various configurations of DEM simulations can be

evaluated. An experimental validation of this batch screening process under the influence of moisture can be found in a previous publication by the authors [298].

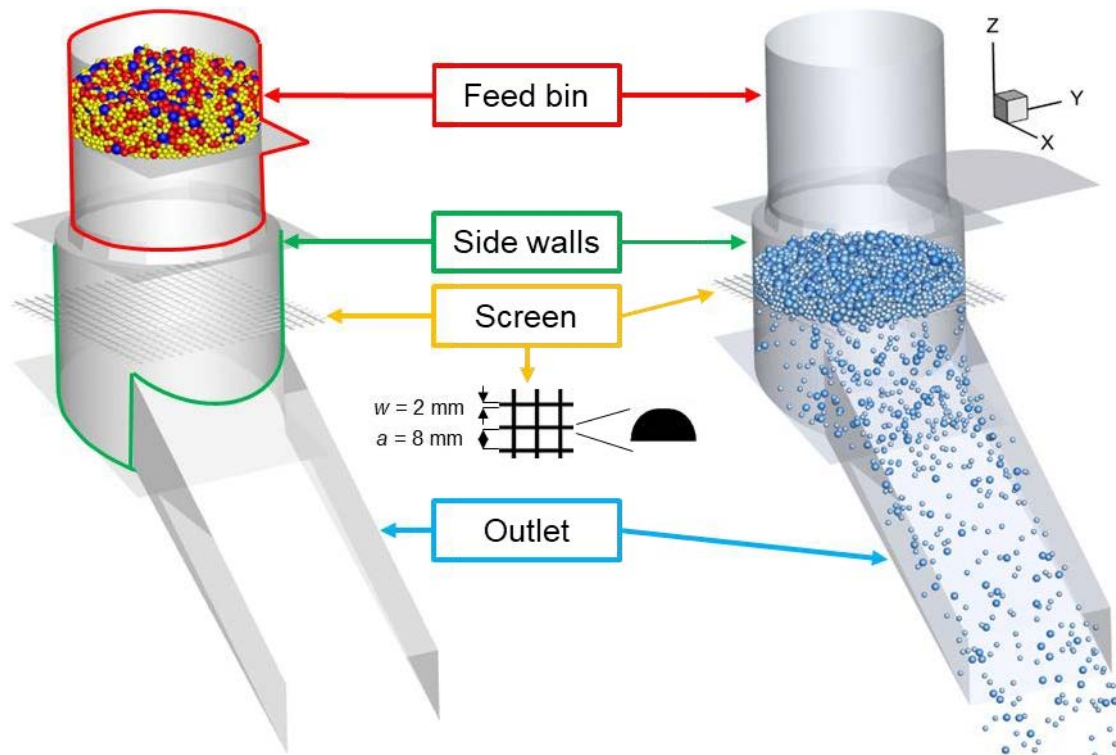


Fig. 128: Batch screening apparatus and close-up of the applied screen surface in the DEM simulations. Particles are coloured according to (left) size at $t = 0$ s and (right) liquid amount at $t = 3$ s.

The mechanical and physical particle and wall properties, which are relevant in the simulations, are presented in Table 31. In this investigation, glass spheres are applied in three different equally distributed discrete size classes of $d_1 = 5$ mm, $d_2 = 7$ mm and $d_3 = 10$ mm. The particles and the aperture size have the relation $d_1 < d_2 < a < d_3$. In the following the particle classes are called small (d_1), near mesh (d_2), which has the additional relationship $0.8a < d_2 < a$, and large (d_3). The contact angles between the different materials and water as outlined in Table 31 as well as the respective transfer ratios after a rupture event were obtained in a previous work by the authors [298].

Table 31: Mechanical and physical particle and wall properties.

| Mechanical particle property | Particles | Walls | |
|---|---|----------|----------|
| | Glass | Steel | PVC |
| Diameter d [mm] | 5 / 7 / 10 \pm 0.1 | - | - |
| Mass m [g] | 0.1636 / 0.4490 / 1.3090 \pm 0.02 | - | - |
| Density ρ [kg/m ³] | 2.5351E+03 / 2.5373E+03 / 2.5300E+03 \pm 1.50 | 7.85E+03 | 1.30E+03 |
| Young's modulus E [N/m ²] | 5.00E+10 | 2.08E+11 | 2.20E+09 |
| Poisson's ratio ν [-] | 0.2 | 0.30 | 0.4 |
| Stiffness k_{PP}^n / k_{PW}^n [N/m] | 1.00E+05 | - | - |
| Contact angle θ [°] | 15 | 45 | 50 |

The properties for the batch screening DEM simulations can be found in Table 32. The glass spheres are filled into the feed bin with a mass of $m_p \approx 1410$ g. Three different liquid amounts in the range of $0 \% \leq M \leq 5 \%$ are applied in order to maintain a pendular regime. At the start of each simulation, the walls are dry and each particle holds the same liquid film thickness P_{lf} (comp. [267]). The wires in the DEM simulations are approximated as horizontal bars with a semicircular profile. According to the screen applied in the experimental setup, the bars have a diameter of $w = 2$ mm resulting in aperture sizes of $a = 8$ mm.

The 3D screen motion is obtained by measurements of an accelerometer (“Sequoia FastTracer PA”) fixed under the screen (comp. [298]). Initially, the amplitude is set to $A = 1$ mm resulting in a frequency of approximately $f = 50.6$ Hz. The motion is elliptical but mainly in vertical direction (z- direction of the screen of about 0.9 mm) while the motion in x- and y- directions is low with maximum amplitudes of $A < 0.1$ mm. In the following, the set amplitude is used to differentiate the cases. In addition to the liquid amount, either the amplitude or the frequency is varied according to the values in Table 32.

Table 32: Properties for batch screening DEM simulations.

| Properties | Values |
|-------------------------|-----------------------------|
| Particle mass [kg] | ~1.41 |
| Liquid amount [%] | 0 / 2.5 / 5 |
| Surface tension [N/m] | 0.07275 |
| Aperture size [mm] | 8.00 ± 0.02 |
| Aperture shape [-] | square |
| Wire diameter [mm] | 2.00 ± 0.01 |
| Screen wire profile [-] | semicircular |
| Set amplitude [mm] | 0.8 / 1 / 1.2 |
| Frequency [Hz] | 45.8 / 50.6 / 55.4 |
| Stroke behavior | Elliptical, mainly vertical |

The DEM parameters coulomb friction μ_c , rolling friction μ_{roll} and the coefficient of restitution e^n can be found in Table 33 for contacts of glass spheres with steel and other glass spheres. A detailed strategy to obtain these parameters is outlined in a work by Elskamp et al. [263].

Table 33: DEM parameters for glass spheres and various contact partners.

| Contact partner 1 | Contact partner 2 | μ_c [-] | μ_{roll} [m] | e^n [-] |
|-------------------|--|-------------|------------------|-----------|
| Glass sphere | Steel (side walls, screen wires, bottom, outlet walls) | 0.2866 | 1.09E-04 | 0.4351 |
| Glass sphere | Glass sphere | 0.1966 | 8.95E-05 | 0.7808 |

All parameters for the performed DEM batch screening simulations and the process models are listed in Table 34.

Table 34: Overview of parameters for the performed DEM simulations and the process models.

| Case No. | Amplitude A [mm] | Frequency f [Hz] | Liquid amount M [%] | Case No. | Amplitude A [mm] | Frequency f [Hz] | Liquid amount M [%] |
|----------|---------------------|---------------------|------------------------|----------|---------------------|---------------------|------------------------|
| 1 | 0.8 | 45.8 | 0 | 15 | 1.0 | 55.4 | 2.5 |
| 2 | 0.8 | 50.6 | 0 | 16 | 1.2 | 45.8 | 2.5 |
| 3 | 0.8 | 55.4 | 0 | 17 | 1.2 | 50.6 | 2.5 |
| 4 | 1.0 | 45.8 | 0 | 18 | 1.2 | 55.4 | 2.5 |
| 5 | 1.0 | 50.6 | 0 | 19 | 0.8 | 45.8 | 5 |
| 6 | 1.0 | 55.4 | 0 | 20 | 0.8 | 50.6 | 5 |
| 7 | 1.2 | 45.8 | 0 | 21 | 0.8 | 55.4 | 5 |
| 8 | 1.2 | 50.6 | 0 | 22 | 1.0 | 45.8 | 5 |
| 9 | 1.2 | 55.4 | 0 | 23 | 1.0 | 50.6 | 5 |
| 10 | 0.8 | 45.8 | 2.5 | 24 | 1.0 | 55.4 | 5 |
| 11 | 0.8 | 50.6 | 2.5 | 25 | 1.2 | 45.8 | 5 |
| 12 | 0.8 | 55.4 | 2.5 | 26 | 1.2 | 50.6 | 5 |
| 13 | 1.0 | 45.8 | 2.5 | 27 | 1.2 | 55.4 | 5 |
| 14 | 1.0 | 50.6 | 2.5 | | | | |

5. Results and discussions

After performing the DEM simulations according to Table 34, the outcome is used to study the fraction retained per size class for different configurations. In addition, the influence of the subprocesses stratification and passage on the screening process is investigated. In the following, parameters of process models are adjusted to fit the DEM screening results and a comparison of the fraction retained per size class between DEM simulations and process models is carried out. As the main novelty, the adjusted parameters are then applied in the process models to predict the fraction retained per size class for various other configurations. Therein, the results of screening processes with operational parameters and liquid amounts between the values of the adjusted cases (interpolation) as well as with larger or lower values (extrapolation) are predicted. Subsequently, the predicted fraction retained values are compared to the results obtained from DEM simulations.

5.1 Numerical investigations of batch screening under the influence of moisture

In a first step, only the fraction retained per size class of DEM simulations with various amplitudes, frequencies and liquid amounts are compared. Note that the particles need at least 0.5 s to reach the end of the outlet resulting in a constant fraction retained until $t = 0.5$ s. In all simulations (Fig. 129 and Fig. 130), most of the particles pass the apertures in the first 5 seconds, while after $t = 5$ s the fraction retained per size class declines only slowly. Additionally, the fraction retained value of the small particles declines faster than the value of near mesh sized particles in all cases. The smaller particles stratify faster through the gaps of the coarse material and pass the apertures more easily. In the first investigations, dry glass spheres with diameters of $d_{1/2/3} = 5/7/10$ mm are screened with an aperture size of $a = 8$ mm (comp. Figs. 129a,b). Approximately until $t = 4.5$ s, the values of the fraction retained of the small and the near mesh sized particles decline fast but nearly unaffected by the screen

agitation. In contrast, after $t = 4.5$ s obvious influences of the operational parameters are revealed by a different reduction of the fraction retained per size class. The particles in the lower layers are nearly directly able to pass the apertures, whereas the particles of the upper layers have to stratify to the bottom layer, which is intensely influenced by the operating parameters.

First, the amplitude is varied from the initial value of $A = 1$ mm to 0.8 mm and 1.2 mm (Fig. 129a). In the initial case, approximately 80 % of the near mesh sized and 87 % of the small particles have already passed the apertures at $t = 5$ s. At $t = 10$ s only 10 % and 1.5 % of near mesh and small particles remain on the screen, respectively. After $t = 15$ s, nearly all undersized particles were able to pass through the apertures. When increasing the amplitude to $A = 1.2$ mm, the fraction retained values for both size classes decline faster between $t = 5$ s and $t = 10$ s, resulting in an earlier depletion of the small particles. However, the near mesh sized particles need about the same time as before under the influence of the initial amplitude. By applying a larger stroke length, the stratification for the small particles due to a loosening of the layers seems to be supported. A decrease of the amplitude to $A = 0.8$ mm leads to a reduced decline of the fraction retained values for both size classes after $t = 5$ s and to an appreciable amount of particles remaining on the screen after $t = 20$ s. The length of the stroke is not long enough to clear the apertures from pegging particles and to give the smaller particles enough possibilities to stratify through the larger ones to the screen surface.

Thereafter, the amplitude is kept constant and the initial frequency of $f = 50.6$ Hz is changed to 45.8 Hz and 55.4 Hz (Fig. 129b). Besides the earlier depletion of the near mesh sized particles, an increase of the frequency to $f = 55.4$ Hz results in nearly the same intensification of the inclination like an increase of the amplitude to $A = 1.2$ mm due to the same reason. In contrast, a reduction of the frequency to $f = 45.8$ Hz has a lower impact than a decrease of the amplitude to $A = 0.8$ mm. Nevertheless, some of the particles remain on the screen after $t = 20$ s. The intensity of the stroke is too low to induce large throws of the coarse material to build up gaps for the small particles to pass through them.

In the next investigations, the liquid amount is increased from $M = 0$ % to $M = 2.5$ % (Figs. 129c,d) and $M = 5$ % (Figs. 129e,f), including variations in the amplitude and the frequency equivalent to those for dry screening. The qualitative results are similar to those with dry particles. A larger amplitude slightly increases the decline of the fraction retained while a larger frequency has a stronger decreasing influence on this value. In contrast, lower amplitudes and frequencies reduce the particle passage and thereby the decline of the fraction retained per size class. In addition, several particles remain on the screen after $t = 20$ s.

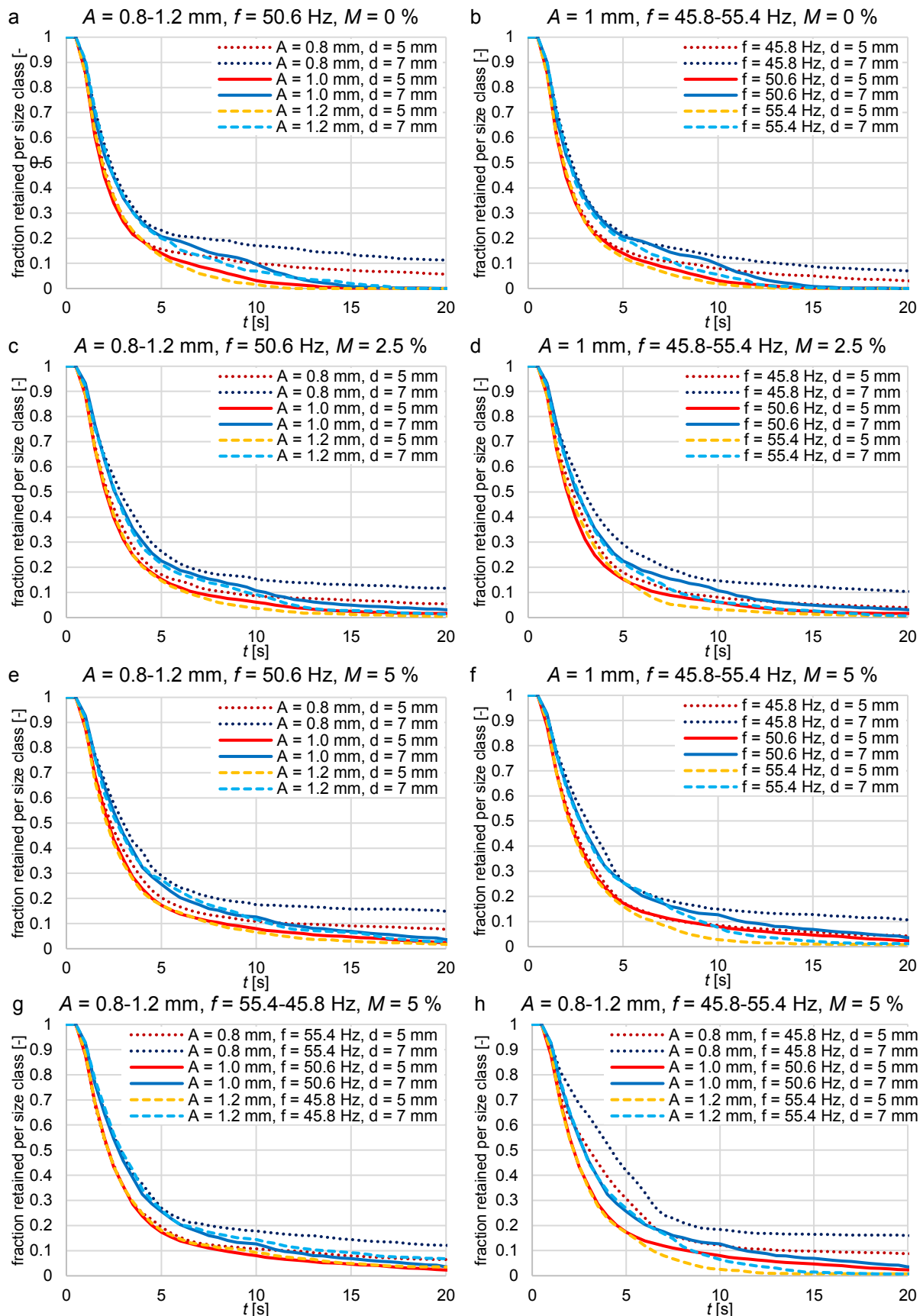


Fig. 129: Fraction retained on the screen over time presented for the small ($d_3 = 5$ mm) and near mesh sized particle fractions ($d_2 = 7$ mm) applying (a,b) dry ($M = 0\%$) and (c-h) wet glass spheres ($M = 2.5/5\%$) with $a = 8$ mm ($d_{1/2/3} = 5/7/10$ mm) and (a,c,e) a variation in the amplitude, (b,d,f) a variation in the frequency and (g,h) a variation in the amplitude and the frequency. All results are obtained by DEM simulations.

The influence of changes in both operating parameters (amplitude and frequency) with a liquid amount of $M = 5\%$ is shown in Figs. 129g,h. For an increase in amplitude and a decrease in frequency, the simulation results are very similar to the initial ones, whereas a larger frequency is not able to compensate for the influence of a lower amplitude when a liquid amount of $M = 5\%$ is applied (compare Fig. 129g). Although the frequency is enlarged, a low amplitude under moist conditions leads to short strokes, which are not able to provide enough opportunities for the undersized particles to stratify towards the apertures to pass through them. In Fig. 129h, under the influence of $M = 5\%$, the operating parameters are both increased or both decreased, respectively. As expected, these simulation results reveal the fastest and the slowest decrease of the fraction retained when applying the same liquid amount.

In order to find out the influence of the added water, simulations with various liquid amounts and constant operational parameters were performed and are shown in Fig. 130. For the initial configuration with $A = 1\text{ mm}$ and $f = 50.6\text{ Hz}$ (Fig. 130a) an increase of the liquid amount results in a lower passage rate and thereby to larger values for the fraction retained per size class independent of particle size. After $t = 20\text{ s}$, some small and near mesh moist particles are still on the screen surface. By adding a small liquid amount, the particles stick to each other and the loosening of the particle layers and thereby the stratification is reduced.

In the next investigations, one operational parameter is changed in each case in comparison to the initial configuration. The results for the simulations with a lower amplitude of $A = 0.8\text{ mm}$ (Fig. 130b) reveal a similar impact of the added water, but after $t = 5\text{ s}$ the curves for the dry particles stagnate more intensively than the other curves due to a larger amount of blocked apertures and the difference to the configuration with $M = 2.5\%$ is equalized. If the amplitude is increased to $A = 1.2\text{ mm}$ (Fig. 130c), the influence of the liquid amount is similar to the initial case. The fraction retained is larger if more water is in the system and at $t = 20\text{ s}$, some of the moist undersized particles are still on the screen.

The results for a lower frequency of $f = 45.8\text{ Hz}$ (Fig. 130d) reveal an equivalent difference between the cases under dry and slightly moist conditions ($M = 2.5\%$) as in the initial configuration. However, a larger liquid amount has only a negligible influence on the fraction retained per size class. If the frequency is increased to $f = 55.4\text{ Hz}$ (Fig. 130e), the passage rate is slowed down for a larger liquid amount and hence, the fraction retained per size class is larger as in the initial configuration. In contrast, the differences between the small particles under the influence of various liquid amounts ($M = 2.5/5\%$) are marginal and all particles are screened after $t = 20\text{ s}$. For a lower amplitude of $A = 0.8\text{ mm}$ and a larger frequency of $f = 55.4\text{ Hz}$ (Fig. 130f), the decrease of the fraction retained is slightly lower for $M = 2.5\%$ in comparison to dry screening, but obviously lower for $M = 5\%$. In the dry case, the larger frequency is able to compensate for the low amplitude, which is not possible for a larger liquid amount.

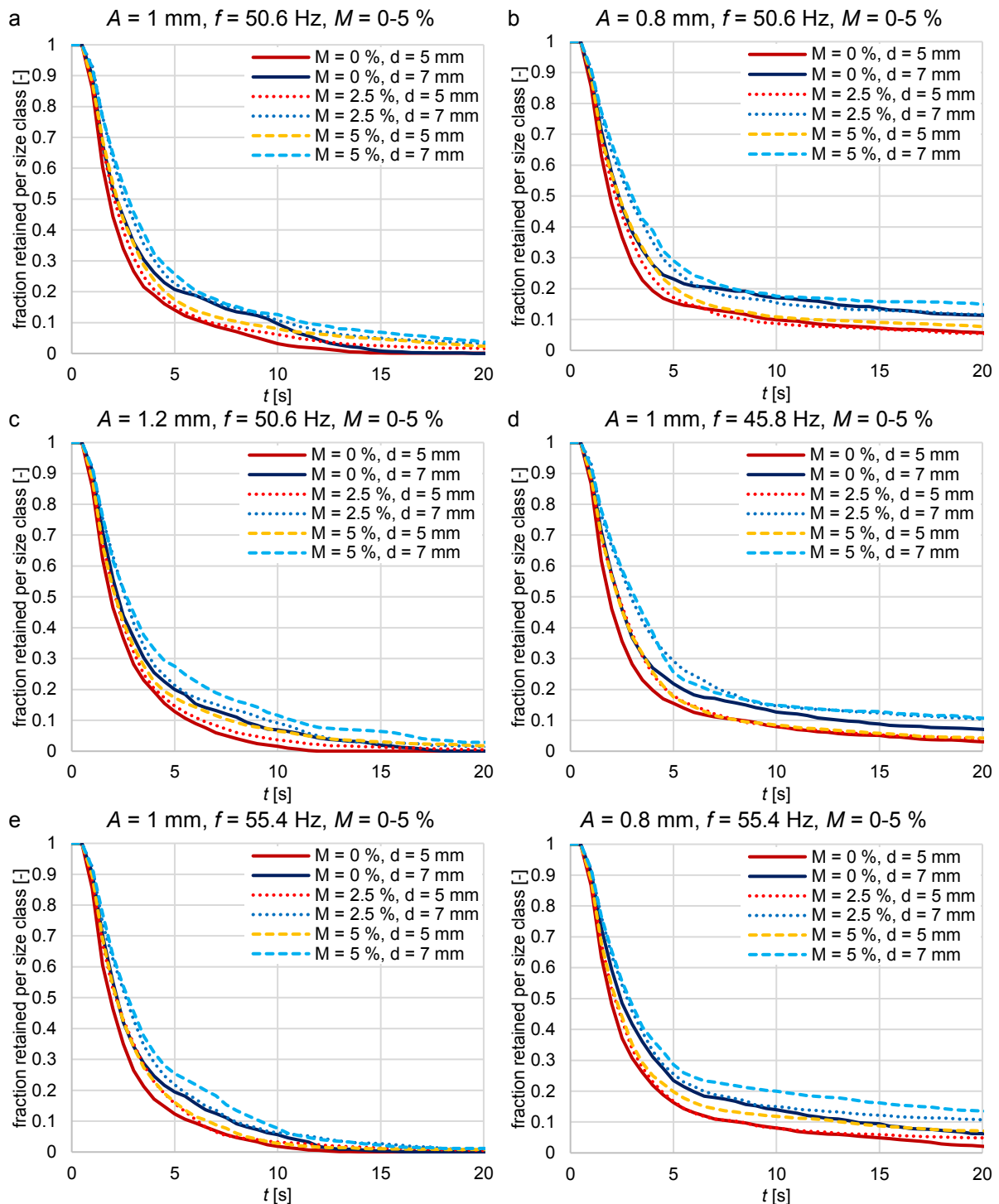


Fig. 130: Fraction retained on the screen over time presented for the small ($d_3 = 5$ mm) and near mesh sized particle fractions ($d_2 = 7$ mm) applying glass spheres with a varying amount of liquid ($M = 0/2.5/5\%$) with $a = 8$ mm ($d_{1/2/3} = 5/7/10$ mm) and (a) initially $A = 1$ mm and $f = 50.6$ Hz. The amplitude is changed to (b) $A = 0.8$ mm and (c) $A = 1.2$ mm as well as the frequency to (d) $f = 45.8$ Hz and (e) $f = 55.4$ Hz. The amplitude and frequency are changed to (f) $A = 0.8$ mm and $f = 55.4$ Hz. All results are obtained by DEM simulations.

5.2 Stratification and passage under the influence of moisture

By analyzing the previous results, it is only possible to compare the passage combined with the stratification. In the following, both subprocesses are studied separately to figure out the relevance of considering them individually in a process model for batch screening.

From a previous work by the authors [241], it is already known that larger amplitudes and frequencies can lead to a faster stratification up to a critical value. That statement has to be verified for the setup applied in this investigation. Additionally, the influence of the liquid amount on the stratification is studied. In order to evaluate the particle stratification, several possibilities are available (comp. [236,241]).

For the first one, the already performed simulations are sufficient. Therein, the particle bed in the screening process is divided in the bottom layer (comp. section 3) and the particles above the bottom layer (top layer). The average time, which the undersized particles need to stratify from the top layer to the bottom layer, is compared in Fig. 131 for the near mesh sized (t_{d2}) and small particles (t_{d3}). In all the simulations, the particles with the larger diameter d_2 need more time to stratify to the bottom layer than the particles with the smaller diameter d_3 . In the initial case, the near mesh sized and small particles need averagely $t_{d2} = 3.62$ s and $t_{d3} = 2.05$ s, respectively. While an increase in amplitude and frequency reduces the residence time for both particle sizes, a larger liquid amount extends it in all cases. By applying larger operational parameters and a lower liquid amount, the particle throws are enlarged and thereby, the loosening of the particle bed is supported, resulting in gaps for the small particles to stratify towards the screen surface.

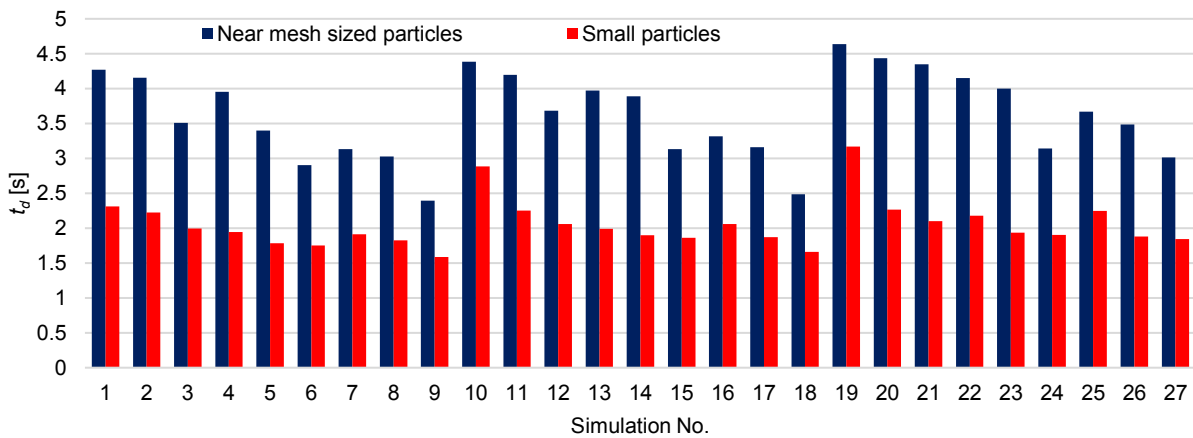


Fig. 131: Average residence time of near mesh sized (t_{d2}) and small particles (t_{d3}) in the top layer for all simulations according to Table 34.

In order to completely separate the stratification process from the passage process, the same setup as before is applied but the screen surface is replaced by a plate without apertures ($a = 0$) and the particles are directly placed on this surface. The plate is vibrated for a time of $t = 10$ s and the positions of the particles are tracked. Thereafter, the accumulated deviation of the average particle height per particle size class from the total average particle height over time t as parameter for comparison is calculated, which is given as

$$h^* = \sum_{j=1}^{n_{class}} \left| \left(\sum_{i=1}^{n_{part,j}} z_{i,j} / n_{part,j} \right) - \left(\sum_{i=1}^{n_{part}} z_i / n_{part} \right) \right|, \quad (293)$$

where n_{class} is the number of size classes, n_{part} is the total number of particles, $n_{part,j}$ is the number of particles in the respective size class j , z_i is the height of a particle i and $z_{i,j}$ is the height of particle i belonging to size class j in the system. In Fig. 132 the accumulated deviation h^* over time t is shown for the initial case ($A = 1$ mm, $f = 50.6$ Hz, $M = 0$ %) and different amplitudes, frequencies and liquid amounts, where only one parameter is varied at a time.

At $t = 0$ s, the particles are well mixed resulting in $h^* = 0$, whereas this value increases for a progressive stratification. The results confirm the observations made before. A larger amplitude or frequency increases the value of h^* faster than lower operational parameters. In addition, a larger liquid amount slows down the stratification process and thus the increase of h^* .

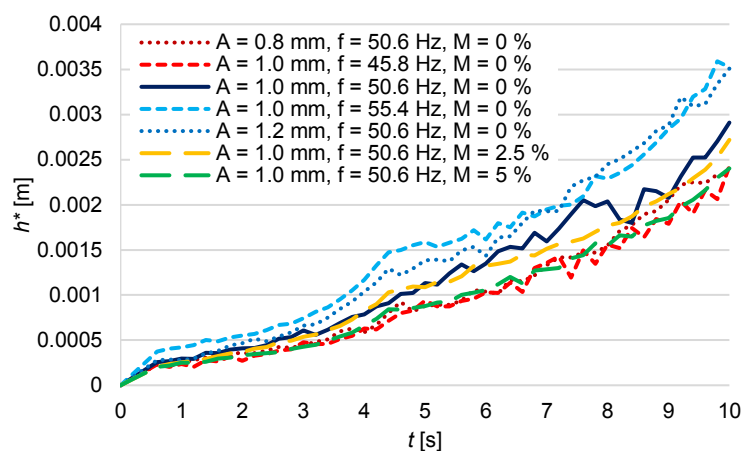


Fig. 132: Accumulated deviation of the average particle height per size class from the total average particle height h^* for different amplitudes, frequencies and liquid amounts in comparison to the initial configuration ($A = 1$ mm, $f = 50.6$ Hz, $M = 0$ %) over time t in the batch apparatus without apertures ($a = 0$). Only one parameter is varied in each simulation.

Concerning the subprocess passage, it is known from the work by Dong et al. [49], that larger amplitudes and frequencies result in less attempts for the particles to pass the apertures. This is only valid for a screening process with a thin layer of particles. Therefore, the initial setup is applied, but only a quarter of the particles is directly placed above the screen surface. The passage of a particle is recorded as soon as it is tracked below the screen surface. The simulations are compared by the fraction retained per size class over a time period of 5 s and their results are presented in Fig. 133. The operational parameters and the liquid amount are changed according to Table 32, but only one parameter is varied at a time.

Particularly for the near mesh sized particles, but also for the small particles, the fraction retained decreases faster for a lower amplitude or frequency and vice versa (comp. Fig. 133a). The particle throws are shorter and thereby, the particles get more attempts to pass the apertures. In Fig. 133b the liquid amount is increased from $M = 0$ % to 2.5 % and 5 %. The passage of the small particles is slightly increased for a larger liquid amount, whereas the near mesh sized particles reveal varying results. While an increase to $M = 2.5$ % slows down the passage, the fraction retained value decreases faster for a larger liquid amount of $M = 5$ %. The reason for this varying behavior is that the throws of the particles under the influence of

liquid are shorter giving the particles more attempts to pass the apertures, whereas the liquid bridges between the particles and the screen wires aggravate the passage.

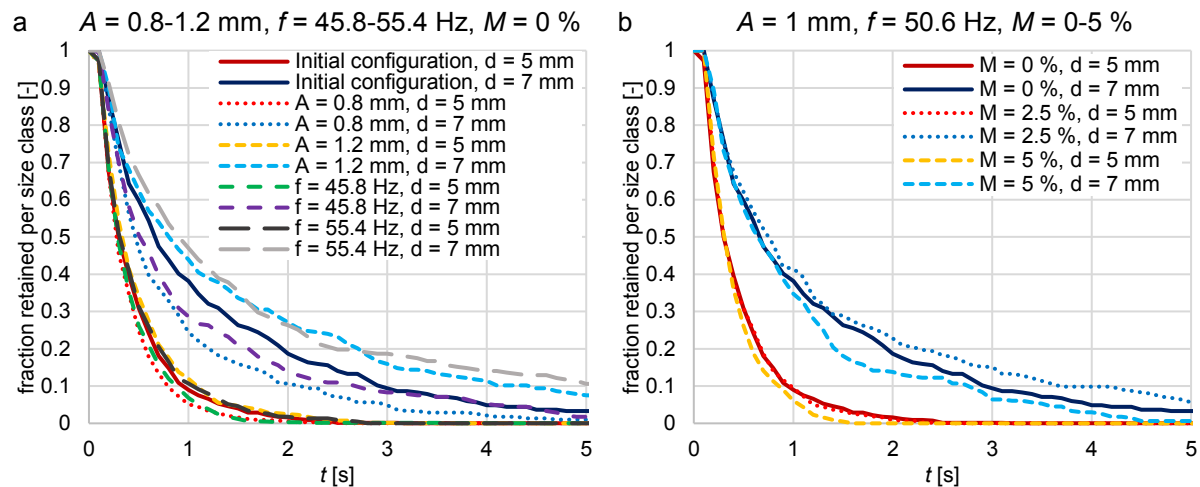


Fig. 133: Fraction retained on the screen over time presented for the small ($d_3 = 7$ mm) and near mesh sized particle fractions ($d_2 = 7$ mm) applying a thin layer of glass spheres with $a = 8$ mm ($d_{1/2/3} = 5/7/10$ mm) and initially $A = 1$ mm, $f = 50.6$ Hz and $M = 0$ %. This initial case is compared to simulations where either (a) the amplitude or frequency or (b) the liquid amount is varied according to Table 32.

In summary, the amplitude, the frequency and the liquid amount influence the two subprocesses stratification and passage contrarily to some extent. Therefore, these processes should be considered separately in a process model, which is further discussed in the following section.

5.3 Application of extended process models for batch screening under the influence of moisture

In this section, the three introduced modified process models for batch screening under the influence of moisture are compared by adjusting their parameters to fit the results obtained by DEM simulations. Thereby, the model results are first adjusted with one set of parameters to all DEM simulation results, giving information about the quality of representing a broad range of various batch screening configurations. In order to quantify these results, the obtained deviations are compared with the lowest possible deviations that could be obtained when applying one set of parameters for each configuration in the process models. Thereby, the deviations of one case are only dependent on the accuracy of the model equation in representing the progression of the fraction retained of this case. Subsequently, the capability of the process models to predict results of batch screening under dry and moist conditions is investigated for the first time. Therein, the adjusted parameters are applied to predict screening results with operational parameters or liquid amounts between the adjusted ones (interpolation) and with lower or larger values (extrapolation), which could be relevant for quantifying the feasibility in industrial applications.

First, one set of adjustable parameters of the process models are adjusted to best fit the results of the fraction retained per size class of all investigated simulations according to Table 34.

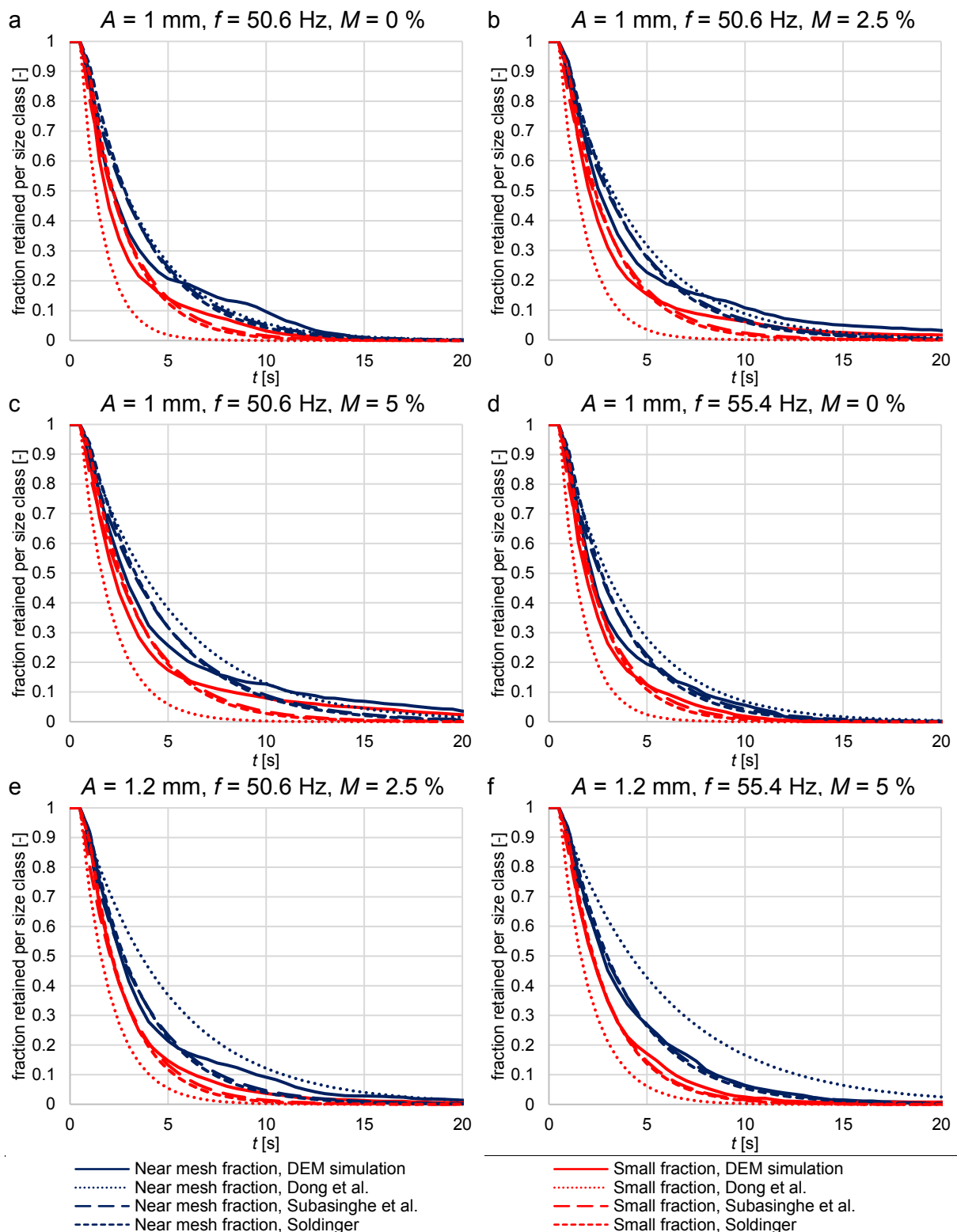


Fig. 134: Fraction retained on the screen over time presented for the small ($d_3 = 5$ mm) and near mesh sized particle fractions ($d_2 = 7$ mm) for various phenomenological screening process models and the DEM simulations applying glass spheres with $a = 8$ mm ($d_{1/2/3} = 5/7/10$ mm). Results are obtained for (a) $A = 1$ mm, $f = 50.6$ Hz and $M = 0$ %, (b) $A = 1$ mm, $f = 50.6$ Hz and $M = 2.5$ %, (c) $A = 1$ mm, $f = 50.6$ Hz and $M = 5$ %, (d) $A = 1$ mm, $f = 55.4$ Hz and $M = 0$ %, (e) $A = 1.2$ mm, $f = 50.6$ Hz and $M = 0$ % as well as for (f) $A = 1.2$ mm, $f = 55.4$ Hz and $M = 5$ %.

In Fig. 134, some examples of the progression of the fraction retained per size class until $t = 20$ s for the initial case (Fig. 134a), two different liquid amounts (Figs. 134b,c), a larger frequency (Fig. 134d), a larger amplitude combined with a small liquid amount (Figs. 134c,e) as well as a large amplitude, frequency and liquid amount (Figs. 134f) obtained by DEM

simulations and process models are presented. It is obvious, that model No. 1 underpredicts the fraction retained of the small particles and mostly overpredicts the fraction retained of the near mesh particles for all configurations shown here. The other models reveal only slight deviations, whereby the results of model No. 2 are a bit closer to the simulation results. A finding of section 5.1 was that a lower amount of liquid as well as a more intense screen motion support the decline of the fraction retained and that smaller particles pass the apertures faster than the near mesh sized particles. These facts are qualitatively represented by the models No. 2 and No. 3 in all cases and by model No. 1 in most cases (comp. Fig. 134).

For a larger frequency (Fig. 134d) or amplitude (Fig. 134e) or both (Fig. 134f) in comparison with the initial operational parameters (Figs. 134a,b), model No. 1 obtains a slightly larger value for the fraction retained per size class. Due to being adjusted with one set of parameters to all simulation results and not considering the stratification process, model No. 1 is not able to compensate the delaying influence on the passage by the supporting impacts on the stratification when larger operating parameters are applied. Conversely, the deviations for configurations with a larger amount of liquid would be more intense, if the results of this model are fitted more accurately to cases with larger operational parameters. Both other models consider the stratification and the passage with different adjustable parameters and therefore, they are able to balance the contrasting effects and to provide results close to the simulated ones. However, it should be noted, that these better results are accompanied by applying twice the number of adjustable parameters.

To benchmark the introduced models over a larger number of investigations, an average deviation of the fraction retained per size class obtained by DEM simulations and process models is calculated. For the different undersized particle classes i , the average of the obtained fractional deviations is given by $(\sum_{i=1}^l (\sum_{k=1}^j |Y_{mod}(i, k) - Y_{sim}(i, k)|)) / (j \cdot r)$, where j is the total number of considered time steps k and r is the total number of undersized fractions (here $r = 2$). Note that the time of the screening process $t = 20$ s is divided into intervals of $\Delta t = 0.5$ s.

The averaged deviations between the fraction retained per size class obtained by phenomenological screening models sorted according to Table 30 and discrete element simulations summed up for all investigated simulations according to Table 34 are presented in Fig. 135 and Fig. 136. In Fig. 135, the process models are adjusted to the simulation results applying one set of parameters for all simulations (bars left of each model number referred to as "left bars" in the following). The average deviations for the models are 0.0593 (No. 1), 0.0387 (No. 2) and 0.0417 (No. 3). Therein, the parameter sets for the three models are as follows:

- No. 1: $k = 1142.6444$, $\alpha = -0.0193$, $\gamma = -161.2886$

- No. 2: $k_s = 1.3883$, $\alpha = 0.8288$, $\gamma = 2.2026$, $k_p = 0.0542$, $\beta = -5.5913$, $\delta = 0.4581$

- No. 3: $k_s = 5.3935$, $\alpha = -9.3318$, $\gamma = 9.6818$, $k_p = 5.0896$, $\beta = 0.7160$, $\delta = 2.4247$

Additionally, these results are compared to the best possible adjustment when one set of parameters for each simulation is used (Fig. 135, bars on the right side of each model number referred to as “right bars” in the following; parameter sets not shown here). Here, the best possible average deviations for the models are 0.0392 (No. 1 / No. 2) and 0.0403 (No. 3). The deviations are very similar for all three models, because the quality of the adjustment in comparison to the other models is independent of the values of the operational parameters or the liquid amount (comp. Fig. 135, right bars).

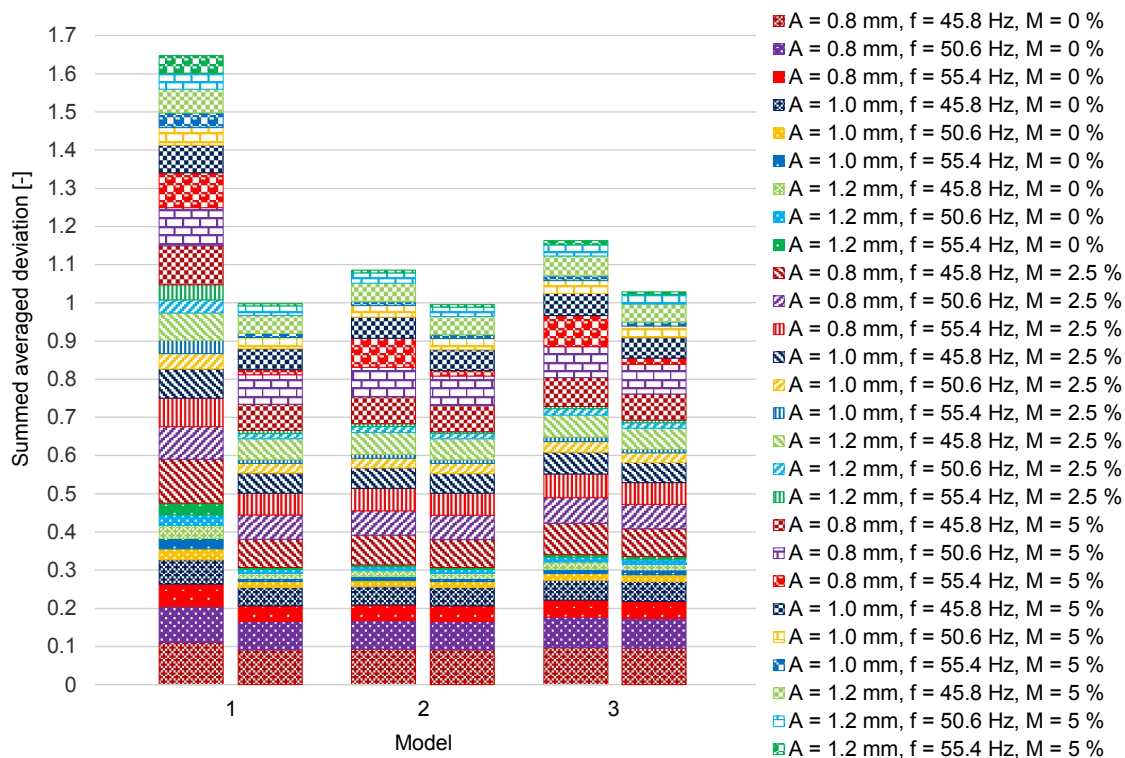


Fig. 135: Deviations between the fraction retained per size class obtained by phenomenological screening models sorted according to Table 30 and discrete element simulations summed up for all investigated simulations according to Table 34. The process models are adjusted to the simulation results by applying one set of parameters for all simulations (bars on the left side of each model number) and by applying one set of parameters for each simulation, showing the best possible adjustment (bars on the right side of each model number).

Overall, all models are better in representing simulations with a faster decline of the fraction retained, whereas the deviations increase for a slower decline of the fraction retained due to lower amplitudes, frequencies and larger liquid amounts. If the models are adjusted with one set of parameters to all simulation results (comp. Fig. 135, left bars), the ranking of the models from the lowest to the largest deviation is No. 2, No. 3 and No. 1, for each configuration. Thereby, the results for the models No. 2 and No. 3 are similar whether one set of parameters is used for all simulations (Fig. 135, left bars) or one for each simulation (Fig. 135, right bars), which represents the best possible adjustment for the respective model. In contrast, the deviations for model No. 1 are much larger if only one set of parameters is applied. It can be

concluded, that the functional forms of all three models are able to represent the progression of the fraction retained per size class for one individual configuration well. However, in batch screening with several particle layers, it is essential to consider the subprocesses stratification and passage like in model No. 2 and No. 3 to represent the results of a wider range of simulation configurations.

The capability of the extended process models to predict simulation results by applying one set of parameters adjusted to simulation results under different configurations is investigated in the following and the summed averaged deviation is shown in Fig. 136. Note that only the deviations of the predicted results to the DEM simulations and not those of the adjusted ones are compared. In this analysis, the process models are adjusted to the first named simulations (numbers in front of the arrows in Fig. 136) before the adjusted parameter set is applied to predict the second named simulations (numbers behind the arrows in Fig. 136). The ranking of the models summed up for all configurations is again No. 2, No. 3 and No. 1, but the individual deviations reveal some interesting particularities. In Figs. 136a-c, only one value of the operational parameters or the liquid amount is varied, while the others are kept constant on the initial, the lower or the larger value. Thereby, the red, blue and green parts of the bars indicate a change in the liquid amount, the amplitude or the frequency, respectively.

In Fig. 136a, the value of one operational parameter (indicated as blue (amplitude) and green bars (frequency)) or the liquid amount (indicated as red bars) of one predicted result is located between the values of two adjusted ones (e.g. $M = 0 \% / M = 5 \% \rightarrow M = 2.5 \%$). The results reveal that all models are able to predict these interpolated values for the fraction retained per size class very well. If only the liquid amount is varied and the operational parameters are kept constant, the results for the models Nos. 1 and 2 are equal. The functional forms of both models are able to predict these results well, because the fraction retained values of the respective predicted configuration are located mostly between those of the adjusted ones. In contrast, model No. 1 reveals more deviations when simulation results with different operational parameters should be predicted. Under these conditions, nearly the same results are obtained by applying the models Nos. 2 and 3, because they both consider the subprocesses stratification and passage which are influenced contrarily by the operational parameters.

In Fig. 136b, the values of the liquid amount or of the operational parameters of two adjusted results are larger than the value of one predicted configuration (e.g. $M = 2.5 \% / M = 5 \% \rightarrow M = 0 \%$). These extrapolated results reveal overall more deviations than in the investigation before, although the outcomes with different liquid amounts are predicted more precisely and nearly independent of the applied model. Larger deviations occur when the result of one simulation with a low amplitude or frequency should be predicted. The process models can predict the outcome of the configurations with larger operational parameters with a fast decline in the fraction retained value very well. As a negative consequence, particularly model No. 1

fails to satisfactorily predict simulation results obtained with lower operational parameters, which are nearly stagnating.

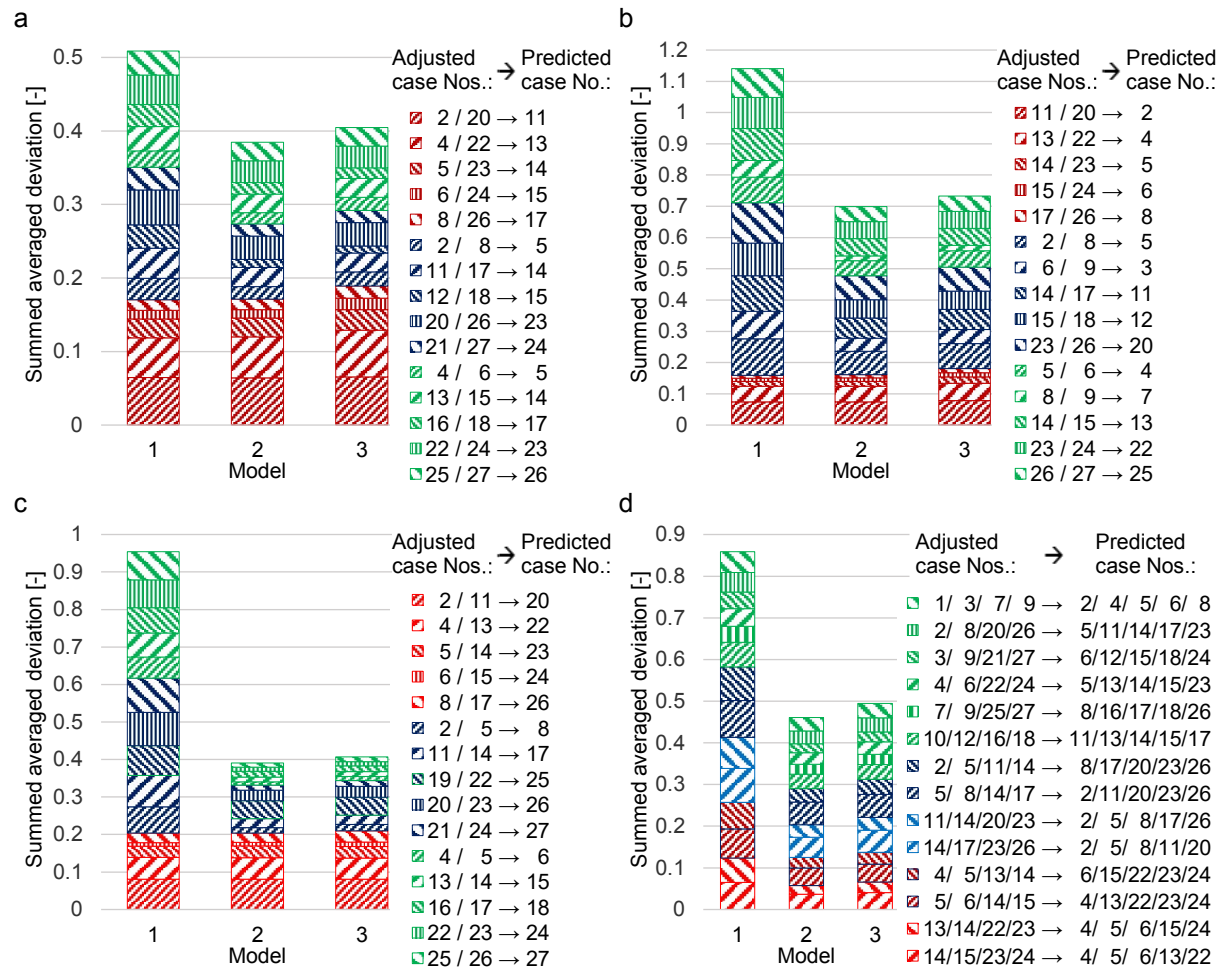


Fig. 136: Summed up deviations between the fraction retained per size class obtained predictively by the process models sorted according to Table 30 and DEM simulations for various configurations according to Table 34. The process models are adjusted to the first named simulations (numbers in front of the arrow) before the adjusted parameters are applied to predict the second named simulations (numbers behind the arrow). The amplitude, frequency or liquid amount of one predicted result is (a) located between (interpolation), (b) lower than or (c) larger than the value of two adjusted ones (extrapolation). (d) Five predicted results are obtained with one set of parameters of four adjusted cases.

The results of predicting the fraction retained per size class for configurations with larger operational parameters or liquid amounts (e.g. $M = 0\%$ / $M = 2.5\%$ → $M = 5\%$) are shown in Fig. 136c. Although the prediction of the simulation results applying a large amount of liquid are worse for all models, the overall results for the models Nos. 2 and 3 are better than in the two previous investigations. These models can predict a fast decline in the fraction retained caused by an intense screen motion very well. In contrast, the results of model No. 1 reveal twice as large deviations as the other two models. In summary, the prediction of simulations with operational parameters that have to be extrapolated is far less accurate if model No. 1 is applied instead of the models Nos. 2 and 3.

In the last investigation, five simulation results are predicted with one set of parameters, which have been adjusted to best fit four different configurations. In Fig. 136d, the average deviations of each five predictions to the simulation results are presented. Therein, the green parts of the

bars indicate that the values of the operational parameters and the liquid amount of the predicted configurations are located between those of the adjusted ones or have the same values. All models are able to predict these results quite well. The parts of the bars in dark blue and blue show the results for predicting different amplitudes as well as larger and lower liquid amounts, respectively. Results with different frequencies in combination with larger and lower liquid amounts are also predicted and depicted as dark red and red parts of the bars in Fig. 136d, respectively. The models Nos. 2 and 3 predict all these configurations very well, but again model No. 1 reveals larger deviations due to the missing ability to compensate for the opposing subprocesses stratification and passage when values have to be extrapolated.

6. Conclusions

In this work, batch screening investigations under the influence of various amounts of liquid have been performed by using the discrete element method (DEM) extended by capillary and viscous forces arising out of the existence of liquid bridge contacts as well as by models for the formation and rupture of liquid bridges. Therein, three particle size classes (coarse, near mesh, fine) as well as various operational parameters (amplitude and frequency) were applied and the resulting values of the fraction retained on the screen surface per size class were compared for the different configurations. The results of the DEM batch screening simulations reveal that larger vibration amplitudes and frequencies predominantly support the decline of the fraction retained for undersized particle classes at least up to the values applied in the investigation here. In contrast, in literature concerning screening with a thin particle bed [49] a lower passage rate is observed for a more intense screen motion due to fewer contacts between the particles and the screen surface leading to a lower number of trials for the particles to pass the apertures. An increase of the liquid amount up to $M = 5\%$ mostly leads to a reduced passage rate and thus to a slower decline of the fraction retained.

From these results, the necessity to study the two subprocesses stratification and passage separately was recognized. Therefore, in a first investigation, the residence time was recorded which the particles need to stratify through the particle bed in the batch screening process. In a further study, the screen surface was replaced by a surface without apertures to analyze the stratification process. The outcomes of both investigations reveal an improvement of the stratification process by enlarging the vibration amplitude and frequency and by reducing the liquid amount. Furthermore, the bulk masses were reduced on the initial screen surface to focus on the passage process of a thin particle bed. The obtained results indicate nearly a contrary impact of the operational parameters and the liquid amount on the passage as on the stratification. The particle passage is faster for lower amplitudes and frequencies in the investigated range giving more attempts for the particles to pass the apertures. Furthermore, a larger amount of liquid leads to shorter particle throws giving them more attempts to pass,

but also to a hindered passage due to the liquid bridges between the particles and the screen wires.

Additionally, as main novelty of this study, phenomenological screening process models have been extended to represent and predict the results of batch screening simulations under the influence of moisture and different operational conditions. First, a benchmark of the extended models to represent all investigated DEM simulation results with one set of adjusted parameters was performed. Overall, all models reveal larger deviations for representing screening results with low amplitudes or frequencies leading to almost stagnating fraction retained curves. On the contrary, the fitting is more accurate for faster declining curves. The results also indicate that the concurrent subprocesses stratification and passage should be considered in the process models. Therefore, the results of the extended models No. 2 by Subasinghe et al. [227] and No. 3 by Soldinger [8], which both take these subprocesses into account fit the simulation results more accurately than the model No. 1 by Dong et al. [49]. In a final investigation, the capability of the extended process models to predict results of batch screening simulations by applying parameters adjusted for different operational parameters or liquid amounts was tested. All investigated models were able to predict the outcome of simulations where only the liquid amount was different or when the varied operational parameter was located between the ones of the adjusted configurations. In contrast, particularly model No. 1 fails to predict the outcome of screening simulations, where the operational parameters of the adjusted configurations are all larger or all lower. However, the models Nos. 2 and 3 are also able to predict these extrapolated results quite well. Therefore, after an appropriate adjustment to the given properties of the screening apparatus and the material, these models (Nos. 2 and 3) can be used to predict results of batch screening simulations of dry material or of particles under the influence of moisture and are suitable to be integrated in the process simulation framework Dyssol [205] in a further step. Note that the outcome of the process models could also be adjusted and compared with experimental results, applying the same procedure. However, in this investigation, previously validated DEM simulations were used within this innovative method to easier obtain a large range of screening results with various operational parameters, to provide the possibility to easily apply this procedure to different screening processes and to give additional information about the subprocesses stratification and passage.

In future investigations, the process models will also be applied for wet screening. For this purpose, some aspects have to be considered. For a small amount of liquid, the screening efficiency decreases with an increase of the liquid amount up to a critical value when the particles are entirely covered by the liquid and the drag forces equal out the adhering forces. From this point on, an increase of the liquid amount results in an increase of the screening

efficiency [9]. Therefore, the introduced models have to be applied with varying parameters for the two different regions also realizing for their transition.

Acknowledgements

The authors gratefully acknowledge the support by DFG within project SPP 1679 through grant number KR3446/7-2 and KR3446/7-3. The original form of the DEM code “DEM-Calc“ applied is based on a development of LEAT, Ruhr-Universität Bochum, Germany. The code “DEM-Calc” has then been continuously extended both at Ruhr-Universität Bochum and Technische Universität Berlin, Germany. We thank all who have contributed.

Compliance with ethical standards

The authors declare that there is no conflict of interest related to this manuscript.

5. Conclusions and perspective

5.1 Conclusion

The overall topic and intention of the DFG project “Development of a dynamic-physical process model for sieving” in the SPP 1679 and of this thesis was to investigate the dynamics of screening as well as its subprocesses under different environmental, material or process related conditions and to provide ways to derive phenomenological process models for the process step screening based on analyzes and benchmarks of existing models, whereby several complementary investigations had to be carried out as well. These tasks were driven forward over the last years resulting in the previously shown publications, of which the particular outcome is summed up in the following.

In publication I, continuously operated screening simulations applying spherical and various non-spherical particles in the DEM have been performed and compared with experimental results from literature (comp. [20]). Thereby, low deviations occurred, which were probably caused by a differing particle feed or the screen wire approximation. Overall, the particle passage is mainly influenced by the particle size and shape, whereby in this investigation, volume equivalent cylinders reveal the best passage rate followed by spheres and non-spherical particles with the same minor axis as the spheres. However, stratification and transport processes are enhanced by the application of spherical particles, followed by symmetrically shaped non-spherical particles. In addition, larger feed rates and shares of coarse material on the screen support the passage of near mesh sized particles. The transport velocity is increased by inclining the screen surface, resulting in a shorter residence time for oversized particles and in a longer residence time for near mesh sized particles due to a spatial later passage.

Batch sieving investigations with various operational parameters, particle and sieve characteristics including their inherent transient effects were carried out in publication II applying discrete element simulations. The findings of publication I are partially confirmed concerning the stratification of spherical and non-spherical particles, but in case of batch sieving, the best passage rate is obtained with spheres. In addition, larger amplitudes and frequencies support the sieving process until a limiting value is reached. An oscillating motion is preferred over a vertically motion and the applied mass should be adapted to the size of the sieve surface. In contrast, a more polydisperse material and the application of a semicircular instead of a rectangular screen bar profile reduce the stratification and the passage rate, respectively. A downscaling of the batch sieving apparatus including a reduction of the amount of particles to reduce the computational effort is possible to some extent. Phenomenological sieving process models were benchmarked based on these results, whereby the models by

Andreev et al. [47], Standish [45], Subasinghe et al. [228], Ferrara et al. [225] and Soldinger [8] reveal the best results. Low sieving rates, represented by flat residual mass curves, are a challenge for all models. The sieving process models, which existed at this time, were apparatus and material dependent, needed adjustable parameters and therefore, they were not predictive. Complex sieving process models do not necessarily offer better results than simpler models and need more time for calculations, but their parameters have a physical meaning and they provide additional information, which could help to increase the predictability of such process models.

In publication III, a similar DEM investigation is performed on a continuously operated screen with a more polydisperse feed than for batch sieving, including additional variations in the inclination angle and the mass flow. Due to the existence of many particle sizes very close to the aperture size, the spherical particles peg the apertures and reveal slower passage rates than non-spherical shapes, which can be prevented by slightly inclining the screen surface. The amplitudes and frequencies with the largest passage rate for the applied configuration are intermediate values of 1.76 mm and 27.6 Hz, respectively and the most effective stroke angle is between 45° and 60° . Note that the choice of an appropriate mass flow rate is dependent on the screen size and particle characteristics. In addition, the fraction retained of some particle shapes is negatively influenced by the geometry of the screen wires. Finally, a screening process with smaller particles and apertures results in a lower value of the fraction retained for spheres and a lower one for non-spherical particles. For the representation of continuous screening, the process models by Grozubinsky et al. [3], Andreev et al. [226], Subasinghe et al. [227] and Soldinger [7] reveal the lowest deviations when the undersized material is taken into account as one lumped fraction. If the undersized material is considered as separated size classes, the model by Standish [45] using one adjustable parameter per size class and the model by Ferrara et al. [225] with less adjustable parameters obtain the most accurate results, respectively. In case of screening models for steady state separation curves, the lowest deviations can be obtained with the model by Plitt [218] and a model based on the mathematical formulation of Trawinski [223]. The discussed advantages and drawbacks of the complex screening models and the findings concerning the predictability are similar to those for batch sieving.

In addition to the previous publication, a finding of publication IV is that the fraction retained is larger for a circular vibration on a horizontally aligned screen in comparison to a linear vibration of ideally 45° . Furthermore, different banana screen approximations were compared with a horizontal as well as two inclined screens in publication V. Thereby, besides the parameters varied in publication III, the inclination angle at the discharge end was varied. Inclined and curved screens revealed a higher screening rate for spheres than for non-spherical particles and an approximation with 5 deck divisions is enough to represent a curved banana screen.

Overall, the investigations confirmed that banana screens have a delayed but reliable particle passage with a lower risk of accumulations, which can be further reduced by larger screen inclinations at the discharge end. They are more sensitive to changes in operational conditions and are capable of handling larger flow rates.

DEM batch sieving investigations under altered operational conditions in addition to the inherent mass loss have been performed with various particle characteristics after an appropriate validation against experiments in publication VI. In accordance with publication II, a change to a larger frequency or amplitude as well as to an oscillating motion with a larger horizontal component during the process supports the sieving. However, an alteration to an oscillating motion with a larger vertical component decelerates the classification. The possibility to predict the results of batch sieving simulations under altered operational conditions by using the known information about the remaining particles of sieving simulations under steady operational conditions was shown to a certain extent. In addition, phenomenological sieving process models have been extended to represent batch sieving simulations under altered operational conditions applying parameters adjusted to unchanged operations. Different modifications had to be realized for the various groups of process models, namely a combination of parameters from initial and altered operational conditions for kinetic models, an aggregation of attempts to pass the apertures before and after the alteration for probabilistic models and a simple change of the parameters in case of the more complex, time step based models. The best results were obtained applying the model by Andreev et al. [226]. However, it considers the undersized particles as one lumped fraction. If the different particle fractions should be taken into account by not adjusting one parameter for each fraction, the model by Solding [8] presents the lowest deviations. However, larger deviations occur, particularly for the model by Subasinghe et al. [228], when the passage rates for different sized particles are similar. The complex, time step based models (comp. [7,8]) reveal larger deviations when abrupt induced reductions of the passage rate occur, due to an overprediction of particles in the layer directly above the sieve surface caused by the initial operational conditions. Overall, the extended models by Andreev et al. [226] and Solding [8] are most suitable to represent batch sieving simulations under altered operational conditions without a new adjustment of parameters. Hence, performing certain simulations or experiments to investigate the resulting repercussions and possible process intensifications can be omitted.

In publication VII, DEM parameters for POM spheres and quartz gravel particles have first been determined by single particle tests including a preceding approximation algorithm for the representation of non-spherical particles. Later, these obtained values were applied in DEM simulations to be adjusted to the results of small bulk experiments (dynamic bed height, static and dynamic angle of repose). Thereby, the DEM parameters were adjusted automatically with an optimization tool, minimizing the deviations between simulations and experiments

progressively. After that, the adjusted DEM parameters were applied to batch sieving simulations and compared to respective experiments, revealing a good match for POM spheres and a satisfying agreement for quartz gravel. To conclude, results of single particle tests can only be used as initial values for the DEM, needing a further automatic adjustment with particles as bulk material, before the DEM parameters can further be applied in more complex processes like sieving.

A comparison between experimental and numerical results of continuously operated screening and air classifying processes under low material loadings has been performed in publication VIII. Thereby, the accuracy when modeling the screening process in the DEM was increased by applying multi-sphere particles instead of spheres to approximate quartz gravel particles. This must also be considered for the representation with the process model by Dong et al. [49], which is suitable for thin layer screening by considering the particle contacts appropriately. Furthermore, experimental investigations for various rotational speeds of a deflector wheel classifier were carried out, whereby a vortex occurs for $n > 6000 \text{ min}^{-1}$, which focused the particles on the pursuing paddle. The experimentally obtained particle trajectories, the cut sizes and the separation curves were represented very well by the DEM simulations, providing possibilities to determine parameters more accurately and to improve respective models. In summary, the DEM can be applied for both classification processes after an appropriate validation. Besides the convenient and detailed investigations, the DEM provides the possibility to derive respective process models and to determine the required adjustable parameters.

In publication IX, the existing DEM code was extended for the simulation of sieving processes under the influence of moisture by capillary and viscous forces caused by the existence of liquid bridges as well as by models for their formation and rupture. Various force models were successfully validated against data from literature, whereby the most accurate models were the one by Rabinovich et al. [104] for capillary forces and the models by Pitois et al. [109] and Goldman et al. [108] for the normal and tangential viscous forces, respectively. Furthermore, the rupture distance is taken from the model of Willett et al. [105] extended by Pitois et al. [110] and the formation and rupture processes including the transfer ratios for the liquid redistribution by applying a look-up table are based on the model by Shi and McCarthy [112]. A batch sieving apparatus was modified to perform experiments with dry particles and material under the influence of moisture. The numerical sieving process was successfully validated against experiments applying materials with a large (glass) and a low wettability (polyoxymethylene) as well as various particle sizes, amplitudes and liquid amounts of up to $M = 10 \%$. According to these investigations, the sieving efficiency is increased for larger amplitudes and larger particle sizes as well as decreased for a larger amount of liquid. The differences between results obtained from experiments and simulations are very low for dry particles and slightly

larger for moist particles, due to the underprediction of water assigned to the undersized material. The main reason for this is that the liquid in the DEM simulations only persists on particles, walls and in liquid bridges, whereas in the experiments, the liquid exists also separated in free motion due to vibrating dewatering, which is not representable by present liquid bridge models.

In publication X, the previously obtained DEM simulation results have been extended by variations in frequency and the results of the fraction retained per size class were first used to adjust process models to later predict batch sieving results under the influence of moisture. Thereby, the supporting effects of a large amplitude and frequency as well as of a low liquid amount concerning the stratification were confirmed. In addition, it was observed that the pure particle passage is reduced contrarily. For the prediction of batch sieving processes under moist conditions, existing phenomenological process models have been extended and benchmarked after their parameters were adjusted to fit results of DEM simulations. The models by Subasinghe et al. [227] and Soldingier [8] obtain low deviations, particularly for results revealing fast passage rates, due to considering the concurrent subprocesses stratification and passage. These models are also capable to predict the progression of the fraction retained of sieving investigations by applying parameters adjusted for different operational parameters or liquid amounts.

To conclude, the findings in these publications provide various aspects concerning the relevant subprocesses stratification, passage and transport as well as particularities of screening like the wire geometry, operational parameters and particle characteristics including their influence on time or spatial dependent outcomes like the fraction retained. The modeling of screening processes with the discrete element method was further improved and extended by the possibility to perform batch sieving under the influence of a certain liquid amount. In addition, a general straightforward procedure to determine DEM simulation parameters exactly and reliably was developed. Furthermore, appropriate validations against experiments have been carried out in order to underline the correctness of the DEM simulations and to apply the respective models for further investigations as already accomplished with regard to air classifying. With the information and data obtained from steady state and dynamic DEM simulations, process models could be benchmarked and successfully extended for representing alterations during the sieving process or sieving under moist conditions. Additionally, suitable models that take the interrelated subprocesses of sieving (stratification and passage) into account could be further improved to predict sieving results for different operational parameters and liquid amounts after being adjusted to fit results of DEM simulations applying the same material- and apparatus-specific parameters. Consequently, the derived process models can be applied as prototypes in dynamic process simulation frameworks of combined solids processes.

5.2 Perspective

In order to complete the performed investigations, some additions can be carried out concerning process models for continuous screening. Alterations during DEM simulations of continuously operated screens have already been studied (not presented in this thesis), but respective process models were not yet derived. In addition, more investigations should be related to the stratification and passage and the adjustment of parameters based on these subprocesses.

One topic that needs to be further investigated in the simulations is that liquid not only persists on particles, walls and in liquid bridges as it is taken into account by existing models. An extension should be implemented to represent liquid separated from particles and walls in free motion like in a vibrating dewatering, which is particularly required for calculating the transition between moist and wet conditions. Another logical continuation concerning screening simulations under the influence of moisture is the consideration of continuously operated screening processes. Therefore, only minor modifications have to be accomplished regarding the simulations, but an appropriate validation based on data from literature or experiments will be challenging. Furthermore, an extension for applying non-spherical particles in screening processes under moist conditions is a relevant topic. In case of multi-sphere particles (comp. Fig. 137), the liquid bridge force calculation would be analogously and the contact detection rules have to be combined with routines for the detection of these non-spherical particles. In addition, the liquid distribution on the individual spheres must be calculated differently. To conclude, screening results of both extensions should be used for the further development of process models.

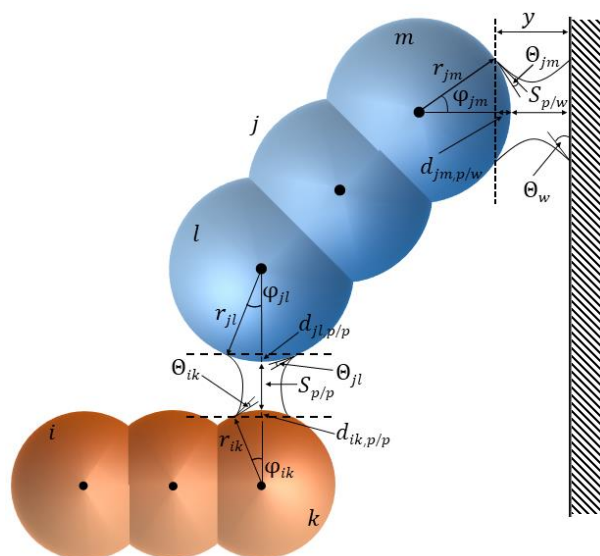


Fig. 137: Liquid bridge contact between two multi-sphere particles as well as between one multi-sphere particle and a wall.

According to Fig. 3, the project plans related to the SPP 1679 include further experimental and simulative investigations under wet conditions. Current work is accomplished concerning the

extension of an experimental batch sieving apparatus for wet screening, which is very challenging due to the large amount of water and its satisfactory control. Furthermore, the coupling of the DEM code with the SPH has to be improved for the appropriate representation of wet batch sieving processes (comp. Fig. 138). Based on this, also continuously operated processes and non-spherical particles should be taken into account in later investigations. The obtained results can form the basis for developing process models for wet screening.

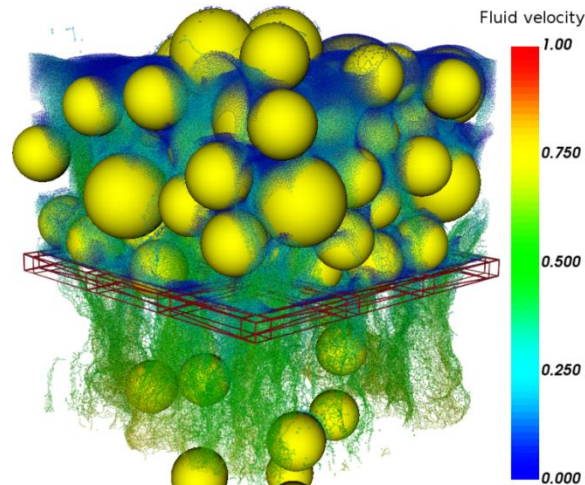


Fig. 138: Wet sieving performed by a coupled DEM and SPH simulation (resolved flow).

Another important task is to further improve the predictability of screening process models by reducing the need for adjustments based on the findings and achievements in this thesis.

Besides the provision of appropriate screening models for the process simulation framework Dyssol, some connections of solids process units will be calculated for testing purposes. Reasonable process chains would consist of several classification processes connected in series or comminution classification circuits.

References

- [1] M. Stieß, *Mechanische Verfahrenstechnik - Partikeltechnologie 1*, 3rd ed., Springer-Verlag, Berlin, Heidelberg (2009).
- [2] K. Liu, Some factors affecting sieving performance and efficiency, *Powder Technology* 193 (2), 208–213 (2009).
- [3] V. Grozubinsky, E. Sultanovitch, I.J. Lin, Efficiency of solid particle screening as a function of screen slot size, particle size, and duration of screening - The theoretical approach, *International Journal of Mineral Processing* 52 (4), 261–272 (1998).
- [4] F. Elskamp, H. Kruggel-Emden, M. Hennig, U. Teipel, Discrete element investigation of process models for batch screening under altered operational conditions, *Powder Technology* 301, 78–95 (2016).
- [5] Y. Yoshida, S. Ishikawa, A. Shimosaka, Y. Shirakawa, J. Hidaka, Estimation Equation for Sieving Rate Based on the Model for Undersized Particles Passing through Vibrated Particle Bed, *Journal of Chemical Engineering of Japan* 46 (2), 116–126 (2013).
- [6] P.W. Cleary, M.D. Sinnott, R.D. Morrison, Separation performance of double deck banana screens – Part 1: Flow and separation for different accelerations, *Minerals Engineering* 22 (14), 1218–1229 (2009).
- [7] M. Solding, Interrelation of stratification and passage in the screening process, *Minerals Engineering* 12 (5), 497–516 (1999).
- [8] M. Solding, Influence of particle size and bed thickness on the screening process, *Minerals Engineering* 13 (3), 297–312 (2000).
- [9] J.W. Fernandez, P.W. Cleary, M.D. Sinnott, R.D. Morrison, Using SPH one-way coupled to DEM to model wet industrial banana screens, *Minerals Engineering* 24, 741–753 (2011).
- [10] P.A. Cundall, O.D.L. Strack, A discrete numerical model for granular assemblies, *Geotechnique* 29 (1), 47–65 (1979).
- [11] M. Zogg, *Einführung in die Mechanische Verfahrenstechnik*, 3rd ed., Teubner Verlag, Stuttgart (1993).
- [12] H. Schubert, *Handbuch der mechanischen Verfahrenstechnik*, Wiley-VCH Verlag, Weinheim (2003).
- [13] S.M. Iveson, J.D. Litster, K. Hapgood, B.J. Ennis, Nucleation, growth and breakage phenomena in agitated wet granulation processes: a review, *Powder Technology* 117, 3–39 (2001).

- [14] K. Washino, K. Miyazaki, T. Tsuji, T. Tanaka, A new contact liquid dispersion model for discrete particle simulation, *Chemical Engineering Research and Design* 110, 123–130 (2016).
- [15] W. Müller, *Mechanische Verfahrenstechnik und ihre Gesetzmäßigkeiten*, 2nd ed., De Gruyter Oldenbourg, Berlin, Boston (2014).
- [16] R. Kruse, *Mechanische Verfahrenstechnik - Grundlagen der Flüssigkeitsförderung und der Partikeltechnologie*, Wiley-VCH Verlag, Weinheim (1999).
- [17] H. Masuda, K. Higashitani, H. Yoshida, *Powder Technology Handbook*, 3rd ed., CRC Press, Taylor & Francis Group, Boca Raton (2006).
- [18] R. Clift, J.R. Grace, M.E. Weber, *Bubbles, Drops, and Particles*, Academic Press, New York, San Francisco, London (1978).
- [19] M. Bohnet, *Mechanische Verfahrenstechnik*, Wiley-VCH Verlag, Weinheim (2004).
- [20] G.W. Delaney, P.W. Cleary, M. Hilden, R.D. Morrison, Testing the validity of the spherical DEM model in simulating real granular screening processes, *Chemical Engineering Science* 68 (1), 215–226 (2012).
- [21] D. Schulze, *Pulver und Schüttgüter - Fließeigenschaften und Handhabung*, 3rd ed., Springer-Verlag, Berlin, Heidelberg (2014).
- [22] K. Höffl, *Zerkleinerungs- und Klassiermaschinen*, Springer-Verlag, Berlin, Heidelberg (1986).
- [23] K. Schwister, *Taschenbuch der Verfahrenstechnik*, 5th ed., Carl Hanser Verlag, München (2017).
- [24] A.M. Gaudin, *Principles of Mineral Dressing*, McGraw-Hill, New York, USA (1939).
- [25] R. Bunge, *Mechanische Aufbereitung - Primär- und Sekundärrohstoffe*, 1st ed., Wiley-VCH Verlag, Weinheim (2012).
- [26] P. Schmidt, R. Körber, M. Coppers, *Sieben und Siebmaschinen - Grundlagen und Anwendungen*, Wiley-VCH Verlag, Weinheim (2003).
- [27] M. Hennig, U. Teipel, Grade efficiency for sieve classification processes, *Canadian Journal of Chemical Engineering* 96, 259–264 (2017).
- [28] H. Jiang, Y. Zhao, C. Duan, C. Zhang, H. Diao, Z. Wang, X. Fan, Properties of technological factors on screening performance of coal in an equal-thickness screen with variable amplitude, *Fuel* 188, 511–521 (2017).
- [29] H. Rumpf, The Strength of Granules and Agglomerates, in: W.A. Knepper (Editor), *Agglomeration*, Wiley Interscience, New York, 379–413 (1962).

- [30] M.R. Smith, L. Collis, P.G. Fookes, *Aggregates: Sand, gravel and crushed rock aggregates for construction purposes*, 3rd ed., The Geological Society, London (2001).
- [31] F.S. Guerreiro, R. Gedraite, C.H. Ataíde, Residual moisture content and separation efficiency optimization in pilot-scale vibrating screen, *Powder Technology* 287, 301–307 (2016).
- [32] A. Govender, J.C. van Dyk, Effect of wet screening on particle size distribution and coal properties, *Fuel* 82, 2231–2237 (2003).
- [33] J. Robertson, C.J. Thomas, B. Caddy, A.J.M. Lewis, Particle Size Analysis of Soils - A Comparison of Dry and Wet Sieving Techniques, *Forensic Science International* 24, 209–217 (1984).
- [34] M.M. Hilden, Dimensional analysis approach to the scale-up and modelling of industrial screens, Ph.D. thesis, University of Queensland (2007).
- [35] H. Dong, C. Liu, Y. Zhao, L. Zhao, Influence of vibration mode on the screening process, *International Journal of Mining Science and Technology* 23 (1), 95–98 (2013).
- [36] L. Zhao, Y. Zhao, C. Bao, Q. Hou, A. Yu, Optimisation of a circularly vibrating screen based on DEM simulation and Taguchi orthogonal experimental design, *Powder Technology* 310, 307–317 (2017).
- [37] J. Wessel, *Grundlagen des Siebens und Sichtens - Das Siebklassieren Teil 2, Aufbereitungs-Technik* 4, 167–180 (1967).
- [38] C. Liu, S. Zhang, H. Zhou, J. Li, Y. Xia, L. Peng, H. Wang, Dynamic analysis and simulation of four-axis forced synchronizing banana vibrating screen of variable linear trajectory, *Journal of Central South University of Technology* 19, 1530–1536 (2012).
- [39] G. Asbjörnsson, M. Bengtsson, E. Hulthén, M. Evertsson, Model of banana screen for robust performance, *Minerals Engineering* 91, 66–73 (2016).
- [40] X. Xiong, L. Niu, C. Gu, Y. Wang, Vibration characteristics of an inclined flip-flow screen panel in banana flip-flow screens, *Journal of Sound and Vibration* 411, 108–128 (2017).
- [41] Z. Gangfeng, Z. Jinbo, X. Wandong, L. Shili, Banana flip-flow screen benefits coal preparation, *Filtration and Separation* 53 (4), 38–41 (2016).
- [42] Y.-S. Chen, S.-S. Hsiau, H.-Y. Lee, Y.-P. Chyou, C.-J. Hsu, Size separation of particulates in a trommel screen system, *Chemical Engineering and Processing: Process Intensification* 49, 1214–1221 (2010).
- [43] B. Bellocq, T. Ruiz, G. Delaplace, A. Duri, B. Cuq, Screening efficiency and rolling effects of a rotating screen drum used to process wet soft agglomerates, *Journal of*

- Food Engineering 195, 235–246 (2017).
- [44] A. Meinel, *Fein und Feinstsiegung, Aufbereitungstechnik* 51 (1), 60–70 (2010).
- [45] N. Standish, *The Kinetics of Batch Sieving, Powder Technology* 41, 57–67 (1985).
- [46] A. Shimosaka, S. Higashihara, J. Hidaka, *Estimation of the sieving rate of powders using computer simulation, Advanced Powder Technology* 11 (4), 487–502 (2000).
- [47] M. Trumic, N. Magdalinovic, *New model of screening kinetics, Minerals Engineering* 24, 42–49 (2011).
- [48] T.J. Napier-Munn, S. Morrell, R.D. Morrison, T. Kojovic, *Mineral Comminution Circuits: Their Operation and Optimisation, Julius Kruttschnitt Mineral Research Centre, The University of Queensland, Brisbane, Queensland* (1996).
- [49] K.J. Dong, B. Wang, A.B. Yu, *Modeling of Particle Flow and Sieving Behavior on a Vibrating Screen: From Discrete Particle Simulation to Process Performance Prediction, Industrial & Engineering Chemistry Research* 52 (33), 11333–11343 (2013).
- [50] J. Li, C. Webb, S.S. Pandiella, G.M. Campbell, *Discrete particle motion on sieves — a numerical study using the DEM simulation, Powder Technology* 133, 190–202 (2003).
- [51] K. Dong, A.H. Esfandiary, A.B. Yu, *Discrete particle simulation of particle flow and separation on a vibrating screen: Effect of aperture shape, Powder Technology* 314, 195–202 (2017).
- [52] A. Dehghani, A.J. Monhemius, R.J. Gochin, *Evaluating the Nakajima et al. model for rectangular-aperture screens, Minerals Engineering* 15, 1089–1094 (2002).
- [53] O. Molerus, *Stochastisches Modell der Gleichgewichtssichtung, Chemie Ingenieur Technik* 39 (13), 792–796 (1967).
- [54] H. Rumpf, K. Sommer, M. Stieß, *Berechnung von Trennkurven für Gleichgewichtssichter, Verfahrenstechnik* 8, 261–263 (1974).
- [55] M.M.G. Senden, *Stochastic Models for Individual Particle Behavior in Straight and Zig Zag Air Classifier, Ph.D. thesis, Eindhoven University of Technology* (1979).
- [56] M.M.G. Senden, M. Tels, *Trennschärfe und mittlere Teilchenverweilzeit im Gleichgewichtssichter, Chemie Ingenieur Technik* 10 (49), 839 (1977).
- [57] K. Husemann, *Modellierung des Sichtprozesses am Abweiserad, Aufbereitungstechnik* 31, 359–366 (1990).
- [58] H. Rumpf, K. Leschonski, *Prinzipien und neuere Verfahren der Windsichtung, Chemie Ingenieur Technik* 39 (21), 1231–1241 (1967).

- [59] O.R. Walton, R.L. Braun, Viscosity, Granular-Temperature, and Stress Calculations for Shearing Assemblies of Inelastic, Frictional Disks, *Journal of Rheology* 30, 949–980 (1986).
- [60] H.P. Zhu, Z.Y. Zhou, R.Y. Yang, A.B. Yu, Discrete particle simulation of particulate systems: Theoretical developments, *Chemical Engineering Science* 62 (13), 3378–3396 (2007).
- [61] H.P. Zhu, Z.Y. Zhou, R.Y. Yang, A.B. Yu, Discrete particle simulation of particulate systems: A review of major applications and findings, *Chemical Engineering Science* 63 (23), 5728–5770 (2008).
- [62] P.W. Cleary, Large scale industrial DEM modelling, *Engineering Computations* 21 (2/3/4), 169–204 (2004).
- [63] G. Lu, J.R. Third, C.R. Müller, Discrete element models for non-spherical particle systems: From theoretical developments to applications, *Chemical Engineering Science* 127, 425–465 (2015).
- [64] D. Höhner, Experimentelle und numerische Untersuchungen zum Einfluss von Partikelgeometrie auf das mechanische Verhalten von Schüttgütern mit Hilfe der Diskreten Elemente Methode, Ph.D. thesis, Ruhr-University Bochum (2014).
- [65] D. Höhner, S. Wirtz, H. Kruggel-Emden, V. Scherer, Comparison of the multi-sphere and polyhedral approach to simulate non-spherical particles within the discrete element method: Influence on temporal force evolution for multiple contacts, *Powder Technology* 208 (3), 643–656 (2011).
- [66] A. Wachs, L. Girolami, G. Vinay, G. Ferrer, Grains3D, a flexible DEM approach for particles of arbitrary convex shape - Part I: Numerical model and validations, *Powder Technology* 224, 374–389 (2012).
- [67] H. Mio, A. Shimosaka, Y. Shirakawa, J. Hidaka, Optimum Cell Size for Contact Detection in the Algorithm of the Discrete Element Method, *Journal of Chemical Engineering of Japan* 38 (12), 969–975 (2005).
- [68] C. Hogue, Shape representation and contact detection for discrete element simulations of arbitrary geometries, *Engineering Computations* 15 (3), 374–390 (1998).
- [69] H. Kruggel-Emden, S. Rickelt, S. Wirtz, V. Scherer, A study on the validity of the multi-sphere Discrete Element Method, *Powder Technology* 188 (2), 153–165 (2008).
- [70] C.M. Wensrich, A. Katterfeld, Rolling friction as a technique for modelling particle shape in DEM, *Powder Technology* 217, 409–417 (2012).
- [71] P.W. Cleary, The effect of particle shape on simple shear flows, *Powder Technology*

- 179 (3), 144–163 (2008).
- [72] S.R. Mead, P.W. Cleary, G.K. Robinson, Characterising the failure and repose angles of irregularly shaped three-dimensional particles using DEM, in: Ninth International Conference on CFD in the Minerals and Process Industries, Melbourne, Australia, 1–6 (2012).
- [73] G.W. Delaney, P.W. Cleary, The packing properties of superellipsoids, *Europhysics Letters* 89 (3), (2010).
- [74] P.A. Cundall, Formulation of a Three-dimensional Distinct Element Model - Part I. A Scheme to Detect and Represent Contacts in a System Composed of Many Polyhedral Blocks, *International Journal of Rock Mechanics and Mining Sciences & Geomechanics Abstracts* 25 (3), 107–116 (1988).
- [75] E.G. Nezami, Y.M.A. Hashash, D. Zhao, J. Ghaboussi, A fast contact detection algorithm for 3-D discrete element method, *Computers and Geotechnics* 31 (7), 575–587 (2004).
- [76] E.G. Nezami, Y.M.A. Hashash, D. Zhao, J. Ghaboussi, Shortest link method for contact detection in discrete element method, *International Journal for Numerical and Analytical Methods in Geomechanics* 30 (8), 783–801 (2006).
- [77] R.P. Jensen, P.J. Bosscher, M.E. Plesha, T.B. Edil, DEM simulation of granular media-structure interface: Effects of surface roughness and particle shape, *International Journal for Numerical and Analytical Methods in Geomechanics* 23 (6), 531–547 (1999).
- [78] J.F. Favier, M.H. Abbaspour-Fard, M. Kremmer, A.O. Raji, Shape representation of axisymmetrical, non-spherical particles in discrete element simulation using multielement model particles, *Engineering Computations* 16 (4), 467–480 (1999).
- [79] J.F. Favier, M.H. Abbaspour-Fard, M. Kremmer, Modeling nonspherical particles using multisphere discrete elements, *Journal of Engineering Mechanics* 127 (10), 971–977 (2001).
- [80] L. Vu-Quoc, X. Zhang, O.R. Walton, A 3-D discrete element method for dry granular flows of ellipsoidal particles, *Computer Methods in Applied Mechanics and Engineering* 187, 483–528 (2000).
- [81] D. Markauskas, R. Kačianauskas, Investigation of rice grain flow by multi-sphere particle model with rolling resistance, *Granular Matter* 13 (2), 143–148 (2011).
- [82] A. Munjiza, J.P. Latham, N.W.M. John, 3D dynamics of discrete element systems comprising irregular discrete elements— integration solution for finite rotations in 3D, *International Journal for Numerical Methods in Engineering* 56 (1), 35–55 (2003).

- [83] K. Han, Y.T. Feng, D.R.J. Owen, Performance comparisons of tree-based and cell-based contact detection algorithms, *Engineering Computations* 24 (2), 165–181 (2007).
- [84] A. Munjiza, K.R.F. Andrews, NBS contact detection algorithm for bodies of similar size, *International Journal for Numerical Methods in Engineering* 43 (1), 131–149 (1998).
- [85] J.R. Williams, E. Perkins, B. Cook, A contact algorithm for partitioning N arbitrary sized objects, *Engineering Computations* 21 (2/3/4), 235–248 (2004).
- [86] A. Munjiza, E. Rougier, N.W.M. John, MR linear contact detection algorithm, *International Journal for Numerical Methods in Engineering* 66 (1), 46–71 (2006).
- [87] K. He, S. Dong, Z. Zhou, Multigrid contact detection method, *Physical Review E* 75 (3), 1–7 (2007).
- [88] J. Bonet, J. Peraire, An alternating digital tree (ADT) algorithm for 3D geometric searching and intersection problems, *International Journal for Numerical Methods in Engineering* 31 (1), 1–17 (1991).
- [89] Y.T. Feng, D.R.J. Owen, An augmented spatial digital tree algorithm for contact detection in computational mechanics, *International Journal for Numerical Methods in Engineering* 55 (2), 159–176 (2002).
- [90] H. Kruggel-Emden, R. Kačianauskas, Discrete element analysis of experiments on mixing and bulk transport of wood pellets on a forward acting grate in discontinuous operation, *Chemical Engineering Science* 92, 105–117 (2013).
- [91] H. Kruggel-Emden, F. Sudbrock, S. Wirtz, V. Scherer, Experimental and numerical investigation of the bulk behavior of wood pellets on a model type grate, *Granular Matter* 14 (6), 681–693 (2012).
- [92] H. Kruggel-Emden, E. Simsek, S. Rickelt, S. Wirtz, V. Scherer, Review and extension of normal force models for the Discrete Element Method, *Powder Technology* 171 (3), 157–173 (2007).
- [93] A. Di Renzo, F.P. Di Maio, Comparison of contact-force models for the simulation of collisions in DEM-based granular flow codes, *Chemical Engineering Science* 59 (3), 525–541 (2004).
- [94] H. Kruggel-Emden, S. Wirtz, V. Scherer, A study on tangential force laws applicable to the discrete element method (DEM) for materials with viscoelastic or plastic behavior, *Chemical Engineering Science* 63 (6), 1523–1541 (2008).
- [95] H. Kruggel-Emden, S. Rickelt, S. Wirtz, V. Scherer, A Numerical Study on the Sensitivity of the Discrete Element Method for Hopper Discharge, *Journal of Pressure Vessel Technology* 131 (3), 031211 (2009).

- [96] P.W. Cleary, M.L. Sawley, DEM modelling of industrial granular flows: 3D case studies and the effect of particle shape on hopper discharge, *Applied Mathematical Modelling* 26 (2), 89–111 (2002).
- [97] D. Höhner, S. Wirtz, V. Scherer, Experimental and numerical investigation on the influence of particle shape and shape approximation on hopper discharge using the discrete element method, *Powder Technology* 235, 614–627 (2013).
- [98] A. Di Renzo, F.P. Di Maio, An improved integral non-linear model for the contact of particles in distinct element simulations, *Chemical Engineering Science* 60 (5), 1303–1312 (2005).
- [99] J. Ai, J.-F. Chen, J.M. Rotter, J.Y. Ooi, Assessment of rolling resistance models in discrete element simulations, *Powder Technology* 206 (3), 269–282 (2011).
- [100] Y.C. Zhou, B.D. Wright, R.Y. Yang, B.H. Xu, A.B. Yu, Rolling friction in the dynamic simulation of sandpile formation, *Physica A* 269, 536–553 (1999).
- [101] W. Ge, L. Wang, J. Xu, F. Chen, G. Zhou, L. Lu, Q. Chang, J. Li, Discrete simulation of granular and particle-fluid flows: From fundamental study to engineering application, *Reviews in Chemical Engineering* 33 (6), 551–623 (2017).
- [102] K.L. Johnson, K. Kendall, A.D. Roberts, Surface Energy and the Contact of Elastic Solids, *Proceedings of the Royal Society A* 324 (1558), 301–313 (1971).
- [103] B.V. Derjaguin, V.M. Muller, Y.U.P. Toporov, Effect of contact deformation on the adhesion of particles, *Journal of Colloid and Interface Science* 53 (2), 314–326 (1975).
- [104] Y.I. Rabinovich, M.S. Esayanur, B.M. Moudgil, Capillary Forces between Two Spheres with a Fixed Volume Liquid Bridge: Theory and Experiment, *Langmuir* 21 (24), 10992–10997 (2005).
- [105] C.D. Willett, M.J. Adams, S.A. Johnson, J.P.K. Seville, Capillary Bridges between Two Spherical Bodies, *Langmuir* 16 (10), 9396–9405 (2000).
- [106] T. Weigert, S. Ripperger, Calculation of the Liquid Bridge Volume and Bulk Saturation from the Half-filling Angle, *Particle & Particle Systems Characterization* 16 (5), 238–242 (1999).
- [107] M.J. Adams, V. Perchard, The Cohesive Forces Between Particles with Interstitial Liquid, *Inst. Chem. Eng. Symp. Ser.* 91, 147–160 (1985).
- [108] A.J. Goldman, R.G. Cox, H. Brenner, Slow viscous motion of a sphere parallel to a plane wall—I Motion through a quiescent fluid, *Chemical Engineering Science* 22 (4), 653–660 (1967).

- [109] O. Pitois, P. Moucheront, X. Chateau, Liquid Bridge between Two Moving Spheres: An Experimental Study of Viscosity Effects, *Journal of Colloid and Interface Science* 231, 26–31 (2000).
- [110] O. Pitois, P. Moucheront, X. Chateau, Rupture energy of a pendular liquid bridge, *The European Physical Journal B* 23, 79–86 (2001).
- [111] X. Pepin, D. Rossetti, S.M. Iveson, S.J.R. Simons, Modeling the Evolution and Rupture of Pendular Liquid Bridges in the Presence of Large Wetting Hysteresis, *Journal of Colloid and Interface Science* 232, 289–297 (2000).
- [112] D. Shi, J.J. McCarthy, Numerical simulation of liquid transfer between particles, *Powder Technology* 184, 64–75 (2008).
- [113] G. Lian, C. Thornton, M.J. Adams, A Theoretical Study of the Liquid Bridge Forces between Two Rigid Spherical Bodies, *Journal of Colloid and Interface Science* 161, 138–147 (1993).
- [114] G. Lian, J. Seville, The capillary bridge between two spheres: New closed-form equations in a two century old problem, *Advances in Colloid and Interface Science* 227, 53–62 (2016).
- [115] A. Gladkyy, R. Schwarze, Comparison of different capillary bridge models for application in the discrete element method, *Granular Matter* 16 (6), 911–920 (2014).
- [116] T. Mikami, H. Kamiya, M. Horio, Numerical simulation of cohesive powder behavior in a fluidized bed, *Chemical Engineering Science* 53 (10), 1927–1940 (1998).
- [117] K. Washino, E.L. Chan, K. Miyazaki, T. Tsuji, T. Tanaka, Time step criteria in DEM simulation of wet particles in viscosity dominant systems, *Powder Technology* 302, 100–107 (2016).
- [118] S. Schmelzle, H. Nirschl, DEM simulations: mixing of dry and wet granular material with different contact angles, *Granular Matter* 20:19, (2018).
- [119] S. Radl, E. Kalvoda, B.J. Glasser, J.G. Khinast, Mixing characteristics of wet granular matter in a bladed mixer, *Powder Technology* 200 (3), 171–189 (2010).
- [120] L. Scholtès, B. Chareyre, F. Nicot, F. Darve, Discrete modelling of capillary mechanisms in multi-phase granular media, *Computer Modeling in Engineering & Sciences* 52 (3), 297–318 (2009).
- [121] K. Melnikov, R. Mani, F.K. Wittel, M. Thielmann, H.J. Herrmann, Grain scale modeling of arbitrary fluid saturation in random packings, *Physical Review E* 92 (2), 022206 (2015).

- [122] J. Wang, E. Gallo, B. François, F. Gabrieli, P. Lambert, Capillary force and rupture of funicular liquid bridges between three spherical bodies, *Powder Technology* 305, 89–98 (2017).
- [123] H.-J. Butt, M. Kappl, *Surface and Interfacial Forces*, Wiley-VCH Verlag, Weinheim (2010).
- [124] Z. Asaf, D. Rubinstein, I. Shmulevich, Determination of discrete element model parameters required for soil tillage, *Soil and Tillage Research* 92 (1–2), 227–242 (2007).
- [125] M. Marigo, E.H. Stitt, Discrete element method (DEM) for industrial applications: Comments on calibration and validation for the modelling of cylindrical pellets, *KONA Powder and Particle Journal* 32 (32), 236–252 (2015).
- [126] C.J. Coetzee, Review: Calibration of the discrete element method, *Powder Technology* 310, 104–142 (2017).
- [127] C.J. Coetzee, Calibration of the discrete element method and the effect of particle shape, *Powder Technology* 297, 50–70 (2016).
- [128] T.A.H. Simons, R. Weiler, S. Strege, S. Bensmann, M. Schilling, A. Kwade, A ring shear tester as calibration experiment for DEM simulations in agitated mixers - A sensitivity study, *Procedia Engineering* 102, 741–748 (2015).
- [129] A.P. Grima, P.W. Wypych, Investigation into calibration of discrete element model parameters for scale-up and validation of particle–structure interactions under impact conditions, *Powder Technology* 212 (1), 198–209 (2011).
- [130] G.K.P. Barrios, R.M. de Carvalho, A. Kwade, L.M. Tavares, Contact parameter estimation for DEM simulation of iron ore pellet handling, *Powder Technology* 248, 84–93 (2013).
- [131] M.D. Sinnott, P.W. Cleary, The effect of particle shape on mixing in a high shear mixer, *Computational Particle Mechanics* 3 (4), 477–504 (2016).
- [132] M. Ucgul, J.M. Fielke, C. Saunders, Three-dimensional discrete element modelling of tillage: Determination of a suitable contact model and parameters for a cohesionless soil, *Biosystems Engineering* 121, 105–117 (2014).
- [133] M.O. Ciantia, M. Arroyo, J. Butlanska, A. Gens, DEM modelling of cone penetration tests in a double-porosity crushable granular material, *Computers and Geotechnics* 73, 109–127 (2016).
- [134] Y.T. Feng, K. Han, D.R.J. Owen, J. Loughran, On upscaling of discrete element models: similarity principles, *Engineering Computations* 26 (6), 599–609 (2009).

- [135] T. Roessler, A. Katterfeld, Scaling of the angle of repose test and its influence on the calibration of DEM parameters using upscaled particles, *Powder Technology* 330, 58–66 (2018).
- [136] W. Smith, D. Melanz, C. Senatore, K. Iagnemma, H. Peng, Comparison of discrete element method and traditional modeling methods for steady-state wheel-terrain interaction of small vehicles, *Journal of Terramechanics* 56, 61–75 (2014).
- [137] D. Markauskas, R. Kačianauskas, A. Džiugys, R. Navakas, Investigation of adequacy of multi-sphere approximation of elliptical particles for DEM simulations, *Granular Matter* 12 (1), 107–123 (2010).
- [138] R. Caulkin, W. Tian, M. Pasha, A. Hassanpour, X. Jia, Impact of shape representation schemes used in discrete element modelling of particle packing, *Computers and Chemical Engineering* 76, 160–169 (2015).
- [139] M. Pasha, C. Hare, M. Ghadiri, A. Gunadi, P.M. Piccione, Effect of particle shape on flow in discrete element method simulation of a rotary batch seed coater, *Powder Technology* 296, 29–36 (2016).
- [140] K.C. Williams, W. Chen, S. Weeger, T.J. Donohue, Particle shape characterisation and its application to discrete element modelling, *Particuology* 12 (1), 80–89 (2014).
- [141] G. Mollon, J. Zhao, Generating realistic 3D sand particles using Fourier descriptors, *Granular Matter* 15 (1), 95–108 (2013).
- [142] M. Lu, G.R. McDowell, The importance of modelling ballast particle shape in the discrete element method, *Granular Matter* 9, 69–80 (2007).
- [143] C. González-Montellano, J.M. Fuentes, E. Ayuga-Téllez, F. Ayuga, Determination of the mechanical properties of maize grains and olives required for use in DEM simulations, *Journal of Food Engineering* 111 (4), 553–562 (2012).
- [144] D. Höhner, S. Wirtz, V. Scherer, A study on the influence of particle shape and shape approximation on particle mechanics in a rotating drum using the discrete element method, *Powder Technology* 253, 256–265 (2014).
- [145] P.W. Cleary, DEM prediction of industrial and geophysical particle flows, *Particuology* 8 (2), 106–118 (2010).
- [146] J. Härtl, J.Y. Ooi, Numerical investigation of particle shape and particle friction on limiting bulk friction in direct shear tests and comparison with experiments, *Powder Technology* 212 (1), 231–239 (2011).
- [147] J. Härtl, J.Y. Ooi, Experiments and simulations of direct shear tests: Porosity, contact friction and bulk friction, *Granular Matter* 10 (4), 263–271 (2008).

- [148] M.D. Sinnott, P.W. Cleary, R.D. Morrison, Combined DEM and SPH simulation of overflow ball mill discharge and trommel flow, *Minerals Engineering* 108, 93–108 (2017).
- [149] S. Just, G. Toschkoff, A. Funke, D. Djuric, G. Scharrer, J. Khinast, K. Knop, P. Kleinebudde, Experimental Analysis of Tablet Properties for Discrete Element Modeling of an Active Coating Process, *AAPS PharmSciTech* 14 (1), 402–411 (2013).
- [150] Y.-C. Chung, J.Y. Ooi, A study of influence of gravity on bulk behaviour of particulate solid, *Particuology* 6 (6), 467–474 (2008).
- [151] K. Senetakis, M.R. Coop, M.C. Todisco, The inter-particle coefficient of friction at the contacts of Leighton Buzzard sand quartz minerals, *Soils and Foundations* 53 (5), 746–755 (2013).
- [152] M. Molenda, J. Horabik, J. Łukaszuk, J. Wiącek, Variability of intergranular friction and its role in DEM simulation of direct shear of an assembly of rapeseeds, *International Agrophysics* 25, 361–368 (2011).
- [153] M. Ucgul, J.M. Fielke, C. Saunders, Defining the effect of sweep tillage tool cutting edge geometry on tillage forces using 3D discrete element modelling, *Information Processing in Agriculture* 2 (2), 130–141 (2015).
- [154] Y.C. Chung, C.K. Lin, J. Ai, Mechanical behaviour of a granular solid and its contacting deformable structure under uni-axial compression-Part II: Multi-scale exploration of internal physical properties, *Chemical Engineering Science* 144, 421–443 (2016).
- [155] D. Kretz, S. Callau-Monje, M. Hitschler, A. Hien, M. Raedle, J. Hesser, Discrete element method (DEM) simulation and validation of a screw feeder system, *Powder Technology* 287, 131–138 (2016).
- [156] H.T. Chou, C.F. Lee, Y.C. Chung, S.S. Hsiau, Discrete element modelling and experimental validation for the falling process of dry granular steps, *Powder Technology* 231, 122–134 (2012).
- [157] F. Alonso-Marroquín, Á. Ramírez-Gómez, C. González-Montellano, N. Balaam, D.A.H. Hanaor, E.A. Flores-Johnson, Y. Gan, S. Chen, L. Shen, Experimental and numerical determination of mechanical properties of polygonal wood particles and their flow analysis in silos, *Granular Matter* 15 (6), 811–826 (2013).
- [158] H. Chen, Y.L. Liu, X.Q. Zhao, Y.G. Xiao, Y. Liu, Numerical investigation on angle of repose and force network from granular pile in variable gravitational environments, *Powder Technology* 283, 607–617 (2015).
- [159] B. Majidi, K. Azari, H. Alamdari, M. Fafard, D. Ziegler, Simulation of vibrated bulk density of anode-grade coke particles using discrete element method, *Powder Technology* 261,

- 154–160 (2014).
- [160] Y. Li, Y. Xu, C. Thornton, A comparison of discrete element simulations and experiments for 'sandpiles' composed of spherical particles, *Powder Technology* 160 (3), 219–228 (2005).
- [161] F. Sudbrock, E. Simsek, S. Rickelt, S. Wirtz, V. Scherer, Discrete element analysis of experiments on mixing and stoking of monodisperse spheres on a grate, *Powder Technology* 208 (1), 111–120 (2011).
- [162] C.X. Wong, M.C. Daniel, J.A. Rongong, Energy dissipation prediction of particle dampers, *Journal of Sound and Vibration* 319 (1–2), 91–118 (2009).
- [163] H. Dong, M.H. Moys, Measurement of impact behaviour between balls and walls in grinding mills, *Minerals Engineering* 16 (6), 543–550 (2003).
- [164] D.A. Gorham, A.H. Kharaz, The measurement of particle rebound characteristics, *Powder Technology* 112 (3), 193–202 (2000).
- [165] D.B. Hastie, Experimental measurement of the coefficient of restitution of irregular shaped particles impacting on horizontal surfaces, *Chemical Engineering Science* 101, 828–836 (2013).
- [166] L. Wang, W. Zhou, Z. Ding, X. Li, C. Zhang, Experimental determination of parameter effects on the coefficient of restitution of differently shaped maize in three-dimensions, *Powder Technology* 284, 187–194 (2015).
- [167] C.J. Coetzee, D.N.J. Els, Calibration of discrete element parameters and the modelling of silo discharge and bucket filling, *Computers and Electronics in Agriculture* 65 (2), 198–212 (2009).
- [168] C.J. Coetzee, D.N.J. Els, Calibration of granular material parameters for DEM modelling and numerical verification by blade-granular material interaction, *Journal of Terramechanics* 46, 15–26 (2009).
- [169] C.J. Coetzee, D.N.J. Els, G.F. Dymond, Discrete element parameter calibration and the modelling of dragline bucket filling, *Journal of Terramechanics* 47 (1), 33–44 (2010).
- [170] P. Frankowski, M. Morgeneyer, Calibration and validation of DEM rolling and sliding friction coefficients in angle of repose and shear measurements, *AIP Conference Proceedings* 1542, 851–854 (2013).
- [171] M. Combarros, H.J. Feise, H. Zetzener, A. Kwade, Segregation of particulate solids: Experiments and DEM simulations, *Particuology* 12 (1), 25–32 (2014).
- [172] D.A. Santos, M.A.S. Barrozo, C.R. Duarte, F. Weigler, J. Mellmann, Investigation of

- particle dynamics in a rotary drum by means of experiments and numerical simulations using DEM, *Advanced Powder Technology* 27 (2), 692–703 (2016).
- [173] R. Cabisco, J.H. Finke, A. Kwade, Calibration and interpretation of DEM parameters for simulations of cylindrical tablets with multi-sphere approach, *Powder Technology* 327, 232–245 (2018).
- [174] C. González-Montellano, Á. Ramírez, E. Gallego, F. Ayuga, Validation and experimental calibration of 3D discrete element models for the simulation of the discharge flow in silos, *Chemical Engineering Science* 66 (21), 5116–5126 (2011).
- [175] Z. Yan, S.K. Wilkinson, E.H. Stitt, M. Marigo, Discrete element modelling (DEM) input parameters: understanding their impact on model predictions using statistical analysis, *Computational Particle Mechanics* 2 (3), 283–299 (2015).
- [176] S.M. Derakhshani, D.L. Schott, G. Lodewijks, Micro-macro properties of quartz sand: Experimental investigation and DEM simulation, *Powder Technology* 269, 127–138 (2015).
- [177] Q. Li, M. Feng, Z. Zou, Validation and Calibration Approach for Discrete Element Simulation of Burden Charging in Pre-reduction Shaft Furnace of COREX Process, *ISIJ International* 53 (8), 1365–1371 (2013).
- [178] R.J. Goetsch, J.D. Regele, Discrete element method prediction of particle curtain properties, *Chemical Engineering Science* 137, 852–861 (2015).
- [179] M.A. Sadek, Y. Chen, J. Liu, Simulating shear behavior of a sandy soil under different soil conditions, *Journal of Terramechanics* 48 (6), 451–458 (2011).
- [180] Z. Wang, G. Jing, Q. Yu, H. Yin, Analysis of ballast direct shear tests by discrete element method under different normal stress, *Measurement* 63, 17–24 (2015).
- [181] A. Salazar, E. Sáez, G. Pardo, Modeling the direct shear test of a coarse sand using the 3D Discrete Element Method with a rolling friction model, *Computers and Geotechnics* 67, 83–93 (2015).
- [182] C.J. Coetzee, E. Horn, Calibration of the Discrete Element Method Using a Large Shear Box, *International Journal of Mechanical and Mechatronic Engineering* 8 (12), 2105–2114 (2014).
- [183] Y.C. Chung, H.H. Liao, S.S. Hsiao, Convection behavior of non-spherical particles in a vibrating bed: Discrete element modeling and experimental validation, *Powder Technology* 237, 53–66 (2013).
- [184] D. Höhner, S. Wirtz, V. Scherer, A numerical study on the influence of particle shape on hopper discharge within the polyhedral and multi-sphere discrete element method,

- Powder Technology 226, 16–28 (2012).
- [185] T. Zhao, F. Dai, N.W. Xu, Y. Liu, Y. Xu, A composite particle model for non-spherical particles in DEM simulations, *Granular Matter* 17 (6), 763–774 (2015).
- [186] J. Wiącek, M. Molenda, J. Horabik, J.Y. Ooi, Influence of grain shape and intergranular friction on material behavior in uniaxial compression: Experimental and DEM modeling, *Powder Technology* 217, 435–442 (2012).
- [187] P. Parafiniuk, M. Molenda, J. Horabik, Influence of particle shape and sample width on uniaxial compression of assembly of prolate spheroids examined by discrete element method, *Physica A* 416, 279–289 (2014).
- [188] K.L. Tung, T.H. Chang, Y. Lin, C. Chyang, DEM Simulation of a 3D Vertical Vibratory Screening Process: The Study of a Simulated Woven-Mesh Structure, *AIChE Journal* 57 (4), 918–928 (2011).
- [189] J. Li, C. Webb, S.S. Pandiella, G.M. Campbell, A numerical simulation of separation of crop seeds by screening - effect of particle bed depth, *Trans IChemE* 80 (Part C), 109–117 (2002).
- [190] H. Alkhalidi, P. Eberhard, Particle screening phenomena in an oblique multi-level tumbling reservoir: a numerical study using discrete element simulation, *Granular Matter* 9, 415–429 (2007).
- [191] H. Alkhalidi, C. Ergenzinger, F. Fleißner, P. Eberhard, Comparison between two different mesh descriptions used for simulation of sieving processes, *Granular Matter* 10, 223–229 (2008).
- [192] L. Zhao, Y. Zhao, C. Liu, J. Li, H. Dong, Simulation of the screening process on a circularly vibrating screen using 3D-DEM, *Mining Science and Technology (China)* 21 (5), 677–680 (2011).
- [193] L. Zhao, Y. Zhao, C. Bao, Q. Hou, A. Yu, Laboratory-scale validation of a DEM model of screening processes with circular vibration, *Powder Technology* 303, 269–277 (2016).
- [194] Z. Yin, H. Zhang, T. Han, Simulation of particle flow on an elliptical vibrating screen using the discrete element method, *Powder Technology* 302, 443–454 (2016).
- [195] K.J. Dong, A.B. Yu, I. Brake, DEM simulation of particle flow on a multi-deck banana screen, *Minerals Engineering* 22, 910–920 (2009).
- [196] C. Liu, H. Wang, Y. Zhao, L. Zhao, H. Dong, DEM simulation of particle flow on a single deck banana screen, *International Journal of Mining Science and Technology* 23 (2), 273–277 (2013).

- [197] M. Jahani, A. Farzanegan, M. Noaparast, Investigation of screening performance of banana screens using LIGGGHTS DEM solver, *Powder Technology* 283, 32–47 (2015).
- [198] P.W. Cleary, M.D. Sinnott, R.D. Morrison, Separation performance of double deck banana screens – Part 2: Quantitative predictions, *Minerals Engineering* 22 (14), 1230–1244 (2009).
- [199] P.W. Cleary, Large scale industrial DEM modelling, *Engineering Computations* 21 (2/3/4), 169–204 (2004).
- [200] H. Li, Y. Li, F. Gao, Z. Zhao, L. Xu, CFD–DEM simulation of material motion in air-and-screen cleaning device, *Computers and Electronics in Agriculture* 88, 111–119 (2012).
- [201] M.D. Sinnott, P.W. Cleary, Particulate and water mixing in the feed box for a screen, *Minerals Engineering* 109, 109–125 (2017).
- [202] K.J. Dong, A.B. Yu, Numerical simulation of the particle flow and sieving behaviour on sieve bend/low head screen combination, *Minerals Engineering* 31, 2–9 (2012).
- [203] P.W. Cleary, P. Wilson, M.D. Sinnott, Effect of particle cohesion on flow and separation in industrial vibrating screens, *Minerals Engineering* 119, 191–204 (2018).
- [204] B. Barbabela e Silva, E.R. da Cunha, R.M. de Carvalho, L.M. Tavares, Modeling and simulation of green iron ore pellet classification in a single deck roller screen using the discrete element method, *Powder Technology* 332, 359–370 (2018).
- [205] V. Skorych, M. Dosta, E.-U. Hartge, S. Heinrich, Novel system for dynamic flowsheet simulation of solids processes, *Powder Technology* 314, 665–679 (2017).
- [206] A. Dimian, C. Bildea, A. Kiss, *Integrated Design and Simulation of Chemical Processes*, Elsevier 13, 73–156 (2014).
- [207] M. Dosta, S. Heinrich, J. Werther, Fluidized bed spray granulation: Analysis of the system behaviour by means of dynamic flowsheet simulation, *Powder Technology* 204 (1), 71–82 (2010).
- [208] W. Marquardt, *Dynamic Process Simulation - Recent Progress and Future Challenges*, in: *Chemical Process Control CPC-IV*, CACHE Publications, 131–180 (1991).
- [209] E.U. Hartge, M. Pogodda, C. Reimers, D. Schwier, G. Gruhn, J. Werther, Flowsheet simulation of solids processes, *KONA* 24, 146–158 (2006).
- [210] D. Schwier, E.U. Hartge, J. Werther, G. Gruhn, Global sensitivity analysis in the flowsheet simulation of solids processes, *Chemical Engineering and Processing: Process Intensification* 49 (1), 9–21 (2010).
- [211] W.L. Luyben, Aspen Dynamics simulation of a middle-vessel batch distillation process,

- Journal of Process Control 33, 49–59 (2015).
- [212] F. Boukouvala, V. Niotis, R. Ramachandran, F.J. Muzzio, M.G. Ierapetritou, An integrated approach for dynamic flowsheet modeling and sensitivity analysis of a continuous tablet manufacturing process, *Computers & Chemical Engineering* 42, 30–47 (2012).
- [213] F. Alobaid, R. Starkloff, S. Pfeiffer, K. Karner, B. Epple, H.G. Kim, A comparative study of different dynamic process simulation codes for combined cycle power plants-Part A: Part loads and off-design operation, *Fuel* 153, 692–706 (2015).
- [214] M. Farina, G.P. Ferrari, F. Manenti, E. Pizzi, Assessment and comparison of distributed model predictive control schemes: Application to a natural gas refrigeration plant, *Computers and Chemical Engineering* 89, 192–203 (2016).
- [215] M. Dosta, S. Antonyuk, E.-U. Hartge, S. Heinrich, Parameter Estimation for the Flowsheet Simulation of Solids Processes, *Chemie Ingenieur Technik* 86 (7), 1073–1079 (2014).
- [216] J. Haus, E.U. Hartge, S. Heinrich, J. Werther, Dynamic flowsheet simulation of gas and solids flows in a system of coupled fluidized bed reactors for chemical looping combustion, *Powder Technology* 316, 628–640 (2017).
- [217] C. Reimers, J. Werther, G. Gruhn, Flowsheet simulation of solids processes. Data reconciliation and adjustment of model parameters, *Chemical Engineering and Processing: Process Intensification* 47 (1), 138–158 (2008).
- [218] L.R. Plitt, The Analysis of Solid - Solid Separations in Classifiers, *CIM Bulletin* 64, 42–47 (1971).
- [219] R.S.C. Rogers, A Classification Function for Vibrating Screens, *Powder Technology* 31, 135–137 (1982).
- [220] C.C. Hatch, A.L. Mular, Simulation of the Brenda Mines Ltd. secondary crusher, in: *SME-AIME Annual Meeting*, 54–79 (1979).
- [221] R.P. King, *Modeling and Simulation of Mineral Processing Systems*, Butterworth Heinemann, Oxford (2001).
- [222] O. Molerus, H. Hoffmann, Darstellung von Windsichtertrennkurven durch ein stochastisches Modell, *Chemie Ingenieur Technik* 41 (5+6), 340–344 (1969).
- [223] H. Trawinski, Die mathematische Formulierung der Tromp-Kurve, *Aufbereitungstechnik* 17, 248–254, 449–459 (1976).
- [224] N. Standish, I.A. Meta, Some Kinetic Aspects of Continuous Screening, *Powder*

- Technology 41, 165–171 (1985).
- [225] G. Ferrara, U. Preti, G.D. Schena, Computer-aided Use of a Screening Process Model, in: Twentieth International Symposium on the Application of Computers and Mathematics in the Mineral Industries, 153–166 (1987).
- [226] S.E. Andreev, V.A. Perov, V.V. Zverevic, Droblenie izmelcenie i grohocenie poleznyh iskopaemyh, Nedra, Moscow (1980).
- [227] G.K.N.S. Subasinghe, W. Schaap, E.G. Kelly, Modelling Screening as a Conjugate Rate Process, International Journal of Mineral Processing 28, 289–300 (1990).
- [228] G.K.N.S. Subasinghe, W. Schaap, E.G. Kelly, Modelling the Screening Process: A Probabilistic Approach, Powder Technology 59, 37–44 (1989).
- [229] Y. Nakajima, W.J. Whiten, Behaviour of non-spherical particles in screening, Transactions of Institution of Mining and Metallurgy 88, C88–C92 (1979).
- [230] G. Ferrara, U. Preti, A contribution to screening kinetics, in: Proceedings of the 11th IMPC, Cagliari, Italy (1975).
- [231] G. Ferrara, U. Preti, G.D. Schena, Modelling of screening operations, International Journal of Mineral Processing 22, 193–222 (1988).
- [232] S. Mabote, Development of a wet fine screen model integrating the effect of operating and design variables on screening performance, Ph.D. thesis, University of Cape Town (2016).
- [233] V.P. Nadutyi, E.C. Lapshin, Probabilistic simulation of vibratory screening under high loading conditions, Refractories and Industrial Ceramics 45 (6), 2–5 (2004).
- [234] M. Soldinger, Transport velocity of a crushed rock material bed on a screen, Minerals Engineering 15, 7–17 (2002).
- [235] Y. Chen, S. Hsiau, H. Lee, Y. Chyou, C. Hsu, Size separation of particulates in a trommel screen system, Chemical Engineering & Processing 49, 1214–1221 (2010).
- [236] H. Kruggel-Emden, F. Elskamp, Modeling of Screening Processes with the Discrete Element Method Involving Non-Spherical Particles, Chemical Engineering & Technology 37 (5), 847–856 (2014).
- [237] J. Xiao, X. Tong, Particle stratification and penetration of a linear vibrating screen by the discrete element method, International Journal of Mining Science and Technology 22 (3), 357–362 (2012).
- [238] J. Xiao, X. Tong, Characteristics and efficiency of a new vibrating screen with a swing trace, Particuology 11 (5), 601–606 (2013).

- [239] J. Duran, *Sands, Powders, and Grains*, Springer-Verlag, New York (2000).
- [240] D.E. Goldberg, *Genetic Algorithms in Search, Optimization and Machine learning*, Addison-Wesley Longman, Boston, Massachusetts (1989).
- [241] F. Elskamp, H. Kruggel-Emden, Review and benchmarking of process models for batch screening based on discrete element simulations, *Advanced Powder Technology* 26, 679–697 (2015).
- [242] B.K. Mishra, C.V.R. Murty, On the determination of contact parameters for realistic DEM simulations of ball mills, *Powder Technology* 115 (3), 290–297 (2001).
- [243] Z. Ma, Y. Li, L. Xu, Discrete-element method simulation of agricultural particles' motion in variable-amplitude screen box, *Computers and Electronics in Agriculture* 118, 92–99 (2015).
- [244] F. Elskamp, H. Kruggel-Emden, M. Hennig, U. Teipel, Benchmarking of process models for continuous screening based on discrete element simulations, *Minerals Engineering* 83, 78–96 (2015).
- [245] V. Skorych, M. Dosta, E.-U. Hartge, S. Heinrich, Modelling Framework for the Dynamic Flowsheet Simulation of Solids Processes, in: *Proceedings of the 7th International Granulation Workshop*, (2015).
- [246] S. Natsui, S. Ueda, M. Oikawa, Z. Fan, J. Kano, R. Inoue, T. Ariyama, Optimization of Physical Parameters of Discrete Element Method for Blast Furnace and Its Application to the Analysis on Solid Motion around Raceway, *ISIJ International* 49 (9), 1308–1315 (2009).
- [247] J. Horabik, M. Molenda, Parameters and contact models for DEM simulations of agricultural granular materials: A review, *Biosystems Engineering* 147, 206–225 (2016).
- [248] P.B. Dobrohotoff, S.I. Azeezullah, F. Maggi, F. Alonso-Marroquin, Optimal description of two-dimensional complex-shaped objects using spheropolygons, *Granular Matter* 14, 651–658 (2012).
- [249] D. Höhner, S. Wirtz, V. Scherer, A study on the influence of particle shape on the mechanical interactions of granular media in a hopper using the Discrete Element Method, *Powder Technology* 278, 286–305 (2015).
- [250] C.Q. Li, W.J. Xu, Q.S. Meng, Multi-sphere approximation of real particles for DEM simulation based on a modified greedy heuristic algorithm, *Powder Technology* 286, 478–487 (2015).
- [251] L. Benvenuti, C. Kloss, S. Pirker, Identification of DEM simulation parameters by Artificial Neural Networks and bulk experiments, *Powder Technology* 291, 456–465

- (2016).
- [252] H. Kruggel-Emden, F. Stepanek, A. Munjiza, A comparative study of reaction models applied for chemical looping combustion, *Chemical Engineering Research and Design* 89 (12), 2714–2727 (2011).
- [253] M. Stender, K. Legenhausen, A.P. Weber, Visualisierung der Partikelbewegung in einem Abweiseradsichter, *Chemie Ingenieur Technik* 87 (10), 1392–1401 (2015).
- [254] Y. Nakajima, W.J. Whiten, M.E. White, Method for measurement of particle-shape distribution by sieves, *Transactions of Institution of Mining and Metallurgy* 87, C194–C203 (1978).
- [255] M. Hennig, U. Teipel, Siebklassierung von Mineralischen Rohstoffen, in: 4. Symposium Rohstoffeffizienz Und Rohstoffinnovationen, Tutzing (2016).
- [256] H. Rumpf, J. Raasch, Desagglomeration in Strömungen, in: Symposium Zerkleinern, Verlag Chemie, Weinheim (1962).
- [257] K. Husemann, Persönliche Mitteilung, Clausthal (2012).
- [258] C. Spötter, K. Legenhausen, A.P. Weber, Separation Characteristics of a Deflector Wheel Classifier in Stationary Conditions and at High Loadings: New Insights by Flow Visualization, *KONA Powder and Particle Journal* 35, 172–185 (2018).
- [259] C. Spötter, K. Legenhausen, A.P. Weber, Dynamische Trenncharakteristik von Abweiseradsichtern, in: *Produktgestaltung in Der Partikeltechnologie*, Band 7, Fraunhofer Verlag, Berlin (2015).
- [260] R. Di Felice, The voidage function for fluid-particle interaction systems, *International Journal of Multiphase Flow* 20 (1), 153–159 (1994).
- [261] A. Hölzer, M. Sommerfeld, New simple correlation formula for the drag coefficient of non-spherical particles, *Powder Technology* 184 (3), 361–365 (2008).
- [262] T. Oschmann, J. Hold, H. Kruggel-Emden, Numerical investigation of mixing and orientation of non-spherical particles in a model type fluidized bed, *Powder Technology* 258, 304–323 (2014).
- [263] F. Elskamp, M. Hennig, H. Kruggel-Emden, U. Teipel, A strategy to determine DEM parameters for spherical and non-spherical particles, *Granular Matter* 19:46, (2017).
- [264] K. Keller, Schwingentwässerung von körnigen Produkten, Ph.D. thesis, Universität Karlsruhe (1997).
- [265] P. Lambert, A. Chau, A. Delchambre, Comparison between Two Capillary Forces Models, *Langmuir* 24 (7), 3157–3163 (2008).

- [266] J.N. Israelachvili, *Intermolecular and Surface Forces*, 3rd ed., Academic Press, London (2011).
- [267] Y. Tsunazawa, D. Fujihashi, S. Fukui, M. Sakai, C. Tokoro, Contact force model including the liquid-bridge force for wet-particle simulation using the discrete element method, *Advanced Powder Technology* 27 (2), 652–660 (2016).
- [268] P.Y. Liu, R.Y. Yang, A.B. Yu, DEM study of the transverse mixing of wet particles in rotating drums, *Chemical Engineering Science* 86, 99–107 (2012).
- [269] C. Song, D. Liu, J. Ma, X. Chen, CFD-DEM simulation of flow pattern and particle velocity in a fluidized bed with wet particles, *Powder Technology* 314, 346–354 (2017).
- [270] J. Fu, M.J. Adams, G.K. Reynolds, A.D. Salman, M.J. Hounslow, Impact deformation and rebound of wet granules, *Powder Technology* 140 (3), 248–257 (2004).
- [271] S. Antonyuk, S. Heinrich, N. Deen, H. Kuipers, Influence of liquid layers on energy absorption during particle impact, *Particuology* 7 (4), 245–259 (2009).
- [272] S. Antonyuk, M. Dosta, S. Heinrich, Numerical estimation of the restitution coefficient for dry and wet agglomerates, *AIP Conference Proceedings* 1542 (2013), 951–954 (2013).
- [273] B. Crüger, V. Salikov, S. Heinrich, S. Antonyuk, V.S. Sutkar, N.G. Deen, J.A.M. Kuipers, Coefficient of restitution for particles impacting on wet surfaces: An improved experimental approach, *Particuology* 25, 1–9 (2016).
- [274] B. Crüger, S. Heinrich, S. Antonyuk, N.G. Deen, J.A.M. Kuipers, Experimental study of oblique impact of particles on wet surfaces, *Chemical Engineering Research and Design* 110 (1), 209–219 (2016).
- [275] V.S. Sutkar, N.G. Deen, J.T. Padding, J.A.M. Kuipers, V. Salikov, B. Crüger, S. Antonyuk, S. Heinrich, A Novel Approach to Determine Wet Restitution Coefficients Through a Unified Correlation and Energy Analysis, *AIChE Journal* 61 (3), 769–779 (2015).
- [276] M.S. van Buijtenen, N.G. Deen, S. Heinrich, S. Antonyuk, J.A.M. Kuipers, A discrete element study of wet particle-particle interaction during granulation in a spout fluidized bed, *Canadian Journal of Chemical Engineering* 87 (2), 308–317 (2009).
- [277] P.A. Kralchevsky, K. Nagayama, Capillary interactions between particles bound to interfaces, liquid films and biomembranes, *Advances in Colloid and Interface Science* 85, 145–192 (2000).
- [278] F. Gabrieli, P. Lambert, S. Cola, F. Calvetti, Micromechanical modelling of erosion due to evaporation in a partially wet granular slope, *International Journal for Numerical and*

- Analytical Methods in Geomechanics 36, 918–943 (2012).
- [279] R.A. Fisher, On the capillary forces in an ideal soil; correction of formulae given by W. B. Haines, *The Journal of Agricultural Science* 16 (3), 492–505 (1926).
- [280] F. Soulié, F. Cherblanc, M.S. El Youssoufi, C. Saix, Influence of liquid bridges on the mechanical behaviour of polydisperse granular materials, *International Journal for Numerical and Analytical Methods in Geomechanics* 30 (3), 213–228 (2006).
- [281] V. Richefeu, M.S. El Youssoufi, R. Peyroux, F. Radja, A model of capillary cohesion for numerical simulations of 3D polydisperse granular media, *International Journal for Numerical and Analytical Methods in Geomechanics* 32, 1365–1383 (2008).
- [282] Y. Song, R. Turton, Study of the effect of liquid bridges on the dynamic behavior of two colliding tablets using DEM, *Powder Technology* 178 (2), 99–108 (2007).
- [283] S.T. Nase, W.L. Vargas, A.A. Abatan, J.J. McCarthy, Discrete characterization tools for cohesive granular material, *Powder Technology* 116, 214–223 (2001).
- [284] M. Wu, S. Radl, J.G. Khinast, A Model to Predict Liquid Bridge Formation Between Wet Particles Based on Direct Numerical Simulations, *AIChE Journal* 62 (6), 1877–1897 (2016).
- [285] S.C. Yang, S.S. Hsiau, The simulation of powders with liquid bridges in a 2D vibrated bed, *Chemical Engineering Science* 56 (24), 6837–6849 (2001).
- [286] R.Y. Yang, R.P. Zou, A.B. Yu, Numerical study of the packing of wet coarse uniform spheres, *AIChE Journal* 49 (7), 1656–1666 (2003).
- [287] P.G. Rognon, J.N. Roux, D. Wolf, M. Naaïm, F. Chevoir, Rheophysics of cohesive granular materials, *Europhysics Letters* 74 (4), 644–650 (2006).
- [288] S. Khamseh, J.-N. Roux, F. Chevoir, Flow of wet granular materials: a numerical study, *Physical Review E* 92 (2), 022201 (2015).
- [289] M. Heine, S. Antonyuk, L. Fries, G. Niederreiter, S. Heinrich, S. Palzer, Modeling of the spray zone for particle wetting in a fluidized bed, *Chemie Ingenieur Technik* 85 (3), 280–289 (2013).
- [290] E.W.C. Lim, Density segregation of dry and wet granular mixtures in vibrated beds, *Advanced Powder Technology* 27, 2478–2488 (2016).
- [291] Y. He, W. Peng, T. Tang, S. Yan, Y. Zhao, DEM numerical simulation of wet cohesive particles in a spout fluid bed, *Advanced Powder Technology* 27 (1), 93–104 (2016).
- [292] T. Young, An Essay on the Cohesion of Fluids, *Philosophical Transactions of the Royal Society* 95, 65–87 (1805).

- [293] H. Mio, A. Shimosaka, Y. Shirakawa, J. Hidaka, Cell optimization for fast contact detection in the discrete element method algorithm, *Advanced Powder Technology* 18 (4), 441–453 (2007).
- [294] R. Kačianauskas, A. Maknickas, A. Kačeniauskas, D. Markauskas, R. Balevičius, Parallel discrete element simulation of poly-dispersed granular material, *Advances in Engineering Software* 41, 52–63 (2010).
- [295] S. Natsui, A. Sawada, K. Terui, Y. Kashihara, T. Kikuchi, R.O. Suzuki, DEM-SPH study of molten slag trickle flow in coke bed, *Chemical Engineering Science* 175, 25–39 (2018).
- [296] W. Batel, Untersuchungen zur Absiebung feuchter, feinkörniger Haufwerke auf Schwingsieben, Ph.D. thesis, Aachen (1954).
- [297] D. Dopfer, S. Palzer, S. Heinrich, L. Fries, S. Antonyuk, C. Haider, A.D. Salman, Adhesion mechanisms between water soluble particles, *Powder Technology* 238, 35–49 (2013).
- [298] F. Elskamp, H. Kruggel-Emden, DEM simulations of screening processes under the influence of moisture, *Chemical Engineering Research and Design* 136, 593–609 (2018).